

## University of Southampton Research Repository

Copyright © and Moral Rights for this thesis and, where applicable, any accompanying data are retained by the author and/or other copyright owners. A copy can be downloaded for personal non-commercial research or study, without prior permission or charge. This thesis and the accompanying data cannot be reproduced or quoted extensively from without first obtaining permission in writing from the copyright holder/s. The content of the thesis and accompanying research data (where applicable) must not be changed in any way or sold commercially in any format or medium without the formal permission of the copyright holder/s.

When referring to this thesis and any accompanying data, full bibliographic details must be given, e.g.

Thesis: Author (Year of Submission) "Full thesis title", University of Southampton, name of the University Faculty or School or Department, PhD Thesis, pagination.

Data: Author (Year) Title. URI [dataset]

**University of Southampton**

Faculty of Engineering and Physical Sciences

School of Chemistry and Chemical Engineering

**Transition Metal and Group 13 Triazamacrocyclic  
Complexes: Coordination Chemistry and  
Applications in  $^{18}\text{F}$  PET Imaging**

by

**Charley O'Callaghan**

ORCID ID 0000-0002-1839-0591

Thesis for the degree of Doctor of Philosophy

February 2025

*“Don’t let the fear of the time it will take to accomplish something stand in the way of your doing it. The time will pass anyway; we might just as well put that passing time to the best possible use”*

# University of Southampton

## Abstract

Faculty of Engineering and Physical Sciences

School of Chemistry and Chemical Engineering

Doctor of Philosophy

### **Transition Metal and Group 13 Triazamacrocyclic Complexes: Coordination Chemistry and Applications in $^{18}\text{F}$ PET Imaging**

by

Charley O'Callaghan

Three novel triazacyclononane ligands bearing phenylacetamide or isopropylacrylamide pendant arms ( $\text{L}^1$ ,  $\text{L}^2$ ,  $\text{L}^3$ ) are reported with their full spectroscopic data, alongside known triazacyclononane ligands with carboxylate ( $\text{H}_2\text{-Bn-NODA}$ ) and phosphinate ester (NOTP-OMe) functionality. New automated purification techniques have also been developed.

The coordination chemistry of the tris(amide) ligands  $\text{L}^1$  and  $\text{L}^2$  has been established with the divalent first-row transition metals,  $\text{Co}^{2+}$ ,  $\text{Ni}^{2+}$ ,  $\text{Cu}^{2+}$  and  $\text{Zn}^{2+}$ , and the complexes characterised using IR,  $^1\text{H}$  and  $^{13}\text{C}\{^1\text{H}\}$  NMR (Zn only) and UV-Vis spectroscopy,  $\text{ESI}^+$  MS, microanalysis and SCXRD. Molecular structures of Co, Ni and Cu complexes of  $\text{L}^1$  and  $\text{L}^2$  are reported, with the ligands adopting hexadentate coordination with an  $\text{N}_3\text{O}_3$  or  $\text{N}_4\text{O}_2$  donor set. Preliminary methods towards Ni, Cu and Zn complexes of NOTP-OMe are discussed.

Routes towards  $\text{MF}_3$  complexes of  $\text{L}^1$ ,  $\text{L}^2$  and  $\text{L}^3$  using a molecular  $\text{MF}_3$  precursor,  $\text{FeF}_3 \cdot 3\text{H}_2\text{O}$  or  $[\text{MF}_3(\text{dmsO})(\text{OH}_2)_2]$  are reported. The products are characterised using IR,  $^1\text{H}$ ,  $^{13}\text{C}\{^1\text{H}\}$  NMR,  $^{19}\text{F}\{^1\text{H}\}$  NMR spectroscopy, microanalysis,  $\text{ESI}^+$  MS and SCXRD. The coordinative properties of the ligands with  $\text{MF}_3$  are determined *via* the molecular structures for  $[\text{GaF}_3(\text{L}^1)]$ ,  $[\text{InF}_3(\text{L}^2)]$ ,  $[\text{GaF}_3(\text{L}^3)]$  and  $[\text{FeF}_3(\text{L}^3)]$ . Any supramolecular features or extended hydrogen-bonded networks are discussed. Potential candidates for  $^{18}\text{F}$ -radiolabelling experiments are identified based on the characterisation data, with consideration towards metal-fluoride bond strength, hydrogen-bonded interactions involving fluoride ligands and the stability of the complexes in solution.

New HPLC methodologies were developed for analysis of the radiochemical reactions involving  $[\text{GaF}_3(\text{L}^1)]$  and  $[\text{GaF}_3(\text{L}^3)]$ .  $[\text{GaF}_3(\text{L}^1)]$  shows  $^{18}\text{F}$  incorporation under various conditions, with a maximum RCY of 20% achieved after 10 min at 80 °C ( $3 \mu\text{mol mL}^{-1}$ ). The crude product was purified using an SPE cartridge and formulated in 10:90 EtOH/ $\text{H}_2\text{O}$  and EtOH/PBS. The starting RCP's were 68% and 64%, respectively, with 7% and 5% degradation observed after 2 h. Meanwhile,  $[\text{GaF}_3(\text{L}^3)]$  does not undergo radiofluorination under any conditions.

Alternative routes towards Group 13 fluoride complexes have been explored, using the Lewis acidic  $\text{M}^{3+}$  cations. The stability of amide-pendant arms is investigated *via* coordination of  $\text{L}^1$  to  $\text{Fe}^{3+}$ ,  $\text{Ga}^{3+}$  and  $\text{In}^{3+}$ . Additionally, various pathways involving  $\text{L}^1$ ,  $\text{H}_3\text{-NOTA}$ ,  $\text{H}_2\text{-Bn-NODA}$  and  $\text{H}_2\text{-Bn-NODP}$  have been explored, *via* addition of  $\text{K}^{19}\text{F}$  to six- or seven-coordinate complexes thereof. From this, the coordination chemistry of the known  $[\text{In}(\text{NOTA})]$  complex has been further examined using electron diffraction analysis, showing a highly unusual tetrameric species. In developing methods towards new Al-F complexes, the chemistry of the ' $\text{Al-}^{19}\text{F}^{2+}$ ' reaction has been probed at a preparative scale, with the previously unobserved  $[\text{Al}(\text{Bn-NODA})(\text{OAc})]$  species identified as a reaction product in addition to  $[\text{AlF}(\text{Bn-NODA})]$ .



# Table of Contents

<b>Table of Contents .....</b>	<b>i</b>
<b>Table of Tables .....</b>	<b>vi</b>
<b>Table of Figures .....</b>	<b>viii</b>
<b>Table of Schemes .....</b>	<b>xvi</b>
<b>Table of Equations .....</b>	<b>xix</b>
<b>List of Accompanying Materials .....</b>	<b>xx</b>
<b>Research Thesis: Declaration of Authorship .....</b>	<b>xxi</b>
<b>Acknowledgements .....</b>	<b>xxii</b>
<b>Definitions and Abbreviations.....</b>	<b>xxiii</b>
<b>Chapter 1 Introduction.....</b>	<b>1</b>
1.1 Positron Emission Tomography .....	1
1.1.1 PET Radioisotopes and Their General Properties .....	2
1.1.2 Traditional Radiotracers and Their Limitations.....	4
1.2 Inorganic Approaches to <sup>18</sup> F Radiopharmaceuticals.....	6
1.2.1 Main Group (Boron and Silicon) .....	7
1.2.2 Transition Metal and Lanthanide Metal Fluorides .....	13
1.3 Coordination Chemistry of Group 13 Macrocyclic Complexes.....	16
1.3.1 Macrocyclic Ligands.....	16
1.3.2 General Properties and Reactivity of the Group 13 Metals .....	20
1.3.3 Applications of Group 13 Macrocyclic Complexes in Radiochemistry .....	21
1.4 Radiochemistry and Characterisation of Radio-Products .....	26
1.4.1 Radiation Safety Measures .....	26
1.4.2 General Radiolabelling Techniques .....	28
1.4.3 Purification via Solid-Phase Extraction and Stability Studies .....	29
1.4.4 High-Performance Liquid Chromatography (HPLC) Analysis .....	30
1.5 Characterisation Techniques .....	31

1.5.1 Infrared Spectroscopy .....	31
1.5.2 NMR Spectroscopy.....	32
1.5.3 Mass Spectrometry .....	33
1.5.4 Elemental Analysis .....	34
1.5.5 UV-Vis Spectroscopy.....	34
1.5.6 Single Crystal X-Ray Diffraction (SCXRD).....	35
1.5.7 Electron Diffraction (ED) .....	39
1.6 Project Aims .....	40
1.7 References .....	41
<b>Chapter 2 Routes Towards N-Functionalised Triazamacrocyclic Ligands: Design Considerations and Synthetic Procedures .....</b>	<b>49</b>
2.1 Introduction .....	49
2.1.1 Triazacyclononane – A Versatile Framework for Functionalisation .....	49
2.1.2 Ligand Design Rationale .....	56
2.1.3 Aims .....	56
2.2 Results and Discussion.....	57
2.2.1 Synthesis of Triazacyclononane and Its Precursors .....	57
2.2.2 Synthesis of Triazacyclononane Ligands with Carboxylate Functionality .....	59
2.2.3 Synthesis and Characterisation of Amide-Functionalised Triazacyclononane Ligands .....	60
2.2.4 Synthesis and Characterisation of Phosphinate-Functionalised Tacn Ligands.....	67
2.3 Conclusions .....	70
2.4 Experimental .....	71
2.4.1 Triazacyclononane .....	71
2.4.2 Amide-Functionalised Triazacyclononane Ligands (L <sup>1</sup> , L <sup>2</sup> and L <sup>3</sup> ).....	73
2.4.3 Carboxylate-Functionalised Triazacyclononane Ligands .....	78
2.4.4 Phosphinate-Ester Functionalised Triazacyclononane Ligands .....	78
2.5 X-Ray Crystallographic Data.....	80

2.6 References .....	81
<b>Chapter 3 Divalent Transition Metal Complexes with Neutral N-Functionalised Triazacyclononane Ligands .....</b>	<b>84</b>
3.1 Introduction .....	84
3.1.1 Properties and Characteristics of First-Row Transition Metals Relevant to This Work .....	84
3.1.2 Transition Metal Complexes of Amide-Functionalised Triazacyclononane Ligands .	86
3.1.3 Transition Metal Complexes of Anionic Hexadentate Phosphinate Tacn Ligands ....	92
3.1.4 Aims .....	95
3.2 Results and Discussion.....	95
3.2.1 Transition Metal Complexes of L <sup>1</sup> and L <sup>2</sup> .....	95
3.2.2 Attempted Formation of Divalent Transition Metal Complexes of NOTP-OMe .....	115
3.3 Conclusions .....	118
3.4 Experimental .....	120
3.4.1 Tris-1,4,7-Phenylacetamide-1,4,7-Triazacyclononane (L <sup>1</sup> ) Complexes .....	120
3.4.2 Tris-1,4,7-Isopropylacrylamide-1,4,7-Triazacyclononane (L <sup>2</sup> ) Complexes .....	122
3.4.3 NOTP-OMe Complexes.....	123
3.5 X-ray Crystallographic Data .....	125
3.6 References .....	128
<b>Chapter 4 Coordination of Metal Trifluorides (M = Al, Ga, In, Fe) with Amide-Functionalised Triazacyclononane Ligands .....</b>	<b>131</b>
4.1 Introduction .....	131
4.1.1 Supramolecular Assemblies with MF <sub>3</sub> Coordination Complexes .....	133
4.1.2 MF <sub>3</sub> Complexes as Metalloligands .....	134
4.1.3 Formation of MF <sub>3</sub> Triazacyclononane Complexes .....	135
4.1.4 Aims .....	137
4.2 Results and Discussion.....	137
4.2.1 Formation of [MF <sub>3</sub> (L <sup>n</sup> )] <i>via</i> [MF <sub>3</sub> (dmsO)(OH <sub>2</sub> ) <sub>2</sub> ] (M = Al, Ga, In) and FeF <sub>3</sub> ·3H <sub>2</sub> O .....	137
4.2.2 Characterisation of Novel MF <sub>3</sub> (L <sup>n</sup> )] Complexes – Solid State and NMR Studies.....	138

4.2.3 Molecular Structures of $[\text{GaF}_3(\text{L}^1)]$ , $[\text{InF}_3(\text{L}^2)]$ , $[\text{GaF}_3(\text{L}^3)]$ and $[\text{FeF}_3(\text{L}^3)]$ and Hydrogen Bonding Interactions.....	150
4.3 Conclusions .....	158
4.4 Experimental .....	159
4.4.1 Ligand 1 Complexes .....	159
4.4.2 Ligand 2 Complexes .....	160
4.4.3 Ligand 3 Complexes .....	162
4.5 X-Ray Crystallographic Data.....	164
4.6 References .....	166
<b>Chapter 5 Radiolabelling of <math>[\text{GaF}_3(\text{L}^1)]</math> and <math>[\text{GaF}_3(\text{L}^3)]</math> via <math>^{19}\text{F}/^{18}\text{F}</math> Isotopic Exchange .....</b>	<b>168</b>
5.1 Introduction .....	168
5.1.1 Group 13 Triazacyclononane Complexes in $^{18}\text{F}$ PET Imaging .....	168
5.1.2 Aims .....	174
5.2 Results and Discussion.....	175
5.2.1 $^{19}\text{F}/^{18}\text{F}$ Exchange Reactions of $[\text{GaF}_3(\text{L}^3)]$ .....	176
5.2.2 $^{19}\text{F}/^{18}\text{F}$ exchange reactions using $[\text{GaF}_3(\text{L}^1)]$ .....	183
5.2.3 Purification Protocol Using Solid-Phase Extraction (SPE) .....	185
5.3 Conclusions .....	187
5.4 Experimental .....	188
5.4.1 Analytical HPLC Method .....	189
5.4.2 $^{19}\text{F}/^{18}\text{F}$ Isotopic Exchange Radiolabelling Procedure .....	190
5.4.3 SPE Purification Protocol.....	190
5.5 References .....	191
<b>Chapter 6 Exploring Routes Towards Group 13 Fluoride Complexes with Penta- and Hexa-dentate Triazacyclononane Ligands .....</b>	<b>193</b>
6.1 Introduction .....	193
6.1.1 Radiochemical Applications of $\text{M}^{3+}$ ( $\text{M} = \text{Al}, \text{Ga}, \text{In}, \text{Fe}$ ) .....	193
6.1.2 Aims .....	200

6.2 Results and Discussion.....	201
6.2.1 Amide-Functionalised Triazacyclononane Ligands with Trivalent, Lewis Acidic Fe <sup>3+</sup> , Ga <sup>3+</sup> and In <sup>3+</sup> Cations.....	201
6.2.2 Synthesis of Ga <sup>3+</sup> and In <sup>3+</sup> Complexes of NOTA and Attempted Fluorination .....	207
6.2.3 Attempted Formation of {MF(L)} Complexes (M = Al, In; L = Bn-NODA, Bn-NODP).	213
6.3 Conclusions .....	218
6.4 Experimental .....	219
6.4.1 Trivalent M <sup>3+</sup> Complexes of L <sup>1</sup> .....	220
6.4.2 Complexes of 1,4,7-Triazacyclononane-1,4,7-Triacetic acid (H <sub>3</sub> -NOTA) .....	221
6.4.3 Complexes of 1-Benzyl-4,7-Diacetic Acid-1,4,7-Triazacyclononane (H <sub>2</sub> -Bn-NODA) .....	222
6.4.4 Complexes of 1,4-Diphosphinate-7-Benzyl-1,4,7-Triazacyclononane (H <sub>2</sub> -Bn-NODP) .....	223
6.4.5 X-ray Crystallographic Data .....	224
6.4.6 Electron Diffraction Crystallographic Data .....	226
6.5 References .....	227
<b>Chapter 7 Summary and Outlook.....</b>	<b>229</b>
7.1 References .....	231
<b>Appendix A General Experimental Details .....</b>	<b>232</b>
A.1 References.....	234
<b>Appendix B Crystallographic Information Files .....</b>	<b>235</b>

## Table of Tables

Table 1.1 – Physical properties of the major PET imaging radioisotopes. ....	3
Table 1.2 – Average M-F bond dissociation enthalpies (kJ mol <sup>-1</sup> ) for the various systems relevant to or discussed in this work. ....	7
Table 1.3 – The range of reaction conditions used for <sup>19</sup> F/ <sup>18</sup> F isotopic exchange reactions of [FeF <sub>3</sub> (BnMe <sub>2</sub> -tacn)]. All reactions were performed in aqueous MeCN at RT or 80 °C, for 10 minutes. ....	13
Table 1.4 – General properties of selected radioisotopes used within the theranostic field.....	15
Table 1.5 – Structures, names and abbreviations for common aza-macrocyclic ligands, and those relevant to, or used within this work. ....	17
Table 1.6 – General NMR properties of the nuclei studied within this project.....	32
Table 1.7 – The seven crystal systems and their associated parameters. ....	36
Table 3.1 – Electronic properties of the transition metal ions used in this work. O <sub>h</sub> , octahedral; LS, low-spin; HS, high-spin.....	85
Table 3.2 – Summary of the UV-Vis spectroscopic data for Co, Ni and Cu complexes of the tris(amide) ligands, L <sup>1</sup> , L <sup>2</sup> and TCMT.....	103
Table 3.3 – Selected geometric parameters for the crystallographically characterised L <sup>1</sup> and L <sup>2</sup> complexes.....	105
Table 4.1 – Selected IR and NMR spectroscopic data for [MF <sub>3</sub> (L)] (M = Al, Ga, Fe).....	139
Table 4.2 – Summary of the bond lengths (Å) and bond angles (°) given by the SCXRD data for [GaF <sub>3</sub> (L <sup>1</sup> )]·1.5MeOH·0.5H <sub>2</sub> O, [InF <sub>3</sub> (L <sup>2</sup> )], [GaF <sub>3</sub> (L <sup>3</sup> )]·0.067H <sub>2</sub> O and [FeF <sub>3</sub> (L <sup>3</sup> )]·2.4H <sub>2</sub> O. ....	157
Table 5.1 – Various radiolabelling conditions for [MF <sub>3</sub> (BnMe <sub>2</sub> -tacn)] complexes (M = Al, Ga; Fe). ....	173
Table 5.2 – Radio-HPLC and corresponding UV-HPLC traces of the crude <sup>18</sup> F [GaF <sub>3</sub> (L <sup>3</sup> )] reaction mixture, diluted to 10, 20 and 50 percent organic content before injection into the HPLC. ...	180
Table 5.3 – Summary of the results from <sup>18</sup> F/ <sup>19</sup> F isotopic exchange with [GaF <sub>3</sub> (L <sup>1</sup> )] using a range of conditions. Numbers highlighted in blue correlate with the optimised conditions i.e. the conditions which gave the highest RCY%.....	184

Table 5.4 – Summary of the results from SPE purification of $[\text{Ga}^{18}\text{FF}_2(\text{L}^1)]$ in $\text{H}_2\text{O}/\text{EtOH}$ and $\text{PBS}/\text{EtOH}$ over 2 h. ....	187
Table 5.5 – Gradient used for analytical HPLC analysis of $[\text{GaF}_3(\text{L}^3)]$ . ....	189
Table 5.6 – Gradient used for analytical HPLC analysis of $[\text{GaF}_3(\text{L}^1)]$ . ....	189
Table 6.1 – Selected bond distances ( $\text{\AA}$ ) for the seven-coordinate $[\text{In}(\text{NOTA})]$ and $[\text{InCl}(\text{NOTA})][\text{H}]\cdot 2\text{H}_2\text{O}$ complexes. ....	211

## Table of Figures

Figure 1.1 – $\beta^+$ decay process and annihilation event.....	2
Figure 1.2 – Cyclotron production of $[^{18}\text{F}]\text{F}^-$ via proton irradiation of $^{18}\text{O}-\text{H}_2\text{O}$ . ....	3
Figure 1.3 – Structures of $[^{18}\text{F}]\text{-FDG}$ (left) and $[^{18}\text{F}]\text{-DOPA}$ (right). ....	5
Figure 1.4 – Structures of $[^{19}\text{F}]\text{-RGD-Pyr-BF}_3^-$ and $[^{19}\text{F}]\text{-RGD-Ar-BF}_3^-$ .....	9
Figure 1.5 – Zwitterionic onium borates first reported by Wade et al. ....	9
Figure 1.6 – Structures of the $\text{Si-}^{18}\text{F}$ compounds first reported by Schirmacher et al.....	11
Figure 1.7 – SiFA $\text{Tyr}^3\text{-octreotate}$ system developed by Schirmacher et al. ....	12
Figure 1.8 – Structure of SiFAlin developed by Wängler and co-workers. ....	12
Figure 1.9 – Structures of $[\text{Sc}(\text{mpatcn})(\text{OH}_2)]$ (left) and $[^{18}\text{F}][\text{ScF}(\text{mpatcn})]^-$ (right) reported by Boros and co-workers. ....	15
Figure 1.10 – Structure of $[\text{Al}^{18}\text{F}(\text{IMP485})]$ reported by McBride et al.....	22
Figure 1.11 – Structures of the $\text{N}_2\text{O}_3$ acyclic chelating ligands developed by Cleeren et al. ....	23
Figure 1.12 – Structure of the tetraaza-macrocyclic PET imaging agent, $[^{68}\text{Ga}]\text{-[Ga(DOTATATE)]}$ , used for the diagnosis of neuroendocrine tumours. ....	24
Figure 1.13 – Lead-lined workstation used in the KCL research labs at St Thomas' Hospital. ..	27
Figure 1.14 – Two representative unit cells with the cell lengths (a, b, c), reference axes (x, y, z) and inter-axial angles ( $\alpha$ , $\beta$ , $\gamma$ ) labelled accordingly.....	36
Figure 1.15 – Illustration of Bragg's Law. Incoming X-rays of the same wavelength ( $\lambda$ ) and incident angle ( $\theta$ ) are diffracted from the lattice plane, resulting in constructive interference from the two diffracted X-rays. The relationship between the two X-rays can be defined by $d \sin\theta$ .....	37
Figure 2.1 – Several examples of N-substituted triazacyclononane ligands with various pendant arms, developed by Blake and co-workers.....	50
Figure 2.2 – Structures of (a) $\text{Me}_3\text{-tacn}$ and (b) $\text{BnMe}_2\text{-tacn}$ . ....	51
Figure 2.3 – The four $\text{H}_3\text{-NOTA}$ derivatives reported by McBride et al. in the formation of $\text{Al-}^{18}\text{F}$ -chelate complexes and their corresponding radiochemical yields (%). ....	53



Figure 2.4 – Pendant arms reported for novel phosphinic-acid functionalised triazacyclononane ligands. ....	55
Figure 2.5 – Proposed structure of $[M(\text{NOTP-OMe})]^{n+}$ complexes.....	55
Figure 2.6 – Amide pendant arms used throughout the literature. ....	56
Figure 2.7 – Pendant arms used in the ligands $L^1$ , $L^2$ and $L^3$ . ....	60
Figure 2.8 – The novel amide-functionalised triazacyclononane ligands, $L^1$ , $L^2$ and $L^3$ . ....	61
Figure 2.9 – $^1\text{H}$ NMR spectra of $L^1$ (bottom; blue) and $L^1\cdot\text{HCl}$ (top; orange) ( $\text{CD}_3\text{OD}$ ). ....	63
Figure 2.10 – View of the structure of $L^1\cdot\text{HCl}$ showing the atom numbering scheme and a weakly H-bonded centrosymmetric dimer, arising from the amide NH functions and a chloride counter-ion. Ellipsoids are drawn at the 50% probability level and H atoms (except those involved in H-bonding) are omitted for clarity.....	64
Figure 2.11 – $^1\text{H}$ NMR spectra of $L^3$ (bottom; green) and $[L^3][\text{H}^+]$ (top; purple) ( $\text{CD}_3\text{OD}$ ). ....	67
Figure 2.12 – Chromatogram (obtained from $\text{ESI}^+$ MS analysis) of the crude product containing the NOTP-OMe ligand. ....	68
Figure 2.13 – Purification of NOTP-OMe using a Biotage Selekt flash chromatography system. ....	69
Figure 2.14 – Chromatogram (obtained from $\text{ESI}^+$ MS) of the purified ligand, NOTP-OMe.....	70
Figure 3.1 – Structures of the triazacyclononane ligands, $L^1$ , $L^2$ and NOTP-OMe, which will be the subject of this chapter. ....	84
Figure 3.2 – Typical Jahn-Teller distortions for an octahedral $\text{Cu}^{2+}$ complex. The $e_g$ orbitals are split into an $a_{1g}$ and $b_{1g}$ subset, reducing the overall energy of the complex. ....	86
Figure 3.3 – Structures of the tris-amide functionalised ligands, $L$ and $\text{MeL}$ .....	87
Figure 3.4 – Extensive hydrogen-bonded network of $[\text{Ni}(\text{tcet})][\text{ClO}_4]_2$ reported by Liu et al. Redrawn from CCDC 602837. Hydrogen and cation atoms (excluding those involved in hydrogen bonding) omitted for clarity. Atom colours: dark green, Ni; green, Cl; red, O; blue, N; white, H. ....	88
Figure 3.5 – Structures of the two diisopropyl mono-amide triazacyclononane ligands reported by Berreau et al. $R$ and $R' = \text{H}$ and/or $\text{Me}$ . ....	89

Figure 3.6 – [Cu(tris-1,4,7-quinolinylnacetamide-tacn)][NO <sub>3</sub> ] <sub>2</sub> reported by Garau et al. Redrawn from CCDC 1889394. Hydrogen atoms (excluding those involved in hydrogen bonding) omitted for clarity. ....	90
Figure 3.7 – Structures of the Fe <sup>2+</sup> (tris)pyridyl-triazacyclononane complexes reported by Tsitovich et al. The addition of a methyl and amino group to the ligand results in a high-spin complex, whereas the unsubstituted analogue is low-spin.....	91
Figure 3.8 – [Co(TCMT)][NO <sub>3</sub> ] <sub>2</sub> reported by Abozeid et al. Redrawn from CCDC 1586385. Hydrogen and nitrate cation atoms (excluding those involved in hydrogen bonding) omitted for clarity. ....	92
Figure 3.9 – General structure of the [M(NOTP)] <sup>–</sup> complexes reported by Parker and co-workers. ....	93
Figure 3.10 – General structure of the [M(NOTP <sup>tfe</sup> )] <sup>n–</sup> complexes reported by Koucký et al. ....	93
Figure 3.11 – Crystal structures of (a) [Co(NOTP <sup>tfe</sup> )] <sup>–</sup> in octahedral geometry and (b)[Co(NOTP <sup>tfe</sup> )] <sup>–</sup> in distorted trigonal prismatic geometry. Trigonal planes are represented by the green and red triangles. Redrawn from CCDC 2327154 and 2327158 respectively. Cations removed for clarity. Atom colours: dark blue, Co; purple, P; green, F; red, O; blue, N; grey, C; white, H.....	94
Figure 3.12 – <sup>1</sup> H NMR spectrum of [Zn(L <sup>1</sup> )] [NO <sub>3</sub> ] <sub>2</sub> (CD <sub>3</sub> OD). ....	98
Figure 3.13 – <sup>1</sup> H NMR spectrum of [Zn(L <sup>2</sup> )] [NO <sub>3</sub> ] <sub>2</sub> (CD <sub>3</sub> OD). ....	99
Figure 3.14 – UV-Vis absorbance spectra for [Co(L <sup>1</sup> )] [NO <sub>3</sub> ] <sub>n</sub> and [Co(L <sup>2</sup> )] [NO <sub>3</sub> ] <sub>n</sub> in MeOH (10 <sup>–3</sup> M). The background noise between 800 – 900 nm is due to a grating change. ....	100
Figure 3.15 – UV-Vis absorbance spectra for [Ni(L <sup>1</sup> )] [NO <sub>3</sub> ] <sub>2</sub> and [Ni(L <sup>2</sup> )] [NO <sub>3</sub> ] <sub>2</sub> in MeOH (10 <sup>–3</sup> M). ....	102
Figure 3.16 – View of the structure of [Co(L <sup>1</sup> -H)] [NO <sub>3</sub> ] <sub>2</sub> ·2MeOH showing the atom numbering scheme and the H-bonding between the nitrate anions and the N5 and N6 atoms of the carboxamide-bound amide arms. Ellipsoids are drawn at the 50% probability level and H and solvent atoms (except those involved in H-bonding) are omitted for clarity. H-bond distances: N5...O104 = 2.74, N6...O103' = 2.736, O107... O105 = 2.764 Å.....	107
Figure 3.17 – View of the structure of [Co(L <sup>2</sup> )] [NO <sub>3</sub> ] <sub>3</sub> showing the atom numbering scheme and H-bonding between the nitrate anions and the N2 atoms of the carboxamide-bound amide arms. Ellipsoids are drawn at the 50% probability level and H and solvent atoms (except those involved in H-bonding) are omitted for clarity. ....	108

Figure 3.18 – Views of the structures present in (a)  $[\text{Ni}(\text{L}^1)][\text{NO}_3]_2 \cdot 1.5\text{MeOH}$  and (b)  $[\text{Ni}(\text{L}^2)][\text{NO}_3]_2 \cdot 0.443\text{H}_2\text{O}$  showing the atom numbering schemes and the H-bonding between nitrate anions and each of the amide NH groups. Ellipsoids are drawn at the 50% probability level and H and solvent atoms (except those involved in H-bonding) are omitted for clarity.. 110

Figure 3.19 – View showing the extended hydrogen-bonded network of (a)  $[\text{Ni}(\text{L}^1)][\text{NO}_3]_2$  and (b)  $[\text{Ni}(\text{L}^2)][\text{NO}_3]_2$ , which both form an infinite 1D chain with one bridging nitrate anion between two molecules. Atom colours: purple, Ni; red, O; blue, N; white, H. .... 111

Figure 3.20 – View of the structure of  $[\text{Cu}(\text{L}^1)][\text{NO}_3]_2 \cdot 1.25\text{Et}_2\text{O} \cdot \text{MeOH}$  (note that there are three crystallographically independent cations and six nitrate anions in the asymmetric unit) showing the H-bonding between nitrate anions and amide N-H groups. The copper cations are labelled (Cu1, Cu2 and Cu3); nitrogen = dark blue; oxygen = red; carbon = grey. Ellipsoids are drawn at the 50% probability level and H and solvent atoms (except those involved in H-bonding) are omitted for clarity. .... 112

Figure 3.21 – (a) View showing the extended hydrogen-bonded network of  $[\text{Cu}(\text{L}^1)][\text{NO}_3]_2$ , which forms a 2D sheet. A nitrate anion bridges alternating Cu2 and Cu3 molecules; (b) The Cu1 molecule sits within the cavity but is only engaged in hydrogen-bonding to nitrate anions. Atom colours: light blue, Cu; red, O; dark blue, N; white, H. .... 113

Figure 3.22 – View of the structure of  $[\text{Cu}(\text{L}^2)]^{2+}$  showing the atom numbering scheme and the H-bonding between nitrate anions and each of the amide NH groups. Ellipsoids are drawn at the 50% probability level and H atoms (except those involved in H-bonding) are omitted for clarity. .... 114

Figure 3.23 – View showing the extended hydrogen-bonded network of  $[\text{Cu}(\text{L}^2)][\text{NO}_3]_2$ , which forms an infinite 1D chain with one bridging nitrate anion between two molecules. Atom colours: light blue, Cu; red, O; dark blue, N; white, H. .... 114

Figure 3.24 – IR spectra obtained for NOTP-OMe (as a film) and the Ni, Cu and Zn complexes (Nujol mull) thereof. The band assigned as the P=O stretch is highlighted in pink and labelled accordingly..... 116

Figure 3.25 –  $^{31}\text{P}\{^1\text{H}\}$  spectrum of  $[\text{Zn}(\text{NOTP-OMe})][\text{BPh}_4]_2 (\text{CD}_3\text{CN})$ ..... 118

Figure 4.1 –  $[\text{GaF}_3\text{L}]_2 \cdot (\text{MeOH})_6$  reported by Penkert et al.: (a) view down the  $S_6$ -axis and (b) side-view showing the hydrogen-bonded hexamer of MeOH molecules. Images redrawn from CCDC 1220143. Hydrogen atoms omitted for clarity. Atom colours: pale pink, Ga; green, F; red, O; blue, N. .... 133

Figure 4.2 – Extended hydrogen-bonding network of $[\text{InF}_3(\text{Me}_3\text{-tacn})]\cdot 4\text{H}_2\text{O}$ . Redrawn from CCDC 926505. Hydrogen atoms (excluding those involved in hydrogen bonded) omitted for clarity. Atom colours: pale purple, In; green, F; red, O; blue, N; grey, C; white, H.....	134
Figure 4.3 – Structure of a $[\text{GaF}_3(\text{BnMe}_2\text{-tacn})\text{K}_2(\text{OH}_2)_4(\text{PF}_6)_2]\cdot \text{H}_2\text{O}$ dimer with coordination to $\text{K}^+$ via fluoride ligands. Redrawn from CCDC 1008583. Hydrogen atoms omitted for clarity. ....	135
Figure 4.4 – (a) $^{19}\text{F}\{^1\text{H}\}$ and (b) $^{27}\text{Al}$ NMR spectra of the $[\text{AlF}_4]^-$ anion isolated from the overnight reaction of $[\text{AlF}_3(\text{dmsO})(\text{OH}_2)_2]$ with $\text{L}^1$ ( $\text{d}_6\text{-dmsO}$ ). ....	141
Figure 4.5 – $^{19}\text{F}\{^1\text{H}\}$ (left; green) and $^1\text{H}$ NMR (right; blue) spectra of the reaction of $[\text{GaF}_3(\text{dmsO})(\text{OH}_2)_2]$ with $\text{L}^1$ taken at time intervals 0, 1, 24 and 48 h ( $\text{CD}_3\text{OD}$ ). Impurities in the $^{19}\text{F}\{^1\text{H}\}$ spectra are annotated with a ‘o’. The rolling baseline in the $^{19}\text{F}\{^1\text{H}\}$ NMR spectra is due to Teflon in the probe. ....	145
Figure 4.6 – (a) $^{19}\text{F}\{^1\text{H}\}$ (298 K, 376 MHz) and (b) $^1\text{H}$ NMR spectra of $[\text{GaF}_3(\text{L}^1)]$ ( $\text{CD}_3\text{OD}$ ). ....	147
Figure 4.7 – $^{71}\text{Ga}$ NMR spectra (298 K, 122 MHz) of (a) $[\text{GaF}_3(\text{L}^1)]$ , $^1J_{^{71}\text{Ga}-^{19}\text{F}} = 510$ Hz and (b) $[\text{GaF}_3(\text{L}^2)]$ , $^1J_{^{71}\text{Ga}-^{19}\text{F}} = 520$ Hz. Both spectra show the expected 1:3:3:1 quartet arising from the coupling of the three fac $^{19}\text{F}$ atoms to the quadrupolar $^{71}\text{Ga}$ nucleus. ....	148
Figure 4.8 – (a) $^{19}\text{F}\{^1\text{H}\}$ (298 K, 376 MHz) and (b) $^1\text{H}$ NMR spectra of $[\text{GaF}_3(\text{L}^3)]$ ( $\text{CD}_3\text{OD}$ ). ....	149
Figure 4.9 – (a) View of the structure of the component of $[\text{GaF}_3(\text{L}^1)]\cdot \text{MeOH}\cdot 0.5\text{H}_2\text{O}$ , showing the atom numbering scheme and H-bonding between amide $\text{NH}\cdots\text{F}$ and lattice $\text{H}_2\text{O}/\text{MeOH}\cdots\text{F}$ . Ellipsoids are drawn at the 50% probability level and H and solvent atoms (except those involved in H-bonding) are omitted for clarity. (b) View of part of the H-bonded extended structure showing the 1D chain formed via intermolecular $\text{F}\cdots\text{H}\cdots\text{N}$ interactions ( $\text{F2}\cdots\text{H4N4} = 1.758$ Å, $\text{F3}\cdots\text{H}_2\text{O} = 1.695$ Å).....	151
Figure 4.10 – (a) View of the structure of $[\text{InF}_3(\text{L}^2)]$ showing the atom numbering scheme and H-bonding between amide $\text{NH}$ and F ligands. Ellipsoids are drawn at the 50% probability level and H atoms (except those involved in H-bonding) are omitted for clarity; (b) View down the a-axis showing the intermolecular $\text{F1}\cdots\text{H2N2}$ hydrogen bonding contacts (1.888 Å). ....	153
Figure 4.11 – View of the isostructural metal complexes present in (a) $[\text{GaF}_3(\text{L}^3)]$ and (b) $[\text{FeF}_3(\text{L}^3)]$ , showing the atom numbering schemes and the intermolecular ‘head-to-tail’ $\text{F2}\cdots\text{H4}\cdots\text{N4}$ hydrogen bonding interactions ( $\text{M} = \text{Ga}, 1.769$ Å; $\text{M} = \text{Fe}, 1.787$ Å), giving weakly associated dimers. Ellipsoids are drawn at the 50% probability level and H and atoms (excluding those involved in H-bonding) are omitted for clarity.....	154

Figure 4.12 – View of part the structure of $[\text{GaF}_3(\text{L}^3)]$ viewed down the c-axis showing the hexagonal arrangement adopted by the weakly associated dimers (the same arrangement is present in $[\text{FeF}_3(\text{L}^3)]$ ).....	155
Figure 4.13 – View of $[\text{GaF}_3(\text{L}^3)]$ down (a) the b-axis and (b) offset from the b-axis, depicting the solvent-accessible voids. Void diameter = 2.4 Å. ....	156
Figure 5.1 – The free carboxylate arm of the $\text{H}_3$ -NOTA derivative IMP449 competes with $^{18}\text{F}$ for the sixth coordination site of aluminium, resulting in low radiochemical yields.....	169
Figure 5.2 – Radiochemical purity of $[\text{M}^{18}\text{F}(\text{Bn-NODP})]$ over 4 h in EtOH/ $\text{H}_2\text{O}$ and EtOH/PBS... ..	171
Figure 5.3 – (a) UV-HPLC trace of $[\text{GaF}_3(\text{L}^3)]$ , $R_t = 5:14$ min; (b) Radio-HPLC trace of $[\text{GaF}_3(\text{L}^3)]$ . Peak 1 $R_t = 2.07$ min. Peak 2 $R_t = 5:17$ min.....	177
Figure 5.4 – (a) UV-HPLC trace of $[\text{GaF}_3(\text{L}^3)]$ , $R_t = 10:46$ min; (b) Radio-HPLC trace of $[\text{GaF}_3(\text{L}^3)]$ . ....	179
Figure 5.5 – (a) UV-HPLC trace of $[\text{GaF}_3(\text{L}^3)]$ , $R_t = 5:35$ min; (b) Radio-HPLC trace of crude $^{18}\text{F}$ $[\text{GaF}_3(\text{L}^3)]$ reaction mixture, $R_t = 1:15$ min ( $[\text{F}^{18}\text{F}]$ ).....	182
Figure 5.6 – Timeline summary of the development of the HPLC method and conditions for $[\text{GaF}_3(\text{L}^3)]$ . ....	183
Figure 5.7 – (a) Analytical UV-HPLC trace of the reference standard compound $[\text{GaF}_3(\text{L}^1)]$ , $R_t = 09:16$ min; (b) Analytical radio-HPLC trace of the crude product from radiofluorination of $[\text{GaF}_3(\text{L}^1)]$ . Peak 1: $R_t = 00:37$ min 80% ( $[\text{F}^{18}\text{F}]$ ). Peak 2: $R_t = 09:17$ min 20% ( $[\text{Ga}^{18}\text{FF}_2(\text{L}^1)]$ ). ..	185
Figure 5.8 – Analytical radio-HPLC traces of the SPE purified $[\text{Ga}^{18}\text{FF}_2(\text{L}^1)]$ in 10:90 EtOH: $\text{H}_2\text{O}$ (left) and 10:90 EtOH:PBS (right) at: $t = 0, 30, 80$ and 120 min. ....	186
Figure 6.1 – Structures of the two bis(phosphonate) triazacyclononane ligands reported by Holub et al.....	194
Figure 6.2 – Structures of the two gallium complexes with the benzylacetamide mono-amide derivative of $\text{H}_3$ -NOTA. The gallium ion is bound to the oxygen of the amide at pH = 3, and to the nitrogen of the amide at pH = 5.....	195
Figure 6.3 – $[\text{Ga}^{67}(\text{NO}_2\text{A-Bn-PSMA})]$ conjugate bound to a serum albumin binding moiety via a serine (amide) linker. Polarisation of the carbonyl-amide bound to the Lewis acidic $\text{Ga}^{3+}$ centre leads to the autolytic cleavage of the amide bond.....	197
Figure 6.4 – Structure of $[\text{In}^{111}]\text{-}[\text{In}(\text{NOTA-Z08698-HEHEHE})]^+$ .....	198

Figure 6.5 – View of the structure of the [Fe(NOTA)] complex with the atom numbering scheme. Ellipsoids are drawn at the 50% probability level and H atoms are omitted for clarity.....	202
Figure 6.6 – $^1\text{H}$ NMR spectra following the reaction of $\text{Ga}(\text{NO}_3)_3 \cdot 9\text{H}_2\text{O}$ and $\text{L}^1$ (left, room temperature and right, $80^\circ\text{C}$ ) taken at time intervals 15 min, 60 min, 2.5 h, 6 h, and 24 h ( $\text{CD}_3\text{OD}$ ). Peaks relating to hydrolysis products annotated with “*” .....	203
Figure 6.7 – View of the structure of the hydrolysis product from the reaction of $\text{Ga}(\text{NO}_3)_3 \cdot 9\text{H}_2\text{O}$ + $\text{L}^1$ with the atom numbering scheme and showing the H-bonding between the amide NH group and the nitrate counter-anion. Ellipsoids are drawn at the 50% probability level and H atoms (except those involved in H-bonding) are omitted for clarity. ....	205
Figure 6.8 – $^{19}\text{F}\{^1\text{H}\}$ NMR spectrum from the reaction of $[\text{In}(\text{L}^1)](\text{NO}_3)_3$ with 3 mol. eqv. KF ( $\text{CD}_3\text{OD}$ ). .....	206
Figure 6.9 – View of the electron diffraction structure of the $[\text{In}(\text{NOTA})]$ tetramer. Ellipsoids are drawn at the 50% probability level and H atoms are removed for clarity. Atom colours: beige-pink, In; red, O; blue, N; grey, C. ....	208
Figure 6.10 – Schematic of the seven-coordinate $[\text{In}(\text{NOTA})]$ structure obtained by electron diffraction, which shows an $\text{N}_3\text{O}_4$ coordination sphere. The asymmetric, bridging carboxylate of the third NOTA pendant arm forms only very long-range, and weak interactions with one indium centre (In-O5), whilst coordinated to an adjacent indium (In-O6). Atom numbering scheme is given for N and O atoms.....	209
Figure 6.11 – View of the structure of $[\text{InCl}(\text{NOTA})][\text{H}]$ with the atom numbering scheme and showing the H-bonding between the protonated carboxylate group and a carboxylate of an adjacent molecule. Ellipsoids are drawn at the 50% probability level and H atoms (except those involved in H-bonding) are omitted for clarity.....	210
Figure 6.12 – $^{19}\text{F}\{^1\text{H}\}$ NMR spectra following the reaction of $[\text{InCl}(\text{NOTA})]^-$ and KF, at 10 min, 6 h and 24 h ( $\text{D}_2\text{O}$ ). ....	212
Figure 6.13 – View of the structure of $[\text{Al}(\text{Bn-NODA})(\text{OAc})] \cdot 2\text{H}_2\text{O}$ showing the atom numbering scheme and H-bonding between carboxylate and lattice $\text{H}_2\text{O}$ molecules. Ellipsoids are drawn at the 50% probability level and H and solvent atoms (except those involved in H-bonding) are omitted for clarity. ....	214
Figure 6.14 – Structures of the two different geometric isomers which are possible for $[\text{MX}(\text{Bn-NODP})]$ and $[\text{MX}(\text{Bn-NODA})]$ complexes, relative to the position of the coordinated P-O donor to the other tacn(N)-substituents. When Y = C, the R group is not present. When Y = P, R = Ph.	215

Figure 6.15 – (a) View of the two  $[\text{Al}(\text{Bn-NODA})(\text{OAc})]\cdot 2\text{H}_2\text{O}$  molecules in the asymmetric unit linked via hydrogen-bonding interactions arising from carboxylate and acetate groups and lattice  $\text{H}_2\text{O}$ ; (b) View of the extended structure assembled through intermolecular H-bonding between  $[\text{Al}(\text{Bn-NODA})(\text{OAc})]\cdot 2\text{H}_2\text{O}$  and lattice  $\text{H}_2\text{O}$  molecules. Atom colours: light-pink, Al; red, O; blue, N; white, H..... 216

## Table of Schemes

Scheme 1.1 – Kryptofix 2.2.2 binds to $K^+$ to prevent the formation of $[^{18}F]KF$ and increase the reactivity of $^{18}F^-$ . .....	6
Scheme 1.2 – Conversion of an aryl boronic ester conjugate to the corresponding aryl trifluoroborate conjugate using nucleophilic $[^{18}F]KHF_2$ in an isotopic exchange reaction. X represents a linking functional group i.e an amide. ....	8
Scheme 1.3 – $^{19}F/^{18}F$ isotopic exchange of $[FeF_3(BnMe_2-tacn)]$ . ....	13
Scheme 1.4 – One-pot synthesis of an $[Al^{18}F(NOTA)]$ complex, conjugated to a biomolecule via a peptide bond. ....	21
Scheme 1.5 – Various Ga- $^{18}F$ radiochemical experiments explored previously in the Reid group. (1) = $Cl/^{18}F$ isotopic exchange of $[GaCl_3(BnMe_2-tacn)]$ ; (2) = $^{19}F/^{18}F$ isotopic exchange of $[GaF_3(BnMe_2-tacn)]$ ; (3) = $Cl/^{18}F$ isotopic exchange of $[GaCl(Bn-NODA)]$ . ....	25
Scheme 2.1 – Direct synthesis of 1,4,7-trimethyl-1,4,7-triazacyclononane from N,N',N''-tris(p-tolylsulfonyl)-1,4,7-triazacyclononane. ....	51
Scheme 2.2 – Synthesis of 1-benzyl-4,7-dimethyl-1,4,7-triazacyclononane ( $BnMe_2-tacn$ ) as first published by Belousoff and co-workers. ....	52
Scheme 2.3 – Synthesis of 1,4,7-triacetic acid-1,4,7-triazacyclononane ( $H_3-NOTA$ ). ....	53
Scheme 2.4 – Synthesis of $H_2-Bn-NODP$ via its intermediate phosphinate-ester derivative. ....	54
Scheme 2.5 – Synthesis of N,N',N''-tris-(p-tolylsulfonyl)diethylene triamine ( $Ts_3-DET$ ). ....	57
Scheme 2.6 – Synthesis of 1,2-bis-[(p-tolylsulfonyl)oxy]ethane (EGT). ....	57
Scheme 2.7 – Synthesis of N,N',N''-tris(p-tolylsulfonyl)-1,4,7-triazacyclononane ( $Ts_3-tacn$ ). ..	58
Scheme 2.8 – Isolation of 1,4,7-triazacyclononane ( $tacn$ ) from $Ts_3-tacn$ . ....	58
Scheme 2.9 – Formation of 1-(p-tolylsulfonyl)-1,4,7-triazacyclononane ( $Ts-tacn$ ) via selective deprotection of $Ts_3-tacn$ . ....	59
Scheme 2.10 – Synthesis of $H_2-Bn-NODA$ via $NO_2A^tBu$ . ....	60
Scheme 2.11 – Synthesis of 1,4,7-tris-phenylacetamide-1,4,7-triazacyclononane (Ligand 1, $L^1$ ). ....	61



Scheme 2.12 – Synthesis of 1,4,7-tris-isopropylacrylamide-1,4,7-triazacyclononane (Ligand 2, L <sup>2</sup> ). .....	65
Scheme 2.13 – Multi-step synthesis of 1-phenylacetamide-4,7-diisopropyl-1,4,7-triazacyclononane (Ligand 3, L <sup>3</sup> ) via Ts-tacn.....	66
Scheme 2.14 – Synthesis of NOTP-OMe and H <sub>3</sub> -NOTP.....	68
Scheme 3.1 – Various hydrolysis pathways and products from the reactions of [M(L)], M = Cr <sup>3+</sup> , Fe <sup>2+</sup> . .....	88
Scheme 3.2 – Formation of transition metal complexes of L <sup>1</sup> and L <sup>2</sup> (in MeOH, at RT) via M(NO <sub>3</sub> ) <sub>2</sub> ·xH <sub>2</sub> O precursors (M = Co, Ni, Cu, Zn).....	96
Scheme 3.3 – Suggested pathway and structure of divalent transition metal complexes of NOTP-OMe (Ni, Cu, Zn). .....	115
Scheme 4.1 - Reactions of [MF <sub>3</sub> (dmsO)(OH <sub>2</sub> ) <sub>2</sub> ] with various N-donor ligands. ....	137
Scheme 4.2 – Assumed synthetic route towards [MF <sub>3</sub> (L <sup>n</sup> )] complexes; M = Al, Ga, In, Fe; L <sup>n</sup> = L <sup>1</sup> , L <sup>2</sup> , L <sup>3</sup> . .....	138
Scheme 5.1 – <sup>18</sup> F/Cl halide exchange reaction on a pre-formed [GaCl(Bn-NODA)] complex..	170
Scheme 5.2 – Cl/ <sup>19</sup> F halide exchange of a pre-formed [AlCl <sub>3</sub> (BnMe <sub>2</sub> -tacn)] complex. ....	172
Scheme 5.3 – <sup>18</sup> F/Cl halide exchange reaction on a pre-formed [GaCl <sub>3</sub> (BnMe <sub>2</sub> -tacn)] complex. ....	172
Scheme 5.4 – Initial isotopic exchange experimental conditions for the target [Ga <sup>18</sup> FF <sub>2</sub> (L <sup>3</sup> )] complex. ....	176
Scheme 5.5 – General isotopic exchange experimental conditions for the target [Ga <sup>18</sup> FF <sub>2</sub> (L <sup>1</sup> )] complex. ....	183
Scheme 6.1 – N, O-acyl rearrangement of mono-amide (serine) [Ga(NO <sub>2</sub> A)] complexes for both N <sub>3</sub> O <sub>3</sub> (low pH) and N <sub>4</sub> O <sub>2</sub> coordination modes. ....	196
Scheme 6.2 – General synthetic route towards <sup>18</sup> F-radiolabelled indium(III) bis-thiosemicarbazone complexes (R <sub>n</sub> = Me, Et, Ph, H). ....	199
Scheme 6.3 – Reaction pathways of L <sup>1</sup> with the Lewis acidic cations Fe <sup>3+</sup> , Ga <sup>3+</sup> and In <sup>3+</sup> and the various reaction conditions used. [Fe(NOTA)] and the Ga <sup>+</sup> complex were isolated as single-crystals from a product mixture containing multiple (unidentified) species/hydrolysis products. ....	201

Scheme 6.4 – Synthesis of [M(NOTA)] complexes (M = Ga or In).....	207
Scheme 6.5 – Formation of [AlX(Bn-NODA)] complexes following [Al <sup>18</sup> F] <sup>2+</sup> chelation methods previously reported (X = OAc, F).....	213
Scheme 6.6 – Various pathways towards [MX(Bn-NODP)] complexes (M = Al, In; X = Cl, F, NO <sub>3</sub> ). .....	217

## Table of Equations

Equation 1.1 – <b>Beer-Lambert Law</b> . A = absorbance, I = intensity, $I_0$ = initial intensity, $\epsilon$ = molar extinction coefficient ( $\text{mol}^{-1}\text{dm}^3\text{cm}^{-1}$ ), l = path length (cm), c = concentration ( $\text{mol dm}^{-3}$ ).....	35
Equation 1.2 – <b>Bragg's Law</b> . n = diffraction order, $\lambda$ = wavelength of the X-Ray beam, d = interplanar distance, $\theta$ = incident angle. ....	37
Equation 1.3 – <b>Forward Fourier Transform</b> (the diffraction experiment). 1 = Total diffracted wave in hkl direction; 2 = sum of the X-rays scattered by individual atoms; 3 + 4 = scattering of X-rays by individual atoms; 5 = position of atoms. Terms: $f_j$ = atomic scattering factor; $u_j$ = isotropic displacement parameter; $x_j, y_j, l_j$ = coordinates relative to the unit cell. ....	38
Equation 1.4 – <b>Reverse Fourier Transform</b> (the recombination calculation). 1 = electron density; 2 = sum of diffracted beams; 3 = reflection amplitude; 4 = intrinsic wave phase; 5 = phase shift at each geometric position. ....	38
Equation 1.5 – <b>Patterson Synthesis</b> . $F_o$ = observed diffraction beam amplitudes. ....	38

## List of Accompanying Materials

Appendix A: General Experimental Details

Appendix B: Crystallographic Information Files

All the cif files of single crystal X-ray structures described in this thesis are included in the ESI, as well as spectroscopic data for the reported compounds. These can be found at DOI:

<https://doi.org/10.5258/SOTON/D3321>.

## Research Thesis: Declaration of Authorship

Print name: Charley O'Callaghan

Title of thesis: Transition Metal and Group 13 Triazamacrocyclic Complexes: Coordination Chemistry and Applications in  $^{18}\text{F}$  PET Imaging

I declare that this thesis and the work presented in it is my own and has been generated by me as the result of my own original research.

I confirm that:

1. This work was done wholly or mainly while in candidature for a research degree at this University;
2. Where any part of this thesis has previously been submitted for a degree or any other qualification at this University or any other institution, this has been clearly stated;
3. Where I have consulted the published work of others, this is always clearly attributed;
4. Where I have quoted from the work of others, the source is always given. With the exception of such quotations, this thesis is entirely my own work;
5. I have acknowledged all main sources of help;
6. Where the thesis is based on work done by myself jointly with others, I have made clear exactly what was done by others and what I have contributed myself;
7. Parts of this work have been published as:

Synthesis and properties of metal trifluoride complexes with amide-functionalised tacn macrocycles and radiofluorination of  $[\text{GaF}_3(\text{L}^1)]$  by  $^{18}\text{F}/^{19}\text{F}$  isotopic exchange. Charley O'Callaghan, Victoria K. Greenacre, Rhys P. King, Julian Grigg, Julie M. Herniman, Graeme McRobbie, Gillian Reid. *Dalton Transactions*. 2024. **53**. 14897.

Di- and tri-valent metal complexes with tris-amide-functionalised 1,4,7-triazacyclononane chelators. Charley O'Callaghan, Victoria K. Greenacre, Gillian Reid. *New Journal of Chemistry*. Accepted, manuscript identification: NJ-ART-12-2024-005327.

Signature:

Date: 11<sup>th</sup> February 2025

## Acknowledgements

The work in this thesis is a culmination of four (+ a bit) years of work which I couldn't have done without the incredible guidance and support of my supervisor, Professor Gill Reid. Your seemingly endless source of wisdom and knowledge will always be a marvel to me. Mostly I'd like to thank your confidence and optimism in this project and myself even when things weren't going as expected; it's testament to the fact I made it through.

Thanks to all at GE Healthcare, especially Dr Graeme McRobbie. Your expertise in getting the radiochemistry off the ground was invaluable. I learnt so much from you during our time at St Thomas', and I really appreciate all your help throughout.

Thanks to everyone in the department. Especially Vicki & Rob, for all your advice and insight, whether chemistry, life or crystal-related – your skills with Olex really are proof that magic is real. To Rhys, for never making any of my questions feel silly, and for running the same  $^{27}\text{Al}$  NMR countless times. Dr Julie Herniman, for the direct injection/HR MS. Then, to Rich, Kelsey, Maddie and Daniie, Mark & Keith, and those in the NCS, for all your help and excellent conversation.

Thanks to my family, for all the love and encouragement throughout. Thanks especially to my Mum for taking me to the Science Museum when I was eight. Without that, would I even be here? Probably not (I wouldn't have seen what astronauts ate in space, and I'd be on the ISS by now). To my Dad, whose belief in me and all-round optimism has kept me going. Reagan, your interest in 'molecules' and my work has always meant the world, despite the fact I may as well be speaking Elvish. To Mila, for being a never-ending source of joy. Also to Pat & Tan – no words can describe my appreciation for everything you've done for me. Crystal-themed T-shirts on the way.

To all my friends, but especially to Alice, Lara, Viv & Josh – hopefully, you might see my "sorry I was too busy to reply to your message for six weeks!" was somewhat justified; thanks for sticking by all these years regardless. Then to 'Mansoor's Movers', thanks for keeping me sane (caffeinated) in the final few months. Liam & India, I'll save the mushy stuff for when I'm a tequila or ten down. All I'll say is I enjoyed my time at the farm, and I appreciate you both endlessly.

Thanks to the University of Southampton & King's College London for the facilities, all those involved in MITHRAS, and the EPSRC for funding the project.

Finally, I wanted to end this on the person I am most grateful to: my incredibly understanding, patient, love of my life and best friend, Angus. I'm truly blessed to have had your unwavering love and support throughout this whole thing. Without you, I wouldn't have made it this far.

## Definitions and Abbreviations

{ <sup>1</sup> H}	Proton decoupled
<sup>18</sup> F	Fluorine-18
<sup>18</sup> F-DOPA	<sup>18</sup> F-fluorodopa
<sup>18</sup> F-FDG	<sup>18</sup> F-fluorodeoxyglucose
Bn	Benzyl
BnMe <sub>2</sub> -tacn	1-benzyl-4,7-dimethyl-1,4,7-triazacyclononane
br	Broad
ClO <sub>4</sub>	Perchlorate
CT	Computed Tomography
d (NMR)	Doublet
DET	Diethylene triamine
DMF	Dimethylformamide
dmsO	Dimethyl sulfoxide
ED	Electron Diffraction
efg	Electric Field Gradient
EGT	Ethylene Glycol Tosylate
ESI	Electrospray Ionisation
Et	Ethyl
Et <sub>2</sub> O	Diethyl ether
EtOH	Ethanol
GBq	Gigabecquerel
GMP	Good Manufacturing Practice
<i>Facial</i>	<i>Fac</i>
H <sub>2</sub> -Bn-NODA	1-benzyl-4,7-diacetic acid-1,4,7-triazacyclononane
H <sub>2</sub> -Bn-NODP	1-benzyl-4,7-phenylphosphinic acid-1,4,7-triazacyclononane
H <sub>3</sub> -NOTA	1,4,7-triazacyclononane-1,4,7-triacetic acid
H <sub>3</sub> -NOTP	1,4,7-phenylphosphinic acid-1,4,7-triazacyclononane

H <sub>4</sub> -DOTA	1,4,7,10-tetraazacyclododecane-1,4,7,10-tetraacetic acid
HLB	Hydrophilic Lipid Balanced
HPLC	High-Performance Liquid Chromatography
HR	High Resolution
HSA	Human Serum Albumin
Hz	Hertz
<sup>i</sup> Pr	Isopropyl
IR	Infrared
J	Coupling constant
KCL	King's College London
keV	Kilo electron volt
Kryptofix 2.2.2	4,7,13,16,21,24-hexaoxa-1,10-diazabicyclo[8.8.8]hexacosane
L <sup>1</sup>	1,4,7-tris-phenylacetamide-1,4,7-triazacyclononane
L <sup>2</sup>	1,4,7-tris-isopropylacrylamide-1,4,7-triazacyclononane
L <sup>3</sup>	1-phenylacetamide-4,7-diisopropyl-1,4,7-triazacyclononane
LMCT	Ligand-to-Metal Charge Transfer
m (IR)	Medium
m (NMR)	Multiplet
MBq	Megabecquerel
Me	Methyl
Me <sub>3</sub> -tacn	1,4,7-trimethyl-1,4,7-triazacyclononane
MeCN	Acetonitrile
MeOH	Methanol
<i>Meridional</i>	<i>Mer</i>
MeV	Mega electron volt
MLCT	Metal-to-Ligand Charge Transfer
MRI	Magnetic Resonance Imaging
MS	Mass spectrometry
mSv	Millisievert
<i>m/z</i>	Mass-to-charge ratio



NMR	Nuclear Magnetic Resonance
NO <sub>3</sub>	Nitrate
NOTP-OMe	Trimethyl-1,4,7-triazacyclononane-1,4,7-triyltris[methylene(phenylphosphinate)]
OAc	Acetate
O <sub>h</sub>	Octahedral
OTf	Triflate
ParaCEST	Paramagnetic Chemical Exchange Saturation Transfer
PBS	Phosphate Buffered Saline
PET	Positron Emission Tomography
Ph	Phenyl
ppm	Parts per million
PSMA	Prostate-Specific Membrane Antigen
Pyr	Pyridyl
RBF	Round-Bottom Flask
RCP	Radiochemical Purity
RCY	Radiochemical Yield
RGD	Arginylglycylaspartic acid
RP	Reverse Phase
R <sub>t</sub>	Retention Time
RT	Room Temperature
s (IR)	Strong
s (NMR)	Singlet
SCXRD	Single Crystal X-ray Diffraction
sh (IR)	Shoulder
SiFA	Silicon Fluoride Acceptor
SPE	Solid Phase Extraction
SPECT	Single Photon Emission Computed Tomography
t (NMR)	Triplet
Tacn	1,4,7-triazacyclononane

<sup>t</sup> Bu	<i>Tert</i> -butyl
tcet	3,3',3''-(1,4,7-triazacyclononane-1,4,7-triyl)tripropanamide
TCMT	1,4,7-tris-carbamoylmethyl-1,4,7-triazacyclononane
TEM	Transmission Electron Microscope
TFA	Trifluoroacetic acid
THF	Tetrahydrofuran
Ts	Tosyl
q (NMR)	Quartet
QMA	Quaternary Methyl Ammonium
w (IR)	Weak
UV-Vis	Ultraviolet-visible
$\epsilon$	Molar extinction coefficient
$\delta$	Chemical shift
$\lambda$	Wavelength
$\tilde{\nu}$	Wavenumber

## Chapter 1 Introduction

This thesis will describe the synthetic routes towards known and novel macrocyclic triazacyclononane ligands, and transition metal and Group 13 complexes thereof.

Current  $^{18}\text{F}$  PET imaging radiopharmaceuticals are limited by complex synthetic techniques and lack of specificity towards biological targets of interest, including various diseases such as cancers. The concept of inorganic-based radiotracers, which exploit the formation of strong M-F bonds and can be conjugated to receptor-specific targeting moieties, has gained increasing interest in recent years. Hence, in this thesis, much of the focus will be put towards Group 13 fluoride complexes, which have been shown to be promising candidates for  $^{18}\text{F}$  radiolabelling – as discussed below. The coordination chemistry, properties and behaviours of these novel complexes will be explored to assess their viability for  $^{18}\text{F}$  PET imaging applications.

### 1.1 Positron Emission Tomography

Positron emission tomography (PET) is a well-established nuclear imaging technique used across a variety of medical disciplines. Often used in conjunction with computed tomography (CT) or magnetic resonance imaging (MRI), it enables the real-time metabolic activity of cells to be visualised and measured. Within research, it can be used to establish the pharmacokinetic properties of trial therapeutics, or the mechanisms of disease initiation and progression, for example.<sup>1,2</sup> Primarily, PET imaging is used in a clinical setting, within oncology, cardiology and neurology departments, for the diagnosis of various cancers or neurodegenerative diseases such as Alzheimer's.<sup>3,4</sup>

PET imaging requires the use of radioactive pharmaceuticals (also known as radiotracers), which most often consist of a biomolecule to target specific receptors or tissues, and a radioisotope that can undergo  $\beta^+$  decay. As shown by Figure 1.1, this decay process releases a positron, which will travel a short distance (mm) before colliding with an electron in the surrounding tissue. This collision – referred to as an 'annihilation event' – results in the emission of two 511 keV photons ( $\gamma$ -rays) in a coincidence line,  $180^\circ$  to each other.<sup>5</sup> These photons are subsequently detected by an external gamma camera, which translates the photons into electrical signals, to produce a high-resolution, three-dimensional image.<sup>6</sup>

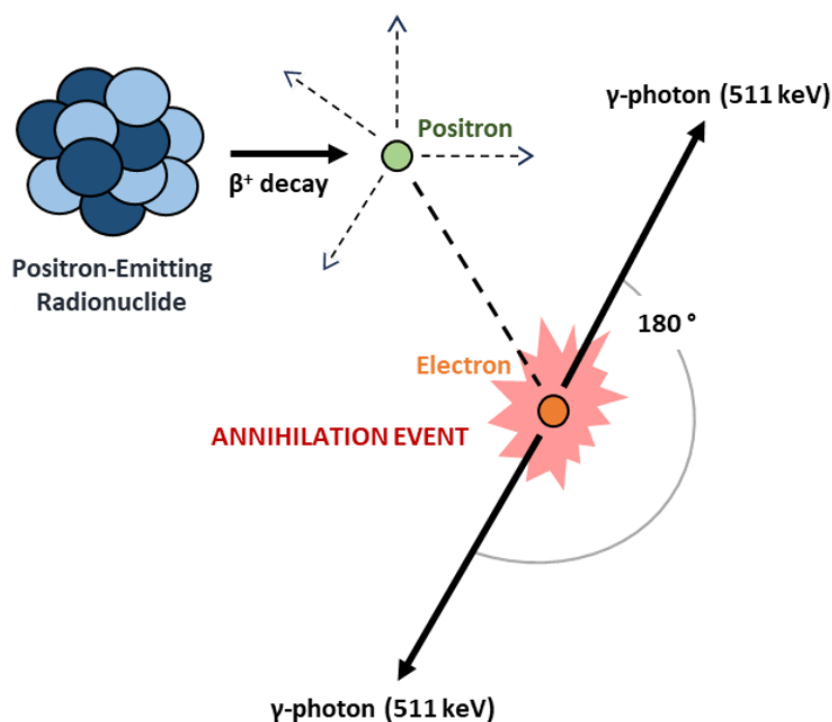


Figure 1.1 –  $\beta^+$  decay process and annihilation event.

### 1.1.1 PET Radioisotopes and Their General Properties

There are several factors to consider when assessing the suitability of a radioisotope for PET imaging. A short half-life is important, as this means the isotope decays quickly and keeps the patient radiation dose as low as possible. However, it also needs to be long enough to ensure enough radioactivity is present at the time of patient administration, following generation and transportation of the radioisotope, and incorporation into and purification of the radiotracer. Most routinely used PET radioisotopes have half-lives between a few minutes and a few hours.<sup>7</sup> Similarly, an isotope that produces a low-energy positron with a short linear range (prior to annihilation) in tissue is important, to increase the accuracy and resolution of the image produced. This also ensures minimal damage to the surrounding cells in the target area. The radioisotope also needs to be high in purity and have a lack of side emission – meaning, the primary decay route must be *via* positron emission.

Table 1.1 summarises the properties of several common positron-emitting radionuclides used in PET imaging.<sup>8</sup> The accessibility of the isotope also needs to be considered. It is recommended that a patient be administered a radiotracer within three half-lives from radioisotope production, for the scan to be effective.<sup>9</sup> Therefore, production of the radioisotope should ideally be on-site or within close proximity to where the radiotracer is prepared and used. All of the isotopes listed below are made available *via* cyclotrons, except for  $^{68}\text{Ga}$ , which is eluted *via* commercially available benchtop generators.<sup>10</sup>

Table 1.1 – Physical properties of the major PET imaging radioisotopes.

Radioisotope	Half-life / min	Positron linear range, $R_{\max}$ / mm	Positron energy, $E_{\max}$ / keV	Positron emission / %
$^{18}\text{F}$	110	2.30	645	97.0
$^{11}\text{C}$	20.4	4.20	960	99.8
$^{13}\text{N}$	10.0	5.40	1200	100
$^{15}\text{O}$	2.20	8.40	1740	99.9
$^{68}\text{Ga}$	67.7	9.20	1899	89.1

Due to its favourable properties,  $^{18}\text{F}$  is the most used isotope in PET imaging. Modern technological advances have also led to an increased availability of cyclotrons at hospitals for its production.<sup>11</sup> Additionally, the chemistry of  $^{18}\text{F}$  is very versatile. Most of the work involves incorporation into organic molecules *via* nucleophilic substitution (as  $[^{18}\text{F}]\text{F}^-$ ) or electrophilic substitution (as  $[^{18}\text{F}]\text{-F}_2$ ), but metal-fluoride coordination (also as  $[^{18}\text{F}]\text{F}^-$ ) is known.<sup>12,13</sup> The production method is different for  $[^{18}\text{F}]\text{F}^-$  vs.  $[^{18}\text{F}]\text{-F}_2$ , with the latter produced from deuteron-irradiation of neon. However, the former is much more common and is produced *via* proton irradiation of  $^{18}\text{O}$ -enriched water (Figure 1.2).

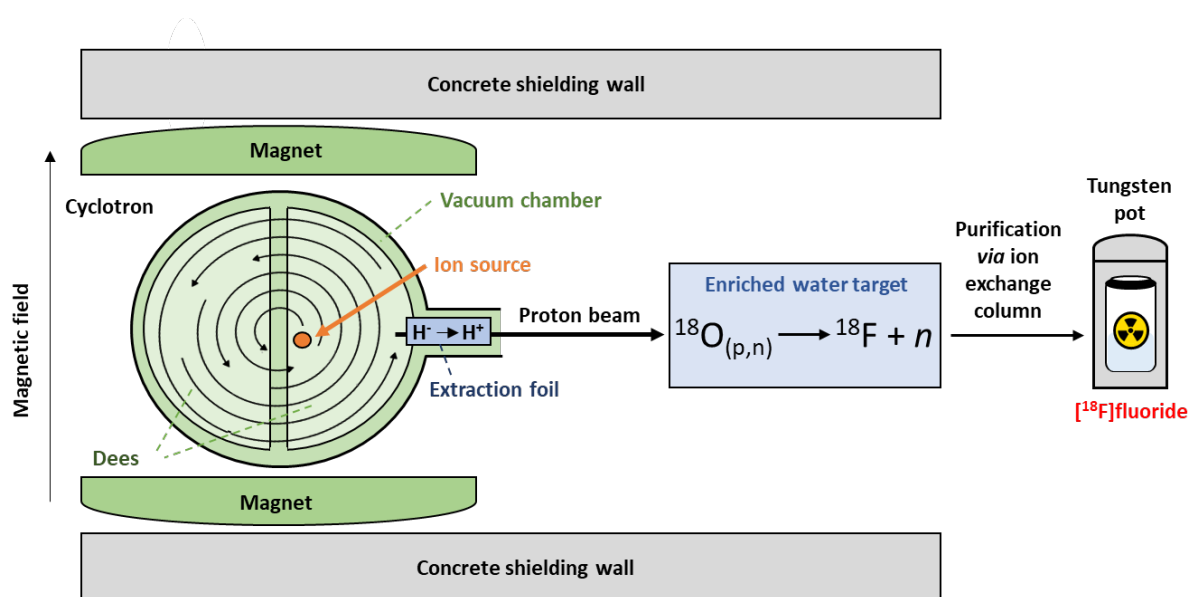


Figure 1.2 – Cyclotron production of  $[^{18}\text{F}]\text{F}^-$  via proton irradiation of  $^{18}\text{O}\text{-H}_2\text{O}$ .

As Figure 1.2 shows, a cyclotron consists of two semi-circular electrodes (called ‘Dees’ due to their shape), positioned between the poles of an electromagnet. There is a narrow gap between the two electrodes, and they are held within a vacuum chamber to avoid side reactions. During operation, a constant, uniform magnetic field is applied, and a high-frequency oscillator is used to alternate the electrical field between the two Dees.  $\text{H}^-$  is produced from the ionisation of hydrogen gas, which is injected into the centre of the cyclotron. This is then immediately

accelerated into the positively-charged Dee, where it then continues in a circular path due to the magnetic field. As it approaches the gap between the two halves, the electric field of the two Dees is reversed, and the ion is accelerated across the gap, gaining energy in the process.<sup>14</sup> This process is repeated until the ion reaches sufficient energy – for a negative-ion cyclotron (widely used for PET isotopes) a typical energy range is 10 – 20 MeV.<sup>15</sup> The ions are extracted from the cyclotron by a thin (20  $\mu\text{m}$ ) carbon stripper foil, which converts  $\text{H}^-$  to  $\text{H}^+$ , resulting in a proton beam which can be directed towards the target.<sup>16</sup>

$[\text{}^{18}\text{F}]\text{F}^-$  is produced from the  $^{18}\text{O}(\text{p}, \text{n})$  reaction, whereby an  $^{18}\text{O}$  nucleus captures a proton and ejects an energetic neutron. The secondary neutrons are the main contributors to both the radiation dose outside of the shielding and the multitude of radioactive side-products; thick concrete walls are required to effectively minimise the risk of radiation exposure.<sup>17, 18</sup> It is for this reason that purification is also required – this is performed remotely using a computerised system, due to the high levels of radiation. Depending on the use (e.g. nucleophilic substitution or isotopic/halide exchange), the  $[\text{}^{18}\text{F}]\text{F}^-$  can be processed further. Nowadays, the production of  $[\text{}^{18}\text{F}]\text{F}^-$  can be done in very high activities ( $10^2$  GBq), with moderate-to-high molar activity ( $A_m$ ), which is defined as the ratio of radioactivity of a compound with respect to its molar mass (typically 40–400 GBq  $\mu\text{mol}^{-1}$ ).<sup>19</sup>

### 1.1.2 Traditional Radiotracers and Their Limitations

Traditional approaches to  $^{18}\text{F}$  radiolabelling have often involved late-stage introduction of the isotope *via* a covalent C– $^{18}\text{F}$  bond.<sup>20</sup> Although considered a covalent bond, the C–F bond is highly polarised due to the electronegativity of fluorine. Therefore, the nature of the bond is much more electrostatic, and much stronger than a typical covalent bond (and other organic bonds). The average bond dissociation enthalpy of a C–F bond is 536 kJ  $\text{mol}^{-1}$ ; for a C–C bond, this value is 346 kJ  $\text{mol}^{-1}$ .<sup>21</sup> These characteristics make the use of C–F bonds in PET tracers advantageous, leading to greater thermal stability and lower toxicity when compared with other radioisotopes.<sup>22</sup>

Figure 1.3 depicts two of the most widely used carbon-based radiotracers: fluorodeoxyglucose ( $[\text{}^{18}\text{F}]\text{-FDG}$ ) and fluorodopa ( $[\text{}^{18}\text{F}]\text{-DOPA}$ ). Limited permeability of the blood-brain barrier is the main challenge in the design of neurological diagnostic and therapeutic agents.<sup>23</sup> However,  $[\text{}^{18}\text{F}]\text{-DOPA}$  is an analogue of levodopa, which is made naturally in the human body as a precursor to the neurotransmitter, dopamine. It is able to cross the blood-brain barrier and is primarily used for the diagnosis and examination of patients affected by Parkinson's disease.<sup>24,25</sup> It can also be used in the diagnoses of certain brain tumours and neuroendocrine tumours.<sup>26</sup> However, despite multiple medical uses and its importance as a PET radiotracer, the existing syntheses of  $[\text{}^{18}\text{F}]\text{-$

DOPA are complex and typically present low radiochemical yields.<sup>27,28</sup> This includes the electrophilic destannylation of a trimethylstannyl precursor, which remains the current most common route used in the clinic.<sup>28</sup> The former radiotracer, [<sup>18</sup>F]-FDG, is a closely related analogue of glucose and mimics its behaviour in the body. Cancerous lesions generally have increased glucose uptake and glycolysis in comparison to normal cells; [<sup>18</sup>F]-FDG can provide a valuable depiction of metabolic abnormalities before morphological changes occur.<sup>29,30</sup> The clinical production of [<sup>18</sup>F]-FDG follows a well-established synthetic route, involving the nucleophilic substitution of a mannose triflate precursor. However, the lack of specificity in the uptake of [<sup>18</sup>F]-FDG and the variable affinity for some cancers are key limitations.<sup>31</sup>

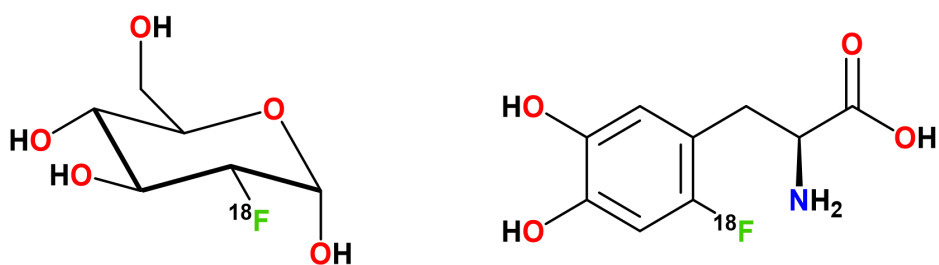
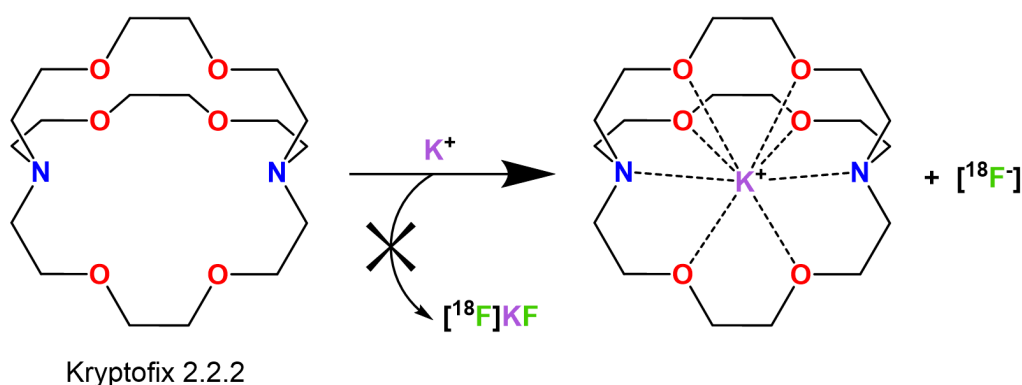


Figure 1.3 – Structures of [<sup>18</sup>F]-FDG (left) and [<sup>18</sup>F]-DOPA (right).

As mentioned, organic radiotracers are labelled *via* electrophilic substitution using [<sup>18</sup>F]-F<sub>2</sub>, or nucleophilic substitution using [<sup>18</sup>F]F<sup>-</sup>. Both come with disadvantages. Electrophilic substitution is a carrier-added, low specific-activity approach, where specific activity (A<sub>s</sub>) relates to the amount of radioactivity per gram of compound (e.g. GBq μg<sup>-1</sup>).<sup>32</sup> Fluorine-19 gas is required, to act as a carrier to extract [<sup>18</sup>F]-F<sub>2</sub> from the target. However, this means the <sup>18</sup>F nuclei are greatly outnumbered by the <sup>19</sup>F nuclei, and only a maximum of 50% of the <sup>18</sup>F produced by the <sup>20</sup>Ne(d,α) reaction can be incorporated into the final product. This synthesis, alongside the reactivity of the electrophilic fluorine, lead to a mixture of isomers and unwanted by-products. This reduces the theoretical yield further, and means extensive purification is necessary to meet the regulatory requirements for high purity pharmaceuticals.<sup>33,34</sup> Electrophilic substitution only produces [<sup>18</sup>F]-F<sub>2</sub> on a 100-600 MBq μmol<sup>-1</sup> scale, therefore synthesis of radiotracers is limited to those which do not require a high specific activity.<sup>35</sup> Conventionally, both [<sup>18</sup>F]-FDG and [<sup>18</sup>F]-DOPA were prepared *via* electrophilic substitution, but advances in the field mean better yields are now obtained *via* nucleophilic substitution.<sup>36,37</sup> Production is also limited by the number of PET centres equipped with the facilities for [<sup>18</sup>F]-F<sub>2</sub> gas production.<sup>38</sup>

In contrast, nucleophilic [<sup>18</sup>F]F<sup>-</sup> can be produced on the 10<sup>2</sup> GBq μmol<sup>-1</sup> scale.<sup>33</sup> It is typically isolated directly from the cyclotron as an aqueous solution, which is also much easier to handle than the electrophilic [<sup>18</sup>F]-F<sub>2</sub>, as leakage and contamination are minimised.<sup>39</sup> However, strong

hydrogen bonds between the  $^{18}\text{F}^-$  and  $\text{H}_2\text{O}$  result in a decrease in nucleophilicity, reducing the rate of the nucleophilic substitution reaction. Therefore, the nucleophilicity must first be increased *via* a multi-step process. This involves trapping the  $^{18}\text{F}^-$  on an ion-exchange column and subsequently eluting with an  $\text{MeCN}/\text{H}_2\text{O}$  solution containing a counter-cation complexed to a phase transfer catalyst.<sup>40</sup> This is then followed by azeotropic drying.<sup>41</sup> For the production of  $^{18}\text{F}$ -FDG and other leading and emerging organic  $^{18}\text{F}$ -radiotracers – such as  $^{18}\text{F}$ -3'-deoxy-3'-fluorothymidine ( $^{18}\text{F}$ -FLT) and  $^{18}\text{F}$ -fluoroazomycin arabinoside ( $^{18}\text{F}$ -FAZA) – potassium ions bound to Kryptofix 2.2.2 are used as the standard.<sup>42,43,44,45</sup> Kryptofix 2.2.2 is a macrobicyclic cryptand that binds to the potassium ion to prevent the formation of  $^{18}\text{F}\text{KF}$  (Scheme 1.1). Thus, the encapsulated potassium cation acts as the counter ion of  $^{18}\text{F}^-$  to enhance its reactivity but does not interfere with the synthesis. Another reason for using Kryptofix 2.2.2 is that many reagents used to synthesise these organic tracers are not tolerant of aqueous conditions. However, because Kryptofix 2.2.2 is toxic ( $\text{LD}_{50}$  (rat) = 35 mg/kg), the radiolabelled tracers must be purified further and analysed for residual levels of Kryptofix 2.2.2 before administration to patients.<sup>42,46</sup>



*Scheme 1.1 – Kryptofix 2.2.2 binds to  $\text{K}^+$  to prevent the formation of  $^{18}\text{F}\text{KF}$  and increase the reactivity of  $^{18}\text{F}^-$ .*

Often, larger and more complicated C- $^{18}\text{F}$  radiotracers – such as the dimeric cyclic RGDyK peptide,  $^{18}\text{F}$ FPPRGD2 – cannot simply undergo electrophilic or nucleophilic substitution with radioactive fluorine, and a prosthetic group is required.<sup>47,48</sup> This often consists of a small  $^{18}\text{F}$ -bearing synthon, designed to react with moieties such as amino, amido, hydroxy, carboxy and thiol groups.<sup>49,50,51</sup> However, this increases the number of synthetic steps and the overall time taken, from the production of the radioactive fluorine to the production of the final purified radiotracer. As a result, the final radiochemical yields are often poor.

## 1.2 Inorganic Approaches to $^{18}\text{F}$ Radiopharmaceuticals

With the half-life of  $^{18}\text{F}$  in consideration, radiolabelling must be fast and efficient, involving few reaction steps, simple purification processes and giving a good yield. Ideally, radiofluorination



would be done in a single step to reduce synthesis times and the risk of failure that occurs with a multi-step synthesis. There is also a requirement for radiofluorination to occur under mild conditions (ambient temperatures and neutral pH) to ensure that the labelling conditions are compatible with an array of biologically sensitive molecules.<sup>52</sup>

To this end, several inorganic fluoride complexes have been reported as possible alternatives to traditional organofluorine radiopharmaceuticals and are discussed below. These systems exploit the formation of strong bonds between transition and main group metals and fluorine, while offering lower activation energies for formation, high bond dissociation enthalpies, and the ability to incorporate  $^{18}\text{F}$  under physiologically-friendly conditions.

Many of the metals considered are examples of hard Lewis acids, which describes a species that has low-lying unoccupied orbitals capable of accepting an electron pair. These bind favourably to hard Lewis bases, such as fluoride – this describes a species with high-lying occupied orbitals, considered to be an electron-pair donor.<sup>53</sup> Hardness, or softness, refers to the polarizability of the acid or base – smaller atoms with a greater charge density are not very polarisable, and are said to be ‘hard’, and *vice versa* for soft atoms.<sup>54</sup> Where the data has been recorded, the average bond dissociation enthalpies relevant to the systems discussed in this work are given in Table 1.2.

Table 1.2 – Average M-F bond dissociation enthalpies ( $\text{kJ mol}^{-1}$ ) for the various systems relevant to or discussed in this work.<sup>55</sup>

Element	Average M-F Bond Dissociation Enthalpy, 298 K / $\text{kJ mol}^{-1}$
C	536
B	766
Al	664
Ga	577
In	506
Si	540
Sc	589
Lu	569

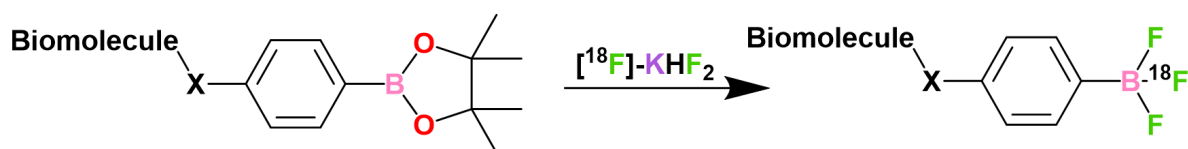
### 1.2.1 Main Group (Boron and Silicon)

This section will focus on the prevalent literature surrounding the non-metallic boron and silicon fluoride species that have applications in  $^{18}\text{F}$  PET imaging. Main group metal complexes (mainly,

aluminium and gallium) are also well-known and are directly relevant to this work. These will be discussed in further detail in *Section 1.3.3* and throughout this thesis.

#### 1.2.1.1 Organotrifluoroborate systems

Boron, the lightest of the Group 13 elements, displays an extremely high affinity for the fluoride anion, and forms strong covalent (B–F) bonds that are resistant to cleavage by biological processes.<sup>56</sup> One pathway to radiolabelled fluoroborate species takes advantage of the high stability of the B–F bond, by converting aryl boronic acids and esters to the corresponding [<sup>18</sup>F]-aryltrifluoroborate compound in a single-step, using a carrier-added source of nucleophilic [<sup>18</sup>F]-fluoride (Scheme 1.2).<sup>57,58</sup> These reactions are rapid (< 1 h), and they can be carried out in aqueous media, negating the need for time-consuming azeotropic drying of the nucleophilic [<sup>18</sup>F]F<sup>–</sup> (and is also compatible with most biomolecules). As the radiofluorination is also specific to the single boron, the synthesis is clean and does not require multiple purification steps.



Scheme 1.2 – Conversion of an aryl boronic ester conjugate to the corresponding aryl trifluoroborate conjugate using nucleophilic [<sup>18</sup>F]KHF<sub>2</sub> in an isotopic exchange reaction. X represents a linking functional group i.e an amide.

In one of the earliest examples using this chemistry towards radiolabelled compounds for <sup>18</sup>F PET imaging, Perrin and co-workers generated a biotinylated-phenylfluoroborate salt.<sup>59</sup> Their initial results showed good radiochemical yield (ca. 80%) and promising stability (no loss of <sup>18</sup>F after one hour in serum or blood). Since then, they have further developed the chemical understanding of aryltrifluoroborate systems as PET imaging agents, by altering the functional groups attached to the aromatic ring. Investigation into the hydrolytic stability of the compounds found that, in cases involving electron-deficient aryl groups, the aryltrifluoroborate undergoes hydrolysis to the corresponding boronic acid or ester.<sup>60,61</sup> However, the use of exocyclic electron-withdrawing substituents, in addition to an electron-withdrawing heteroaromatic species, improves *in vivo* stability.<sup>62</sup> For example, a heteroaryl <sup>18</sup>F-PyrBF<sub>3</sub><sup>–</sup> species (2-amino-3,5-dibromopyridyl-4-trifluoroborate) was shown to have the same kit-like radiolabelling capabilities but had enhanced solvolytic and serum stability, in comparison to an <sup>18</sup>F-ArBF<sub>3</sub><sup>–</sup> species previously reported (Figure 1.4).<sup>63,64</sup> The rate of solvolysis of the B–F bond was calculated to be 16000 min for the <sup>18</sup>F-PyrBF<sub>3</sub><sup>–</sup> vs. 1100 min for the <sup>18</sup>F-ArBF<sub>3</sub><sup>–</sup>; the former showed negligible (< 1%) degradation/defluoridation in plasma over 150 min (vs. 7% decomposition over 120 min for the latter). <sup>19</sup>F-Pyr-BF<sub>3</sub><sup>–</sup> can be readily conjugated to a peptide sequence in a simple copper-

catalysed click reaction prior to radiofluorination, with less than 45 min required for the total radiosynthetic procedure, including HPLC purification. The isotopic exchange reaction occurs in 15 min with gentle heating (40 °C) under acidic conditions (pH 2), in good radiochemical yield.

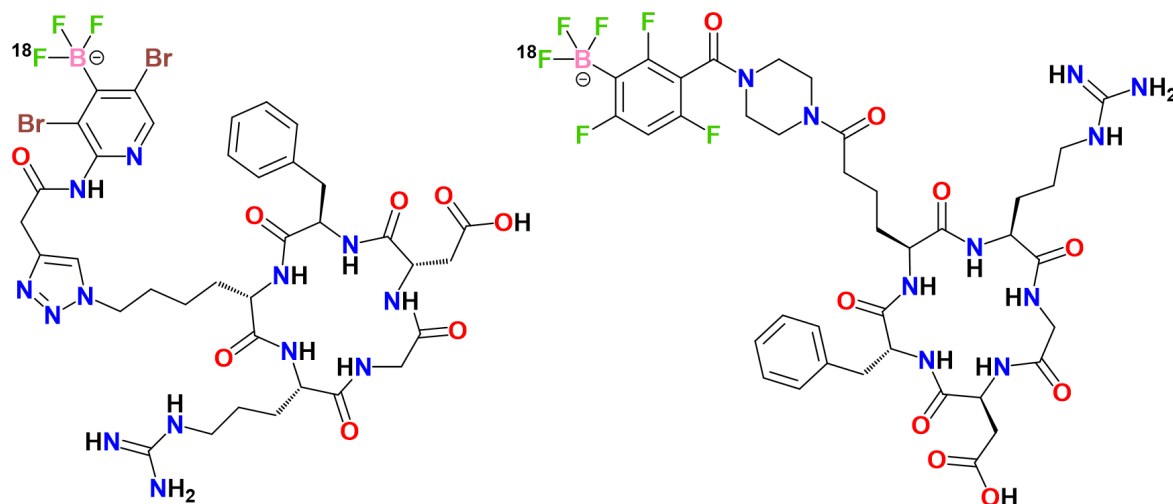


Figure 1.4 – Structures of  $[^{18}\text{F}]\text{-RGD-Pyr-BF}_3^-$  and  $[^{18}\text{F}]\text{-RGD-Ar-BF}_3^-$ .

Another approach using boron for  $^{18}\text{F}$  PET imaging purposes is *via* zwitterionic onium trifluoroborates, such as **1**, **2**, and **3** provided as examples in Figure 1.5.<sup>65</sup> Investigations into the anion-binding properties of such species show that the presence of the cationic group greatly enhances the fluoride ion affinity of the boranes.<sup>66,67</sup> These species can be radiolabelled analogously to the  $\text{ArBF}_3^-/\text{PyrBF}_3^-$  species. In addition, Gabbaï and co-workers<sup>52</sup> report a method by which the radiolabelled compounds can be accessed *via* isotopic exchange reactions; **1** has been shown to undergo fast and efficient radiolabelling (RCY = 87%) by stirring with aqueous  $^{18}\text{F}^-$  (pH 1.5) at room temperature for 20 min.

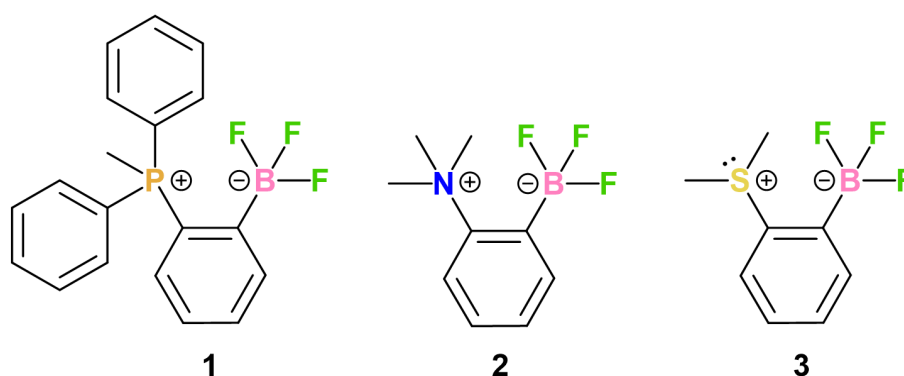


Figure 1.5 – Zwitterionic onium borates first reported by Wade et al.<sup>65</sup>

However, it has been observed that the more stable the fluoroborate is, the more difficult it is to radiolabel (due to the intrinsic thermodynamic stability of the B–F bonds).<sup>68</sup> The use of a carrier-added source of fluoride, such as tetrabutylammonium  $[^{18}\text{F}]\text{-fluoride}$  ( $[^{18}\text{F}]\text{-TBAF}$ ), and a Lewis

acid promoter (to activate the B-F bond), such as  $\text{SnCl}_4$ , can circumvent these issues – but it can lead to more complicated purification steps and lower specific activity.

Another drawback to organotrifluoroborate systems is the pH dependency of the radiochemical reactions, which will not be compatible with many biomolecules/peptides.<sup>69</sup> For the organofluoroborate ( $\text{ArBF}_3^-/\text{PyrBF}_3^-$ ) systems, acidification is necessary to form three B-F bonds (to the potassium salt of the ions).<sup>70</sup> It also reduces the concentration of competitive hydroxide anions and, therefore, the likelihood of hydrolysis to the corresponding organoboronate *in situ* (in comparison to higher/basic pH).

#### 1.2.1.2 Silicon-Fluoride-Acceptors

Silicon-fluoride compounds are of interest in terms of  $^{18}\text{F}$  radiochemistry owing to the high bond dissociation enthalpy of the Si-F bond ( $540 \text{ kJ mol}^{-1}$ ).<sup>55</sup> Additionally, the greater covalent radius of silicon vs. carbon contributes to the enhanced driving force of nucleophilic substitution at the silicon centre compared to carbon-centred analogues.<sup>71</sup> These properties are central to the development of Si- $^{18}\text{F}$  radiotracers, with some of the prominent research in this field highlighted below.

The first use of [ $^{18}\text{F}$ ]-fluorosilanes for PET imaging was proposed by Rosenthal *et al.*<sup>72</sup> in 1985, who treated chlorotrimethylsilane with  $^{18}\text{F}^-$  in aqueous acetonitrile to form the corresponding [ $^{18}\text{F}$ ]-fluorotrimethylsilane in 65% yield. However, *in vivo* results showed that the compound underwent rapid hydrolysis, accompanied by high  $^{18}\text{F}$  uptake in bone, and was subsequently ruled as being unsuitable for further radiopharmaceutical applications. It was concluded that more sterically hindered Si- $^{18}\text{F}$  compounds would have better hydrolytic stability.

With this in mind, early work by Schirmacher *et al.*<sup>73</sup> looked towards the design of silicon fluoride compounds which were stable under physiological conditions. As suggested by Rosenthal, it was found that the stability of the Si- $^{18}\text{F}$  bond was enhanced by linking sterically bulky substituents to the fluorinated silicon atom. The reaction of three different triorganochlorosilane precursors ( $\text{Ph}_3\text{SiCl}$ ,  $^t\text{BuPh}_2\text{SiCl}$ ,  $^t\text{Bu}_2\text{PhSiCl}$ ) with azeotropically dried  $^{18}\text{F}^-/\text{Kryptofix 2.2.2}/\text{K}^+$  formed the [ $^{18}\text{F}$ ]-organofluorosilane products (Figure 1.6) in an almost quantitative radiochemical yield.

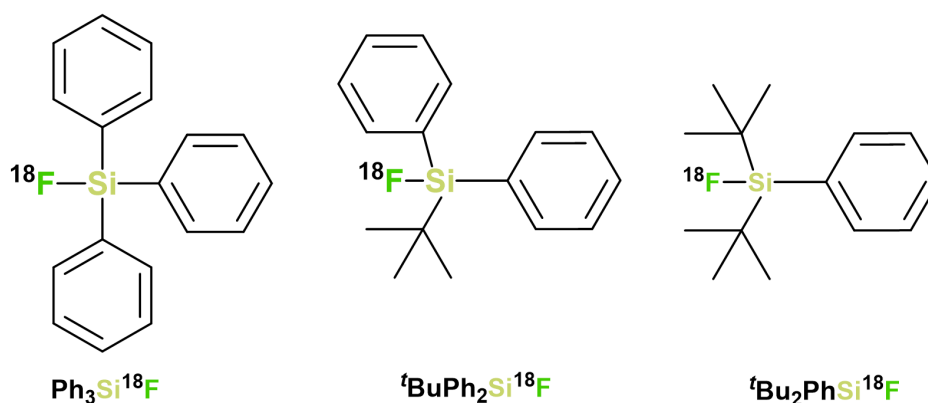


Figure 1.6 – Structures of the Si- $^{18}\text{F}$  compounds first reported by Schirmacher et al.<sup>73</sup>

*In vitro* studies showed that the tris(phenyl) compound was stable in water over 4 h, but not in human serum albumin (HSA, pH 7.4 – 7.6, 37.4 °C), with rapid degradation observed after 10 min. The mono- and di- tert-butyl precursors displayed high stability in water and in HSA, with their respective radiochemical purities maintained near 100% after 1 h. However, the use of hydrolytically unstable chloro-silanes during synthesis meant that they were incompatible for further conjugation to peptides or other biomolecules, where an aqueous work up is unavoidable.

However, from this initial work, the SiFA (silicon-fluoride-acceptor) method was developed; this involves the use of organosilicon compounds containing a central silicon atom, two tert-butyl groups, and a phenyl ring which is amenable to modifications.<sup>74</sup> The first example of a Si- $^{18}\text{F}$  radiolabelled peptide is given in Figure 1.7, which achieved radiochemical yields between 95–97% after the reaction (at room temperature, 10–15 min) of the [ $^{19}\text{F}$ ]-SiFA Tyr<sup>3</sup>-octreotate precursor with  $^{18}\text{F}$ /Kryptofix 2.2.2/ $\text{K}^+$ . Purification was achieved using an SPE cartridge-based method (details of this purification method can be found in Section 1.4.3), with isolation of the final radiotracer in radiochemical yields between 55–65%, and >98% radiochemical purity. However, *in vitro* studies using tumour-bearing mice showed that the highly lipophilic nature of the tert-butyl groups prevented efficient imaging in the target cells, as the tracer was effectively siphoned from the bloodstream by the liver, where it was found to accumulate.

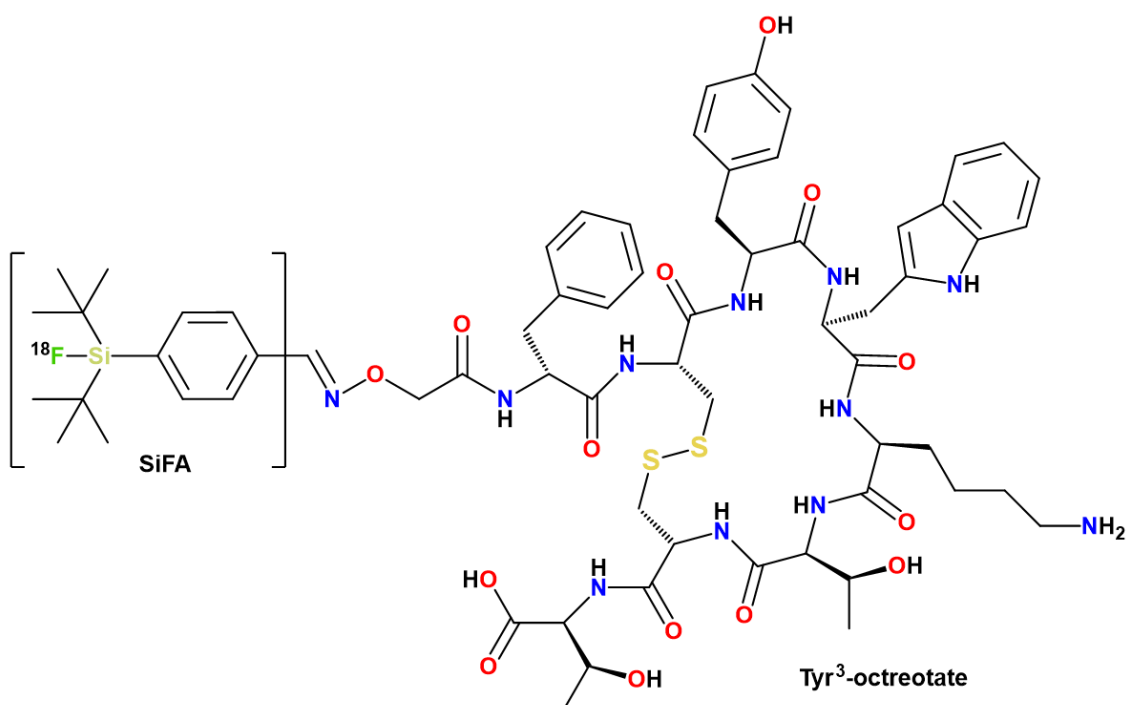


Figure 1.7 – SiFA Tyr<sup>3</sup>-octreotate system developed by Schirmacher et al.<sup>73</sup>

Later developments of SiFA-octreotate conjugates by Wängler and co-workers<sup>75,76</sup> found that the addition of functional groups with high hydrophilicity (carbohydrates and polyethylene glycols) into the peptide sequence could reduce the overall lipophilicity of the tracer. The most promising results from these systems involve the use of a permanent positive charge on the SiFA building block (SiFAlin, Figure 1.8) as well as two asparagine (Asn) side-chains and an acylated amino-sugar (AcNH- $\beta$ -Glc).<sup>77</sup> The third-generation radiotracer was synthesised in a kit-like manner, with radiochemical yields up to 53%, and showed favourable *in vivo* pharmacokinetic properties. Improvements to tumour-to-normal tissue uptake ratio and renal clearance resulted in high-quality and high-resolution PET images. Recently, this compound has been translated into the first in-human PET studies.<sup>78,79</sup>

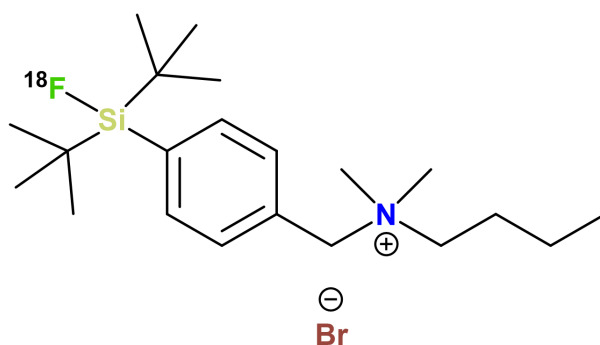
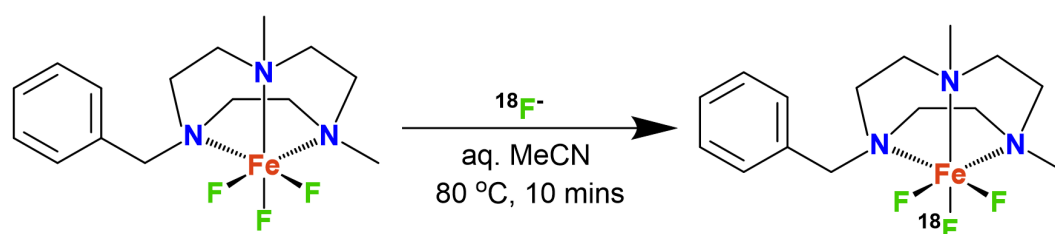


Figure 1.8 – Structure of SiFAlin developed by Wängler and co-workers.<sup>77</sup>

## 1.2.2 Transition Metal and Lanthanide Metal Fluorides

### 1.2.2.1 $\text{FeF}_3$ Complexes

Whilst the radioisotopes of several transition metals (and lanthanides) are already known in a clinical setting, until recently, there has been little research into their  $\text{M}-^{18}\text{F}$  complexes for PET imaging.<sup>80,81</sup> In 2019, work in the Reid group identified the  $[\text{FeF}_3(\text{BnMe}_2\text{-tacn})]$  complex as a suitable candidate for  $^{19}\text{F}/^{18}\text{F}$  isotopic exchange reactions (Scheme 1.3), providing the first reported example of a transition metal complex bound to  $[\text{F}^{18}]\text{F}^-$ .<sup>82</sup>



Scheme 1.3 –  $^{19}\text{F}/^{18}\text{F}$  isotopic exchange of  $[\text{FeF}_3(\text{BnMe}_2\text{-tacn})]$ .<sup>82</sup>

A range of conditions were trialed, using 2360, 236 or 24  $\text{nmol mL}^{-1}$  of precursor. A maximum radiochemical yield of 44% was achieved at a higher concentration ( $80\text{ }^\circ\text{C}$ , 10 min), compared to 6% at room temperature. However, the complex was efficiently purified using an SPE cartridge method and was shown to have excellent *in vivo* stability over two hours in a range of formulations, including 10:90 EtOH/PBS and 10:90 EtOH/HSA.

Table 1.3 – The range of reaction conditions used for  $^{19}\text{F}/^{18}\text{F}$  isotopic exchange reactions of  $[\text{FeF}_3(\text{BnMe}_2\text{-tacn})]$ . All reactions were performed in aqueous MeCN at RT or  $80\text{ }^\circ\text{C}$ , for 10 minutes.

Mass / mg	Concentration / $\text{nmol mL}^{-1}$	Temperature / $^\circ\text{C}$	RCY / %
1	2360	25	$6 \pm 1$
1	2360	80	$44 \pm 6$
0.1	236	80	$40 \pm 6$
0.01	24	80	$13 \pm 5$

This prompted the later development of a fully-automated optimised procedure for the  $[\text{FeF}_3(\text{BnMe}_2\text{-tacn})]$  complex for high-activity work.<sup>83</sup> The radiochemical procedure was translated onto a FASTLab™ synthesis platform (GE Healthcare), with optimisation and automation reported using up to 30 GBq of  $[\text{F}^{18}]\text{-fluoride}$  during the synthesis. Radiofluorination was successful, with radiochemical yields of 42% obtained at high activity. However, higher levels of radioactivity can significantly impact the stability of the radio-product, and a reduction in radiochemical purity from 97% to 78% was observed over five hours, owing to degradation

promoted by radiolysis. Addition of a radio-stabiliser (nicotinamide) improved the stability of the radio-product at high-activity, with radiochemical purity decreasing to only 86% after four hours (in EtOH).

When translating radiopharmaceuticals from a research lab into a clinical setting, implementation of and compliance with good manufacturing practices (GMP) is required. Automated techniques allow the production of a consistent and reproducible product and enable the safe use of radionuclides at a higher activity. For  $^{18}\text{F}$ -labelled PET imaging probes, this is generally within the 50 – 500 GBq range.<sup>84,85</sup> The successful development of an optimised protocol for the automation of the [ $^{18}\text{F}$ ]-fluoride radiolabelling of [ $\text{FeF}_3(\text{BnMe}_2\text{-tacn})$ ] at higher activity provided proof-of-concept that these types of systems may be suitable for later work containing bioconjugated peptides and provided a good starting point for optimising these systems.

Subsequently, the radiochemistry of a new  $\text{Fe-}^{18}\text{F}$  system involving a bis(phosphinate) triazacyclononane ligand has been reported, alongside its  $\text{Ga-}^{18}\text{F}$  analogue.<sup>86</sup> Both will be discussed in *Section 5.1.1.1* within Chapter 5 of this work.

#### *1.2.2.2 ‘Theranostic Pairs’ – Recent Developments in the Radiochemistry of $^{47}\text{Sc-}^{18}\text{F}$*

‘Theranostics’ refers to the combination of a therapeutic agent and diagnostic tool that share a specific target in diseased cells or tissues.<sup>87</sup> This concept has emerged from nuclear medicine; although the term was first coined in 1998, it has been applied to the imaging and treatment of thyroid diseases using radioactive iodine-131 for more than 50 years.<sup>88,89</sup> More recently, the wider accessibility of various metal radionuclides and improved imaging techniques have vastly expanded the field.<sup>90</sup>

Typically, theranostic treatment consists of a disease-related biomarker and a radionuclide. These work in tandem to deliver ionising radiation to a specific target whilst simultaneously or sequentially visualising the target through molecular imaging techniques such as PET.<sup>91</sup> Often, paired radionuclides (theranostic pairs) are used, such as a  $^{68}\text{Ga}$  tracer for PET imaging and  $^{177}\text{Lu}$  tracer ( $\beta^-$  emitter) for therapy.<sup>92</sup> General properties of selected radioisotopes mentioned in this work, often considered for theranostic applications, are given in Table 1.4, although this is not an exhaustive list.



Table 1.4 – General properties of selected radioisotopes used within the theranostic field.<sup>92</sup>

Radioisotope	Particle Emission	Theranostic Role	Half-life
<sup>18</sup> F	β+	<sup>18</sup> F PET Imaging	110 min
<sup>68</sup> Ga	β+	<sup>68</sup> Ga PET Imaging	67.7 min
<sup>177</sup> Lu	β-	Therapeutic	6.65 days
<sup>44</sup> Sc	β+	<sup>44</sup> Sc PET Imaging	3.97 h
<sup>47</sup> Sc	β-	Therapeutic	3.35 days
<sup>131</sup> I	β-	Therapeutic	8 days
<sup>90</sup> Y	β-	Therapeutic	2.67 days

With the aim to find a suitable theranostic pair involving <sup>18</sup>F, the radiochemistry of scandium with <sup>18</sup>F has been recently explored by the Boros group.<sup>93,94</sup> The Sc<sup>3+</sup> ion exhibits hard Lewis acid character, meaning it is an optimal candidate for binding hard Lewis bases such as fluoride. Hence, there is precedence for the development of a single molecule containing both <sup>18</sup>F (imaging) and <sup>47</sup>Sc (therapeutic) radioisotopes. The Boros group has previously identified a chelating, heptadentate tacn-based ligand (mpatchn) for radiometallic <sup>44</sup>Sc/<sup>47</sup>Sc and <sup>44</sup>Sc/<sup>177</sup>Lu theranostic pairs, and the ligand was shown to leave a vacant coordination site on the metal centre, otherwise bound by an inner-sphere water molecule.<sup>95</sup> By using methods directly analogous to those developed in the Al-<sup>18</sup>F chemistry, the [Sc-<sup>18</sup>F]<sup>2+</sup> species was pre-formed *in situ* followed by immediate addition of the mpatchn ligand (Figure 1.9).

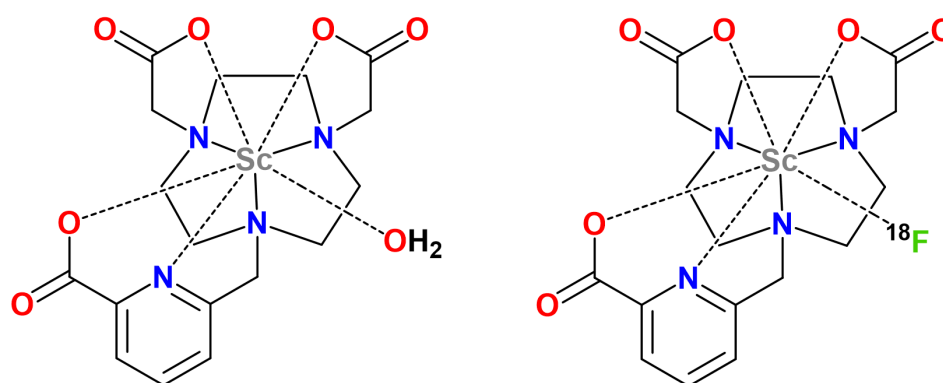


Figure 1.9 – Structures of [Sc(mpatchn)(OH<sub>2</sub>)] (left) and [<sup>18</sup>F][ScF(mpatchn)]<sup>-</sup> (right) reported by Boros and co-workers.<sup>95,93</sup>

Yields of up to 89% were observed when heated to 100 °C, which reduced to 62% at 80 °C and 20% at 60 °C (when heated for 30 min). The formation of the desired radio-product at 60 °C is an improvement from many of the Al-<sup>18</sup>F systems, with no degradation/loss of <sup>18</sup>F<sup>-</sup> observed *in vitro* (PBS, 4 h).

These early results are promising, and very recent work published by the Boros group in 2024 has explored the coordinative properties and chemical reactivity of triaza-macrocyclic ligands in terms of an  $^{18}\text{F}$ -Sc/ $^{44}\text{Sc}$ / $^{177}\text{Lu}$  theranostic triad.<sup>96</sup> The aim of this study was to identify which ligand characteristics (i.e. denticity, donor group, charge) are best suited to stabilising Sc-F, Sc and Lu, as well as improving radiochemical labelling approaches. It is later concluded that future work in this area will look towards accelerating these methods towards clinical translation.

## 1.3 Coordination Chemistry of Group 13 Macrocyclic Complexes

### 1.3.1 Macrocyclic Ligands

#### 1.3.1.1 The Macrocyclic Effect

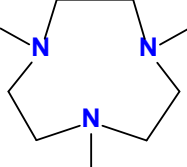
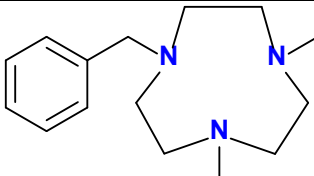
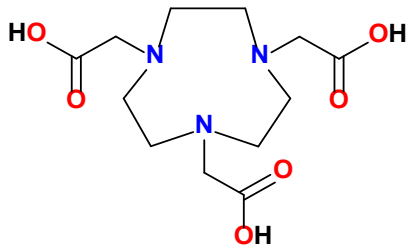
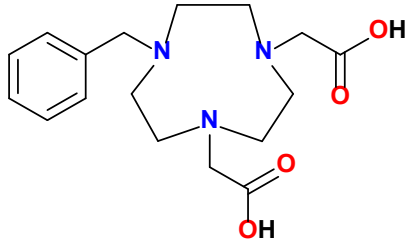
The compounds that will be discussed are bound to multi-dentate (chelating) ligands – due to their cyclic nature, these ligands are referred to as macrocycles. Any ring-structure containing a minimum of nine atoms and three donor sites (*via* heteroatoms such as nitrogen and oxygen) is defined as a macrocycle, which can be further classified by type, depending upon the donor heteroatom.<sup>97</sup> For example, macrocycles with oxygen donor atoms are referred to as crown ethers, and those with nitrogen are termed aza-macrocycles.

Macrocyclic ligands confer more stability than their acyclic counterparts due to a phenomenon called the macrocyclic effect. This is similar to the entropy-driven chelate effect; multi-dentate binding offers increased thermodynamic stability over monodentate ligands, and cyclic ligands have fewer conformational degrees of freedom when unbound in comparison to acyclic ligands. The macrocyclic effect is also greater than the chelate effect due to increased kinetic stability. Dissociation of a macrocycle from a metal centre – a process which requires distortion and elongation of the bonds – is very much energetically unfavourable. Macrocyclic bonds are known to be inflexible and robust. These properties make them ideal for radiopharmaceutical applications, as the resulting complexes are typically inert and resistant to demetallation.<sup>98</sup>

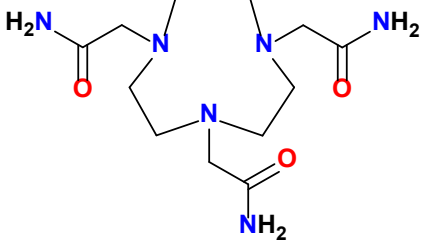
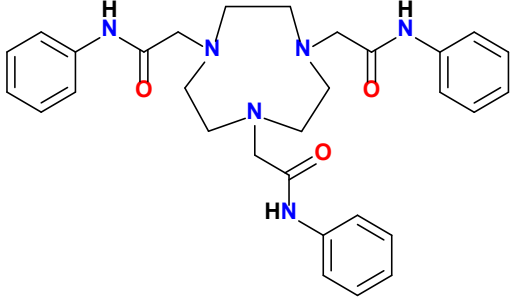
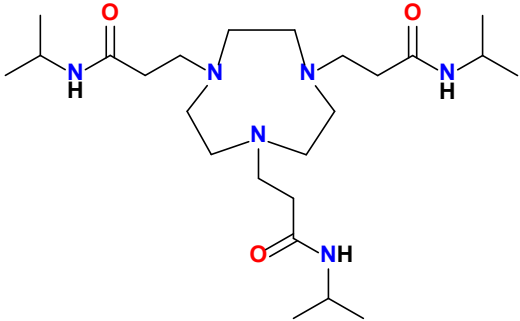
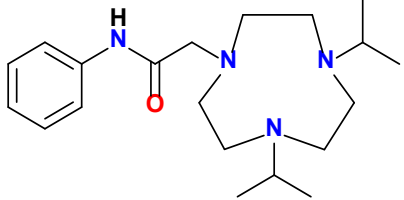
#### 1.3.1.2 Triazacyclononane Ligands Relevant to This Work

Aza-macrocycles coordinate very strongly to main group metals and transition metals. For this reason, nine-membered triazacyclononane ligands are used throughout the entirety of this work. Common triazacyclononane ligands (used within the radiopharmaceutical context) as well as those directly relevant to this work, including those mentioned below, are given in Table 1.5.

Table 1.5 – Structures, names and abbreviations for common aza-macrocyclic ligands, and those relevant to, or used within this work.

Structure	Name	Abbreviation
	1,4,7-trimethyl-1,4,7-triazacyclononane	Me <sub>3</sub> -tacn
	1-benzyl-4,7-dimethyl-1,4,7-triazacyclononane	BnMe <sub>2</sub> -tacn
	1,4,7-triazacyclononane-1,4,7-triacetic acid	H <sub>3</sub> -NOTA
	1-benzyl-4,7-diacetic acid-1,4,7-triazacyclononane	H <sub>2</sub> -Bn-NODA

	<p>1,4,7-phenylphosphinic acid-1,4,7-triazacyclononane</p>	<p>H<sub>3</sub>-NOTP</p>
	<p>1-benzyl-4,7-phenylphosphinic acid-1,4,7-triazacyclononane</p>	<p>H<sub>2</sub>-Bn-NOTP</p>
	<p>Trimethyl-1,4,7-triazacyclononane-1,4,7-triyltris[methylene(phenylphosphinate)]</p>	<p>NOTP-OMe</p>

	1,4,7-tris-carbamoylmethyl-1,4,7-triazacyclononane	TCMT
	1,4,7-tris-phenylacetamide-1,4,7-triazacyclononane	L <sup>1</sup>
	1,4,7-tris-isopropylacrylamide-1,4,7-triazacyclononane	L <sup>2</sup>
	1-phenylacetamide-4,7-diisopropyl-1,4,7-triazacyclononane	L <sup>3</sup>

### 1.3.2 General Properties and Reactivity of the Group 13 Metals

The Group 13 elements consist of boron (non-metallic), aluminium, gallium, indium and thallium (metallic). The trends observed throughout the group are similar to the other main group metals. Generally, as the atomic radii increases down the group, increased shielding from the nucleus means the valence electrons become less tightly bound. However, this is not applicable to gallium, which is reported to have a smaller atomic radius (1.35 Å) compared to aluminium (1.43 Å), due to the poor shielding offered by its inner (and more diffuse) d-orbital electrons.<sup>99</sup>

Down the group, the bonds formed by the larger, heavier atoms become less covalent in character, and can be considered increasingly more ionic.<sup>100</sup> The general increase in atomic radii also means for aluminium and beyond, complexes with coordination numbers of four to six are typically observed, as they are able to accommodate a larger coordination sphere. For the larger elements (indium, thallium), seven- and eight-coordinate species are also possible.<sup>101</sup> With one outer valence electron in the p shell and two in the s shell, the Group 13 metals can be found in either the +1 or +3 state. However, for the lighter metals (B, Al, Ga), the +1 state is very rare.

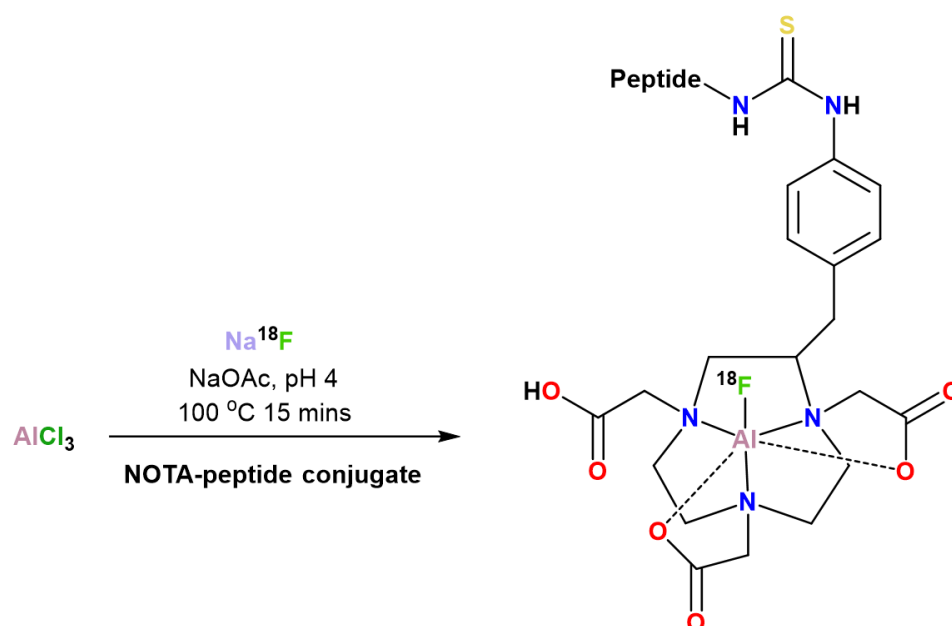
The trivalent cations of the Group 13 metals ( $B^{3+}$ ,  $Al^{3+}$ ,  $Ga^{3+}$ ,  $In^{3+}$ ) are considered hard Lewis acids, and form strong covalently bonded complexes with hard Lewis basic donor atoms such as fluoride, and nitrogen- and oxygen-donor ligands. Hence, they are described as having an inherently high fluorophilicity – although this property decreases down the group as the orbitals become larger and more diffuse (becoming less Lewis acidic).

For this reason, Group 13 fluoride complexes, particularly those of aluminium and gallium, are highly sought after for inorganic  $^{18}F$  PET imaging purposes. As such, the coordination chemistry of the Group 13 halides has been extensively explored with neutral ligands, where the +3 oxidation state dominates.<sup>102</sup> However, the anhydrous trifluoride ( $MF_3$ ,  $M = Al, Ga, In$ ) species are inert and polymeric and are, therefore, generally unreactive towards neutral ligands. The hydrates,  $MF_3 \cdot 3H_2O$ , are more reactive but poorly soluble in organic solvents and water.<sup>103</sup> Until recently, the coordination chemistry of very few  $MF_3$  complexes had been described.<sup>104</sup> Current methods towards  $MF_3$  species include halide exchange<sup>105</sup>, hydrothermal synthesis<sup>106</sup>, or *via* a molecular  $MF_3$  precursor.<sup>107</sup> Some of these examples will be given below in Section 1.3.3, and also discussed in further detail throughout this work.

### 1.3.3 Applications of Group 13 Macrocyclic Complexes in Radiochemistry

#### 1.3.3.1 $\text{Al-}^{18}\text{F}$ systems

In one of the first examples of a metal-based chelate for PET imaging applications, McBride *et al.*<sup>108</sup> reported an  $[\text{}^{18}\text{F}]\text{-AlF-NOTA}$  ( $\text{H}_3\text{-NOTA}$  = 1,4,7-triazacyclononane-1,4,7-triacetic acid) complex.  $[\text{}^{18}\text{F}]\text{F}^-$  is first attached to aluminium as  $[\text{Al}^{18}\text{F}]^{2+}$ , *via* the  $\text{Cl}/^{18}\text{F}$  exchange reaction between  $\text{AlCl}_3 \cdot 6\text{H}_2\text{O}$  (in sodium acetate buffer) and  $[\text{}^{18}\text{F}]\text{KF}$ . In a facile, one-pot synthesis (Scheme 1.4), this can then be reacted directly with the  $\text{H}_3\text{-NOTA}$  ligand, already linked to a relevant biomolecule *via* a peptide bond.



Scheme 1.4 – One-pot synthesis of an  $[\text{Al}^{18}\text{F}(\text{NOTA})]$  complex, conjugated to a biomolecule *via* a peptide bond.

This approach was later applied to a  $\text{NOTA-octreotide}$  conjugate system – octreotide is a synthetic analogue of somatostatin, and used for the detection of neuroendocrine tumours, which express somatostatin receptors.<sup>109</sup> The target  $\text{Al}^{18}\text{F}$  species was formed with high specific activity ( $45000 \text{ GBq mmol}^{-1}$ ), and *in vitro* results found it to be stable in serum for 4 h at  $37^\circ\text{C}$ . *In vivo* studies of this complex found promising results, showing excellent tumour-targeting properties. This system has since been developed further by several other groups, which has included its fully automated synthesis, compliant with good manufacturing processes (a requirement for clinical radiotracers), achieving a 26.1% radiochemical yield (10 min,  $100^\circ\text{C}$ ) which displayed high radiochemical purity and stability (96.3% up to 6 h post-synthesis).<sup>110,111</sup> In 2019, the first clinical trial using  $[\text{}^{18}\text{F}]\text{-AlF-NOTA-octreotide}$  to image neuroendocrine neoplasms using PET/CT was reported.<sup>112</sup>

Similarly, Wan *et al.*<sup>113</sup> have developed a simple, one-step lyophilized kit for a [ $\text{Al}^{18}\text{F}(\text{NOTA-PGRD2})$ ] peptide conjugate (also referred to as [ $^{18}\text{F}$ ]-alfatide), in which the entire radiosynthetic procedure only takes 20 min. Initial in-human clinical trials showed clear uptake in lung tumours, demonstrating that  $^{18}\text{F}$ -alfatide is a viable radiotracer for the assessment of angiogenesis. Like the other examples given above, high temperatures (100–120 °C) are required for the complexation.

Continuing work by the McBride group has investigated similar  $\text{Al}^{18}\text{F}$  complexes with  $\text{H}_2\text{-NODA}$  (1,4,7-triazacyclononane-1,4-diacetate) derivatives.<sup>114,115</sup> It was found that the addition of an aromatic group to a nitrogen within the cyclononane ring of  $\text{H}_2\text{-NODA}$  enhanced the yield for [ $\text{Al}^{18}\text{F}$ ]<sup>2+</sup> complexation, compared to other (alkyl and carboxyl) substituents. This can be attributed to a pentadentate  $\text{N}_3\text{O}_2$  donor set resulting in a site for  $^{18}\text{F}$  coordination, without competition from a third pendant arm.<sup>114,115</sup> A lyophilized kit-based approach has been reported, with a  $\text{H}_2\text{-NODA-MPAA}$ -containing peptide, IMP485 (MPAA = methyl phenylacetic acid) which can be chelated to [ $\text{Al}^{18}\text{F}$ ]<sup>2+</sup> rapidly with heating between 100 – 110 °C, and in good radiochemical yield (55–89%), using a simplified solid-phase extraction (SPE) cartridge-based purification method. However, while this method is compatible with the PGRD2 and IMP485 peptides, the wider clinical applications of this method are limited due to the heat sensitivity of many other relevant biomolecules.

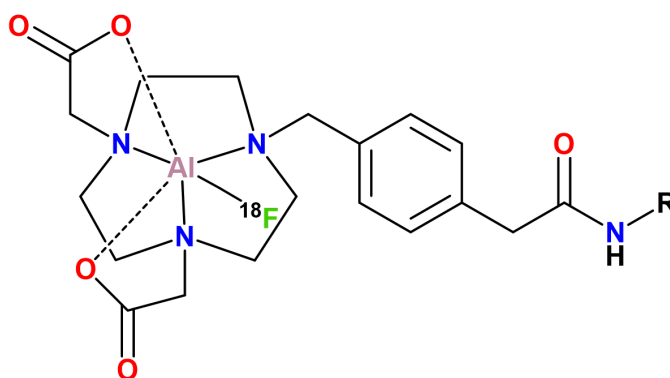


Figure 1.10 – Structure of [ $\text{Al}^{18}\text{F}(\text{IMP485})$ ] reported by McBride *et al.*<sup>116</sup>

More recently, however, Cleeren and co-workers have developed new  $\text{N}_2\text{O}_3$  acyclic ligands (Figure 1.11) that allow efficient chelation of [ $\text{Al}^{18}\text{F}$ ]<sup>2+</sup> at moderate temperature (40 °C).<sup>117,118</sup> Although  $\text{Al}^{18}\text{F-L}_\text{A}$  showed excellent radio-incorporation at room temperature (12 min, RCY > 90%), it was substantially unstable in PBS and in rat serum, resulting in significant demetallation/release of the [ $\text{Al}^{18}\text{F}$ ]<sup>2+</sup> moiety after just 10 min incubation. However, after 240 min, the  $\text{Al}^{18}\text{F-L}_\text{C}$  complex remained 77% and 66% intact in PBS and rat serum, respectively, with an RCY of 77% at 40 °C (12 min). Stability was significantly improved by the addition of a



cyclohexyl group in the ligand architecture ((±)-H<sub>3</sub>RESCA), which conferred enhanced structural rigidity in comparison to H<sub>3</sub>L<sub>A</sub> and H<sub>3</sub>L<sub>C</sub>. The [Al<sup>18</sup>F]<sup>2+</sup> complex of this particular ligand radiolabelled at room temperature in 12 min (RCY = 52–63%) and showed excellent *in vivo* stability in PBS and rat plasma (> 90% after 4 h).

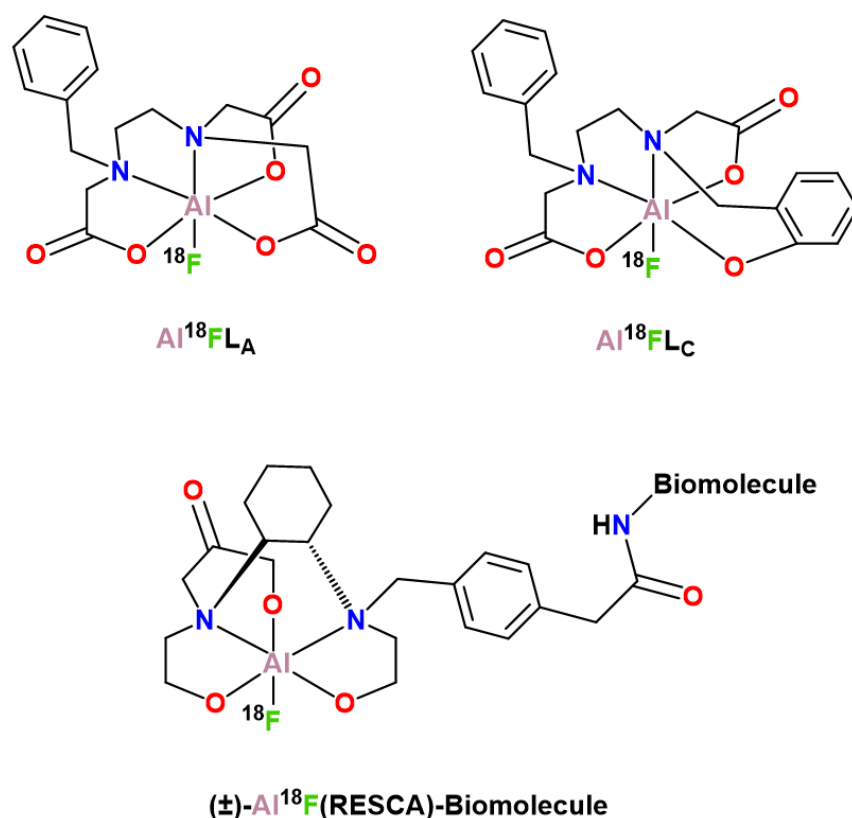


Figure 1.11 – Structures of the N<sub>2</sub>O<sub>3</sub> acyclic chelating ligands developed by Cleeren et al.<sup>117,118</sup>

### 1.3.3.2 Gallium (<sup>67</sup>Ga, <sup>68</sup>Ga)

Trivalent gallium (Ga<sup>3+</sup>) has a well-established role in the radiopharmaceutical field, with the first use of Ga radioisotopes dating back to the 1940s.<sup>119</sup> There are two main gallium radionuclides used within nuclear imaging: <sup>67</sup>Ga and <sup>68</sup>Ga. <sup>67</sup>Ga is a γ-emitter with a half-life of 3.26 days. It has been extensively used in single-photon emission computed tomography (SPECT) as a therapeutic imaging agent in various roles (such as cancer, lymphoma and infection imaging) for over 50 years.<sup>120,121</sup> This work has already mentioned <sup>68</sup>Ga, a positron-emitter, which is increasingly used in diagnostic PET imaging due to its short half-life (68 minutes) and accessibility (it can be synthesised using bench-top generators).<sup>122</sup> It is extensively used in the labelling of biomolecules, such as somatostatin and PSMA inhibitor analogues.<sup>123,124</sup>

The most prominent <sup>68</sup>Ga radiopharmaceuticals include the tetraaza-macrocyclic compounds, <sup>68</sup>Ga-DOTATOC, <sup>68</sup>Ga-DOTATATE (Figure 1.12) and <sup>68</sup>Ga-DOTANOC which are currently in use for

imaging somatostatin receptors.<sup>10</sup> However, harsh conditions (high temperature and low pH) are often required for the chelation of the H<sub>4</sub>-DOTA derivatives to <sup>68</sup>Ga<sup>3+</sup>, which – like much of the work surrounding the Al<sup>18</sup>F chemistry – will not often favour conjugated biomolecules.

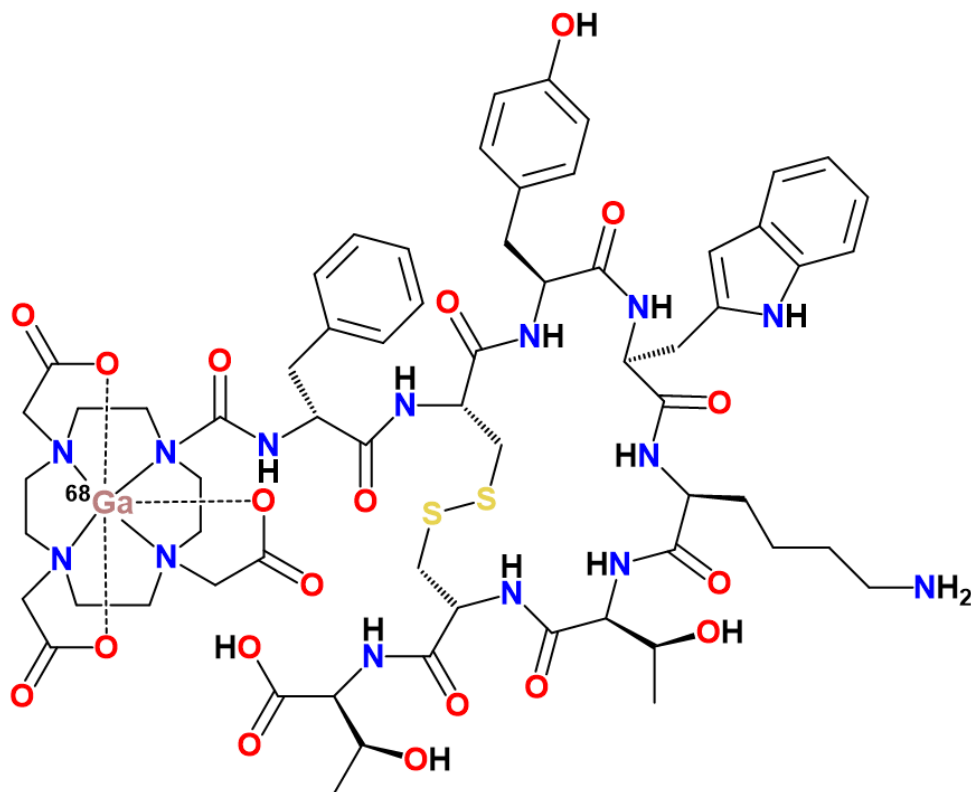


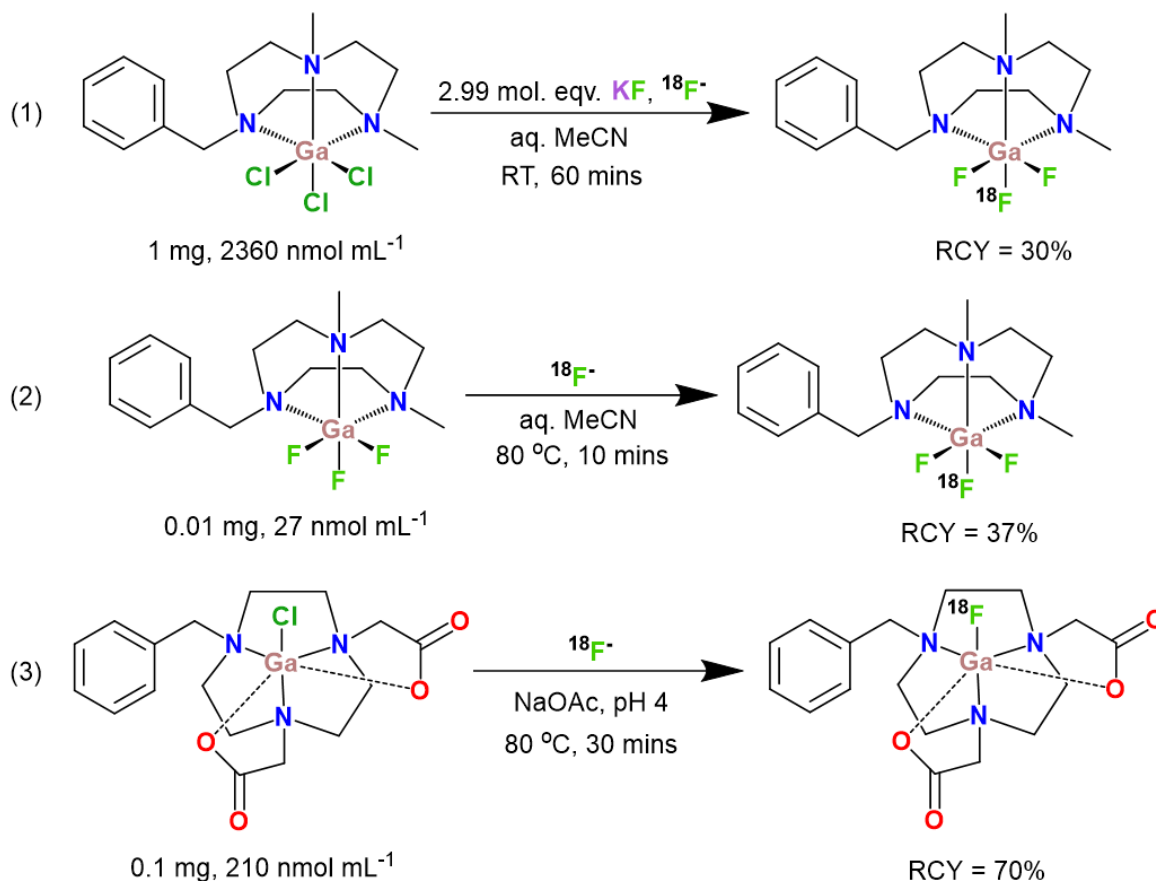
Figure 1.12 – Structure of the tetraaza-macrocylic PET imaging agent, [<sup>68</sup>Ga]-[Ga(DOTATATE)], used for the diagnosis of neuroendocrine tumours.

More recently, triaza-macrocylic ligands (primarily, H<sub>3</sub>-NOTA derivatives) have been shown to possess superior <sup>68</sup>Ga binding abilities, in comparison to the H<sub>4</sub>-DOTA systems.<sup>125</sup> Currently, several H<sub>3</sub>-NOTA-derived <sup>68</sup>Ga radiopharmaceuticals are being assessed in clinical trials.<sup>126,127,128</sup> Additionally, triazacyclononane-phosphinate (TRAP) chelators – such as the tris-phosphinic acid tacn ligand, H<sub>3</sub>-NOTP – have also shown favourable binding properties with <sup>68</sup>Ga. Due to the pentavalency of the pendant arm phosphorus atom, their main advantage over the H<sub>3</sub>-NOTA systems is the ability to functionalise all three arms, whilst retaining tridentate coordination to gallium *via* the three ring-nitrogen atoms.<sup>129</sup> TRAP-based ligands have been used to form a wide range of <sup>68</sup>Ga radiotracers, which can be conjugated to several biological target structures.<sup>130</sup>

#### 1.3.3.2.1 Previous Work in the Reid Group (Ga–<sup>18</sup>F)

The success of using triazacyclononane ligands for stable coordination to Ga<sup>3+</sup>, combined with the strength of the Ga–F bond, has opened up the potential of inorganic-based radiochemistry, with the option of using gallium fluoride macrocyclic complexes in <sup>18</sup>F PET imaging. Much of the

surrounding literature will be discussed in Chapter 4 and Chapter 5 of this work, with a brief overview given below – Scheme 1.5 shows the general radiochemistry of Ga- $^{18}\text{F}$  developed within the Reid group.



Scheme 1.5 – Various Ga- $^{18}\text{F}$  radiochemical experiments explored previously in the Reid group.<sup>105,131,132</sup> (1) =  $\text{Cl}/^{18}\text{F}$  isotopic exchange of  $[\text{GaCl}_3(\text{BnMe}_2\text{-tacn})]$ ; (2) =  $^{19}\text{F}/^{18}\text{F}$  isotopic exchange of  $[\text{GaF}_3(\text{BnMe}_2\text{-tacn})]$ ; (3) =  $\text{Cl}/^{18}\text{F}$  isotopic exchange of  $[\text{GaCl}(\text{Bn-NODA})]$ .

Some of the first examples of gallium trifluoride triaza-macrocyclic complexes were prepared by  $\text{Cl}/^{19}\text{F}$  halide exchange reactions of the analogous  $\text{GaCl}_3$  complex, forming the neutral  $[\text{GaF}_3(\text{Me}_3\text{-tacn})]$  and  $[\text{GaF}_3(\text{BnMe}_2\text{-tacn})]$  species.<sup>105</sup> The  $[\text{GaCl}_3(\text{BnMe}_2\text{-tacn})]$  complex was later translated to  $^{18}\text{F}$  radiolabelling reactions (Scheme 1.5 (1)), where radiofluorination was observed at room temperature in aqueous media (30–60 min), but not at concentrations lower than  $0.26 \mu\text{mol mL}^{-1}$ .<sup>105</sup> In contrast, the  $\text{Al}^{18}\text{F}$  systems have repeatedly been shown to radiolabel at tracer concentration ( $< \text{nmol}$  of Al precursor). This was attributed to slow hydrolysis of the Ga–Cl bond competing with the  $^{18}\text{F}^-$  coordination.

The inertness of the Group 13 fluoride species has traditionally been a limiting factor in the formation of  $\text{MF}_3$  complexes. However, later developments led to the formation of the  $[\text{GaF}_3(\text{dmsO})(\text{OH}_2)_2]$  precursor, which could be used to form  $\text{M}^{19}\text{F}_3$  complexes under ambient

conditions *via* direct addition to the desired ligand.<sup>107</sup> The pre-formed  $[\text{GaF}_3(\text{BnMe}_2\text{-tacn})]$  complex can be radiolabelled at much lower ( $\text{nmol mL}^{-1}$ ) concentrations (Scheme 1.5 (2)).<sup>131</sup>

With the success of using the  $\text{H}_2\text{-Bn-NODA}$  ligand and its derivatives with  $\text{Al-}^{18}\text{F}$ , other work in the group has looked at the formation of the corresponding  $[\text{Ga}^{18}\text{F}(\text{Bn-NODA})]$  complex *via*  $\text{Cl}/^{18}\text{F}$  halide exchange of  $[\text{GaCl}(\text{Bn-NODA})]$  (Scheme 1.5 (3)).<sup>132</sup> Despite successful radiofluorination at  $80^\circ\text{C}$  (achieving up to 70% RCY), the radiolabelled gallium complex did not exhibit the same stability as the aluminium complexes. This indicates that the stronger Lewis acidic nature of the  $\text{Al}^{3+}$  metal is more appropriate for stabilising the anionic  $\text{COO}^-$  coordination.

The radiochemistry described in this work (Chapter 5) will consider gallium trifluoride complexes bound to neutral triazacyclononane ligands with amide pendant donors ( $\text{L}^1$  and  $\text{L}^3$  – Table 1.5). The work described above will serve as a guide to help identify optimal conditions for the radiofluorination of these novel complexes.

#### 1.3.3.3 Indium ( $^{111}\text{In}$ )

Indium is also well-established in the context of nuclear medical imaging. Like  $^{67}\text{Ga}$ ,  $^{111}\text{In}$  is a  $\gamma$ -emitter with a half-life of 2.8 days. It is used in SPECT to image antibodies with longer biological half-lives. Current radiopharmaceuticals containing indium-111 involve open-chain or macrocyclic chelating agents, similar to the inorganic  $^{18}\text{F}$ -containing complexes discussed for PET imaging applications.<sup>133</sup> A fundamental component of many radiopharmaceuticals is the chelating or macrocyclic ligand – this ensures the (radio)metal is bound in a stable coordination sphere, increasing stability and effectively supplying a site-specific radioactive source *in vivo*.<sup>134</sup>

## 1.4 Radiochemistry and Characterisation of Radio-Products

### 1.4.1 Radiation Safety Measures

The radiolabelling experiments carried out in this work were conducted at St Thomas' Hospital (London), where King's College London have research laboratories with the appropriate radiochemical safety measures in place. The hospital has an on-site cyclotron for the production of target water,  $[\text{}^{18}\text{F}]\text{F}/\text{H}_2\text{O}$ , which is used for research and clinical purposes.

The handling of radiation requires very strict containment and protection protocols. The radioactive material was collected (and stored) in tungsten pots and used only in lead-lined workstations (Figure 1.13), to shield users and limit radiation exposure. The amount of radioactive fluoride per user per day was limited to a maximum of 1500 MBq, which was usually obtained in a 1 mL aqueous solution. In the context of this work, radiochemical experiments used 0.25 mL of the  $[\text{}^{18}\text{F}]\text{F}/\text{H}_2\text{O}$ , achieving between 100 – 250 MBq of radioactivity per experiment

(this was measured prior to each experiment, using a Capintec), accounting for radioactive decay and the short half-life of  $^{18}\text{F}$ .



Figure 1.13 – Lead-lined workstation used in the KCL research labs at St Thomas' Hospital.

Body and finger dosimetry (worn as a chest badge, and as a ring per hand) are required to monitor the amount of radiation exposure over time. These are replaced every two months, and the total exposure within this period is recorded. This ensures users do not exceed the government-set dose limits for radiation workers (20 mSv per year).<sup>135</sup> All radioactive work is performed in a lead-lined workstation (as mentioned above), or in fume hoods equipped with lead brick enclosures when heating apparatus is needed. In the context of this work (when radiochemical experiments required heating), a heating mantle or a GE FASTLab™ were available. When possible, the FASTLab™ was used, as it was contained within a separate fume hood with space for only one reaction at a time; the alternative KCL heating blocks often contained more than one radiation source at a time.

Extra-long tongs are used whilst handling any radioactivity, to maximise the distance between user and radioactive source. Lead-lined syringes and pots are used to transport radioactivity within the lab. Radioactive waste is collected in clearly labelled sharps bins (contaminated syringes, vials, needles etc.).

As per the local radiation rules, personal contamination monitoring (using Berthold radiation monitors) must be carried out and recorded at regular intervals and at any time prior to leaving the lab.

### 1.4.2 General Radiolabelling Techniques

The radiolabelling of inorganic halide complexes is typically performed using two methods:  $^{19}\text{F}/^{18}\text{F}$  isotopic exchange, or  $\text{Cl}/^{18}\text{F}$  halide exchange. Typically, for halide exchange reactions of  $[\text{MCl}_3(\text{ligand})]$  complexes, a  $^{19}\text{F}$  carrier agent (e.g.  $\text{KF}$ ,  $\text{NMe}_4\text{F}$ ,  $\text{NBu}_4\text{F}$ ) will be required, to form the target  $\text{M}^{18}\text{F}^{19}\text{F}_2$  complex. However, in this work, only  $^{19}\text{F}/^{18}\text{F}$  isotopic exchange reactions of  $\text{MF}_3$  complexes will be considered; the systems selected for radiochemical studies herein build upon previous work in the group, which demonstrated that the formation of  $\text{MCl}_3$  complexes with the ligands was not possible under the conditions trialled.<sup>136</sup> Radiochemical experiments were performed using either KCL equipment (Eppendorf vials, heating mantle) or GE Healthcare equipment (FastLAB™ reaction vessels, FastLAB™ heating block). In addition to lessened radiation exposure, the advantage of the FastLAB™ compared to the KCL heating block is improved contact from the heat source to the reaction vessel. However, no discernible differences in the radiochemical reactions (under the same conditions with the same complex) were observed between the two heating methods.

A typical isotopic exchange reaction (in relation to this work) first involves the dissolution of the precursor complex (1 – 2 mg) in an appropriate solvent (0.75 mL, MeCN or MeOH), followed by the addition of  $[\text{}^{18}\text{F}]\text{F}^-$  target water (0.25 mL, 100 – 250 MBq). The amount of radioactivity in the reaction mixture is recorded using a Capintec. When required, the reaction mixture was heated (60 – 80 °C) for 10 – 30 min. Chapter 5 will further discuss the radiochemistry undertaken in this work, with specific details of the experimental conditions given in *Section 5.4*.

Once the reaction is complete, a small aliquot of the mixture is diluted with water (to contain around 10% organic content), and the crude radio-product is analysed *via* high-performance liquid chromatography (HPLC). The HPLC is fitted with UV and radio-detectors – providing a complex has a chromophore, a UV trace will be obtained alongside a radiotrace. This allows the chromophore to be tracked in the radio-product, helping to confirm its identity. The radiotrace will almost always contain an additional peak for unreacted  $[\text{}^{18}\text{F}]\text{F}^-$ . Hence, the radiochemical yield of the reaction is obtained by integration of the two radio-peaks. A UV-HPLC trace of the inactive ( $^{19}\text{F}$ ) species is obtained prior to radiolabelling, which acts as a reference standard to enable the identification of the desired radio-product. The retention time ( $R_t$ ) will be dependent upon the nature of the complex and its interaction with the column. If the desired product is formed, a purification step can be carried out as discussed below.

### 1.4.3 Purification via Solid-Phase Extraction and Stability Studies

If the desired radio-product has been identified in the crude analytical HPLC trace, purification can be performed using a solid-phase extraction (SPE) protocol. Purification is also possible using prep-HPLC methods, although this is more time-consuming and complex.<sup>137</sup> SPE-based purification is essential for radiotracer development, as it is a necessary requirement for translation to clinical use.

SPE protocols require the use of a cartridge, such as a quaternary methylammonium (QMA) or hydrophilic lipid-balanced (HLB) cartridges – both frequently used in  $^{18}\text{F}$  radiochemistry.<sup>138,139,140,141</sup> QMA cartridges can be used to trap and separate anionic species (such as  $^{18}\text{F}^-$ ) whilst HLB cartridges are universal reverse-phase cartridges, and are used to trap and separate a range of basic, neutral or acidic species. This work utilises HLB cartridges, with the aim to trap the desired radio-product and remove any unreacted  $^{18}\text{F}^-$ . This is done in four stages:

- 1) Preparation – the HLB cartridge is prepared by washing with ethanol, then followed by water. This is to remove any impurities which may be on the cartridge prior to use.
- 2) Load – the crude reaction mixture is diluted with water and then passed through the HLB cartridge, trapping the desired product.
- 3) Wash – the trapped product is washed with water to remove any unreacted  $^{18}\text{F}^-$ .
- 4) Elute – the radio-product can then be eluted using a small amount of organic solvent. In this work, this was done using EtOH (1 mL).

The organic solution containing the purified product can then be formulated in water or in pH 7.4 aqueous phosphate-buffered solution (PBS). The stability and radiochemical purity (RCP) of the product in both formulations can then be monitored over various time intervals (often between 0 and 240 minutes, accounting for the half-life of  $^{18}\text{F}$ ) *via* HPLC analysis. Ideally, the starting RCP of the product will be > 90%, with minimal change over this time period. As well as degradation due to inherent instability of the radio-product in competitive media, a common reason for any observed instability (measured by the increase of the  $[^{18}\text{F}]\text{F}^-$  peak in the radiotrace) is attributed to radiolysis. This describes the degradation process of the radio-product induced by free radicals, which are produced by interaction of ionising radiation and water. Radicals, such as  $\text{OH}^\bullet$ ,  $\text{H}^\bullet$  and  $\text{O}_2^{\bullet-}$ , can interact with the radiolabelled compound and induce  $[^{18}\text{F}]\text{F}^-$  liberation from the radiolabelled complex. This can be prevented *via* the addition of a radiostabiliser (a non-toxic radical scavenging antioxidant) to the formulated solution of the product, although



this was not used in this work. Another key contributor to instability is hydrolysis, due to the presence of hydroxide (OH<sup>-</sup>) anions at higher pH.

#### 1.4.4 High-Performance Liquid Chromatography (HPLC) Analysis

HPLC is a method which can allow for the identification, quantification, separation and purification of species in a reaction mixture. It is extensively used throughout radiochemistry (especially where work is typically done using very small quantities of a sample), as it is a very sensitive technique which can detect picomolar ( $10^{-12}$  mol) concentrations of a sample.

During this work, an analytical HPLC method was employed, using an Agilent 1260 Infinity II HPLC system (KCL) or an Agilent 1290 HPLC system (GE Healthcare). The general principles of the two systems are the same, with the only two noteworthy differences being the load method (manual injection for KCL; automated for GE Healthcare) and the associated analytical software. For the purposes of this work, initial (trial) experiments were performed using the KCL HPLC system. Final experiments with the optimised radiolabelling conditions and stability studies were performed using the GE Healthcare HPLC system, with help from GE Healthcare colleague, Dr Graeme McRobbie.

An analytical HPLC experiment consists of a sample dissolved in a suitable solvent (typically a 90:10 ratio of water to organic content), a loop of a size appropriate to the injection volume (for the KCL HPLC, typically 20  $\mu$ L) or an automated arm for injection (GE Healthcare system), a pump, a mixture of solvents (typically A and B, making up the mobile phase), a column (stationary phase) and a UV and radiation detector. The pump pushes the mobile phase and the sample onto the column, where the species are separated depending on the nature of the interaction of the species in the mixture with the column. The separate fractions elute from the column at different retention times ( $R_t$ ) and are subsequently detected by the radio-detector and/or the UV detector. These signals are reprocessed to result in the observable analytical HPLC traces.

During this work a reverse-phase HPLC method was employed, consisting of a polar mobile phase and a silica C<sub>18</sub> column. Hydrophilic species are eluted at a shorter  $R_t$  due to little interaction with the column (i.e. [<sup>18</sup>F]F<sup>-</sup>), whilst species containing more organic moieties will elute with a longer  $R_t$ . The gradient of the mobile phase can be adjusted to improve the separation between species. A UV-detector adjoined with a radio-detector allows for identification (based on  $R_t$ ) and quantification (based on the integration of the area under the curve) of species in the HPLC trace.



## 1.5 Characterisation Techniques

Prior to any radiochemical experiments, the coordination chemistry of the ligands and complexes within this work will first be analysed using a variety of techniques, detailed below.

### 1.5.1 Infrared Spectroscopy

Infrared (IR) spectroscopy is a characterisation technique used to determine which types of bonds and functional groups are present within compounds. Each bond within a molecule has a defined set of vibrational energy levels – if infrared radiation of a specific energy corresponds to the energy of a particular vibrational level, then it will be absorbed, resulting in a net change in dipole moment. Subtraction of these absorbed energies from a pre-recorded background gives a characteristic IR spectrum.<sup>142</sup>

Group theory can also be used in conjunction with IR spectroscopy to predict how many bands are expected for a complex, and to ascertain its molecular symmetry. This is particularly useful for many of the distorted octahedral  $\text{MF}_3\text{L}_3$  complexes discussed throughout this work. Three bands in the M–X region would imply the complex is *meridional* and has  $\text{C}_{2v}$  symmetry ( $2a_1 + b_1$ ). two bands would imply it is *facial* with  $\text{C}_{3v}$  ( $a_1 + e$ ); symmetry. However, group theory does not take into account intermolecular bonding interactions. These interactions can cause the peaks to broaden, resulting in fewer observed bands due to overlap, or more bands than predicted – from splitting of degenerate modes due to solid state interactions – than group theory predicts. Therefore, it is important to note that group theory is a predictive tool to be taken as a guide and will not always correspond to experimental results, especially in solid-state compounds.

Many of the complexes discussed within this report will contain coordinated water molecules or hydrogen-bonded water. IR is useful in this case, as a broad peak above  $3000\text{ cm}^{-1}$  and a (weaker) peak around  $1700 - 1650\text{ cm}^{-1}$  will correspond to an O–H stretch and an H–O–H bend respectively.<sup>143</sup> More importantly, however, it will be most useful to help identify any relevant M–F stretches. In the context of this work, these are typically observed within  $600 - 400\text{ cm}^{-1}$  (dependent upon the metal centre). For example, the IR obtained for the Group 13 complexes of  $\text{BnMe}_2\text{-tacn}$  gave stretches ( $\text{cm}^{-1}$ ) at 635, 601 (Al–F), 526, 515 (Ga–F) and 481, 463 (In–F).<sup>105</sup>

IR will be collected as Nujol mulls in the region  $4000\text{ cm}^{-1} - 200\text{ cm}^{-1}$ . Nujol mull is useful for solid-state samples (including air-sensitive compounds) and does not require the complexes to be soluble in common solvents. This is an advantage over other techniques, such as NMR spectroscopy, although it is a destructive technique. It can also be difficult to mull hygroscopic samples, which may result in poorer quality IR spectra.

### 1.5.2 NMR Spectroscopy

Nuclear magnetic resonance (NMR) spectroscopy is a highly sensitive characterisation technique that exploits the magnetic properties of atomic nuclei, to give detailed information on the physical and chemical properties of the atoms or molecules in which they are contained.

The nuclei studied in this project include:  $^1\text{H}$ ,  $^{13}\text{C}$ ,  $^{19}\text{F}$ ,  $^{31}\text{P}$ ,  $^{27}\text{Al}$  and  $^{71}\text{Ga}$ . Their NMR properties, along with other relevant nuclei, are detailed in Table 1.6.

Table 1.6 – General NMR properties of the nuclei studied within this project.<sup>144</sup>

NMR Nucleus	Nuclear Spin ( <i>I</i> )	Chemical Shift Range / ppm	Natural Abundance / %	Quadrupole Moment (Q) / $10^{-28} \text{ m}^2$
$^1\text{H}$	1/2	13	99.9	n/a
$^{13}\text{C}$	1/2	200	1.1	n/a
$^{19}\text{F}$	1/2	700	100	n/a
$^{31}\text{P}$	1/2	500	100	n/a
$^{27}\text{Al}$	5/2	400	100	0.15
$^{71}\text{Ga}$	3/2	1436	39.9	0.11
$^{69}\text{Ga}$	3/2	1436	60.1	0.17
$^{115}\text{In}$	9/2	1100	95.7	0.77

The nuclei of all atoms have an intrinsic property called nuclear spin (*I*), and an associated magnetic moment. Upon the application of an external magnetic field, some nuclear spin states will be aligned accordingly. Those spins which align with the magnetic field are lower in energy, and *vice versa*. The nucleus will always attempt to orientate to the lowest energy. Although this is always possible for nuclei with  $I = \frac{1}{2}$ , this is not possible for nuclei with spin  $> \frac{1}{2}$  (known as quadrupolar nuclei). This is because the nuclei are unable to find an orientation with the lowest energy, where several orientations are possible. In an NMR experiment, a radiofrequency is used to excite the spins into the highest energy state. The energy lost by the relaxation back down to the lower energy states is picked up by a detector, resulting in the characteristic NMR spectrum.<sup>145</sup>

For quadrupolar nuclei such as  $^{115}\text{In}$  and  $^{69}\text{Ga}$ , the associated quadrupole moment significantly reduces the lifetime of the excited state, so relaxation is much faster than for nuclei with  $I = \frac{1}{2}$ . This results in significant line broadening except when the nucleus is in a regular  $\text{O}_h$  or  $\text{T}_d$  environment. This is also true of paramagnetic molecules, wherein their unpaired electron has a much larger magnetic moment than nuclei (658 times greater). This can produce large fluctuating local magnetic fields, effective at relaxing nuclei. Relaxation times from the excited

state to the lower energy states are also much quicker (on a timescale of milli- to micro-seconds, vs. seconds for standard NMR nuclei).<sup>146</sup> Most of the transition metal complexes discussed in Chapter 3 are expected to be paramagnetic and unsuitable for NMR spectroscopy.

Resonances of nuclei close to quadrupolar nuclei are also expected to be broadened, which should be considered in the analysis of the gallium and indium complexes in this work. Additionally, although <sup>69</sup>Ga is almost twice as abundant as <sup>71</sup>Ga, <sup>71</sup>Ga is the isotope of choice for gallium NMR in this work, due its smaller quadrupole moment; linewidths are up to three times narrower (than <sup>69</sup>Ga), which also means there is an improved signal-to-noise ratio.<sup>147</sup> The greater chemical shift range of the heavier nuclei (<sup>19</sup>F, <sup>27</sup>Al, <sup>71</sup>Ga etc.) in comparison to <sup>1</sup>H and <sup>13</sup>C also needs to be considered – the chemical shifts will be much more sensitive to the environment of the nucleus (such as oxidation state, coordination number, and nature of coordinated ligands).

The <sup>27</sup>Al and <sup>19</sup>F NMR spectra are also expected to have broadened baselines due to the presence of Teflon and aluminium in the NMR probes. For <sup>19</sup>F NMR, sharp features relating to F<sup>-</sup> and [HF<sub>2</sub>]<sup>-</sup> are also very common (around -130 and -150 ppm, respectively, dependent on NMR solvent).

### 1.5.3 Mass Spectrometry

Mass spectrometry (MS) is a useful technique which can provide both qualitative (structural) and quantitative (molecular mass) information. In a mass spectrometer, the sample is first introduced to an ionisation source, where the molecules are converted into ions – these can be positively or negatively charged, depending on the chosen technique. Then, these ions will travel through a mass analyser, at a rate dependent on their mass-to-charge ( $m/z$ ) ratio. A detector will pick up the ions, generating an electrical signal, which will be recorded and displayed as a mass spectrum.

Electrospray ionisation (ESI) is a soft ionisation technique that results in little fragmentation. It is used extensively in the characterisation of peptides, macromolecules, organometallics, coordination complexes and other compounds prone to fragmentation.<sup>148</sup> As the sample is in an aerosol, it is also suitable for high molecular weight species (including metal complexes of macrocyclic ligands) and salts. It is also very sensitive, and only requires micromolar quantities of the sample to be analysed. This is typically dissolved in a volatile solvent such as MeOH or MeCN, which is readily evaporated in the MS chamber, which is under a vacuum.

In relation to the metals used in this work, their natural abundances and respective isotope patterns will give a characteristic distribution of peaks in the mass spectrum, which can be easily identified. Isotope patterns can be readily simulated for comparison. Assignments require a good match between the observed  $m/z$  peak and the isotope pattern.

Whilst ESI MS can provide evidence for the formation and purity of the sample analysed, some of the systems described in this work may not be easily ionised. In these instances, the relevant  $m/z$  peak would not be observed. However, when used in conjunction with other spectroscopic techniques, it is an invaluable characterisation tool.

#### 1.5.4 Elemental Analysis

Elemental analysis (also called microanalysis or combustion analysis) is a technique in which a sample is analysed to determine its elemental composition. In the context of this report, CHN analysis will be used. To determine the percentages of these elements within a compound, the sample is first burnt in an excess of  $O_2$ . The gaseous combustion products that form as a result (such as  $CO_2$ ,  $H_2O$ ,  $N_2$ ) are trapped and quantified, to give an accurate measure of their percentage amounts. Suitable results require the percentage compositions to be within  $\pm 0.4\%$  of the theoretical composition, typically.

This method is particularly useful in determining the molecular formula of the bulk sample, assessing the purity of the compound, and whether the compounds are solvent-free (and if not, the nature of the solvate and its extent). It can be combined with other techniques to confirm the presence of any solvent molecules. However, this is a destructive technique which requires a minimum of 5 mg of sample for accurate analysis.

Elemental analysis will be performed offsite and outsourced to Medac.

#### 1.5.5 UV-Vis Spectroscopy

Ultraviolet-Visible (UV-Vis) spectroscopy refers to absorption or reflectance spectroscopy within the ultraviolet and visible range of the electromagnetic spectrum. Within this region, atoms and molecules undergo electronic excitation, whereby valence electrons are promoted across atomic orbitals. Given that atomic orbitals can be associated with discrete, quantised energy levels, only specific frequencies of electromagnetic radiation will promote an electron across the energy gap. Each excitation can be associated with a specific electronic transition, such as a  $d-d$  electron transition or ligand-to-metal or metal-to-ligand charge transfer transitions (LMCT or MLCT).<sup>149</sup> Charge transfer transitions (and also intra-ligand transitions) typically occur at higher energies and can be found typically in the UV region of the electromagnetic spectrum, whereas  $d-d$  are most often observed in the visible region (380 – 700 nm).

Electronic transitions are subject to a set of selection rules, which state whether a transition is ‘allowed’ or forbidden’. For centrosymmetric complexes, allowed transitions must be accompanied by a change in parity,  $g \rightarrow u$  (Laporte rule,  $\Delta l = \pm 1$ ), and the spin of the electron

must remain the same (spin selection rule,  $\Delta S = 0$ ). For transition metals with partially-filled  $d$ -orbitals with octahedral symmetry, excitation of an electron will promote it from the  $t_{2g}$  orbital to the  $e_g$  orbital. Although  $d-d$  transitions are Laporte forbidden, effects from vibronic coupling (which result in temporary distortions in the molecular symmetry) often result in weak transitions being observed. This would be reflected in a low molar extinction coefficient value ( $\epsilon$ ,  $1 - 100 \text{ mol}^{-1} \text{ dm}^3 \text{ cm}^{-1}$ ), which relates to the absorbance of the observed transition by the Beer-Lambert law (Equation 1.1). Meanwhile, LMCT/MLCT and intra-ligand electronic transitions are both spin- and Laporte-allowed and are much more intense ( $\epsilon \geq 10^3 \text{ mol}^{-1} \text{ dm}^3 \text{ cm}^{-1}$ ).

$$A = -\log\left(\frac{I}{I_0}\right) = \epsilon lc$$

*Equation 1.1 – Beer-Lambert Law. A = absorbance, I = intensity, I<sub>0</sub> = initial intensity,  $\epsilon$  = molar extinction coefficient ( $\text{mol}^{-1} \text{ dm}^3 \text{ cm}^{-1}$ ), l = path length (cm), c = concentration ( $\text{mol dm}^{-3}$ ).*

UV-Vis spectroscopy is particularly useful for investigating the oxidation state of transition metals with partially-filled  $d$ -orbitals, and in this work, will be used for the Co, Ni and Cu macrocyclic complexes. In most cases, absorption arising from the  $d-d$  transitions are expected in the visible region, but in some cases also show additional transitions towards the near-IR region.

The spectra obtained in this work (for hexacoordinate transition metal complexes) will be analysed assuming approximate  $O_h$  symmetry. However, the complexes are expected to be *facial* with  $C_{3v}$  symmetry, which complicates the systems in comparison to the high-symmetry  $O_h$  complexes. This may result in additional features being observed in the spectra. It is also expected that some of the complexes (in particular, the  $d^9 \text{ Cu}^{2+}$  complexes) will experience Jahn-Teller distortion, further reducing the symmetry. This effect, alongside the transition-metal-ion-specific properties, will be detailed in Chapter 3.

#### 1.5.6 Single Crystal X-Ray Diffraction (SCXRD)

Single crystal X-ray diffraction (SCXRD) is a powerful and incredibly informative X-ray diffraction technique that is used to determine the solid-state chemical structure of a given compound, provided a suitable crystal can be grown. A single crystal consists of a three-dimensional array of regularly repeating structural elements, which may be entire molecules, atoms, or ions. The repeat component is defined as the unit cell of the crystal, which forms the 3D crystal lattice based on translation operations.

The unit cell contains the asymmetric unit, which includes all the structural and symmetry information, and may relate to entire molecule(s) or portions of a molecule. The unit cell is

obtained by applying the symmetry operations on the asymmetric unit, while the packing of a crystal is obtained by applying translational operations on the unit cell.<sup>150</sup> Hence, each unit cell is related through translational displacements along the x, y and z axes (coincident with the a, b and c lengths of the unit cell, respectively).<sup>151</sup> This is represented by Figure 1.14 below.

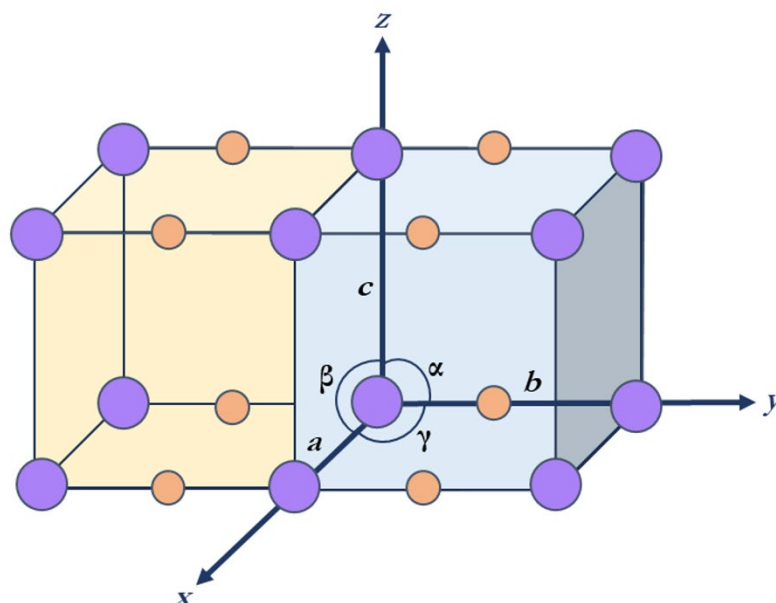


Figure 1.14 – Two representative unit cells with the cell lengths ( $a$ ,  $b$ ,  $c$ ), reference axes ( $x$ ,  $y$ ,  $z$ ) and inter-axial angles ( $\alpha$ ,  $\beta$ ,  $\gamma$ ) labelled accordingly.

The relationship between these different cell parameters defines the nature of the crystal system – these are given in Table 1.7.

Table 1.7 – The seven crystal systems and their associated parameters.

Crystal system	Unit cell parameters
<b>Cubic</b>	$a = b = c$ , $\alpha = \beta = \gamma = 90^\circ$
<b>Hexagonal</b>	$a = b \neq c$ , $\alpha = \beta = 90^\circ$ , $\gamma \neq 120^\circ$
<b>Tetragonal</b>	$a = b \neq c$ , $\alpha = \beta = \gamma = 90^\circ$
<b>Monoclinic</b>	$a \neq b \neq c$ , $\alpha = \gamma = 90^\circ$ , $\beta \neq 90^\circ$
<b>Triclinic</b>	$a \neq b \neq c$ , $\alpha \neq \beta \neq \gamma \neq 90^\circ$
<b>Orthorhombic</b>	$a \neq b \neq c$ , $\alpha = \beta = \gamma = 90^\circ$
<b>Rhombohedral</b>	$a = b = c$ , $\alpha = \beta = \gamma \neq 90^\circ$

A single crystal diffraction experiment involves firing monochromatic X-rays at a crystal and mapping the resultant diffraction pattern. When an X-ray hits a lattice plane of the crystal at an incident angle ( $\theta$ ), it may be diffracted at an equal angle of reflection. Each lattice plane can be

characterised by the Miller indices,  $hkl$ , which define the orientation of the planes with respect to the cell parameters  $a$ ,  $b$  and  $c$ , and each lattice plane in a set  $hkl$  can be considered a separate scattering object. Constructive interference occurs when two or more of the diffracted X-rays (travelling in the same direction) have the same wavelength – this results in a much more intense X-ray beam, which can then be detected. For this to occur (and for an X-ray to be diffracted), the conditions must comply with Bragg's Law (Equation 1.2).

$$n\lambda = 2d_{hkl}\sin\theta$$

Equation 1.2 – **Bragg's Law**.  $n$  = diffraction order,  $\lambda$  = wavelength of the X-Ray beam,  $d$  = interplanar distance,  $\theta$  = incident angle.

Bragg's Law can also be shown figuratively, as depicted in Figure 1.15.

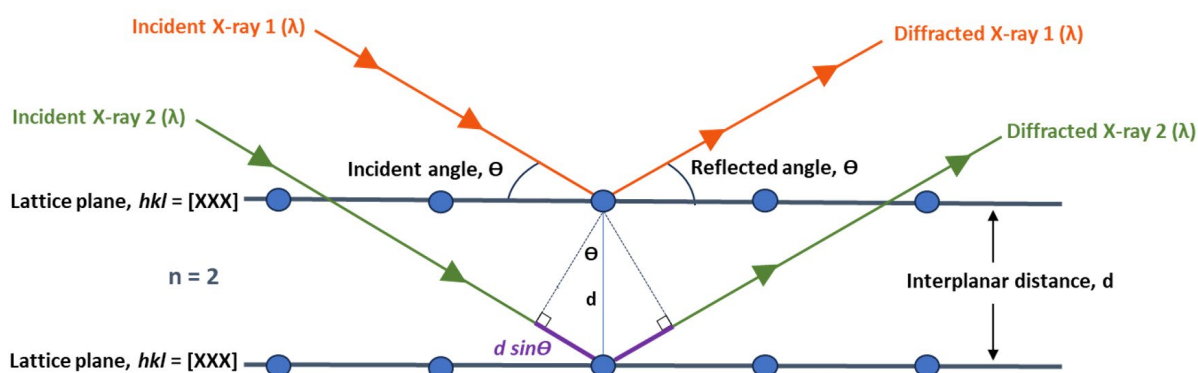


Figure 1.15 – Illustration of Bragg's Law. Incoming X-rays of the same wavelength ( $\lambda$ ) and incident angle ( $\theta$ ) are diffracted from the lattice plane, resulting in constructive interference from the two diffracted X-rays. The relationship between the two X-rays can be defined by  $d \sin\theta$ .

At a single incident angle, only a small number of X-rays will satisfy Bragg's law. Therefore, during an experiment, the crystal will be rotated within the path of the incoming X-ray beam to increase the number of incident angles, so data can be collected for a wider range of lattice planes. The crystal is often cooled to 100 K in this time to minimise thermal atomic motion (bond vibration, bending, stretching). This helps to lower the size of the ellipsoids drawn in the Oak Ridge Thermal Ellipsoid Plot (ORTEP) graphical representation of the given compound and minimises the risk of degradation of the crystal from radiation exposure.

Specifically, it is the electrons associated with the atoms within the crystal that cause the incoming X-ray beam to scatter, and the intensity of the reflection is directly correlated with the atom type ( $Z$  value) and its position in the unit cell. The geometry of the diffraction pattern/position of the spots provide information on the unit cell parameters, whilst the symmetry of the diffraction pattern is closely related with the symmetry of the unit cell.

The intensities of the reflections in the diffraction pattern and the arrangement of atoms in the unit cell are related through Fourier transformation: the diffraction pattern is the Fourier transform of the electron density, and *vice versa*. Each reflection (associated with its own discrete Miller indices) holds structural information and can be assigned with its individual structure factor,  $F(hkl)$ , which comprise of the amplitude ( $|F(hkl)|$ ) and phase ( $\phi$ ). Summation of the Fourier transform of the structure factors for each reflection produce a diffraction pattern (Equation 1.3).

$$F(hkl) = \sum_j f_j(\theta) \cdot \exp\left(-\frac{8\pi U_j \sin^2 \theta}{\lambda^2}\right) \cdot \exp[2\pi i(hx_j + ky_j + ly_j)]$$

1                      2      3                                      4                                      5

*Equation 1.3 – Forward Fourier Transform* (the diffraction experiment). 1 = Total diffracted wave in  $hkl$  direction; 2 = sum of the X-rays scattered by individual atoms; 3 + 4 = scattering of X-rays by individual atoms; 5 = position of atoms. Terms:  $f_j$  = atomic scattering factor;  $u_j$  = isotropic displacement parameter;  $x_j, y_j, l_j$  = coordinates relative to the unit cell.

Thus, the reverse Fourier transform gives the electron density (Equation 1.4).

$$p(xyz) = \frac{1}{V} \sum_{hkl} |F(hkl)| \cdot \exp(i\phi(hkl)) \cdot \exp[-2\pi i(hx_j + ky_j + ly_j)]$$

1                      2                      3                                      4                                      5

*Equation 1.4 – Reverse Fourier Transform* (the recombination calculation). 1 = electron density; 2 = sum of diffracted beams; 3 = reflection amplitude; 4 = intrinsic wave phase; 5 = phase shift at each geometric position.

However, during an experiment, information on the phase of the reflection is lost, so the calculation of the reverse Fourier transform is not possible. To overcome this ‘phase problem’, the Patterson synthesis can be used (Equation 1.5), which assumes the phases are all equal to zero, relying only on the observed reflection intensities.

$$p(xyz) = \frac{1}{V} \sum_{hkl} |F_0(hkl)|^2 \cdot \exp[-2\pi i(hx_j + ky_j + ly_j)]$$

*Equation 1.5 – Patterson Synthesis.*  $F_0$  = observed diffraction beam amplitudes.

This produces a Patterson map, which looks similar to an electron density map – but rather than depicting information on the positions of atoms in the structure, it instead is a map of the vectors between pairs of atoms in the structure. The map shows where the pair of atoms exist in relation to each other, but not to the unit cell origin. If a structure contains only a few heavy atoms, the map will depict a larger peak which can be assigned accordingly, and a partial structure can be



obtained. For full structure elucidation, a diffraction pattern based upon a model structure with a complete set of structure factors ( $F_c$ , amplitude and phase) can be compared against the experimental diffraction pattern, obtained from the observed structure factors ( $F_o$ , amplitude only). These are compared *via* the residual factor (R factor), defined as:

$$R = \frac{\sum ||F_o| - |F_c||}{\sum |F_o|}$$

For a correct and complete crystal structure, there should be resemblance between the model and experimental diffraction pattern, and the R factor would be expected to be around 0.02 – 0.07. However, disorder is common in many crystal structures, particularly where solvent or labile systems are involved, which can often increase the R factor. Dynamic disorder, which occurs due to thermal motion of the bonds, is prevented by running the experiment at 100 K. Static disorder is caused by the random variation in the position of the atoms within the crystal but can often be modelled in the refinement process.

Hence, SCXRD provides information on the positions of the atoms within the unit cell, and the bond lengths and bond angles between different atoms. Most complexes in this work are expected to be six-coordinate, *pseudo*-octahedral (or *pseudo*-trigonal prismatic). From their crystal structures, the exact geometry can be determined through calculation of their twist angles,  $\Theta$ , between the opposite triangular planes of the complex (for true octahedral geometry,  $\Theta = 60^\circ$ ; for trigonal prismatic,  $\Theta = 0^\circ$ ).<sup>152</sup>

However, although it is incredibly useful, it is necessary to recognise that the crystal structure obtained may not be representative of the bulk product or the species in solution. The growing of suitable crystals, and their quality, is a key limiting factor.

### 1.5.7 Electron Diffraction (ED)

The concept of electron diffraction was first demonstrated in 1927, by Davisson and Germer<sup>153</sup>, who reported the diffraction of an electron beam incident upon a nickel crystal and discovered that the reflected electrons displayed a discrete distribution of scattering angles, comparable to the diffraction of an X-ray beam. A series of electron diffraction experiments followed in the next decade, but this technique has only recently found a new resurgence for structure determination, primarily due to significant advancements in data collection techniques.<sup>154,155,156,157</sup>

Although the general concepts (in terms of structure determination) between X-ray and electron diffraction are the same, the beams have very different properties. X-rays are chargeless,

massless quanta, and interact weakly with matter. Crystals of at least  $10^5 \mu\text{m}^3$  in volume are required to generate enough signal for structure determination.<sup>157</sup> However, negatively-charged electrons (with nonzero mass) experience electrostatic attraction toward protons in atomic nuclei, in addition to repulsion from local electron density. As a consequence of these strong Coulombic interactions, an electron beam can produce substantial diffraction from crystallite sizes much smaller than those required during a SCXRD experiment ( $10^{-2} \mu\text{m}^3$ ). It also means a very good signal-to-noise ratio can be achieved, with easier identification of smaller and lighter elements (such as hydrogen). However, unlike an X-ray beam, the amplitude of electron scattering is not always linear with atom size (due to the influence of repulsion by valence electrons), and the strong interactions can result in intensities that are difficult to interpret.<sup>158</sup>

A typical electron diffraction experiment first involves the dispersal of the microcrystalline sample onto an electron microscope grid. Data collection uses a (modified) transmission electron microscope (TEM) for crystallite selection and is performed under a high vacuum (to prevent the electron beam interacting with air molecules). Cryo-cooling is often required to maintain the stability and structure of the crystallites under vacuum, particularly when solvent molecules may be present. The electron beam is then focused onto the target crystallite, and the diffraction pattern collected (using the same detectors used for SCXRD analysis).

## 1.6 Project Aims

The overarching aim of this project was to synthesise inorganic metal and metal fluoride complexes with both new and known N-functionalised triaza-macrocyclic ligands derived from the 9-membered tacn ring, with respect to the development of novel inorganic  $^{18}\text{F}$ -based PET imaging agents. The primary objectives of this thesis can be described by the following:

- To develop synthetic routes towards known and novel triaza-macrocyclic ligands with various functionality (including those with carboxylate, phosphinate-ester and amide- pendant arms), and their subsequent complexation towards transition metal ions, Group 13 metal ions, and Group 13 metal fluoride units.
- Prior to any  $^{18}\text{F}$  radiochemistry, to research and develop the coordination chemistry of carboxylate, phosphinate-ester and amide-functionalised triazacyclononane ligands, and to gain an understanding of the coordinative properties and behaviours of the ligands. The objective is to identify suitable synthetic pathways for future radiolabelling reactions, and to establish whether these systems are promising for potential applications in PET imaging.

- To investigate the radiochemistry of gallium trifluoride complexes with tris- and mono-functionalised triazacyclononane ligands, and to discover the optimal radiochemical and HPLC methodologies for both the radiofluorination and the subsequent assessment of the radiolabelled systems. At the outset of this work, there were no existing amide-tactn  $\text{MF}_3$  systems described in the literature for  $^{18}\text{F}$  PET imaging purposes. However, the use of amide (peptide) bonds are well documented in this field, and can be found in many examples of existing and developing radiotracers (for conjugation to tissue-specific biomolecules). This work will assess the suitability of using neutral  $\text{N}_3\text{O}_3$  ligands with strong hydrogen-bonding capabilities, and what affect they may have on  $^{18}\text{F}$  radiochemistry.
- To assess the suitability of existing and novel Group 13 complexes for radiochemical applications, based on the effect of chelate size and metal ion radius on the observed coordinative behaviour, with the aim to shed further insight into the ideal properties and behaviours of future inorganic triazacyclononane complexes in  $^{18}\text{F}$  PET imaging.

## 1.7 References

1. G. Crişan, N. S. Moldovean-Cioroianu, D.-G. Timaru, G. Andrieş, C. Căinap and V. Chiş, *Int. J. Mol. Sci.*, 2022, **23**, 5023.
2. P. J. Myburgh and K. K. S. Sai, *ACS Pharmacol. Transl. Sci.*, 2023, **6**, 1616.
3. A. M. J. Paans, A. van Waarde, P. H. Elsinga, A. T. M. Willemsen and W. Vaalburg, *Methods*, 2002, **27**, 195.
4. K. Herholz, S. F. Carter and M. Jones, *Br. J. Radiol.*, 2007, **80**, 160.
5. S. R. Cherry and M. Dahlborn, *PET: Physics, Instrumentation, and Scanners*, Springer, New York, 1st edn., 2006.
6. A. Berger, *Br. Med. J.*, 2003, **326**, 1449.
7. K. Duncan, *J. Nucl. Med. Technol.*, 1998, **26**, 228.
8. A. K. Shukla and U. Kumar, *J. Med. Phys.*, 2006, **31**, 13.
9. P. W. Miller, N. J. Long, R. Vilar and A. D. Gee, *Angew. Chem. Int. Ed.*, 2008, **47**, 8998.
10. S. R. Banerjee and M. G. Pomper, *Appl. Radiat. Isot.*, 2013, **76**, 2.
11. J. D. Young, M. Jauregui-Osoro, W.-L. Wong, M. S. Cooper, G. Cook, S. F. Barrington, M. T. Ma, P. J. Blower and E. O. Aboagye, *Nucl. Med. Commun.*, 2021, **42**, 1301.
12. O. Jacobson, D. O. Kiesewetter and X. Chen, *Bioconjug. Chem.*, 2015, **26**, 1.
13. T. Wang, S. Lv, Z. Mou, Z. Zhang, T. Dong and Z. Li, *Bioconjug. Chem.*, 2023, **34**, 140.

14. K. Strijckmans, *Comput. Med. Imaging Graph.*, 2001, **25**, 69.
15. R. Gallerani, G. Cicoria, E. Fantuzzi, M. Marengo and D. Mostacci, *Prog. Nuclear Energy*, 2008, **50**, 939.
16. F. Daghihian, R. Sumida and M. E. Phelps, *J. Nucl. Med. Technol.*, 1990, **18**, 5.
17. M. Bakhtiari, L. M. Oranj, N.-S. Jung, A. Lee and H.-S. Lee, *Radiat. Phys. Chem.*, 2020, **177**, 1.
18. J. C. Chaves, M. J. Vargas and R. S. Sánchez, *Radiat. Phys. Chem.*, 2016, **126**, 32.
19. B. Y. Yang, S. Telu, M. B. Haskali, C. L. Morse and V. W. Pike, *Sci. Rep.*, 2019, **9**, 14835.
20. J. S. Wright, L. S. Sharninghausen, A. Lapsys, M. S. Sanford and P. J. H. Scott, *ACS Cent. Sci.*, 2024, **10**, 1674.
21. D. M. Lemal, *J. Org. Chem.*, 2004, **69**, 1.
22. D. O'Hagan, *Chem. Soc. Rev.*, 2008, **37**, 308.
23. F. M. G. Cornelissen, G. Markert, G. Deutsch, M. Antonara, N. Faaij, I. Bartelink, D. Noske, W. P. Vandertop, A. Bender and B. A. Westerman, *J. Med. Chem.*, 2023, **66**, 7253.
24. P. K. Morrish, G. V. Sawle and D. J. Brooks, *J. Neurol. Neurosurg. Psychiatry*, 1995, **59**, 597.
25. G. N. Stormezand, L. T. Chaves, D. Vázquez García, J. Doorduyn, B. M. De Jong, K. L. Leenders, B. P. H. Kremer and R. A. J. O. Dierckx, *NeuroImage Clin.*, 2020, **25**, 102161.
26. C. Nanni, S. Fanti and D. Rubello, *J. Nucl. Med.*, 2007, **48**, 1577.
27. Â. C. B. Neves, I. Hrynychak, I. Fonseca, V. H. P. Alves, M. M. Pereira and A. Falcão, *EJNMMI Radiopharm. Chem.*, 2021, **6**, 1.
28. R. Edwards and T. Wirth, *J. Label. Compd. Radiopharm.*, 2015, **58**, 183.
29. E. M. Rohren, T. G. Turkington and R. E. Coleman, *Radiology*, 2004, **231**, 305.
30. F. Castell and G. J. R. Cook, *Br. J. Cancer*, 2008, **98**, 1597.
31. A. Almuhaideb, N. Papathanasiou and J. Bomanji, *Ann. Saudi Med.*, 2011, **31**, 3.
32. H. H. Coenen, A. D. Gee, M. Adam, G. Antoni, C. S. Cutler, Y. Fujibayashi, J. M. Jeong, R. H. Mach, T. L. Mindt, V. W. Pike and A. D. Windhorst, *Ann. Nucl. Med.*, 2018, **32**, 236.
33. H. H. Coenen, presented in part at the Ernst Schering Research Foundation Workshop, 2007.
34. J. S. Fowler, *J. Nucl. Med.*, 2020, **61**, 105S.
35. E. Hess, G. Blessing, H. H. Coenen and S. M. Qaim, *Appl. Radiat. Isot.*, 2000, **52**, 1431.
36. J. S. Fowler and T. Ido, *Semin. Nucl. Med.*, 2002, **32**, 6.
37. M. Pretze, C. Wängler and B. Wängler, *Biomed. Res. Int.*, 2014, 674063.

38. S. G. Nerella, P. Singh, T. Sanam and C. S. Digwal, *Front. Med.*, 2022, **9**, 812270.
39. M. Tredwell and V. Gouverneur, *Angew. Chem. Int. Ed.*, 2012, **51**, 11426.
40. S. Preshlock, M. Tredwell and V. Gouverneur, *Chem. Rev.*, 2016, **116**, 719.
41. J. Ajenjo, G. Destro, B. Cornelissen and V. Gouverneur, *EJNMMI Radiopharm. Chem.*, 2021, **6**, 33.
42. P. J. H. Scott and M. R. Kilbourn, *Appl. Radiat. Isot.*, 2007, **65**, 1359.
43. A. G. Nappi, G. Santo, L. Jonghi-Lavarini, A. Miceli, A. Lazzarato, F. La Torre, F. Dondi and J. Gorica, *Hematol Rep.*, 2024, **16**, 32.
44. P. Mapelli, E. Incerti, V. Bettinardi, G. M. Conte, F. Fallanca, M. Bailo, M. Vuozzo, M. Callea, L. Gianolli and M. Picchio, *Clin. Transl. Imaging*, 2017, **5**, 389.
45. P. Mapelli and M. Picchio, *Int. J. Biol. Markers*, 2020, **35**, 42.
46. S. Yu, *Biomed. Imaging Interv. J.*, 2006, **2**, e57.
47. L. Lang, W. Li, N. Guo, Y. Ma, L. Zhu, D. O. Kiesewetter, S. Baozhong, G. Niu and X. Chen, *Bioconjug. Chem.*, 2011, **22**, 2415.
48. E. Cole, M. Stewart, R. Littich, R. Hoareau and P. Scott, *Curr. Top. Med. Chem.*, 2014, **14**, 875.
49. R. Schirmacher, B. Wängler, J. Bailey, V. Bernard-Gauthier, E. Schirmacher and C. Wängler, *Semin. Nucl. Med.*, 2017, **47**, 474.
50. W. Cai, X. Zhang, Y. Wu and X. Chen, *J. Nucl. Med.*, 2006, **47**, 1172.
51. J. Marik and J. L. Sutcliffe, *Appl. Radiat. Isot.*, 2007, **65**, 199.
52. K. Chansaenpak, B. Vabre and F. P. Gabbaï, *Chem. Soc. Rev.*, 2016, **45**, 954.
53. D. Nicholls, in *Complexes and First-Row Transition Elements*, The Macmillan Press Ltd, London, 1974, ch. 2, pp. 9-16.
54. R. G. Pearson, *Hard and Soft Acids and Bases*, Dowden, Hutchinson & Ross, Stroudsburg, 1st edn., 1973.
55. J. A. Dean, *Lange's Handbook of Chemistry*, McGraw-Hill Inc., New York, 15th edn., 1999.
56. V. Bernard-Gauthier, M. L. Lepage, B. Waengler, J. J. Bailey, S. H. Liang, D. M. Perrin, N. Vasdev and R. Schirmacher, *J. Nucl. Med.*, 2018, **59**, 568.
57. Q. I. Churches, J. F. Hooper and C. A. Hutton, *J. Org. Chem.*, 2015, **80**, 5428-5435.
58. G. E. Smith, H. L. Sladen, S. C. G. Biagini and P. J. Blower, *Dalton Trans.*, 2011, **40**, 6196.
59. R. Ting, M. J. Adam, T. J. Ruth and D. M. Perrin, *J. Am. Chem. Soc.*, 2005, **127**, 13094.
60. R. Ting, C. Harwig, U. Auf Dem Keller, S. McCormick, P. Austin, C. M. Overall, M. J. Adam, T. J. Ruth and D. M. Perrin, *J. Am. Chem. Soc.*, 2008, **130**, 12045.

61. R. Ting, J. Lo, M. J. Adam, T. J. Ruth and D. M. Perrin, *J. Fluorine Chem.*, 2008, **129**, 349.
62. L. Ying, A. Asadi and D. M. Perrin, *J. Fluorine Chem.*, 2009, **130**, 377.
63. Z. Liu, N. Hundal-Jabal, M. Wong, D. Yapp, K. S. Lin, F. Bénard and D. M. Perrin, *MedChemComm*, 2014, **5**, 171.
64. Z. Liu, Y. Li, J. Lozada, M. Q. Wong, J. Greene, K.-S. Lin, D. Yapp and D. M. Perrin, *Nucl. Med. Biol.*, 2013, **40**, 841.
65. C. R. Wade, H. Zhao and F. P. Gabbaï, *Chem. Commun.*, 2010, **46**, 6380.
66. M. H. Lee, T. Agou, J. Kobayashi, T. Kawashima and F. P. Gabbaï, *Chem. Commun.*, 2007, 1133.
67. T. W. Hudnall, Y.-M. Kim, M. W. P. Bebbington, D. Bourissou and F. P. Gabbaï, *J. Am. Chem. Soc.*, 2008, **130**, 10890.
68. H. Hong, L. Zhang, F. Xie, R. Zhuang, D. Jiang, H. Liu, J. Li, H. Yang, X. Zhang, L. Nie and Z. Li, *Nat. Commun.*, 2019, **10**, 1.
69. K. Chansaenpak, M. Wang, Z. Wu, R. Zaman, Z. Li and F. P. Gabbaï, *Chem. Commun.*, 2015, **51**, 12439.
70. Y. Li, Z. Liu, J. Lozada, M. Q. Wong, K.-S. Lin, D. Yapp and D. M. Perrin, *Nucl. Med. Biol.*, 2013, **40**, 959.
71. V. Bernard-Gauthier, C. Wängler, E. Schirmacher, A. Kostikov, K. Jurkschat, B. Wängler and R. Schirmacher, *Biomed. Res. Int.*, 2014, 454503.
72. M. S. Rosenthal, A. L. Bosch, R. J. Nickles and S. J. Gatley, *Int. J. Appl. Radiat. Isot.*, 1985, **36**, 318.
73. R. Schirmacher, G. Bradtmöller, E. Schirmacher, O. Thews, J. Tillmanns, T. Siessmeier, H. G. Buchholz, P. Bartenstein, B. Wängler, C. M. Niemeyer and K. Jurkschat, *Angew. Chem. Int. Ed.*, 2006, **45**, 6047.
74. R. Schirmacher, C. Wängler and E. Schirmacher, *Mini Rev. Org. Chem.*, 2007, **4**, 317.
75. C. Wängler, B. Waser, A. Alke, L. Iovkova, H.-G. Buchholz, S. Niedermoser, K. Jurkschat, C. Fottner, P. Bartenstein, R. Schirmacher, J.-C. Reubi, H.-J. Wester and B. Wängler, *Bioconjug. Chem.*, 2010, **21**, 2289.
76. C. Wängler, S. Niedermoser, J. Chin, K. Orchowski, E. Schirmacher, K. Jurkschat, L. Iovkova-Berends, A. P. Kostikov, R. Schirmacher and B. Wängler, *Nat. Protoc.*, 2012, **7**, 1946.
77. S. Niedermoser, J. Chin, C. Wängler, A. Kostikov, V. Bernard-Gauthier, N. Vogler, J. P. Soucy, A. J. McEwan, R. Schirmacher and B. Wängler, *J. Nucl. Med.*, 2015, **56**, 1100.
78. H. Ilhan, A. Todica, S. Lindner, G. Boening, A. Gosewisch, C. Wängler, B. Wängler, R. Schirmacher and P. Bartenstein, *Eur. J. Nucl. Med. Mol. Imaging*, 2019, **46**, 2400.

79. H. Leupe, S. Ahenkorah, J. Dekervel, M. Unterrainer, E. Van Cutsem, C. Verslype, F. Cleeren and C. M. Deroose, *J. Nucl. Med.*, 2023, **64**, 835.
80. I. F. Chaple and S. E. Lapi, *J. Nucl. Med.*, 2018, **59**, 1655.
81. D. S. Macpherson, K. Fung, B. E. Cook, L. C. Francesconi and B. M. Zeglis, *Dalton Trans.*, 2019, **48**, 14547.
82. P. J. Blower, W. Levason, S. K. Luthra, G. McRobbie, F. M. Monzittu, T. O. Mules, G. Reid and M. Nadeem Subhan, *Dalton Trans.*, 2019, **48**, 6767.
83. M. S. Woodward, D. E. Runacres, J. Grigg, I. Khan, W. Levason, G. McRobbie and G. Reid, *Pure Appl. Chem.*, 2024, **96**, 57.
84. R. A. Davis, C. Drake, R. C. Ippisch, M. Moore and J. L. Sutcliffe, *RSC Adv.*, 2019, **9**, 8638.
85. S. M. Ametamey, M. Honer and P. A. Schubiger, *Chem. Rev.*, 2008, **108**, 1501.
86. D. E. Runacres, V. K. Greenacre, J. M. Dyke, J. Grigg, G. Herbert, W. Levason, G. McRobbie and G. Reid, *Inorg. Chem.*, 2023, **62**, 20844.
87. J. F. Gomes Marin, R. F. Nunes, A. M. Coutinho, E. C. Zaniboni, L. B. Costa, F. G. Barbosa, M. A. Queiroz, G. G. Cerri and C. A. Buchpiguel, *Radiographics*, 2020, **40**, 1715.
88. R. Levine and E. P. Krenning, *J. Nucl. Med.*, 2017, **58**, 3S.
89. E. B. Silberstein, *Semin. Nucl. Med.*, 2012, **42**, 164.
90. K. Herrmann, M. Schwaiger, J. S. Lewis, S. B. Solomon, B. J. McNeil, M. Baumann, S. S. Gambhir, H. Hricak and R. Weissleder, *Lancet Oncol.*, 2020, **21**, e146.
91. I. O. Lawal, S. O. Abubakar, H. Ndlovu, K. M. G. Mokoala, S. S. More and M. M. Sathekge, *Mol. Diagn. Ther.*, 2024, **28**, 265.
92. C. Barca, C. Griessinger, A. Faust, D. Depke, M. Essler, A. Windhorst, N. Devoogdt, K. Brindle, M. Schäfers, B. Zinnhardt and A. Jacobs, *Pharmaceuticals*, 2021, **15**, 13.
93. J. N. Whetter, B. A. Vaughn, A. J. Koller and E. Boros, *Angew. Chem. Int. Ed.*, 2022, **61**, e202114203.
94. J. N. Whetter, D. Śmiłowicz and E. Boros, *Acc. Chem. Res.*, 2024, **57**, 933.
95. B. A. Vaughn, A. J. Koller, Z. Chen, S. H. Ahn, C. S. Loveless, S. J. Cingoranelli, Y. Yang, A. Cirri, C. J. Johnson, S. E. Lapi, K. W. Chapman and E. Boros, *Bioconjug. Chem.*, 2021, **32**, 1232.
96. C. A. A. Kelderman, O. M. Glaser, J. N. Whetter, E. Aluicio-Sarduy, J. C. Mixdorf, K. M. Sanders, I. A. Guzei, T. E. Barnhart, J. W. Engle and E. Boros, *Chem. Sci.*, 2024, **15**, 17927.
97. G. Melson, *Coordination Chemistry of Macrocyclic Compounds*, Springer US, New York, 1st edn., 1979.
98. E. C. Constable, in *Metals and Ligand Reactivity*, VCH Verlagsgesellschaft mbH, Weinheim, 2nd edn., 2005, ch. 6, pp. 135-182.

99. in *Chemistry of the Elements*, eds. N. N. Greenwood and A. Earnshaw, Butterworth-Heinemann, Oxford, 2nd edn., 1997, ch. 7, pp. 216-267.
100. I. Bradbury, J. Boyle and A. Morse, *Scientific Principles for Physical Geographers*, Pearson Education Limited, London, 1st edn., 2002.
101. M. A. Malyarick, A. B. Ilyuhin, S. P. Petrosyants and P. Petrosyants, *Main Group Met. Chem.*, 1994, **17**, 707.
102. D. Vidovic and S. Aldridge, *Chem. Sci.*, 2011, **2**, 601.
103. A. J. Downs, *Chemistry of Aluminium, Gallium, Indium and Thallium*, Blackie Academic & Professional, Glasgow, 1st edn., 1993.
104. S. L. Benjamin, W. Levason and G. Reid, *Chem. Soc. Rev.*, 2013, **42**, 1460.
105. R. Bhalla, C. Darby, W. Levason, S. K. Luthra, G. McRobbie, G. Reid, G. Sanderson and W. Zhang, *Chem. Sci.*, 2014, **5**, 381.
106. R. Bhalla, W. Levason, S. K. Luthra, G. McRobbie, F. M. Monzittu, J. Palmer, G. Reid, G. Sanderson and W. Zhang, *Dalton Trans.*, 2015, **44**, 9569.
107. R. Bhalla, J. Burt, A. L. Hector, W. Levason, S. K. Luthra, G. McRobbie, F. M. Monzittu and G. Reid, *Polyhedron*, 2016, **106**, 65.
108. W. J. McBride, R. M. Sharkey, H. Karacay, C. A. D'Souza, E. A. Rossi, P. Laverman, C. H. Chang, O. C. Boerman and D. M. Goldenberg, *J. Nucl. Med.*, 2009, **50**, 991.
109. P. Laverman, W. J. McBride, R. M. Sharkey, A. Eek, L. Joosten, W. J. G. Oyen, D. M. Goldenberg and O. C. Boerman, *J. Nucl. Med.*, 2010, **51**, 454.
110. L. Allott, C. Da Pieve, D. R. Turton and G. Smith, *React. Chem. Eng.*, 2017, **2**, 68.
111. T. Tshibangu, C. Cawthorne, K. Serdons, E. Pauwels, W. Gsell, G. Bormans, C. M. Deroose and F. Cleeren, *EJNMMI Radiopharm. Chem.*, 2020, **5**, 4.
112. T. Long, N. Yang, M. Zhou, D. Chen, Y. Li, J. Li, Y. Tang, Z. Liu, Z. Li and S. Hu, *Clin. Nucl. Med.*, 2019, **44**, 452.
113. W. Wan, N. Guo, D. Pan, C. Yu, Y. Weng, S. Luo, H. Ding, Y. Xu, L. Wang, L. Lang, Q. Xie, M. Yang and X. Chen, *J. Nucl. Med.*, 2013, **54**, 691.
114. C. A. D'Souza, W. J. McBride, R. M. Sharkey, L. J. Todaro and D. M. Goldenberg, *Bioconjug. Chem.*, 2011, **22**, 1793.
115. W. J. McBride, C. A. D'Souza, R. M. Sharkey and D. M. Goldenberg, *Appl. Radiat. Isot.*, 2012, **70**, 200.
116. W. J. McBride, C. A. D'Souza, H. Karacay, R. M. Sharkey and D. M. Goldenberg, *Bioconjug. Chem.*, 2012, **23**, 538.
117. F. Cleeren, J. Lecina, E. M. Billaud, M. Ahamed, A. Verbruggen and G. M. Bormans, *Bioconjug. Chem.*, 2016, **27**, 790.



118. F. Cleeren, J. Lecina, M. Ahamed, G. Raes, N. Devoogdt, V. Caveliers, P. McQuade, D. J. Rubins, W. Li, A. Verbruggen, C. Xavier and G. Bormans, *Theranostics*, 2017, **7**, 2924.
119. R. L. Hayes, *Semin. Nucl. Med.*, 1978, **8**, 183.
120. C. L. Edwards and R. L. Hayes, *J. Nucl. Med.*, 1969, **10**, 103.
121. S. M. Pinsky and R. E. Henkin, *Semin. Nucl. Med.*, 1976, **6**, 397.
122. B. J. B. Nelson, J. D. Andersson, F. Wuest and S. Spreckelmeyer, *EJNMMI Radiopharm. Chem.*, 2022, **7**, 27.
123. A. H. Alnahwi, S. Tremblay, S. Ait-Mohand, J.-F. Beaudoin and B. Guérin, *Appl. Radiat. Isot.*, 2020, **156**, 109014.
124. A. Amor-Coarasa, M. Schoendorf, M. Meckel, S. Vallabhajosula and J. W. Babich, *J. Nucl. Med.*, 2016, **57**, 1402.
125. J. Notni, K. Pohle and H.-J. Wester, *EJNMMI Res.*, 2012, **2**, 28.
126. Y. He, R. Tian, D. Xu, Y. Wu, S. Rina, T. Chen, Y. Guan, T. Xie, T. Ying, F. Xie and J. Han, *Eur. J. Nucl. Med. Mol. Imaging*, 2024.
127. A. Azam, S. Kurbegovic, E. A. Carlsen, T. L. Andersen, V. A. Larsen, I. Law, J. Skjøth-Rasmussen and A. Kjaer, *EJNMMI Res.*, 2024, **14**, 100.
128. Y. Zhang, M. Cao, Y. Wu, S. Malih, D. Xu, E. Yang, M. H. Younis, W. Lin, H. Zhao, C. Wang, Q. Liu, J. W. Engle, M. J. Rasaei, Y. Guan, G. Huang, J. Liu, W. Cai, F. Xie and W. Wei, *J. ImmunoTher. Cancer*, 2024, **12**, e008794.
129. M. A. Zierke, C. Rangger, K. Samadikhah, C. Kreutz, A. M. Schmid and R. Haubner, *J. Med. Chem.*, 2024, **67**, 19668.
130. A. Wurzer, J. Pollmann, A. Schmidt, D. Reich, H.-J. Wester and J. Notni, *Mol. Pharm.*, 2018, **15**, 4296.
131. F. M. Monzittu, I. Khan, W. Levason, S. K. Luthra, G. McRobbie and G. Reid, *Angew. Chem. Int. Ed.*, 2018, **57**, 6658.
132. R. Bhalla, W. Levason, S. K. Luthra, G. McRobbie, G. Sanderson and G. Reid, *Chem. Eur. J.*, 2015, **21**, 4688.
133. J. Nairne, P. B. Iveson and A. Meijer, in *Progress in Medicinal Chemistry*, eds. G. Lawton and D. Witty, Elsevier B.V., Amsterdam, 2015, ch. 5, pp. 231-280.
134. E. W. Price and C. Orvig, *Chem. Soc. Rev.*, 2014, **43**, 260.
135. Radiological protection of people and the environment: generic developed principles, <https://www.gov.uk/government/publications/rsr-generic-developed-principles-regulatory-assessment/radiological-protection-of-people-and-the-environment-generic-developed-principles>, (accessed 12/11/2024).
136. G. Sanderson PhD, University of Southampton, 2015.
137. Y. Dai, R. Sa, F. Guan, Q. Wang, Y. Li and H. Zhao, *Front. Med.*, 2021, **8**, 693632.

138. K. Bratteby, V. Shalgunov, U. M. Battisti, I. N. Petersen, S. L. Van Den Broek, T. Ohlsson, N. Gillings, M. Erlandsson and M. M. Herth, *ACS Pharmacol. Transl. Sci.*, 2021, **4**, 1556.
139. A. V. Mossine, A. F. Brooks, N. Ichiishi, K. J. Makaravage, M. S. Sanford and P. J. H. Scott, *Sci. Rep.*, 2017, **7**, 233.
140. D. H. R. Stimson, Z. Qiao, D. C. Reutens, T. K. Venkatachalam and R. Bhalla, *J. Label. Compd. Radiopharm.*, 2019, **62**, 588.
141. D. Zhou, W. Chu, X. Peng, J. McConathy, R. H. Mach and J. A. Katzenellenbogen, *Tetrahedron Lett.*, 2015, **56**, 952.
142. N. L. Alpert, W. E. Keiser and H. A. Szymanski, *IR: Theory and Practice of Infrared Spectroscopy*, Plenum Press, New York, 2nd edn., 2012.
143. P. L. Silvestrelli, M. Bernasconi and M. Parrinello, *Chem. Phys. Lett.*, 1997, **277**, 478.
144. G. E. Hawkes, in *Encyclopedia of Spectroscopy and Spectrometry*, eds. J. C. Lindon, G. E. Tranter and J. L. Holmes, Academic Press, London, 1999, pp. 2224-2233.
145. J. Keeler, *Understanding NMR Spectroscopy*, John Wiley & Sons, Oxford, 2nd edn., 2011.
146. J. D. Satterlee, *Concepts in Magnetic Resonance*, 1990, **2**, 119-129.
147. J. T. Ash and P. J. Grandinetti, *Magn. Reson. Chem.*, 2006, **44**, 823.
148. L. Konermann and D. J. Douglas, in *Enzymes in Methodology*, ed. D. L. Purich, Academic Press, San Diego, 2002, vol. 354, ch. 3, pp. 50-64.
149. A. Nonat, D. Esteban-Gómez, L. Valencia, P. Pérez-Lourido, J. L. Barriada, L. J. Charbonnière and C. Platas-Iglesias, *Dalton Trans.*, 2019, **48**, 4035.
150. S. Parsons, *Tetrahedron: Asymmetry*, 2017, **28**, 1304.
151. D. E. McRee, in *Practical Protein Crystallography*, Academic Press, San Diego, 2 edn., 1999, ch. 3, pp. 91.
152. A. A. Pinkerton, in *The Rare Earths in Modern Science and Technology*, eds. G. J. McCarthy, J. J. Rhyne and H. B. Silber, Springer US, New York, 1 edn., 1980, vol. 2, pp. 147-152.
153. C. Davisson and L. H. Germer, *Phys. Rev.*, 1927, **30**, 705.
154. G. P. Thomson and A. Reid, *Nature*, 1927, **119**, 890.
155. A. Charlesby, G. I. Finch and H. Wilman, *Pro. Phys. Soc.*, 1939, **51**, 479.
156. M. Gemmi, E. Mugnaioli, T. E. Gorelik, U. Kolb, L. Palatinus, P. Boullay, S. Hovmöller and J. P. Abrahams, *ACS Cent. Sci.*, 2019, **5**, 1315.
157. A. Saha, S. S. Nia and J. A. Rodríguez, *Chem. Rev.*, 2022, **122**, 13883.
158. C. Baerlocher and L. B. McCusker, in *From Zeolites to Porous MOF Materials - The 40th Anniversary of International Zeolite Conference*, eds. R. Xu, Z. Gao, J. Chen and W. Yan, Elsevier, Amsterdam, 2007, vol. 170, pp. 657-665.

## Chapter 2 Routes Towards N-Functionalised Triazamacrocyclic Ligands: Design Considerations and Synthetic Procedures

### 2.1 Introduction

Given the plethora of inorganic-based  $^{18}\text{F}$  radiotracers which involve coordination to triazamacrocyclic ligands, and their favourable properties (detailed below), this chapter will report the synthesis and purification of both known ( $\text{H}_2\text{-Bn-NODA}$  and  $\text{NOTP-OMe}$ ) and novel (amide-functionalised) triazacyclononane ligands. Work in the following chapters will therefore look towards the formation of transition metal and Group 13 complexes of these ligands.

#### 2.1.1 Triazacyclononane – A Versatile Framework for Functionalisation

Applications of 1,4,7-triazacyclononane and its derivative ligands have been an area of increasing interest over the last decades.<sup>1</sup> In part, this is due to the increased thermodynamic and kinetic stability the macrocycles impart on their coordination complexes, and the suitability of the 9-membered ring for fixed *facial* coordination towards many transition metal ions (both high and low valent) and Lewis acidic main group ions.<sup>2</sup> Importantly, the ability to fine-tune the intrinsic properties of the ligand by substitution at the cyclic N- positions makes them incredibly versatile and highly-valued supporting structures.

The development of synthetic methodologies towards tacn-based ligands has led to symmetrical and non-symmetrical functionalisation with a wide array of pendant arms, which can bear different functional groups. Derivatives of the form  $\text{R-tacn}$ ,  $\text{R}_2\text{-tacn}$ ,  $\text{R}_3\text{-tacn}$ , but also  $\text{R}^1\text{R}^2\text{-tacn}$ ,  $\text{R}^1\text{R}_2^2\text{-tacn}$ ,  $\text{R}^1\text{R}^2\text{R}^3\text{-tacn}$  are known.<sup>3</sup> Blake and co-workers made significant early advancements in the field, and have reported several triazacyclononane ligands with varying pendant arm functionalisation – some of which are given as examples in Figure 2.1.<sup>4,5,6,7</sup>

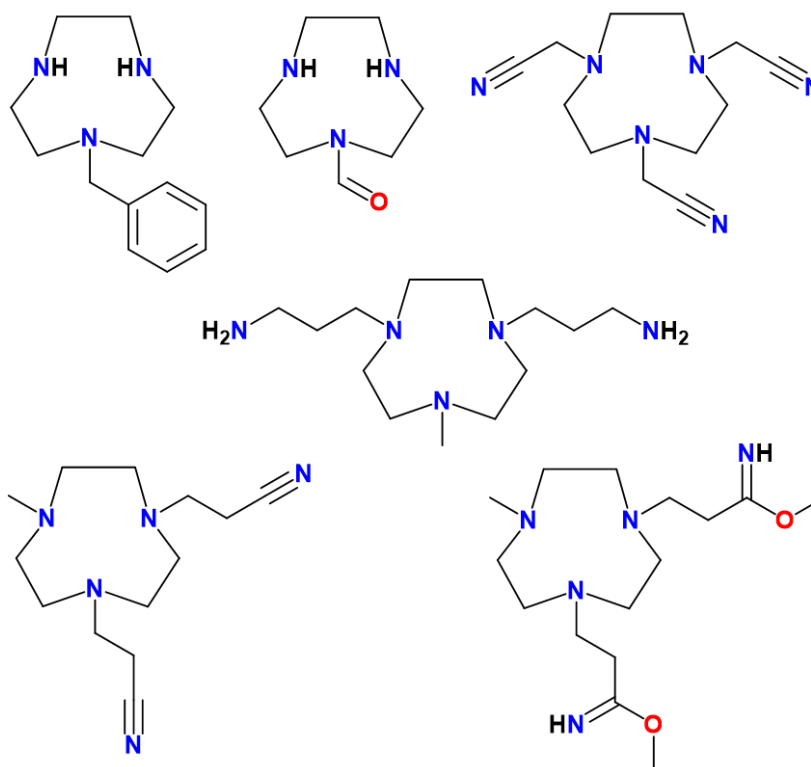


Figure 2.1 – Several examples of *N*-substituted triazacyclononane ligands with various pendant arms, developed by Blake and co-workers.<sup>4,5,6,7</sup>

The majority of synthetic routes towards triazacyclononane and its derivatives still adhere to the general procedure for polycyclic amines, first reported by Richman and Atkins in the 1970s.<sup>8,9</sup> All involve long, multi-step reactions with harsh conditions, and the use of tosylated intermediates, ultimately leading to poor atom economy.<sup>10</sup> However, synthesis is effective and scalable, and the intermediates require little to no purification. Tacn and common derivatives can also be bought directly from specialist commercial suppliers. However, there can often be a high cost associated with the ready accessibility.

#### 2.1.1.1 *N*<sub>3</sub>-Donor Triazacyclononane Ligands

Many tacn-based ligands, like the free base, are tridentate, and include simple groups such as alkyl- and benzyl- substituted at the cyclic *N*- positions.<sup>11</sup> Two notable examples relevant to the work in this thesis include 1,4,7-trimethyl-1,4,7-triazacyclononane (Me<sub>3</sub>-tacn) and 1-benzyl-4,7-dimethyl-1,4,7-triazacyclononane (BnMe<sub>2</sub>-tacn) (Figure 2.2).

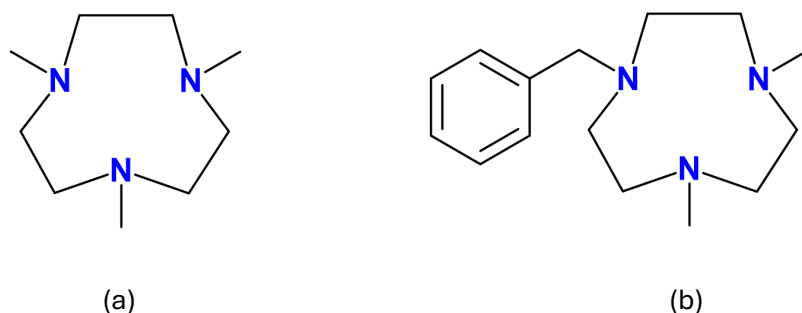
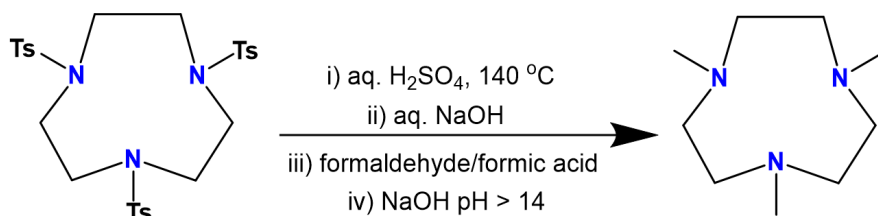


Figure 2.2 – Structures of (a)  $\text{Me}_3\text{-tacn}$  and (b)  $\text{BnMe}_2\text{-tacn}$ .

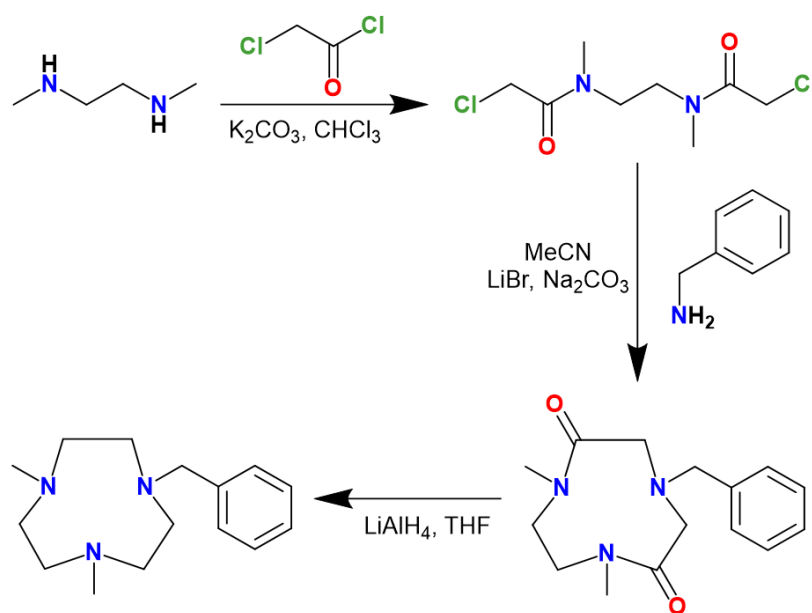
The synthesis of  $\text{Me}_3\text{-tacn}$  was first reported by Wieghardt *et al.*<sup>12</sup> in the 1980s, alongside the first examples of stable binuclear complexes with  $\text{Cr}^{3+}$ ,  $\text{Co}^{3+}$  and  $\text{Rh}^{3+}$  metal cations. In the forty years since, it has been a popular ligand choice for many researchers across a range of disciplines.<sup>13,14</sup> Due to this popularity, its synthesis has been adapted and simplified. In the initial publication by Wieghardt and co-workers,  $\text{H}_3\text{-tacn}$  was isolated prior to methylation. However, in 1994, an alternative route in which  $\text{Me}_3\text{-tacn}$  can be isolated from the tri-tosylated triazacyclononane intermediate in a ‘one-pot’ method was patented.<sup>15</sup> Concentrated sulfuric acid is first used to remove the tosylate groups, and a subsequent work up step is immediately followed by *in situ* addition of formaldehyde and formic acid to methylate the N-atoms of the macrocycle (Scheme 2.1). This avoids the several time-consuming steps involved in the later stages of  $\text{H}_3\text{-tacn}$  synthesis, simultaneously reducing the overall cost of production and environmental impact.



Scheme 2.1 – Direct synthesis of 1,4,7-trimethyl-1,4,7-triazacyclononane from  $N,N',N''\text{-tris}(p\text{-tolylsulfonyl})\text{-1,4,7-triazacyclononane}$ .

Many examples of inorganic radiopharmaceuticals discussed in Chapter 1 involve coordination towards macrocyclic ligands. Although applications of  $\text{Me}_3\text{-tacn}$  in radiopharmaceutical chemistry are limited due to the lack of chromophore and functional group for bioconjugation, it can be used in place of  $\text{BnMe}_2\text{-tacn}$  in the earlier stages of radiotracer development to develop the coordination chemistry with metal fluoride species. For example, previous work in the Reid group first reported the Group 13 metal trichloride complexes ( $\text{AlCl}_3$ ,  $\text{GaCl}_3$  and  $\text{InCl}_3$ ) of  $\text{Me}_3\text{-tacn}$  alongside those of  $\text{BnMe}_2\text{-tacn}$ , to assess the suitability of these complexes for fluorination (using a source of  $[^{19}\text{F}]\text{F}^-$ ) and also their stabilities in solution (in  $\text{H}_2\text{O}$ ,  $\text{MeCN}$ ,  $\text{CH}_2\text{Cl}_2$ ).<sup>16</sup>

Due to the unsymmetrical nature of the ligand, with two different substituents, BnMe<sub>2</sub>-tacn is more complicated to synthesise. The first synthetic route, published by Belousoff *et al.*<sup>17</sup> in 2006, is depicted in Scheme 2.2. This route avoids the typical cyclisation of tosylated intermediates often used in triazacyclononane syntheses. It also involves fewer steps than the alternative route, which forms the ligand *via* the alkylation of 1-benzyl-1,4,7-triazacyclononane.<sup>18</sup> However, care is required when using strongly reducing agents such as LiAlH<sub>4</sub>, which are extremely flammable and react violently upon exposure to air. It must be used under an inert atmosphere, so specialist apparatus such as a glove box or a Schlenk line is preferred.

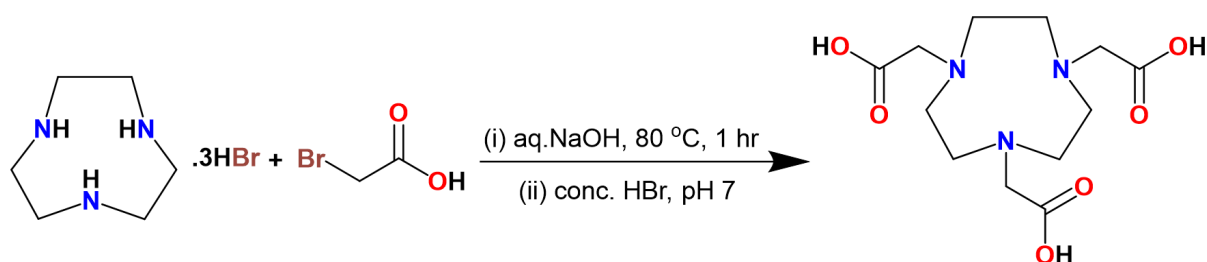


Scheme 2.2 – Synthesis of 1-benzyl-4,7-dimethyl-1,4,7-triazacyclononane (BnMe<sub>2</sub>-tacn) as first published by Belousoff and co-workers.<sup>17</sup>

#### 2.1.1.2 Triazacyclononane Ligands with Pendant Donor Arms

It is also possible to functionalise triazacyclononane with one or more pendant arms containing donor groups capable of binding to the metal centre, such as alkoxides and carboxylates. 1,4,7-triazacyclononane-1,4,7-triacetic acid (H<sub>3</sub>-NOTA) is a well-known example of a tacn framework containing three pendant (anionic) donor arms. This ligand is generally hexadentate, providing an N<sub>3</sub>O<sub>3</sub> donor *via* the amine and carboxylate groups. This makes it ideal for stabilising metals in the +3 oxidation state, such as the Group 13 metals and some transition metals. Following on from their work on the neutral tridentate Me<sub>3</sub>-tacn ligand, the synthesis of H<sub>3</sub>-NOTA (Scheme 2.3) alongside the first examples of its complexes, were published by Wiegardt *et al.*<sup>19</sup> in 1982. It was found that the ligand could adopt either a *pseudo*-octahedral or a distorted trigonal prismatic coordination, which varied according to the central metal ion. Since then, H<sub>3</sub>-NOTA and its derivatives have become highly valued within nuclear imaging, particularly in the

formation of radiopharmaceuticals that require smaller metal isotopes, such as  $^{64}\text{Cu}$  and  $^{68}\text{Ga}$ .<sup>20,21,22,23</sup>



Scheme 2.3 – Synthesis of 1,4,7-triacetic acid-1,4,7-triazacyclononane ( $\text{H}_3\text{-NOTA}$ ).

McBride *et al.*<sup>24</sup> have also explored four different derivatives of  $\text{H}_3\text{-NOTA}$  as chelators for  $\text{Al-}^{18}\text{F}$  radiolabelling. Each contains a single peptide, bound directly to the tacn ring or conjugated to the pendant arm. For the four ligands, radiochemical yields of 5.8% – 87% were observed when similar reaction conditions were used. Figure 2.3 depicts these ligands and their associated radiochemical yields. The highest radiochemical yield was found for IMP467, whose structure is known to give rise to enhanced binding properties and may increase radiolabelling yield.<sup>25</sup> This illustrates that the choice of pendant arm can also directly affect radiolabelling capabilities — something that will be considered in the ligand design rationale later in this work.

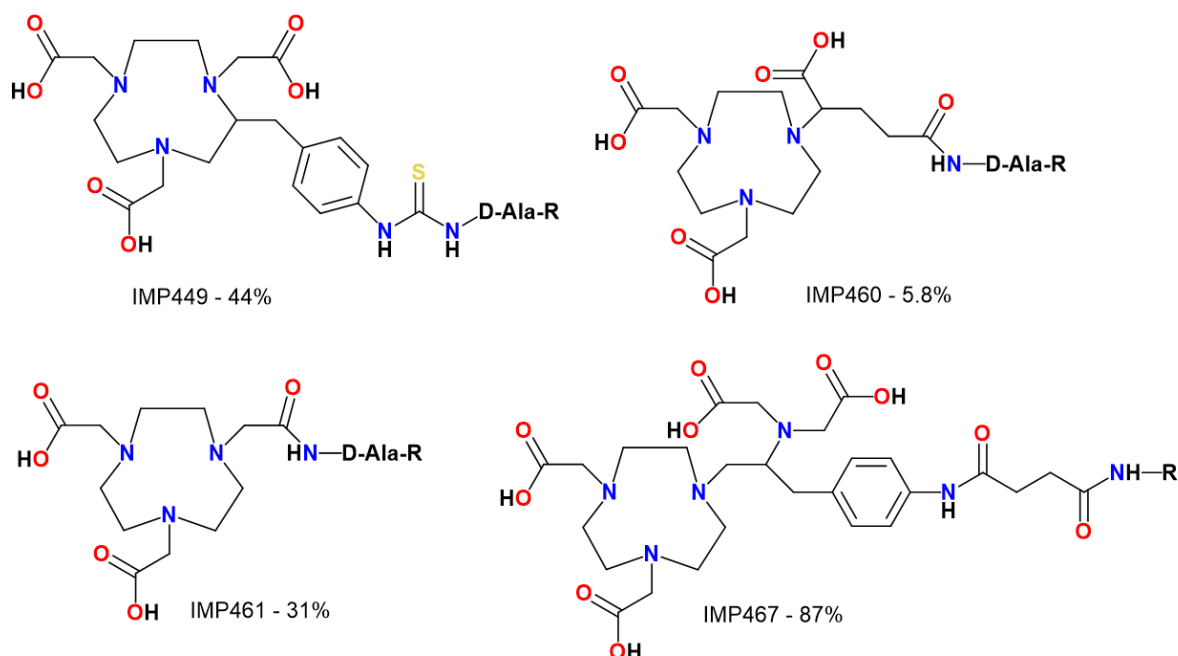
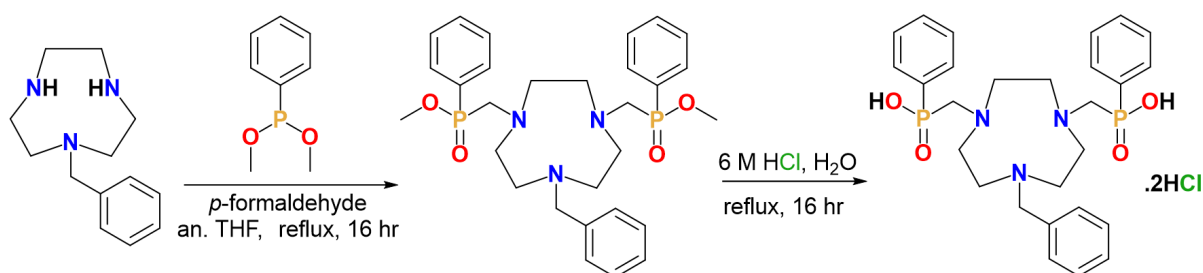


Figure 2.3 – The four  $\text{H}_3\text{-NOTA}$  derivatives reported by McBride *et al.*<sup>24</sup> in the formation of  $\text{Al-}^{18}\text{F}$ -chelate complexes and their corresponding radiochemical yields (%).

A pentadentate equivalent of  $\text{H}_3\text{-NOTA}$ , 1-benzyl-4,7-dicarboxylate-1,4,7-triazacyclononane ( $\text{H}_2\text{-Bn-NODA}$ ), has also been successfully used in the formation of  $\text{Al-}^{18}\text{F}$ -based radiotracers.<sup>26</sup>

Conversely, while the analogous gallium complex,  $[\text{Ga}^{18}\text{F}(\text{Bn-NODA})]$ , is formed with high RCY, the radiocomplex has shown lower stability above pH 7, liberating  $^{18}\text{F}^-$ .<sup>27</sup> This instability has been attributed to the acute bite angles associated with the carboxylate pendant arms, leading to increased chelate ring strain. This was evidenced *via* comparison of the structural data for  $[\text{AlF}(\text{Bn-NODA})]$  vs.  $[\text{GaF}(\text{Bn-NODA})]$ , which depicted the Ga-O bond as being approximately 0.10 Å longer than the analogous Al-O bond.<sup>28</sup> Hence, decomposition may arise due to the destabilisation of the  $\text{Ga}^{3+}$  coordination sphere in the presence of competitive ions/water.

It was suggested that the stability of the metal-fluoride complex could be improved with careful fine-tuning of the steric and electronic properties of the macrocyclic chelator. Recent research (in which the two carboxylate arms have been substituted for two phosphinate arms) has shown that a subtle increase in the bite angle leads to a significant improvement in radiochemical stability over time.<sup>29</sup> This further highlights the effect that pendant arms can have on the properties of the resulting macrocyclic complexes. The synthesis of the parent phosphinic acid ligand, 1-benzyl-4,7-phenylphosphinic acid-1,4,7-triazacyclononane ( $\text{H}_2\text{-Bn-NODP}$ ), is given in Scheme 2.4 below.



Scheme 2.4 – Synthesis of  $\text{H}_2\text{-Bn-NODP}$  via its intermediate phosphinate-ester derivative.

Phosphinic acid functionalised triazacyclononane ligands were first reported by Broan *et al.*<sup>30</sup> in 1992 as an alternative to the carboxylic acid analogues. As phosphinic acids are typically stronger acids than carboxylic acids, protonation of the tacn-ring and the phosphorus-oxygen double bond is prevented.<sup>31</sup> This leads to enhanced kinetic stability of the ensuing metal-ligand complexes, as acid-catalysed dissociation of the metal is prevented. The pentavalency of the phosphorus also means that an array of functional groups may be introduced to further tune the ligand's properties. This is highlighted in Figure 2.4, which depicts the four phosphinic pendant arm variations identified in the 1992 paper.



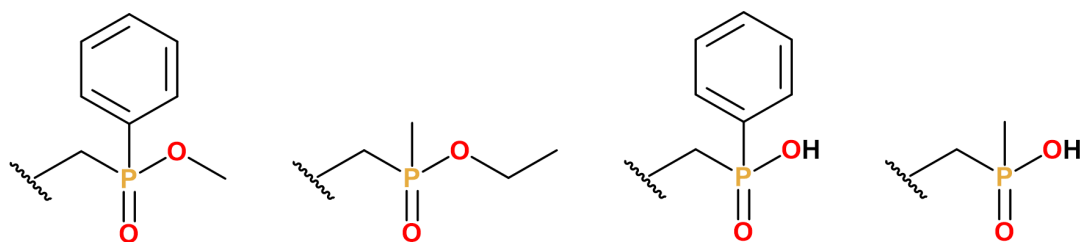


Figure 2.4 – Pendant arms reported for novel phosphinic-acid functionalised triazacyclononane ligands.

Later, work by the same group reported several transition metal and Group 13 metal complexes with the ligand, 1,4,7-triazacyclononane-1,4,7-triyltrimethylenetris(phenylphosphinate) ( $H_3$ -NOTP).<sup>32</sup> Here, the ligand acts as a charged donor, providing an  $N_3O_3$  donor set *via* the tacn nitrogen atoms and the OH groups of the phosphinic acid pendant arm (after deprotonation). The synthesis of  $H_3$ -NOTP forms a phosphinate-ester derivative directly from the free base as an intermediate, preceding acid hydrolysis to remove the methyl ester (OMe) group. The intermediate phosphinate-ester ligand may also have use as a complexing agent for transition metals and Group 13 metals alike; as a neutral donor ligand with no groups for deprotonation, it still may provide a hexadentate  $N_3O_3$  donor set *via* chelation of the oxygen of the phosphorus-oxygen double bond (Figure 2.5).

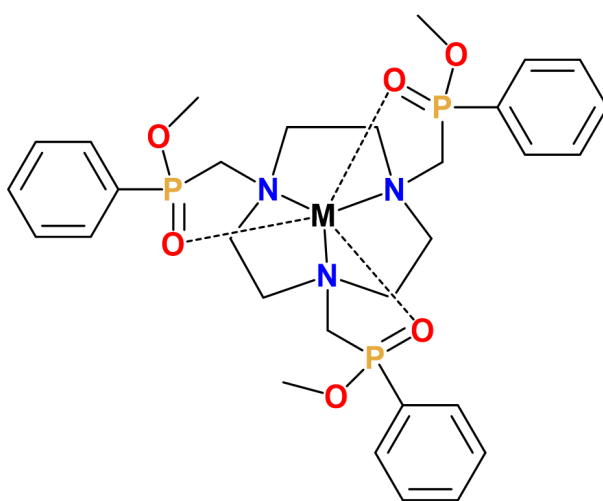


Figure 2.5 – Proposed structure of  $[M(NOTP-OMe)]^n+$  complexes.

A similar coordination mode has been observed for neutral-donor triazacyclononane ligands containing pendant arms with amide functional groups. It has been shown – across a variety of first-row divalent transition metals with tris-amide substituted ligands – that the carbonyl oxygen binds to the metal centre alongside the tacn-ring nitrogens.<sup>33</sup> If the pendant arm contains a primary amide, deprotonation of the  $NH_2$  group may also be observed for certain high-valent transition metals to provide an  $N_4O_2$  donor set.<sup>34</sup> In this case, the interchangeable coordination mode of the ligand can be used to stabilise metal centres in various oxidation states. However,

much of the literature concerns only symmetrical *tris*-substituted tacn ligands with simple amide pendant arms, such as the two shown in Figure 2.6. This work aims to create novel amide-functionalised triazacyclononane ligands with varying complexity and properties.

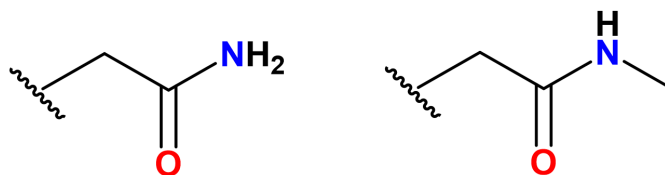


Figure 2.6 – Amide pendant arms used throughout the literature.

### 2.1.2 Ligand Design Rationale

Several factors will be considered in the formation of novel amide-functionalised triazacyclononane ligands, including:

- i) Synthesis of the ligands in high yield and purity;
- ii) The ease with which the pendant donor arms can be incorporated;
- iii) The differing properties of the pendant arm donors e.g. containing a chromophore and/or a site for bioconjugation, lipophilicity, and steric effects;
- iv) The potential hydrogen-bonding interactions;
- v) The denticity and variations thereof, of the final tacn ligand derivative.

### 2.1.3 Aims

This chapter aims to synthesise existing and novel triazacyclononane ligands, with carboxylate, amide and phosphinate functionality. Complete and reliable characterisation data will be obtained for each ligand, including IR and NMR ( $^1\text{H}$  and  $^{13}\text{C}\{^1\text{H}\}$ ;  $^{13}\text{C}$  135-DEPT if required) spectroscopy and ESI<sup>+</sup> mass spectrometry. Where possible, existing synthetic methodologies and purification procedures will be improved upon.

The novel amide-functionalised triazacyclononane ligands will be synthesised according to the ligand rationale design proposed above, with the overall goal of creating scaffolds suitable for the formation of stable  $\text{MF}_3$  complexes for  $^{18}\text{F}$  radiolabelling applications (Chapters 4 and 5). The coordination modes and general properties of these ligands (and the NOTP-OMe ligand) will be further explored in Chapter 3.

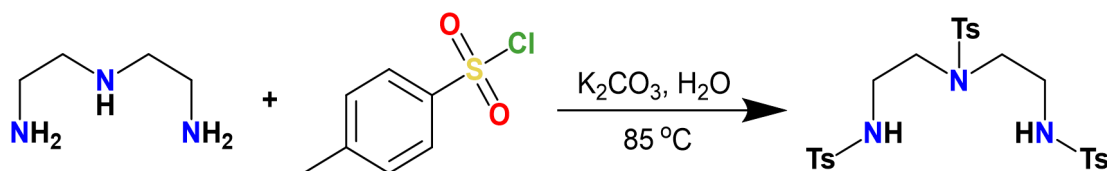
## 2.2 Results and Discussion

### 2.2.1 Synthesis of Triazacyclononane and Its Precursors

#### 2.2.1.1 Synthesis of the Precursors and Ring-Closure

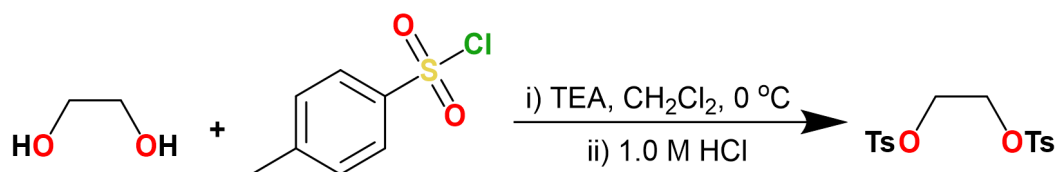
The synthesis of the tris-tosylated form of triazacyclononane follows the route first patented by Stephen Madison in 1994.<sup>15</sup> The initial step involves the formation of the two precursors, N,N',N''-tris(*p*-tolylsulfonyl)diethylene triamine (Ts<sub>3</sub>-DET) and 1,2-bis-[(*p*-tolylsulfonyl)oxy]ethane (EGT). Both are prepared in very high yields (> 90%) and as white powders. Characterisation by NMR spectroscopy confirms the products.

Ts<sub>3</sub>-DET was prepared *via* the reaction of triethylene diamine and tosyl chloride in the presence of potassium carbonate, as shown in Scheme 2.5 below. The tosyl group is retained in the subsequent steps, acting as a protecting group for the amine functions.



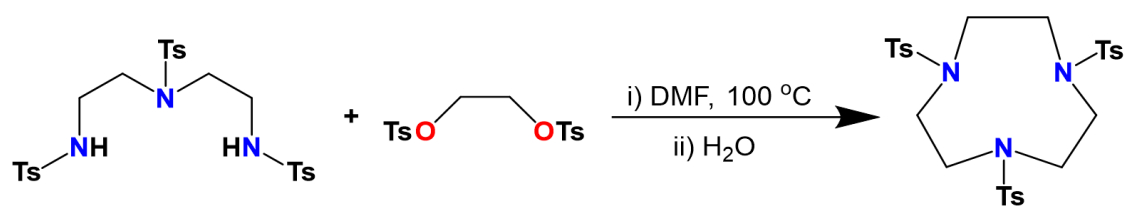
Scheme 2.5 – Synthesis of N,N',N''-tris-(*p*-tolylsulfonyl)diethylene triamine (Ts<sub>3</sub>-DET).

Similarly, EGT was prepared *via* the method depicted in Scheme 2.6. Ethylene glycol is reacted with tosyl chloride in the presence of triethylamine, followed by aqueous work-up using 1.0 M HCl. The OTs fragment will act as a leaving group for the next step.



Scheme 2.6 – Synthesis of 1,2-bis-[(*p*-tolylsulfonyl)oxy]ethane (EGT).

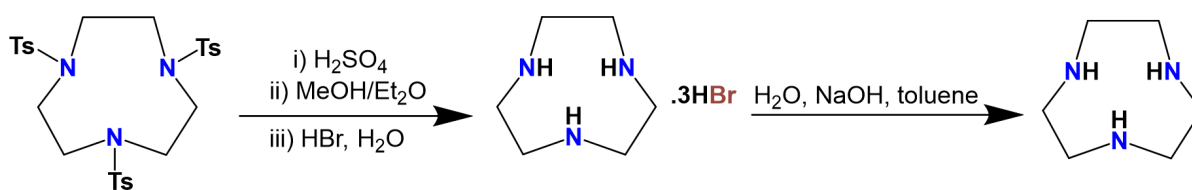
Cyclisation is the second step towards the formation of tacn and is depicted in Scheme 2.7. Ts<sub>3</sub>-DET and EGT are combined in equimolar concentrations in the presence of K<sub>2</sub>CO<sub>3</sub>, following a high-dilution method to ensure ring closure is preferred over polymerisation. The reaction between the two precursors is a 1:1 condensation reaction, combining the fragments such that the desired macrocycle, N,N',N''-tris(*p*-tolylsulfonyl)-1,4,7-triazacyclononane (Ts<sub>3</sub>-tacn) is formed. As a vast quantity of solvent is required, the work-up involves removal of the DMF *via* distillation before washing with water and isolating the final product in good yield (~ 70%) as a white powder. <sup>1</sup>H and <sup>13</sup>C{<sup>1</sup>H} NMR confirm the product in high purity.



Scheme 2.7 – Synthesis of *N,N',N''*-tris(*p*-tolylsulfonyl)-1,4,7-triazacyclononane (*Ts*<sub>3</sub>-*tacn*).

#### 2.2.1.2 Synthesis of the HBr Salt and Isolation of *H*<sub>3</sub>-*Tacn*

Scheme 2.8 shows the two final steps in the formation of *tacn*, following a modified method reported by Richman and Atkins for the syntheses of cyclic polyamines.<sup>9</sup>



Scheme 2.8 – Isolation of 1,4,7-triazacyclononane (*tacn*) from *Ts*<sub>3</sub>-*tacn*.

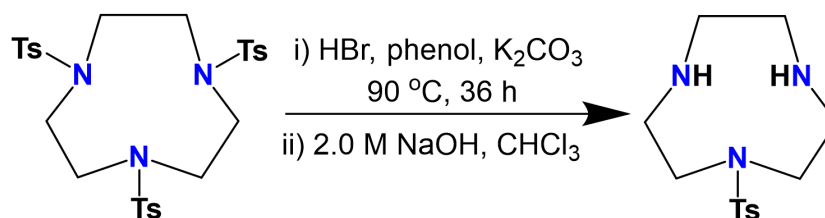
*Ts*<sub>3</sub>-*tacn* was first dissolved and heated in concentrated sulfuric acid overnight to remove all three of the tosylate-protecting groups. Addition of the acidic mixture to cold methanol produced a precipitate, which was washed with ether. Recrystallisation from water and aqueous hydrobromic acid left the product – the hydrobromide salt of the free base – as a beige-coloured powder, in a very good yield (96%). To isolate triazacyclononane, the fourth and final step involves reflux of a mixture of the hydrobromide salt in toluene/water/NaOH. As the reaction proceeds, a sodium bromide crust forms, to leave *H*<sub>3</sub>-*tacn* free in the toluene. Removal of the solvent *via* distillation yielded the ligand as a crystalline yellow solid, which was successfully characterised using <sup>1</sup>H NMR spectroscopy.

#### 2.2.1.3 Selective Deprotection of *Ts*<sub>3</sub>-*Tacn* and Isolation of *Ts*-*Tacn*

For the synthesis of macrocyclic ligands where different functional groups are substituted at the ring-N positions, these groups must be added sequentially. This can be done by selective deprotection of *Ts*<sub>3</sub>-*tacn*, where only one or two tosylate functions are removed at a time. This is typically done by heating the tris-protected macrocycle in the presence of an acid (such as HBr), phenol, and a base. The addition of phenol increases the solubility of *Ts*<sub>3</sub>-*tacn* and acts as a scavenger for free bromine.<sup>35</sup>

The formation of the mono-tosylated derivative, 1-(*p*-tolylsulfonyl)-1,4,7-triazacyclononane, is depicted in Scheme 2.9. *Ts*<sub>3</sub>-*tacn* is refluxed in HBr (33 wt % in H<sub>2</sub>O) alongside phenol and K<sub>2</sub>CO<sub>3</sub> for 36 hours, during which time a solid precipitate forms. The precipitate was filtered and

dissolved in 2.0 M NaOH until pH > 12. Using a smaller volume of water leads to a greater proportion of the product being recovered in the subsequent extraction step. Combining the organic portions and removing the solvent *via* rotary evaporation led to the isolation of the product as an off-white oily solid, in a modest yield (55%).

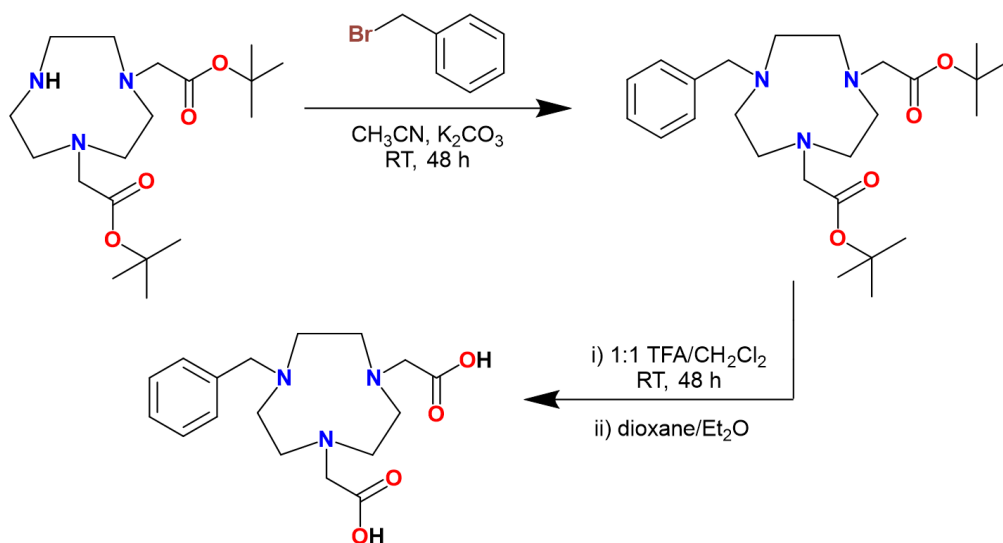


Scheme 2.9 – Formation of 1-(*p*-tolylsulfonyl)-1,4,7-triazacyclononane (*Ts-tacn*) via selective deprotection of *Ts*<sub>3</sub>-*tacn*.

## 2.2.2 Synthesis of Triazacyclononane Ligands with Carboxylate Functionality

The tris-carboxylate *tacn* ligand, H<sub>3</sub>-NOTA, is commercially available. Its benzyl dicarboxylate derivative, H<sub>2</sub>-Bn-NODA, has also been used towards the synthesis of inorganic radiotracers, particularly by McBride and his work on ‘Al-F’ chemistry.<sup>26,36</sup>

Although this ligand is known within the literature, the aim here was to obtain complete and reliable characterisation data prior to coordination chemistry experiments (Chapter 6). H<sub>2</sub>-Bn-NODA was prepared using a method reported by Pujales-Paradela *et al.*<sup>37</sup>, starting from the commercially available derivative, di-*tert*-butyl-2,2’-(1,4,7-triazacyclononane-1,4-diyl)diacetate (NO2A<sup>t</sup>Bu) (Scheme 2.10). The addition of benzyl bromide to NO2A<sup>t</sup>Bu in the presence of K<sub>2</sub>CO<sub>3</sub> formed the *tert*-butyl-protected derivative of the H<sub>2</sub>-Bn-NODA ligand. Acid hydrolysis using trifluoroacetic acid (TFA) in CH<sub>2</sub>Cl<sub>2</sub> led to the product in a very good yield (96%) as a dark brown oil. The ligand was successfully characterised using NMR spectroscopy and ESI<sup>+</sup> MS.



Scheme 2.10 – Synthesis of  $H_2\text{-Bn-NODA}$  via  $\text{NO}_2\text{A}^t\text{Bu}$ .

### 2.2.3 Synthesis and Characterisation of Amide-Functionalised Triazacyclononane Ligands

Three novel amide-functionalised triazacyclononane ligands ( $L^1 - L^3$ ) have been synthesised based upon preliminary work by George Sanderson, which looked towards the formation of new macrocyclic chelator ligands for potential chelators for  $M\text{-}^{18}\text{F}$  radiolabelling.<sup>38</sup> Three different pendant arms (Figure 2.7) were chosen, considering factors such as ease of synthesis, lipophilicity, and the inclusion of a chromophore.

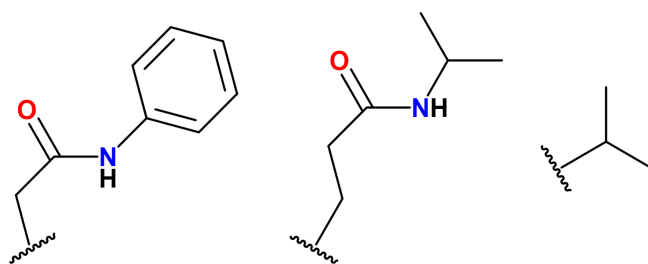


Figure 2.7 – Pendant arms used in the ligands  $L^1$ ,  $L^2$  and  $L^3$ .

The phenyl group is of particular interest in the context of PET imaging, as it may act as a chromophore to follow the radiochemical reactions *via* the HPLC-UV trace, and it may also act as a tether for biomolecules or small peptides to bind. Alkyl substituents were chosen to increase solubility in organic media. The three target ligands  $L^1$  (1,4,7-tris-phenylacetamide-1,4,7-triazacyclononane),  $L^2$  (1,4,7-tris-isopropylacrylamide-1,4,7-triazacyclononane) and  $L^3$  (1-phenylacetamide-4,7-diisopropyl-1,4,7-triazacyclononane) are shown in Figure 2.8.

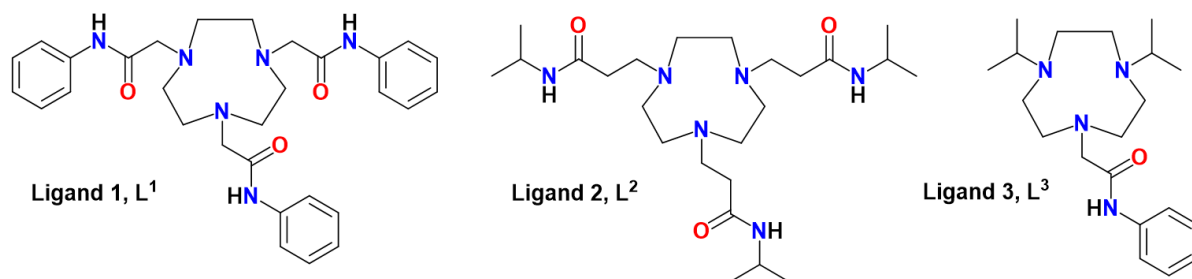
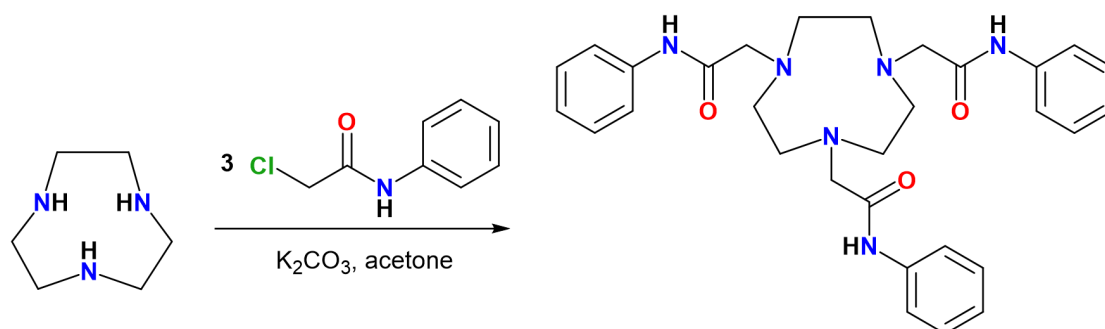


Figure 2.8 – The novel amide-functionalised triazacyclononane ligands,  $L^1$ ,  $L^2$  and  $L^3$ .

Each of the different amide-functionalised ligands can be synthesised from the direct reaction of the parent tacn with the pendant arm precursor. Generally, the syntheses are performed under mild conditions, forming the target ligands in good yield. Purification of the ligands  $L^1$  and  $L^3$  was required, and an appropriate method was developed for use with the automated flash chromatography system using a silica-based stationary phase. The pure ligands were isolated as a white powder ( $L^1$ ), yellow oil ( $L^2$ ) or orange oil ( $L^3$ ) and characterised by  $^1\text{H}$  and  $^{13}\text{C}\{^1\text{H}\}$  NMR and IR spectroscopy, and *via* high-resolution  $\text{ESI}^+$  MS. The IR spectra for all three ligands  $L^1$ - $L^3$  show two strong  $\text{C}=\text{O}$  stretching vibrations, along with the expected  $\nu(\text{NH})$  bands.

For  $L^1$ , three equivalents of the pendant arm precursor, 2-chloro-N-phenylacetamide, are added to triazacyclononane in the presence of an excess of  $\text{K}_2\text{CO}_3$  (Scheme 2.11). The reaction mixture can be left to stir overnight under ambient conditions. This is followed by filtration to remove any salts formed, and then adjustment of the solution to  $\text{pH} > 12$ . Extraction in chloroform and subsequent drying of the organic extracts *in vacuo* affords the crude product mixture as a tan-coloured oil. This was then purified *via* automated flash column chromatography using the Biotage Selekt system.



Scheme 2.11 – Synthesis of 1,4,7-tris(phenylacetamido)-1,4,7-triazacyclononane (Ligand 1,  $L^1$ ).

The Biotage columns used in the purification of  $L^1$  are reverse-phase and use a C18 packing media. Reverse-phase columns typically use polar solvents such as water, acetonitrile or methanol. As better separation can be achieved through dry-loading the product onto a silica

adsorbent (in comparison to wet loading), methanol was avoided. To prevent the amide functions 'sticking' to the column, formic acid (0.1%) was added to both mobile phase solvents, A and B (A = H<sub>2</sub>O, B = MeCN); comparison of the <sup>1</sup>H NMR data pre- and post-purification indicates that the addition of formic acid does not cause protonation. After optimising the conditions, L<sup>1</sup> was eluted as a white powder solid, in high yield (90%). HR ESI<sup>+</sup> MS confirmed the presence of a single product, with *m/z* peaks found at 529.2921 and 551.2738, corresponding to [L<sup>1</sup>+H]<sup>+</sup> and [L<sup>1</sup>+Na]<sup>+</sup>, respectively.

L<sup>1</sup> has limited solubility in most common solvents – a property likely derived from the three phenyl substituents. NMR data of the purified product was collected in CD<sub>3</sub>OD, alongside the <sup>1</sup>H NMR data for the corresponding HCl salt. As Figure 2.9 shows, protonation causes the twelve protons of the tacn-ring to shift significantly higher frequency from that of free ligand (3.66 ppm vs. 3.14 ppm). The six protons corresponding to the methylene bridge of the pendant arm also shift similarly, from 3.87 ppm in the free ligand, to 4.23 ppm in the HCl salt. The values of the shifts corresponding to the 15 aromatic protons remain mostly unchanged between the two, although the coupling appears to become more resolved in L<sup>1</sup>·HCl. This may be due to the reduced symmetry of L<sup>1</sup>·HCl arising from the protonation of the tacn-ring. This may fix the geometry of the ligand, causing it to become more rigid, with the pendant arms becoming less dynamic/fluxional in solution. In the free ligand, the pendant arms are likely free to rotate in solution. Rapid proton exchange between N-H of the ligand and O-H of the methanol means the N-H peak in both cases is not quantitative and cannot be integrated accurately. The acidity of the solution also causes the water present in the CD<sub>3</sub>OD NMR solvent to shift to higher frequency.



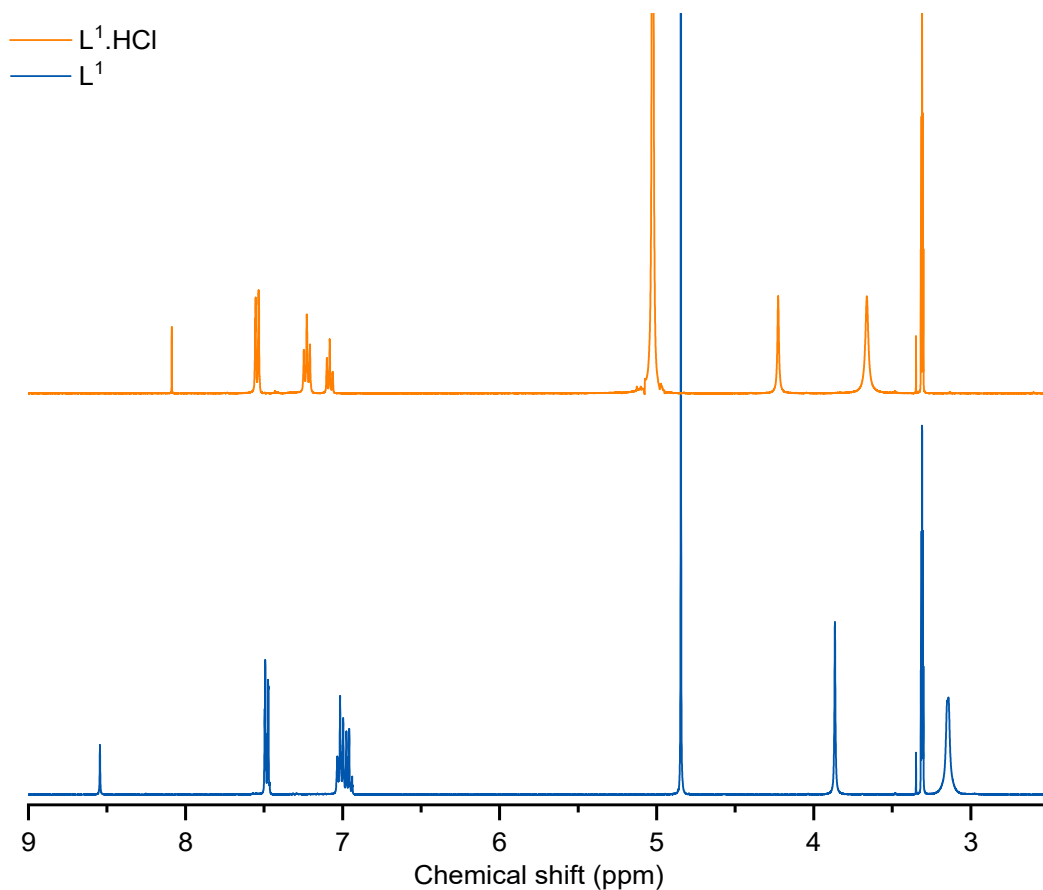


Figure 2.9 –  $^1\text{H}$  NMR spectra of  $\text{L}^1$  (bottom; blue) and  $\text{L}^1\cdot\text{HCl}$  (top; orange) ( $\text{CD}_3\text{OD}$ ).

From the slow evaporation of the NMR solution containing  $\text{L}^1\cdot\text{HCl}$ , crystals suitable for SCXRD were grown. Figure 2.10 shows the structure of  $\text{L}^1\cdot\text{HCl}$ , with mono-protonation of the tacn ring. *Intramolecular*  $\text{N6-H6}\cdots\text{O1(=C)}$  H-bonding between the amide groups is evident between two of the pendant arms of  $\text{L}^1\cdot\text{HCl}$ , while *intermolecular* H-bonding involving the chloride anion and the third amide arm in two adjacent  $\text{L}^1$  moieties,  $\text{N4-H4}\cdots\text{Cl1}\cdots\text{H5-N5}$  gives rise to weakly associated dimers in the solid state ( $\text{N4-H4}\cdots\text{Cl1} = 2.130(15)$ ,  $\text{N5-H5}\cdots\text{Cl1} = 2.166(17)$  Å). No further hydrogen bonding is observed.

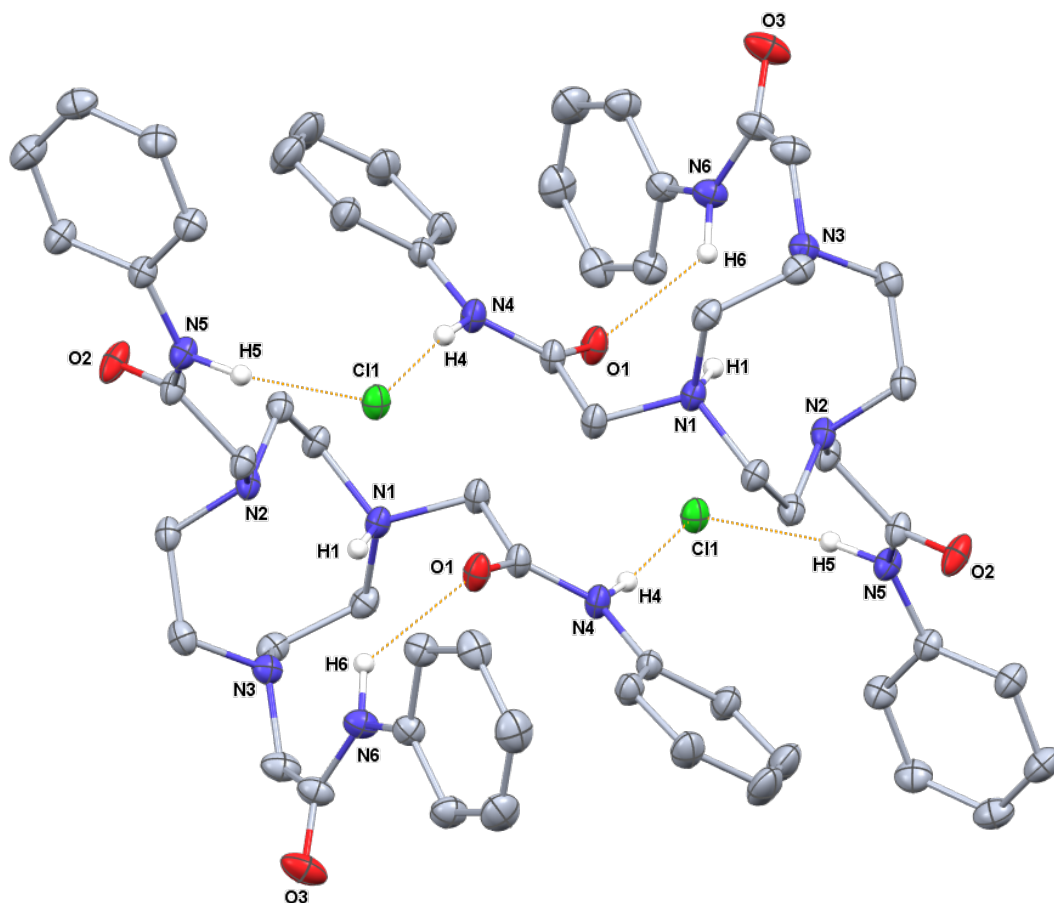
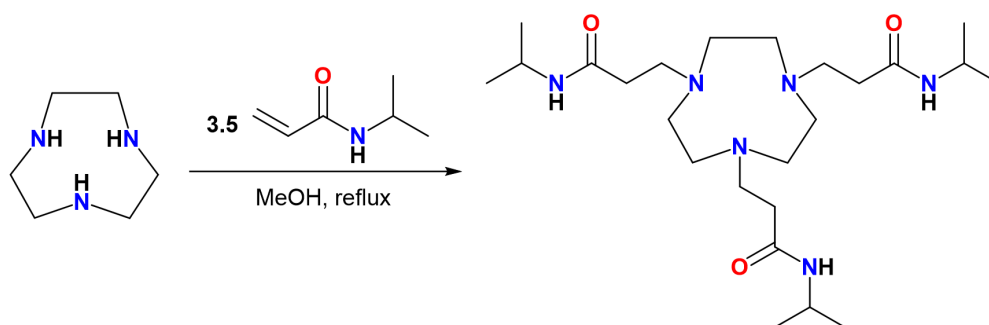


Figure 2.10 – View of the structure of  $L^1 \cdot HCl$  showing the atom numbering scheme and a weakly H-bonded centrosymmetric dimer, arising from the amide NH functions and a chloride counter-ion. Ellipsoids are drawn at the 50% probability level and H atoms (except those involved in H-bonding) are omitted for clarity.

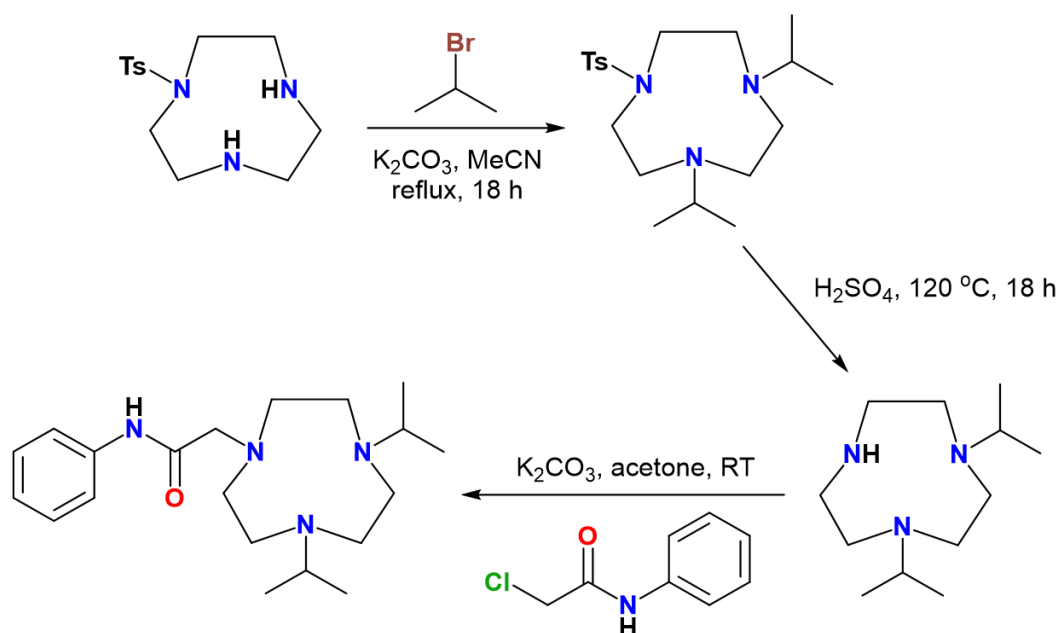
Similar to  $L^1$ ,  $L^2$  is synthesised from the reaction of tacn with a slight excess (3.5 eqv.) of the pendant arm precursor (N-isopropylacrylamide), following a method adapted from previous work (Scheme 2.12). Refluxing the mixture in methanol overnight forms a yellow solution. Following filtration and removal of the solvent *in vacuo*, the oily residue is washed with 1.0 M HCl. Washing in chloroform removes any unreacted amide starting material. The aqueous portion containing the product is then brought to pH > 12, and the ligand isolated *via* extraction in organic solvent. Removal of the solvent *in vacuo* leaves a tan-coloured oil in good yield (89%).



Scheme 2.12 – Synthesis of 1,4,7-tris-isopropylacrylamide-1,4,7-triazacyclononane (Ligand 2,  $L^2$ ).

$L^2$  was fully characterised using HR ESI<sup>+</sup> MS, and IR and NMR spectroscopy. HR ESI MS<sup>+</sup> confirmed the formation of the ligand with  $m/z$  peaks at 469.3863 ( $[L^2+H]^+$ ), 491.3683 ( $[L^2+Na]^+$ ) and 235.1967 ( $L^2+2H^{2+}$ ). An  $m/z$  peak at 356.3019 can be assigned to a di-substituted monovalent  $L^2+H^+$ , whereby one of the pendant arms has been lost. This species is not present in either the  $^1H$  or  $^{13}C\{^1H\}$  NMR spectra, which suggests this was a consequence of fragmentation during the ionisation process rather than a by-product of the reaction. The  $^1H$  NMR spectrum in  $CD_3OD$  shows a doublet centred at 1.14 ppm with a  $^3J_{1H-1H}$  value of 6.6 Hz corresponding to the terminal  $iPr-CH_3$  protons; the  $iPr-CH$  resonates as a septet at 3.98 – 3.92 ppm with a similar  $^3J_{1H-1H}$  coupling value of 6.5 Hz. Two broad triplets are present at 2.81 – 2.78 ppm and 2.29 – 2.26 ppm, corresponding to the  $CH_2$  groups of the ethylene linker, and the 12 tacn protons resonate as a broad singlet at 2.83 ppm.  $^1H$  NMR data was also obtained in  $CDCl_3$ , and the coupling becomes more resolved, with the isopropyl protons and the ethylene bridge protons all forming  $^3J_{1H-1H}$  interactions with values of 6.6 Hz. Attempts to obtain NMR data for the HCl salt of the ligand in the same solvents were unsuccessful due to insolubility of the salt.

The synthesis of  $L^3$  is much more complex than  $L^1$  and  $L^2$  and requires a multi-step procedure following the formation of Ts-tacn (Scheme 2.13). The parent tacn compound, 1,4-diisopropyl-7-N'-1,4,7-triazacyclononane ( $iPr_2$ -tacn), is synthesised according to a method reported in the literature.<sup>39</sup> 2-bromopropane is added to Ts-tacn in the presence of  $K_2CO_3$ , and the mixture is stirred at reflux in acetonitrile overnight. After pH adjustment and removal of the solvent *in vacuo*, 1,4-diisopropyl-7-tosyl-1,4,7-triazacyclononane (1,4- $iPr_2$ -7-Ts-tacn) is isolated as an off-white solid in high yield (91%). The remaining tosyl group is removed *via* acid hydrolysis using conc.  $H_2SO_4$  and heating to 120 °C overnight.  $iPr_2$ -tacn is isolated in high yield (92%) as an amber-coloured oil following pH adjustment and extraction using aqueous NaOH/ $CHCl_3$ . All intermediate ligands were successfully characterised *via*  $^1H$  and  $^{13}C\{^1H\}$  NMR spectroscopy, which confirmed the products in high purity.



Scheme 2.13 – Multi-step synthesis of 1-phenylacetamide-4,7-diisopropyl-1,4,7-triazacyclononane (Ligand 3,  $L^3$ ) via Ts-tacn.

Using the same pendant arm precursor as  $L^1$ , this is reacted in equimolar concentration to  $iPr_2$ -tacn under ambient conditions in the presence of  $K_2CO_3$ . After work-up involving pH adjustment and extraction in chloroform, the crude product is isolated as a dark-coloured oil. Purification was performed similarly to  $L^1$ , using the Biotage Selekt flash-chromatography system and the same mobile solvents. After purification, the initial product was confirmed using HR ESI<sup>+</sup> MS, with peaks at 347.2812 ( $[L^3+H]^+$ ) and 305.2341 ( $[L^3-iPr][H^+]$ ). However, although the spectroscopic data also matched the data reported earlier by George Sanderson, further experiments (which include several attempted and unsuccessful reactions with  $MF_3$  precursors,  $M = Al, Ga, In$  and  $Fe$ ) indicated that the ligand was protonated. Given the experimental conditions, the isolated product is likely to be the HCl salt, as a result of the loss of chloride from the pendant arm during the initial synthesis. With this in mind, the first isolated species was washed with aqueous triethylamine. The target ligand remained undissolved in the basic solution, so this was separated and taken into  $CHCl_3$ . The organic phase was washed with aqueous base and separated. The volatiles were removed *via* rotary evaporation to yield the pure ligand,  $L^3$ . HR ESI<sup>+</sup> MS again confirmed the ligand, with a peak at 347.2812 ( $[L^3+H]^+$ ). Although HR ESI<sup>+</sup> MS is indistinguishable between the two isolated species, Figure 2.11 shows the comparison of the  $^1H$  NMR spectra obtained for the initial species,  $[L^3][H^+]$ , and the final product,  $L^3$ .

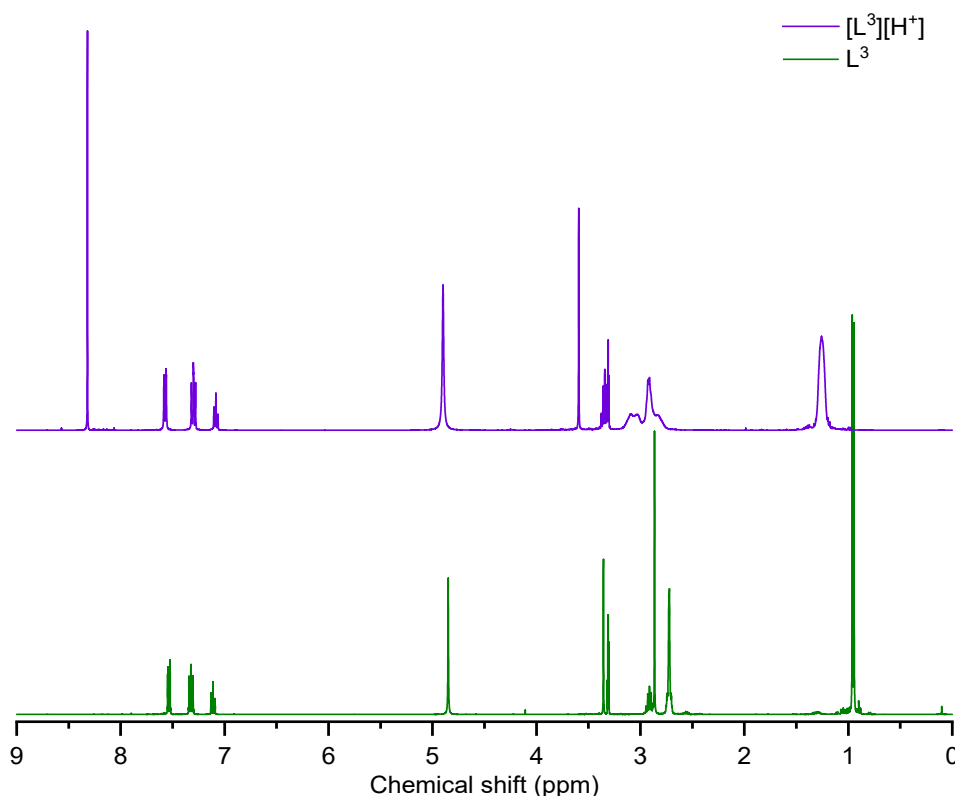


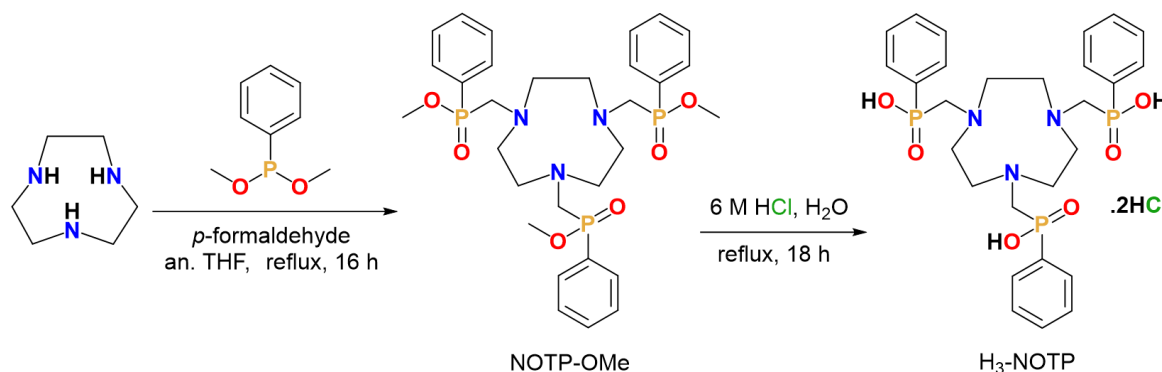
Figure 2.11 –  $^1\text{H}$  NMR spectra of  $\text{L}^3$  (bottom; green) and  $[\text{L}^3][\text{H}^+]$  (top; purple) ( $\text{CD}_3\text{OD}$ ).

The chemical shifts of almost all groups change noticeably between the two different  $^1\text{H}$  NMR spectra. Whilst the five aromatic protons remain mostly unchanged,  $[\text{L}^3][\text{H}^+]$  has a sharp peak at 8.32 ppm corresponding to the N-H of the mono-protonated tacn ring, which is absent in the free base,  $\text{L}^3$ . The two  $\text{CH}_2$  protons of the methylene bridge have also shifted to higher frequency, from 3.36 ppm in the pure  $\text{L}^3$ , to 3.59 ppm in the protonated ligand. This is also true of the  $i\text{Pr-CH}$  proton (2.96 – 2.87 ppm vs 3.39 – 3.32 ppm), which resonates as a septet due to  $^3J_{\text{H-H}}$  coupling to the six neighbouring  $i\text{Pr-CH}_3$  protons. The tacn resonances in  $\text{L}^3$  are in a well-defined 8:4 split, and at a slightly higher frequency shift of the tacn resonances for  $[\text{L}^3][\text{H}^+]$ . They are also much broader and less defined for the latter, likely due to tautomerisation; the additional proton within the tacn ring may rapidly migrate between the three nitrogens.<sup>40</sup>

## 2.2.4 Synthesis and Characterisation of Phosphinate-Functionalised Tacn Ligands

The phosphinate-ester functionalised triazacyclononane ligand, NOTP-OMe, has been synthesised according to earlier work by Parker and his group, who formed it in an intermediate step towards  $\text{H}_3\text{-NOTP}$  (Scheme 2.14).<sup>30</sup> Whilst transition metal and Group 13 complexes of the ligand  $\text{H}_3\text{-NOTP}$  are known, little work has been reported on the intermediate compound. As mentioned above, NOTP-OMe is expected to have a similar coordination mode to the amide tacn

ligands  $L^1$  and  $L^2$ , forming hexadentate complexes with an  $N_3O_3$  donor set arising from the  $P=O$  bond.



Scheme 2.14 – Synthesis of NOTP-OMe and H<sub>3</sub>-NOTP.

NOTP-OMe is synthesised *via* the direct reaction of the phosphinate arm derivative, dimethylphenylphosphonite, with H<sub>3</sub>-tacn, in the presence of *p*-formaldehyde. As the pendant arm precursor is prone to hydrolysis *in situ*, the reaction is performed under inert conditions using anhydrous THF to minimise the amount of moisture in the reaction mixture. Refluxing overnight yields a pale orange mixture, which is filtered. Removal of the solvent under reduced pressure results in a crude amber oil containing the target product, which requires further purification. Figure 2.12 shows the chromatogram (obtained from ESI<sup>+</sup> MS) for the crude product, which contains a mixture of several species, including the target ligand.

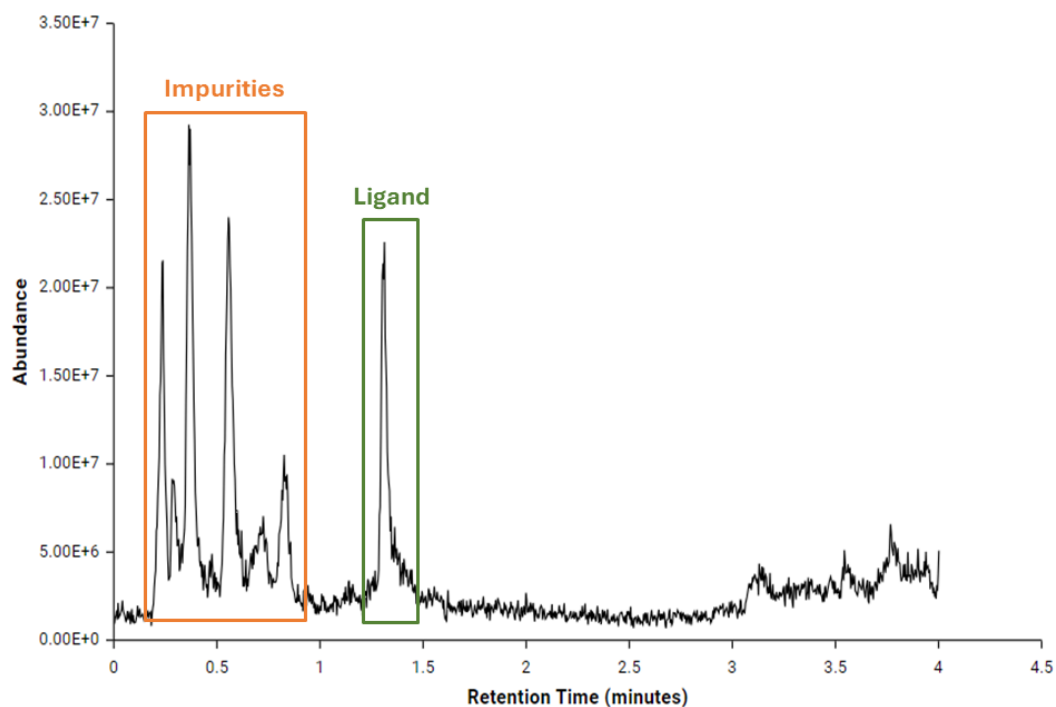


Figure 2.12 – Chromatogram (obtained from ESI<sup>+</sup> MS analysis) of the crude product containing the NOTP-OMe ligand.

The reported method uses normal-phase manual flash column chromatography, with the mobile phase consisting of 100-95% dichloromethane with a gradient of 0-5% methanol. Neutral alumina is used as the stationary phase, as it retains the ligand better than silica (which is slightly acidic). However, it was found that some impurities co-elute alongside the target product, and several time-consuming columns were required, which also decreased the overall yield. Translating the manual purification method onto the automated system was necessary to obtain the clean ligand. The automated system also means the crude product can be purified on a much larger scale at a single time.

As mentioned, a reverse-phase solvent system is needed for the Biotage system. Water and methanol were chosen as solvents A and B, respectively. Neutral alumina was used as the adsorbent media to dry-load the sample before purification. Purification using this method was successful, and much better separation was achieved in comparison to the manual columns. This is highlighted in Figure 2.13, where each coloured peak represents one of the impurities separated from the crude mixture.

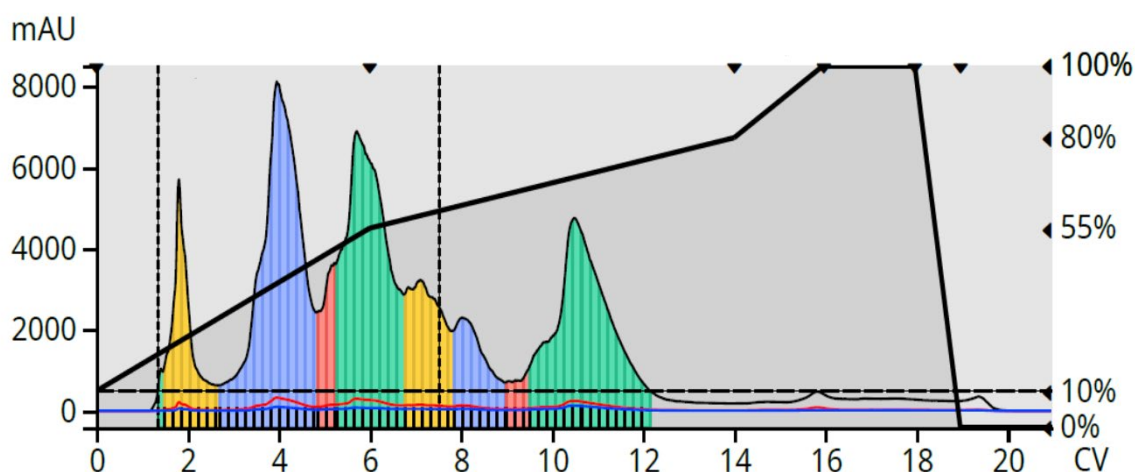


Figure 2.13 – Purification of NOTP-OMe using a Biotage Selekt flash chromatography system.

ESI<sup>+</sup> MS of the final fraction confirmed that the ligand NOTP-OMe was eluted as a single product (chromatogram shown in Figure 2.14), at a gradient containing approximately 70% MeOH and 30% H<sub>2</sub>O. As the ESI<sup>+</sup> MS shows, a peak was observed at  $m/z = 634.31$ , corresponding to [NOTP-OMe+H]<sup>+</sup>. Removal of the solvents under reduced pressure yielded a tan-coloured oil. Only a 15% yield was obtained – attributed to the formation of hydrolysis products during the initial overnight reaction. This would have significantly limited the amount of pendant arm precursor available to form the tris-substituted target ligand.

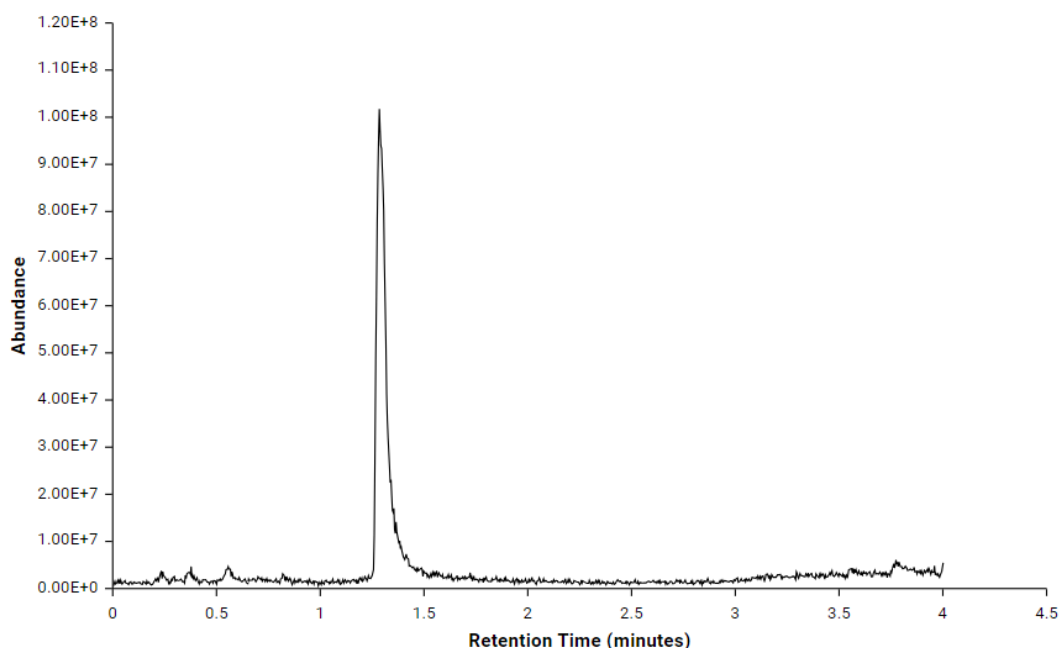


Figure 2.14 – Chromatogram (obtained from ESI<sup>+</sup> MS) of the purified ligand, NOTP-OMe.

The  $^{31}\text{P}\{^1\text{H}\}$  NMR spectrum of the purified product shows a broad singlet at 40.7 ppm, which coincides with the literature data. The phosphorus centre of the pendant arms is chiral, and due to the presence of stereoisomers, multiple peaks might be expected. However, these could be lost under the broad nature of the resonance. The  $^1\text{H}$  NMR differs slightly from the original reported shifts (which included only the tacn and pendant arm protons). Very broad resonances are present at 2.70 ppm and 3.06 ppm, arising from the 12 tacn and six bridging  $\text{CH}_2$  protons of the pendant arms, respectively. A poorly resolved doublet of triplets is observed at 3.63 – 3.58 ppm, corresponding to the  $\text{O-CH}_3$  groups. This has previously been reported as a doublet. In this case, stereoisomerism may lead to the observed splitting pattern. The paper with the comparative data was published in 1992, and the resolution may not have been the same as the current standard. The previously unreported aromatic proton shifts are present as multiplets at 7.79 – 7.72, 7.57 – 7.51 and 7.51 – 7.44 ppm.

## 2.3 Conclusions

This chapter aimed to synthesise several known and novel triaza-macrocyclic ligands derived from tacn, with various pendant arms, building and improving upon existing methodologies. Based upon previous preliminary work, a design rationale for the amide-functionalised triazacyclononane ligands was utilised, to form ligands suitable for use in the following chapters for the formation of stable metal-macrocyclic complexes. This considered several factors, such as the inclusion of a chromophore, the number of amide donors, and the pendant arm length (and hence chelate ring size formed with a metal ion). These structural variations will help



elucidate the ideal properties of the ligands for potential future radiolabelling applications (Chapter 5).

The ligands  $L^1$ ,  $L^2$ , and  $L^3$  were successfully synthesised using modified methods based on those first proposed by George Sanderson.<sup>38</sup>  $L^1$  was synthesised in a high yield and, due to improved purification techniques, isolated as a single, pure species. SCXRD structural data of  $L^1 \cdot HCl$  shows hydrogen bonding is possible between the amide N-H protons and the chloride anion. This property can be further investigated with the  $MF_3$  complexes discussed in Chapter 4 of this work.  $L^2$  was also successfully synthesised, with an adjusted work-up stage, to yield the final ligand in pure form. Whilst the reported data for  $L^1$  and  $L^2$  was consistent with the ligands in their final form, it was found that the reported data for  $L^3$  was related to the protonated ligand – likely to result from the initial reaction conditions.  $L^3$  was isolated as a novel species, and this work reports the complete spectroscopic data.

The phosphinate-ester ligand, NOTP-OMe, was successfully synthesised according to the previously reported method<sup>30</sup>, alongside complete spectroscopic characterisation. A new automated method for the purification of the ligand was established, which can provide a basis for future purification methods for similar ligands. This has also greatly improved the general ease of synthesis. The reaction and purification can now be performed on a much larger scale (this was previously limited by the manual flash column chromatography technique used). Notably, NOTP-OMe has previously only been used as an intermediate step towards the formation of  $H_3$ -NOTP, and its preferred coordination environment has not been studied. Chapter 3 will discuss some preliminary novel transition metal complexes with this ligand.

## 2.4 Experimental

For general experimental methods, see Appendix A.  $NO_2A^tBu$  (ChemATech), *P*-toluenesulfonyl chloride, benzyl bromide, *N*-isopropylacrylamide, 2-bromopropane, dimethylphenylphosphonite, diethylphenylphosphonite (Sigma-Aldrich), and HBr (33 wt% in  $H_2O$ ) (Fisher) were used as supplied. The 2-chloro-*N*-phenylacetamide was synthesised according to the literature.<sup>41</sup> All solvents used were of HPLC-chromatography grade.

### 2.4.1 Triazacyclononane

#### 2.4.1.1 *N,N',N''*-tris(*p*-tolylsulfonyl)diethylene triamine ( $Ts_3$ -DET)

In a 1 L, three-necked RBF equipped with magnetic stirring and a reflux condenser, anhydrous  $K_2CO_3$  (107.0 g, 0.774 mol) was dissolved in deionised water (900 mL). The mixture was stirred vigorously. Diethylene triamine (23.5 g, 0.228 mol) was added all at once.  $TsCl$  (130.4 g, 0.884

mol) was added in portions over a period of 20 minutes, after this time a slight persistent warming of the reaction mixture was observed. This was left to stir at room temperature for 2.5 hours. After this, the reaction was stirred at 85 °C for 1.5 hours. The solid was filtered from solution and washed with deionised water. The off-white powder product was dried in the oven at 70 °C. Yield: 122.2 g, 0.216 mol (95%). <sup>1</sup>H NMR (295 K, CDCl<sub>3</sub>): δ (ppm) = 7.78 – 7.76 (ArH, m, [4H]), 7.63 – 7.61 (ArH, m, [2H]), 7.34 – 7.30 (ArH, m, [6H]), 3.22 – 3.11 (m, [8H], Et-CH<sub>2</sub>), 2.44 (s, [9H], CH<sub>3</sub>), 1.60 (s, H<sub>2</sub>O).

#### 2.4.1.2 1,2-bis-[(*p*-tolylsulfonyl)oxy]ethane (EGT)

In a 2 L, three-necked RBF equipped with magnetic stirring and a reflux condenser, TsCl (291.8 g, 1.53 mol) was dissolved in CH<sub>2</sub>Cl<sub>2</sub> (1.2 L). Ethylene glycol (45 g, 0.725 mol) and triethylamine (220.1 g, 2.18 mol) were added. The solution was stirred at 0 °C for six hours and then at room temperature overnight. The solution turned yellow, and a precipitate formed (triethylamine hydrochloride). The mixture was washed with 1.0 M HCl (2 L). The solution split into two layers, with the precipitate dissolved in the aqueous portion. The organic phase was collected, and the solvent removed *via* rotary evaporation to leave a white solid. Yield: 253.1 g, 0.683 mol (94%). <sup>1</sup>H NMR (295 K, CDCl<sub>3</sub>): δ (ppm) = 7.75 – 7.73 (d, [4H], ArH), *J* = 8.32 Hz, 7.35 – 7.33 (d, [4H], ArH), 4.19 (s, [4H], Et-CH<sub>2</sub>), 2.46 (s, [6H], CH<sub>3</sub>).

#### 2.4.1.3 *N,N',N''*-tris(*p*-tolylsulfonyl)-1,4,7-triazacyclononane (Ts<sub>3</sub>-tacn)

In a 2 L RBF equipped with a mechanical stirrer and reflux condenser, Ts<sub>3</sub>-DET (71.0 g, 0.123 mol) and K<sub>2</sub>CO<sub>3</sub> (41.1 g, 0.297 mol) were dissolved in DMF (425 mL). The mixture was stirred vigorously whilst heating to 100 °C. EGT (46.5 g, 0.123 mol) was dissolved in DMF (225 mL), placed into a pressure-equalising dropping funnel, and added dropwise to the RBF overnight. Stirring was maintained at 100 °C. The DMF was then removed *via* distillation under atmospheric pressure. The remaining slurry was added to ice-cold di H<sub>2</sub>O (1.5 L) whilst stirring vigorously, causing precipitation of an off-white solid. This was then filtered and washed with fresh di H<sub>2</sub>O. The off-white solid product was dried in an oven at 70 °C. Yield: 96.3 g, 0.163 mol (66%). <sup>1</sup>H NMR (295 K, CD<sub>2</sub>Cl<sub>2</sub>): δ (ppm) = 7.69 – 7.67 (d, [6H], ArH), 7.37 – 7.35 (d, [6H], ArH), 3.39 (s, [12H], tacn-CH<sub>2</sub>), 2.44 (s, [9H], CH<sub>3</sub>), 1.58 (s, H<sub>2</sub>O). <sup>13</sup>C{<sup>1</sup>H} NMR (295 K, CD<sub>2</sub>Cl<sub>2</sub>): δ (ppm) = 144.6 (ArC), 135.2 (ArC), 130.4 (ArC), 127.9 (ArC), 52.6 (tacn-CH<sub>2</sub>), 21.8 (CH<sub>3</sub>).

#### 2.4.1.4 Triazacyclononane trihydrobromide (Tacn·3HBr)

Concentrated H<sub>2</sub>SO<sub>4</sub> (210 mL) was purged with N<sub>2</sub> and then heated to 70 °C in a 500 mL RBF equipped with magnetic stirring. A glass tap adapter was used to vent the reaction. Ts<sub>3</sub>-tacn (70.0 g, 0.118 mol) was added and the reaction mixture was stirred to 100 °C for 18 hours. The solution

had turned a translucent black-brown colour. This was cooled and transferred to a dropping funnel. A large beaker containing chilled methanol (630 mL) was held in an ice bath, and the acidic solution was added slowly and dropwise maintaining a temperature below 20 °C. A precipitate formed upon addition. Diethyl ether (420 mL) was added and the solution filtered, leaving a beige-coloured solid. This was dissolved in a minimal amount of hot di H<sub>2</sub>O (40 mL), and two volumetric equivalents of HBr (48 wt % in H<sub>2</sub>O) were added. A beige-coloured solid precipitated, which was isolated, washed with diethyl ether and dried. Yield: 42.1 g, 0.113 mol (96%). <sup>1</sup>H NMR (295 K, D<sub>2</sub>O): δ (ppm) = 2.58 (s, [12H], tacn-CH<sub>2</sub>).

#### 2.4.1.5 Triazacyclononane (Tacn)

In a 500 mL RBF equipped with magnetic stirring and a Dean & Stark trap, tacn-3HBr (19.86 g, 0.053 mol), toluene (297 mL), di H<sub>2</sub>O (20 mL) and NaOH (12.87 g, 0.322 mol) were added and heated at reflux overnight. A NaBr crust had formed. The water was extracted and the toluene decanted. Additional toluene (120 mL) was added and heated at 70 °C for two hours, to extract any remaining product from the NaBr crust. This was then decanted and combined with the previous toluene extract. The majority of the toluene was removed by distillation under atmospheric pressure. The remaining few mL was removed *via* vacuum transfer – the remaining solution was cooled to below freezing using liquid nitrogen, and placed under a vacuum whilst warming to room temperature. The product was isolated as a pale yellow, hygroscopic solid. Yield: 4.18 g, 0.032 mol (60%). <sup>1</sup>H NMR (295 K, CDCl<sub>3</sub>): δ (ppm) = 2.73 (s, [12H], tacn-CH<sub>2</sub>), 2.10 (br s, [3H], NH).

### 2.4.2 Amide-Functionalised Triazacyclononane Ligands (L<sup>1</sup>, L<sup>2</sup> and L<sup>3</sup>)

#### 2.4.2.1 1,4,7-tris-phenylacetamide-1,4,7-triazacyclononane (Ligand 1, L<sup>1</sup>)

Tacn (0.506 g, 3.92 mmol) was added to a rapidly stirring mixture of K<sub>2</sub>CO<sub>3</sub> (6.50 g, 47.0 mmol) in acetone (80 mL) in a 250 mL RBF equipped with magnetic stirring. This was stirred for 10 min. at room temperature. A solution of 2-chloro-N-phenylacetamide (2.00 g, 11.8 mmol, 3 mol. eq.) in acetone (40 mL) was then added dropwise and the reaction mixture stirred at room temperature overnight. The resulting yellow mixture was filtered and the filtrate was adjusted to pH 12 with 1.5 M NaOH (*ca.* 150 mL). This solution was extracted with CHCl<sub>3</sub> (3 x 150 mL) and the organic extracts were combined. The solvent was removed using a rotary evaporator to leave a tan coloured oil. This was subsequently purified by flash chromatography. The crude ligand L<sup>1</sup> was dissolved in a minimal volume of CHCl<sub>3</sub> and four mass equivalents of silica was added to the solution, creating a slurry. The CHCl<sub>3</sub> solvent was removed by rotary evaporation to leave a free-flowing orange powder. This was dry-loaded onto the Biotage (gradient = 40% – 60%

H<sub>2</sub>O/MeCN each containing 0.01 % formic acid, over 4 column volumes where: CV = 164 mL and flow rate = 50 mL min<sup>-1</sup>). The fractions corresponding to L<sup>1</sup> were combined and the solvent was removed *in vacuo*. The residue was washed with fresh MeCN, causing precipitation of a white solid, which was collected by filtration and dried. Yield: 1.96 g, 3.53 mmol (90%). <sup>1</sup>H NMR (295 K, CD<sub>3</sub>OD): δ (ppm) = 8.55 (s, NH), 7.50 – 7.46 (m, [6H], ArH), 7.03 – 6.94 (m, [9H], ArH), 4.85 (s, H<sub>2</sub>O), 3.86 (br s, [6H], CH<sub>2</sub>), 3.14 (br s, [12H], tacn-CH<sub>2</sub>). <sup>13</sup>C{<sup>1</sup>H} NMR (295 K, CD<sub>3</sub>OD): δ (ppm) = 169.5 (C=O), 139.4 (ArC), 129.8 (ArC), 125.4 (ArC), 121.4 (ArC), 59.5 (CH<sub>2</sub>), 51.1 (tacn-CH<sub>2</sub>). <sup>13</sup>C 135-DEPT NMR (295 K, CD<sub>3</sub>OD): δ (ppm) = 129.6 (ArC), 125.1 (ArC), 121.1 (ArC), 59.2 (CH<sub>2</sub>), 50.1 (tacn-CH<sub>2</sub>). HR ESI<sup>+</sup> MS (CH<sub>3</sub>OH): found: *m/z* = 529.2921 [L<sup>1</sup>+H]<sup>+</sup> (calculated for [C<sub>30</sub>H<sub>37</sub>N<sub>6</sub>O<sub>3</sub>]<sup>+</sup>: *m/z* = 529.2927); 551.2738 [L<sup>1</sup>+Na]<sup>+</sup> (calculated for [C<sub>30</sub>H<sub>36</sub>N<sub>6</sub>O<sub>3</sub>Na]<sup>+</sup>: *m/z* = 551.2747). IR (Nujol, ν / cm<sup>-1</sup>): 3344 m, 3180 w (NH), 1682 s, 1596 s (C=O).

#### 2.4.2.2 [Ligand 1][HCl]

L<sup>1</sup> was converted to its HCl salt for X-ray structure analysis. One drop of 12 M HCl was added to a solution of L<sup>1</sup> (0.01 g, 0.019 mmol) in deuterated methanol (2 mL). Crystals suitable for X-ray diffraction were grown *via* slow evaporation of solvent over a period of four weeks in the fridge. <sup>1</sup>H NMR (298 K, CD<sub>3</sub>OD): δ (ppm) = 8.09 (s, NH), 7.56 – 7.53 (m, [6H], ArH), 7.25 – 7.21 (m, [6H], ArH), 7.10 – 7.06 (m, [3H], ArH), 5.03 (s, H<sub>2</sub>O), 4.23 (br s, [6H], CH<sub>2</sub>), 3.66 (br s, [12H], tacn-CH<sub>2</sub>). <sup>13</sup>C{<sup>1</sup>H} NMR (298 K, CD<sub>3</sub>OD): δ (ppm) = 167.8 (C=O), 139.0 (ArC), 130.0 (ArC), 126.0 (ArC), 121.6 (ArC), 59.9 (CH<sub>2</sub>), 52.9 (tacn-CH<sub>2</sub>).

#### 2.4.2.3 1,4,7-tris-isopropylacrylamide-1,4,7-triazacyclononane (Ligand 2, L<sup>2</sup>)

Tacn (0.650 g, 5.03 mmol) and N-isopropylacrylamide (1.74 g, 15.3 mmol, 5% mol. excess) were placed into a 250 mL RBF equipped with magnetic stirring and a reflux condenser and degassed MeOH (100 mL) was added. The mixture was heated at reflux for 18 h. The resulting pale-yellow solution was filtered through celite to remove any particulates, and the volatiles were then removed *via* rotary evaporation, leaving a pale-yellow oil. This was dissolved in 1.0 M HCl (20.5 mL) and extracted with CHCl<sub>3</sub> (3 x 50 mL) to remove the excess N-isopropylacrylamide. The organic phases were discarded. The pH of the remaining aqueous phase was adjusted to > 12 using 2 M KOH (50 mL) and extracted with 3 x 50 mL CHCl<sub>3</sub>. The combined organic extracts were dried over MgSO<sub>4</sub>, filtered, and the volatiles removed *via* rotary evaporation. This left the product as a viscous yellow oil. Yield: 2.01 g, 4.46 mmol (89%). <sup>1</sup>H NMR (298 K, CD<sub>3</sub>OD): δ (ppm) = 4.85 (s, H<sub>2</sub>O), 3.98 – 3.92 (septet, <sup>3</sup>J<sub>1H-1H</sub> = 6.5 Hz, [3H], <sup>i</sup>Pr-CH), 3.01 – 2.87 (br m, [6H], CH<sub>2</sub>), 2.83 (br s, [12H], tacn-CH<sub>2</sub>), 2.38 – 2.34 (br t, [6H], CH<sub>2</sub>), 1.14 (d, <sup>3</sup>J<sub>1H-1H</sub> = 6.6 Hz, [18H], <sup>i</sup>Pr-CH<sub>3</sub>). <sup>1</sup>H NMR (298 K, CDCl<sub>3</sub>): δ (ppm) = 6.72 (br, [3H], NH), 4.11 – 4.01 (septet, <sup>3</sup>J<sub>1H-1H</sub> = 6.6 Hz, [3H], <sup>i</sup>Pr-CH), 2.81 – 2.78 (t, <sup>3</sup>J<sub>1H-1H</sub> = 6.5 Hz, [6H], CH<sub>2</sub>), 2.76 (s, [12H], tacn-CH<sub>2</sub>), 2.29 – 2.26 (t, <sup>3</sup>J<sub>1H-1H</sub> = 6.5 Hz,

[6H],  $\text{CH}_2$ ), 1.14 (d,  $^3J_{\text{H-H}} = 6.6$  Hz, [18H],  $^i\text{Pr-CH}_3$ ).  $^{13}\text{C}\{^1\text{H}\}$  NMR (298 K,  $\text{CDCl}_3$ ):  $\delta$  (ppm) = 171.3 ( $\text{C=O}$ ), 55.6 (tacn- $\text{CH}_2$ ), 54.8 ( $\text{CH}_2$ ), 41.0 ( $^i\text{Pr-CH}$ ), 34.3 ( $\text{CH}_2$ ), 22.9 ( $^i\text{Pr-CH}_3$ ).  $^{13}\text{C}$  DEPT-135 NMR (298 K,  $\text{CDCl}_3$ ):  $\delta$  (ppm) = 55.4 (tacn- $\text{CH}_2$ ), 54.6 ( $\text{CH}_2$ ), 40.8 ( $^i\text{Pr-CH}$ ), 34.1 ( $\text{CH}_2$ ), 22.7 ( $^i\text{Pr-CH}_3$ ). HR ESI<sup>+</sup> MS ( $\text{CH}_3\text{OH}$ ): found:  $m/z$  = 491.3683 [ $\text{L}^2+\text{Na}$ ]<sup>+</sup> (calculated for  $[\text{C}_{24}\text{H}_{48}\text{N}_6\text{O}_3\text{Na}]^+$ :  $m/z$  = 491.3680), 469.3863 [ $\text{L}^2+\text{H}$ ]<sup>+</sup> (calculated for  $[\text{C}_{24}\text{H}_{49}\text{N}_6\text{O}_3]^+$ :  $m/z$  = 469.3861), 356.3019 [ $^i\text{PrC}(\text{O})\text{NH}(\text{CH}_2)_2$ -tacn+H]<sup>+</sup> (calculated for  $[\text{C}_{18}\text{H}_{37}\text{N}_5\text{O}_2]^+$ :  $m/z$  = 356.30), 235.1967 [ $\text{L}^2+2\text{H}$ ]<sup>2+</sup> (calculated for  $[\text{C}_{24}\text{H}_{50}\text{N}_6\text{O}_3]^{2+}$ :  $m/z$  = 235.1967). IR (neat film,  $\nu$  /  $\text{cm}^{-1}$ ): 3460 br, 3287 br (OH), 3078 br (NH), 1644 vs, 1554 s ( $\text{C=O}$ ).

#### 2.4.2.4 1-(*p*-tolylsulfonyl)-1,4,7-triazacyclononane (Ts-tacn)

Ts<sub>3</sub>-tacn (37.0 g, 62.6 mmol) and phenol (44.0 g, 470 mmol) were placed into a 1 L RBF equipped with magnetic stirring, a condenser equipped with an acid scrubber containing water and  $\text{NaHCO}_3$ , and an  $\text{N}_2$  inlet. The mixture was dissolved in HBr (33 wt% in AcOH) (500 mL). This was left to stir at 90 °C for 36 hours (at around 70 °C, gaseous HBr fumes were given out and consequently neutralised by the scrubber. This effervescence persisted for around four hours). The solution turned black overnight. After heating, the mixture was allowed to cool, then filtered and washed with copious amounts of  $\text{Et}_2\text{O}$ . The remaining beige solid was dissolved in 2.0 M NaOH until pH > 12, at which point the solution turned pink. This was extracted with 3 x 150 mL  $\text{CHCl}_3$ . The organic phases were collected and combined, and then dried over  $\text{MgSO}_4$ . This was then filtered and the volatiles removed *via* rotary evaporation, to leave an off-white, waxy solid. Yield: 9.76 g, 34.4 mmol (55%).  $^1\text{H}$  NMR (295 K,  $\text{CDCl}_3$ ):  $\delta$  (ppm) = 7.71 – 7.67 (m, [2H], ArH), 7.32 – 7.30 (m, [2H], ArH), 3.20 – 3.17 (m, [4H], tacn- $\text{CH}_2$ ), 3.09 – 3.07 (m, [4H], tacn- $\text{CH}_2$ ), 2.89 (s, [4H], tacn- $\text{CH}_2$ ), 2.43 (s, [3H],  $\text{CH}_3$ ), 1.73 (br s, [2H], NH).  $^{13}\text{C}$  NMR (295 K,  $\text{CDCl}_3$ ):  $\delta$  (ppm) = 143.2 (ArC), 135.6 (ArC), 129.6 (ArC), 127.2 (ArC), 54.0 (tacn- $\text{CH}_2$ ), 49.7 (tacn- $\text{CH}_2$ ), 49.5 (tacn- $\text{CH}_2$ ), 21.5 ( $\text{CH}_3$ ).

#### 2.4.2.5 1,4-diisopropyl-7-tosyl-1,4,7-triazacyclononane ( $^i\text{Pr}_2$ -Ts-tacn)

Ts-tacn (6.50 g, 23.0 mmol) was placed into a 50 mL round-bottom Schlenk flask equipped with magnetic stirring and a condenser. This was placed under an inert  $\text{N}_2$  atmosphere. 2-bromopropane (11.2 g, 91.1 mmol) and degassed MeCN (25 mL) were added *via* needle and syringe.  $\text{Na}_2\text{CO}_3$  (10.2 g, 96.6 mmol) was also added. The mixture was heated at reflux (85 °C) for 18 hours whilst stirring. A yellow mixture had formed, which was filtered and washed with MeCN. The filtrate was concentrated *in vacuo* to leave a yellow oil. This was redissolved in  $\text{CHCl}_3$  (50 mL) and washed with 1.5 M NaOH (50 mL). The organic layer was separated and the aqueous phase was extracted with 3 x 50 mL  $\text{CHCl}_3$ . The organic extracts were combined and dried over  $\text{MgSO}_4$ . The solution was filtered and the solvent removed *in vacuo* to leave an off-white solid.

Yield: 7.72 g, 21.0 mmol (91%).  $^1\text{H}$  NMR (295 K,  $\text{CDCl}_3$ ):  $\delta$  (ppm) = 7.69 – 7.62 (d, [2H], ArH), 7.29 – 7.27 (d, [2H], ArH), 3.31 – 3.26 (m, [4H] tacn-CH<sub>2</sub>), 2.87 – 2.85 (m, [4H] tacn-CH<sub>2</sub>), 2.82 – 2.72 (septet, [2H],  $^i\text{Pr}$ -CH), 2.46 (s, [4H], tacn-CH<sub>2</sub>), 2.42 (s, [3H], Ar-CH<sub>3</sub>), 0.94 – 0.92 (d, [12H],  $^i\text{Pr}$ -CH<sub>3</sub>).  $^{13}\text{C}$  NMR (295 K,  $\text{CDCl}_3$ ):  $\delta$  (ppm) = 142.6 (ArC), 136.7 (ArC), 129.5 (ArC), 127.2 (ArC), 53.7 ( $^i\text{Pr}$ -CH), 52.3 (tacn-CH<sub>2</sub>), 50.3 (tacn-CH<sub>2</sub>), 21.4 (Ar-CH<sub>3</sub>), 18.3 ( $^i\text{Pr}$ -CH<sub>3</sub>).

#### 2.4.2.6 1,4-diisopropyl-7-*N*'-1,4,7-triazacyclononane ( $^i\text{Pr}_2$ -tacn)

$^i\text{Pr}_2$ -Ts-tacn (7.71 g, 23.0 mmol) and conc.  $\text{H}_2\text{SO}_4$  (26.1 mL) were placed into a 50 mL RBF equipped with magnetic stirring. The mixture was heated to 120 °C for 18 hours whilst stirring under an inert  $\text{N}_2$  atmosphere. A black solution formed, which was then cooled and poured into a beaker containing crushed ice (130 g). The resulting solution was brought to pH > 11 using 1.5 M NaOH (approx. 200 mL). A heterogeneous mixture formed. This was extracted with 5 x 100 mL  $\text{CHCl}_3$  (until the organic extracts were colourless). These were then combined and dried over  $\text{MgSO}_4$ . The solution was filtered and the solvent removed *via* rotary evaporation. An amber-coloured oil remained. Yield: 4.50 g, 21.1 mmol (92%).  $^1\text{H}$  NMR (295 K,  $\text{CDCl}_3$ ):  $\delta$  (ppm) = 5.06 (br s, [1H], NH), 2.79 – 2.69 (septet, [2H],  $^i\text{Pr}$ -CH), 2.62 – 2.59 (m, [4H], tacn-CH<sub>2</sub>), 2.49 – 2.46 (m, [4H], tacn-CH<sub>2</sub>), 2.37 (s, [4H], tacn-CH<sub>2</sub>), 0.89 – 0.87 (d, [12H],  $^i\text{Pr}$ -CH<sub>3</sub>).  $^{13}\text{C}$  NMR (295 K,  $\text{CDCl}_3$ ):  $\delta$  (ppm) = 52.6 ( $^i\text{Pr}$ -CH), 47.8 (tacn-CH<sub>2</sub>), 46.1 (tacn-CH<sub>2</sub>), 45.7 (tacn-CH<sub>2</sub>), 18.5 ( $^i\text{Pr}$ -CH<sub>3</sub>).

#### 2.4.2.7 [1,4-diisopropyl-7-phenylacetamide-1,4,7-triazacyclononane][H<sup>+</sup>] ([L<sup>3</sup>][H<sup>+</sup>])

In a 100 mL RBF equipped with magnetic stirring,  $^i\text{Pr}_2$ -tacn (4.50 g, 21.1 mmol) was dissolved in degassed acetone (100 mL). Powdered  $\text{K}_2\text{CO}_3$  (4.50 g, 32.5 mmol) was added. This was stirred at room temperature for 15 min. and 2-chloro-*N*-phenylacetamide (3.57 g, 21.1 mmol) dissolved in degassed acetone (100 mL) was then added dropwise. The reaction mixture was stirred at room temperature overnight. After filtering through celite, the filtrate was adjusted to pH 12 using aqueous 1.5 M NaOH (ca. 200 mL). This was extracted with 3 x 200 mL  $\text{CHCl}_3$ , and the organic phases collected and combined. The solvent was removed *via* rotary evaporation to leave a tan-coloured oil. This crude product was purified in batches by flash chromatography using a Biotage Selekt flash chromatography system (dry-loaded; gradient = 30% – 40%  $\text{H}_2\text{O}/\text{MeCN}$  each containing 0.01 % formic acid, over 4 column volumes where: CV = 164 mL and flow rate = 50 mL min<sup>-1</sup>). A portion of the crude product (3.00 g) was dissolved in a minimal amount of  $\text{CHCl}_3$ . Then, four mass equivalents of chromatography-grade silica was added to the solution, creating a tan-coloured slurry. The  $\text{CHCl}_3$  solvent was removed *via* the rotary evaporator to leave a free-flowing orange powder. The pure fractions containing  $\text{L}^3\cdot\text{HCl}$  were collected, and the solvent was removed *in vacuo* leaving a viscous, tan-coloured oil. After washing with MeCN and further drying, the product was isolated as the protonated ligand salt,  $\text{L}^3\cdot\text{HCl}$ . Yield = 2.50 g.  $^1\text{H}$  NMR

(295 K, CD<sub>3</sub>OD):  $\delta$  (ppm) = 8.32 (s, NH), 7.57 (m, [2H], ArH), 7.30 (m, [2H], ArH), 7.09 (m, [1H], ArH), 4.90 (H<sub>2</sub>O), 3.59 (s, [2H], CH<sub>2</sub>), 3.39 – 3.32 (septet, [2H], <sup>i</sup>Pr-CH), 3.10 – 3.03 (br m, [4H], tacn-CH<sub>2</sub>), 2.96 – 2.87 (br m, [4H], tacn-CH<sub>2</sub>), 2.84 – 2.74 (br m, [4H], tacn-CH<sub>2</sub>), 1.25 (br d, [12H], <sup>i</sup>Pr-CH<sub>3</sub>). <sup>13</sup>C{<sup>1</sup>H} NMR (295 K, CD<sub>3</sub>OD):  $\delta$  (ppm) = 167.4 (C=O), 139.9 (ArC), 130.0 (ArC), 125.3 (ArC), 121.1 (ArC), 58.5 (CH<sub>2</sub>), 55.3 (<sup>i</sup>Pr-CH), 50.3 (tacn-CH<sub>2</sub>), 48.3 (tacn-CH<sub>2</sub>), 46.3 (tacn-CH<sub>2</sub>), 18.4 (<sup>i</sup>Pr-CH<sub>3</sub>), 18.1 (<sup>i</sup>Pr-CH<sub>3</sub>). 135-DEPT <sup>13</sup>C NMR (295 K, CD<sub>3</sub>OH):  $\delta$  (ppm) = 129.7 (ArC), 125.0 (ArC), 120.8 (ArC), 58.2 (CH<sub>2</sub>), 55.0 (<sup>i</sup>Pr-CH), 50.0 (tacn-CH<sub>2</sub>), 48.0 (tacn-CH<sub>2</sub>), 46.0 (tacn-CH<sub>2</sub>), 18.1 (<sup>i</sup>Pr-CH<sub>3</sub>), 17.8 (<sup>i</sup>Pr-CH<sub>3</sub>). HR ESI<sup>+</sup> MS (CH<sub>3</sub>OH): found:  $m/z$  = 347.2812 [L<sup>3</sup>+H]<sup>+</sup> (calculated for [C<sub>20</sub>H<sub>35</sub>N<sub>4</sub>O]<sup>+</sup>:  $m/z$  = 347.2805), 305.2341 [<sup>i</sup>Pr(CH<sub>2</sub>CONHPh)-tacn+H]<sup>+</sup> (calculated for [C<sub>17</sub>H<sub>29</sub>N<sub>4</sub>O]<sup>+</sup>:  $m/z$  = 305.2336).

#### 2.4.2.8 1,4-diisopropyl-7-phenylacetamide-1,4,7-triazacyclononane (Ligand 3, L<sup>3</sup>)

L<sup>3</sup>·HCl (2.20 g, 5.74 mmol) was treated with a solution of NEt<sub>3</sub> (20% by volume in deionised water) until pH > 12 (ca. 150 mL). A white precipitate formed initially, which then dissolved, and an orange oil was deposited. CHCl<sub>3</sub> (100 mL) was added to dissolve the oil and the organic phase was separated and retained. Removal of the CHCl<sub>3</sub> solvent *in vacuo* yielded a tan-coloured oil. Addition of pentane (25 mL) produced a dark-yellow solution, leaving a small amount of brown residue, which was discarded. The pentane was removed *in vacuo*, leaving the final product as a dark yellow oil (1.10 g, 55%). <sup>1</sup>H NMR (295 K, CD<sub>3</sub>OD):  $\delta$  (ppm) = 7.53 (m, [2H], ArH), 7.32 (m, [2H], ArH), 7.11 (m, [1H], ArH), 4.85 (H<sub>2</sub>O), 3.36 (s, [2H], CH<sub>2</sub>), 2.96 – 2.87 (septet, <sup>3</sup>J<sub>1H-1H</sub> = 6.6 Hz, [2H], <sup>i</sup>Pr-CH), 2.86 (s, [4H], tacn-CH<sub>2</sub>), 2.76 – 2.69 (br m, [8H], tacn-CH<sub>2</sub>), 0.95 (d, <sup>3</sup>J<sub>1H-1H</sub> = 6.6 Hz, [12H], <sup>i</sup>Pr-CH<sub>3</sub>). <sup>13</sup>C{<sup>1</sup>H} NMR (295 K, CD<sub>3</sub>OD):  $\delta$  (ppm) = 173.6 (C=O), 139.4 (ArC), 129.8 (ArC), 125.4 (ArC), 121.5 (ArC), 62.9 (CH<sub>2</sub>), 59.8 (tacn-CH<sub>2</sub>), 56.0 (<sup>i</sup>Pr-CH), 18.3 (<sup>i</sup>Pr-CH<sub>3</sub>). 135-DEPT <sup>13</sup>C NMR (295 K, CD<sub>3</sub>OD):  $\delta$  (ppm) = 129.9 (ArC), 125.5 (ArC), 121.7 (ArC), 63.0 (CH<sub>2</sub>), 59.9 (tacn-CH<sub>2</sub>), 56.1 (<sup>i</sup>Pr-CH), 49.7 (tacn-CH<sub>2</sub>), 18.4 (<sup>i</sup>Pr-CH<sub>3</sub>). <sup>1</sup>H NMR (295 K, CDCl<sub>3</sub>):  $\delta$  (ppm) = 10.84 (s, [1H], NH), 7.58 (m, [2H], ArH), 7.31 (m, [2H], ArH), 7.08 (m, [1H], ArH), 3.37 (s, [2H], CH<sub>2</sub>), 2.88 (septet, <sup>3</sup>J<sub>1H-1H</sub> = 6.1 Hz [2H], <sup>i</sup>Pr-CH), 2.82 (br s, [4H], tacn-CH<sub>2</sub>), 2.70 (br s, [8H], tacn-CH<sub>2</sub>), 1.56 (H<sub>2</sub>O), 0.93 (d, <sup>3</sup>J<sub>1H-1H</sub> = 6.6 Hz, [12H], <sup>i</sup>Pr-CH<sub>3</sub>). <sup>13</sup>C{<sup>1</sup>H} NMR (295 K, CDCl<sub>3</sub>):  $\delta$  (ppm) = 171.3 (C=O), 139.6 (ArC), 128.7 (ArC), 123.7 (ArC), 119.9 (ArC), 62.5 (CH<sub>2</sub>), 59.4 (tacn-CH<sub>2</sub>), 55.8 (<sup>i</sup>Pr-CH), 54.9 (tacn-CH<sub>2</sub>), 49.1 (tacn-CH<sub>2</sub>), 18.0 (<sup>i</sup>Pr-CH<sub>3</sub>). HR ESI<sup>+</sup> MS (CH<sub>3</sub>OH): found:  $m/z$  = 347.2812 [L<sup>3</sup>+H]<sup>+</sup> (calculated for [C<sub>20</sub>H<sub>35</sub>N<sub>4</sub>O]<sup>+</sup>  $m/z$  = 347.2805). IR (neat film,  $\nu$  / cm<sup>-1</sup>): 3400 br, 3200 br (OH), 3053, 3033 w (NH), 2961, 2930, 2812 (C–H stretch), 1678 br s, 1600 (C=O).



## 2.4.3 Carboxylate-Functionalised Triazacyclononane Ligands

### 2.4.3.1 Di-tert-butyl 2,2'-(7-benzyl-1,4,7-triazacyclononane-1,4-diyl)diacetate (Bn-NO2A<sup>t</sup>Bu)

In a 100 mL RBF, NO2A<sup>t</sup>Bu (0.200 g, 0.559 mmol) was dissolved in MeCN (20 mL). K<sub>2</sub>CO<sub>3</sub> (0.134 g, 0.968 mmol) was added. Benzyl bromide (0.096 g, 0.559 mmol) in MeCN (20 mL) was added dropwise and slowly to the RBF. Stirring was continued for 48 h. After, the reaction mixture was filtered and the volatiles removed *in vacuo* to leave a yellow oil. Yield: 0.250 g, 0.559 (100%). <sup>1</sup>H NMR (295 K, CDCl<sub>3</sub>): δ (ppm) = 7.37 – 7.35 (m, [2H], ArH), 7.32 – 7.27 (m, [2H], ArH), 7.24 – 7.20 (m, [1H], ArH), 3.68 (br s, [2H], CH<sub>2</sub>), 3.31 (br s, [4H], CH<sub>2</sub>), 2.94 (br s, [4H], tacn-CH<sub>2</sub>), 2.86 – 2.77 (br m, [8H], tacn-CH<sub>2</sub>), 1.46 (s, [18H], <sup>t</sup>Bu-CH<sub>3</sub>). ESI<sup>+</sup> MS (CH<sub>3</sub>OH): found: *m/z* = 448.44 [Bn-NO2A<sup>t</sup>Bu+H]<sup>+</sup> (calculated for [C<sub>25</sub>H<sub>42</sub>N<sub>3</sub>O<sub>4</sub>]<sup>+</sup> *m/z* = 448.32), 470.38 [Bn-NO2A<sup>t</sup>Bu+Na]<sup>+</sup> (calculated for [C<sub>25</sub>H<sub>41</sub>N<sub>3</sub>O<sub>4</sub>Na]<sup>+</sup> *m/z* = 470.30).

### 2.4.3.2 1-benzyl-4,7-diacetic acid-1,4,7-triazacyclononane (H<sub>2</sub>-Bn-NODA)

Bn-NO2A<sup>t</sup>Bu (0.250 g, 0.559 mmol) was dissolved in a 1:1 TFA:CH<sub>2</sub>Cl<sub>2</sub> mixture and stirred at room temperature for 48 h. The solution was then concentrated *in vacuo* and washed several times with water (removing the water each time *via* rotary evaporation). The product was then recrystallised from dioxane/Et<sub>2</sub>O, and after drying *in vacuo*, a dark brown oil remained. Yield: 0.180 g, 0.537 mmol (96%). <sup>1</sup>H NMR (295 K, D<sub>2</sub>O): δ (ppm) = 7.57 – 7.47 (m, [5H], ArH), 4.46 (s, [2H], CH<sub>2</sub>), 3.58 (s, [4H], CH<sub>2</sub>), 3.55 – 3.43 (br m, [4H], tacn-CH<sub>2</sub>), 3.38 – 3.21 (br m, [2H], tacn-CH<sub>2</sub>), 3.13 (br s, tacn-CH<sub>2</sub>), 3.03 – 2.82 (br m, [2H], tacn-CH<sub>2</sub>). <sup>13</sup>C{<sup>1</sup>H} NMR (295 K, D<sub>2</sub>O): δ (ppm) = 174.5 (C=O), 131.0 (ArC), 130.3 (ArC), 129.4 (ArC), 129.3 (ArC), 60.5 (CH<sub>2</sub>), 57.2 (CH<sub>2</sub>), 50.5 (tacn-CH<sub>2</sub>), 48.9 (tacn-CH<sub>2</sub>). ESI<sup>+</sup> MS (H<sub>2</sub>O): found: *m/z* = 336.31 [Bn-NODA+H]<sup>+</sup> (calculated for [C<sub>17</sub>H<sub>26</sub>N<sub>3</sub>O<sub>4</sub>]<sup>+</sup> *m/z* = 336.19).

## 2.4.4 Phosphinate-Ester Functionalised Triazacyclononane Ligands

### 2.4.4.1 Trimethyl-1,4,7-triazacyclononane-1,4,7-triyltris[methylene(phenylphosphinate)] (NOTP-OMe)

Under inert conditions in a 250 mL RBF containing 3 Å molecular sieves, 1,4,7-triazacyclononane (1.00 g, 7.74 mmol), dimethylphenylphosphonite (4.61 g, 27.1 mmol, 3.5 mol eqv.) were combined in an. THF. Paraformaldehyde (1.50 g, 50.0 mmol) was then added. The reaction was heated at reflux overnight. The resultant yellow-orange solution was filtered, and the volatiles removed *via* rotary evaporation to leave a dark orange oil. The crude product was purified by flash chromatography using a Biotage Selekt flash chromatography system (dry-



loaded; gradient = 10% – 100% H<sub>2</sub>O/MeOH, over 16 column volumes where: CV = 164 mL and flow rate = 50 mL min<sup>-1</sup>). The crude product (2.50 g) was dissolved in a minimal amount of CH<sub>2</sub>Cl<sub>2</sub>. Then, four mass equivalents of chromatography-grade neutral alumina was added to the solution, creating a tan-coloured slurry. The CH<sub>2</sub>Cl<sub>2</sub> was removed *via* rotary evaporation to leave a free-flowing yellow powder. The pure fractions containing NOTP-OMe were collected, and the solvent was removed *in vacuo* leaving a viscous dark yellow oil. Yield: 0.750 g, 1.18 mmol (15%). <sup>1</sup>H (295 K, CDCl<sub>3</sub>): δ (ppm) = 7.80 – 7.72 (m, [6H], ArH), 7.57 – 7.51 (m, [3H], ArH), 7.51 – 7.43 (m, [6H], ArH), 3.63 – 3.58 (dt, [9H], CH<sub>3</sub>), 3.15 – 2.97 (br m, [6H], CH<sub>2</sub>), 2.88 – 2.51 (br m, [12H], tacn-CH<sub>2</sub>). <sup>31</sup>P{<sup>1</sup>H} (295 K, CDCl<sub>3</sub>): δ (ppm) = 40.7 (br s). ESI<sup>+</sup> MS (MeOH): found: *m/z* = 634.3 [NOTP-OMe+H]<sup>+</sup> (calculated for [C<sub>30</sub>H<sub>43</sub>N<sub>3</sub>O<sub>6</sub>P<sub>3</sub>]<sup>+</sup> *m/z* = 634.2). IR (neat film, ν / cm<sup>-1</sup>): 3400 v br (OH), 1664 s (HOH), 1203 br, s (P=O), 1027 s (P-O).

## 2.5 X-Ray Crystallographic Data

Compound	<b>L<sup>1</sup>·HCl</b>
Formula	C <sub>30</sub> H <sub>37</sub> ClN <sub>6</sub> O <sub>3</sub>
<i>M</i>	565.12
Crystal system	Monoclinic
Space group (no.)	<i>P</i> 2 <sub>1</sub> /c (14)
<i>a</i> /Å	12.8300(3)
<i>b</i> /Å	23.5152(6)
<i>c</i> /Å	9.6411(2)
$\alpha$ /°	90
$\beta$ /°	99.705(2)
$\gamma$ /°	90
<i>U</i> /Å <sup>3</sup>	2867.09(12)
<i>Z</i>	4
$\mu$ (Mo-K $\alpha$ ) /mm <sup>-1</sup>	0.176
<i>F</i> (000)	1201
Total no. reflns	33643
<i>R</i> <sub>int</sub>	0.029
Unique reflns	8740
No. of params, restraints	694, 651
GOF	0.985
<i>R</i> <sub>1</sub> , <i>wR</i> <sub>2</sub> [ <i>I</i> > 2 $\sigma$ ( <i>I</i> )] <sup>b</sup>	0.038, 0.088
<i>R</i> <sub>1</sub> , <i>wR</i> <sub>2</sub> (all data)	0.057, 0.095

<sup>a</sup> common items: *T* = 100 K; wavelength (Mo-K $\alpha$ ) = 0.71073 Å;  $\theta$ (max) = 27.5°;

<sup>b</sup>  $R_1 = \Sigma||F_o| - |F_c||/\Sigma|F_o|$ ;  $wR_2 = [\Sigma w(F_o^2 - F_c^2)^2 / \Sigma wF_o^4]^{1/2}$

## 2.6 References

1. S. Pulacchini, K. Shastri, N. Dixon and M. Watkinson, *Synthesis*, 2004, **2001**, 2381.
2. P. Chaudhuri and K. Wieghardt, in *Progress in Inorganic Chemistry.*, ed. S. J. Lippard, John Wiley & Sons, Inc., Toronto, 1987, ch. 4, pp. 329-436.
3. E. Macedi, A. Bencini, C. Caltagirone and V. Lippolis, *Coord. Chem. Rev.*, 2020, **407**, 213151.
4. A. J. Blake, I. A. Fallis, S. Parsons, S. A. Ross and M. Schröder, *J. Chem. Soc., Dalton Trans.*, 1996, 525.
5. A. J. Blake, I. A. Fallis, A. Heppeler, S. Parsons, S. A. Ross and M. Schröder, *J. Chem. Soc., Dalton Trans.*, 1996, 31.
6. A. J. Blake, J. P. Danks, W.-S. Li, V. Lippolis and M. Schröder, *J. Chem. Soc., Dalton Trans.*, 2000, 3034.
7. L. Tei, A. J. Blake, V. Lippolis, C. Wilson and M. Schröder, *Dalton Trans.*, 2003, 304.
8. J. E. Richman and T. J. Atkins, *J. Am. Chem. Soc.*, 1974, **96**, 2268.
9. T. J. Atkins, J. E. Richman and W. F. Oettle, *Org. Synth.*, 1978, **58**, 86.
10. P. Désogère, Y. Rousselin, S. Poty, C. Bernhard, C. Goze, F. Boschetti and F. Denat, *Eur. J. Org. Chem.*, 2014, 783.
11. A. Thangavel, M. Wieliczko, J. Bacsá and C. C. Scarborough, *Inorg. Chem.*, 2013, **52**, 13282.
12. K. Wieghardt, P. Chaudhuri, B. Nuber and J. Weiss, *Inorg. Chem.*, 1981, **21**, 3086.
13. C.-X. Zhang, D.-W. Fang, J.-L. Wang, A.-Q. Jia and Q.-F. Zhang, *Inorg. Chim. Acta*, 2020, 507, 119599.
14. B.-F. Qian, J.-L. Wang, A.-Q. Jia, H.-T. Shi and Q.-F. Zhang, *Inorg. Chim. Acta*, 2021, **516**, 120128.
15. NL Pat., WO1994000439A1, 1994.
16. R. Bhalla, C. Darby, W. Levason, S. K. Luthra, G. McRobbie, G. Reid, G. Sanderson and W. Zhang, *Chem. Sci.*, 2014, **5**, 381.
17. M. J. Belousoff, M. B. Duriska, B. Graham, S. R. Batten, B. Moubaraki, K. S. Murray and L. Spiccia, *Inorg. Chem.*, 2006, **45**, 3746.
18. M. Buziková, R. Willmetz and J. Kotek, *Molecules*, 2023, **28**, 7542.
19. K. Wieghardt, U. Bossek, P. Chaudhuri, W. Herrmann, B. C. Menke and J. Weiss, *Inorg. Chem.*, 1982, **21**, 4308.
20. G. Makris, L. L. Radford, M. Kuchuk, F. Gallazzi, S. S. Jurisson, C. J. Smith and H. M. Hennkens, *Bioconjug. Chem.*, 2018, **29**, 4040.

21. F. Y. Adeowo, B. Honarparvar and A. A. Skelton, *J. Phys. Chem. A*, 2017, **121**, 6054.
22. V. Kubíček, Z. Böhmová, R. Ševčíková, J. Vaněk, P. Lubal, Z. Poláková, R. Michalíková, J. Kotek and P. Hermann, *Inorg. Chem.*, 2018, **57**, 3061.
23. J. Notni, K. Pohle and H.-J. Wester, *EJNMMI Res.*, 2012, **2**, 28.
24. W. J. McBride, C. A. D'souza, R. M. Sharkey, H. Karacay, E. A. Rossi, C. H. Chang and D. M. Goldenberg, *Bioconjug. Chem.*, 2010, **21**, 1331.
25. H.-S. Chong, K. Garmestani, D. Ma, D. E. Milenic, T. Overstreet and M. W. Brechbiel, *J. Med. Chem.*, 2002, **45**, 3458.
26. C. A. D'Souza, W. J. McBride, R. M. Sharkey, L. J. Todaro and D. M. Goldenberg, *Bioconjug. Chem.*, 2011, **22**, 1793.
27. R. Bhalla, W. Levason, S. K. Luthra, G. McRobbie, G. Sanderson and G. Reid, *Chem. Eur. J.*, 2015, **21**, 4688.
28. D. Shetty, S. Y. Choi, J. M. Jeong, J. Y. Lee, L. Hoigebazar, Y. S. Lee, D. S. Lee, J. K. Chung, M. C. Lee and Y. K. Chung, *Chem. Commun.*, 2011, **47**, 9732.
29. D. E. Runacres, V. K. Greenacre, J. M. Dyke, J. Grigg, G. Herbert, W. Levason, G. McRobbie and G. Reid, *Inorg. Chem.*, 2023, **62**, 20844.
30. C. J. Broan, E. Cole, K. J. Jankowski, D. Parker, K. Pulukkody, B. A. Boyce, N. R. A. Beeley, K. Millar and A. T. Millican, *Synthesis*, 1992, 63.
31. J. Šimeček, M. Schulz, J. Notni, J. Plutnar, V. c. Kubíček, J. Havlíčková and P. Hermann, *Inorg. Chem.*, 2011, **51**, 577.
32. E. Cole, R. C. B. Copley, J. A. K. Howard, D. Parker, G. Ferguson, J. F. Gallagher, B. Kaitner, A. Harrison and L. Royle, *J. Chem. Soc., Dalton Trans.*, 1994, 1619.
33. S. J. Dorazio, A. O. Olatunde, P. B. Tsitovich and J. R. Morrow, *J. Biol. Inorg. Chem.*, 2014, **19**, 191.
34. T. Weyhermüller, K. Weighardt and P. Chaudhuri, *J. Chem. Soc., Dalton Trans.*, 1998, 3805.
35. G. H. Searle and R. J. Geue, *Aust. J. Chem.*, 1984, **37**, 959.
36. W. J. McBride, C. A. D'Souza, R. M. Sharkey and D. M. Goldenberg, *Appl. Radiat. Isot.*, 2012, **70**, 200.
37. R. Pujales-Paradela, F. Carniato, D. Esteban-Gómez, M. Botta and C. Platas-Iglesias, *Dalton Trans.*, 2019, **48**, 3962.
38. G. Sanderson PhD, University of Southampton, 2015.
39. S. Mahapatra, J. A. Halfen, E. C. Wilkinson, G. Pan, X. Wang, V. G. Young, C. J. Cramer, L. Que Jr. and W. B. Tolman, *J. Am. Chem. Soc.*, 1996, **118**, 11555.
40. R. M. Claramunt, C. López, M. D. Santa María, D. Sanz and J. Elguero, *Prog. Nucl. Magn. Reson. Spectrosc.*, 2006, **49**, 169.

41. L. Zhaowen, Z. Li, X. Chunfen, Y. Yong, Z. Fanbo and H. Kaixun, *Med. Chem. Res.*, 2007, **16**, 380.

## Chapter 3 Divalent Transition Metal Complexes with Neutral N-Functionalised Triazacyclononane Ligands

### 3.1 Introduction

Chapter 2 describes the synthesis of neutral triazacyclononane ligands with (tris)amide and phosphinate-ester pendant arms. This chapter will investigate the coordination chemistry (i.e. determining the denticity, donor set, structural parameters) and behaviour (such as stability towards hydrolysis, hydrogen-bonding properties of the amide functions) of these ligands ( $L^1$ ,  $L^2$  and NOTP-OMe – Figure 3.1) towards divalent metal centres and compare them to the literature surrounding similar complexes.

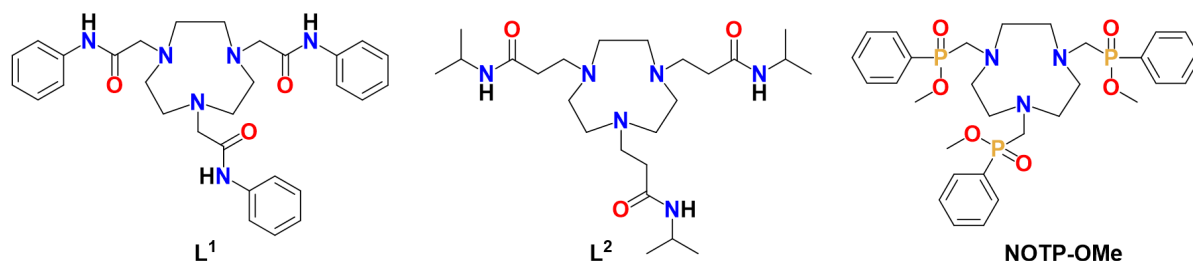


Figure 3.1 – Structures of the triazacyclononane ligands,  $L^1$ ,  $L^2$  and NOTP-OMe, which will be the subject of this chapter.

#### 3.1.1 Properties and Characteristics of First-Row Transition Metals Relevant to This Work

The divalent transition metal ions,  $Fe^{2+}$ ,  $Co^{2+}$ ,  $Ni^{2+}$ ,  $Cu^{2+}$ , and  $Zn^{2+}$ , are the subject of this chapter – their general electronic properties are summarised in Table 3.1. Much of the focus is on the divalent transition metal ions, due to their abundance and accessibility, their relative stability, but also because of the plethora of triaza-macrocyclic complexes that are known from the literature – some of which will be discussed below.<sup>1,2,3</sup>

Table 3.1 – Electronic properties of the transition metal ions used in this work. *O<sub>h</sub>*, octahedral; LS, low-spin; HS, high-spin.

Metal Ion	Electronic Configuration	d-Orbital Configuration ( <i>O<sub>h</sub></i> )		Ground State Free Ion Term	Ground State Molecular Term ( <i>O<sub>h</sub></i> )
<b>Fe<sup>2+</sup></b>	[Ar]3d <sup>6</sup>	t <sub>2g</sub> <sup>6</sup> e <sub>g</sub> <sup>0</sup> (LS)	t <sub>2g</sub> <sup>4</sup> e <sub>g</sub> <sup>2</sup> (HS)	<sup>5</sup> D	<sup>1</sup> A <sub>1g</sub> (LS) <sup>5</sup> T <sub>2g</sub> (HS)
<b>Fe<sup>3+</sup></b>	[Ar]3d <sup>5</sup>	t <sub>2g</sub> <sup>5</sup> e <sub>g</sub> <sup>0</sup> (LS)	t <sub>2g</sub> <sup>3</sup> e <sub>g</sub> <sup>2</sup> (HS)	<sup>6</sup> S	<sup>2</sup> T <sub>2g</sub> (LS) <sup>6</sup> A <sub>1g</sub> (HS)
<b>Co<sup>2+</sup></b>	[Ar]3d <sup>7</sup>	t <sub>2g</sub> <sup>6</sup> e <sub>g</sub> <sup>1</sup> (LS)	t <sub>2g</sub> <sup>5</sup> e <sub>g</sub> <sup>2</sup> (HS)	<sup>4</sup> F	<sup>2</sup> E <sub>g</sub> (LS) <sup>4</sup> T <sub>1g</sub> (HS)
<b>Co<sup>3+</sup></b>	[Ar]3d <sup>6</sup>	t <sub>2g</sub> <sup>6</sup> e <sub>g</sub> <sup>0</sup> (LS)	t <sub>2g</sub> <sup>4</sup> e <sub>g</sub> <sup>2</sup> (HS)	<sup>5</sup> D	<sup>1</sup> A <sub>1g</sub> (LS) <sup>5</sup> T <sub>2g</sub> (HS)
<b>Ni<sup>2+</sup></b>	[Ar]3d <sup>8</sup>	t <sub>2g</sub> <sup>6</sup> e <sub>g</sub> <sup>2</sup>		<sup>3</sup> F	<sup>3</sup> A <sub>2g</sub>
<b>Cu<sup>2+</sup></b>	[Ar]3d <sup>9</sup>	t <sub>2g</sub> <sup>6</sup> e <sub>g</sub> <sup>3</sup>		<sup>2</sup> D	<sup>2</sup> E <sub>g</sub>
<b>Zn<sup>2+</sup></b>	[Ar]3d <sup>10</sup>	t <sub>2g</sub> <sup>6</sup> e <sub>g</sub> <sup>4</sup>		<sup>1</sup> S	No <i>d-d</i> transitions

Unlike main group metal ions, transition metal ions usually have partially filled *d*-orbitals. For each metal, the different *d<sup>n</sup>* configurations correspond to different properties, such as the ease with which they change oxidation state, their ligand substitution kinetics, colour, magnetism, structure, and their reactivity. For example, Fe<sup>2+</sup> is categorised as a borderline hard/soft acid, whereas Fe<sup>3+</sup> (a small and highly polarised cation) is considered a strong Lewis acid, and is not dissimilar from Ga<sup>3+</sup>.<sup>4,5</sup> Fe<sup>2+</sup> may bind more favourably towards a more diverse range of ligand donor groups (e.g. oxygen-, nitrogen- and sulphur- donor ligands), whereas Fe<sup>3+</sup> will prefer hard Lewis bases such as halides or oxygen-donor ligands.<sup>6</sup> In most cases, their electronic configuration limits their ability to be characterised *via* NMR spectroscopy – those with unpaired electrons (high-spin Fe<sup>2+</sup> and Co<sup>3+</sup>, Fe<sup>3+</sup>, Co<sup>2+</sup>, Ni<sup>2+</sup>, Cu<sup>2+</sup>) are paramagnetic, so conventional NMR spectroscopy will be uninformative. Metal ions with paired electrons are diamagnetic and include low-spin Fe<sup>2+</sup> and Co<sup>3+</sup>, and Zn<sup>2+</sup>. The divalent form of zinc has a completely full set of *d*-orbitals (*d<sup>10</sup>*), which also means it is impervious to oxidation or reduction. However, like iron, the +2 and +3 oxidation states of cobalt are both well-known and have even been shown to display reversible aerobic oxidation.<sup>7,8,9</sup> Whilst a source of Co<sup>3+</sup> will not be used directly with the ligands, it oxidises more readily than the other divalent ions (excluding Fe<sup>2+</sup>) and both NMR and UV-Vis spectroscopy could help determine the oxidation state of its complexes.

For some ions (*d<sup>4</sup> – d<sup>7</sup>*), their properties also depend on the ligands to which they are bound e.g. strong-field ligands (which favour the low-spin configuration) vs. weak-field ligands (which favour the high-spin configuration). In some cases, when the ligand-field strength is close to the

crossover point between high-spin and low-spin states, a phenomenon called spin-crossover (SCO) can also be observed.<sup>10</sup>

Six-coordinate complexes of these metal ions are typically expected to have octahedral geometry, although complexes of  $\text{Cu}^{2+}$  ( $d^9$ ) are likely to show Jahn-Teller distortion. This describes the geometric distortion that occurs when non-linear molecules contain degenerate electronic ground states – in this case, the asymmetrically-occupied  $e_g$  subset of  $d$ -orbitals for the  $\text{Cu}^{2+}$  ion is energetically unfavourable, and spontaneously splits in such a way to remove the degeneracy.<sup>11</sup> This effect can be seen in Figure 3.2.

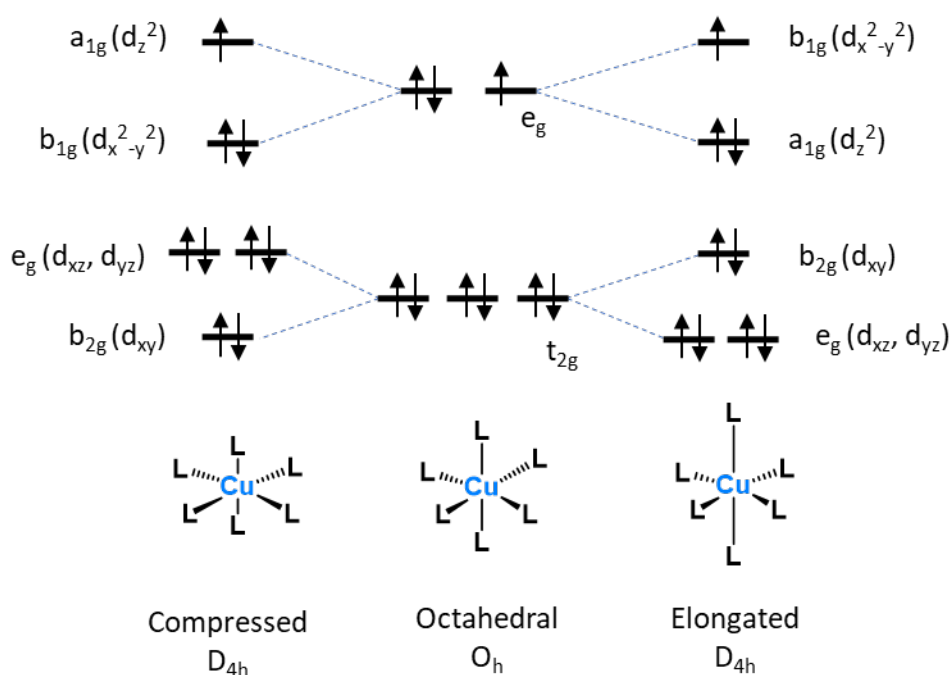


Figure 3.2 – Typical Jahn-Teller distortions for an octahedral  $\text{Cu}^{2+}$  complex. The  $e_g$  orbitals are split into an  $a_{1g}$  and  $b_{1g}$  subset, reducing the overall energy of the complex.

### 3.1.2 Transition Metal Complexes of Amide-Functionalised Triazacyclononane Ligands

So far, much of this work has discussed the widespread use of tacn-based macrocycles for the formation of thermodynamically and kinetically stable metal complexes, with many examples of tacn derivatives containing various pendant arm groups. Some amide-functionalised triazacyclononane ligands have been reported, including 1,4,7-tris(carbamoylmethyl)-1,4,7-triazacyclononane (TCMT) and its methyl derivative, as two of the first examples (Figure 3.3).<sup>12,13</sup>



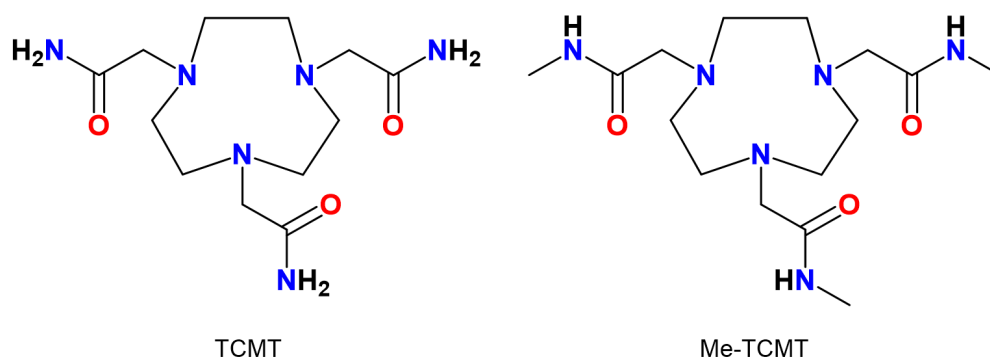
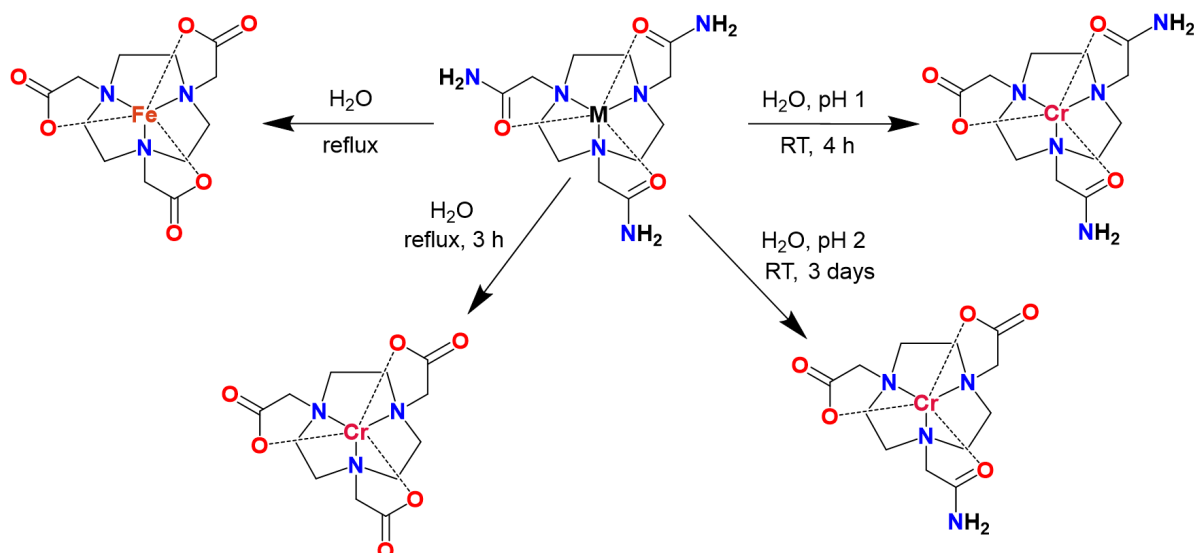


Figure 3.3 – Structures of the tris-amide functionalised ligands, *L* and *MeL*.

These ligands have been used to form coordination complexes with several first-row transition metal ions, including:  $\text{Zn}^{2+}$ ,  $\text{Cu}^{2+}$ ,  $\text{Ni}^{2+}$ ,  $\text{Co}^{2+}$ ,  $\text{Fe}^{2+}$ ,  $\text{Mn}^{2+}$ ,  $\text{Cr}^{2+}$ ,  $\text{Cr}^{3+}$ ,  $\text{V}^{3+}$  and  $\text{V}^{4+}$ .<sup>14</sup> The complexes were formed from the direct reaction of the ligands with the corresponding metal salt in methanol. In most cases, the ligands provided an  $\text{N}_3\text{O}_3$  hexadentate donor set *via* coordination of the three *fac* tacn-nitrogens and O-bound carboxamide groups of the amide pendant arms. This excludes the reaction of TCMT with  $\text{CrCl}_2$ , which causes the deprotonation of a terminal  $\text{NH}_2$  group in solution, yielding a  $\text{CrN}_4\text{O}_2$  complex. Crystallographic data for  $[\text{Ni}(\text{TCMT})]^{2+}$  and  $[\text{Cr}(\text{Me-TCMT})]^{3+}$  show that *pseudo*-octahedral geometry is somewhat favoured over trigonal prismatic geometry, with twist angles of  $44^\circ$  and  $49^\circ$  respectively.

Interestingly, for  $\text{Cr}^{3+}$  and  $\text{Fe}^{2+}$  complexes of TCMT, the amide pendant arms were also observed to undergo hydrolysis to the corresponding carboxylate group. The extent of the hydrolysis was dependent upon the metal ion and the reaction conditions (Scheme 3.1). Three separate  $\text{Cr}^{3+}$  complexes were isolated, with the loss of one, two or three amide groups; the resulting carboxylate group(s) coordinated to the metal centre in place of the carbonyl of the amide. For the  $\text{Fe}^{2+}$  complex, complete hydrolysis of all three pendant arms was observed when refluxed in the presence of water, alongside oxidation of the metal centre to  $\text{Fe}^{3+}$  (this formed the known  $[\text{Fe}(\text{NOTA})]$  complex).<sup>15</sup>



Scheme 3.1 – Various hydrolysis pathways and products from the reactions of  $[M(L)]$ ,  $M = Cr^{3+}$ ,  $Fe^{2+}$ .<sup>14</sup>

A similar  $[Ni(tcet)][ClO_4]_2$  ( $tcet = 3,3',3''$ -(1,4,7-triazacyclononane-1,4,7-triyl)tripropanamide) complex has also been reported.<sup>16</sup> Again, the coordination geometry around the central metal ion is *pseudo*-octahedral, with a slightly larger twist angle of  $53.2^\circ$ . In the solid state, complex cations are linked *via* hydrogen bonds between an NH of one amide group, to a C=O of another amide on a neighbouring complex. This forms zig-zag chains, which are then organised into an extended three-dimensional network by hydrogen bonding to the  $[ClO_4]^-$  anions. (Figure 3.4).

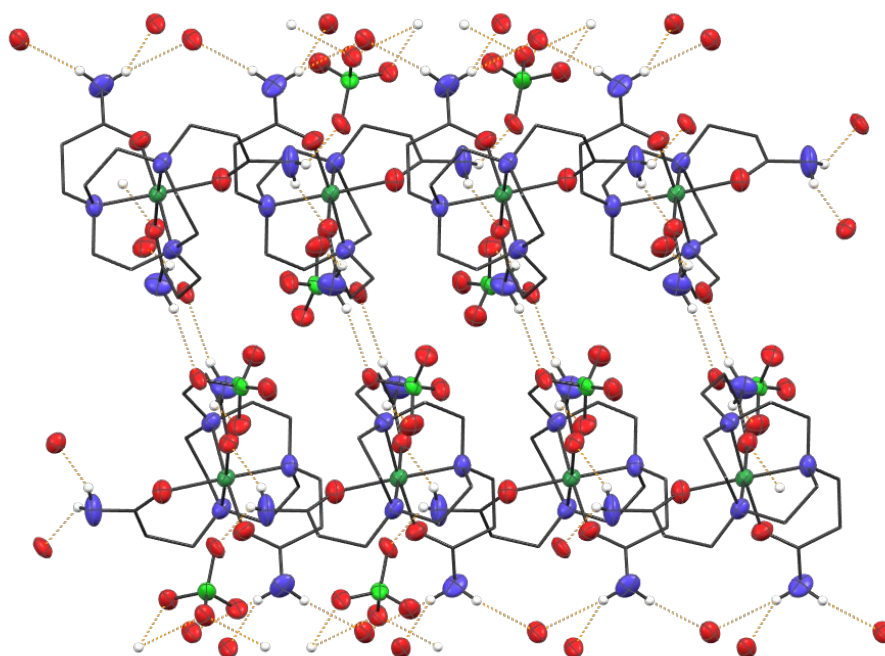


Figure 3.4 – Extensive hydrogen-bonded network of  $[Ni(tcet)][ClO_4]_2$  reported by Liu et al.<sup>16</sup> Redrawn from CCDC 602837. Hydrogen and cation atoms (excluding those involved in hydrogen bonding) omitted for clarity. Atom colours: dark green, Ni; green, Cl; red, O; blue, N; white, H.

An investigation into the coordination chemistry of  $\text{Cu}^+$  and  $\text{Cu}^{2+}$  complexes of mono-amide tacn ligands has also been reported (Figure 3.5).<sup>17</sup> Two different ligands have been synthesised, with the length of the alkyl tether and orientation of the amide group varied between both.

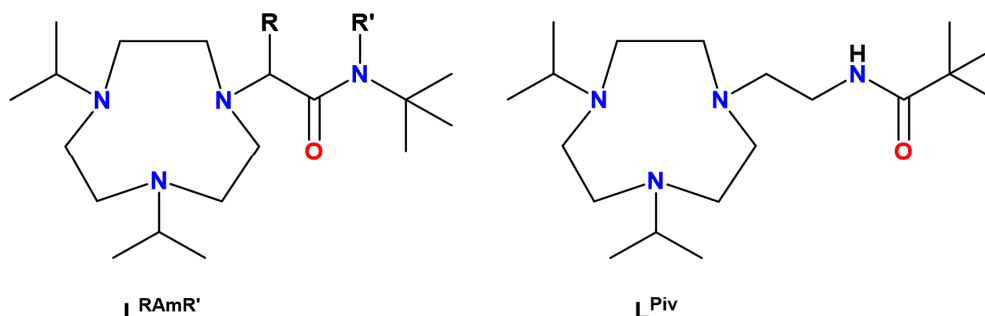


Figure 3.5 – Structures of the two diisopropyl mono-amide triazacyclononane ligands reported by Berreau *et al.*<sup>17</sup>  $R$  and  $R' = \text{H}$  and/or  $\text{Me}$ .

For the four-coordinate  $\text{Cu}(\text{I})$  complexes, there was no indication of an amide-bonding interaction between the pendant arm and the metal centre in any of the isolated structures, with the metal centre bound to the *facial* tacn(N), and the fourth coordination site occupied by an acetonitrile (N-donor) or carbonyl (O-donor) ligand. However, the  $\text{Cu}^{2+}$  ions were found to form five-coordinate complexes, with the carboxamide oxygen bound to the metal centre regardless of the length of the pendant arm or orientation of the amide group. The observed coordination sphere around the central  $\text{Cu}^{2+}$  ion was  $\text{N}_4\text{OCl}$  (chloride ligand) or  $\text{N}_4\text{O}_2$  (triflate ligand). This suggests that, within the context of the work in this thesis, the metal complexes of  $\text{L}^1$  and  $\text{L}^2$  may show similar coordinative behaviour. However, more recent work by Garau *et al.*<sup>18</sup> has reported the  $\text{Cu}^{2+}$  complex of a tris(amide) ligand with a similar structure to  $\text{L}^1$  (containing a quinolinylacetamide group, rather than a phenylacetamide group), whereby the tacn is bound *facially*, but only one of the amide groups is coordinated in the axial position. The other two equatorial sites are instead completed by coordination *via* the two nitrogen atoms of the deprotonated N-8-quinolinylacetamide group, emphasising the effect that steric crowding can have on the observed bonding domains. Figure 3.6 shows the crystal structure of the complex.

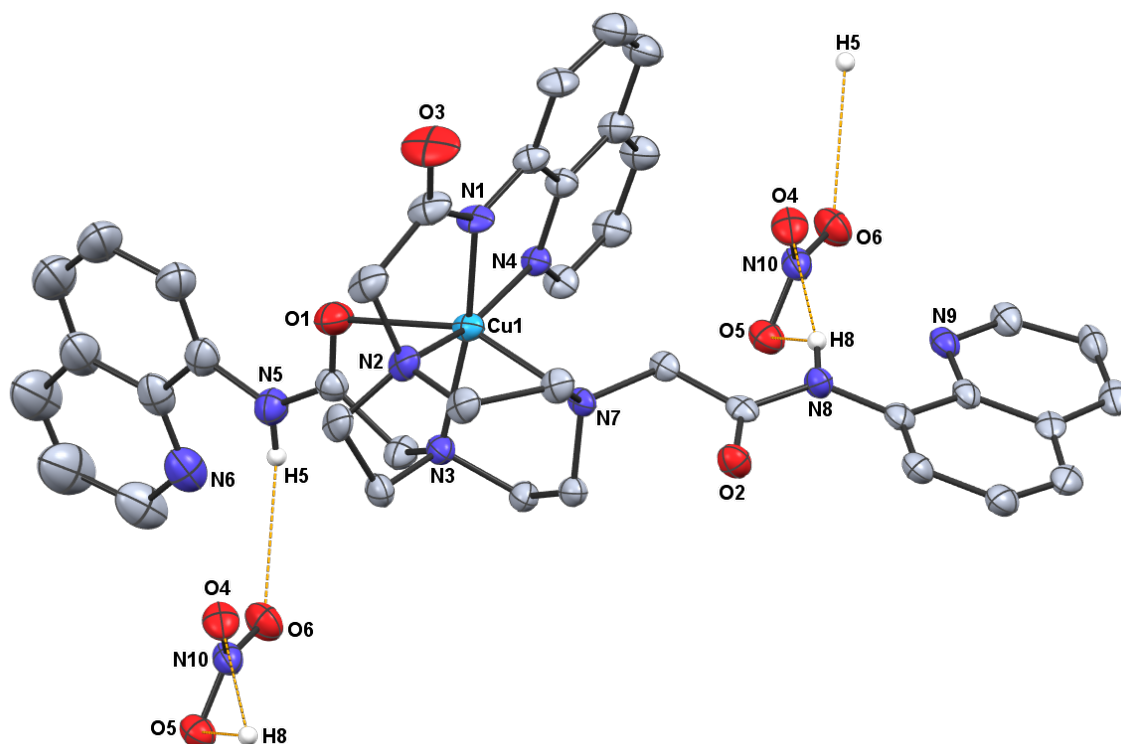


Figure 3.6 –  $[\text{Cu}(\text{tris-1,4,7-quinolinylnacetamide-tacn})][\text{NO}_3]_2$  reported by Garau *et al.*<sup>18</sup>. Redrawn from CCDC 1889394. Hydrogen atoms (excluding those involved in hydrogen bonding) omitted for clarity.

#### 3.1.2.1 Use as paraCEST MRI Imaging Agents

Paramagnetic transition metal complexes are of interest in the development of paraCEST (paramagnetic chemical exchange saturation transfer) MRI imaging contrast agents. Recent focus has been towards  $\text{Mn}^{2+}$ ,  $\text{Fe}^{2+}$ ,  $\text{Co}^{2+}$  or  $\text{Ni}^{2+}$  complexes of macrocyclic ligands with pendant arms containing exchangeable OH or NH protons.<sup>19,20</sup> Extending on the earlier work by Weyhermüller *et al.*<sup>14</sup> detailed above,  $\text{Fe}^{2+}$ ,  $\text{Co}^{2+}$  and  $\text{Ni}^{2+}$  complexes of TCMT have been reported as potential paraCEST MRI imaging agents due to their kinetic inertness and well-characterised coordination chemistry.<sup>21,22,23,24</sup> The  $[\text{Fe}(\text{TCMT})]^{2+}$  complex (prepared under inert conditions from the  $\text{Fe}(\text{OTf})_2$  precursor) was found to have a very high reduction potential of 860 mV vs. the normal hydrogen electrode (NHE), corresponding to a highly stabilised  $\text{Fe}^{2+}$  oxidation state.<sup>25,5</sup> This reflects on the effect of the neutral amide pendant groups on stabilising the divalent metal centre, which limits its reactivity towards anions and oxygen. In this case, TCMT was also observed to stabilise high-spin  $\text{Fe}^{2+}$ ; amide-functionalised macrocycles are considered weak field ligands and are generally found to promote the high-spin metal ions.<sup>21</sup>

However, to emphasise how subtle changes in the structure of a ligand can affect the properties of its complexes, two complexes of  $\text{Fe}^{2+}$  have been reported, which contain structurally similar (tris)pyridyl-triazacyclononane ligands (Figure 3.7).<sup>26,27</sup> The addition of an amino and a methyl group to the pyridine ring gives a high-spin  $\text{Fe}^{2+}$  complex, whereas the unsubstituted analogue is

low-spin.<sup>5</sup> The different substituents (aromatic vs. alkyl) may induce different electronic effects in their respective complexes.

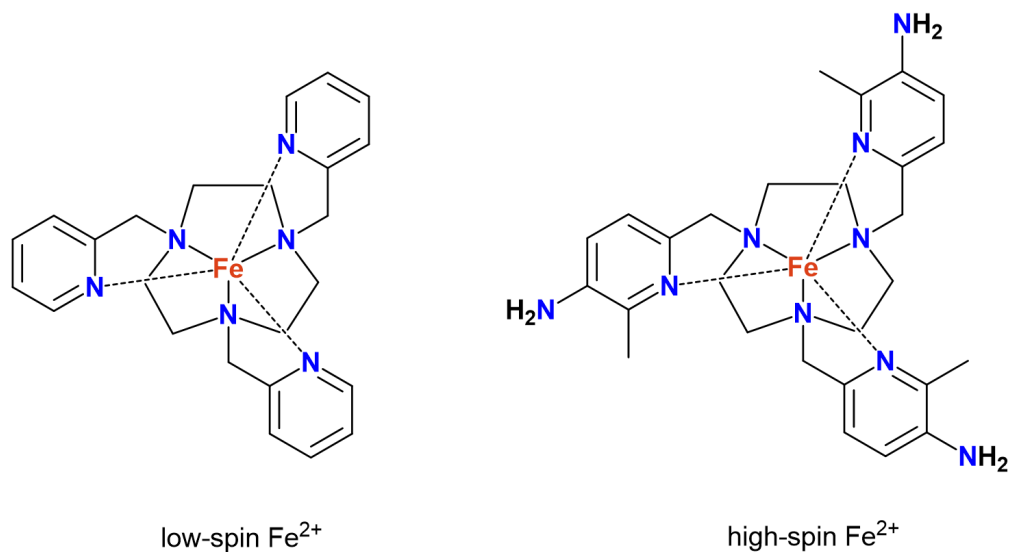


Figure 3.7 – Structures of the Fe<sup>2+</sup> (tris)pyridyl-triazacyclononane complexes reported by Tsitovich et al.<sup>5</sup> The addition of a methyl and amino group to the ligand results in a high-spin complex, whereas the unsubstituted analogue is low-spin.

Similar to the [Ni(TCMT)]<sup>2+</sup> complex described above, crystallographic data later obtained by Abozeid *et al.*<sup>22</sup> for [Co(TCMT)][ClO<sub>4</sub>]<sub>2</sub> and [Co(TCMT)][NO<sub>3</sub>]<sub>2</sub> showed that the ligand provides a hexadentate N<sub>3</sub>O<sub>3</sub> donor set. The geometry around the metal centre was distorted trigonal prismatic in both complexes, with twist angles of 17.2° (perchlorate) and 18.2° (nitrate). This has also been observed for the analogous Zn<sup>2+</sup> complex.<sup>28</sup> These complexes exhibit extensive hydrogen-bonding interactions between one of the NH protons of the amide group and a C=O oxygen of another complex, as well as hydrogen bonding from the terminal NH<sub>2</sub> groups of the pendant arm towards the cations – Figure 3.8 shows the structure obtained for [Co(TCMT)][NO<sub>3</sub>]<sub>2</sub>, including the oxygen atoms of the nitrate cations involved in hydrogen bonding.

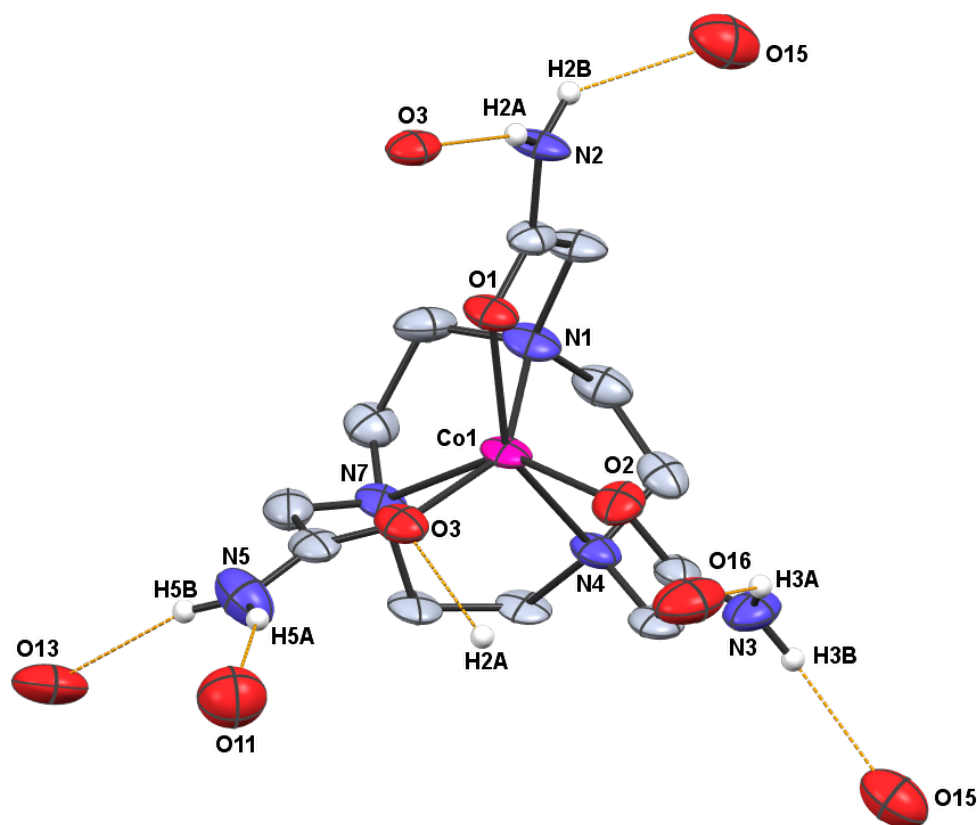


Figure 3.8 –  $[\text{Co}(\text{TCMT})][\text{NO}_3]_2$  reported by Abozeid *et al.*<sup>22</sup> Redrawn from CCDC 1586385. Hydrogen and nitrate cation atoms (excluding those involved in hydrogen bonding) omitted for clarity.

$\text{Ni}^{2+}$  complexes of  $\text{L}^2$  have been previously reported by George Sanderson.<sup>29</sup> No other transition metal complexes were explored at this time, but across the different metal ions, including those of  $\text{L}^1$ , the complexes may be expected to share the same hexadentate  $\text{N}_3\text{O}_3$  coordination.

### 3.1.3 Transition Metal Complexes of Anionic Hexadentate Phosphinate Tacn Ligands

Parker and co-workers<sup>30</sup> reported the formation of several divalent transition metal complexes with the anionic  $\text{H}_3\text{-NOTP}$  ligand. Akin to this earlier work, this chapter will investigate the complexation chemistry of NOTP-OMe (synthesised in Chapter 2), which, thus far, has only been used as an intermediate ligand for the formation of the phosphinic acid derivative.<sup>31</sup> Like  $\text{H}_3\text{-NOTP}$ , this is also expected to provide an  $\text{N}_3\text{O}_3$  donor set (but will be a neutral ligand, rather than anionic).

The  $[\text{M}(\text{NOTP})]^-$  complexes ( $\text{M} = \text{Co}^{2+}$ ,  $\text{Ni}^{2+}$ ,  $\text{Cu}^{2+}$ ,  $\text{Zn}^{2+}$ , as reported by Parker *et al.*<sup>30</sup>), were isolated as  $[\text{H}_3\text{O}]^+$  salts, with spontaneous deprotonation of the phosphinic acid groups, and were found to be in a distorted octahedral environment (Figure 3.9). This creates a new stereogenic centre at the phosphorus, rendering the oxygens diastereotopic. Although this can result in two (chiral) diastereoisomers (*RRR/SSS* and *RSR/SRS*), X-ray structural analysis showed that only a single

diastereoisomer (RRR or SSS at each phosphorus centre) was formed for all four transition metal complexes in the solid-state (which were isostructural).

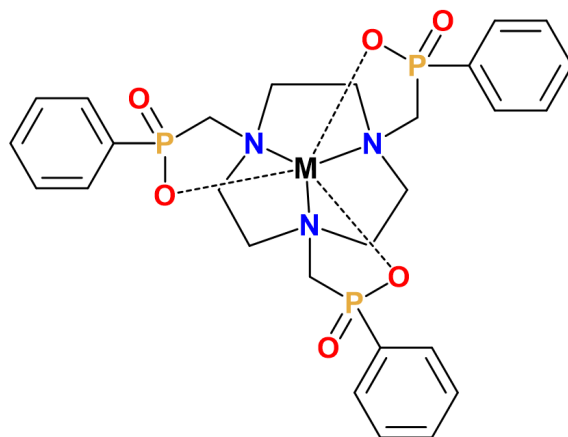


Figure 3.9 – General structure of the  $[M(\text{NOTP})]^-$  complexes reported by Parker and co-workers.<sup>31</sup>

It was determined that the coordination environment around the metal centre was a result of the minimisation of intramolecular ligand interactions, particularly from the PPh groups. Additionally, the  $\text{Cu}^{2+}$  complex only underwent Jahn-Teller distortion below 100 K – above this temperature, the observed  $C_3$  symmetry may be considered to result from 'time averaging' of vibronic couplings. Slow oxidation was also observed for the  $\text{Co}^{2+}$  complex, which formed the dark blue, neutral  $[\text{Co}(\text{NOTP})]$  complex over a period of 5-6 weeks in aerated aqueous solvent, or following the addition of hydrogen peroxide.

More recent work has reported the design of a new tacn-based ligand containing three [methylene-(2,2,2-trifluoroethyl)phosphinic acid] pendant arms,  $\text{H}_3\text{-NOTP}^{\text{tf6}}$ , and several paramagnetic divalent ( $\text{Mg}^{2+}$ ,  $\text{Ca}^{2+}$ ,  $\text{Mn}^{2+}$ ,  $\text{Fe}^{2+}$ ,  $\text{Co}^{2+}$ ,  $\text{Ni}^{2+}$ ,  $\text{Cu}^{2+}$ ,  $\text{Zn}^{2+}$ ) and trivalent ( $\text{Cr}^{3+}$ ,  $\text{Fe}^{3+}$ ,  $\text{Co}^{3+}$ ) metal complexes thereof.<sup>32</sup>

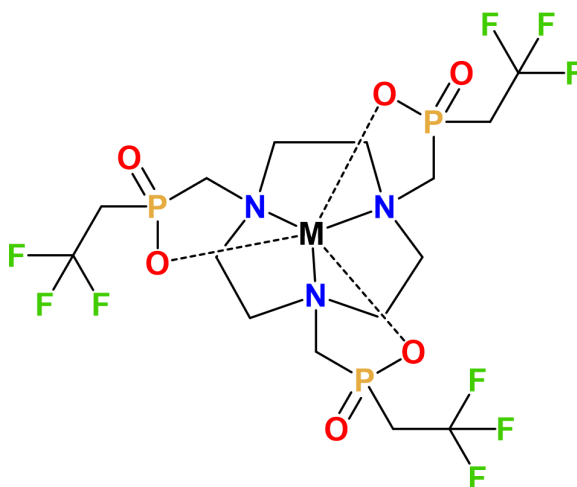


Figure 3.10 – General structure of the  $[M(\text{NOTP}^{\text{tf6}})]^{n-}$  complexes reported by Koucký et al.<sup>32</sup>

The structural properties of the complexes were evaluated. Generally, it was found that the larger metal ion,  $\text{Mn}^{2+}$ , adopted a distorted trigonal prismatic geometry, with a larger coordination cavity and smaller torsion of the pendant arms. The smaller divalent ions,  $\text{Ni}^{2+}$ ,  $\text{Cu}^{2+}$  and  $\text{Zn}^{2+}$ , formed *pseudo*-octahedral complexes, with a smaller cavity and greater pendant arm torsion. Interestingly,  $\text{Co}^{2+}$  (with an intermediate-sized radius) was observed in both arrangements (Figure 3.11).

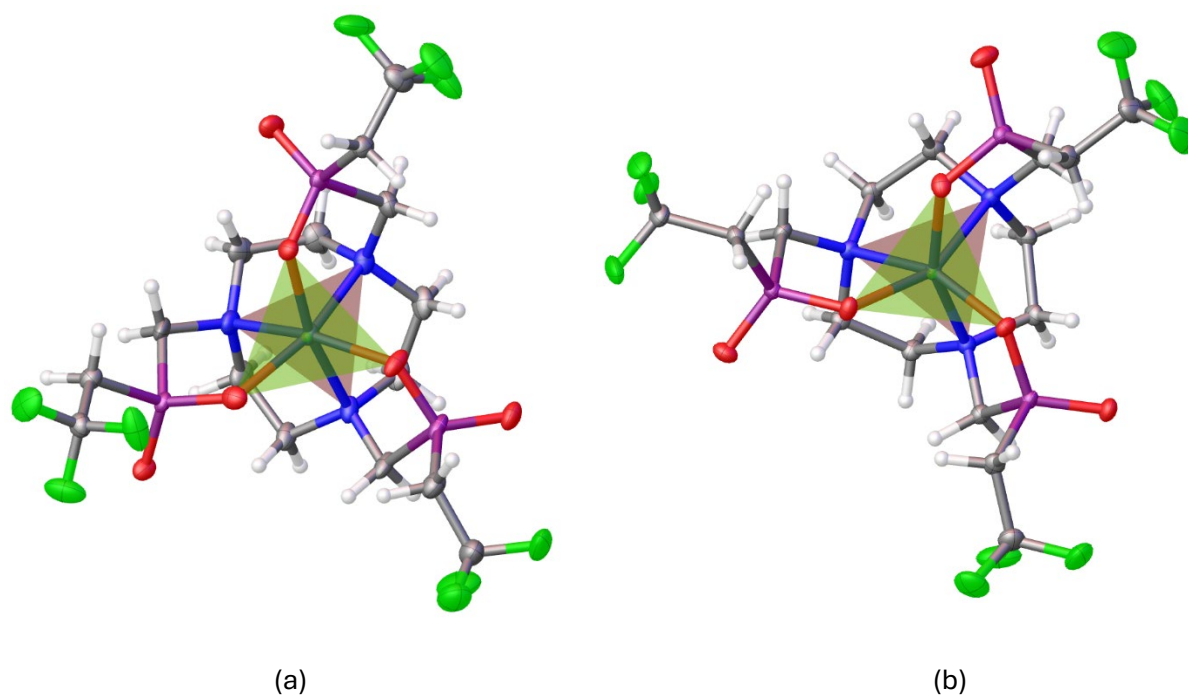


Figure 3.11 – Crystal structures of (a)  $[\text{Co}(\text{NOTP}^{\text{tfe}})]^-$  in octahedral geometry and (b)  $[\text{Co}(\text{NOTP}^{\text{tfe}})]^-$  in distorted trigonal prismatic geometry. Trigonal planes are represented by the green and red triangles. Redrawn from CCDC 2327154 and 2327158 respectively. Cations removed for clarity. Atom colours: dark blue, Co; purple, P; green, F; red, O; blue, N; grey, C; white, H.

The  $\text{H}_3\text{NOTP}^{\text{tfe}}$  ligand was found to provide a relatively weak-field, resulting in predominantly high-spin complexes. However, the neutral  $\text{Co}^{3+}$  complex of the ligand (produced by chemical oxidation, using  $\text{K}_2\text{S}_2\text{O}_8$  or  $\text{H}_2\text{O}_2$ ) was observed as the diamagnetic, low-spin form. This was confirmed by UV-Vis spectrometry, exhibiting two absorbance bands for the  $\text{Co}^{3+}$  complex, corresponding to the two spin-allowed transitions from the low-spin ground state  $^1\text{A}_{1g}$ , to  $^1\text{T}_{1g}$  and  $^1\text{T}_{2g}$ .

Like the  $\text{H}_3\text{-NOTP}$  ligand described above, complexes of the  $\text{H}_3\text{NOTP}^{\text{tfe}}$  ligand can exist in one of several possible isomers, due to the stereogenic phosphorus centre created upon coordination of the OH group to the metal centre, but also due to clockwise and anti-clockwise torsion of the  $\text{CH}_2$  groups upon coordination of the tacn-unit to the metal centre (denoted  $\delta$  or  $\lambda$ ), and of the pendant arms upon binding to the metal centre (denoted  $\Delta$  or  $\Lambda$ ). However,  $^{19}\text{F}$  and  $^{31}\text{P}$  NMR



spectra of the diamagnetic  $\text{Zn}^{2+}$  complex indicated the presence of only one single enantiomeric pair of a single diastereomer.

### 3.1.4 Aims

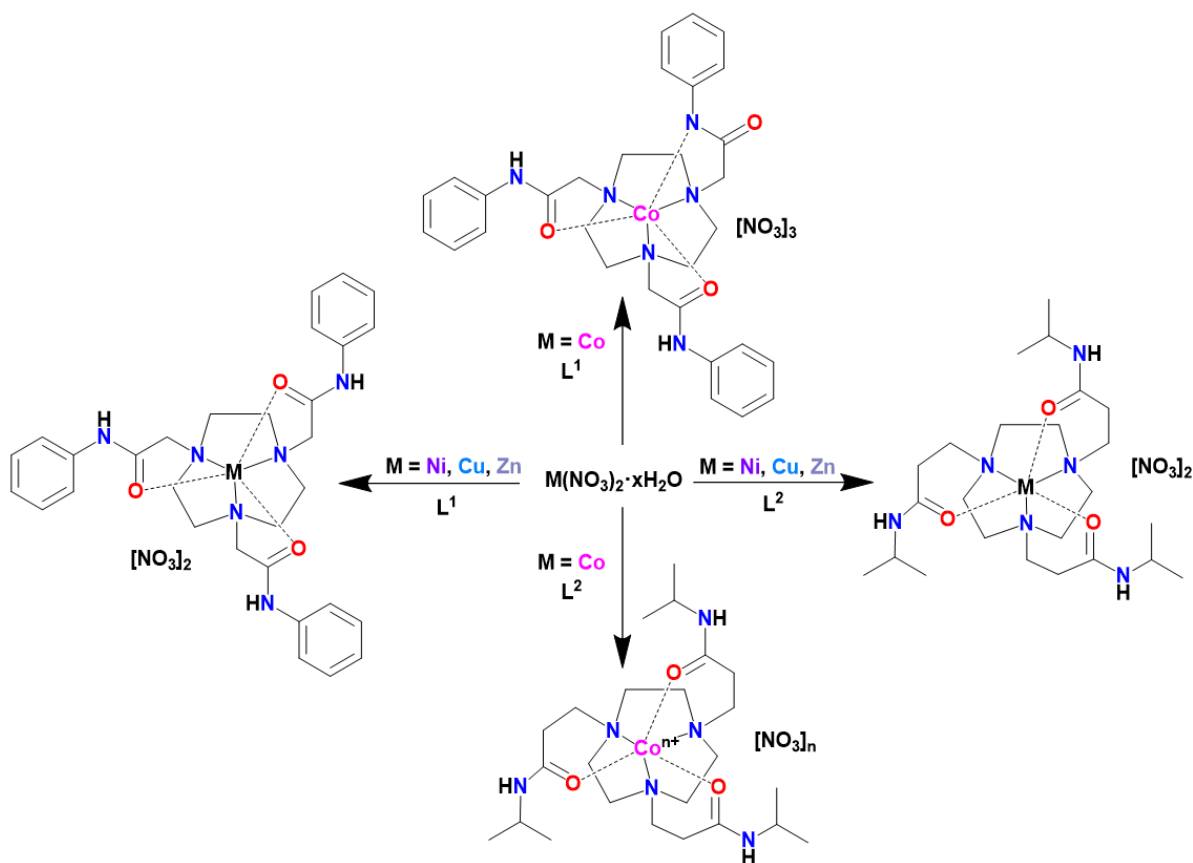
This chapter aims to form divalent transition metal complexes (Co, Ni, Cu, Zn) with the novel tris(amide) triazacyclononane ligands ( $\text{L}^1$  and  $\text{L}^2$ ), and the tris(phosphinate ester) ligand (NOTP-OMe) previously synthesised in Chapter 2.

Hence, prior to any work involving [ $^{18}\text{F}$ ]-fluoride, the coordination chemistry and behaviour of the ligands will first be established. UV-Vis spectroscopy and SCXRD data will be particularly useful for analysis of the paramagnetic complexes ( $\text{Co}^{2+}$ ,  $\text{Ni}^{2+}$ ,  $\text{Cu}^{2+}$ ), in conjunction with solid-state characterisation (elemental analysis and IR) and  $\text{ESI}^+$  MS. Based on literature for similar complexes, all three ligands are expected to provide an  $\text{N}_3\text{O}_3$  coordination sphere *via* the tacn-nitrogen and C=O or P=O groups.

## 3.2 Results and Discussion

### 3.2.1 Transition Metal Complexes of $\text{L}^1$ and $\text{L}^2$

The divalent transition metal complexes of  $\text{L}^1$  and  $\text{L}^2$  were prepared by the direct addition of the relevant metal nitrate precursor ( $\text{M}(\text{NO}_3)_2 \cdot x\text{H}_2\text{O}$ ,  $\text{M} = \text{Co}, \text{Ni}, \text{Cu}$  and  $\text{Zn}$ ) to the ligand, in methanol (Scheme 3.2). The solutions were left to stir at room temperature overnight, with the products subsequently isolated as coloured powder solids in good yield. For the cobalt complexes, the reactions were performed under an inert  $\text{N}_2$  atmosphere to minimise the likelihood of oxidation of the  $\text{Co}^{2+}$  metal centre to  $\text{Co}^{3+}$ . Due to the paramagnetic nature of the cobalt, nickel and copper complexes, NMR was only obtained for the diamagnetic zinc complex. Otherwise, characterisation was achieved using elemental analysis,  $\text{ESI}^+$  MS, IR, UV-Vis spectroscopy and SCXRD.



Scheme 3.2 – Formation of transition metal complexes of  $L^1$  and  $L^2$  (in MeOH, at RT) via  $M(\text{NO}_3)_2 \cdot x\text{H}_2\text{O}$  precursors ( $M = \text{Co, Ni, Cu, Zn}$ ).

In the majority of cases, and particularly for  $L^2$ , elemental analysis of the products indicated the presence of lattice water or MeOH. This was unsurprising, especially for the complexes of  $L^2$ , which were found to be very hygroscopic, and rapidly formed waxy solids upon exposure to air. SCXRD analysis of the cobalt and nickel complexes of  $L^1$ , and the nickel complex of  $L^2$ , also confirmed the presence of hydrogen-bonded water or methanol within the crystal structure. This highlights the propensity for the amide-functionalised tacn ligands to form hydrogen-bonding interactions with protic solvent molecules. This was in accord with the IR data obtained for the complexes, which (excluding the cobalt complex of  $L^1$ ) all depicted a broad peak over  $3000\text{ cm}^{-1}$  corresponding to an O-H stretch, and a sharper peak between  $1600 - 1700\text{ cm}^{-1}$  for the H-O-H bend. This was not observed in the IR data of the  $[\text{Co}(L^1)][\text{NO}_3]_n$  complex, possibly reflecting on the increased time the complex was left to dry *in vacuo* prior to storing in the glove box. The IR spectra for all the complexes depict two strong bands around  $1600\text{ cm}^{-1}$  which relate to the C=O stretch. Identification of the nitrate anions was not possible due to overlap with the ligand peaks.

ESI  $\text{MS}^+$  data for complexes of  $L^1$  and  $L^2$  (MeOH) confirmed the presence of the target  $[\text{M}(L^n)]^{2+}$  species ( $M = \text{Ni, Cu, Zn}$ ), and  $[\text{Co}(L^1\text{-H})]^{2+}$ . The nickel, copper and zinc complexes each show the

expected isotope splitting patterns. ESI<sup>+</sup> MS also gave evidence for the [Co(L<sup>2</sup>)]<sup>2+</sup> complex when obtained immediately after synthesis. However, analysis of crystals grown from an aerated solution containing the complex over several weeks showed *m/z* peaks relating to both [Co(L<sup>2</sup>)]<sup>2+</sup> and [Co(L<sup>2</sup>)]<sup>3+</sup>. Likewise, elemental analysis of the L<sup>2</sup> complex of cobalt was in accord with the oxidised [Co(L<sup>2</sup>)](NO<sub>3</sub>)<sub>3</sub> complex (+ ½ Et<sub>2</sub>O). This suggests that the cobalt metal centres undergo ready oxidation upon exposure to air.

The <sup>1</sup>H NMR spectrum (Figure 3.12) of [Zn(L<sup>1</sup>)](NO<sub>3</sub>)<sub>2</sub> (CD<sub>3</sub>OD) is consistent with coordinated ligand, with the tacn-CH<sub>2</sub> resonance (which was observed as a singlet at 3.14 ppm in the free ligand) observed as two adjacent multiplets, at 3.22 – 3.12 ppm and 3.02 – 2.91 ppm. Two separate resonances arise due to the inequivalent axial and equatorial protons of the tacn ring upon complexation of the ligand. The resonance relating to the CH<sub>2</sub> protons of the pendant arm also shifts towards higher-frequency from uncoordinated ligand, from 3.87 ppm to 4.04 ppm, and the aromatic region now depicts three multiplets at 7.66 – 7.64 [6H], 7.41 – 7.37 [6H] and 7.26 – 7.22 [3H] ppm. This is another indication that the amide pendant arm is bound to the metal centre. The spectrum shows the presence of a small amount of diethyl ether, which is also consistent with the microanalysis obtained for the sample. The <sup>13</sup>C{<sup>1</sup>H} NMR spectrum also suggests the target complex was formed in high purity. The expected resonances are present, with shifts from uncoordinated ligand in all cases. This is most notable for the C=O resonance, which shifts to higher frequency, from 169.5 ppm to 173.6 ppm.

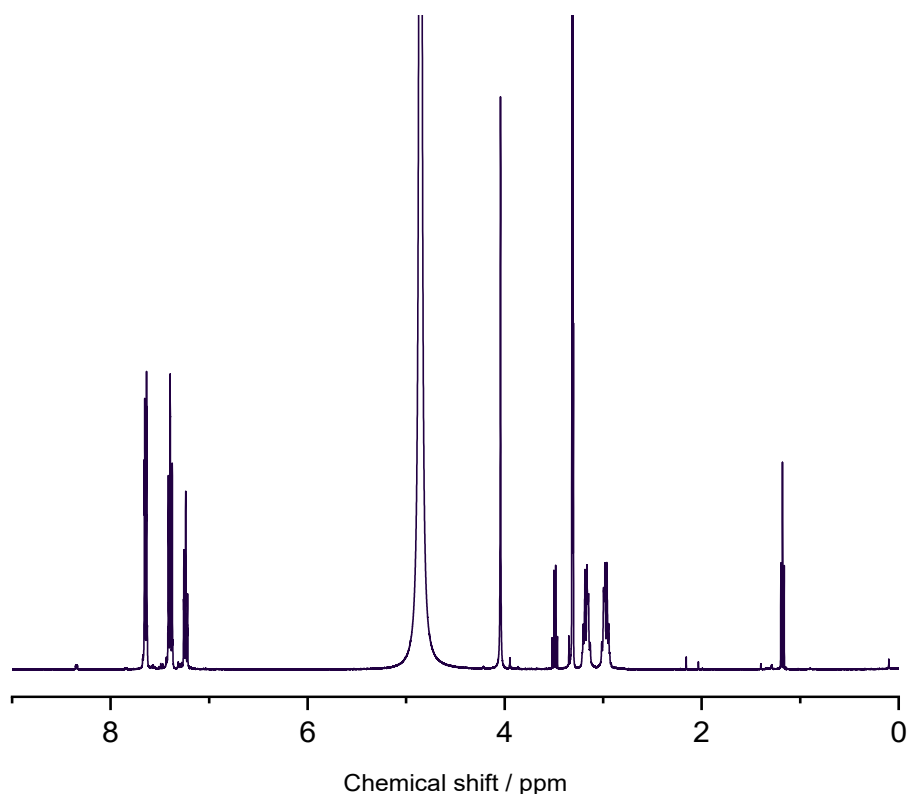


Figure 3.12 –  $^1\text{H}$  NMR spectrum of  $[\text{Zn}(\text{L}^1)][\text{NO}_3]_2$  ( $\text{CD}_3\text{OD}$ ).

The  $^1\text{H}$  NMR spectrum (Figure 3.13) of  $[\text{Zn}(\text{L}^2)][\text{NO}_3]_2$  ( $\text{CD}_3\text{OD}$ ) also shows the expected differences from uncoordinated ligand, although the shifts are much broader in comparison to the  $[\text{Zn}(\text{L}^1)][\text{NO}_3]_2$  complex. However, most of the resonances in this case are much closer in chemical shift and may appear broader due to some overlap. The tacn- $\text{CH}_2$  protons again resonate as two multiplets, at 2.98 – 2.89 and 2.88 – 2.74 ppm. The six  $\text{CH}_2$  protons of the pendant arm ethyl linker appear at 3.03 – 3.00 and 2.74 – 2.62 ppm. The change in the terminal isopropyl groups is minimal, as their chemical and steric environment is not significantly affected upon coordination of the ligand. The trends in the  $^{13}\text{C}\{^1\text{H}\}$  NMR spectrum are similar to those observed in  $[\text{Zn}(\text{L}^1)][\text{NO}_3]_2$ , again indicating coordination of the carboxamide oxygens of the pendant arm to the metal.

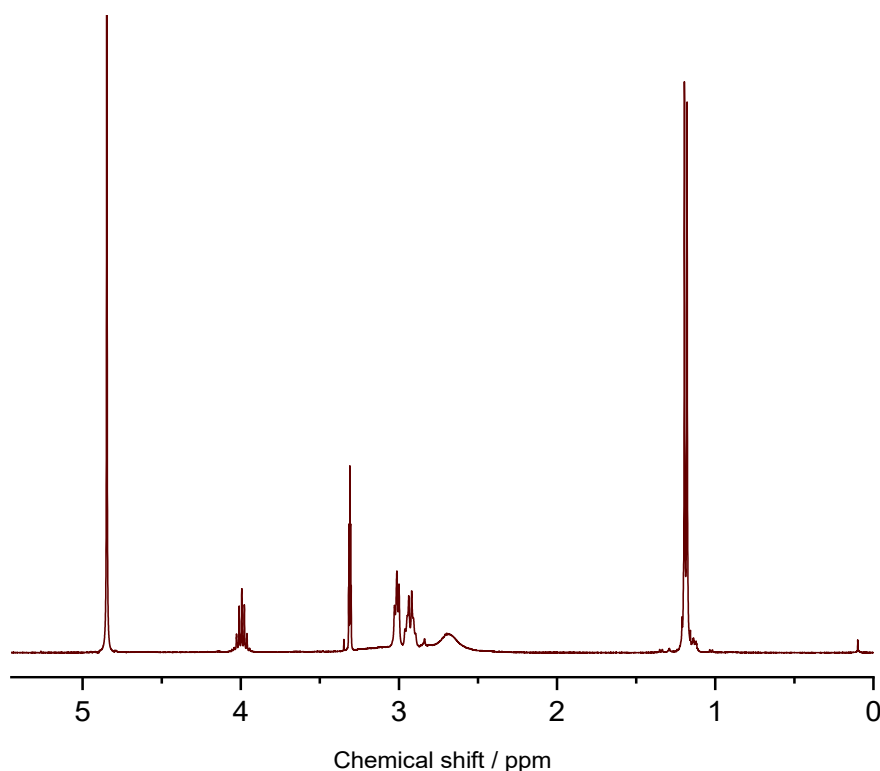


Figure 3.13 –  $^1\text{H}$  NMR spectrum of  $[\text{Zn}(\text{L}^2)][\text{NO}_3]_2$  ( $\text{CD}_3\text{OD}$ ).

#### 3.2.1.1 UV-Vis Spectroscopy for the Co, Ni and Cu Complexes of $\text{L}^1$ and $\text{L}^2$

The UV-Vis spectra for the Co, Ni and Cu complexes of  $\text{L}^1$  and  $\text{L}^2$  were obtained from methanol solutions containing a  $10^{-3}$  M concentration of the relevant sample and were analysed in the visible to near-IR region.

##### 3.2.1.1.1 Cobalt

Based on literature for similar  $d^7$   $\text{Co}^{2+}$  complexes (with approximate octahedral symmetry), the cobalt complexes of  $\text{L}^1$  and  $\text{L}^2$  are expected to be high-spin.<sup>14,22</sup> In this case, three spin-allowed  $d-d$  transitions are expected. Two transitions originate from the ground state  $^4\text{T}_{1g}$  term, and one from the low-lying  $^4\text{P}$  excited term:  $^4\text{T}_{2g}(\text{F}) \leftarrow ^4\text{T}_{1g}(\text{v}_1)$ ,  $^4\text{A}_{2g}(\text{F}) \leftarrow ^4\text{T}_{1g}(\text{v}_2)$  and  $^4\text{T}_{1g}(\text{P}) \leftarrow ^4\text{T}_{1g}(\text{v}_3)$ . However, the  $\text{v}_2$  transition is formally considered a ‘two-electron jump’ and is usually very weak.<sup>33,34</sup> In most instances, it is not observed, or may appear as a shoulder.<sup>35</sup> Additional structures within the visible region may also arise from spin-forbidden transitions. However, several literature examples have also highlighted the ease with which  $\text{Co}^{2+}$  complexes can be oxidised to the corresponding  $d^6$   $\text{Co}^{3+}$  complexes.<sup>7,8,9</sup> The majority of  $\text{Co}^{3+}$  complexes are diamagnetic and low-spin, and are expected to show two transitions from the octahedral ground-state  $^1\text{A}_{1g}$  term, to the excited  $^1\text{T}_{1g}$  and  $^1\text{T}_{2g}$  states; rarely, high-spin  $\text{Co}^{3+}$  complexes are observed.<sup>36,37</sup> In the  $[\text{Co}(\text{NOTP}^{\text{tfe}})]$  example given above, the ligand was found to provide a weak-

field (consistent with other literature examples of  $\text{N}_3\text{O}_3$ -donor tacn ligands), resulting in a high-spin  $\text{Co}^{2+}$  complex.<sup>32</sup> Upon oxidation to  $\text{Co}^{3+}$ , however, the low-spin complex was observed.

$[\text{Co}(\text{L}^1)]^{2+}$  and  $[\text{Co}(\text{L}^2)]^{2+}$  are expected to show absorption spectra similar to  $[\text{Co}(\text{TCMT})]^{2+}$  (discussed above), which was reported to have three distinct absorbance bands relating to the spin-allowed  $d-d$  transitions – two in the visible, and one in the near-IR region.<sup>22</sup> Figure 3.14 shows the UV-Vis spectra obtained for the cobalt complexes of  $\text{L}^1$  and  $\text{L}^2$ . The background noise between 800 – 900 nm is due to a grating change during data collection.

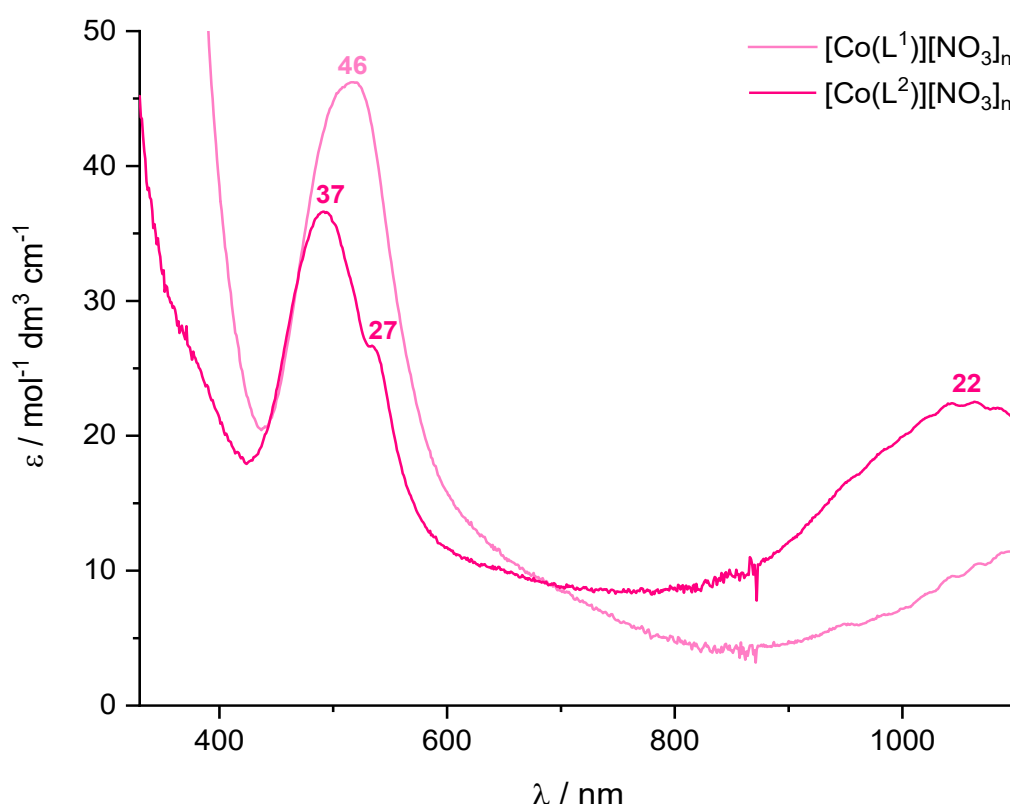


Figure 3.14 – UV-Vis absorbance spectra for  $[\text{Co}(\text{L}^1)][\text{NO}_3]_n$  and  $[\text{Co}(\text{L}^2)][\text{NO}_3]_n$  in MeOH ( $10^{-3}$  M). The background noise between 800 – 900 nm is due to a grating change.

Based on the above information, it is not possible to assign the metal centre in the cobalt complex of  $\text{L}^1$  as either  $\text{Co}^{2+}$  or  $\text{Co}^{3+}$ . A single broad absorption band is observed in the visible region at 521 nm ( $19200\text{ cm}^{-1}$ ). For a high-spin  $\text{Co}^{2+}$  complex, an absorption band would also be expected around  $8000 - 10000\text{ cm}^{-1}$  (near-IR region), but this may be obscured by the background noise beyond 1100 nm. However, a low-spin  $\text{Co}^{3+}$   $d^6$  complex would be expected to show two principal regions of absorption – which could be hidden underneath much more energetic charge transfer bands (both spectra show significant absorption below 400 nm).

The absorption spectrum of the cobalt complex of  $\text{L}^2$  shows two principal regions of absorption at 1062 nm ( $9420\text{ cm}^{-1}$ ) and 493 nm ( $20300\text{ cm}^{-1}$ ), and a shoulder is observed at 535 nm ( $18700\text{ cm}^{-1}$ ).

cm<sup>-1</sup>). Although this aligns with previously reported literature for octahedral high-spin Co<sup>2+</sup> complexes, the expected C<sub>3v</sub> nature of the complex reduces the symmetry, which may lead to additional absorption bands. Like the L<sup>1</sup> complex, the cobalt metal centre of the L<sup>2</sup> complex cannot be conclusively assigned to either oxidation state.

Molar extinction coefficients for the observed transitions of either complex do not exceed 46 mol<sup>-1</sup> dm<sup>3</sup> cm<sup>-1</sup>, as expected for spin-allowed and Laporte-forbidden electronic transitions.

### 3.2.1.1.2 Nickel

Three spin-allowed transitions are expected for a d<sup>8</sup> metal ion with octahedral symmetry: <sup>3</sup>T<sub>2g</sub>(F) ← <sup>3</sup>A<sub>2g</sub> (7000 – 13000 cm<sup>-1</sup>), <sup>3</sup>T<sub>1g</sub>(F) ← <sup>3</sup>A<sub>2g</sub> (11000 – 20000 cm<sup>-1</sup>), <sup>3</sup>T<sub>1g</sub>(P) ← <sup>3</sup>A<sub>2g</sub> (19000 – 27000 cm<sup>-1</sup>). In addition, two spin-forbidden transitions can often be prominent: <sup>1</sup>E<sub>g</sub> ← <sup>3</sup>A<sub>2g</sub> and <sup>1</sup>T<sub>2g</sub> ← <sup>3</sup>A<sub>2g</sub>.<sup>35</sup> The former is considered to arise from a ‘spin-flip’ transition and is reported by Weyhermüller *et al.*<sup>14</sup> for the [Ni(TCMT)]<sup>2+</sup> complex, appearing as an absorbance band at 802 nm. [Ni(TCMT)]<sup>2+</sup> was also reported to have transitions at 920 nm (10900 cm<sup>-1</sup>), 561 nm (17800 cm<sup>-1</sup>) and 354 nm (28200 cm<sup>-1</sup>).

The UV-Vis spectra for the [Ni(L<sup>1</sup>)](NO<sub>3</sub>)<sub>2</sub> and [Ni(L<sup>2</sup>)](NO<sub>3</sub>)<sub>2</sub> are shown in Figure 3.15. Both complexes are very similar to [Ni(TCMT)]<sup>2+</sup> (as expected due to the shared N<sub>3</sub>O<sub>3</sub> coordination sphere around the nickel ion) and can be assigned accordingly. For [Ni(L<sup>1</sup>)](NO<sub>3</sub>)<sub>2</sub>, the three spin-allowed transitions are observed at 933 nm (10700 cm<sup>-1</sup>), 563 nm (17800 cm<sup>-1</sup>) and 354 nm (28200 cm<sup>-1</sup>). Hence, the absorbance band at 800 nm (12500 cm<sup>-1</sup>) is tentatively assigned as the spin-forbidden <sup>1</sup>E<sub>g</sub> ← <sup>3</sup>A<sub>2g</sub> transition. However, these complexes are also expected to possess C<sub>3v</sub> symmetry, and deviation from true O<sub>h</sub> symmetry often result in splitting of the observed absorbance bands. The values for the [Ni(L<sup>2</sup>)](NO<sub>3</sub>)<sub>2</sub> complex are very similar, at 928 nm (10800 cm<sup>-1</sup>), 790 nm (12700 cm<sup>-1</sup>), 569 nm (17600 cm<sup>-1</sup>) and 354 nm (28200 cm<sup>-1</sup>). The molar extinction coefficient values for the observed transitions (both complexes) transition range between 22 – 62 mol<sup>-1</sup> dm<sup>3</sup> cm<sup>-1</sup>, in line with expected values for *pseudo*-octahedral d<sup>8</sup> nickel species.

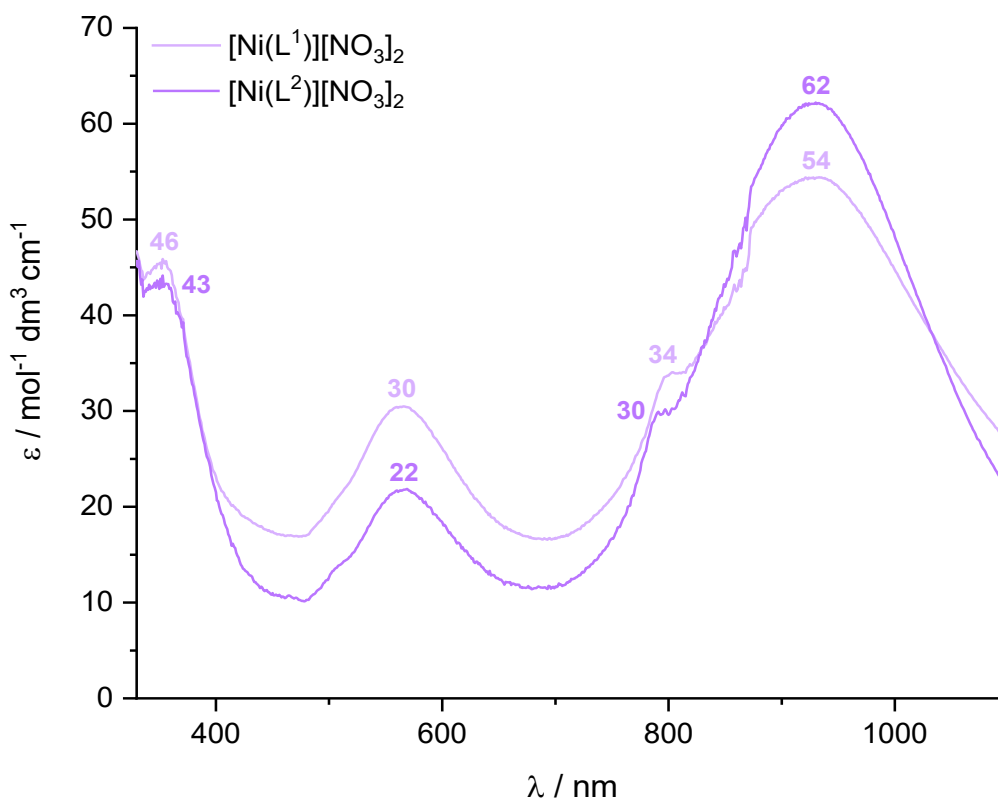


Figure 3.15 – UV-Vis absorbance spectra for  $[\text{Ni}(\text{L}^1)][\text{NO}_3]_2$  and  $[\text{Ni}(\text{L}^2)][\text{NO}_3]_2$  in MeOH ( $10^{-3} \text{ M}$ ).

#### 3.2.1.1.3 Copper

For octahedral  $d^9 \text{Cu}^{2+}$  complexes, as a result of Jahn-Teller distortion, the  ${}^2\text{E}_g$  and  ${}^2\text{T}_g$  orbital subsets are split into  ${}^2\text{B}_{1g}/{}^2\text{A}_{1g}$  and  ${}^2\text{B}_{2g}/{}^2\text{E}_g$  orbitals, respectively. Three spin-allowed transitions are possible. However, because these transitions are relatively weak and close in energy, the majority of  $\text{Cu}^{2+} d^9$  complexes produce a UV-Vis spectrum consisting of a single, broad, poorly resolved band in the visible region.<sup>35,38</sup> The UV-Vis spectra for the  $[\text{Cu}(\text{L}^1)][\text{NO}_3]_2$  and  $[\text{Cu}(\text{L}^2)][\text{NO}_3]_2$  complexes both show a single, broad absorption band, observed at 733 nm ( $13600 \text{ cm}^{-1}$ ) for the  $\text{L}^1$  complex and 772 nm ( $13000 \text{ cm}^{-1}$ ) for the  $\text{L}^2$  complex. As a result of distortion and, therefore, loss of symmetry, the molar extinction coefficients are an order of magnitude higher (ca.  $100 \text{ mol}^{-1} \text{ dm}^3 \text{ cm}^{-1}$ ) than those observed for the cobalt and nickel complexes (ca.  $40 \text{ mol}^{-1} \text{ dm}^3 \text{ cm}^{-1}$ ).

#### 3.2.1.1.4 Summary of the UV-Vis Spectra for Ni, Co and Cu Complexes of Tris(Amide) Tacn Ligands

Table 3.2 provides a summary of the UV-Vis spectra (including wavelength, wavenumber and molar extinction coefficients for each observed transition, and where possible, the assignment) for the transition metal complexes of  $\text{L}^1$  and  $\text{L}^2$ , as well as the related TCMT complexes reported by Weyhermüller *et al.*<sup>14</sup>



Table 3.2 – Summary of the UV-Vis spectroscopic data for Co, Ni and Cu complexes of the tris(amide) ligands, L<sup>1</sup>, L<sup>2</sup> and TCMT.

Complex	$\lambda$ / nm	$\tilde{\nu}$ / cm <sup>-1</sup>	$\epsilon$ / mol <sup>-1</sup> dm <sup>3</sup> cm <sup>-1</sup>	Transition	Description
<b>[Co(TCMT)]<sup>2+</sup></b>	1146	8700	15	${}^4T_{2g}(F) \leftarrow {}^4T_{1g}$	<i>d-d</i> spin-allowed
	668	15000	5	${}^4A_{2g}(F) \leftarrow {}^4T_{1g}$	<i>d-d</i> spin-allowed 'two-electron jump'
	500	20000	20	${}^4T_{1g}(P) \leftarrow {}^4T_{1g}$	<i>d-d</i> spin-allowed
<b>[Co(L<sup>1</sup>)]<sup>n+</sup></b>	521	19200	46	-	-
<b>[Co(L<sup>2</sup>)]<sup>n+</sup></b>	1062	9420	22	-	-
	535 (sh)	18700	27	-	-
	493	20300	37	-	-
<b>[Ni(TCMT)]<sup>2+</sup></b>	920	10900	39	${}^3T_{2g}(F) \leftarrow {}^3A_{2g}$	<i>d-d</i> spin-allowed
	802	12500	20	${}^1E_g \leftarrow {}^3A_{2g}$	'spin-flip' transition
	561	17800	15	${}^3T_{1g}(F) \leftarrow {}^3A_{2g}$	<i>d-d</i> spin-allowed
	354	28200	20	${}^3T_{1g}(P) \leftarrow {}^3A_{2g}$	<i>d-d</i> spin-allowed
<b>[Ni(L<sup>1</sup>)]<sup>2+</sup></b>	933	10700	54	${}^3T_{2g}(F) \leftarrow {}^3A_{2g}$	<i>d-d</i> spin-allowed
	800	12500	34	${}^1E_g \leftarrow {}^3A_{2g}$	'spin-flip' transition <u>OR</u> <i>d-d</i> spin-forbidden (C <sub>3v</sub> symmetry)
	563	17800	30	${}^3T_{1g}(F) \leftarrow {}^3A_{2g}$	<i>d-d</i> spin-allowed
	354	28200	46	${}^3T_{1g}(P) \leftarrow {}^3A_{2g}$	<i>d-d</i> spin-allowed
<b>[Ni(L<sup>2</sup>)]<sup>2+</sup></b>	928	10800	62	${}^3T_{2g}(F) \leftarrow {}^3A_{2g}$	<i>d-d</i> spin-allowed
	790	12700	30	${}^1E_g \leftarrow {}^3A_{2g}$	'spin-flip' transition <u>OR</u> <i>d-d</i> spin-forbidden (C <sub>3v</sub> symmetry)
	569	17600	22	${}^3T_{1g}(F) \leftarrow {}^3A_{2g}$	<i>d-d</i> spin-allowed
	354	28200	43	${}^3T_{1g}(P) \leftarrow {}^3A_{2g}$	<i>d-d</i> spin-allowed
<b>[Cu(TCMT)]<sup>2+</sup></b>	764	13100	97	-	<i>d-d</i> spin-allowed (Jahn-Teller)
<b>[Cu(L<sup>1</sup>)]<sup>2+</sup></b>	733	13600	95	-	<i>d-d</i> spin-allowed (Jahn-Teller)
<b>[Cu(L<sup>2</sup>)]<sup>2+</sup></b>	772	13000	101	-	<i>d-d</i> spin-allowed (Jahn-Teller)

### 3.2.1.2 Molecular Structures of Co, Ni and Cu Complexes of $L^1$ and $L^2$

To confirm the coordination environments and investigate both the influence of the metal  $d^n$  configurations and the effect of the different amide linking groups from the tacn N-donor atoms, X-ray crystallographic studies were undertaken on five examples,  $[\text{Co}(\text{1-H})][\text{NO}_3]_2$  and  $[\text{M}(\text{L})][\text{NO}_3]_2$  ( $\text{M} = \text{Ni}, \text{Cu}$ ;  $\text{L} = \text{L}^1$  or  $\text{L}^2$ ). Key bond distances and angles involving the tacn ring and the five- or six-membered chelate rings involving the pendant amides formed by  $\text{L}^1$  and  $\text{L}^2$ , respectively, are presented in Table 3.3. Below, these metrics and their associated trends will be discussed in further detail for each of the individual complexes.

Table 3.3 – Selected geometric parameters for the crystallographically characterised  $L^1$  and  $L^2$  complexes.

Complex	d(M-N)	d(M-O)	<N-M-N	<N-M-O	Twist angle, $\theta^a$
	/ Å	/ Å	/°	/°	/°
<b>[Co(L<sup>1</sup>-H)][NO<sub>3</sub>]<sub>2</sub> •2MeOH</b>	Co-N1: 1.948(2) Co-N2: 1.9221(19) Co-N3: 1.9288(19) Co-N4: 1.928(2)	Co-O1: 1.9222(16) Co-O2: 1.9349(17)	N1-Co-N2: 88.68(8) N1-Co-N4: 88.46(8) N2-Co-N4: 89.45(8) N3-Co-N4: 84.96(8)	N2-Co-O2: 85.12(8) N1-Co-O1: 85.31(8)	52.26(6)
<b>[Ni(L<sup>1</sup>)] [NO<sub>3</sub>]<sub>2</sub> •1.5MeOH</b>	Ni-N1: 2.079(2) Ni-N2: 2.072(2) Ni-N3: 2.049(3)	Ni-O1: 2.0558(16) Ni-O2: 2.032(2) Ni-O3: 2.0805(15)	N1-Ni-N2: 85.50(9) N1-Ni-N3: 85.79(12) N2-Ni-N3: 85.93(9)	N1-Ni-O1: 82.38(8) N2-Ni-O2: 82.63(9) N3-Ni-N3: 81.62(8)	48.84(6)
<b>[Ni(L<sup>2</sup>)] [NO<sub>3</sub>]<sub>2</sub> •0.443H<sub>2</sub>O</b>	Ni-N1: 2.138(2) Ni-N2: 2.142(2) Ni-N3: 2.137(2)	Ni-O1: 2.0647(18) Ni-O2: 2.078(2) Ni-O3: 2.064(2)	N1-Ni-N2: 83.96(9) N1-Ni-N3: 83.52(10) N2-Ni-N3: 83.36(9)	N1-Ni-N2: 91.38(10) N2-Ni-O3: 90.12(9) N3-Ni-O1: 91.73(8)	56.78(7)

Table 3.3 cont. –

Complex	d(M-N)	d(M-O)	<N-M-N	<N-M-O	Twist angle, $\theta^a$
	/ Å	/ Å	/°	/°	/°
<b>[Cu(L<sup>1</sup>)] [NO<sub>3</sub>]<sub>2</sub>· 1.25Et<sub>2</sub>O·MeOH</b>	Cu1-N1: 2.116(2)	Cu1-O1: 2.193(2)	N1-Cu1-N2: 84.20(9)	N1-Cu1-O1: 77.61(8)	26.16(7)
	Cu1-N2: 2.043(2)	Cu1-O2: 2.019(2)	N1-Cu1-N3: 81.32(9)	N2-Cu1-O2: 81.67(9)	
	Cu1-N3: 2.198(2)	Cu1-O3: 2.061(2)	N3-Cu1-N2: 83.23(9)	N3-Cu1-O3: 78.12(8)	
	Cu2-N7: 2.091(3)	Cu2-O4: 1.989(2)	N7-Cu2-N8: 82.48(10)	N8-Cu2-O4: 81.34(9)	
	Cu2-N8: 2.203(3)	Cu2-O5: 2.045(2)	N7-Cu2-N9: 85.61(10)	N9-Cu2-O5: 82.73(9)	46.31(7)
	Cu2-N9: 2.019(2)	Cu2-O6: 2.215(2)	N8-Cu2-N9: 85.67(9)	N7-Cu2-O6: 79.77(9)	
	Cu3-N13: 2.126(2)	Cu3-O7: 2.063(2)	N14-Cu3-N13: 80.89(9)	N15-Cu3-O7: 80.96(9)	27.13(7)
	Cu3-N14: 2.179(2)	Cu3-O8: 2.162(2)	N15-Cu3-N13: 83.04(9)	N13-Cu3-O8: 78.48(9)	
	Cu3-N15: 2.077(2)	Cu3-O9: 2.119(2)	N14-Cu3-N15: 82.66(9)	N14-Cu3-O9: 77.60(8)	
<b>[Cu(L<sup>2</sup>)] [NO<sub>3</sub>]<sub>2</sub></b>	Cu-N1: 2.3231(8)	Cu-O1: 1.9678(6)	N1-Cu-N1: 81.02(3)	N1-Cu-O1: 89.62(3)	56.12(2)
	Cu-N2: 2.0845(8)	Cu-O2: 2.3599(7)	N1-Cu-N3: 84.59(3)	N2-Cu-O2: 89.48(3)	
	Cu-N3: 2.0184(7)	Cu-O3: 1.9780(6)	N2-Cu-N3: 87.07(3)	N3-Cu-O3: 93.69(3)	

<sup>a</sup> the twist angle,  $\theta$ , between the triangular N<sub>3</sub> face from the coordinated tacn and the opposite triangular face containing the amide/carboxamide/carboxylate pendant donor groups; trigonal prismatic:  $\theta = 0^\circ$ ; octahedral:  $\theta = 60^\circ$ .

For  $[\text{Co}(\text{L}^1\text{-H})][\text{NO}_3]_2$  (Figure 3.16) the ligand provides an  $\text{N}_4\text{O}_2$  donor set following deprotonation of one of the NH groups of a single amide pendant arm, and coordination to an oxidised  $\text{Co}^{3+}$  metal centre. The three tacn N-donor atoms are bound *facially*, alongside two carboxamide O-donor atoms from the two other two pendant arms. Two nitrate counter-ions are present, which are found to form hydrogen-bonding interactions with one of the ‘intact’, O-bonded (amide)NH functions. The observed (but unexpected)  $\text{N}_4\text{O}_2$  coordination is supported by the comparison of the M-N(tacn) bond distances (ca. 1.93 Å for M = Co) vs. the M-N(tacn) bond distances in the nickel and copper complexes of  $\text{L}^1$  and  $\text{L}^2$ , which are considerably shorter. Additionally, M-N(tacn) bond distances with related  $\text{Co}^{2+}$  and  $\text{Co}^{3+}$  complexes with tacn ligands also strongly support the presence of a central  $\text{Co}^{3+}$  ion.<sup>39,40</sup> For example, in the  $[\text{Co}(\text{TCMT})][\text{NO}_3]_2$  complex mentioned above, the average Co–N bond distance is ca. 2.15 Å – around 0.2 Å longer than the  $[\text{Co}(\text{L}^1\text{-H})][\text{NO}_3]_2$  complex.

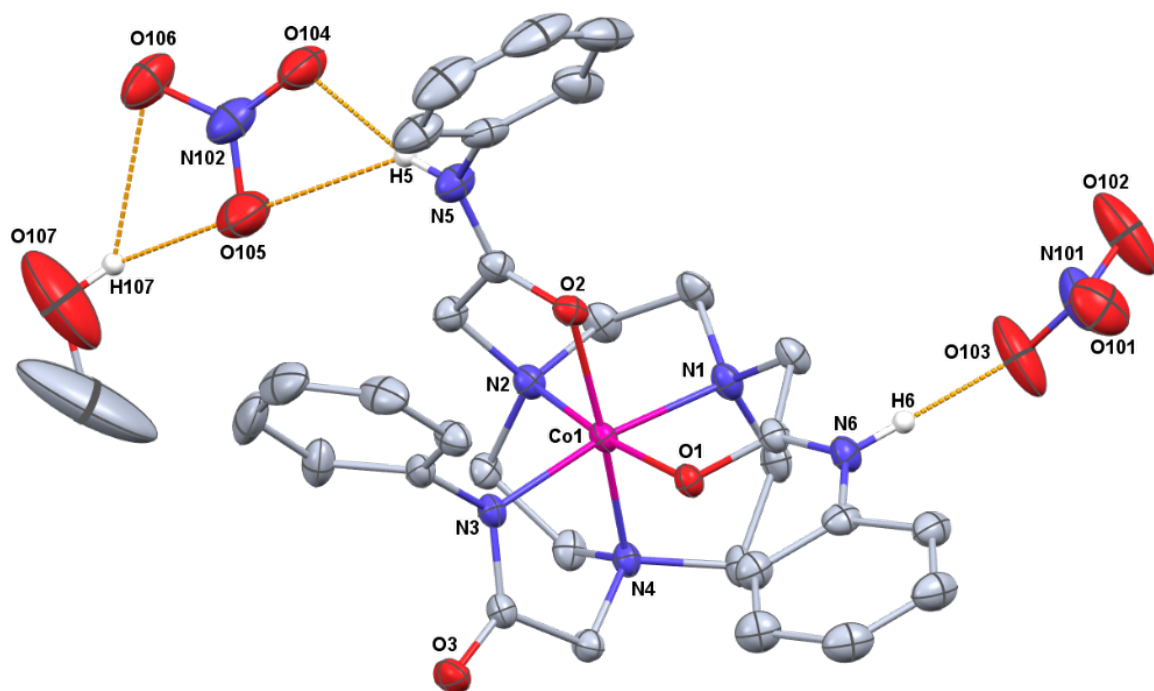


Figure 3.16 – View of the structure of  $[\text{Co}(\text{L}^1\text{-H})][\text{NO}_3]_2 \cdot 2\text{MeOH}$  showing the atom numbering scheme and the H-bonding between the nitrate anions and the N5 and N6 atoms of the carboxamide-bound amide arms. Ellipsoids are drawn at the 50% probability level and H and solvent atoms (except those involved in H-bonding) are omitted for clarity. H-bond distances:  $\text{N5} \cdots \text{O104} = 2.74$ ,  $\text{N6} \cdots \text{O103} = 2.736$ ,  $\text{O107} \cdots \text{O105} = 2.764$  Å.

A similar coordination mode was also observed with the trivalent  $\text{Cr}^{3+}$  complex of TCMT, as reported by Weyhermüller *et al.*<sup>14</sup> (Section 3.1.2). Deprotonation of one amide NH group occurs, giving rise to an  $\text{N}_4\text{O}_2$  donor set around the central metal ion, as the anionic amide-nitrogen binds in place of the (more commonly observed) carboxamide-oxygen. The Cr-N(tacn) bond distances were ca. 0.2 Å longer than the Cr-N(amide) distances, whereas all four Co-N distances of the

$[\text{Co}(\text{L}^1\text{-H})]^{2+}$  cation are very similar. This reflects on the smaller ionic radius of  $\text{Co}^{3+}$  compared to  $\text{Cr}^{3+}$  and the reduced strain in the coordinated tacn unit. However, the strain imposed by the geometry at the deprotonated amide is apparent by the slightly longer Co-N1 distance (by ca. 0.03 Å) and the smaller N3-Co-N4 chelate angle (by 4°).

Several crystals of a  $[\text{Co}(\text{L}^2)][\text{NO}_3]_3$  complex were also analysed *via* SCXRD. In all cases, the crystals were significantly twinned and, therefore, the data was of lower quality, with a minimum R-factor value of 0.1120 across the datasets (ideally, this would be no greater than 0.070). However, all the structures obtained were shown to contain the oxidised  $\text{Co}^{3+}$  metal ion (Figure 3.17). Rather than deprotonation of one of the amide pendants, like  $[\text{Co}(\text{L}^1\text{-H})][\text{NO}_3]_2$ , all three of the pendant arms are coordinated via the carboxamide-O, with three  $[\text{NO}_3]^-$  counter-ions. Although accurate comparisons cannot be made from this complex due to the lower quality data, the average Co-N(tacn) bond length is 1.928(5) Å, and the average Co-O bond is 1.915(4) Å, both which are in line with  $\text{Co}^{3+}$ .<sup>39,40</sup> The complex appears to have *pseudo*-octahedral geometry, with a twist angle,  $\Theta$ , of 54.2°.

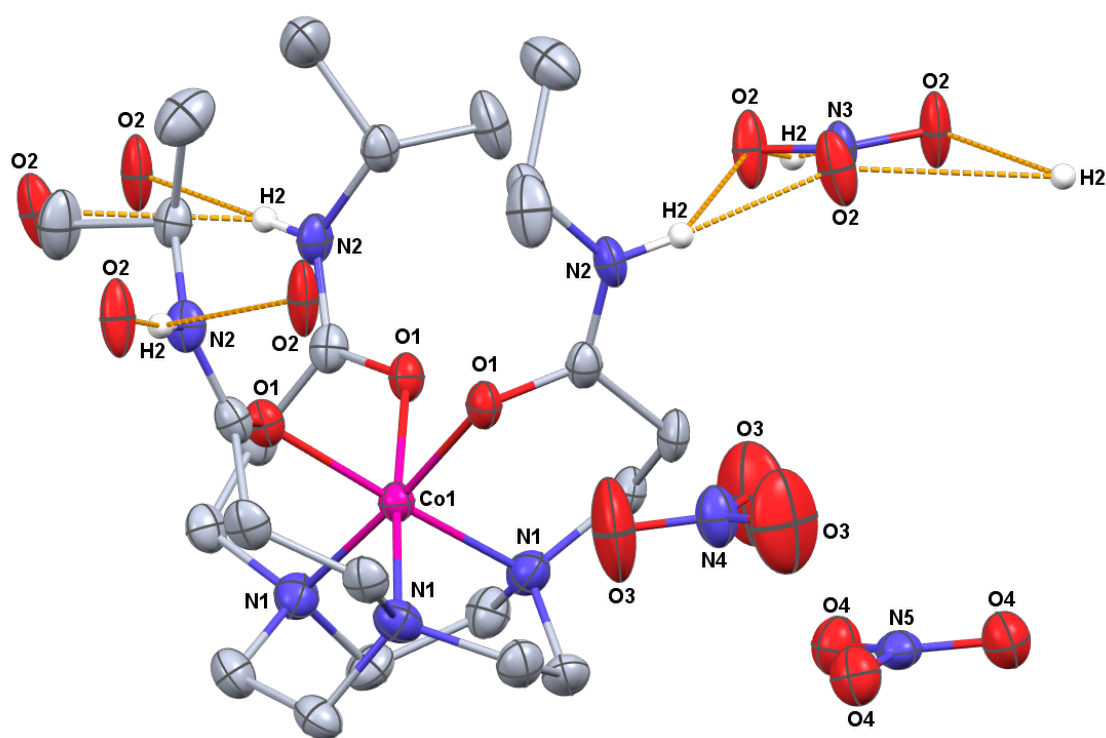
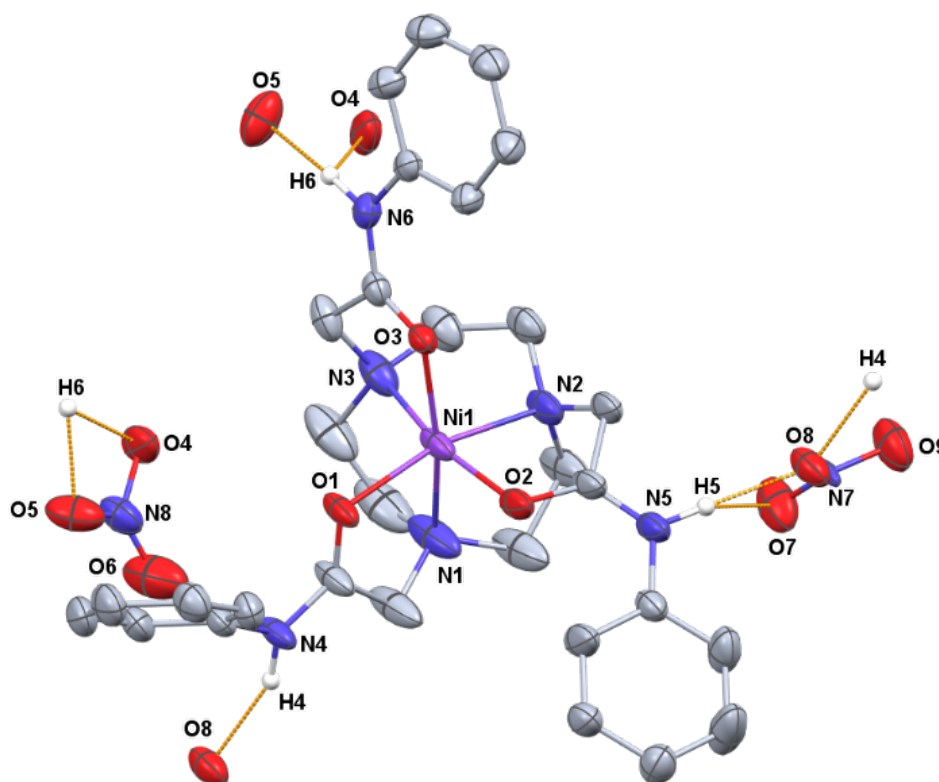


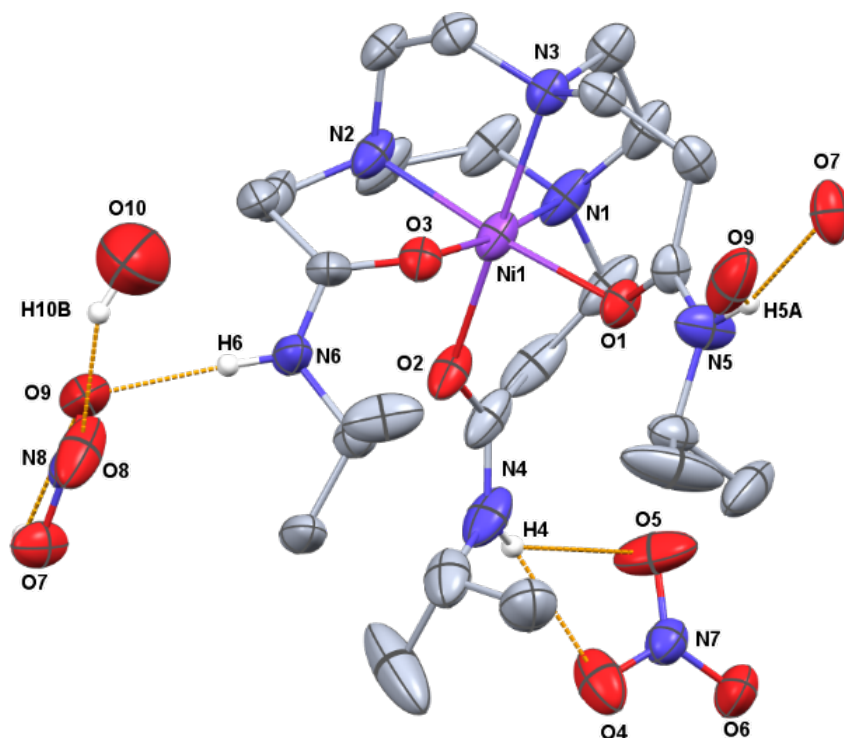
Figure 3.17 – View of the structure of  $[\text{Co}(\text{L}^2)][\text{NO}_3]_3$  showing the atom numbering scheme and H-bonding between the nitrate anions and the N2 atoms of the carboxamide-bound amide arms. Ellipsoids are drawn at the 50% probability level and H and solvent atoms (except those involved in H-bonding) are omitted for clarity.

The structures of  $[\text{Ni}(\text{L}^1)]^{2+}$  and  $[\text{Ni}(\text{L}^2)]^{2+}$  are given in Figure 3.18. In both complexes, the ligands are hexadentate and provide an  $\text{N}_3\text{O}_3$  donor set to the central  $\text{Ni}^{2+}$  ions. The observed twist angles are consistent with *pseudo*-octahedral geometry (46.84(6)° for the  $\text{L}^1$  complex and 56.78(7)° for

the  $L^2$  complex). As expected, the shorter alkyl linker of  $L^1$  leads to a smaller twist angle. The five-membered chelate rings involving the amide O atoms in  $[Ni(L^1)]^{2+}$  also result in much more acute N-Ni-O bond angles (*ca.*  $82^\circ$ ) compared to the N-Ni-O bond angles of  $[Ni(L^2)]^{2+}$  (*ca.*  $91^\circ$ ), which has a six-membered chelate ring. The Ni-N bonds are also slightly shorter and the N-Ni-N angles are slightly larger in  $[Ni(L^1)]^{2+}$  compared to  $[Ni(L^2)]^{2+}$ . The latter complex has metrics similar to the  $[Ni(tcet)]^{2+}$  complex given as an earlier example.<sup>16</sup>



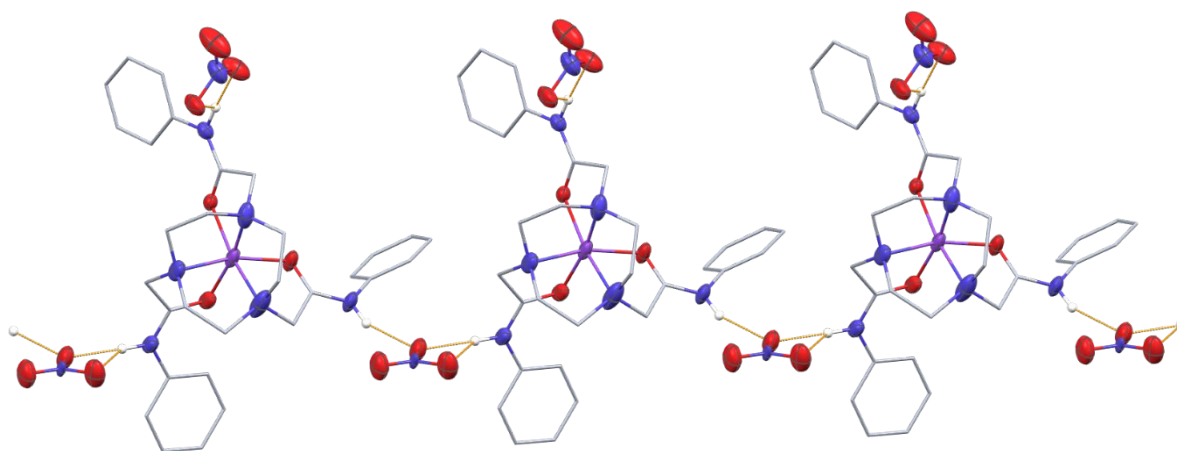
(a)



(b)

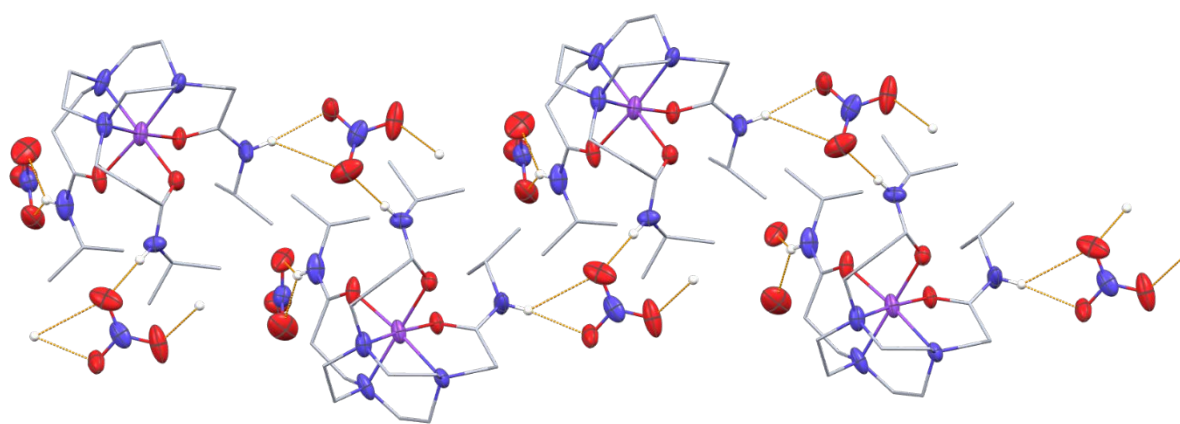
Figure 3.18 – Views of the structures present in (a)  $[\text{Ni}(\text{L}^1)][\text{NO}_3]_2 \cdot 1.5\text{MeOH}$  and (b)  $[\text{Ni}(\text{L}^2)][\text{NO}_3]_2 \cdot 0.443\text{H}_2\text{O}$  showing the atom numbering schemes and the H-bonding between nitrate anions and each of the amide NH groups. Ellipsoids are drawn at the 50% probability level and H and solvent atoms (except those involved in H-bonding) are omitted for clarity.

The extended hydrogen-bonded networks for the two nickel complexes are given in Figure 3.19, with both structures forming infinite one-dimensional sheets. One nitrate anion bridges two molecules in both  $[\text{Ni}(\text{L}^1)]^{2+}$  and  $[\text{Ni}(\text{L}^2)]^{2+}$ , with an average N(amide)---O(nitrate) distance of 3.0 Å for  $[\text{Ni}(\text{L}^1)][\text{NO}_3]_2$  and 3.1 Å for  $[\text{Ni}(\text{L}^2)][\text{NO}_3]_2$ .



(a)





(b)

Figure 3.19 – View showing the extended hydrogen-bonded network of (a)  $[\text{Ni}(\text{L}^1)][\text{NO}_3]_2$  and (b)  $[\text{Ni}(\text{L}^2)][\text{NO}_3]_2$ , which both form an infinite 1D chain with one bridging nitrate anion between two molecules. Atom colours: purple, Ni; red, O; blue, N; white, H.

The structure obtained for the  $[\text{Cu}(\text{L}^1)]^{2+}$  complex shows three crystallographically independent  $[\text{Cu}(\text{L}^1)]^{2+}$  cations (Figure 3.20). The complexes involving Cu1 and Cu3 are very similar, whereas the complex involving Cu2 is notably different. The measured twist angles ( $\theta$ ) of each cation are as follows: Cu1 =  $26.16(7)^\circ$ , Cu2 =  $46.31(7)^\circ$ , Cu3 =  $27.13(7)^\circ$ . The Cu1 and Cu3-centered complexes have geometries closer to trigonal prismatic, while the Cu2-centered complex has a much larger twist angle, indicating it is closer to octahedral. Despite the observed differences, these values are within reasonable ranges for transition metal ion complexes of tris-substituted tacn derivatives. Twist angles of octahedral and trigonal prismatic are  $60^\circ$  and  $0^\circ$ , respectively – most reported complexes contain intermediate geometries in the range  $25^\circ - 50^\circ$ .<sup>5,41</sup> For the  $[\text{Cu}(\text{L}^1)]^{2+}$  complexes, the large differences between the twist angles in the three independent cations may result from crystal packing and/or weak secondary bonding interactions in the lattice.

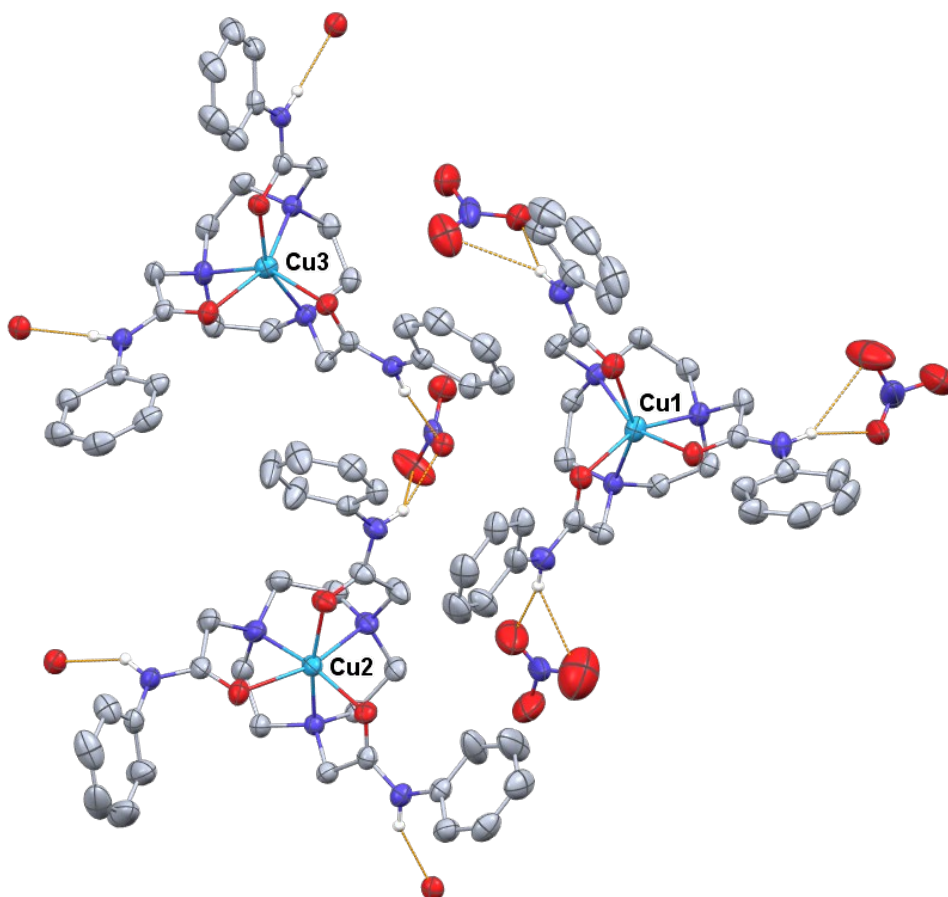
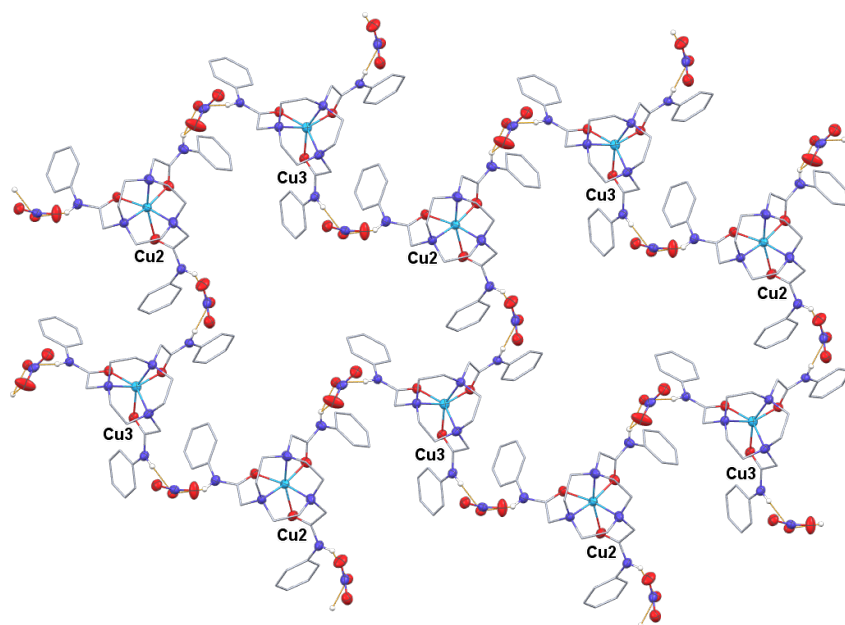


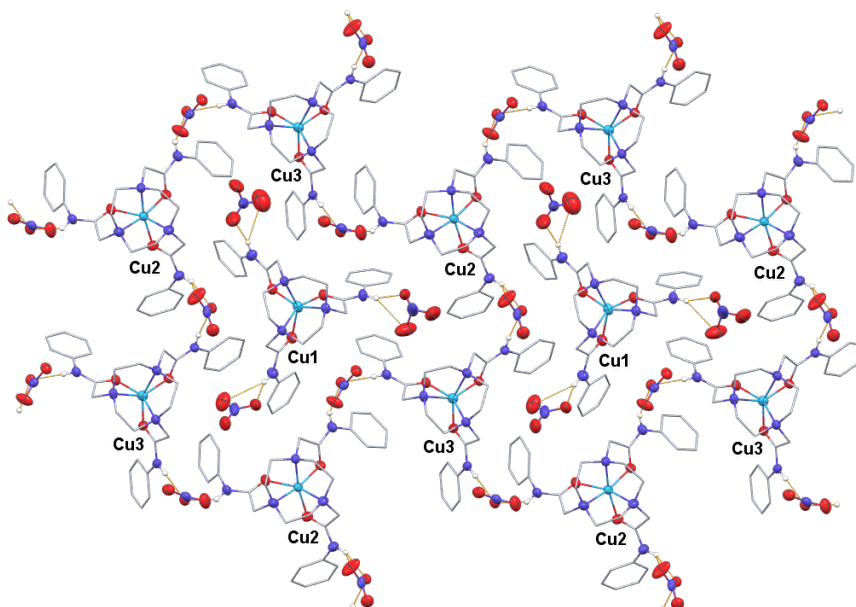
Figure 3.20 – View of the structure of  $[\text{Cu}(\text{L}^1)][\text{NO}_3]_2 \cdot 1.25\text{Et}_2\text{O} \cdot \text{MeOH}$  (note that there are three crystallographically independent cations and six nitrate anions in the asymmetric unit) showing the H-bonding between nitrate anions and amide N-H groups. The copper cations are labelled (Cu1, Cu2 and Cu3); nitrogen = dark blue; oxygen = red; carbon = grey. Ellipsoids are drawn at the 50% probability level and H and solvent atoms (except those involved in H-bonding) are omitted for clarity.

For octahedral  $d^9$   $\text{Cu}^{2+}$  complexes, Jahn-Teller distortion is expected. For the distorted octahedral  $[\text{Cu}(\text{L}^1)]^{2+}$  cation containing Cu2, this distortion is evidenced through tetragonal elongation along the N8-Cu-O6 axis. As expected, this is much less obvious for the distorted trigonal prismatic  $[\text{Cu}(\text{L}^1)]^{2+}$  complexes containing Cu1 and Cu3, with minimal differences between the Cu-N and Cu-O bond distances ( $\sim 0.05\text{--}0.08$  Å). These findings align with the literature on similar divalent  $\text{Cu}^{2+}$  complexes involving tacn-derived ligands – for example, the  $[\text{Cu}(\text{NOTA})]^-$  complex reported by Hermann and co-workers<sup>42</sup> was isolated in both *pseudo*-octahedral and distorted trigonal-prismatic geometries.

The extended structure of the  $[\text{Cu}(\text{L}^1)][\text{NO}_3]_2$  complex shows that the complexes containing Cu2 and Cu3 form a two-dimensional sheet (Figure 3.21a) with a nitrate ion bridging two alternating Cu2 and Cu3 molecules. The Cu1 molecule sits within the cavity (Figure 3.21b), with its three amide(NH) groups engaged in hydrogen-bonding to nitrate anions, with no further intermolecular bonding between other complexes.



(a)



(b)

Figure 3.21 – (a) View showing the extended hydrogen-bonded network of  $[\text{Cu}(\text{L}^1)](\text{NO}_3)_2$ , which forms a 2D sheet. A nitrate anion bridges alternating Cu2 and Cu3 molecules; (b) The Cu1 molecule sits within the cavity but is only engaged in hydrogen-bonding to nitrate anions. Atom colours: light blue, Cu; red, O; dark blue, N; white, H.

The  $\text{L}^2$  ligand, like  $\text{L}^1$ , also provides an  $\text{N}_3\text{O}_3$  donor set to a central  $\text{Cu}^{2+}$  ion *via* coordination of the tacn amine functions and the amide carboxamide pendant arm groups (Figure 3.22). The larger chelate bite angle of  $\text{L}^2$  more readily accommodates octahedral arrangement compared to  $\text{L}^1$ , with a twist angle,  $\theta$ , measured at  $56.12(2)^\circ$ . As a result, the bond distances for the  $[\text{Cu}(\text{L}^2)]^{2+}$  cation indicate significant Jahn-Teller distortion. Along the N1-Cu-O2 axis, the Cu-N1 bond is

longer than the other two Cu-N bonds by  $\sim 0.25$  Å, while the Cu-O2 distance shows even greater lengthening, by  $\sim 0.4$  Å, compared to the other Cu-O distances. This is consistent with a tetragonal elongation, and the increased flexibility provided by the six-membered chelate ring involving O2.

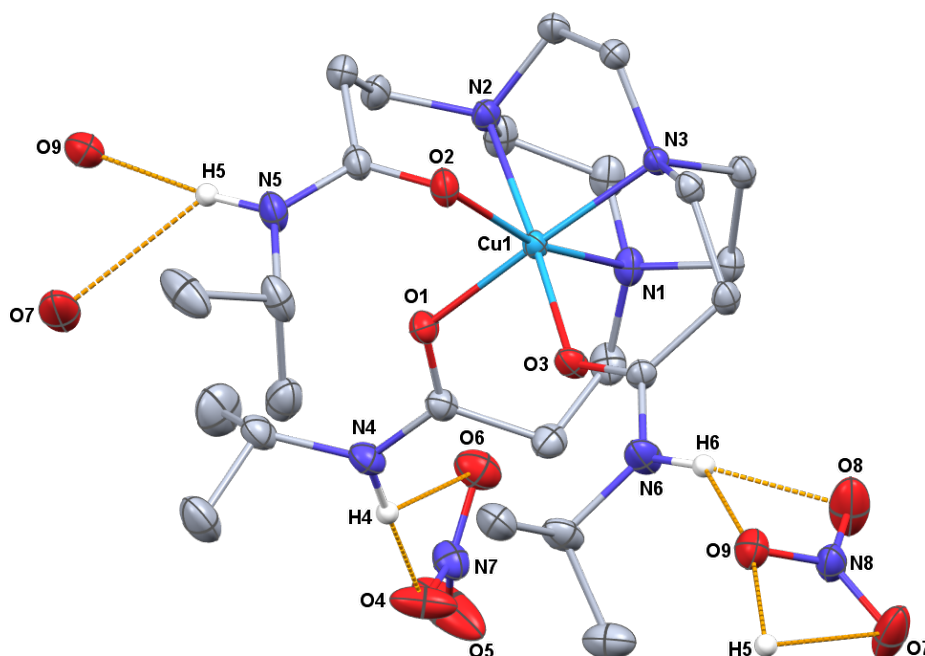


Figure 3.22 – View of the structure of  $[\text{Cu}(\text{L}^2)]^{2+}$  showing the atom numbering scheme and the H-bonding between nitrate anions and each of the amide NH groups. Ellipsoids are drawn at the 50% probability level and H atoms (except those involved in H-bonding) are omitted for clarity.

Much like the analogous nickel complex, the extended hydrogen-bonded network of  $[\text{Cu}(\text{L}^2)][\text{NO}_3]_2$  shows the complex forms infinite one-dimensional chains (Figure 3.23), with one bridging nitrate anion between two molecules. The other amide-NH group is bound to the second nitrate counter-ion, which is not engaged in further intermolecular bonding.

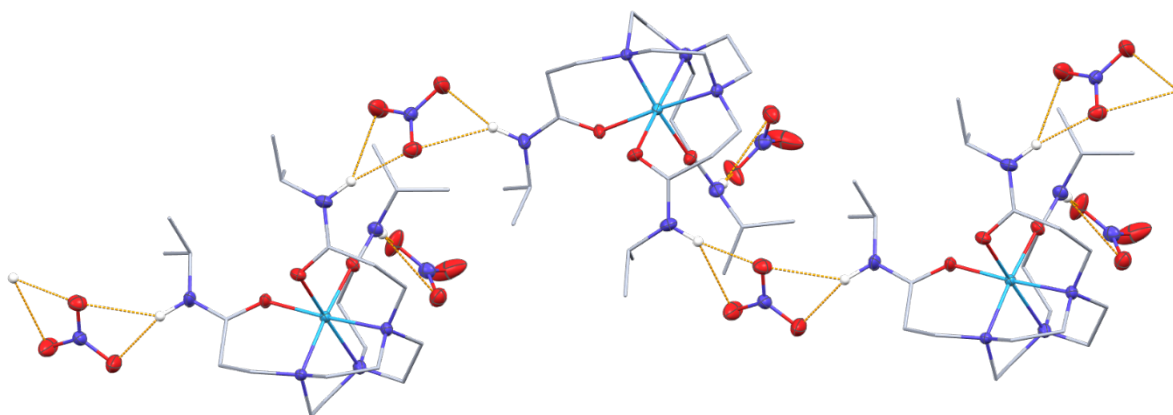
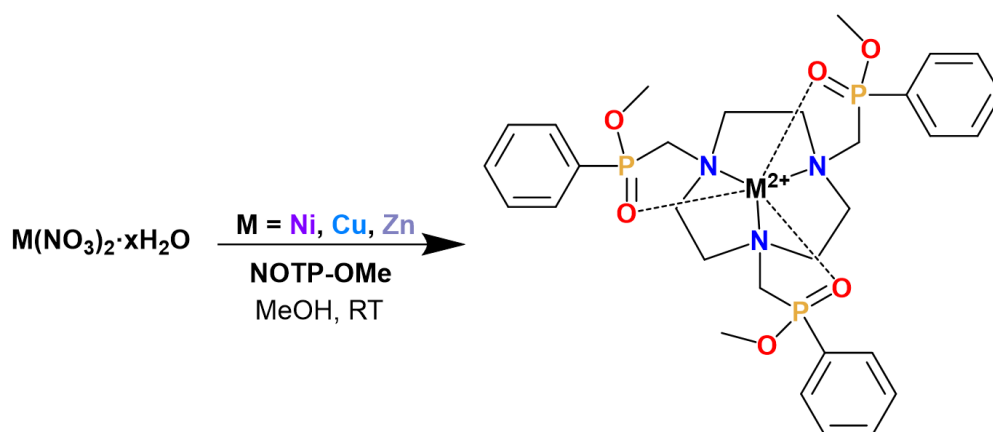


Figure 3.23 – View showing the extended hydrogen-bonded network of  $[\text{Cu}(\text{L}^2)][\text{NO}_3]_2$ , which forms an infinite 1D chain with one bridging nitrate anion between two molecules. Atom colours: light blue, Cu; red, O; dark blue, N; white, H.

### 3.2.2 Attempted Formation of Divalent Transition Metal Complexes of NOTP-OMe

This section presents preliminary methods towards, and (partial) characterisation of, transition metal ( $\text{Ni}^{2+}$ ,  $\text{Cu}^{2+}$ ) and  $\text{Zn}^{2+}$  complexes of NOTP-OMe. It is anticipated that, like the carboxamide  $\text{C}=\text{O}$  group of  $\text{L}^1$  and  $\text{L}^2$ , the  $\text{P}=\text{O}$  bond within the pendant arm of the NOTP-OMe ligand will coordinate preferentially to the metal centre (rather than the oxygen of the -OMe ester group). However, in this work, only IR will be able to suggest the coordination mode, as no crystal structures were obtained in the time-frame of the project.

Attempted formation of the complexes followed the direct addition of the relevant metal nitrate precursor ( $\text{M}(\text{NO}_3)_2 \cdot x\text{H}_2\text{O}$ ,  $\text{M} = \text{Ni}$ ,  $\text{Cu}$  and  $\text{Zn}$ ) to the ligand, in methanol (Scheme 3.3). The solutions were left to stir at room temperature overnight ( $\text{Ni}$ ,  $\text{Cu}$ ) or under an inert  $\text{N}_2$  atmosphere for two hours ( $\text{Zn}$ ).



*Scheme 3.3 – Suggested pathway and structure of divalent transition metal complexes of NOTP-OMe (Ni, Cu, Zn).*

To the zinc reaction mixture, two molar equivalents of  $\text{NaBPh}_4$  were added to the solution, with the aim to precipitate the target  $[\text{Zn}(\text{NOTP-OMe})][\text{BPh}_4]_2$  salt. It was assumed that the more sterically bulky counter-ions ( $\text{BPh}_4$  vs.  $\text{NO}_3$ ) would increase the likelihood of growing suitable crystals for SCXRD. The products from the reactions of nickel and copper with the ligand were isolated as hygroscopic green powder solids in good yield (88%).  $^1\text{H}$ ,  $^{31}\text{P}$  NMR analysis was only obtained for the product isolated from reaction of NOTP-OMe with diamagnetic  $\text{Zn}^{2+}$ . Otherwise, characterisation was achieved using IR, ESI $^+$  MS and UV-Vis. Elemental analysis was obtained for the  $[\text{Ni}(\text{NOTP-OMe})][\text{NO}_3]_2$  complex with 7.5  $\text{H}_2\text{O}$  molecules; although solvated water is reasonable (given the hygroscopic nature of the complex and the hexahydrate nickel(II) nitrate starting material), this is much more solvent than is typically expected for similar metal complexes, including those of  $\text{L}^1$  and  $\text{L}^2$  above. Therefore, it may not be an accurate reflection of the state of the bulk material. However, the IR spectrum (Figure 3.24) depicts a large, broad peak

around  $3300\text{ cm}^{-1}$  relating to an O-H stretch, which confirms water is present in the isolated product.

Figure 3.24 shows the IR spectra obtained for the ligand (obtained as a film) and the three transition metal complexes (obtained as Nujol mull) thereof. The band at  $1203\text{ cm}^{-1}$  in the uncoordinated ligand is assigned as the P=O stretch. Upon coordination of the ligand to the metal centres (Ni, Cu and Zn), this band appears to shift to lower frequency ( $1181$ ,  $1158$  and  $1153\text{ cm}^{-1}$ , respectively), which is consistent with coordination of the P=O function to the metal centre. As well as the NOTP-OMe ligand, the nickel and copper complexes show a significant broad band around  $3400 - 3300\text{ cm}^{-1}$  (O-H stretch) alongside a band around  $1650\text{ cm}^{-1}$  (H-O-H bend), which indicates the presence of water. The nickel and copper complexes were isolated as nitrate salts – the anions of which often form intermolecular hydrogen bonds to solvent and water molecules. However, the zinc complex was instead isolated as a tetraphenylborate salt, which is much less likely to form hydrogen-bonded interactions – this is reflected in the absence of a peak above  $3000\text{ cm}^{-1}$ .

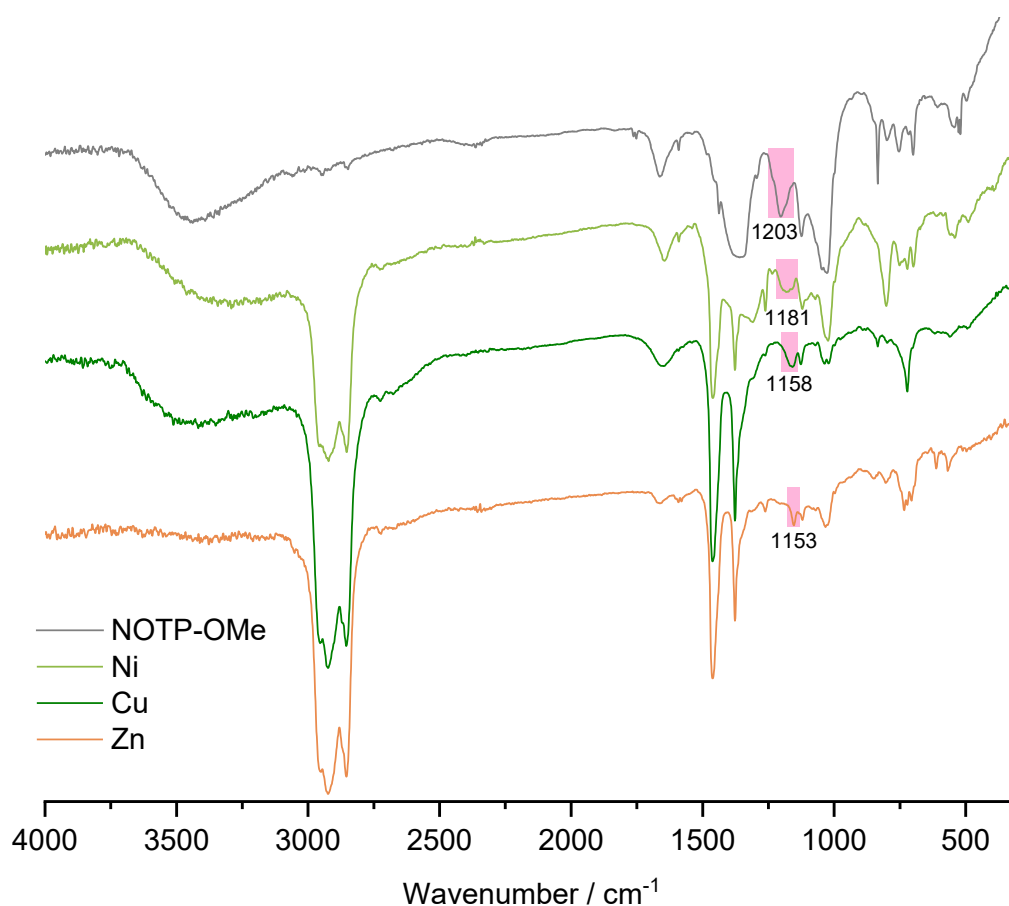


Figure 3.24 – IR spectra obtained for NOTP-OMe (as a film) and the Ni, Cu and Zn complexes (Nujol mull) thereof. The band assigned as the P=O stretch is highlighted in pink and labelled accordingly.

The UV-Vis spectrum for  $[\text{Ni}(\text{NOTP-OMe})][\text{NO}_3]_2$  shows three spin-allowed transitions (as expected for octahedral  $d^8$  complexes), which can be assigned as the following:  ${}^3\text{T}_{2g}(\text{F}) \leftarrow {}^3\text{A}_{2g}$  (994 nm,  $10100\text{ cm}^{-1}$ ),  ${}^3\text{T}_{1g}(\text{F}) \leftarrow {}^3\text{A}_{2g}$  (599 nm,  $16700\text{ cm}^{-1}$ ),  ${}^3\text{T}_{1g}(\text{P}) \leftarrow {}^3\text{A}_{2g}$  (505 nm,  $19800\text{ cm}^{-1}$ ). Weaker features are observed at 696 nm ( $14400\text{ cm}^{-1}$ ) and 801 nm ( $12500\text{ cm}^{-1}$ ). As mentioned above, the spin-forbidden transitions,  ${}^1\text{E}_g \leftarrow {}^3\text{A}_{2g}$  and  ${}^1\text{T}_{2g} \leftarrow {}^3\text{A}_{2g}$  are often observed in  $\text{Ni}^{2+}$  absorbance spectra.<sup>35</sup> However, like the amide-tacn complexes, these complexes are expected to have  $\text{C}_{3v}$  symmetry; the additional bands may arise due to the lower symmetry. The UV-Vis spectrum obtained for the  $[\text{Cu}(\text{NOTP-OMe})][\text{NO}_3]_2$  complex is akin to the  $[\text{Cu}(\text{L}^1)][\text{NO}_3]_2$  and  $[\text{Cu}(\text{L}^2)][\text{NO}_3]_2$  complexes, and depicts a single, poorly resolved broad absorption band at 764 nm ( $13100\text{ cm}^{-1}$ ) – as expected for Jahn-Teller distorted  $d^9$  complexes.

The  ${}^{31}\text{P}\{^1\text{H}\}$  spectrum for the  $[\text{Zn}(\text{NOTP-OMe})][\text{BPh}_4]_2$  complex is given in Figure 3.25. It is known from previous work with similar complexes of phosphinate-functionalised tacn ligands that multiple isomers are possible, upon coordination of the ligand. These derive from a stereogenic phosphorous centre, and clockwise/anti-clockwise pendant arm and tacn-ring rotations. The below spectrum indicates the presence of multiple isomers, with four resonances which are shifted to significantly higher frequency from the broad resonance observed in the uncoordinated ligand (40.7 ppm). However, it is not possible to definitively assign a particular isomer to an individual shift in the  ${}^{31}\text{P}\{^1\text{H}\}$  NMR spectrum – especially without any SCXRD data which would help elucidate possible isomeric conformations.

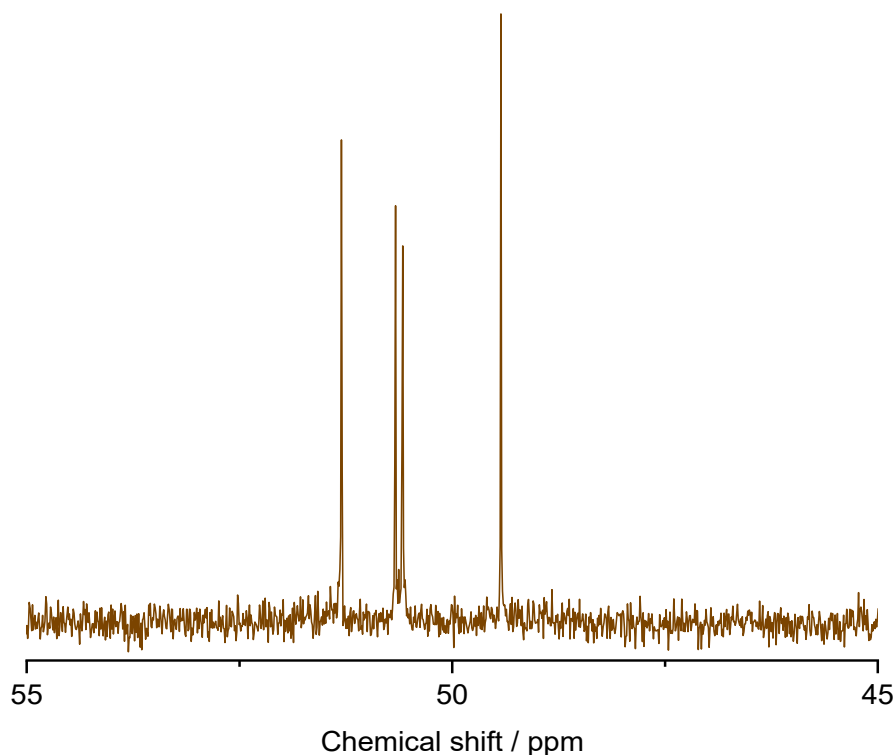


Figure 3.25 –  $^{31}\text{P}\{^1\text{H}\}$  spectrum of  $[\text{Zn}(\text{NOTP-OMe})][\text{BPh}_4]_2$  ( $\text{CD}_3\text{CN}$ ).

The  $^1\text{H}$  NMR spectrum – as expected for a species with multiple isomeric forms – is very complicated. Many of the peaks overlap, so accurate integration is not possible. However, the spectrum clearly shows four doublets (between 3.89 – 3.70 ppm), with coupling constants of around 10.5 Hz ( $^3J_{31\text{P}-1\text{H}}$ ). Based on the ligand shifts and coupling constants reported in Chapter 2 and the original literature, these can be assigned as the  $\text{CH}_3$  protons of the ester group.<sup>31</sup> This also coincides with the four isomers observed in the  $^{31}\text{P}\{^1\text{H}\}$  NMR spectrum. The  $\text{CH}_2$  protons of the methyl linker are also split by the  $^{31}\text{P}$  nucleus; combined with multiple isomers, this region appears as a broad series of individual peaks between 3.69 – 3.32 ppm. Hence, a value for the  $^2J_{1\text{H}-31\text{P}}$  coupling interactions cannot be deduced. Both the tacn- $\text{CH}_2$  protons and the aromatic protons of the P-Ph group resonate as broad multiplets. The  $[\text{BPh}_4]^-$  aromatic protons are much more defined in comparison to the complex, with three multiplets observed at 7.30 – 7.24, 7.02 – 6.97, and 6.86 – 6.82 ppm.

### 3.3 Conclusions

This chapter has demonstrated the successful formation of a series of divalent  $\text{Ni}^{2+}$ ,  $\text{Cu}^{2+}$  and  $\text{Zn}^{2+}$  complexes of the tris(amide) ligands,  $\text{L}^1$  and  $\text{L}^2$ . For most complexes, the solid-state analysis (elemental analysis, IR spectroscopy) was consistent with the bulk product consisting of the solvated  $[\text{M}(\text{L}^n)]^{2+}$  species, which can be attributed to the hydrogen-bonding properties of the amide pendant arms. Solution UV-Vis data for the  $\text{Ni}^{2+}$  complexes was in good agreement with



the previously reported tris(amide)  $[\text{Ni}(\text{TCMT})]^{2+}$  complex, and the copper complexes were also consistent with Jahn-Teller distorted  $d^9$  complexes.

Molecular structures for the  $\text{Ni}^{2+}$  and  $\text{Cu}^{2+}$  complexes depicted distorted trigonal prismatic or octahedral coordination *via* an  $\text{N}_3\text{O}_3$  donor set. The complexes of  $\text{L}^1$  tend to have slightly smaller twist angles than those of  $\text{L}^2$ , indicative of a larger trigonal prismatic distortion due to the smaller five-membered chelate ring. In contrast, the more flexible  $\text{L}^2$  ligand (with a six-membered chelate ring) tends towards distorted octahedral geometries. This also meant Jahn-Teller distortion is much more apparent in the  $[\text{Cu}(\text{L}^2)]^{2+}$  complex in comparison to  $[\text{Cu}(\text{L}^1)]^{2+}$ . The crystal structure of the latter shows three crystallographically independent cations ( $\text{Cu1}$ ,  $\text{Cu2}$  and  $\text{Cu3}$ ), with  $\text{Cu2}$  adopting a *pseudo*-octahedral geometry with distortion along the  $\text{N8-Cu-O6}$  axis. The  $\text{Cu2}$  and  $\text{Cu3}$  anions form a two-dimensional hydrogen-bonded network *via* bridging nitrate cations. This forms a cavity in which the  $\text{Cu1}$  anion is situated. The  $\text{Cu1}$  molecule is only involved in hydrogen bonding to nitrate anions, and no other intermolecular interactions are observed. The structures of  $[\text{Ni}(\text{L}^1)][\text{NO}_3]_2$ ,  $[\text{Ni}(\text{L}^2)][\text{NO}_3]_2$  and  $[\text{Cu}(\text{L}^2)][\text{NO}_3]_2$  also show secondary H-bonding from the amide N-H groups to nitrate anions, leading to extended one-dimensional networks.

The susceptibility of  $\text{Co}^{2+}$  to undergo ready oxidation to  $\text{Co}^{3+}$  was evidenced by the reaction of  $\text{Co}(\text{NO}_3)_2 \cdot 6\text{H}_2\text{O}$  with  $\text{L}^1$  in  $\text{MeOH}$ , which led to the isolation of the  $\text{Co}^{3+}$  complex,  $[\text{Co}(\text{L}^1\text{-H})][\text{NO}_3]_2$ . SCXRD analysis showed deprotonation of one of the pendant arm amide(N) functions and an  $\text{N}_4\text{O}_2$  donor set. This was also supported by  $\text{ESI}^+$  MS, although the UV-Vis data in this case was not sensitive to either  $\text{Co}^{2+}$  or  $\text{Co}^{3+}$  oxidation states. The characterisation data obtained for the cobalt complex of  $\text{L}^2$  was slightly more ambiguous, and although IR,  $\text{ESI}^+$  MS, elemental analysis and UV-Vis all indicated towards complex formation, the oxidation state of the metal remains unclear. The  $\text{Co}^{3+}$  ion was directly observed *via* SCXRD analysis, although the crystals were grown after several weeks in non-anhydrous methanol, and the data was of lower quality. It is possible that both  $\text{Co}^{2+}$  and  $\text{Co}^{3+}$  complexes were isolated.

Although not included in the discussion, it is noteworthy to mention that attempts to form the  $[\text{Fe}(\text{L}^1)][\text{OTf}]_2$  complex were unsuccessful.  $\text{ESI}^+$  MS of the isolated product indicated the target complex was formed, however, colourless weakly diffracting crystals (grown from the slow evaporation of the product in methanol) were shown to be the known  $[\text{Fe}(\text{NOTA})]$  complex. This is similar to the behaviour observed with  $\text{Fe}^{2+}$  and TCMT reported by Weyhermüller *et al.*<sup>14</sup>, in which the amide pendant arms of the ligand were found to hydrolyse to the corresponding carboxylate, coinciding with oxidation of the central  $\text{Fe}^{2+}$  ion to  $\text{Fe}^{3+}$ . Bulk analysis of the product

was indicative of multiple species. The behaviour of  $L^1$  with more highly Lewis acidic  $M^{3+}$  cations will be explored further in Chapter 6 of this work.

This chapter also described preliminary work on the attempted formation of the divalent Ni, Cu and Zn metal complexes of NOTP-OMe. In this case, despite several attempts, no single crystals were obtained, and satisfactory elemental analysis could not be obtained. However, IR data indicated a lower-frequency shift in the pendant arm P=O function, supporting complex formation *via* coordination of the tacn(N) and P=O groups. UV-Vis (Ni, Cu) and ESI<sup>+</sup> MS (Ni, Cu, Zn) also indicated that the target divalent  $M^{2+}$  species were isolated. For zinc,  $^{31}\text{P}\{^1\text{H}\}$  and  $^1\text{H}$  NMR spectra suggested the formation of four different  $[\text{Zn}(\text{NOTP-OMe})][\text{BPh}_4]_2$  isomers. However, further work is clearly necessary in future to confirm the identity of the products from these reactions. Inert conditions and anhydrous precursors (such as  $\text{M}(\text{OTf})_2$ ) may be better suited to the NOTP-OMe ligand, to prevent hydrolysis of the pendant arm function.

The following chapter will look at the formation of  $\text{MF}_3$  coordination complexes of the ligands  $L^1$  and  $L^2$ , as well as the mono-amide derivative,  $L^3$  ( $M = \text{Al, Ga, In, Fe}$ ). This chapter has demonstrated the propensity of the amide functions to form intermolecular hydrogen-bonded interactions, which will be explored further.

## 3.4 Experimental

For general experimental methods, see Appendix A. The ligands  $L^1$ ,  $L^2$  and NOTP-OMe were used as prepared in Chapter 2.  $\text{Co}(\text{NO}_3)_2 \cdot 6\text{H}_2\text{O}$ ,  $\text{Ni}(\text{NO}_3)_2 \cdot 6\text{H}_2\text{O}$  (BDH Laboratories),  $\text{Cu}(\text{NO}_3)_2 \cdot 3\text{H}_2\text{O}$ ,  $\text{Zn}(\text{NO}_3)_2 \cdot 6\text{H}_2\text{O}$  (Alfa Aesar),  $\text{Fe}(\text{OTf})_2$ , and  $\text{NaBPh}_4$  (Sigma-Aldrich) used as supplied. All solvents used were of HPLC-chromatography grade.

### 3.4.1 Tris-1,4,7-Phenylacetamide-1,4,7-Triazacyclononane ( $L^1$ ) Complexes

#### 3.4.1.1 $[\text{Co}(L^1)][\text{NO}_3]_2$

Under inert conditions,  $L^1$  (30.0 mg, 0.057 mmol) and  $\text{Co}(\text{NO}_3)_2 \cdot 6\text{H}_2\text{O}$  (16.5 mg, 0.057 mmol) were dissolved in anhydrous MeOH. The pink solution was left to stir overnight. The solvent volume was then decreased *in vacuo* to approx. 1 mL, and excess an.  $\text{Et}_2\text{O}$  was added, causing precipitation of a pink solid. The solid was filtered and dried *in vacuo*. Yield: 29.0 mg, 0.041 mmol (72%). Crystals suitable for single crystal X-ray analysis were grown *via* the vapour diffusion of  $\text{Et}_2\text{O}$  into a methanol solution containing the product. ESI<sup>+</sup> MS ( $\text{CH}_3\text{OH}$ ): found:  $m/z = 293.7$   $[\text{Co}(L^1\text{-H})]^{2+}$  (calculated for  $[\text{Co}(L^1\text{-H})]^{2+}$ :  $m/z = 293.1$ ). UV-VIS ( $4.1 \times 10^{-3} \text{ mol dm}^{-3}/\text{MeOH}$ ):  $\tilde{\nu} \text{ cm}^{-1}$  ( $\epsilon \text{ mol}^{-1} \text{ dm}^3 \text{ cm}^{-1}$ ) = 19200 (46). IR (Nujol,  $\nu / \text{cm}^{-1}$ ): 3293 ww, 3272 w (NH), 1626 m, 1595 m (C=O).

#### 3.4.1.2 [Ni(L<sup>1</sup>)]/[NO<sub>3</sub>]<sub>2</sub>

A solution of Ni(NO<sub>3</sub>)<sub>2</sub>·6H<sub>2</sub>O (27.5 mg, 0.095 mmol) in MeOH (5 mL) was added to a solution of L<sup>1</sup> (50 mg, 0.095 mmol) in MeOH (5 mL). The solution was left to stir overnight, over which time it had turned from green to purple. The solvent volume was reduced *in vacuo* and excess Et<sub>2</sub>O was added, causing precipitation of a purple solid. The solid was isolated *via* filtration and dried *in vacuo*. Yield: 54.0 mg, 0.083 mmol (87%). Crystals suitable for X-Ray diffraction were grown *via* the vapour diffusion of Et<sub>2</sub>O into a methanol solution containing the product. Analysis required for C<sub>30</sub>H<sub>36</sub>NiN<sub>8</sub>O<sub>9</sub>·0.25Et<sub>2</sub>O·0.5H<sub>2</sub>O: C, 50.74; H, 5.59; N, 14.79. Found: C, 51.09; H, 5.34; N, 14.46%. ESI<sup>+</sup> MS (CH<sub>3</sub>OH): found: *m/z* = 293.3 [Ni(L<sup>1</sup>)]<sup>2+</sup> (calculated for [Ni(L<sup>1</sup>)]<sup>2+</sup>: *m/z* = 293.1). UV-VIS (6.7×10<sup>-3</sup> mol dm<sup>-3</sup>/MeOH):  $\tilde{\nu}$  cm<sup>-1</sup> ( $\epsilon$  mol<sup>-1</sup> dm<sup>3</sup> cm<sup>-1</sup>) = 28200 (46), 17800 (30), 12500 (34), 10700 (54). IR (Nujol,  $\nu$  / cm<sup>-1</sup>): 3444 br, 3266 br (OH), 3198 m, 3145 m (NH), 1686 m (HOH), 1622 s, 1596 s (C=O).

#### 3.4.1.3 [Cu(L<sup>1</sup>)]/[NO<sub>3</sub>]<sub>2</sub>

A solution of Cu(NO<sub>3</sub>)<sub>2</sub>·3H<sub>2</sub>O (46.0 mg, 0.190 mmol) in MeOH (5 mL) was added to a solution of L<sup>1</sup> (100 mg, 0.190 mmol) in MeOH (5 mL). This was left to stir for 3 h. The solvent volume was reduced *in vacuo* and excess Et<sub>2</sub>O was added, causing precipitation of a blue solid. The solid was isolated *via* filtration and dried *in vacuo*. Yield: 101 mg, 0.141 mmol (74%). Crystals suitable for X-ray analysis were grown *via* the vapour diffusion of Et<sub>2</sub>O into a methanol solution containing the product. Analysis required for C<sub>30</sub>H<sub>36</sub>CuN<sub>8</sub>O<sub>9</sub>·1.5H<sub>2</sub>O: C, 48.48; H, 5.29; N, 15.08. Found: C, 48.88; H, 5.49; N, 14.71%. ESI<sup>+</sup> MS (CH<sub>3</sub>OH): found: *m/z* = 295.8 [Cu(L<sup>1</sup>)]<sup>2+</sup> (calculated for [Cu(L<sup>1</sup>)]<sup>2+</sup>: *m/z* = 295.6). UV-VIS (2.8 × 10<sup>-3</sup> mol dm<sup>-3</sup>/MeOH):  $\tilde{\nu}$  cm<sup>-1</sup> ( $\epsilon$ /mol<sup>-1</sup> dm<sup>3</sup> cm<sup>-1</sup>) = 13600 (95). IR (Nujol,  $\nu$  / cm<sup>-1</sup>): 3429 br, 3267 br (OH), 3207 w, 3143 w (NH), 1652 sh (HOH), 1621 s, 1594 s (C=O).

#### 3.4.1.4 [Zn(L<sup>1</sup>)]/[NO<sub>3</sub>]<sub>2</sub>

A solution of Zn(NO<sub>3</sub>)<sub>2</sub>·6H<sub>2</sub>O (56.9 mg, 0.191 mmol) in MeOH (5 mL) was added to a solution of L<sup>1</sup> (100 mg, 0.191 mmol) in MeOH (5 mL). This was left to stir overnight. The solvent volume was reduced *in vacuo* to approx. 2 mL, and excess Et<sub>2</sub>O was added, causing precipitation of a white solid. The solid was isolated *via* filtration and dried *in vacuo*. Yield: 95.9 mg, 0.134 mmol (70%). Analysis required for C<sub>30</sub>H<sub>36</sub>ZnN<sub>8</sub>O<sub>9</sub>·1.5H<sub>2</sub>O: C, 48.36; H, 5.28; N, 15.04. Found: C, 48.19; H, 5.54; N, 14.50%. <sup>1</sup>H NMR (295 K, CD<sub>3</sub>OD):  $\delta$  (ppm) = 7.66 – 7.63 (m, [6H], ArH), 7.41 – 7.37 (m, [6H], ArH), 7.26 – 7.22 (m, [3H], ArH), 4.85 (H<sub>2</sub>O), 4.04 (s, [6H], CH<sub>2</sub>), 3.21 – 3.13 (m, [6H], tacn-CH<sub>2</sub>), 3.01 – 2.93 (m, [6H], tacn-CH<sub>2</sub>). <sup>13</sup>C{<sup>1</sup>H} NMR (295 K, CD<sub>3</sub>OD):  $\delta$  (ppm) = 173.6 (C=O), 137.8 (ArC), 130.4 (ArC), 127.5 (ArC), 122.5 (ArC), 59.9 (CH<sub>2</sub>), 52.2 (tacn-CH<sub>2</sub>). ESI<sup>+</sup> MS (CH<sub>3</sub>OH): found: *m/z*

= 296.4  $[\text{Zn}(\text{L}^1)]^{2+}$  (calculated for  $[\text{Zn}(\text{L}^1)]^{2+}$ :  $m/z$  = 296.1). IR (Nujol,  $\nu$  /  $\text{cm}^{-1}$ ): 3450 br, 3278 br (OH), 3214 w, 3154 w (NH), 1696 sh (HOH), 1626 s, 1596 s (C=O).

#### 3.4.1.5 Attempted synthesis of $[\text{Fe}(\text{L}^1)][\text{OTf}]_2$

Under inert conditions,  $\text{Fe}(\text{OTf})_2$  (26.5 mg, 0.075 mmol) was added to a solution of  $\text{L}^1$  (39.6 mg, 0.075 mmol) in an. MeOH (5 mL). The solution was initially colourless, and turned pale yellow after ca. 15 min. This was left to stir at room temperature for 2 h, at which point the solution was a much darker yellow/orange colour. The solvent was removed *in vacuo* leaving a brown-purple solid. ESI<sup>+</sup> MS ( $\text{CH}_3\text{OH}$ ): found:  $m/z$  = 291.9  $[\text{Fe}(\text{L}^1)]^{2+}$  (calculated for  $[\text{Fe}(\text{L}^1)]^{2+}$ :  $m/z$  = 292.1). Colourless crystals grown from the slow evaporation of a methanol solution containing the product mixture were shown to be the hydrolysed species,  $[\text{Fe}(\text{NOTA})]$ .

### 3.4.2 Tris-1,4,7-Isopropylacrylamide-1,4,7-Triazacyclononane ( $\text{L}^2$ ) Complexes

#### 3.4.2.1 $[\text{Co}(\text{L}^2)][\text{NO}_3]_2$

Under inert conditions,  $\text{L}^2$  (33.4 mg, 0.071 mmol) and  $\text{Co}(\text{NO}_3)_2 \cdot 6\text{H}_2\text{O}$  (20.7 mg, 0.071 mmol) were dissolved in an. MeOH. The dark pink solution was left to stir overnight. The solvent volume was then decreased *in vacuo* to approx. 1 mL, and excess an.  $\text{Et}_2\text{O}$  was added, causing the precipitation of a red-pink solid. The solid was filtered and dried *in vacuo*. Yield: 36.6 mg, 0.056 mmol (79%). Analysis required for  $\text{C}_{24}\text{H}_{42}\text{CoN}_9\text{O}_{12} \cdot 0.5\text{Et}_2\text{O}$ : C, 41.60; H, 7.12; N, 16.79. Found: C, 41.84; H, 7.08; N, 16.80%. ESI<sup>+</sup> MS ( $\text{CH}_3\text{OH}$ ): found:  $m/z$  = 263.7  $[\text{Co}(\text{L}^2)]^{2+}$  (calculated for  $[\text{Co}(\text{L}^2)]^{2+}$ :  $m/z$  = 263.7). UV VIS ( $4.5 \times 10^{-3}$  mol  $\text{dm}^{-3}$  / MeOH):  $\tilde{\nu}$   $\text{cm}^{-1}$  ( $\epsilon$  /  $\text{mol}^{-1} \text{dm}^3 \text{cm}^{-1}$ ) = 20300 (37), 18700 (27), 9420 (22). IR (Nujol,  $\nu$  /  $\text{cm}^{-1}$ ): 3400 br (OH), 3250 br (OH), 3100 br (NH), 1602 s (HOH), 1610 s, 1574 s (C=O). Crystals suitable for X-ray diffraction were grown from vapour diffusion of  $\text{Et}_2\text{O}$  into a methanol solution containing the product, over a period of several weeks. These were shown to be the oxidised  $[\text{Co}(\text{L}^2)][\text{NO}_3]_3$  complex. ESI<sup>+</sup> MS (crystals) ( $\text{CH}_3\text{OH}$ ): found:  $m/z$  = 263.8  $[\text{Co}(\text{L}^2)]^{2+}$  (calculated for  $[\text{Co}(\text{L}^2)]^{2+}$ :  $m/z$  = 263.7); 176.0  $[\text{Co}(\text{L}^2)]^{3+}$  (calculated for  $[\text{Co}(\text{L}^2)]^{3+}$ :  $m/z$  = 175.8).

#### 3.4.2.2 $[\text{Ni}(\text{L}^2)][\text{NO}_3]_2$

A solution of  $\text{Ni}(\text{NO}_3)_2 \cdot 6\text{H}_2\text{O}$  [15.5 mg, 0.053 mmol] in MeOH (5 mL) was added to a solution of  $\text{L}^2$  (25.0 mg, 0.053 mmol) in MeOH (5 mL). This was left to stir for two hours, and the solution changed colour from pale green to pale purple. The solvent volume was reduced *in vacuo* and excess  $\text{Et}_2\text{O}$  was added, causing precipitation of a hygroscopic purple solid. The solid was isolated *via* filtration and dried *in vacuo*. Yield: 27.1 mg, 0.043 mmol (81%). Crystals suitable for X-ray diffraction were grown *via* the vapour diffusion of  $\text{Et}_2\text{O}$  into a methanol solution containing

the product. Analysis required for  $C_{24}H_{42}NiN_8O_9 \cdot 2.5H_2O$ : C, 41.39; H, 7.67; N, 16.09. Found: C, 41.51; H, 7.52 N, 16.42%. ESI<sup>+</sup> MS ( $CH_3OH$ ): found:  $m/z = 263.3$  [ $Ni(L^2)$ ]<sup>2+</sup> (calculated for  $Ni(L^2)$ ]<sup>2+</sup>:  $m/z = 263.2$ ). UV-VIS ( $3.6 \times 10^{-3}$  mol  $dm^{-3}$ /MeOH):  $\tilde{\nu}$   $cm^{-1}$  ( $\epsilon$  mol<sup>-1</sup>  $dm^3$   $cm^{-1}$ ) = 28200 (43), 17600 (22), 12700 (30), 10800 (62). IR (Nujol,  $\nu$  /  $cm^{-1}$ ): 3300 v br (OH) 3100 v br (NH), 1640 s (HOH), 1610 s, 1564 s (C=O).

#### 3.4.2.3 $[Cu(L^2)][NO_3]_2$

A solution of  $Cu(NO_3)_2 \cdot 3H_2O$  [28.7 mg, 0.0119 mmol] in MeOH (5 mL) was added to a solution of  $L^2$  [55.7 mg, 0.119 mmol] in MeOH (5 mL). The blue-coloured solution was left to stir overnight. The solvent volume was reduced *in vacuo* and excess  $Et_2O$  was added, causing precipitation of a dark blue solid. The solid was isolated *via* filtration and dried *in vacuo*. Yield: 58.5 mg, 0.089 mmol (75%). Crystals suitable for X-Ray diffraction were grown *via* the slow evaporation of  $Et_2O$ /MeOH. ESI<sup>+</sup> MS ( $CH_3OH$ ): found:  $m/z = 266.0$  [ $Cu(L^2)$ ]<sup>2+</sup> (calculated for [ $Cu(L^2)$ ]<sup>2+</sup>:  $m/z = 266.1$ ). UV-VIS ( $5.9 \times 10^{-3}$  mol  $dm^{-3}$ /MeOH):  $\tilde{\nu}$   $cm^{-1}$  ( $\epsilon$ /mol<sup>-1</sup>  $dm^3$   $cm^{-1}$ ) = 13000 (101). IR (Nujol,  $\nu$  /  $cm^{-1}$ ): 3450 br, 3274 br (OH), 3102 br (NH), 1639 sh (HOH), 1609 m, 1594 m (C=O).

#### 3.4.2.4 $[Zn(L^2)][NO_3]_2$

A solution of  $Zn(NO_3)_2 \cdot 6H_2O$  [22.2 mg, 0.075 mmol] in MeOH (5 mL) was added to a solution of  $L^2$  [35.0 mg, 0.075 mmol] in MeOH (5 mL). The colourless solution was left to stir overnight. The solvent volume was reduced *in vacuo* and excess  $Et_2O$  was added, causing precipitation of a white solid. The solid was isolated *via* filtration and dried *in vacuo*. Yield: 37.4 mg, 0.057 mmol (76%). Analysis required for  $C_{24}H_{42}ZnN_8O_9 \cdot 2.5H_2O$ : C, 41.53; H, 7.55; N, 16.14. Found: C, 41.17; H, 7.12 N, 16.55%. <sup>1</sup>H NMR (295 K,  $CD_3OD$ ):  $\delta$  (ppm) = 4.85 ( $H_2O$ ), 4.04 – 3.94 (septet,  $^3J_{1H-1H} = 6.5$  Hz, [3H], <sup>i</sup>Pr-**CH**), 3.03 – 3.00 (br m, [6H], **CH**<sub>2</sub>), 2.98 – 2.89 (br m, [8H], tacn-**CH**<sub>2</sub>), 2.88 – 2.74 (br m, [4H], tacn-**CH**<sub>2</sub>), 2.74 – 2.62 (br m, [6H], **CH**<sub>2</sub>), 1.20 – 1.17 (d,  $^3J_{1H-1H} = 6.6$  Hz, [18H], <sup>i</sup>Pr<sub>2</sub>-**CH**<sub>3</sub>). <sup>13</sup>C NMR (295 K,  $CD_3OD$ ):  $\delta$  (ppm) = 176.4 (C=O), 56.2 (tacn-**CH**<sub>2</sub>), 55.0 (**CH**<sub>2</sub>), 43.5 (<sup>i</sup>Pr-**CH**), 31.8 (**CH**<sub>2</sub>), 22.3 (<sup>i</sup>Pr-**CH**<sub>3</sub>). ESI<sup>+</sup> MS ( $CH_3OH$ ): found:  $m/z = 266.2$  [ $Zn(L^2)$ ]<sup>2+</sup> (calculated for [ $Zn(L^2)$ ]<sup>2+</sup>:  $m/z = 266.2$ ). IR (Nujol,  $\nu$  /  $cm^{-1}$ ): 3264 br (OH), 3100 br (NH), 1633 m (HOH), 1601 s, 1575 sh (C=O).

### 3.4.3 NOTP-OMe Complexes

#### 3.4.3.1 $[Ni(NOTP-OMe)][NO_3]_2$

A solution of  $Ni(NO_3)_2 \cdot 6H_2O$  (9.2 mg, 0.032 mmol) in MeOH (3 mL) was added to a solution of NOTP-OMe (20 mg, 0.032 mmol) in MeOH (3 mL). The resultant green solution was left to stir at room temperature overnight. The solvent volume was reduced *in vacuo* and excess  $Et_2O$  was added, causing precipitation of a green solid. The solid was isolated *via* filtration and dried *in*

*vacuo* (very hygroscopic). Yield: 19.7 mg, 0.028 mmol (88%). ESI<sup>+</sup> MS (CH<sub>3</sub>OH): found:  $m/z$  = 345.9 [Ni(NOTP-OMe)]<sup>2+</sup> (calculated for [Ni(NOTP-OMe)]<sup>2+</sup>:  $m/z$  = 345.6). UV-VIS (2.4x10<sup>-3</sup> mol dm<sup>-3</sup>/MeOH):  $\tilde{\nu}$  cm<sup>-1</sup> ( $\epsilon$  mol<sup>-1</sup> dm<sup>3</sup> cm<sup>-1</sup>) = 19800 (24), 16700 (28), 10100 (48). IR (Nujol,  $\nu$  / cm<sup>-1</sup>): 3300 br (OH), 1645 m (HOH), 1181 br (P=O).

#### 3.4.3.2 [Cu(NOTP-OMe)][NO<sub>3</sub>]<sub>2</sub>

A solution of Cu(NO<sub>3</sub>)<sub>2</sub>·3H<sub>2</sub>O (9.9 mg, 0.041 mmol) in MeOH (3 mL) was added to a solution of NOTP-OMe (26 mg, 0.041 mmol) in MeOH (3 mL). The resultant green solution was left to stir at room temperature overnight. The solvent volume was reduced *in vacuo* and excess Et<sub>2</sub>O was added, causing precipitation of a vivid green solid. The solid was isolated *via* filtration and dried *in vacuo*. Yield: 19.7 mg, 0.028 mmol (88%). ESI<sup>+</sup> MS (CH<sub>3</sub>OH): found:  $m/z$  = 348.4 [Cu(NOTP-OMe)]<sup>2+</sup> (calculated for [Cu(NOTP-OMe)]<sup>2+</sup>:  $m/z$  = 348.1). UV-Vis (2.2x10<sup>-3</sup> mol dm<sup>-3</sup>/MeOH):  $\tilde{\nu}$  cm<sup>-1</sup> ( $\epsilon$  mol<sup>-1</sup> dm<sup>3</sup> cm<sup>-1</sup>) = 13000 (83). IR (Nujol,  $\nu$  / cm<sup>-1</sup>): 3400 br (OH), 1645 br (HOH), 1158 m (P=O).

#### 3.4.3.3 [Zn(NOTP-OMe)][BPh<sub>4</sub>]<sub>2</sub>

Under an inert N<sub>2</sub> atmosphere, Zn(NO<sub>3</sub>)<sub>2</sub>·6H<sub>2</sub>O (9.4 mg, 0.032 mmol) was added to a solution of NOTP-OMe [20 mg, 0.032 mmol] in an. MeOH (5 mL). The colourless solution was left to stir for three hours. NaBPh<sub>4</sub> (21.6 mg, 0.064 mmol, 2 mol. eqv.) was added, causing the immediate precipitation of a white solid. The solid was isolated *via* filtration and dried *in vacuo*. Yield: 15.2 mg, 0.022 mmol (69%). <sup>1</sup>H NMR (295 K, CD<sub>3</sub>CN):  $\delta$  (ppm) = 8.01 – 7.92 (m, ArH), 7.86 – 7.75 (m, ArH), 7.73 – 7.41 (br m, ArH), 7.30 – 7.24 (m, ArH), 7.02 – 6.97 (m, ArH), 6.86 – 6.82 (m, ArH), 3.89 – 3.86 (d, <sup>3</sup>J<sub>1H-31P</sub> = 11.5 Hz, CH<sub>3</sub>), 3.89 – 3.86 (d, <sup>3</sup>J<sub>1H-31P</sub> = 11.5 Hz, CH<sub>3</sub>), 3.77 – 3.74 (d, <sup>3</sup>J<sub>1H-31P</sub> = 11.5 Hz, CH<sub>3</sub>), 3.73 – 3.70 (d, <sup>3</sup>J<sub>1H-31P</sub> = 11.5 Hz, CH<sub>3</sub>), 3.69 – 3.47 (m, CH<sub>2</sub>), 3.38 – 3.32 (m, CH<sub>2</sub>), 3.13 – 2.76 (br m, tacn-CH<sub>2</sub>). <sup>31</sup>P NMR (295 K, CD<sub>3</sub>CN):  $\delta$  (ppm) = 51.3 (s, [1P]), 50.7 (s, [1P]), 50.6 (s, [1P]), 49.4 (s, [1P]). ESI<sup>+</sup> MS (CH<sub>3</sub>OH): found:  $m/z$  = 348.9 [Zn(NOTP-OMe)]<sup>2+</sup> (calculated for [Zn(NOTP-OMe)]<sup>2+</sup>:  $m/z$  = 348.6). IR (Nujol,  $\nu$  / cm<sup>-1</sup>): 1153 m (P=O).

### 3.5 X-ray Crystallographic Data

Complex	<b>[Co(L<sup>1</sup>-H)][NO<sub>3</sub>]<sub>2</sub>·2MeOH</b>	<b>[Co(L<sup>2</sup>)](NO<sub>3</sub>)<sub>2</sub>·1.5H<sub>2</sub>O</b>
Formula	C <sub>30</sub> H <sub>35</sub> CoN <sub>8</sub> O <sub>9</sub> ·2CH <sub>4</sub> O	C <sub>24</sub> H <sub>48</sub> CoN <sub>9</sub> O <sub>12</sub> ·1.5H <sub>2</sub> O
<i>M</i>	774.67	740.658
Crystal system	Monoclinic	Trigonal
Space group (no.)	<i>P</i> 2 <sub>1</sub> /c (14)	<i>P</i> -3 (147)
<i>a</i> /Å	10.8001(2)	9.8338(4)
<i>b</i> /Å	17.3514(3)	9.8338(4)
<i>c</i> /Å	19.5643(3)	20.3850(9)
$\alpha$ /°	90	90
$\beta$ /°	96.185(2)	90
$\gamma$ /°	90	120
<i>U</i> /Å <sup>3</sup>	3644.95(11)	1707.20(12)
<i>Z</i>	4	2
$\mu$ (Mo-K $\alpha$ ) /mm <sup>-1</sup>	0.540	0.578
<i>F</i> (000)	1624	787.341
Total no. reflns	74317	37332
<i>R</i> <sub>int</sub>	0.043	0.1049
Unique reflns	9423	3734
No. of params, restraints	494, 4	142, 24
GOF	1.071	0.8115
<i>R</i> <sub>1</sub> , <i>wR</i> <sub>2</sub> [ <i>I</i> > 2 $\sigma$ ( <i>I</i> )] <sup>b</sup>	0.057, 0.164	0.1120, 0.2698
<i>R</i> <sub>1</sub> , <i>wR</i> <sub>2</sub> (all data)	0.064, 0.169	0.1188, 0.2754

Complex	<b>[Ni(L<sup>1</sup>)] [NO<sub>3</sub>]<sub>2</sub>·1.5MeOH</b>	<b>[Ni(L<sup>2</sup>)] [NO<sub>3</sub>]<sub>2</sub>·0.443H<sub>2</sub>O</b>
Formula	C <sub>30</sub> H <sub>36</sub> N <sub>8</sub> NiO <sub>9</sub> ·1.5CH <sub>4</sub> O	C <sub>24</sub> H <sub>48</sub> N <sub>8</sub> NiO <sub>9</sub> ·0.443H <sub>2</sub> O
<i>M</i>	759.426	659.38
Crystal system	Monoclinic	Monoclinic
Space group (no.)	<i>P</i> 2 <sub>1</sub> /c (14)	<i>P</i> 2 <sub>1</sub> /n (14)
<i>a</i> /Å	16.2195(5)	17.7391(7)
<i>b</i> /Å	19.5074(8)	11.5230(4)
<i>c</i> /Å	11.0872(3)	18.2239(7)
<i>α</i> /°	90	90
<i>β</i> /°	95.999(3)	119.134(5)
<i>γ</i> /°	90	90
<i>U</i> /Å <sup>3</sup>	3488.8(2)	3253.8(3)
<i>Z</i>	4	4
<i>m</i> (Mo-K <sub>α</sub> ) /mm <sup>-1</sup>	0.625	0.656
<i>F</i> (000)	1598.644	1410
Total no. reflns	45487	81694
<i>R</i> <sub>int</sub>	0.058	0.065
Unique reflns	8997	8412
No. of params, restraints	755, 740	466, 1
GOF	1.0487	1.025
<i>R</i> <sub>1</sub> , <i>wR</i> <sub>2</sub> [ <i>I</i> > 2σ( <i>I</i> )] <sup>b</sup>	0.057, 0.135	0.058, 0.138
<i>R</i> <sub>1</sub> , <i>wR</i> <sub>2</sub> (all data)	0.090, 0.149	0.086, 0.152



Complex	<b>[Cu(L<sup>1</sup>)] [NO<sub>3</sub>]<sub>2</sub> · 1.25Et<sub>2</sub>O · MeOH</b>	<b>[Cu(L<sup>2</sup>)] [NO<sub>3</sub>]<sub>2</sub></b>
Formula	[C <sub>30</sub> H <sub>36</sub> CuN <sub>6</sub> O <sub>3</sub> ] <sub>3</sub> [NO <sub>3</sub> ] <sub>6</sub> · 1.25C <sub>4</sub> H <sub>10</sub> O · CH <sub>4</sub> O	C <sub>24</sub> H <sub>48</sub> CuN <sub>8</sub> O <sub>9</sub>
<i>M</i>	2273.340	656.243
Crystal system	triclinic	monoclinic
Space group (no.)	<i>P</i> -1 (2)	<i>P</i> 2 <sub>1</sub> /n (14)
<i>a</i> /Å	17.6146(3)	16.4229(3)
<i>b</i> /Å	17.6300(3)	10.9307(2)
<i>c</i> /Å	20.0301(3)	17.9733(3)
<i>α</i> /°	85.355(1)	90
<i>β</i> /°	80.554(1)	103.813(2)
<i>γ</i> /°	60.327(2)	90
<i>U</i> /Å <sup>3</sup>	5331.28(19)	3133.15(10)
<i>Z</i>	2	4
<i>m</i> (Mo-K <sub>α</sub> ) /mm <sup>-1</sup>	0.681	0.758
<i>F</i> (000)	2382.868	1398.432
Total no. reflns	124966	85801
<i>R</i> <sub>int</sub>	0.067	0.038
Unique reflns	27524	10252
No. of params, restraints	1387, 53	811, 0
GOF	1.0317	1.0629
<i>R</i> <sub>1</sub> , <i>wR</i> <sub>2</sub> [ <i>I</i> > 2σ( <i>I</i> )] <sup>b</sup>	0.062, 0.150	0.024, 0.051
<i>R</i> <sub>1</sub> , <i>wR</i> <sub>2</sub> (all data)	0.099, 0.170	0.036, 0.056

<sup>a</sup> common items: *T* = 100 K; wavelength (Mo-K<sub>α</sub>) = 0.71073 Å; θ(max) = 27.5°;

<sup>b</sup>  $R_1 = \sum ||F_o| - |F_c|| / \sum |F_o|$ ;  $wR_2 = [\sum w(F_o^2 - F_c^2)^2 / \sum wF_o^4]^{1/2}$

### 3.6 References

1. C. Van Cleave and D. C. Crans, *Inorganics*, 2019, **7**, 111.
2. R. M. Couñago, M. P. Ween, S. L. Begg, M. Bajaj, J. Zuegg, M. L. O'Mara, M. A. Cooper, A. G. McEwan, J. C. Paton, B. Kobe and C. A. McDevitt, *Nat. Chem. Biol.*, 2014, **10**, 35.
3. I. A. Fallis, R. D. Farley, K. M. A. Malik, D. M. Murphy and H. J. Smith, *J. Chem. Soc., Dalton Trans.*, 2000, 3632.
4. A. L. Crumbliss and S. Banerjee, *J. Inorg. Biochem.*, 2021, **219**, 111411.
5. P. B. Tsitovich and J. R. Morrow, *Inorg. Chim. Acta*, 2012, **393**, 3.
6. M. Sánchez, L. Sabio, N. Gálvez, M. Capdevila and J. M. Dominguez-Vera, *IUBMB Life*, 2017, **69**, 382.
7. C. N. Verani, S. Gallert, E. Bill, T. Weyhermüller, K. Wieghardt and P. Chaudhuri, *Chem. Commun.*, 1999, 1747.
8. D. Herebian, P. Ghosh, H. Chun, E. Bothe, T. Weyhermüller and K. Wieghardt, *Eur. J. Inorg. Chem.*, 2002, 1957.
9. J. Liu, S. C. Lorraine, B. S. Dolinar and J. M. Hoover, *Inorg. Chem.*, 2022, **61**, 6008.
10. S. Hayami, Y. Komatsu, T. Shimizu, H. Kamihata and Y. H. Lee, *Coord. Chem. Rev.*, 2011, **255**, 1981.
11. M. A. Halcrow, *Chem. Soc. Rev.*, 2013, **42**, 1784.
12. S. Amin, C. Marks, L. M. Toomey, M. R. Churchill and J. R. Morrow, *Inorg. Chim. Acta*, 1996, **246**, 99.
13. R. Kataký, K. E. Matthes, P. E. Nicholson, D. Parker and H.-J. Buschmann, *J. Chem. Soc., Perkin Trans. 2*, 1990, 1425.
14. T. Weyhermüller, K. Weighardt and P. Chaudhuri, *J. Chem. Soc., Dalton Trans.*, 1998, 3805.
15. K. Wieghardt, U. Bossek, P. Chaudhuri, W. Herrmann, B. C. Menke and J. Weiss, *Inorg. Chem.*, 1982, **21**, 4308.
16. R. Liu, Y. Z. Li, Z. Zhang and Z. L. Wang, *Acta Crystallogr. Sect. E: Struct. Rep. Online*, 2006, **62**, m1064.
17. L. M. Berreau, J. A. Halfen, V. G. Young and W. B. Tolman, *Inorg. Chem.*, 1998, **37**, 1091.
18. A. Garau, A. Bencini, A. J. Blake, C. Caltagirone, L. Conti, F. Isaia, V. Lippolis, R. Montis, P. Mariani and M. A. Scorciapino, *Dalton Trans.*, 2019, **48**, 4949.
19. C. S. Bonnet and É. Tóth, *Curr. Opin. Chem. Biol.*, 2021, **61**, 154.
20. A. Gupta, P. Caravan, W. S. Price, C. Platas-Iglesias and E. M. Gale, *Inorg. Chem.*, 2020, **59**, 6648.

21. S. J. Dorazio, A. O. Olatunde, P. B. Tsitovich and J. R. Morrow, *J. Biol. Inorg. Chem.*, 2014, **19**, 191.
22. S. M. Abozeid, E. M. Snyder, T. Y. Tittiris, C. M. Steuerwald, A. Y. Nazarenko and J. R. Morrow, *Inorg. Chem.*, 2018, **57**, 2085.
23. S. M. Abozeid, E. M. Snyder, A. P. Lopez, C. M. Steuerwald, E. Sylvester, K. M. Ibrahim, R. R. Zaky, H. M. Abou-El-Nadar and J. R. Morrow, *Eur. J. Inorg. Chem.*, 2018, 1902.
24. A. O. Olatunde, C. J. Bond, S. J. Dorazio, J. M. Cox, J. B. Benedict, M. D. Daddario, J. A. Sperryak and J. R. Morrow, *Chem. Eur. J.*, 2015, **21**, 18290.
25. S. J. Dorazio, P. B. Tsitovich, S. A. Gardina and J. R. Morrow, *J. Inorg. Biochem.*, 2012, **117**, 212.
26. L. Christiansen, D. N. Hendrickson, H. Toftlund, S. R. Wilson and C.-L. Xie, *Inorg. Chem.*, 1986, **25**, 2813.
27. S. J. Dorazio, P. B. Tsitovich, K. E. Sitters, J. A. Sperryak and J. R. Morrow, *J. Am. Chem. Soc.*, 2011, **133**, 14154.
28. Z. Zhang, Y. He, Q. Zhao, W. Xu, Y.-Z. Li and Z.-L. Wang, *Inorg. Chem. Commun.*, 2006, **9**, 269.
29. G. Sanderson PhD, University of Southampton, 2015.
30. E. Cole, R. C. B. Copley, J. A. K. Howard, D. Parker, G. Ferguson, J. F. Gallagher, B. Kaitner, A. Harrison and L. Royle, *J. Chem. Soc., Dalton Trans.*, 1994, 1619.
31. C. J. Broan, E. Cole, K. J. Jankowski, D. Parker, K. Pulukkody, B. A. Boyce, N. R. A. Beeley, K. Millar and A. T. Millican, *Synthesis*, 1992, 63-67.
32. F. Koucký, T. Dobrovolná, J. Kotek, I. Císařová, J. Havlíčková, A. Liška, V. Kubíček and P. Hermann, *Dalton Trans.*, 2024, **53**, 9267.
33. P. Askalani, *Transition Met. Chem.*, 1986, **11**, 469.
34. W. Klæui, W. Eberspach and P. Guetlich, *Inorg. Chem.*, 1987, **26**, 3977.
35. A. B. P. Lever, *Inorganic Electronic Spectroscopy*, Elsevier, Amsterdam, 2nd edn., 1984.
36. S. E. Neale, D. A. Pantazis and S. A. Macgregor, *Dalton Trans.*, 2020, **49**, 6478.
37. H. B. Lee, N. Ciolkowski, C. Winslow and J. Rittle, *Inorg. Chem.*, 2021, **60**, 11830.
38. M. J. Gajewska, W.-M. Ching, Y.-S. Wen and C.-H. Hung, *Dalton Trans.*, 2014, **43**, 14726.
39. H.-J. Küppers, A. Neves, C. Pomp, D. Ventur, K. Wieghardt, B. Nuber and J. Weiss, *Inorg. Chem.*, 1986, **25**, 2400.
40. G. H. Searle, D.-N. Wang, S. Larsen and L. Erik, *Acta Chem. Scand.*, 1992, **46**, 38.
41. A. A. Pinkerton, in *The Rare Earths in Modern Science and Technology*, eds. G. J. McCarthy, J. J. Rhyne and H. B. Silber, Springer US, New York, 1 edn., 1980, pp. 147-152.

42. V. Kubíček, Z. Böhmová, R. Ševčíková, J. Vaněk, P. Lubal, Z. Poláková, R. Michalicová, J. Kotek and P. Hermann, *Inorg. Chem.*, 2018, **57**, 3061.

## Chapter 4 Coordination of Metal Trifluorides (M = Al, Ga, In, Fe) with Amide-Functionalised Triazacyclononane Ligands

This chapter will investigate the behaviour of the amide-triazacyclononane ligands, L<sup>1</sup>, L<sup>2</sup> and L<sup>3</sup> towards the formation of novel metal fluoride complexes of the trivalent Al, Ga, In and Fe ions. These complexes are fully characterised using a range of analytical techniques, both in the solid state (microanalysis, IR spectroscopy, SCXRD) and in solution (NMR spectroscopy, ESI<sup>+</sup> MS). Where single-crystal structures have been obtained, the supramolecular features (such as an extended-hydrogen bonded network) are discussed. The suitability of the MF<sub>3</sub> complexes for <sup>18</sup>F/<sup>19</sup>F isotopic exchange reactions are assessed based upon their ease of synthesis, behaviour and relative stabilities in solution, and identification of any supramolecular features that are postulated to assist in the radiochemical reaction – for example, hydrogen-bonding interactions involving the fluoride ligands.

### 4.1 Introduction

The last decade has seen considerable research into new metal-fluoride complexes, much of which has been motivated by their potential as carriers for the positron-emitting <sup>18</sup>F radioisotope for positron emission tomography (PET) imaging in medicine.<sup>1,2,3</sup> The key features of many of these complexes are strong metal-halide bonds, which facilitate the late-stage incorporation of <sup>18</sup>F *via* isotopic or halide exchange.<sup>4,5</sup> Furthermore, many of the reported complexes contain neutral or anionic tacn-based ligand scaffolds, which allow for tailored properties (e.g. by including receptor-specific peptides on the pendant arm) and give additional stability *via* the macrocyclic effect.<sup>6,7,8,9</sup> Such scaffolds are ideal for binding smaller metal ions, such as the first-row transition metals and some main group metals. Chapter 1 has given several examples of systems incorporating aluminium(III), gallium(III), iron(III) and scandium(III) fluoride species.<sup>1,2,3,9,10,11</sup> Chapter 3 has also detailed the scope of triazacyclononane ligands coordinated to various divalent transition metal ions, with a focus on those containing amide-pendant arms. In most cases, the amide pendant arms act as a donor *via* the carboxamide function; the behaviour of these ligands towards neutral, uncharged metal fragments – such as MF<sub>3</sub> – is unknown.

Hence, the work in this chapter will describe the first routes towards MF<sub>3</sub> complexes of amide-functionalised triazacyclononane ligands using the novel L<sup>1</sup>, L<sup>2</sup> and L<sup>3</sup> ligands (synthesised in Chapter 2). The previous chapter has already discussed the coordination chemistry of the tris-substituted ligands, L<sup>1</sup> and L<sup>2</sup>, with divalent metal ions, and (with one exception) has found both

ligands provide a hexadentate  $\text{N}_3\text{O}_3$  donor set *via* coordination of the tacn-nitrogens and the carboxamide-oxygens. However, a molecular  $\text{MF}_3$  precursor will be used to synthesise the complexes in this chapter. Due to their high bond dissociation enthalpies, it is assumed that the metal-fluoride bonds will not be displaced *via* coordination of the carboxamide of the pendant arms, and the neutral  $[\text{MF}_3(\text{L}^n)]$  complexes will be formed.

This follows from previous work in the group, which has identified the  $[\text{MF}_3(\text{BnMe}_2\text{-tacn})]$  ( $\text{M} = \text{Ga}, \text{Fe}$ ) systems as suitable candidates for  $^{19}\text{F}/^{18}\text{F}$  isotopic exchange reactions.<sup>5,12</sup> Recently, the  $[\text{FeF}_3(\text{BnMe}_2\text{-tacn})]$  system has been used as a model complex for the translation of  $\text{MF}_3$  complexes to high-activity work, so there is an increasing interest in the development of  $\text{MF}_3$  systems for  $^{18}\text{F}$ -radiochemistry.<sup>10</sup> However, in contrast to the  $\text{BnMe}_2\text{-tacn}$  ligand (with no donor pendant groups), the amide functions of  $\text{L}^1$ ,  $\text{L}^2$  and  $\text{L}^3$  may be free to engage in hydrogen-bonding interactions. Structural analysis of the tris(amide) transition metal complexes in Chapter 3 gave evidence of extensive hydrogen-bonding interactions from amide(NH) functions towards nitrate counter-ions and lattice solvent molecules. It is not known what effect this will have on  $^{18}\text{F}$ -radiolabelling reactions. Prior to radiofluorination experiments, and in addition to the complete characterisation of the novel  $\text{MF}_3$  complexes, this work will investigate if, and to what extent, hydrogen-bonding interactions occur.

Aside from the possibility of influencing radiochemistry, hydrogen-bonding can also lead to interesting supramolecular arrays. A supramolecule can be defined as ‘a set of molecular components held together by intermolecular interactions’.<sup>13</sup> There are many examples of metal complexes with nitrogen-based macrocycles, which represent a notable subset of supramolecular chemistry. These include complexes of triazacyclononane and its derivatives, cyclen/cyclam derivatives, porphyrins, corrins, and chlorins.<sup>14,15,16,17</sup>

With careful consideration of the ligand architecture and possible non-covalent bonds, supramolecules can be purposefully designed for a range of functional applications in chemistry, biology and medicine (e.g. drug delivery, catalysis, molecular sensors, and cosmetics).<sup>18,19,20</sup> For example, in this manner, Hajjaj *et al.*<sup>21</sup> have reported the rapid formation of zinc-imidazolyl porphyrin dimers that arise from non-covalent  $\pi$ -stacking interactions. This leads to interesting pentagonal and hexagonal supramolecular arrays, with potential applications as photosynthetic light-harvesting antennae.

Recently, the role of ‘ $\text{MF}_3$ ’ fragments in triazacyclononane complexes have emerged as interesting subunits for supramolecular assemblies. The *fac*-trifluoride moiety offers a region of high electronegativity, capable of forming weak electrostatic or dative interactions, as well as acting as a hydrogen-bond acceptor. Importantly, intermolecular hydrogen bonding can be

considered one of the primary interactions that underpin the self-assembly of supramolecular structures.<sup>22</sup>

#### 4.1.1 Supramolecular Assemblies with MF<sub>3</sub> Coordination Complexes

The coordination chemistry and packing motifs of several MF<sub>3</sub> systems and other similar complexes have been investigated. For example, Penkert *et al.*<sup>23</sup> have reported an [GaF<sub>3</sub>(L)] species (L = 1,4,7-tris(2-amino-3,5-di-tert-butylbenzyl)-1,4,7-triazacyclononane) whereby the metal is bound to three fluoride ligands and the tacn ring-nitrogen atoms. The tacn pendant arms remain uncoordinated and adopt a conformation that creates a hydrophobic ‘surface’ via six tertiary butyl groups. Packing of the [GaF<sub>3</sub>(L)] molecules brings two adjacent hydrophobic surfaces together, creating a ‘dimer’ held together by weak van der Waals forces. The cavity on the inside of this dimer holds a hexamer of staggered MeOH molecules, which adopt S<sub>6</sub>-symmetry (Figure 4.1).

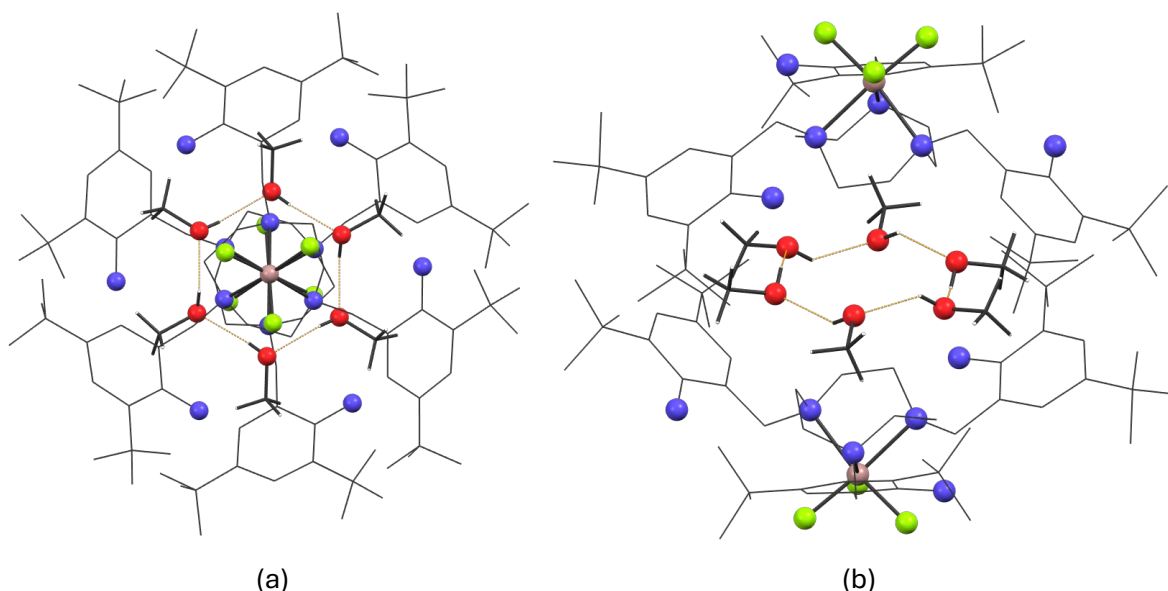


Figure 4.1 – [GaF<sub>3</sub>L]<sub>2</sub>·(MeOH)<sub>6</sub> reported by Penkert *et al.*<sup>23</sup>: (a) view down the S<sub>6</sub>-axis and (b) side-view showing the hydrogen-bonded hexamer of MeOH molecules. Images redrawn from CCDC 1220143. Hydrogen atoms omitted for clarity. Atom colours: pale pink, Ga; green, F; red, O; blue, N.

MF<sub>3</sub> complexes with Me<sub>3</sub>-tacn and BnMe<sub>2</sub>-tacn, such as [InF<sub>3</sub>(Me<sub>3</sub>-tacn)]·4H<sub>2</sub>O depicted in Figure 4.2 below, have also been shown to form extended H-bonding networks with lattice water molecules via F⋯HOH interactions.<sup>12</sup>

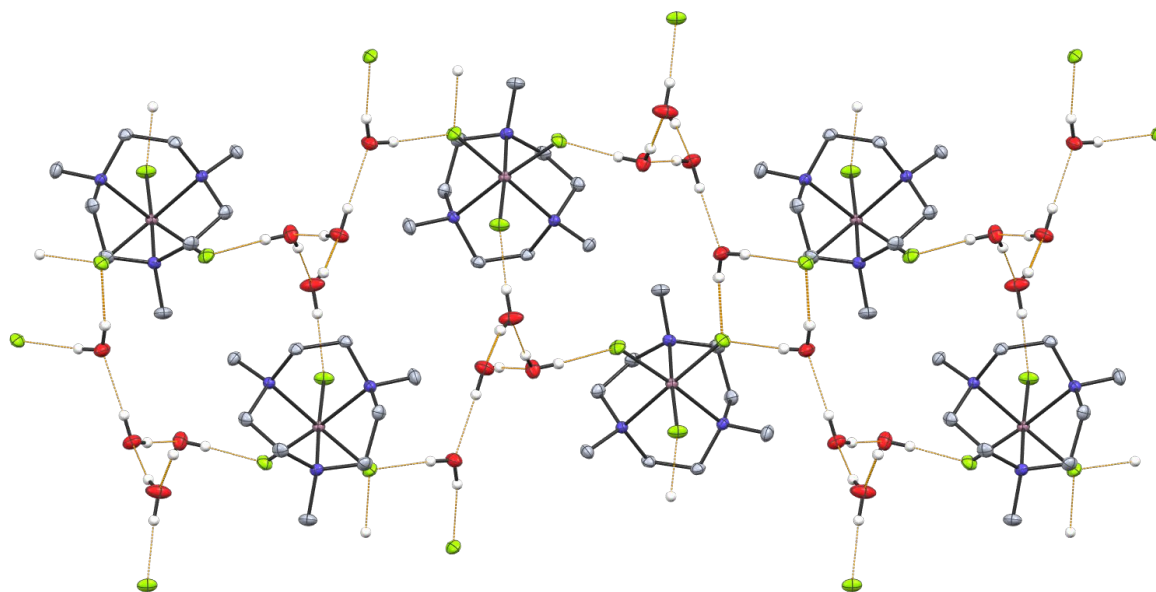


Figure 4.2 – Extended hydrogen-bonding network of  $[\text{InF}_3(\text{Me}_3\text{-tacn})]\cdot 4\text{H}_2\text{O}$ . Redrawn from CCDC 926505. Hydrogen atoms (excluding those involved in hydrogen bonded) omitted for clarity. Atom colours: pale purple, In; green, F; red, O; blue, N; grey, C; white, H.<sup>12</sup>

#### 4.1.2 $\text{MF}_3$ Complexes as Metalloligands

Other examples also show the *fac*- $[\text{MF}_3(\text{R}_3\text{-tacn})]$  complexes acting as metalloligands towards different cations, leading to unexpected supramolecular assemblies. This can give rise to novel functional properties. For instance, in pursuit of molecular magnetic refrigerants, Pedersen and co-workers<sup>24</sup> report a series of hydrated  $[\text{MF}_3(\text{Me}_3\text{-tacn})]\cdot x\text{H}_2\text{O}$  ( $\text{M} = \text{Cr}^{3+}$ ,  $\text{Fe}^{3+}$ ,  $\text{Ga}^{3+}$ ) complexes, capable of forming fluoride-bridged complexes to  $\text{Gd}^{3+}$ .  $[\text{GaF}_3(\text{BnMe}_2\text{-tacn})]$  has also been shown to behave as a metalloligand towards alkali metal cations ( $\text{Li}^+$ ,  $\text{Na}^+$ ,  $\text{K}^+$ ), as well as  $[\text{NH}_4]^+$ .<sup>25</sup> Figure 4.3 below shows the crystal structure obtained for  $[\text{GaF}_3(\text{BnMe}_2\text{-tacn})]$  with  $\text{KPF}_6$ , presented as a dimer. Both of the gallium complexes in the dimer are bonded *via* two of the fluorides to  $\text{K}^+$ , to form an eight-coordinate  $\text{K}^+$  cation. This further highlights the scope of possible bonding motifs presented by  $\text{MF}_3$  complexes.



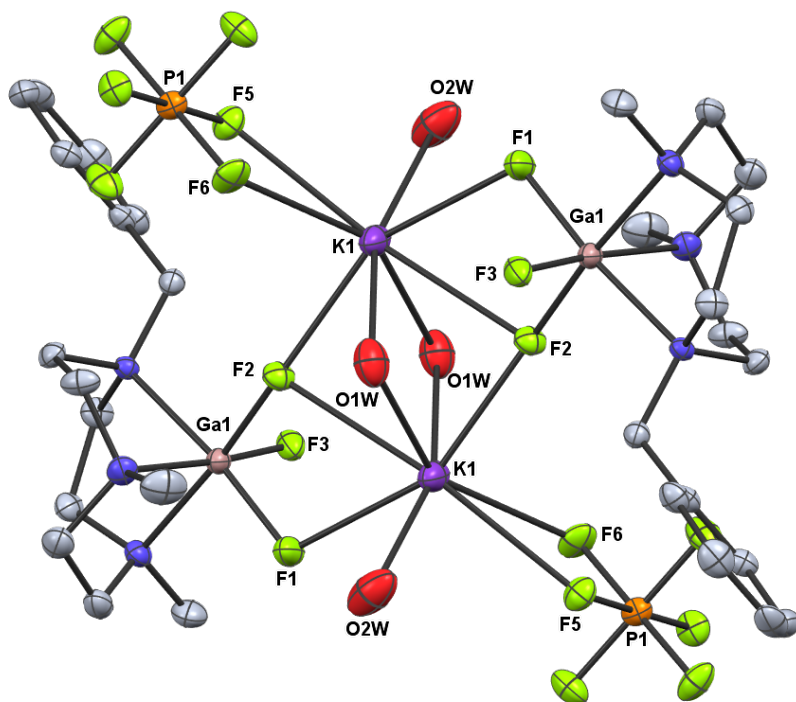


Figure 4.3 – Structure of a  $[GaF_3(BnMe_2-tacn)K_2(OH_2)_4(PF_6)_2] \cdot H_2O$  dimer with coordination to  $K^+$  via fluoride ligands. Redrawn from CCDC 1008583. Hydrogen atoms omitted for clarity.<sup>25</sup>

This chapter will focus on expanding the coordination chemistry of these ‘ $MF_3$ ’ fragments ( $M = Al, Ga, In, Fe$ ) with the tacn derivatives containing amide pendant arms ( $L^1, L^2$  and  $L^3$ ). Based on the above, and the expectation that the amide functions will act as hydrogen-bonding groups, it is not unreasonable to expect metal trifluoride complexes of  $L^1, L^2$  and  $L^3$  to exhibit supramolecular properties. Solid-state characterisation of the transition metal complexes of  $L^1$  and  $L^2$  have highlighted the propensity for the amide(NH) functions to engage in hydrogen-bonding between counter-ions and protic solvent molecules. Therefore, it is possible that the amide pendant arms may interact with highly electronegative fluoride – including both bound ligands from the resultant  $MF_3$  complexes, and any incoming  $^{18}F^-$  from isotopic exchange reactions. It is suggested that these interactions may assist the delivery of highly electronegative fluoride ions to the metal in the process of radiofluorination, which may increase the radiochemical yield. They may also help to increase the overall stability of the complexes in the solid-state and solution.

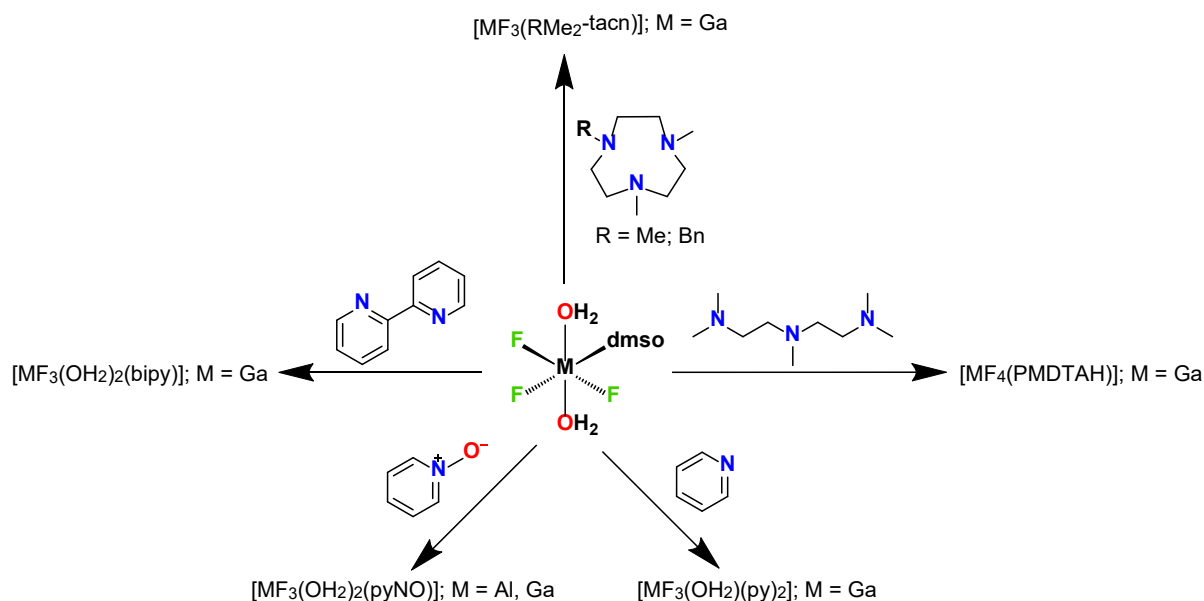
#### 4.1.3 Formation of $MF_3$ Triazacyclononane Complexes

Group 13 complexes of the alkylated  $Me_3-tacn$  and  $BnMe_2-tacn$  ligands have been synthesised successfully using several techniques, including hydrothermal synthesis and *via* Cl/F exchange of a pre-formed chloro-complex.<sup>26,8</sup>

However, similar efforts to form  $\text{MF}_3$  complexes ( $\text{M} = \text{Ga}, \text{In}$ ) with ligands  $\text{L}^1$ ,  $\text{L}^2$  and  $\text{L}^3$  were unsuccessful.<sup>27</sup> A hydrothermal approach was used to attempt to form  $[\text{GaF}_3(\text{L}^1)]$ . Whilst the poorly soluble (and mostly polymeric)  $\text{MF}_3 \cdot 3\text{H}_2\text{O}$  ( $\text{M} = \text{Al}, \text{Ga}, \text{In}$ ) precursors can provide a source of ' $\text{MF}_3$ ' for coordination to certain ligands, no identifiable products were isolated in this instance.<sup>26,28</sup> It was suggested that the reaction conditions (involving high temperature and pressure) led to the extensive hydrolysis of the ligands in the solution. These results show much milder reaction conditions are required.

Attempts to access the gallium and indium trichloride complexes of  $\text{L}^2$  and  $\text{L}^3$  were also unsuccessful. Spectroscopic data of the products formed from the reaction of anhydrous  $\text{MCl}_3$  with the ligands indicated the presence of protonated ligand  $[\text{HL}^n]^+$  and the corresponding tetrachlorometallate anion,  $[\text{MCl}_4]^-$ , only.

Previous work in the Reid group has shown that the molecular  $[\text{MF}_3(\text{dmsO})(\text{OH}_2)_2]$  precursors are often more suitable due to their higher solubilities under milder reaction conditions.<sup>29</sup> Therefore, they are more compatible with a wider range of ligand types and functionalities. Scheme 4.1 summarises some of the reactions with  $[\text{MF}_3(\text{dmsO})(\text{OH}_2)_2]$  previously reported.<sup>30</sup>  $\text{MF}_3$  complexes of several triazacyclononane ligands can now be accessed *via* the direct reaction of the precursor with the ligand in weak donor solvents, such as  $\text{CH}_2\text{Cl}_2$  or  $\text{MeCN}$ . Utilising a molecular form of  $\text{MF}_3$  also avoids the more highly Lewis-acidic  $\text{M}^{3+}$  cations. Chapter 3 mentions the behaviour of the borderline hard Lewis acid,  $\text{Fe}^{2+}$ , which was observed to promote complete hydrolysis of all three of the amide arms in the TCMT ligand – and although not discussed in detail, the reaction of  $\text{Fe}(\text{OTf})_2$  with  $\text{L}^1$  also led to the observation of the known  $[\text{Fe}(\text{NOTA})]$  complex.<sup>31</sup> Instead, the behaviour of amide ligands with hard Lewis acids ( $\text{Fe}^{3+}$ ,  $\text{Ga}^{3+}$ ,  $\text{In}^{3+}$ ) will be probed further in Chapter 6.



Scheme 4.1 - Reactions of  $[MF_3(dmsO)(OH_2)_2]$  with various N-donor ligands.

#### 4.1.4 Aims

This chapter aims to form novel amide-tacn ( $L^1$ ,  $L^2$  and  $L^3$ ) complexes with iron, aluminium, gallium and indium fluorides ( $MF_3$ ). For the Group 13 complexes, the molecular  $MF_3$  precursor,  $[MF_3(dmsO)(OH_2)_2]$  will be used. To explore their coordination chemistry and their properties in solution and in the solid-state, the novel complexes will be fully characterised using IR and NMR ( $^1H$ ,  $^{19}F\{^1H\}$ ,  $^{13}C\{^1H\}$ ,  $^{71}Ga$ ,  $^{27}Al$ ) spectroscopy, ESI<sup>+</sup> MS, elemental analysis, and where suitable crystals can be grown, SCXRD.

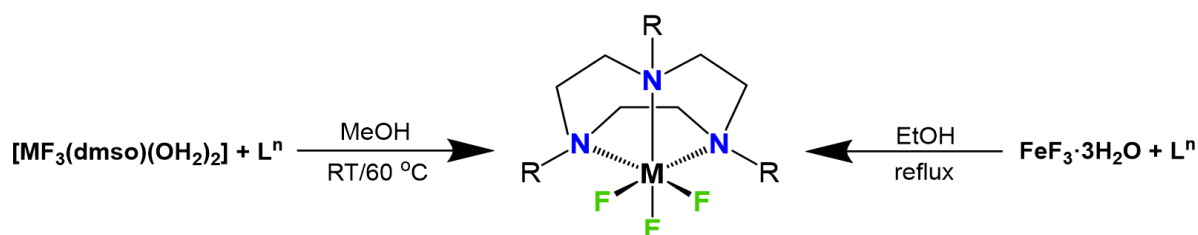
SCXRD data will be used to help to identify any non-covalent interactions between the fluorides and amide-NH functions, which may influence isotopic exchange reactions with  $^{18}F$ . The work in this chapter will therefore also allow potential candidate complexes for future radiolabelling experiments to be identified – these will be discussed further in Chapter 5.

## 4.2 Results and Discussion

### 4.2.1 Formation of $[MF_3(L^n)]$ via $[MF_3(dmsO)(OH_2)_2]$ ( $M = Al, Ga, In$ ) and $FeF_3 \cdot 3H_2O$

The (target) synthetic routes towards  $[MF_3(L^n)]$  ( $M = Al, Ga, In, Fe$ ;  $L^n = L^1, L^2, L^3$ ) are given in Scheme 4.2, alongside the structure of the target  $MF_3$  complex. The  $MF_3$  ( $M = Al, Ga, In$ ) complexes of  $L^n$  were synthesised *via* the reaction of the molecular precursors,  $[MF_3(dmsO)(OH_2)_2]$ , with one mol. eqv. of the macrocyclic ligand in MeOH, either at room temperature (Al, In) or heating to 60 °C (Ga).<sup>29</sup> Whilst  $FeF_3 \cdot 3H_2O$  is poorly soluble, heating at reflux with one mol. eqv. of the ligands in EtOH (4–12 h) led to full dissolution and formation of the three desired complexes as pale-yellow solids. Based on a previously reported method and

successful formation of  $[\text{FeF}_3(\text{BnMe}_2\text{-tacn})]$ , formation of the  $\text{FeF}_3$  complexes by refluxing in *n*-BuOH (130 °C) using shorter reaction times was attempted.<sup>12</sup> However, this led to the decomposition of the ligands in solution, indicating instability of the amide functions at elevated temperatures. The reaction products were isolated in good yield (60–80%), although characterisation data was indicative of multiple species in some cases (primarily, complexes of indium). The spectroscopic and structural data are discussed in further detail below.



Scheme 4.2 – Assumed synthetic route towards  $[\text{MF}_3(\text{L}^n)]$  complexes;  $\text{M} = \text{Al}, \text{Ga}, \text{In}, \text{Fe}$ ;  $\text{L}^n = \text{L}^1, \text{L}^2, \text{L}^3$ .

## 4.2.2 Characterisation of Novel $[\text{MF}_3(\text{L}^n)]$ Complexes – Solid State and NMR Studies

### 4.2.2.1 Infrared, Microanalysis, and ESI<sup>+</sup> MS

As expected for *fac*- $\text{MX}_3\text{L}_3$  complexes with  $\text{C}_{3v}$  symmetry, the powdered  $[\text{MF}_3(\text{L}^n)]$  ( $\text{M} = \text{Al}, \text{Ga}, \text{Fe}$ ) products largely show two ( $a_1 + e$ ) stretching bands in the far IR regions, with the exception of  $[\text{FeF}_3(\text{L}^2)]$ , which shows one very broad Fe–F stretch at  $512 \text{ cm}^{-1}$ . In this instance, the broadness of the peak likely obscures a second IR band. Although IR spectra were collected for the products isolated from reactions of  $[\text{InF}_3(\text{dmsO})(\text{OH}_2)_2]$  and  $\text{L}^1$ ,  $\text{L}^2$  and  $\text{L}^3$ , the expected In–F stretches ( $400 - 500 \text{ cm}^{-1}$ ) of the target complexes were not observed and potentially lost in the background/fingerprint region of the complex.

The observed frequencies compare well with the literature data for the  $[\text{MF}_3(\text{Me}_3\text{-tacn})]$  ( $\text{M} = \text{Al}, \text{Ge}, \text{Fe}$ ) complexes previously reported by the group – Table 4.1 provides a summary of the IR (and NMR) characteristics of the  $\text{MF}_3$  amide-tacn complexes and similar complexes reported in the literature.<sup>8,12</sup> The M–F stretching region can be expected to be observed at ca.  $600 - 700 \text{ cm}^{-1}$  for Al–F, and ca.  $500 - 600 \text{ cm}^{-1}$  for Ga–F and Fe–F.

Table 4.1 – Selected IR and NMR spectroscopic data for  $[MF_3(L)]$  ( $M = Al, Ga, Fe$ ).

Complex	IR M–F bands / $\text{cm}^{-1}$	NMR Solvent	$\delta(^{19}\text{F}\{^1\text{H}\})$ / ppm	$\delta(^{27}\text{Al}/^{71}\text{Ga})$ / ppm
$[\text{AlF}_3(\text{Me}_3\text{-tacn})]^8$	633, 614	MeCN	-176.1	19.0
		H <sub>2</sub> O	-169.9	18.5
$[\text{AlF}_3(\text{BnMe}_2\text{-tacn})]^8$	635, 601	MeCN	-161.5 [F], -161.7 [2F]	19.8
$[\text{AlF}_3(\text{L}^1)]$	694, 673	MeOH	-174 br	not observed
		H <sub>2</sub> O*	-	
$[\text{AlF}_3(\text{L}^2)]$	667, 616	MeOH	-174.5 br	not observed
		H <sub>2</sub> O	-155.8 br	
$[\text{AlF}_3(\text{L}^3)]$	642, 592	MeOH	-196 br	not observed
		H <sub>2</sub> O	-155.2 [F], -156.1 [2F]	
$[\text{GaF}_3(\text{Me}_3\text{-tacn})]^8$	530, 492	CH <sub>2</sub> Cl <sub>2</sub>	-181 br	42.0 (br q) ( $^1J_{71\text{Ga}19\text{F}} \sim 490$ Hz)
		H <sub>2</sub> O	-173 br	44.6 (br q) ( $^1J_{71\text{Ga}19\text{F}} \sim 490$ Hz)
$[\text{GaF}_3(\text{BnMe}_2\text{-tacn})]^8$	526, 515	H <sub>2</sub> O	-172.8 br	44.9
$[\text{GaF}_3(\text{L}^1)]$	583, 543	MeOH	-180 v br	46.6 (br q) ( $^1J_{71\text{Ga}19\text{F}} \sim 510$ Hz)
$[\text{GaF}_3(\text{L}^2)]$	528, 510	MeOH	-178 v br	41.0 (br q) ( $^1J_{71\text{Ga}19\text{F}} \sim 520$ Hz)
$[\text{GaF}_3(\text{L}^3)]$	539, 520	MeOH	-171.5 [2F], -172.3 [F]	not observed
$[\text{FeF}_3(\text{Me}_3\text{-tacn})]^{12}$	529, 512	***	-	-
$[\text{FeF}_3(\text{Bn-Me}_2\text{-tacn})]^{12}$	537, 517	***	-	-
$[\text{FeF}_3(\text{L}^1)]$	550, 537	***	-	-
$[\text{FeF}_3(\text{L}^2)]$	512**	***	-	-
$[\text{FeF}_3(\text{L}^3)]$	539, 521	***	-	-

\* complex not sufficiently soluble

\*\* very broad IR band

\*\*\* Complexes contain  $d^5$  paramagnetic  $\text{Fe}^{3+}$  so NMR is not suitable

The IR spectra also confirm the presence of H<sub>2</sub>O, with a broad peak over 3000 cm<sup>-1</sup>. In some cases, uncoordinated dmso is also present in the isolated products, with the S=O stretch observed as a band just above 1000 cm<sup>-1</sup> (coordinated dmso is present just below 1000 cm<sup>-1</sup> in the [MF<sub>3</sub>(dmso)(OH<sub>2</sub>)<sub>2</sub>] complexes). This was also consistent with microanalytical data, and not unexpected – dmso has a high boiling point (189 °C) and is difficult to remove, even with repeated washing and drying *in vacuo*. Much like the transition metal complexes of L<sup>2</sup>, the MF<sub>3</sub> complexes of L<sup>2</sup> were observed as very hygroscopic, and their microanalytical data also concurs with the presence of solvated water in the bulk material.

ESI<sup>+</sup> MS of the complexes typically showed peaks with the expected isotopic pattern associated with [MF<sub>2</sub>(L)]<sup>+</sup> or [MF<sub>3</sub>(L)+H]<sup>+</sup>, although often with low intensities (M = Al, Ga, Fe). The loss of fluoride ligands from the metal centre is observed due to the ionisation conditions during the MS experiment. Interestingly, however, the Al complexes of all three ligands (L<sup>1</sup>, L<sup>2</sup> and L<sup>3</sup>) were detected as the [AlF<sub>3</sub>(L<sup>3</sup>)]<sup>+</sup> ions, which may reflect on the higher Al–F bond strength (664 kJ mol<sup>-1</sup>) vs. Ga–F (577 kJ mol<sup>-1</sup>), for example. Peaks for [L+H]<sup>+</sup> are also observed in some cases. ESI<sup>+</sup> MS did not detect any mass peaks relating to ions of [InF<sub>3</sub>(L<sup>1</sup>)], [InF<sub>3</sub>(L<sup>2</sup>)] and [InF<sub>3</sub>(L<sup>3</sup>)] or similar.

While the expected ν(Fe–F) bands are present in the IR spectra and the expected peaks are evident in the ESI<sup>+</sup> MS for [FeF<sub>2</sub>(L<sup>2</sup>)]<sup>+</sup> and [FeF<sub>2</sub>(L<sup>3</sup>)]<sup>+</sup>, the paramagnetic nature of the iron complexes (Fe<sup>3+</sup>, d<sup>5</sup>) precludes NMR analysis.

#### 4.2.2.2 Solution NMR Studies of the Group 13 Complexes

The Group 13 complexes, and particularly those of L<sup>1</sup> (containing three aromatic phenyl rings), were found to have limited solubility in non-protic solvents, and so NMR characterisation data was obtained from CD<sub>3</sub>OD or D<sub>2</sub>O solutions. For reasons indicated above, NMR analysis was not undertaken on the three iron trifluoride systems. Their respective <sup>19</sup>F{<sup>1</sup>H} NMR shifts (and, where appropriate, multinuclear NMR shifts) are given in Table 4.1 above, but will be discussed in further detail below.

##### 4.2.2.2.1 Aluminium Trifluoride Complexes

The three aluminium trifluoride complexes were analysed using <sup>1</sup>H (*I* = ½, 99.9%), <sup>19</sup>F{<sup>1</sup>H} (*I* = ½, 100%) and <sup>13</sup>C{<sup>1</sup>H} (*I* = ½, 1.1%) NMR spectroscopy. Attempts were made to obtain <sup>27</sup>Al (*I* = 5/2, 60.4%) NMR spectra for each of the complexes, but this was unsuccessful for reasons which will be specified below.

The synthesis of [AlF<sub>3</sub>(L<sup>1</sup>)] was optimised following a series of trial conditions, which involved varying the time the reaction was allowed to proceed (between 2 h and 48 h) and/or varying the

reaction temperature (RT to 80 °C). Solution NMR analysis was impeded due to the limited solubility of the isolated product(s). However, NMR analysis was able to show that shorter reaction times led to a greater yield of the final (target) product. Longer reaction times (> 12 hours) resulted in the precipitation of a poorly soluble white solid;  $^{19}\text{F}\{^1\text{H}\}$  and  $^{27}\text{Al}$  NMR analysis (Figure 4.4) showed this to contain the tetrafluoroaluminate anion,  $[\text{AlF}_4]^-$ . The remaining undissolved particulates in the NMR solution may be due to another, unknown impurity (with no evidence of starting material or target species). The  $^{19}\text{F}\{^1\text{H}\}$  spectrum of this solid depicts a six-line coupling pattern centred around -190 ppm, which arises from the coupling of the four fluorine nuclei to the quadrupolar aluminium centre.<sup>32</sup> The  $^{27}\text{Al}$  spectrum shows a broad peak at around 49 ppm. A quintet would typically be expected for the  $[\text{AlF}_4]^-$  anion; however, the quadrupolar nature of the aluminium nucleus can lead to considerable line broadening, and the coupling pattern may not be observed – particularly on a concentrated sample. It is proposed that the strongly coordinating behaviour of the dmsol liberated from the metal precursor may lead to competition for binding to the metal ion. Over an extended period, this could cause some decomposition to produce the  $[\text{AlF}_4]^-$  anion and protonated ligand.

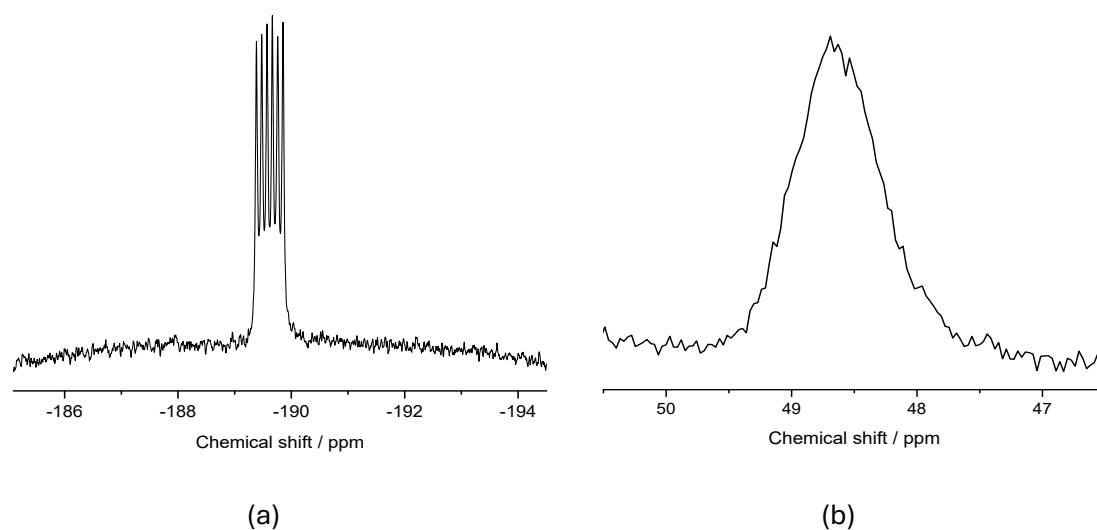


Figure 4.4 – (a)  $^{19}\text{F}\{^1\text{H}\}$  and (b)  $^{27}\text{Al}$  NMR spectra of the  $[\text{AlF}_4]^-$  anion isolated from the overnight reaction of  $[\text{AlF}_3(\text{dmsol})(\text{OH}_2)_2]$  with  $\text{L}^1$  ( $d_6$ -dmsol).

The  $[\text{AlF}_4]^-$  by-product was easily removed from the reaction *via* filtration, and the target complex could be isolated from the solution after removal of the solvent *in vacuo*. This left a white solid in good yield, although it was poorly soluble in typical organic solvents, including MeOH,  $\text{H}_2\text{O}$ , and non-protic solvents such as  $\text{CHCl}_3$  and  $\text{CH}_2\text{Cl}_2$ . This meant a  $^{27}\text{Al}$  NMR spectrum of the isolated complex was not obtained. The  $^1\text{H}$  NMR and  $^{19}\text{F}\{^1\text{H}\}$  NMR spectra were collected in  $\text{CD}_3\text{OD}$ . These are much quicker NMR experiments than  $^{27}\text{Al}$  NMR, and so are less affected by

the poor solubility of the product, despite it precipitating from the NMR solution over a short time period (< 10 min).

The  $^1\text{H}$  NMR spectrum of  $[\text{AlF}_3(\text{L}^1)]$  showed little deviation from the  $^1\text{H}$  NMR spectrum of  $\text{L}^1$  itself, except for a significant difference in the tacn- $\text{CH}_2$  resonances. Rather than a singlet at 3.16 ppm as observed in uncoordinated ligand, this was now present as a broadened multiple (3.21 – 3.09 ppm), characteristic of a *facially*-bound tacn moiety. The  $^{19}\text{F}\{^1\text{H}\}$  NMR spectrum produced a broadened singlet around -174.1 ppm, which is consistent with three equivalent fluoride ligands bound *facially* to a central metal ion, and in a similar range to the  $[\text{AlF}_3(\text{Me}_3\text{-tacn})]$  complex (-176.1 ppm in  $\text{CD}_3\text{CN}$  and -169.9 ppm in  $\text{D}_2\text{O}$ ).<sup>8</sup> This is also in contrast to the  $^{19}\text{F}\{^1\text{H}\}$  spectrum of the  $[\text{AlF}_3(\text{dmsO})(\text{OH}_2)_2]$  precursor, which depicts two sharp resonances in a 2:1 ratio at -173.6 ppm and -177.2 ppm (as opposed to one singlet, in the same solvent).

The reaction of  $[\text{AlF}_3(\text{dmsO})(\text{OH}_2)_2]$  with  $\text{L}^2$  at room temperature overnight resulted in a colourless solution, and no precipitation was observed, unlike the reaction with  $\text{L}^1$ . Removal of the solvent *in vacuo* left a very sticky, oily solid. Subsequent washing with diethyl ether to remove any liberated dmsO and drying *in vacuo* left a white, hygroscopic powdered solid in good yield. The product was partially soluble in  $\text{CD}_3\text{OD}$  and  $\text{D}_2\text{O}$ , more so than  $[\text{AlF}_3(\text{L}^1)]$  – most likely a consequence of the lipophilic isopropyl groups on the pendant arms. However, the limited solubility meant a  $^{27}\text{Al}$  NMR spectrum could not be acquired for the product due to the amount of material required for the experiment.

The  $^1\text{H}$  NMR spectrum shows the expected shifts to higher frequency for the tacn- $\text{CH}_2$  and the pendant arm  $\text{CH}_2$  resonances from those observed in the uncoordinated ligand. The pendant arm  $\text{CH}_2$  resonances (observed as 1:2:1 triplets at 3.17–3.13 and 2.51–2.48 ppm) also become much more resolved in  $\text{CD}_3\text{OD}$ , in comparison to the uncoordinated ligand resonances, which were very broad in the same solvent. However, unlike the multiplet observed for the tacn- $\text{CH}_2$  protons of  $[\text{AlF}_3(\text{L}^1)]$ , the tacn- $\text{CH}_2$  protons of  $[\text{AlF}_3(\text{L}^2)]$  resonate as a broad singlet at 2.94 ppm (a small higher-frequency shift from the ligand at 2.83 ppm). The resonances relating to the isopropyl groups are unchanged, which is as expected given that their chemical environment is largely unaffected by coordination of  $\text{L}^2$  to  $\text{AlF}_3$ .

The  $^{19}\text{F}\{^1\text{H}\}$  NMR spectrum of the product was initially collected in  $\text{CD}_3\text{OD}$ , followed by  $\text{D}_2\text{O}$ . The spectrum obtained from the product in  $\text{CD}_3\text{OD}$  shows a very broad resonance at -195 ppm, which is akin to the chemical shift of the  $[\text{AlF}_4]^-$  anion, except that no six-line coupling pattern is observed. To confirm whether this was  $[\text{AlF}_4]^-$  or a solvent effect, a second  $^{19}\text{F}\{^1\text{H}\}$  spectrum of the product was obtained in  $\text{D}_2\text{O}$ . This showed a significant shift of the very broad resonance present in the  $\text{CD}_3\text{OD}$  sample, to -155 ppm. No peak was observed at -195 ppm. In the  $[\text{AlF}_3(\text{Me}_3\text{-$



tacn)] example, the  $^{19}\text{F}\{^1\text{H}\}$  NMR shifts change by about 7 ppm in  $\text{CD}_3\text{OD}$  vs.  $\text{CD}_3\text{CN}$ , and different shifts are to be expected between different solvents.<sup>8</sup> For  $[\text{AlF}_3(\text{L}^2)]$ , the large shift could be attributed to hydrogen-bonding effects as a result of the amide pendant arms. These values are still within a reasonable range for  $\text{AlF}_3$  complexes, with the fluorine resonances for  $[\text{AlF}_3(\text{BnMe}_2\text{-tacn})]$  appearing at -161.5 [F] and -161.7 [2F] ppm (in  $\text{D}_2\text{O}$ ) in its corresponding  $^{19}\text{F}\{^1\text{H}\}$  NMR.<sup>8</sup> Therefore, these resonances can be attributed to the  $\text{AlF}_3$  moiety of the target complex.

The reaction of  $[\text{AlF}_3(\text{dmsO})(\text{OH}_2)_2]$  and  $\text{L}^3$  in a MeOH solution was carried out with stirring at room temperature overnight. The solvent was concentrated *in vacuo* and diethyl ether was added, precipitating a white solid. This was filtered and dried *in vacuo* to leave a white solid in good yield (67%).

The  $^1\text{H}$  NMR spectrum is indicative of coordination of the macrocycle to the  $\text{AlF}_3$  fragment, with significant changes in multiplicity and chemical shift for the tacn- $\text{CH}_2$  and isopropyl- $\text{CH}_3$  groups. In  $\text{L}^3$ , the tacn- $\text{CH}_2$  protons resonate as two distinct, broad singlets, but when bound, become complex multiplets which have shifted to higher frequency. The isopropyl methyl groups now resonate as two distinct doublets, rather than a single doublet as observed in uncoordinated ligand, indicating that they are now diastereotopic.<sup>33,34</sup> A shift in the amide pendant arm  $\text{CH}_2$  group is observed, from 3.36 ppm in  $\text{L}^3$ , to 3.59 ppm in  $[\text{AlF}_3(\text{L}^3)]$ , as well as the isopropyl CH proton, from 2.91 to 3.36 ppm,  $\text{L}^3$  vs.  $[\text{AlF}_3(\text{L}^3)]$ .

In accordance with the  $[\text{AlF}_3(\text{BnMe}_2\text{-tacn})]$  complex, two  $^{19}\text{F}$  NMR resonances are expected for the lower symmetry  $[\text{AlF}_3(\text{L}^3)]$  complex. These are observed at -155.2 ([F]) and -156.1 ([2F]) ppm in  $\text{CD}_3\text{OD}$ . Although coupling from the  $^{19}\text{F}$  nuclei to the  $^{27}\text{Al}$  nuclei would be expected, this may not be observed due to the quadrupolar nature of  $^{27}\text{Al}$ . Like the  $[\text{AlF}_3(\text{L}^2)]$  complex, the  $^{19}\text{F}\{^1\text{H}\}$  NMR spectra also indicate significant solvent-dependency (with a broad peak observed for the complex, at -196 ppm in  $\text{D}_2\text{O}$ ). No resonance was detected in the  $^{27}\text{Al}$  NMR spectrum, possibly a consequence of the loss of symmetry in the asymmetrically substituted tacn-N donor atoms (this is because asymmetric coordination environments increase the line broadening, in addition to the quadrupolar  $^{27}\text{Al}$  nuclei).<sup>35,36</sup>

#### 4.2.2.2.2 Gallium Trifluoride Complexes

The three gallium trifluoride complexes were analysed using  $^1\text{H}$ ,  $^{19}\text{F}\{^1\text{H}\}$ ,  $^{13}\text{C}\{^1\text{H}\}$  and  $^{71}\text{Ga}$  ( $I = 3/2$ , 39.6%) NMR spectroscopy, and the results are discussed below.

Preliminary reactions of  $[\text{GaF}_3(\text{dmsO})(\text{OH}_2)_2]$  with  $\text{L}^1$  were left to stir at room temperature overnight, and unlike the analogous aluminium complex, no precipitation was observed. Subsequent work-up left the product as a white powdered solid in good yield, which was poorly

soluble in most solvents, except for MeOH. However,  $^1\text{H}$  NMR analysis was indicative of either a second species (e.g. the target product and protonated ligand), or an incomplete reaction (e.g. the target product and unreacted starting material). Hence, to rule out any unreacted starting material and to ascertain the nature of the peaks observed in this initial  $^1\text{H}$  NMR spectra, the progress of the reaction was monitored *via*  $^1\text{H}$  and  $^{19}\text{F}\{^1\text{H}\}$  NMR spectroscopy. NMR data were collected over various time intervals up to 48 hours. The results are shown in Figure 4.5 below. The sharp resonance at 2.65 ppm in the  $^1\text{H}$  NMR spectrum of  $[\text{GaF}_3(\text{L}^1)]$  ( $\text{CD}_3\text{OD}$ ) can be assigned to uncoordinated dmso in the  $\text{CD}_3\text{OD}$  solution containing the reaction mixture. It is important to note that although not shown, the  $^{19}\text{F}\{^1\text{H}\}$  NMR spectra depicted resonances at around -155 ppm (relating to  $[\text{HF}_2]^-$ ), and around -130 ppm (relating to  $\text{F}^-$ ). Both are commonly observed by-products in  $^{19}\text{F}\{^1\text{H}\}$  NMR spectra of metal fluoride complexes.<sup>37</sup>

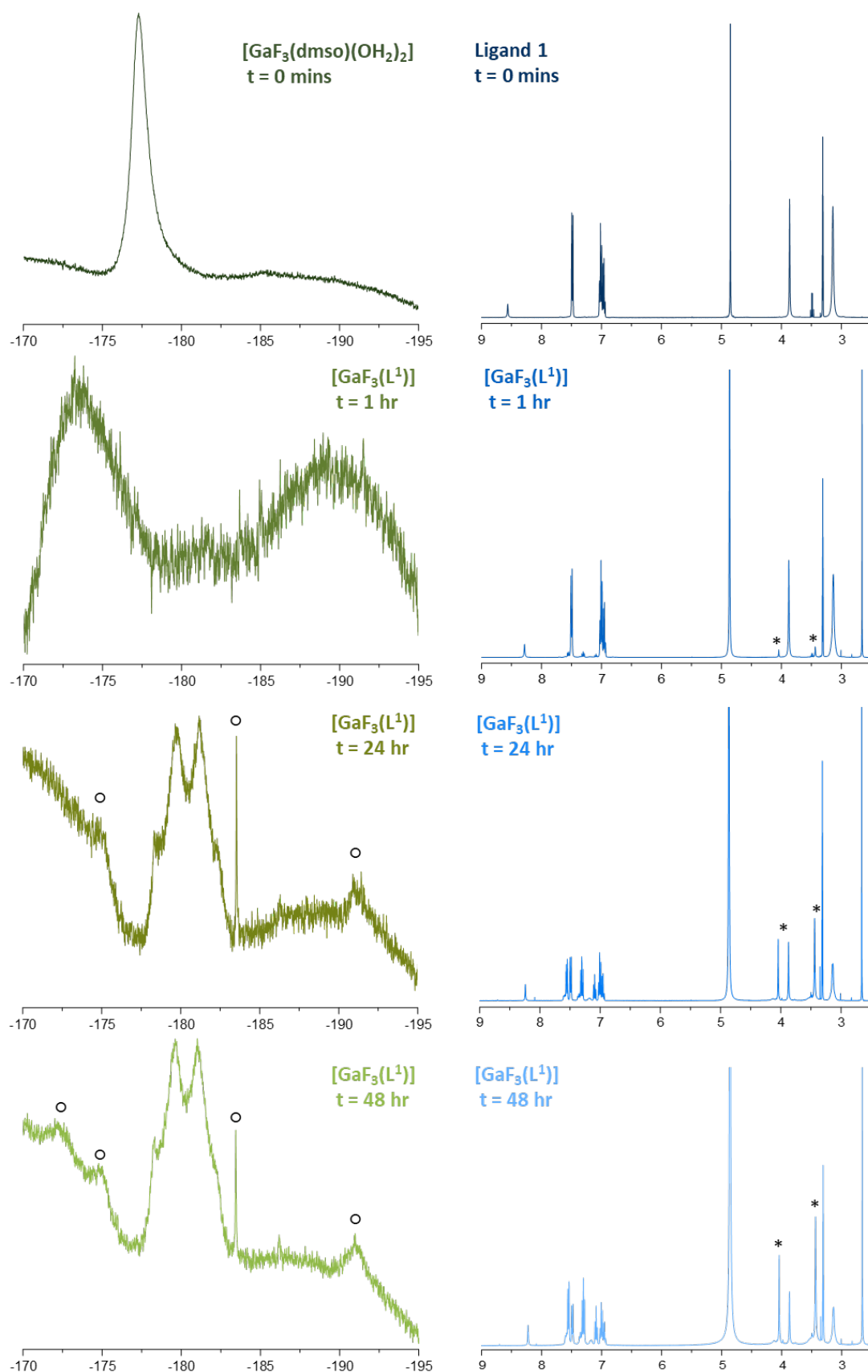


Figure 4.5 –  $^{19}\text{F}\{^1\text{H}\}$  (left; green) and  $^1\text{H}$  NMR (right; blue) spectra of the reaction of  $[\text{GaF}_3(\text{dmsO})(\text{OH}_2)_2]$  with  $\text{L}^1$  taken at time intervals 0, 1, 24 and 48 h ( $\text{CD}_3\text{OD}$ ). Impurities in the  $^{19}\text{F}\{^1\text{H}\}$  spectra are annotated with a 'o'. The rolling baseline in the  $^{19}\text{F}\{^1\text{H}\}$  NMR spectra is due to Teflon in the probe.

After 1 h, the  $^{19}\text{F}\{^1\text{H}\}$  NMR spectrum shows a complete loss of the broad singlet at -177 ppm corresponding to the  $[\text{GaF}_3(\text{dmsO})(\text{OH}_2)_2]$  precursor. New but very minor resonances (\*) are observed in the  $^1\text{H}$  NMR spectrum alongside the resonances which coincide with uncoordinated  $\text{L}^1$ . These may represent the target  $[\text{GaF}_3(\text{L}^1)]$  complex that is beginning to form. After 24 h, these smaller peaks increase in intensity considerably, and the ligand resonances become relatively weaker. The  $^{19}\text{F}\{^1\text{H}\}$  NMR spectrum also shows the growth of a new  $\text{GaF}_3$  species, with a broad resonance observed around -180 ppm. This is on par with similar  $\text{GaF}_3$  complexes reported in the literature. For example, the  $[\text{GaF}_3(\text{Me}_3\text{-tacn})]$  and  $[\text{GaF}_3(\text{Bn-NODA})]$  complexes each produce a broad  $^{19}\text{F}\{^1\text{H}\}$  resonance at -181 ppm ( $\text{CD}_2\text{Cl}_2$ ) and -185 ppm, respectively.<sup>8,4</sup> After 48 h, the  $^1\text{H}$  NMR spectrum shows the new species as the major product, although some ligand is still present, which proved to be difficult to separate from the target complex. The  $^{19}\text{F}\{^1\text{H}\}$  NMR spectrum is mostly unchanged, although some minor impurities appear more pronounced (annotated with a 'o'). These are likely to be a result of the length of time of the reaction. Stability studies of this complex (in water, varying pH, etc.) could not be carried out due to the limited solubility.

Using an alternative method, the reaction solution was gently heated to 60 °C for 4 h to promote full conversion of the starting materials to the final product, and to minimise the formation of by-products and impurities, such as  $[\text{GaF}_4]^-$  or hydrolysed/protonated ligand. Figure 4.6 shows the  $^{19}\text{F}\{^1\text{H}\}$  and  $^1\text{H}$  NMR spectra of the final isolated product. The  $^1\text{H}$  NMR spectrum shows resonances for the target  $[\text{GaF}_3(\text{L}^1)]$  complex only. A very broad resonance is observed in the  $^{19}\text{F}\{^1\text{H}\}$  NMR spectra at around -180 ppm, caused by two overlapping, partially resolved *pseudo*-quartets, arising from the coupling of the three *fac*  $^{19}\text{F}$  atoms to both the  $^{69}\text{Ga}$  and  $^{71}\text{Ga}$  NMR-active nuclei (each of which has  $I = 3/2$ ), respectively, in the approximately  $\text{C}_{3v}$  symmetry molecules. The appearance of the multiplicity in the solution phase reflects on the high-symmetry of the complex, which generates a small electric field gradient and allows the coupling interaction to be observed.

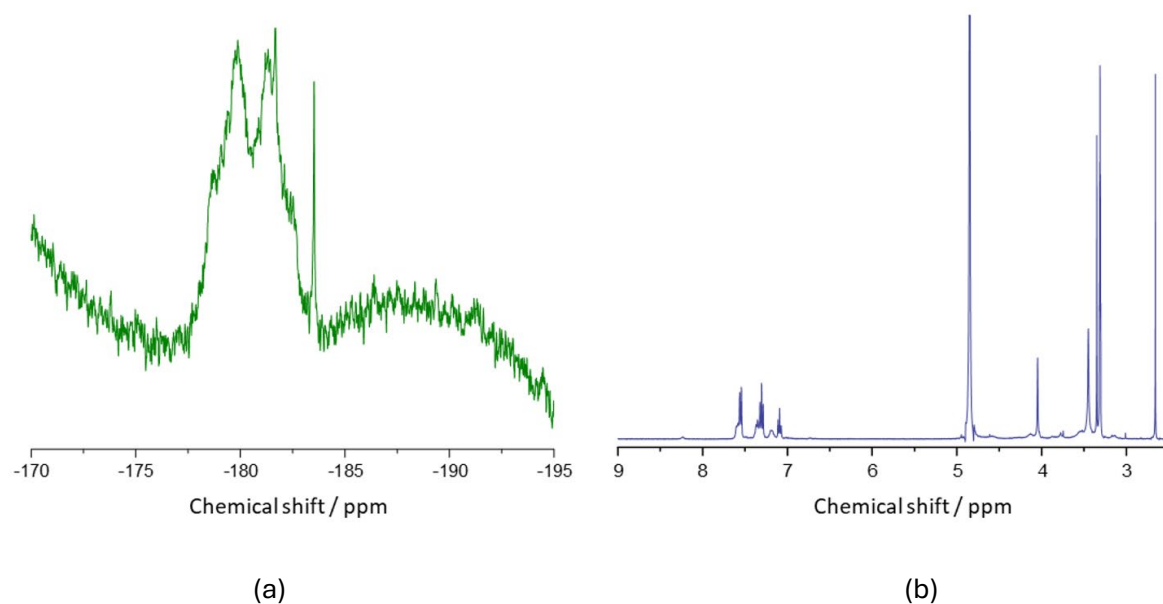


Figure 4.6 – (a)  $^{19}\text{F}\{^1\text{H}\}$  (298 K, 376 MHz) and (b)  $^1\text{H}$  NMR spectra of  $[\text{GaF}_3(\text{L}^1)]$  ( $\text{CD}_3\text{OD}$ ).

The isolated product from the reaction of  $[\text{GaF}_3(\text{dmsO})(\text{OH}_2)_2]$  with  $\text{L}^2$  (48 h at room temperature) was also shown to have a similar  $^{19}\text{F}\{^1\text{H}\}$  NMR spectrum, with a very broadened multiplet at -178.2 ppm. Again, this is in line with previously reported  $\text{GaF}_3$  triazacyclononane complexes.<sup>8,4</sup> For both complexes, the coupling is also observed in their respective  $^{71}\text{Ga}$  NMR spectra (Figure 4.7), which both show a broadened 1:3:3:1 quartet around 40 ppm, where  $^1J_{^{71}\text{Ga}-^{19}\text{F}}$  is approximately equal to 510 or 520 Hz. These values are within the expected ranges for  $\text{GaF}_3$ -tacn complexes;  $[\text{GaF}_3(\text{Me}_3\text{-tacn})]$ , 42.0 ppm ( $^1J_{^{71}\text{Ga}-^{19}\text{F}} = 490$  Hz) and  $[\text{GaF}_3(\text{BnMe}_2\text{-tacn})]$ , 44.8 ( $^1J_{^{71}\text{Ga}-^{19}\text{F}} = 445$  Hz).<sup>8</sup>

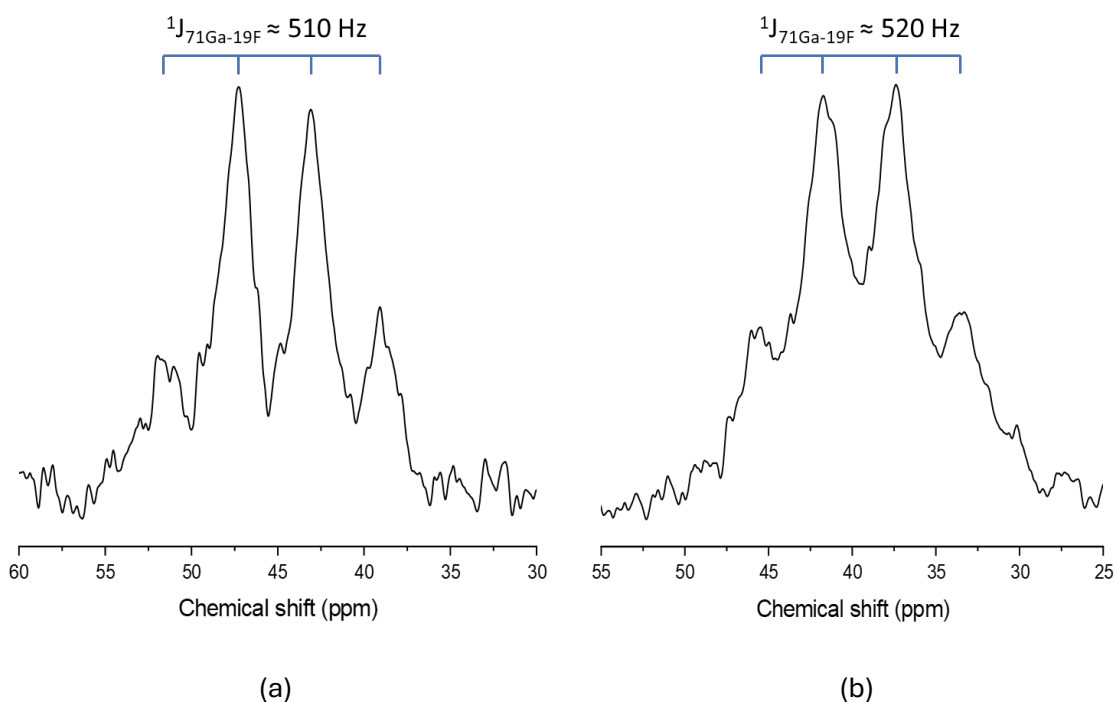


Figure 4.7 –  $^{71}\text{Ga}$  NMR spectra (298 K, 122 MHz) of (a)  $[\text{GaF}_3(\text{L}^1)]$ ,  $^1J_{^{71}\text{Ga}-^{19}\text{F}} = 510$  Hz and (b)  $[\text{GaF}_3(\text{L}^2)]$ ,  $^1J_{^{71}\text{Ga}-^{19}\text{F}} = 520$  Hz. Both spectra show the expected 1:3:3:1 quartet arising from the coupling of the three fac  $^{19}\text{F}$  atoms to the quadrupolar  $^{71}\text{Ga}$  nucleus.

The  $^1\text{H}$  NMR spectrum of  $[\text{GaF}_3(\text{L}^2)]$  showed the expected changes in the resonances of the tacn- $\text{CH}_2$  protons and pendant arm  $\text{CH}_2$  protons when compared to the uncoordinated ligand. The tacn- $\text{CH}_2$  resonance appears to be split over two adjacent multiplets (3.16–3.06 and 2.88–2.76 ppm), each with an integral of six protons. Both sets of protons for each of the  $\text{CH}_2$  groups of the pendant arms have shifted to higher frequency, from 2.91 ppm in  $\text{L}^2$  to 3.42–3.38 ppm (of the complex), and 2.38–2.34 ppm in  $\text{L}^2$ , to 2.53–2.49 ppm (of the complex).

The  $[\text{GaF}_3(\text{L}^3)]$  complex was synthesised in the same manner as described for the  $[\text{AlF}_3(\text{L}^3)]$  complex above, *via* the direct reaction of  $[\text{GaF}_3(\text{dmsO})(\text{OH}_2)_2]$  and  $\text{L}^3$  in a MeOH solution with stirring at room temperature overnight. After work-up, the product was isolated as a white powder in good yield (61%).

The  $^1\text{H}$  NMR spectrum shows similar changes from uncoordinated ligand observed in the analogous  $[\text{AlF}_3(\text{L}^3)]$  complex. Resonances at -171.5 ([2F]) and -172.3 ppm ([F]) are observed in the  $^{19}\text{F}\{^1\text{H}\}$  NMR spectrum ( $\text{CD}_3\text{OD}$ ), although the F–F couplings may be lost in the line widths. It may also result from the complex being dynamic at room temperature, with a rapid exchange of the three fluoride ligands in solution. This shift is very similar to that observed for  $[\text{GaF}_3(\text{BnMe}_2\text{-tacn})]$ , in which the  $\text{GaF}_3$  environment gave rise to a broad singlet at -172.8 ppm. In this case, the two expected resonances for the inequivalent  $^{19}\text{F}$  nuclei were likely obscured by the broad nature of the resonance due to the quadrupolar gallium nuclei. The  $^1\text{H}$  and  $^{19}\text{F}\{^1\text{H}\}$  NMR spectra

for the  $[\text{GaF}_3(\text{L}^3)]$  complex are given in Figure 4.8. No  $^{71}\text{Ga}$  NMR resonance was observed for  $[\text{GaF}_3(\text{L}^3)]$ , possibly due to fast quadrupolar relaxation in the lower symmetry species.

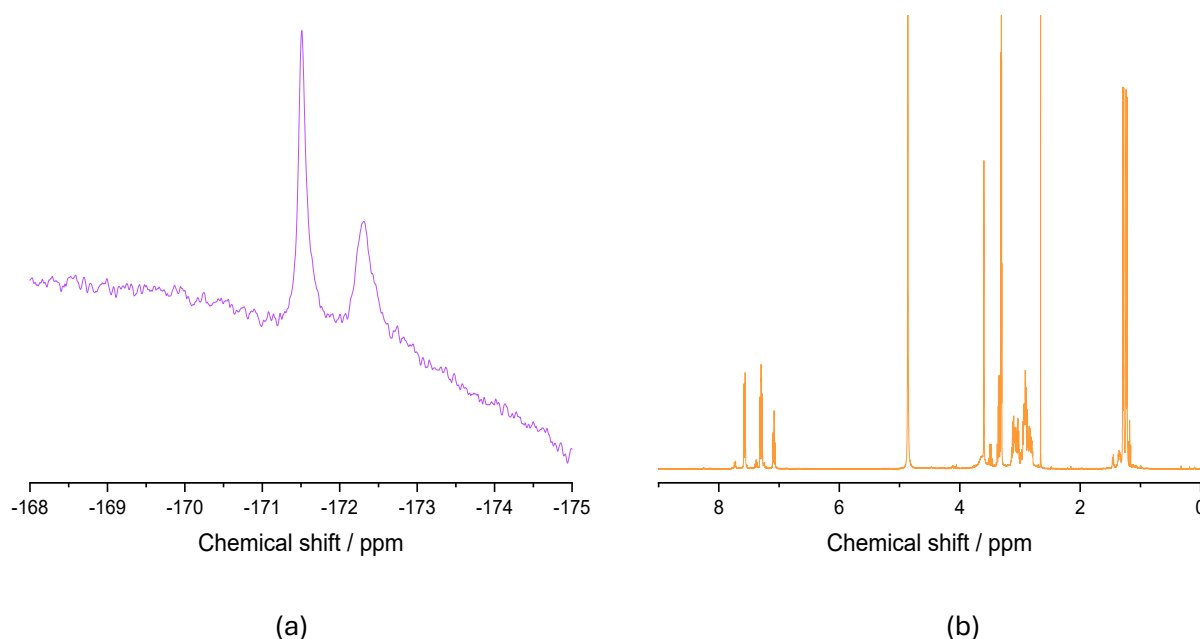


Figure 4.8 – (a)  $^{19}\text{F}\{^1\text{H}\}$  (298 K, 376 MHz) and (b)  $^1\text{H}$  NMR spectra of  $[\text{GaF}_3(\text{L}^3)]$  ( $\text{CD}_3\text{OD}$ ).

With fewer aromatic substituents,  $[\text{GaF}_3(\text{L}^3)]$  displayed improved solubility compared to the  $\text{L}^1$  analogue. Stability studies of the complex in aqueous conditions were conducted and analysed *via*  $^{19}\text{F}\{^1\text{H}\}$  NMR spectroscopy. The spectrum obtained immediately after sample preparation gave a broad resonance at -152.4 ppm (and some free fluoride at around -120 ppm). The shift in resonance – when comparing the spectra obtained in  $\text{CD}_3\text{OD}$  to  $\text{D}_2\text{O}$  – is not dissimilar to that observed for  $[\text{AlF}_3(\text{L}^2)]$  and is likely a consequence of hydrogen bonding. No change in the  $^{19}\text{F}\{^1\text{H}\}$  NMR spectrum was observed after 4 h, indicating the  $\text{GaF}_3$  moiety remains intact under aqueous conditions.

#### 4.2.2.2.3 Attempted Formation of Indium Trifluoride Complexes

For the reactions involving  $[\text{InF}_3(\text{dmsO})(\text{OH}_2)_2]$  with the ligands  $\text{L}^1$ ,  $\text{L}^2$ , and  $\text{L}^3$ , none of the isolated products appeared to contain a pure and single species which was identifiable as the target complex, despite varying the reaction conditions (time and temperature). Instead, in all cases, the obtained NMR spectra of the final isolated products indicated multiple species were present as a mixture. This may be a consequence of the weaker M–F bonds present in the  $\text{In}^{3+}$  species compared to  $\text{Al}^{3+}$  and  $\text{Ga}^{3+}$ , resulting in competition for coordination to  $\text{In}^{3+}$  of one or more amide pendant groups and loss of  $\text{F}^-$ .

However, the  $^{19}\text{F}\{^1\text{H}\}$  NMR spectrum of the product isolated from the reaction involving  $\text{L}^2$  suggests a new  $\text{InF}_3$  species forms, with a very broad peak around -198 ppm. The  $\text{InF}_3$  complexes

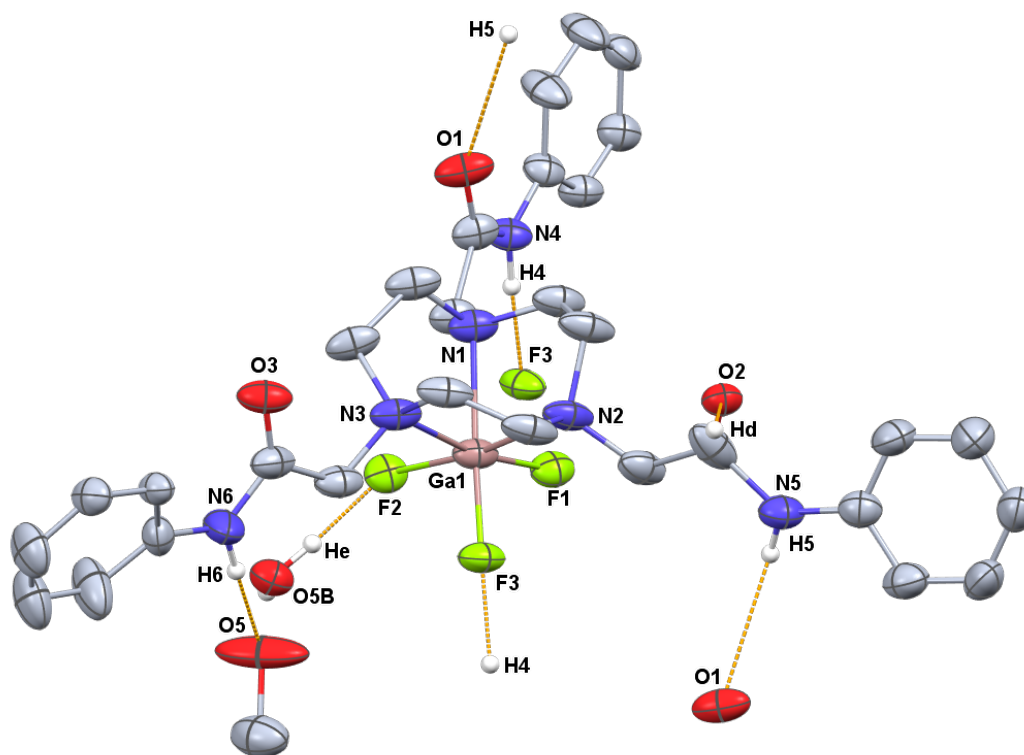
of Me<sub>3</sub>-tacn and BnMe<sub>2</sub>-tacn are also reported to have broad resonances in their respective <sup>19</sup>F[<sup>1</sup>H] NMR spectra, at a lower frequency than the analogous AlF<sub>3</sub> and GaF<sub>3</sub> complexes.<sup>8</sup> These appear between -190 and -220 ppm, depending on the NMR solvent. There is also a smaller broad peak at -202 ppm, again indicating a mix of species. It also gave evidence of a significant loss of fluoride, with a large, sharp peak at -130 ppm. Slow evaporation of the NMR solvent (CD<sub>3</sub>OD) later led to the formation of suitable crystals for SCXRD, which confirmed the target species, [InF<sub>3</sub>(L<sup>2</sup>)] was formed – this will be discussed in further detail below. However, SCXRD is not always representative of the bulk material, and it is likely that the [InF<sub>3</sub>(L<sup>2</sup>)] complex preferentially crystallises from the solution instead of any other (unknown) byproducts.

#### 4.2.3 Molecular Structures of [GaF<sub>3</sub>(L<sup>1</sup>)], [InF<sub>3</sub>(L<sup>2</sup>)], [GaF<sub>3</sub>(L<sup>3</sup>)] and [FeF<sub>3</sub>(L<sup>3</sup>)] and Hydrogen Bonding Interactions

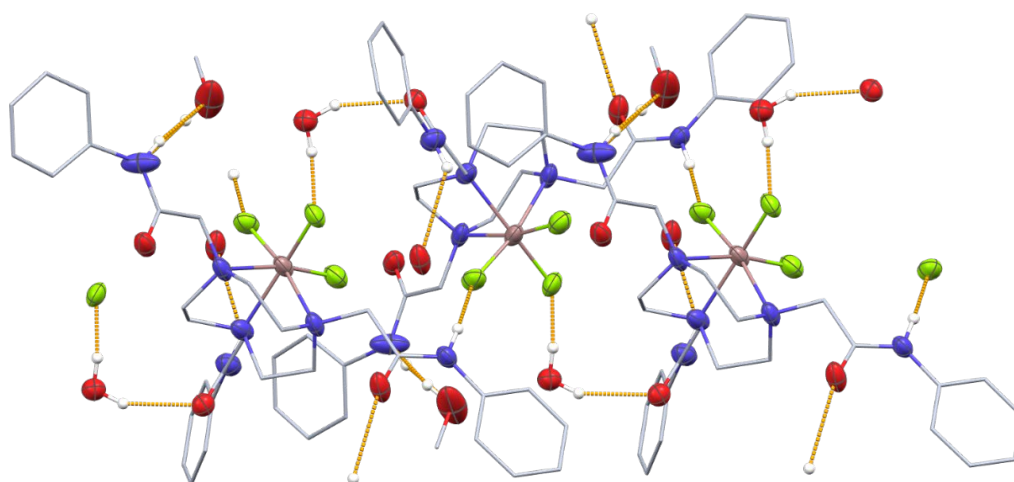
Single-crystal X-ray analyses further confirmed the molecular structures and the nature and extent of hydrogen bonding present in [GaF<sub>3</sub>(L<sup>1</sup>)]·1.5MeOH·0.5H<sub>2</sub>O, [InF<sub>3</sub>(L<sup>2</sup>)], [GaF<sub>3</sub>(L<sup>3</sup>)] and [FeF<sub>3</sub>(L<sup>3</sup>)].

Crystals of [GaF<sub>3</sub>(L<sup>1</sup>)]·1.5MeOH·0.5H<sub>2</sub>O were obtained *via* the vapour diffusion of diethyl ether into a methanol solution containing the product. The crystal forms in the monoclinic *P*2<sub>1</sub>/*n* space group, and the structure (Figure 4.9a) shows the central Ga<sup>3+</sup> atom in a distorted octahedral coordination environment. Like the transition metal complexes described in Chapter 3, and other triazacyclononane complexes, the tridentate tacn ring occupies one face of the metal centre (Ga-N1 = 2.157(2), Ga-N2 = 2.162(2), Ga-N3 = 2.165(3) Å). However, where it was shown previously that the amide pendant arms may act as donors towards a metal centre, the three *facial* fluorides are now instead situated *trans* to the amine N-donor atoms (Ga-F1 = 1.8287(18), Ga-F2 = 1.8487(17), Ga-F3 = 1.8493(16) Å). The amide pendant arms are positioned as far from each other as possible to minimise steric repulsion. The structure is disordered, with two distinct forms modelled (each with 50% occupancy) displaying different orientations for one of the pendant amide arms (at the carboxamide carbon) and for one of the phenyl rings in another. For the amide(NH) group of the disordered pendant arm, the two different orientations mean it is only engaged in hydrogen-bonded interactions 50% of the time. The hydrogen-bonded component is shown below, where hydrogen bonding is evident between an amide(NH) group and a lattice water molecule, or the fluoride ligands in an adjacent molecule. This forms an extended network of 1D chains, as shown in Figure 4.9b.





(a)

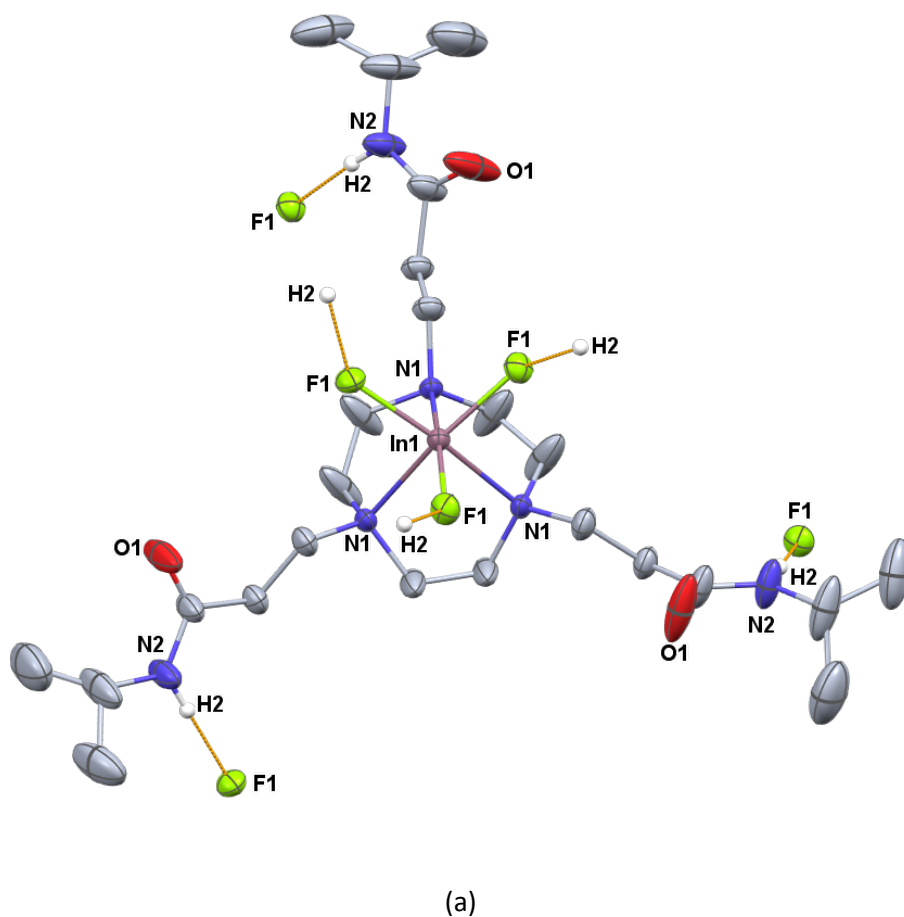


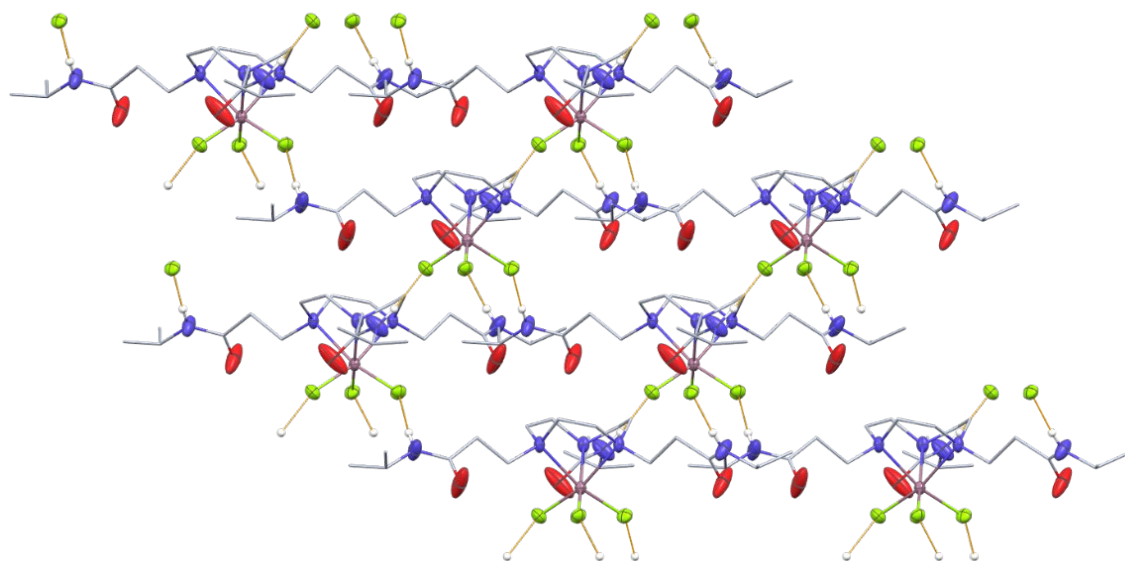
(b)

Figure 4.9 – (a) View of the structure of the component of  $[\text{GaF}_3(\text{L}^1)] \cdot \text{MeOH} \cdot 0.5\text{H}_2\text{O}$ , showing the atom numbering scheme and H-bonding between amide  $\text{NH} \cdots \text{F}$  and lattice  $\text{H}_2\text{O}/\text{MeOH} \cdots \text{F}$ . Ellipsoids are drawn at the 50% probability level and H and solvent atoms (except those involved in H-bonding) are omitted for clarity. (b) View of part of the H-bonded extended structure showing the 1D chain formed via intermolecular  $\text{F} \cdots \text{H-N}$  interactions ( $\text{F2} \cdots \text{H4N4} = 1.758 \text{ \AA}$ ,  $\text{F3} \cdots \text{H}_2\text{O} = 1.695 \text{ \AA}$ ).

As previously mentioned, crystals of  $[\text{InF}_3(\text{L}^2)]$  were grown *via* the slow evaporation of a  $\text{CD}_3\text{OD}$  solution containing the product mixture. The obtained structure (Figure 4.10a) shows it to crystallise in the trigonal space group  $R\bar{3}c$ , with three-fold crystallographic symmetry. Like the

[GaF<sub>3</sub>(L<sup>1</sup>)] complex, the indium(III) metal centre is in a distorted octahedral environment, with three *facial* fluorides and the three N-donor atoms from the tacn ring, d(In-F) = 2.071(2), d(In-N) = 2.299(3) Å. The F-In-F angles are 97.99(8)°, while the N-In-N angles involving the macrocycle are much more acute (78.04(10)°). Disorder was modelled for the pendant arm isopropyl groups – to be expected with free rotation of the group around the central carbon atom. The pendant amide groups – in this case, with the amide groups extended further from the macrocyclic amine functions by the extra CH<sub>2</sub> unit – are not involved in coordination to the metal centre. However, they each form one intermolecular N-H...F H-bond, d(N...F) = 1.888 Å, to an adjacent molecule. Figure 4.10b depicts the hydrogen-bonded network of [InF<sub>3</sub>(L<sup>2</sup>)] as viewed down the *a*-axis, which forms two-dimensional sheets.





(b)

Figure 4.10 – (a) View of the structure of  $[\text{InF}_3(\text{L}^2)]$  showing the atom numbering scheme and H-bonding between amide NH and F ligands. Ellipsoids are drawn at the 50% probability level and H atoms (except those involved in H-bonding) are omitted for clarity; (b) View down the a-axis showing the intermolecular  $\text{F1} \cdots \text{H2N2}$  hydrogen bonding contacts (1.888 Å).

Crystals of  $[\text{GaF}_3(\text{L}^3)]$  and  $[\text{FeF}_3(\text{L}^3)]$  were both grown *via* the slow evaporation of a solvent/solvent mix containing the product. Single-crystal structural data shows both complexes to be isostructural, crystallising in the  $R\bar{3}$  space group (Figure 4.11a,  $[\text{GaF}_3(\text{L}^3)]$  and Figure 4.11b,  $[\text{FeF}_3(\text{L}^3)]$ ). Each complex shows *fac*-tridentate coordination of  $\text{L}^3$  to the metal ion *via* its tacn N(amine) donor atoms, with the three fluoride ligands occupying the other face and giving a distorted octahedral species. Both complexes form weakly-associated ‘head-to-tail’ H-bonded dimers *via* hydrogen bonding from the amide NH group in one molecule, with one F atom in the second molecule ( $\text{M} = \text{Ga}$ :  $\text{F} \cdots \text{HN}$  distance = 1.769 Å;  $\text{M} = \text{Fe}$ :  $\text{F} \cdots \text{HN}$  distance = 1.787 Å).

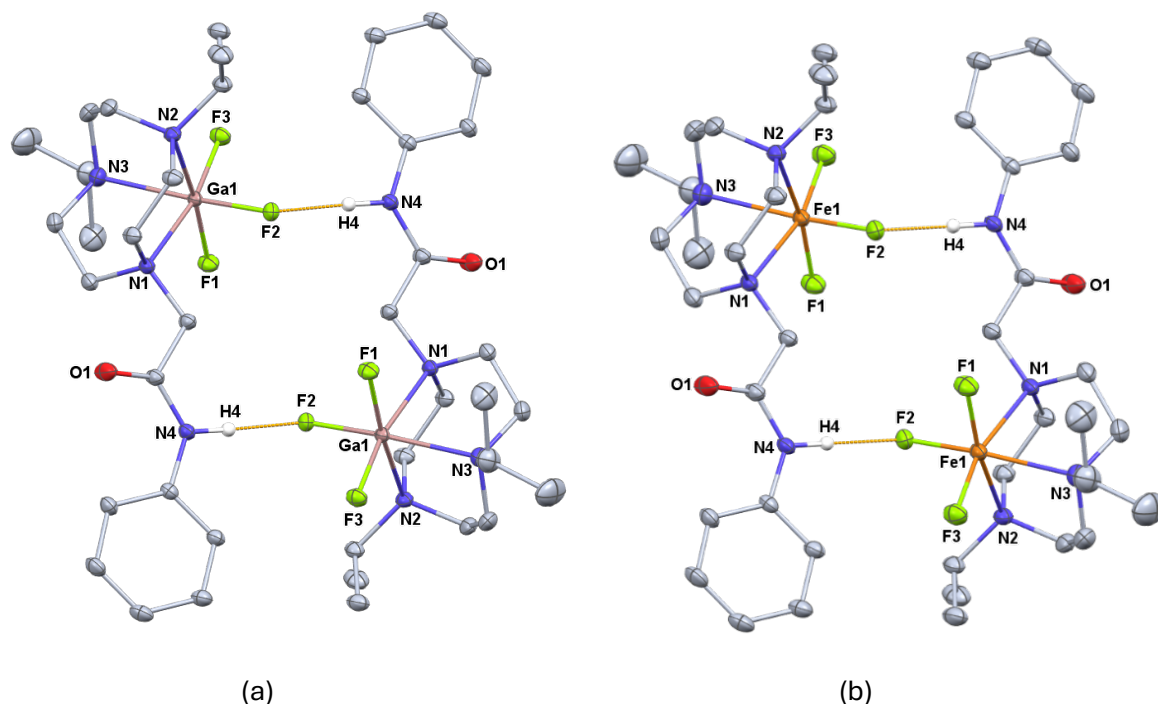


Figure 4.11 – View of the isostructural metal complexes present in (a)  $[\text{GaF}_3(\text{L}^3)]$  and (b)  $[\text{FeF}_3(\text{L}^3)]$ , showing the atom numbering schemes and the intermolecular ‘head-to-tail’  $\text{F2} \cdots \text{H4-N4}$  hydrogen bonding interactions ( $M = \text{Ga}$ , 1.769 Å;  $M = \text{Fe}$ , 1.787 Å), giving weakly associated dimers. Ellipsoids are drawn at the 50% probability level and H and atoms (excluding those involved in H-bonding) are omitted for clarity.

The extended structures of each complex show that the dimer units are arranged in a hexagonal ‘windmill’-like array when viewed down the c-axis (Figure 4.12). Unlike the literature examples involving porphyrins, the supramolecular assembly of these complexes appears to be held only by hydrogen-bonding interactions; no overlap of the  $\pi$ -orbitals of the phenyl rings is observed.<sup>21</sup> Two closely related compounds,  $[\text{FeF}_3(\text{BnMe}_2\text{-tacn})]$  and  $[\text{FeF}_3(\text{terpy})]$ , were also observed to form  $\pi$ -stacking interactions, in addition to hydrogen-bonding (from fluoride ligands to lattice water molecules), in their respective extended structures.<sup>12</sup>

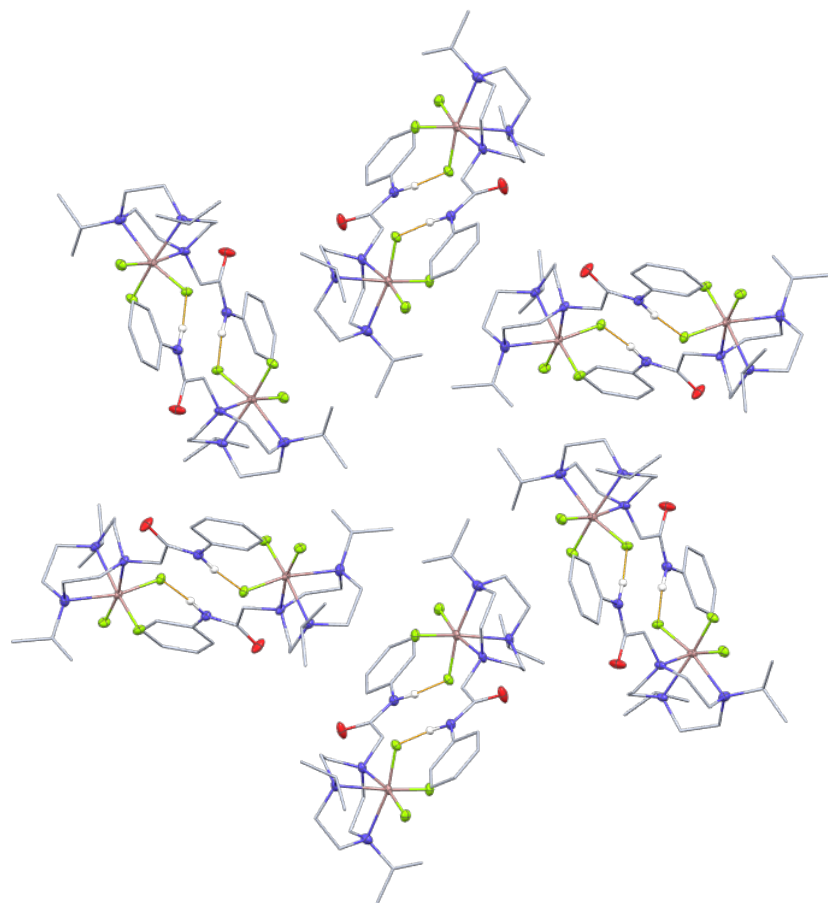


Figure 4.12 – View of part the structure of  $[\text{GaF}_3(\text{L}^3)]$  viewed down the  $c$ -axis showing the hexagonal arrangement adopted by the weakly associated dimers (the same arrangement is present in  $[\text{FeF}_3(\text{L}^3)]$ ).

However, the  $[\text{GaF}_3(\text{L})]$  complex reported by Penkert *et al.*<sup>23</sup> (mentioned in Section 4.1.1) bears some resemblance. Their triazacyclononane ligand, 'L', also contains hydrophobic alkyl substituents in the way of *tert*-butyl groups, not dissimilar to the isopropyl groups of  $\text{L}^3$ , and forms a dimer held together only by van der Waals forces. These created a cavity accessible by solvent MeOH molecules. Similarly, the supramolecular arrangement of  $[\text{GaF}_3(\text{L}^3)]$  leaves solvent-accessible voids in the lattice. This contained disordered  $\text{H}_2\text{O}$ , which was modelled using a solvent mask and is consistent with *ca.* 0.067 and 2.4  $\text{H}_2\text{O}$  molecules per unit cell for the Ga and Fe species, respectively. These voids can be seen in Figure 4.13. This view (down the  $b$ -axis, and slightly offset from) shows that the material is not truly porous, as the view down the  $c$ -axis may suggest. However, the complexes were found to be highly hygroscopic, with the powders and crystals rapidly becoming sticky upon exposure to air over a few minutes.

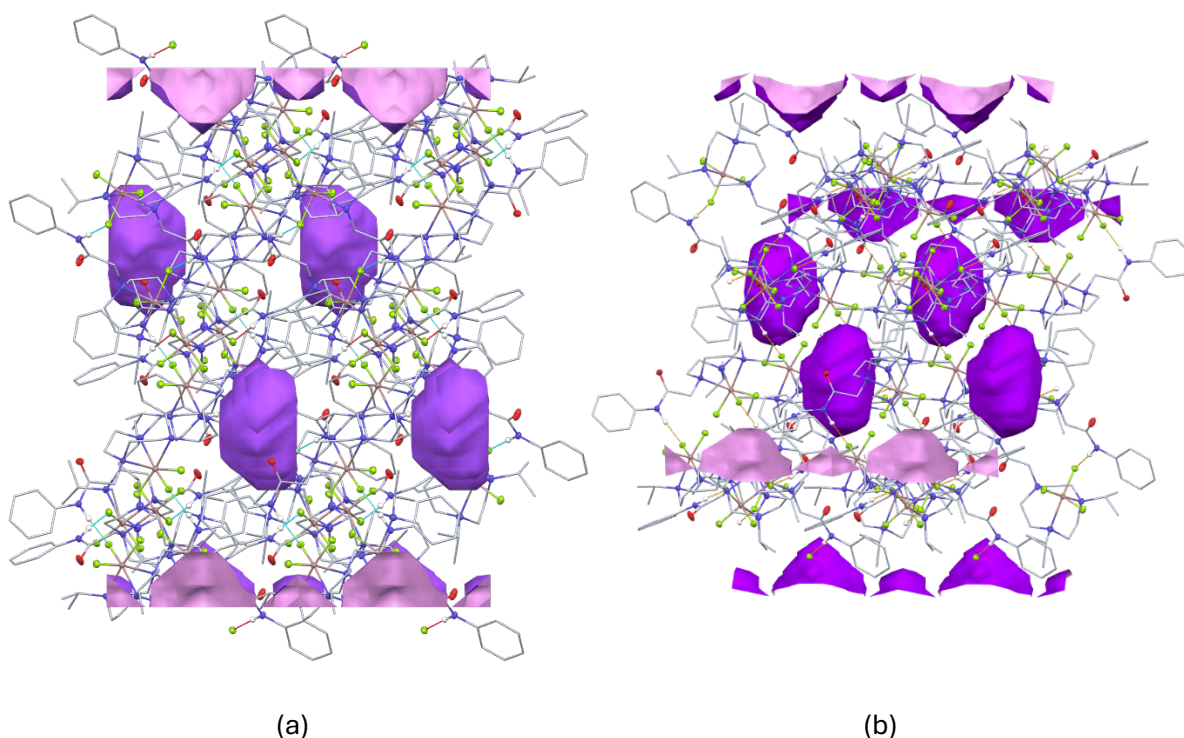


Figure 4.13 – View of  $[\text{GaF}_3(\text{L}^3)]$  down (a) the b-axis and (b) offset from the b-axis, depicting the solvent-accessible voids. Void diameter = 2.4 Å.

#### 4.2.3.1 Summary of the SCXRD Structural Parameters for the $[\text{MF}_3(\text{L}^n)]$ Complexes

The M–N and M–F bond lengths (Å) and bond angles (°) gathered from the SCXRD data above are given in Table 4.2 below. These values are in good agreement with those previously reported for the crystal structures of Ga, In and Fe complexes, with  $\text{Me}_3\text{-tacn}$  and  $\text{BnMe}_2\text{-tacn}$ .<sup>8,12</sup> In accordance with their respective ionic radii (and bond dissociation enthalpies), the In–F bond length (2.071(2) Å) observed in the  $[\text{InF}_3(\text{L}^2)]$  complex is significantly longer (ca. 12%) than the average bond lengths observed for Ga–F (1.842 Å) and Fe–F (1.826 Å) in the  $\text{L}^1$  and  $\text{L}^3$  complexes.<sup>38,39</sup> There is a negligible difference between the gallium complexes of  $\text{L}^1$  and  $\text{L}^3$ , and between the gallium/iron complexes of  $\text{L}^3$ . As mentioned above, the N–In–N bond angle is more acute in comparison to the other complexes, which reflects on the elongated In–N bond distance.

Table 4.2 – Summary of the bond lengths (Å) and bond angles (°) given by the SCXRD data for  $[\text{GaF}_3(\text{L}^1)] \cdot 1.5\text{MeOH} \cdot 0.5\text{H}_2\text{O}$ ,  $[\text{InF}_3(\text{L}^2)]$ ,  $[\text{GaF}_3(\text{L}^3)] \cdot 0.067\text{H}_2\text{O}$  and  $[\text{FeF}_3(\text{L}^3)] \cdot 2.4\text{H}_2\text{O}$ .

Complex	M–N Bond Lengths / Å	M–F Bond Lengths / Å	M–N Bond Angles / °	M–F Bond Angles / °
<b><math>[\text{GaF}_3(\text{L}^1)] \cdot 1.5\text{MeOH} \cdot 0.5\text{H}_2\text{O}</math></b>	Ga–N1: 2.157(2)	Ga–F1: 1.8287(18)	N1–Ga–N2: 82.80(9)	F2–Ga–F1: 96.23(8)
	Ga–N2: 2.162(2)	Ga–F2: 1.8487(17)	N1–Ga–N3: 82.30(9)	F3–Ga–F1: 96.31(8)
	Ga–N3: 2.165(3)	Ga–F3: 1.8493(16)	N2–Ga–N3: 81.86(11)	F2–Ga–F3: 96.23(8)
<b><math>[\text{InF}_3(\text{L}^2)]</math></b>	In–N1: 2.299(3)	In–F1: 2.071(2)	N1–In–N1: 78.04(10)	F1–In–F1: 97.99(8)
<b><math>[\text{GaF}_3(\text{L}^3)] \cdot 0.067\text{H}_2\text{O}</math></b>	Ga–N1: 2.1674(4)	Ga–F1: 1.8392(3)	N1–Ga–N2: 82.582(14)	F2–Ga–F1: 93.541(13)
	Ga–N2: 2.2007(4)	Ga–F2: 1.8613(3)	N1–Ga–N3: 81.818(15)	F3–Ga–F1: 95.564(12)
	Ga–N3: 2.2057(4)	Ga–F3: 1.824(3)	N2–Ga–N3: 82.448(15)	F2–Ga–F3: 98.067(12)
<b><math>[\text{FeF}_3(\text{L}^3)] \cdot 2.4\text{H}_2\text{O}</math></b>	Fe–N1: 2.2643(10)	Fe–F1: 1.8446(7)	N1–Fe–N2: 80.04(4)	F1–Fe–F2: 101.01(3)
	Fe–N2: 2.2668(10)	Fe–F2: 1.8824(7)	N1–Fe–N3: 79.47(4)	F1–Fe–F3: 97.95(3)
	Fe–N3: 2.2328(9)	Fe–F3: 1.8605(7)	N2–Fe–N3: 80.06(3)	F2–Fe–F3: 94.91(3)

### 4.3 Conclusions

This chapter has demonstrated that the neutral  $[\text{MF}_3(\text{L}^n)]$  complexes ( $\text{M} = \text{Al}, \text{Ga}, \text{Fe}$  and  $\text{L}^n = \text{L}^1, \text{L}^2$  and  $\text{L}^3$ ) can be accessed directly and in good yield, from the molecular Group 13  $\text{MF}_3$  precursor  $[\text{MF}_3(\text{dmsO})(\text{OH}_2)_2]$ , without the need for harsh hydrothermal conditions. Attempts to form the  $[\text{FeF}_3(\text{L}^n)]$  complexes *via* refluxing  $\text{FeF}_3 \cdot 3\text{H}_2\text{O}$  with the ligands in *n*-BuOH (120 °C) further highlighted the instability of the ligands at elevated temperatures. Instead, these were formed by refluxing in EtOH (80 °C) over a shorter time period. The complexes were fully characterised using IR and NMR spectroscopy, ESI<sup>+</sup> MS, elemental analysis, and SCXRD, which confirmed that the target products were formed and were consistent with the literature on similar complexes. The complexes showed the expected trends in solubility. For example, complexes of  $\text{L}^1$  were poorly soluble in all conventional solvents (except for methanol), whereas complexes of  $\text{L}^3$  were readily soluble in most, probably due to the inclusion of lipophilic isopropyl groups.

Reactions of  $\text{L}^n$  with  $[\text{InF}_3(\text{dmsO})(\text{OH}_2)_2]$  resulted in the isolation of a mixture of species, as evidenced by complicated and undiscernible  $^1\text{H}$  and  $^{19}\text{F}\{^1\text{H}\}$  NMR spectra. In the case of  $[\text{InF}_3(\text{L}^2)]$ , slow evaporation of the NMR solvent produced a few small crystals, which confirmed that the target product had been formed. However, the  $^1\text{H}$  and  $^{19}\text{F}\{^1\text{H}\}$  NMR spectra indicated the presence of at least one other indium species. Comparison of the In–F and Ga–F/Fe–F bond lengths from SCXRD structural data also showed that, as expected, the In–F bond was significantly longer and, therefore, weaker. This may explain why several species were isolated in attempts to form the indium complexes – the In–F bond may have been displaced by a coordinating amide arm, for example. Significant loss of fluoride is also evident in the  $[\text{InF}_3(\text{L}^2)]$   $^{19}\text{F}\{^1\text{H}\}$  NMR spectrum.

SCXRD data of  $[\text{GaF}_3(\text{L}^1)]$ ,  $[\text{GaF}_3(\text{L}^3)]$  and  $[\text{FeF}_3(\text{L}^3)]$  and  $[\text{InF}_3(\text{L}^2)]$  showed, in all cases, that the metals were in a distorted octahedral coordination environment, with the tacn(N) and three fluoride ligands bound *facially*. Unlike the transition metal complexes of  $\text{L}^1$  and  $\text{L}^2$  described in Chapter 3, the ligands provided an  $\text{N}_3$  coordination sphere, and all pendant arms remained unbound. The amide(NH) functions were involved in either intra- or inter-molecular hydrogen bonding to fluoride ligands (or lattice solvent).  $[\text{GaF}_3(\text{L}^1)]$  was shown to form an extended three-dimensional hydrogen-bonded network.  $[\text{InF}_3(\text{L}^2)]$  formed two-dimensional, hydrogen-bonded sheets.  $[\text{GaF}_3(\text{L}^3)]$  and  $[\text{FeF}_3(\text{L}^3)]$  were isostructural and formed ‘head-to-tail’ hydrogen-bonded dimers. Packing of these dimers led to an interesting hexagonal, supramolecular array, resulting in the formation of solvent-accessible voids.



Following the complete characterisation of the MF<sub>3</sub> complexes and given the limitations caused by poor solubility and relative M–F bond strengths (aluminium complexes), only the gallium and iron complexes of L<sup>1</sup> and L<sup>3</sup> (which contain a chromophore, unlike L<sup>2</sup>) can be considered for future isotopic exchange reactions. Although stability studies of the L<sup>1</sup> complexes were not possible due to limited solubility, the [GaF<sub>3</sub>(L<sup>3</sup>)] complex was stable in water after 4 h, with no degradation or hydrolysis of the amide pendant arms observed. Hence, these systems will be discussed further in the next chapter of this work, Chapter 5.

## 4.4 Experimental

For general experimental methods, see Appendix A. The ligands L<sup>1</sup>, L<sup>2</sup> and L<sup>3</sup> were used as prepared in Chapter 2. Metal trifluoride precursor complexes, [MF<sub>3</sub>(dmsO)(OH<sub>2</sub>)<sub>2</sub>] (M = Al, Ga, In), prepared according to the previously reported method.<sup>29</sup> FeF<sub>3</sub>·3H<sub>2</sub>O (Sigma-Aldrich) used as supplied. All solvents used were of HPLC-chromatography grade.

### 4.4.1 Ligand 1 Complexes

#### 4.4.1.1 [AlF<sub>3</sub>(L<sup>1</sup>)]

A solution of [AlF<sub>3</sub>(dmsO)(OH<sub>2</sub>)<sub>2</sub>] (0.011 g, 0.057 mmol) in MeOH (5 mL) was added to a solution of L<sup>1</sup> (0.030 g, 0.057 mmol) in MeOH (5 mL). This was stirred at room temperature overnight, during which time a white precipitate had formed. This was separated from the reaction solution *via* filtration. The solvent volume was then reduced to approx. 2 mL *in vacuo* and diethyl ether (20 mL) was added, causing precipitation of a white solid. This was filtered and dried *in vacuo*. Yield: 0.027 g, 0.035 mmol (62%). Analysis required for C<sub>30</sub>H<sub>36</sub>AlF<sub>3</sub>N<sub>6</sub>O<sub>3</sub>·2dmsO: C, 53.11; H, 6.29; N, 10.93. Found: C, 51.30; H, 6.13; N, 11.24%. <sup>1</sup>H NMR (CD<sub>3</sub>OD, 298 K): δ (ppm) = 7.50 – 7.48 (m, [6H], ArH), 7.03 – 6.94 (m, [9H], ArH), 4.85 (H<sub>2</sub>O), 3.87 (s, [6H], CH<sub>2</sub>), 3.21 – 3.09 (br m, [12H], tacn-CH<sub>2</sub>), 2.66 (dmsO). <sup>19</sup>F{<sup>1</sup>H} NMR (CD<sub>3</sub>OD, 298 K): δ (ppm) = -174.1 (br s). <sup>13</sup>C{<sup>1</sup>H} NMR (CD<sub>3</sub>OD, 298 K): δ (ppm) = 168.5 (C=O), 139.4 (ArC), 129.8 (ArC), 125.4 (ArC), 121.4 (ArC), 59.5 (CH<sub>2</sub>), 51.1 (tacn-CH<sub>2</sub>), 40.6 (dmsO). HR ESI<sup>+</sup> MS (CH<sub>3</sub>OH): found: 529.2934 [L<sup>1</sup>+H]<sup>+</sup> (calculated for [L<sup>1</sup>+H]<sup>+</sup>: *m/z* = 529.2927), 551.2744 [L<sup>1</sup>+Na]<sup>+</sup> (calculated for [L<sup>1</sup>+Na]<sup>+</sup>: *m/z* = 551.2747), 613.2666 [AlF<sub>3</sub>(L<sup>1</sup>)+H]<sup>+</sup> (calculated for [AlF<sub>3</sub>(L<sup>1</sup>)+H]<sup>+</sup>: *m/z* = 613.2689). IR (Nujol, ν / cm<sup>-1</sup>): 3450 br, 3300 m (OH), 3146 w (NH), 1673 m (C=O), 1621 w (HOH), 1600 m (C=O), 1032 br (S=O, dmsO), 694 m, 673 sh (Al-F).

#### 4.4.1.2 [GaF<sub>3</sub>(L<sup>1</sup>)]

A solution of [GaF<sub>3</sub>(dmsO)(OH<sub>2</sub>)<sub>2</sub>] (0.034 g, 0.142 mmol) in MeOH (5 mL) was added to a solution of L<sup>1</sup> (0.075 g, 0.142 mmol) in MeOH (5 mL). This was left to stir at room temperature for 4 h, then

heated at 60 °C for 2 h. The solvent was then removed *in vacuo*, and the product was isolated as an off-white solid. Yield: 0.060 g, 0.091 mmol (64%). Analysis required for  $C_{30}H_{36}F_3GaN_6O_3 \cdot dmsol \cdot H_2O$ : C, 51.14; H, 5.90; N, 11.18. Found: C, 51.43; H, 5.95; N, 11.58%.  $^1H$  NMR (298 K,  $CD_3OD$ ):  $\delta$  (ppm) = 7.55 (m, [6H], ArH), 7.30 (m, [6H], ArH), 7.18 (br s, [NH]), 7.09 (m, [3H], ArH), 4.85 (s,  $H_2O$ ), 4.05 (s, [6H],  $CH_2$ ), 3.45 (br s, [12H], tacn- $CH_2$ ), 2.66 (s, dmsol).  $^{13}C\{^1H\}$  NMR ( $CD_3OD$ , 298 K):  $\delta$  (ppm) = 168.3 ( $C=O$ ), 139.6 (ArC), 130.0 (ArC), 125.5 (ArC), 121.4 (ArC), 58.5 ( $CH_2$ ), 50.2 (tacn- $CH_2$ ), 40.6 (dmsol).  $^{19}F\{^1H\}$  NMR ( $CD_3OD$ , 298 K):  $\delta$  (ppm) = -180 (v br with partially resolved coupling to  $^{69/71}Ga$ ).  $^{71}Ga$  NMR ( $CD_3OD$ , 298 K):  $\delta$  (ppm) = 46.6 (br quartet,  $^1J_{71Ga-19F} \sim 510$  Hz). ESI<sup>+</sup> MS ( $CH_3OH$ ): found: 635.4  $[GaF_2(L^1)]^+$  (calculated for  $[GaF_2(L^1)]^+$ :  $m/z$  = 635.2). IR (Nujol,  $\nu / cm^{-1}$ ): 3425 br (OH), 3195 w, 3133 w (NH), 1685 s ( $C=O$ ), 1621 sh (HOH), 1599 s ( $C=O$ ), 1015 m ( $S=O$ , dmsol), 583, 543 w (Ga-F). Crystals suitable for X-ray diffraction were grown *via* vapour diffusion of diethyl ether into a methanol solution of the product.

#### 4.4.1.3 $[FeF_3(L^1)]$

A suspension of  $FeF_3 \cdot 3H_2O$  (0.016 g, 0.095 mmol) in EtOH (7.5 mL) was added to a solution of  $L^1$  (0.050 g, 0.095 mmol) in EtOH (7.5 mL). The reaction mixture was stirred at reflux overnight, giving a clear, colourless solution. The solvent was then removed *in vacuo*, leaving an off-white solid. Yield: 0.041 g, 0.064 mmol (67%). Analysis required for  $C_{30}H_{36}F_3FeN_6O_3 \cdot H_2O \cdot 0.25EtOH$ : C, 54.81; H, 6.08; N, 12.22. Found: C, 54.55; H, 6.05; N, 12.31%. IR (Nujol,  $\nu / cm^{-1}$ ): 3400 br, 3300 br (OH), 3197 m, 3136 w (NH), 1681 s, 1599 s ( $C=O$ ), 550, 537 w (Fe-F). ESI<sup>+</sup> MS (MeOH): not observed.

### 4.4.2 Ligand 2 Complexes

#### 4.4.2.1 $[AlF_3(L^2)]$

A solution of  $[AlF_3(dmsol)(OH_2)_2]$  (0.011 g, 0.054 mmol) in MeOH (5 mL) was added to a solution of  $L^2$  (0.025 g, 0.054 mmol) in MeOH (5 mL). The mixture was stirred overnight at room temperature. The solvent was removed *in vacuo* to leave a sticky hygroscopic solid. This was washed with diethyl ether (3 x 10 mL) and dried *in vacuo*, leaving a white powdered solid. Yield: 0.022 g, 0.040 mmol (74%). Analysis required for  $C_{24}H_{48}AlF_3N_6O_3 \cdot 3H_2O$ : C, 45.36; H, 8.56; N, 13.22. Found: C, 45.19; H, 8.71; N, 13.11%.  $^1H$  NMR ( $CD_3OD$ , 298 K):  $\delta$  (ppm) = 4.85 ( $H_2O$ ), 4.00 – 3.90 (septet,  $^3J_{1H-1H}$  = 6.6 Hz, [3H],  $iPr-CH$ ), 3.17 – 3.13 (br t,  $^3J_{1H-1H}$  = 7.0 Hz, [6H],  $CH_2$ ), 3.03 – 2.85 (br m, [12H], tacn- $CH_2$ ), 2.66 (s, dmsol), 2.51 – 2.48 (t,  $^3J_{1H-1H}$  = 7.0 Hz, [6H],  $CH_2$ ), 1.14 (d,  $^3J_{1H-1H}$  = 6.6 Hz, [18H],  $iPr-CH_3$ ).  $^1H$  NMR ( $D_2O$ , 298 K):  $\delta$  (ppm) = 3.93 – 3.83 (br septet, [3H],  $iPr-CH$ ), 3.15 – 3.11 (br t, [6H],  $CH_2$ ), 2.89 (br s, [12H], tacn- $CH_2$ ), 2.51 – 2.48 (br t, [6H],  $CH_2$ ), 1.11

(br d, [18H],  $^i\text{Pr-CH}_3$ ).  $^{13}\text{C}\{^1\text{H}\}$  NMR ( $\text{CD}_3\text{OD}$ , 298 K):  $\delta$  (ppm) = 172.7 ( $\text{C=O}$ ), 53.1 ( $\text{CH}_2$ ), 51.2 (tacn- $\text{CH}_2$ ), 42.7 ( $^i\text{Pr-CH}$ ), 33.4 ( $\text{CH}_2$ ), 22.8 ( $^i\text{Pr-CH}_3$ ).  $^{13}\text{C}\{^1\text{H}\}$  NMR ( $\text{D}_2\text{O}$ , 298 K):  $\delta$  (ppm) = 172.4 ( $\text{C=O}$ ), 50.9 ( $\text{CH}_2$ ), 48.6 (tacn- $\text{CH}_2$ ), 41.8 ( $^i\text{Pr-CH}$ ), 32.1 ( $\text{CH}_2$ ), 21.4 ( $^i\text{Pr-CH}_3$ ).  $^{19}\text{F}\{^1\text{H}\}$  NMR ( $\text{CD}_3\text{OD}$ , 298 K):  $\delta$  (ppm) = -196 (br); ( $\text{D}_2\text{O}$ , 298 K):  $\delta$  (ppm) = -155 (br). HR ESI<sup>+</sup> MS ( $\text{CH}_3\text{OH}$ ): found: 553.3627  $[\text{AlF}_3(\text{L}^2)+\text{H}]^+$  (calculated for  $[\text{AlF}_3(\text{L}^2)+\text{H}]^+$ :  $m/z$  = 553.3628), 491.3681  $[\text{L}^2+\text{Na}]^+$  (calculated for  $[\text{L}^2+\text{Na}]^+$ :  $m/z$  = 491.3680), 469.3876  $[\text{L}^2+\text{H}]^+$  (calculated for  $[\text{L}^2+\text{H}]^+$ :  $m/z$  = 469.3861). IR (Nujol,  $\nu$  /  $\text{cm}^{-1}$ ): 3430 v br, 3290 br (OH), 3090 br, 3068 br (NH), 1644 s, 1551 s (C=O), 1050 w (S=O, dmso), 667 br, 616 sh (Al-F).

#### 4.4.2.2 $[\text{GaF}_3(\text{L}^2)]$

A solution of  $[\text{GaF}_3(\text{dmso})(\text{OH}_2)_2]$  (0.032 g, 0.134 mmol) in MeOH (5 mL) was added to a solution of  $\text{L}^2$  (0.063 g, 0.134 mmol) in MeOH (5 mL). The mixture was stirred at room temperature for 48 h and then concentrated to ca. 2 mL *in vacuo*. Diethyl ether (20 mL) was added, causing a pale-yellow precipitate to form. This was collected by filtration as a very hygroscopic, sticky solid, which became an off-white powder upon drying *in vacuo*. Yield: 0.067 g, 0.112 mmol (84%). Analysis required for  $\text{C}_{24}\text{H}_{48}\text{F}_3\text{Ga}\text{N}_6\text{O}_3 \cdot 3\text{H}_2\text{O} \cdot 0.3\text{dmso}$ : C, 44.00; H, 7.93; N, 12.70. Found: C, 43.91; H, 8.36; N, 12.49%.  $^1\text{H}$  NMR ( $\text{CD}_3\text{OD}$ , 298 K):  $\delta$  (ppm) = 4.85 ( $\text{H}_2\text{O}$ ), 3.98 – 3.88 (septet,  $^3J_{1\text{H}-1\text{H}}$  = 6.4 Hz [3H],  $^i\text{Pr-CH}$ ), 3.42 – 3.38 (br t, [6H],  $\text{CH}_2$ ), 3.16 – 3.06 (br m, [6H], tacn- $\text{CH}_2$ ), 2.88 – 2.76 (br m, [6H], tacn- $\text{CH}_2$ ), 2.66 (dmso), 2.53 – 2.47 (br m, [6H],  $\text{CH}_2$ ), 1.14 – 1.12 (d,  $^3J_{1\text{H}-1\text{H}}$  = 6.4 Hz, [18H],  $^i\text{Pr-CH}_3$ ).  $^{13}\text{C}\{^1\text{H}\}$  NMR ( $\text{CD}_3\text{OD}$ , 298 K):  $\delta$  (ppm) = 172.6 ( $\text{C=O}$ ), 54.6 ( $^i\text{Pr-CH}$ ), 53.1 ( $\text{CH}_2$ ), 51.2 (tacn- $\text{CH}_2$ ), 42.7 (tacn- $\text{CH}_2$ ), 40.6 (dmso), 33.4 ( $\text{CH}_2$ ), 22.8 ( $^i\text{Pr-CH}_3$ ).  $^{19}\text{F}\{^1\text{H}\}$  NMR ( $\text{CD}_3\text{OD}$ , 298 K):  $\delta$  (ppm) = -178.2 (br).  $^{71}\text{Ga}$  NMR ( $\text{CD}_3\text{OD}$ , 298 K):  $\delta$  (ppm) = 41.0 (br quartet,  $^1J_{71\text{Ga}-19\text{F}}$  ~ 520 Hz). ESI<sup>+</sup> MS ( $\text{CH}_3\text{OH}$ ): found: 575.5  $[\text{GaF}_2(\text{L}^2)]^+$  (calculated for  $[\text{GaF}_2(\text{L}^2)]^+$ :  $m/z$  = 575.3). IR (Nujol,  $\nu$  /  $\text{cm}^{-1}$ ): 3438 br, 3267 br (OH), 3190 sh, 3060 br (NH), 1645 br s, 1548 s (C=O), 1018 w (S=O, dmso), 528 m, 510 sh (Ga-F).

#### 4.4.2.3 Attempted preparation of $[\text{InF}_3(\text{L}^2)]$

A solution of  $[\text{InF}_3(\text{dmso})(\text{OH}_2)_2]$  (0.037 g, 0.128 mmol) in MeOH (5 mL) was added to a solution of  $\text{L}^2$  (0.060 g, 0.128 mmol) in MeOH (5 mL). The mixture was refluxed with stirring for 2 h. The solution was concentrated to ca. 2 mL *in vacuo*, and diethyl ether (20 mL) was added, causing precipitation of an off-white solid. This was isolated *via* filtration as a very hygroscopic, sticky solid. Upon further drying *in vacuo*, a white powder product was obtained. Yield: 0.026 g.  $^1\text{H}$  NMR spectroscopy indicates that the isolated product appears to contain two different indium species, one of which is the target complex, while the second is as yet unidentified; a significant amount of  $\text{F}^-$  is also present ( $^{19}\text{F}$  NMR evidence). Spectroscopic data quoted here are those assigned to the target  $[\text{InF}_3(\text{L}^2)]$  complex.  $^1\text{H}$  NMR ( $\text{CD}_3\text{OD}$ , 298 K):  $\delta$  (ppm) = 4.85 ( $\text{H}_2\text{O}$ ), 3.96

(septet, [3H], <sup>i</sup>Pr-CH), 3.15 (t, CH<sub>2</sub>), 3.12 – 3.02 (br m, [6H], tacn-CH<sub>2</sub>), 2.99 – 2.88 (br m, [6H], tacn-CH<sub>2</sub>), 2.74 – 2.69 (br m, [2H], CH<sub>2</sub>), 2.66 (dmsO), 2.65 – 2.61 (m, [2H], CH<sub>2</sub>), 2.52 – 2.45 (br m, [2H], CH<sub>2</sub>), 1.14 (br d, [18H], <sup>i</sup>Pr-CH<sub>3</sub>). <sup>19</sup>F{<sup>1</sup>H} NMR (CD<sub>3</sub>OD, 298 K): δ (ppm) = -197.8 (br) (a singlet is also observed at -132.6 ppm, suggesting significant liberation of F<sup>-</sup> from the indium(III) during the reaction, along with a minor species giving a broad resonance at -202 ppm). A few small crystals of [InF<sub>3</sub>(L<sup>2</sup>)] were grown *via* slow evaporation from the NMR solution of the product mixture in CD<sub>3</sub>OD and were analysed by single crystal X-ray diffraction.

#### 4.4.2.4 [FeF<sub>3</sub>(L<sup>2</sup>)]

A suspension of FeF<sub>3</sub>·3H<sub>2</sub>O (0.019 g, 0.112 mmol) in EtOH (7.5 mL) was added to a solution of L<sup>2</sup> (0.053 g, 0.112 mmol) in EtOH (7.5 mL). The solution was heated to 80 °C, at which point the solution changed from colourless to orange-yellow and full dissolution was observed. Heating was continued for 4 h, then the solvent was removed *in vacuo*. An off-white solid remained. Yield: 0.036 g, 0.068 mmol (61%). Analysis required for C<sub>24</sub>H<sub>48</sub>FeF<sub>3</sub>N<sub>6</sub>O<sub>3</sub>·3H<sub>2</sub>O: C, 45.36; H, 8.56; N, 13.22. Found: C, 45.73; H, 8.19; N, 13.11%. IR (Nujol, ν / cm<sup>-1</sup>): 3450 s br, 3275 s br (OH), 3091 sh, 3075 m br (NH), 1648 s, 1555 s (C=O), 512 (br, Fe–F). HR ESI<sup>+</sup> MS (CH<sub>3</sub>OH): found: *m/z* = 562.3110 [FeF<sub>2</sub>(L<sup>2</sup>)]<sup>+</sup> (calculated for [FeF<sub>2</sub>(L<sup>2</sup>)]<sup>+</sup>: *m/z* = 562.3105), 449.2263 [FeF<sub>2</sub>{(<sup>i</sup>PrCONH(CH<sub>2</sub>)<sub>2</sub>)<sub>2</sub>-tacn}+H]<sup>+</sup> (calculated for [FeF<sub>2</sub>{(<sup>i</sup>PrCONH(CH<sub>2</sub>)<sub>2</sub>)<sub>2</sub>-tacn}+H]<sup>+</sup>: *m/z* = 449.2265), 262.1578 [Fe(L<sup>2</sup>)]<sup>2+</sup> (calculated for [Fe(L<sup>2</sup>)]<sup>2+</sup>: *m/z* = 262.1563).

### 4.4.3 Ligand 3 Complexes

#### 4.4.3.1 [AlF<sub>3</sub>(L<sup>3</sup>)]

A solution of [AlF<sub>3</sub>(dmsO)(OH<sub>2</sub>)<sub>2</sub>] (0.026 g, 0.130 mmol) in MeOH (5 mL) was added to a solution of L<sup>3</sup> (0.45 g, 0.130 mmol) in MeOH (5 mL). This was left to stir at room temperature overnight. The solvent was then concentrated *in vacuo* to ca. 2 mL, then diethyl ether (10 mL) was added, causing the precipitation of a white solid, which was collected by filtration and dried *in vacuo*. Yield: 0.038 g, 0.087 mmol (67%). Analysis required for C<sub>20</sub>H<sub>34</sub>AlF<sub>3</sub>N<sub>4</sub>O·2H<sub>2</sub>O·dmsO: C, 48.16; H, 7.77; N, 10.70. Found: C, 48.52; H, 8.14; N, 10.29%. <sup>1</sup>H NMR (CD<sub>3</sub>OD, 298 K): δ (ppm) = 7.58 – 7.56 (br d, [2H], ArH), 7.32 – 7.28 (br t, [2H], ArH), 7.10 – 7.07 (br t, [1H], ArH), 4.86 (H<sub>2</sub>O), 3.59 (s, [2H], CH<sub>2</sub>), 3.35 (br septet, overlapping with solvent peaks, <sup>i</sup>Pr-CH), 3.15 – 3.02 (br m, [4H], tacn-CH<sub>2</sub>), 2.97 – 2.80 (br m, [8H], tacn-CH<sub>2</sub>), 2.66 (dmsO), 1.29 – 1.28 (d, <sup>3</sup>J<sub>1H-1H</sub> = 6.5 Hz, [6H], <sup>i</sup>Pr-CH<sub>3</sub>), 1.24 – 1.22 (d, <sup>3</sup>J<sub>1H-1H</sub> = 6.6 Hz, [6H], <sup>i</sup>Pr-CH<sub>3</sub>). <sup>13</sup>C{<sup>1</sup>H} NMR (298 K, CD<sub>3</sub>OD): δ (ppm) = 164.6 (C=O), 140.0 (ArC), 130.0 (ArC), 125.3 (ArC), 121.1 (ArC), 58.6 (CH<sub>2</sub>), 55.3 (<sup>i</sup>Pr-CH), 50.3 (tacn-CH<sub>2</sub>), 48.3 (tacn-CH<sub>2</sub>), 46.3 (tacn-CH<sub>2</sub>), 18.5, 18.1 (<sup>i</sup>Pr-CH<sub>3</sub>). <sup>19</sup>F{<sup>1</sup>H} NMR (CD<sub>3</sub>OD, 298 K): δ (ppm) = -196 (br); (D<sub>2</sub>O, 298 K): δ (ppm) = -155.2 ([F]), -156.1 ([2F]). <sup>27</sup>Al NMR (CD<sub>3</sub>OD, 298 K):

not observed. ESI MS<sup>+</sup> (CH<sub>3</sub>OH) found:  $m/z$  = 431.2570 [AlF<sub>3</sub>(L<sup>3</sup>)+H]<sup>+</sup> (calculated for [AlF<sub>3</sub>(L<sup>3</sup>)+H]<sup>+</sup>:  $m/z$  = 431.2573), 347.2817 [L<sup>3</sup>+H]<sup>+</sup> (calculated for [L<sup>3</sup>+H]<sup>+</sup>:  $m/z$  = 347.2805), 174.1441 [L<sup>3</sup>+2H]<sup>2+</sup> (calculated for [L<sup>3</sup>+2H]<sup>2+</sup>:  $m/z$  = 174.1439). IR (Nujol,  $\nu$  / cm<sup>-1</sup>): 3430 (br, OH), 3266, 3177 (NH), 3155 (aromatic CH), 2727, 2676 (C–H stretch), 1693, 1615, 1600 (C=O), 642, 592 sh (Al–F).

#### 4.4.3.2 [GaF<sub>3</sub>(L<sup>3</sup>)]

A solution of [GaF<sub>3</sub>(dmsO)(OH)<sub>2</sub>] (0.038 g, 0.159 mmol) in MeOH (5 mL) was added to a solution of L<sup>3</sup> (0.55 g, 0.159 mmol) in MeOH (5 mL). This was left to stir at room temperature overnight. The solvent was concentrated *in vacuo* to ca. 2 mL, then diethyl ether (10 mL) was added, causing the precipitation of a white solid. The solid was collected by filtration and dried *in vacuo*. Yield: 0.046 g, 0.097 mmol (61%). Analysis required for C<sub>20</sub>H<sub>34</sub>F<sub>3</sub>GaN<sub>4</sub>O·3H<sub>2</sub>O: C, 45.56; H, 7.65; N, 10.63. Found: C, 45.74; H, 7.28; N, 10.25%. <sup>1</sup>H NMR (CD<sub>3</sub>OD, 298 K):  $\delta$  (ppm) = 7.58 – 7.56 (m, [2H], ArH), 7.32 – 7.28 (m, [2H], ArH), 7.10 – 7.07 (m, [1H], ArH), 4.86 (H<sub>2</sub>O), 3.60 (s, [2H], CH<sub>2</sub>), 3.35 (septet, <sup>3</sup>J<sub>1H-1H</sub> = 6.9 Hz, [2H], <sup>i</sup>Pr-CH), 3.14 – 3.01 (m, [4H], tacn-CH<sub>2</sub>), 2.99 – 2.79 (br m, [8H], tacn-CH<sub>2</sub>), 2.66 (dmsO), 1.30 – 1.28 (d, <sup>3</sup>J<sub>1H-1H</sub> = 6.6 Hz, [6H], <sup>i</sup>Pr-CH<sub>3</sub>), 1.24 – 1.22 (d, <sup>3</sup>J<sub>1H-1H</sub> = 6.6 Hz, [6H], <sup>i</sup>Pr-CH<sub>3</sub>). <sup>13</sup>C{<sup>1</sup>H} NMR (298 K, CD<sub>3</sub>OD):  $\delta$  (ppm) = 171.4 (C=O), 140.0 (ArC), 130.0 (ArC), 125.5 (ArC), 121.1 (ArC), 58.7 (CH<sub>2</sub>), 55.3 (<sup>i</sup>Pr-CH), 50.3 (tacn-CH<sub>2</sub>), 48.3 (tacn-CH<sub>2</sub>), 46.3 (tacn-CH<sub>2</sub>), 40.6 (dmsO), 18.5, 18.1 (<sup>i</sup>Pr-CH<sub>3</sub>). <sup>19</sup>F{<sup>1</sup>H} NMR (CD<sub>3</sub>OD, 298 K):  $\delta$  (ppm) = -171.5 (br s, [2F]) -172.3 (br s, [F]). <sup>71</sup>Ga NMR (298 K, MeOH): not observed. ESI<sup>+</sup> MS (CH<sub>3</sub>OH): found:  $m/z$  = 473.3429 [GaF<sub>3</sub>(L<sup>3</sup>)+H]<sup>+</sup> (calculated for [GaF<sub>3</sub>(L<sup>3</sup>)+H]<sup>+</sup>:  $m/z$  = 473.2019); 453.1950 [GaF<sub>2</sub>(L<sup>3</sup>)]<sup>+</sup> (calculated for [GaF<sub>2</sub>(L<sup>3</sup>)]<sup>+</sup>:  $m/z$  = 453.1956), 347.2817 [L<sup>3</sup>+H]<sup>+</sup> (calculated for [L<sup>3</sup>+H]<sup>+</sup>:  $m/z$  = 347.2805), 305.2331 [L<sup>3</sup>-<sup>i</sup>Pr][H]<sup>+</sup> (calculated for [L<sup>3</sup>-<sup>i</sup>Pr][H]<sup>+</sup>:  $m/z$  = 305.2336). IR (Nujol,  $\nu$  / cm<sup>-1</sup>): 3420, 3307 (OH), 3193, 3132 (NH), 1689, 1622 (C=O), 1032 (S=O, dmsO), 539, 520 (GaF). Crystals suitable for X-ray structure determination were grown *via* slow evaporation from a solution of the complex in acetonitrile.

#### 4.4.3.3 [FeF<sub>3</sub>(L<sup>3</sup>)]

A suspension of FeF<sub>3</sub>·3H<sub>2</sub>O (0.020 g, 0.117 mmol) in EtOH (7.5 mL) was added to a solution of L<sup>3</sup> (0.041 g, 0.117 mmol) in EtOH (7.5 mL). This was stirred at reflux. After 30 min. full dissolution was observed and refluxing was continued for 6 h. The solvent was removed *in vacuo*. An off-white solid remained. Yield: 0.034 g, 0.074 mmol (63%). Analysis required for C<sub>20</sub>H<sub>34</sub>F<sub>3</sub>FeN<sub>4</sub>O·1.5H<sub>2</sub>O: C, 49.39; H, 7.67; N, 11.52. Found: C, 49.76; H, 7.84; N, 11.16%. IR (Nujol,  $\nu$  / cm<sup>-1</sup>): 3428, 3270 (OH), 3206 sh, 3192(NH), 1689 (C=O), 1617 sh (HOH), 1598 (C=O), 539, 521 (FeF). HR ESI<sup>+</sup> MS (CH<sub>3</sub>OH): found:  $m/z$  = 440.2043 [FeF<sub>2</sub>(L<sup>3</sup>)]<sup>+</sup> (calculated for [FeF<sub>2</sub>(L<sup>3</sup>)]<sup>+</sup>:  $m/z$  = 440.2050), 347.2809 [L<sup>3</sup>+H]<sup>+</sup> (calculated for [L<sup>3</sup>+H]<sup>+</sup>:  $m/z$  = 347.2805). Crystals suitable for

X-ray diffraction were grown *via* slow evaporation from a solution of the product in methanol/diethyl ether.

#### 4.5 X-Ray Crystallographic Data

Complex	<b>[GaF<sub>3</sub>(L<sup>1</sup>)]·1.5MeOH·0.5H<sub>2</sub>O</b>	<b>[InF<sub>3</sub>(L<sup>2</sup>)]</b>
Formula	C <sub>30</sub> H <sub>36</sub> F <sub>3</sub> GaN <sub>6</sub> O <sub>5</sub> ·1.5CH <sub>4</sub> O·0.5H <sub>2</sub> O	C <sub>24</sub> H <sub>48</sub> F <sub>3</sub> InN <sub>6</sub> O <sub>3</sub>
<i>M</i>	712.45	640.50
Crystal system	Monoclinic	Trigonal
Space group (no.)	<i>P</i> 2 <sub>1</sub> / <i>n</i> (14)	<i>R</i> 3c (161)
<i>a</i> /Å	17.0116(5)	14.2596(2)
<i>b</i> /Å	12.0324(3)	14.2596(2)
<i>c</i> /Å	17.3324(6)	26.9863(5)
$\alpha$ /°	90	90
$\beta$ /°	115.495(4)	90
$\gamma$ /°	90	120
<i>U</i> /Å <sup>3</sup>	3202.3(2)	4752.13(13)
<i>Z</i>	4	6
$\mu$ (Mo-K $\alpha$ ) /mm <sup>-1</sup>	0.927	0.796
<i>F</i> (000)	1490	2001
Total no. reflns	31373	50509
<i>R</i> <sub>int</sub>	0.039	0.035
Unique reflns	8240	2726
No. of params, restraints	593, 92	115, 65
GOF	1.056	1.032
<i>R</i> <sub>1</sub> , <i>wR</i> <sub>2</sub> [ <i>I</i> > 2σ( <i>I</i> )] <sup>b</sup>	0.053, 0.127	0.035, 0.094
<i>R</i> <sub>1</sub> , <i>wR</i> <sub>2</sub> (all data)	0.086, 0.147	0.037, 0.096

Complex	<b>[FeF<sub>3</sub>(L<sup>3</sup>)]·2.4H<sub>2</sub>O</b>	<b>[GaF<sub>3</sub>(L<sup>3</sup>)]·0.067H<sub>2</sub>O</b>
Formula	C <sub>20</sub> H <sub>34</sub> F <sub>3</sub> FeN <sub>4</sub> O·2.4H <sub>2</sub> O	C <sub>20</sub> H <sub>34</sub> F <sub>3</sub> GaN <sub>4</sub> O·0.0067H <sub>2</sub> O
<i>M</i>	459.36	474.489
Crystal system	Trigonal	Trigonal
Space group (no.)	<i>R</i> -3 (148)	<i>R</i> -3 (148)
<i>a</i> /Å	33.7472(5)	33.4699(7)
<i>b</i> /Å	33.7472(5)	33.4699(7)
<i>c</i> /Å	10.2893(2)	10.3165(2)
$\alpha$ /°	90	90
$\beta$ /°	90	90
$\gamma$ /°	120	120
<i>U</i> /Å <sup>3</sup>	10148.3(4)	10008.6(4)
<i>Z</i>	18	18
$\mu$ (Mo-K $\alpha$ ) /mm <sup>-1</sup>	0.711	1.280
<i>F</i> (000)	4383.6	4484.66
Total no. reflns	147068	31588
<i>R</i> <sub>int</sub>	0.052	0.020
Unique reflns	5824	6970
No. of params, restraints	568, 1209	568, 6970
GOF	1.103	1.011
<i>R</i> <sub>1</sub> , <i>wR</i> <sub>2</sub> [ <i>I</i> > 2 $\sigma$ ( <i>I</i> )] <sup>b</sup>	0.028, 0.057	0.014, 0.026
<i>R</i> <sub>1</sub> , <i>wR</i> <sub>2</sub> (all data)	0.037, 0.061	0.017, 0.027

<sup>a</sup> common items: *T* = 100 K; wavelength (Mo-K $\alpha$ ) = 0.71073 Å;  $\theta$ (max) = 27.5°;

<sup>b</sup>  $R_1 = \Sigma ||F_o| - |F_c|| / \Sigma |F_o|$ ;  $wR_2 = [\Sigma w(F_o^2 - F_c^2)^2 / \Sigma wF_o^4]^{1/2}$

## 4.6 References

1. K. Chansaenpak, B. Vabre and F. P. Gabbaï, *Chem. Soc. Rev.*, 2016, **45**, 954.
2. W. Levason, F. M. Monzittu and G. Reid, *Coord. Chem. Rev.*, 2019, **391**, 90.
3. S. Schmitt and E. Moreau, *Coord. Chem. Rev.*, 2023, **480**, 215028.
4. R. Bhalla, W. Levason, S. K. Luthra, G. McRobbie, G. Sanderson and G. Reid, *Chem. Eur. J.*, 2015, **21**, 4688.
5. F. M. Monzittu, I. Khan, W. Levason, S. K. Luthra, G. McRobbie and G. Reid, *Angew. Chem. Int. Ed.*, 2018, **57**, 6658.
6. W. J. McBride, C. A. D'Souza, H. Karacay, R. M. Sharkey and D. M. Goldenberg, *Bioconjug. Chem.*, 2012, **23**, 538.
7. P. Laverman, W. J. McBride, R. M. Sharkey, A. Eek, L. Joosten, W. J. G. Oyen, D. M. Goldenberg and O. C. Boerman, *J. Nucl. Med.*, 2010, **51**, 454.
8. R. Bhalla, C. Darby, W. Levason, S. K. Luthra, G. McRobbie, G. Reid, G. Sanderson and W. Zhang, *Chem. Sci.*, 2014, **5**, 381.
9. D. E. Runacres, V. K. Greenacre, J. M. Dyke, J. Grigg, G. Herbert, W. Levason, G. McRobbie and G. Reid, *Inorg. Chem.*, 2023, **62**, 20844.
10. M. S. Woodward, D. E. Runacres, J. Grigg, I. Khan, W. Levason, G. McRobbie and G. Reid, *Pure Appl. Chem.*, 2024, **96**, 57.
11. J. N. Whetter, B. A. Vaughn, A. J. Koller and E. Boros, *Angew. Chem. Int. Ed.*, 2022, **61**, e202114203.
12. P. J. Blower, W. Levason, S. K. Luthra, G. McRobbie, F. M. Monzittu, T. O. Mules, G. Reid and M. Nadeem Subhan, *Dalton Trans.*, 2019, **48**, 6767.
13. M. Ghazzali, *Pure Appl. Chem.*, 2013, **85**, 397.
14. E. Macedi, A. Bencini, C. Caltagirone and V. Lippolis, *Coord. Chem. Rev.*, 2020, **407**, 213151.
15. A. B. Rahman, H. Okamoto, Y. Miyazawa and S. Aoki, *Eur. J. Inorg. Chem.*, 2021, 1213.
16. L. F. Lindoy, K.-M. Park and S. S. Lee, *Chem. Soc. Rev.*, 2013, **42**, 1713.
17. H. J. Choi, T. S. Lee and M. P. Suh, *Angew. Chem. Int. Ed.*, 1999, **38**, 1405.
18. D. Braga, F. Grepioni and G. R. Desiraju, *J. Organomet. Chem.*, 1997, **548**, 33.
19. S. B. Khan and S.-L. Lee, *Molecules*, 2021, **26**, 3995.
20. S. A. Svatek, L. M. A. Perdigão, A. Stannard, M. B. Wieland, D. V. Kondratuk, H. L. Anderson, J. N. O'Shea and P. H. Beton, *Nano Lett.*, 2013, **13**, 3391.
21. F. Hajjaj, Z. S. Yoon, M.-C. Yoon, J. Park, A. Satake, D. Kim and Y. Kobuke, *J. Am. Chem. Soc.*, 2006, **128**, 4612.



22. C. Nieuwland, D. Almacellas, M. M. Veldhuizen, L. De Azevedo Santos, J. Poater and C. Fonseca Guerra, *Phys. Chem. Chem. Phys.*, 2024, **26**, 11306.
23. F. N. Penkert, T. Weyhermüller and K. Wieghardt, *Chem. Commun.*, 1998, 557.
24. K. S. Pedersen, G. Lorusso, J. J. Morales, T. Weyhermüller, S. Piligkos, S. K. Singh, D. Larsen, M. Schau-Magnussen, G. Rajaraman, M. Evangelisti and J. Bendix, *Angew. Chem. Int. Ed.*, 2014, **53**, 2394.
25. R. Bhalla, W. Levason, S. K. Luthra, G. McRobbie, G. Reid, G. Sanderson and W. Zhang, *Chem. Commun.*, 2014, **50**, 12673.
26. R. Bhalla, W. Levason, S. K. Luthra, G. McRobbie, F. M. Monzittu, J. Palmer, G. Reid, G. Sanderson and W. Zhang, *Dalton Trans.*, 2015, **44**, 9569.
27. G. Sanderson PhD, University of Southampton, 2015.
28. B. Neumüller, *Coord. Chem. Rev.*, 1997, **158**, 69.
29. R. Bhalla, J. Burt, A. L. Hector, W. Levason, S. K. Luthra, G. McRobbie, F. M. Monzittu and G. Reid, *Polyhedron*, 2016, **106**, 65.
30. F. M. Monzittu, PhD, University of Southampton, 2018.
31. T. Weyhermüller, K. Weighardt and P. Chaudhuri, *J. Chem. Soc., Dalton Trans.*, 1998, 3805.
32. N. Herron, D. L. Thorn, R. L. Harlow and F. Davidson, *J. Am. Chem. Soc.*, 1993, **115**, 3028.
33. G. R. Giesbrecht, A. Gebauer, A. Shafir and J. Arnold, *J. Chem. Soc., Dalton Trans.*, 2000, 4018.
34. K. E. Dalle, S. Dechert and F. Meyer, *Z. Anorg. Allg. Chem.*, 2015, **641**, 2181.
35. S. Berger, J. Nolde, T. Yüksel, W. Tremel and M. Mondeshki, *Molecules*, 2018, **23**, 808.
36. A. Samadi-Maybodi, *Spectrochim. Acta A Mol. Biomol. Spectrosc.*, 2006, **64**, 1025.
37. J. Soriano, J. Shamir, A. Netzer and Y. Marcus, *Inorg. Nucl. Chem. Lett.*, 1969, **5**, 209.
38. B. Cordero, V. Gómez, A. E. Platero-Prats, M. Revés, J. Echeverría, E. Cremades, F. Barragán and S. Alvarez, *Dalton Trans.*, 2008, 2832.
39. J. A. Dean, *Lange's Handbook of Chemistry*, McGraw-Hill Inc., New York, 15th edn., 1999.

## Chapter 5 Radiolabelling of $[\text{GaF}_3(\text{L}^1)]$ and $[\text{GaF}_3(\text{L}^3)]$ via $^{19}\text{F}/^{18}\text{F}$ Isotopic Exchange

### 5.1 Introduction

This chapter follows up on the chemistry developed in Chapter 4, specifically investigating the suitability of the  $[\text{GaF}_3(\text{L}^1)]$  and  $[\text{GaF}_3(\text{L}^3)]$  complexes for radiofluorination via  $^{19}\text{F}/^{18}\text{F}$  isotopic exchange reactions. The objective will be to develop procedures for the incorporation of  $^{18}\text{F}$  and, if successful, to develop reliable cartridge-based purification procedures. Ultimately, their suitability as future potential PET imaging candidates will be evaluated based on their radiochemical yields and their radiochemical stability in competitive media.

#### 5.1.1 Group 13 Triazacyclononane Complexes in $^{18}\text{F}$ PET Imaging

Chapter 1 and Chapter 4 of this work have discussed the suitability of using  $\text{MF}_3$  fragments (particularly those bound to triaza-macrocyclic ligands) to form inorganic macrocyclic complexes for  $^{18}\text{F}$  PET imaging applications. Much of the focus has surrounded transition metals (specifically  $\text{Fe}^{3+}$  and the trivalent Group 13 metals ( $\text{Al}^{3+}$ ,  $\text{Ga}^{3+}$ ), which form inherently strong bonds to fluorine.<sup>1,2</sup> This is imperative for  $^{18}\text{F}$  radiolabelling.<sup>3</sup> For these metal ions, the strength of the M–F bond is undoubtedly essential for the overall radiochemical stability – ensuring the fluoride will remain bound to the metal under physiological conditions.<sup>4</sup> Due to the enhanced thermodynamic and kinetic stability from the macrocyclic effect, coordination of the metal ion to a macrocyclic ligand also reduces the likelihood of by-product formation during radiolabelling, and reduces the risk of hydrolysis and liberation of  $^{18}\text{F}^-$  *in vivo*. Ideally, inorganic metal-fluoride radiotracers will be pre-formed, and the  $^{18}\text{F}^-$  introduced as the final step. A challenge faced by researchers in more recent years has been to develop radiotracers that can be radiolabelled at lower temperatures (below 100 °C and as close to room temperature as possible), which are also stable over a wide pH range, to be more compatible with a broader range of conjugated peptides and proteins.<sup>5</sup>

##### 5.1.1.1 Radiochemistry of $[\text{M}^{18}\text{F}(\text{L})]$ Complexes ( $\text{M} = \text{Al}, \text{Ga}, \text{Fe}$ )

The  $\text{Al}-^{18}\text{F}$  chemistry initially developed by McBride and co-workers<sup>6</sup> provides the earliest examples of Group 13 metal-fluoride complexes in an  $^{18}\text{F}$  PET imaging context, using  $\text{N}_3\text{O}_3$   $\text{H}_3$ -NOTA and  $\text{N}_3\text{O}_2$   $\text{H}_2$ -NODA derived triazacyclononane ligands. Although these ligands are some of the most frequently used  $[\text{F}^{18}]\text{AlF}$  chelators (owing to their commercial availability and ability to form very stable conjugate complexes with a range of peptides), their work also highlights the effect of the macrocycle on the radiolabelling efficiency.<sup>7</sup> Several examples have been

discussed in Chapters 1 and 2, with some Al- $^{18}\text{F}$  NOTA-complexes advanced to clinical trials for imaging of various cancer.<sup>8,9</sup> However, whilst the H<sub>3</sub>-NOTA derived chelates showed excellent *in vivo* stability, radiochemical yields are often poor (up to 20%), attributed to competition from the free carboxylate pendant arm with incoming  $^{18}\text{F}^-$  for the sixth aluminium coordination site (Figure 5.1).<sup>6,10,11</sup>

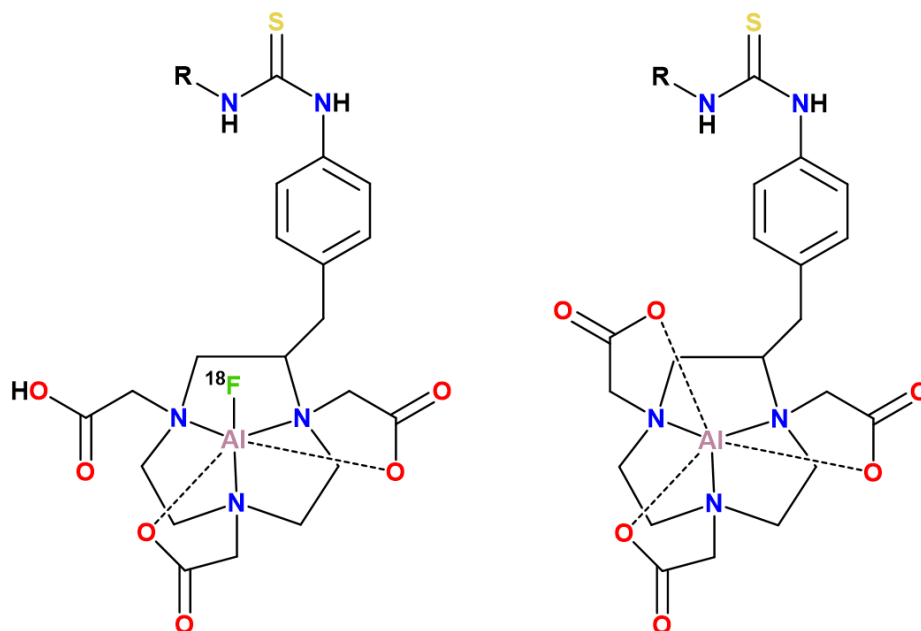
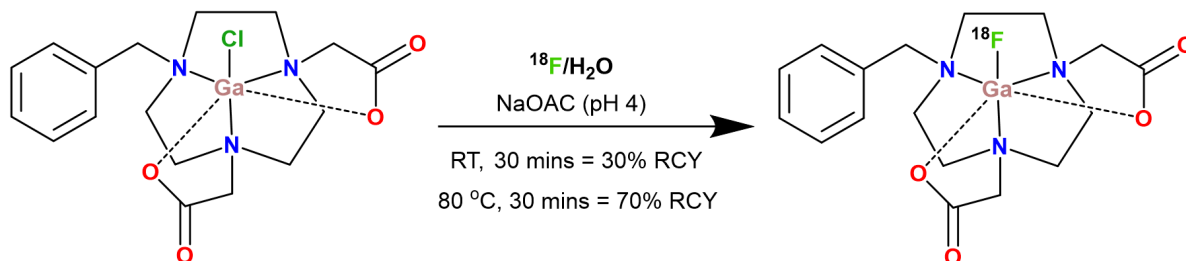


Figure 5.1 – The free carboxylate arm of the H<sub>3</sub>-NOTA derivative IMP449 competes with  $^{18}\text{F}^-$  for the sixth coordination site of aluminium, resulting in low radiochemical yields.<sup>10</sup>

Pentadentate H<sub>2</sub>-NODA derivatives were found to have similar *in vivo* stability but much improved radiochemical yields (up to 90%).<sup>10</sup> For example, Shetty *et al.*<sup>11</sup> reported an [ $^{18}\text{F}$ ]-[AlF(Bn-NODA)] complex, which underwent efficient radiolabelling at 110 °C (RCY = 89%) after 10 min, which was stable in human serum (37 °C) and sodium acetate buffer (pH 4) for 2 h (ca. 95 – 100% RCP). However, only 1.28%  $^{18}\text{F}$  incorporation was observed at room temperature. The wider applications are still somewhat limited, as the radiolabelling conditions for Al- $^{18}\text{F}$  complexes often require elevated temperatures (up to 110 °C) for the chelation of [ $^{18}\text{F}$ ]AlF<sup>2+</sup> into the macrocycle, and narrow pH windows (pH 4 – pH 5) to prevent the formation of aluminium hydroxide species.<sup>12</sup>

The radiochemistry of H<sub>2</sub>-NODA has been probed further by the Reid group, forming [Ga $^{18}\text{F}$ (Bn-NODA)] *via* halide exchange on the pre-formed [GaCl(Bn-NODA)] complex (Scheme 5.1).<sup>13</sup> In this case,  $^{18}\text{F}$ -radiolabelling was achievable at room temperature, with 30% radio-incorporation observed after 30 min. This was significantly improved by heating to 80 °C for 30 min, with radiochemical yields of up to 70% obtained. Purification was fast and efficient using a HLB cartridge, but the stability of the product was strongly dependent on pH. Unlike the Al- $^{18}\text{F}$

equivalents, substantial liberation of  $^{18}\text{F}$  was observed at pH 7.5, which was attributed to the strain caused by the acute chelate bite angles associated with the pendant arms, and weaker carboxylate bonds to  $\text{Ga}^{3+}$  vs.  $\text{Al}^{3+}$  making it susceptible to nucleophilic attack by hydroxide anions.



Scheme 5.1 –  $^{18}\text{F}/\text{Cl}$  halide exchange reaction on a pre-formed  $[\text{GaCl}(\text{Bn-NODA})]$  complex.

More recent work in the group has produced the  $[\text{M}^{18}\text{F}(\text{Bn-NODP})]$  complexes ( $\text{M} = \text{Ga}, \text{Fe}$ ) via halide exchange reactions on the corresponding chloro- complexes.<sup>14</sup> The  $[\text{Bn-NODP}]^{2-}$  ligand, like  $[\text{Bn-NODA}]^{2-}$ , is pentadentate upon deprotonation, but the chelating bite angle from the carboxylate of the phosphinate pendant arm to the metal centre is larger. For the  $[\text{GaF}(\text{Bn-NODP})]$  complex, the O-Ga-N chelate angles were observed at  $86.00(7)$  and  $85.40(6)^\circ$ , some  $3\text{--}4^\circ$  larger than the corresponding O-Ga-N chelate angles in the previously reported structure of  $[\text{GaF}(\text{Bn-NODA})]$ .<sup>13</sup> The pentavalency of the phosphorus also means the ligand properties can be tailored more easily in comparison. This work was developed based on previous studies by Parker and co-workers<sup>15</sup>, who found that the  $\text{H}_3\text{-NOTP}$  ligand (with three phosphinic acid arms, in comparison to the two of  $\text{H}_2\text{-Bn-NODP}$ ) were ideal for binding  $^{68}\text{Ga}^{3+}$ .

Radiofluorination of  $[\text{MF}(\text{Bn-NODP})]$  ( $\text{M} = \text{Ga}$  or  $\text{Fe}$ ) can be achieved in partially aqueous conditions ( $\text{Ga}$ :  $\text{MeCN}/\text{NaOAc}_{\text{aq}}$ ) or in  $\text{EtOH}$  ( $\text{Ga}$  or  $\text{Fe}$ ), with radiochemical yields between 60–80% observed after heating for 10 min at  $80\text{ }^\circ\text{C}$ . Following purification using a HLB cartridge, the  $[\text{Fe}^{18}\text{F}(\text{Bn-NODP})]$  complex was shown to be unstable in both  $\text{EtOH}/\text{H}_2\text{O}$  and  $\text{EtOH}/\text{PBS}$ . Conversely, the  $[\text{Ga}^{18}\text{F}(\text{Bn-NODP})]$  complex shows excellent stability, with a radiochemical purity (RCP) of 99% after 4 h in  $\text{EtOH}/\text{H}_2\text{O}$ , and 95% after 4 h in  $\text{EtOH}/\text{PBS}$ . These trends can be seen in Figure 5.2. Both the metal ion, as well as the nature of the macrocycle (in terms of the behaviour of the pendant arms and the steric constraints they impose), clearly influence the radiolabelling efficiency and the overall stability.

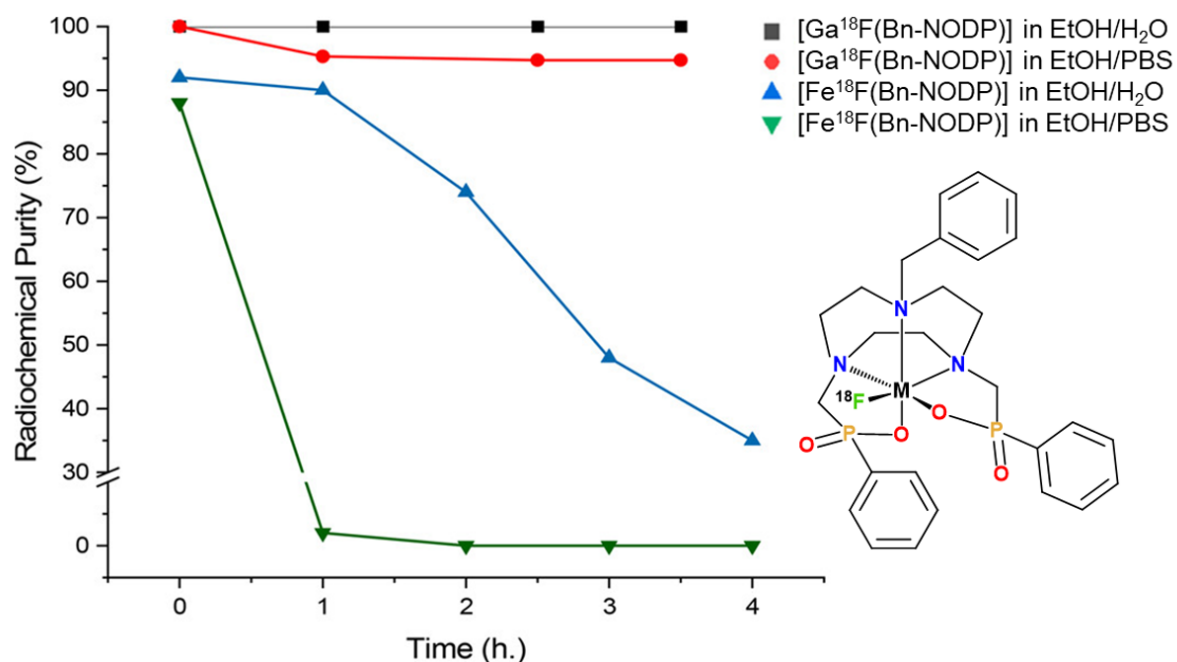
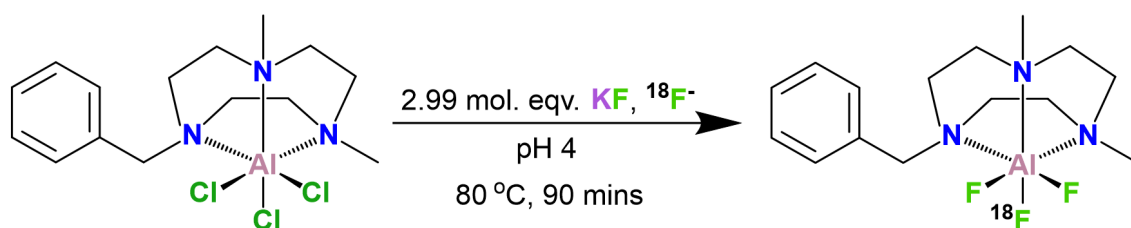


Figure 5.2 – Radiochemical purity of  $[M^{18}\text{F}(\text{Bn-NODP})]$  over 4 h in EtOH/H<sub>2</sub>O and EtOH/PBS.<sup>14</sup>

#### 5.1.1.2 Radiochemistry of $[MX_3(\text{BnMe}_2\text{-tacn})]$ Complexes ( $M = \text{Al, Ga, Fe}$ ; $X = \text{Cl, F}$ )

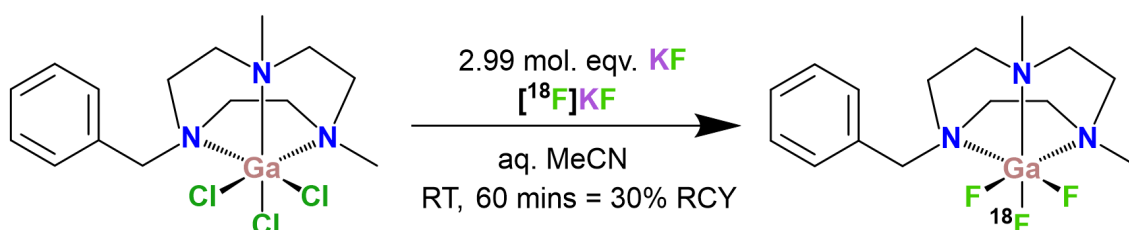
Previous work in the group has also developed several  $MX_3$  ( $M = \text{Al, Ga, In, Fe}$  and  $X = \text{F, Cl}$ ) complexes of functionalised triazacyclononane ligands for  $^{18}\text{F}$  PET imaging – the most notable examples include complexes of  $\text{BnMe}_2\text{-tacn}$ , an asymmetric neutral  $\text{N}_3$ -donor ligand. Due to the poor reactivity of the Group 13 trifluoride hydrates and the harsh hydrothermal conditions required for their complexation, the initial route towards  $[\text{MF}_3(\text{BnMe}_2\text{-tacn})]$  complexes was *via* halide exchange from the  $[\text{MCl}_3(\text{BnMe}_2\text{-tacn})]$  analogues.<sup>16</sup>

Preliminary ‘cold’ fluorination experiments using  $[\text{MCl}_3(\text{Me}_3\text{-tacn})]$  to assess the suitability of the complexes for  $^{18}\text{F}$ -radiolabelling initially ruled out the use of the aluminium complexes;  $\text{AlCl}_3$  did not react with  $\text{NR}_4\text{F}$  ( $R = \text{Me, Bu}$ ) in MeCN at room temperature, and heating led to the decomposition of the complex forming  $[\text{AlF}_4]^-$  and release of the free ligand. However, following adjustment of the reaction conditions (using a pH 4 buffered solution rather than acetonitrile), the successful  $\text{Cl}/^{18}\text{F}$  halide exchange of the pre-formed  $[\text{AlCl}_3(\text{BnMe}_2\text{-tacn})]$  complex was reported (Scheme 5.2).<sup>17</sup> Radiofluorination of the chloro- complex achieved a radiochemical yield of 24% after heating at 80 °C for 90 min. The crude product was successfully purified using a SPE purification protocol and showed very high stability in 50% EtOH/PBS (pH 7.4) after 3 h (RCP > 99%). However, unlike the  $\text{Al-}^{18}\text{F}$  systems, radiofluorination was not observed at lower concentrations (when using 0.1 mg of precursor vs. 1.0 mg).



Scheme 5.2 –  $\text{Cl}/^{19}\text{F}$  halide exchange of a pre-formed  $[\text{AlCl}_3(\text{BnMe}_2\text{-tacn})]$  complex.<sup>17</sup>

Both the gallium and indium complexes fluorinated readily at room temperature using  $\text{NR}_4\text{F}$  ( $\text{R} = \text{Me}, \text{Bu}$ ) or  $\text{KF}$ , although the process was much slower for indium than gallium. Hence, radiofluorination of the indium complex was not considered; instead, the radiochemistry of the  $[\text{GaCl}_3(\text{BnMe}_2\text{-tacn})]$  complex was explored (Scheme 5.3).



Scheme 5.3 –  $^{18}\text{F}/\text{Cl}$  halide exchange reaction on a pre-formed  $[\text{GaCl}_3(\text{BnMe}_2\text{-tacn})]$  complex.<sup>16</sup>

A radiochemical yield of 30% was achieved at room temperature in aqueous MeCN after 60 min, following the addition of 2.99 mol. equiv.  $[\text{F}^{19}]\text{KF}$  and 0.4 mL  $[\text{F}^{18}]\text{KF}$  to a  $2.36 \mu\text{mol mL}^{-1}$  (1.0 mg) solution of  $[\text{GaCl}_3(\text{BnMe}_2\text{-tacn})]$ . After HPLC purification, the  $[\text{Ga}^{18}\text{FF}_2(\text{BnMe}_2\text{-tacn})]$  complex displayed high stability in EtOH/PBS (pH 7.4), with an RCP of 98% after two hours. However, at nanomolar concentrations ( $0.1 \text{ mg}, 260 \text{ nmol mL}^{-1}$ ) the  $[\text{GaCl}_3(\text{BnMe}_2\text{-tacn})]$  complex did not undergo radiofluorination – this could be due to the hydrolytic sensitivity of the Ga-Cl bond, resulting in competition between slow hydrolysis and the  $\text{Cl}/^{19}\text{F}$  exchange.

$[\text{GaF}_3(\text{BnMe}_2\text{-tacn})]$  was later synthesised using the method employed for the Group 13 complexes of  $\text{L}^1$ ,  $\text{L}^2$  and  $\text{L}^3$  described in the previous chapter, *via* the molecular  $[\text{GaF}_3(\text{dmsO})(\text{OH}_2)_2]$  precursor.<sup>18</sup> This negates the use of hydrothermal conditions, and because the Ga-F bond is much more stable in water than the Ga-Cl bond, competitive hydrolysis is avoided.<sup>19</sup> Using this novel route,  $[\text{GaF}_3(\text{BnMe}_2\text{-tacn})]$  could be radiolabelled *via*  $^{18}\text{F}/^{19}\text{F}$  exchange, and at much lower concentrations. For example, a radiochemical yield of 37% was achieved using a  $27 \text{ nmol mL}^{-1}$  concentration of  $[\text{GaF}_3(\text{BnMe}_2\text{-tacn})]$  (0.01 g precursor) and heating for 10 min at  $80^\circ\text{C}$ .<sup>20</sup> The same report trials a wide variety of conditions, adjusting the precursor concentration, temperature, solvent and the length of time of the radiochemical reaction, to establish the effect of each on the  $[\text{F}^{18}]\text{F}^-$  incorporation. Table 5.1 summarises the conditions and outcomes for the isotopic exchange of  $[\text{AlF}_3(\text{BnMe}_2\text{-tacn})]$  and  $[\text{GaF}_3(\text{BnMe}_2\text{-tacn})]$ .

tacn)] complexes, and also includes  $[\text{Fe}^{18}\text{FF}_2(\text{BnMe}_2\text{-tacn})]$  mentioned in Chapter 1, which was one of the first examples of  $^{18}\text{F}$ -radiolabelling of transition metal trifluoride complex and showed promise as an inorganic radiotracer.<sup>1</sup>

Table 5.1 – Various radiolabelling conditions for  $[\text{MF}_3(\text{BnMe}_2\text{-tacn})]$  complexes ( $M = \text{Al}, \text{Ga}; \text{Fe}$ ).

<b><math>^{18}\text{F}</math>-Complex</b>	<b>Precursor concentration / nmol mL<sup>-1</sup></b>	<b>Reaction conditions</b>	<b>RCY / %</b>	<b>Stability after purification</b>
<b><math>[\text{AlF}_3(\text{BnMe}_2\text{-tacn})]^{17}</math></b>	2360	60:40 MeCN:H <sub>2</sub> O 80 °C; 90 min	9	> 99% RCP after 2 h in PBS
<b><math>[\text{AlF}_3(\text{BnMe}_2\text{-tacn})]^{17}</math></b>	2360	NaOAc buffer pH 4 80 °C; 90 min	24	
<b><math>[\text{GaF}_3(\text{BnMe}_2\text{-tacn})]^{20}</math></b>	2680	50:50 MeCN:H <sub>2</sub> O 80 °C; 60 min	23	98% RCP after 2 h in PBS; 83% RCP after 2 h in HSA
<b><math>[\text{GaF}_3(\text{BnMe}_2\text{-tacn})]^{20}</math></b>	2680	75:25 MeCN:H <sub>2</sub> O 80 °C; 10 min	73	
<b><math>[\text{GaF}_3(\text{BnMe}_2\text{-tacn})]^{20}</math></b>	2680	75:25 EtOH:H <sub>2</sub> O 80 °C; 10 min	81	
<b><math>[\text{GaF}_3(\text{BnMe}_2\text{-tacn})]^{20}</math></b>	268	75:25 MeCN:H <sub>2</sub> O 25 °C; 80 min	8	
<b><math>[\text{GaF}_3(\text{BnMe}_2\text{-tacn})]^{20}</math></b>	268	75:25 MeCN:H <sub>2</sub> O 80 °C; 10 min	66	
<b><math>[\text{GaF}_3(\text{BnMe}_2\text{-tacn})]^{20}</math></b>	27	75:25 MeCN:H <sub>2</sub> O 80 °C; 10 min	37	

Table 5.1 cont. –

<b>[<sup>18</sup>F]-Complex</b>	<b>Precursor</b>		<b>RCY / %</b>	<b>Stability after purification</b>
	<b>concentration / nmol mL<sup>-1</sup></b>	<b>Reaction conditions</b>		
<b>[FeF<sub>3</sub>(BnMe<sub>2</sub>-tacn)]<sup>1</sup></b>	2360	75:25 MeCN:H <sub>2</sub> O 80 °C; 10 min	44	> 90% RCP after 2 h in H <sub>2</sub> O or PBS or HSA
<b>[FeF<sub>3</sub>(BnMe<sub>2</sub>-tacn)]<sup>1</sup></b>	2360	75:25 MeCN:H <sub>2</sub> O RT; 10 min	6	
<b>[FeF<sub>3</sub>(BnMe<sub>2</sub>-tacn)]<sup>1</sup></b>	236	75:25 MeCN:H <sub>2</sub> O 80 °C; 10 min	40	
<b>[FeF<sub>3</sub>(BnMe<sub>2</sub>-tacn)]<sup>1</sup></b>	24	75:25 MeCN:H <sub>2</sub> O 80 °C; 10 min	13	

Precursor concentration and temperature of the radiochemical reaction have a clear effect on the radiochemical yields of the complexes. For example, for the [GaF<sub>3</sub>(BnMe<sub>2</sub>-tacn)] complex, a maximum RCY of 81% was observed at higher concentrations (2680 nmol mL<sup>-1</sup>) in aqueous EtOH with heating at 80 °C for 10 min. 268 nmol (0.1 mg) of precursor in aqueous MeCN (1 mL) gave a 66% RCY after heating at 80 °C for 10 min. However, at room temperature, RCY did not exceed 8% (268 nmol mL<sup>-1</sup>, 80 min). Some solvent dependency is also observed for the complex, with poor yields observed in more aqueous conditions, and a slightly better yield in EtOH (81%) vs. MeCN (73%) under the same conditions (2680 nmol mL<sup>-1</sup>, 80 °C, 10 min).

### 5.1.2 Aims

The work in this chapter will provide the first examples of (attempted) radiofluorination of MF<sub>3</sub> amide-tacn species, and will aim to establish the ideal conditions and HPLC methods through a systematic optimisation process.

Based on the previous work undertaken in Chapter 4, and also with the knowledge of the general properties of the Group 13 metals, only the gallium complexes of L<sup>1</sup> and L<sup>3</sup> will be considered. Many examples given in the literature have described the successful radiofluorination of GaF and GaF<sub>3</sub> species.<sup>13,14,20</sup> [FeF<sub>3</sub>(L<sup>1</sup>)] and [FeF<sub>3</sub>(L<sup>3</sup>)] may also represent suitable candidates. However, the work surrounding the [FeF(Bn-NODA)] complexes demonstrated significant decomposition during stability studies (in H<sub>2</sub>O and PBS), and more characterisation data is



available on  $[\text{GaF}_3(\text{L}^1)]$  and  $[\text{GaF}_3(\text{L}^3)]$ , due to the paramagnetic nature of  $d^5 \text{Fe}^{3+}$  being unsuitable for NMR analysis.

Additionally, although some of the work within this project and in the wider field has suggested amide pendant arms may be prone to hydrolysis under certain conditions, this was not observed in the coordination chemistry discussed in Chapter 4.<sup>21,22</sup> There may also be some competition between the amide functions of the pendant arm and  $^{18}\text{F}^-$  for the sixth coordination site. However, M-F bond strength is expected to prevail, and this is consistent with the crystal structures of  $[\text{GaF}_3(\text{L}^1)]$  and  $[\text{GaF}_3(\text{L}^3)]$  in Chapter 4.

The overarching objectives are to understand the role of the amide pendant arms in the radiochemical reaction, and also what effect (if any) they have on the ultimate stability of the radiolabelled product. To this end, the behaviour of the tris(amide) and mono(amide) ligands,  $\text{L}^1$  and  $\text{L}^3$ , will be compared with regard to their radiochemistry – the obvious difference between the two is the number of amide pendant arms and, therefore, the number of H-bonding donors. The work on the divalent transition metal complexes (Chapter 3) and the  $\text{MF}_3$  complexes (Chapter 4) have provided evidence for extensive hydrogen bonding. For  $[\text{GaF}_3(\text{L}^1)]$ , this was observed between adjacent amide(NH) and fluoride ligands of neighbouring molecules in the solid state. It was hypothesised that these interactions may assist in directing the incoming  $^{18}\text{F}^-$  ions towards the metal centre. Thus, this work aims to determine whether the presence of strong H-bonding donor groups affect the radiofluorination chemistry.

Both  $\text{L}^1$  and  $\text{L}^3$  are suitable for radiochemistry, as they contain a chromophore by nature of a phenyl ring, which will help to characterise the radio-products *via* comparison of the radio-HPLC and UV-HPLC traces. Additionally, many examples of inorganic  $^{18}\text{F}$  radiotracers in the literature are bound to a targeting vector i.e. a receptor-specific biomolecule or protein, often through a peptide (amide) bond. Hence, the amide pendant groups may be ideal for radiopharmaceutical applications, as they could allow for easy bioconjugation.

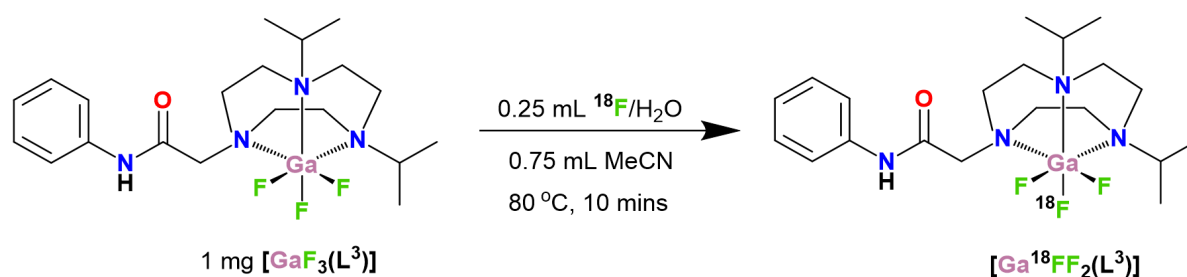
## 5.2 Results and Discussion

As mentioned above, the complexes,  $[\text{GaF}_3(\text{L}^3)]$  and  $[\text{GaF}_3(\text{L}^1)]$ , were identified as suitable candidates for  $^{19}\text{F}/^{18}\text{F}$  exchange reactions due to previous successes in the group with radiolabelling  $\text{GaF}_3$  complexes.<sup>16,20</sup> Additionally, a complete set of characterisation data – including molecular structures – has been obtained for both complexes. Any potential radio-products, e.g.  $[\text{Ga}^{18}\text{FF}_2(\text{L}^3)]$  and  $[\text{Ga}^{18}\text{FF}_2(\text{L}^1)]$ , can be identified by comparison of the  $R_f$  for the radiotracer and UV-HPLC trace of the radio-product, and matching the latter with the UV-HPLC trace of the reference complex.

General details with respect to the typical radiochemical experiments (radiation handling, general experimental method, safety, HPLC methods) are given in Section 1.4.2 of Chapter 1.

### 5.2.1 $^{19}\text{F}/^{18}\text{F}$ Exchange Reactions of $[\text{GaF}_3(\text{L}^3)]$

The initial experimental conditions for  $[\text{GaF}_3(\text{L}^3)]$  mirrored those described in the literature, using ca.  $3\ \mu\text{mol mL}^{-1}$  of complex first dissolved in 0.75 mL of MeCN and followed by the addition of 0.25 mL  $^{18}\text{F}/\text{H}_2\text{O}$ , heating for 10 minutes at 80 °C (Scheme 5.4). Adjustments to the HPLC method and the mobile phase were made depending on the results.



Scheme 5.4 – Initial isotopic exchange experimental conditions for the target  $[\text{Ga}^{18}\text{FF}_2(\text{L}^3)]$  complex.

The preliminary HPLC method was based on the method developed by Monzittu for the  $[\text{GaF}_3(\text{BnMe}_2\text{-tacn})]$  system.<sup>23</sup> The mobile phase consisted of solvents A and B, where A =  $\text{H}_2\text{O}$  + 0.1 % trifluoroacetic acid (TFA) and B = MeCN. TFA is a common mobile phase additive, particularly when UV detection is required, due to its solubility and volatility, and its resolving power as a strong acid (which determines how well two distinct signals will be differentiated).<sup>24,25</sup> It is often used for the separation of peptides (i.e. amide-containing compounds).<sup>26</sup> In this instance, it also mimics the 0.1% formic acid used during the purification of  $\text{L}^3$  described in Chapter 2, which assisted the movement of the ligand through the column. 0.1% formic acid is also used in the mobile phase throughout ESI MS<sup>+</sup> analysis. Before this, attempts to collect a UV-HPLC for the reference standard of  $[\text{GaF}_3(\text{L}^3)]$  using A =  $\text{H}_2\text{O}$  and B = MeCN alone were unsuccessful.

Under these conditions, the ‘cold’ (non-radiolabelled standard) complex was found to elute as a single peak at 5:14 min (Figure 5.3a). The attempted radiofluorination (using the experimental conditions described above) gave the result shown in Figure 5.3b. Initially, these results appeared very promising despite the broad feature on the baseline of the radio-HPLC trace. Two radio-peaks are observed, with a minor peak corresponding to free  $[^{18}\text{F}]\text{F}^-$ , and a second, major peak with a retention time similar to the reference standard (5:17 min). This experiment was repeated three times with the same result each time. Although it appears as though most of the radio-product related to the complex, an accurate radiochemical yield could not be calculated due to the broad baseline, which features at the same time that the (assumed) radio-product

elutes. It was initially presumed that the ‘tailing’ of the baseline was a result of the interaction of the radio-product (which was yet undefined) with the column.

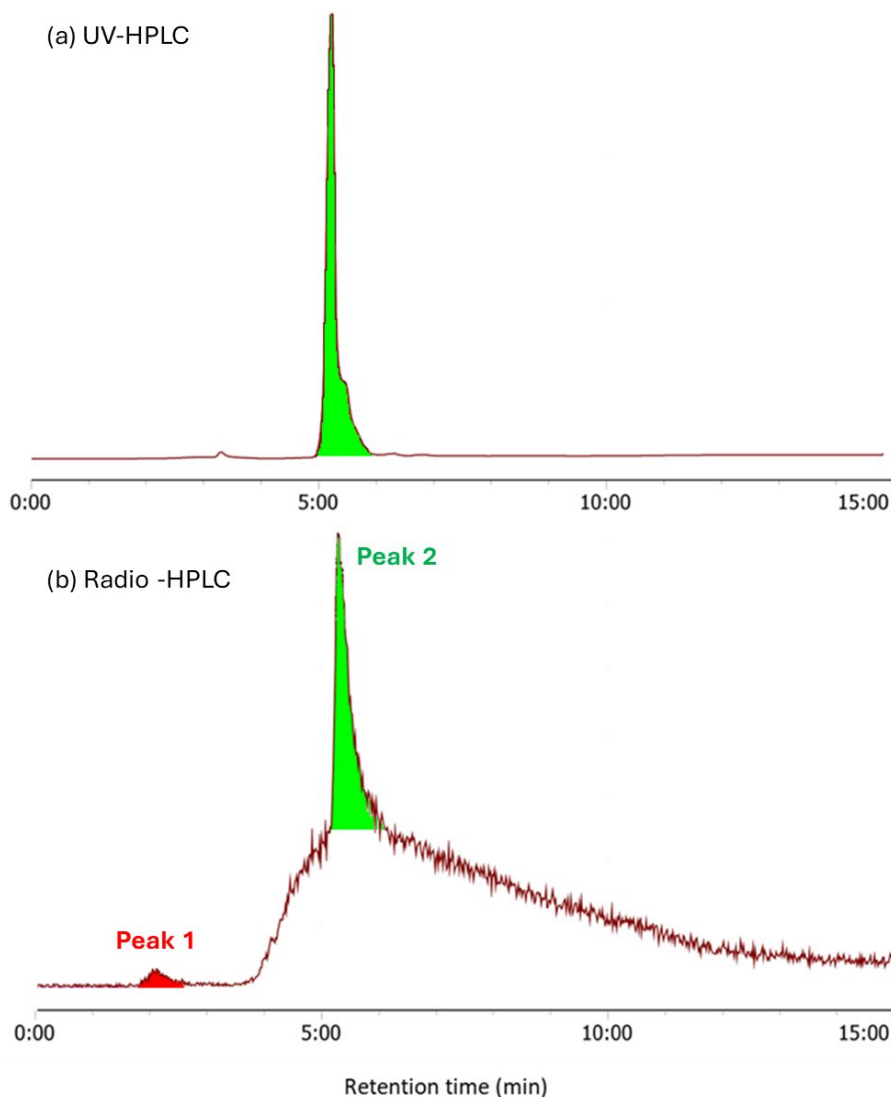


Figure 5.3 – (a) UV-HPLC trace of  $[\text{GaF}_3(\text{L}^3)]$ ,  $R_t = 5:14$  min; (b) Radio-HPLC trace of  $[\text{GaF}_3(\text{L}^3)]$ . Peak 1  $R_t = 2:07$  min. Peak 2  $R_t = 5:17$  min.

The next series of experiments sought to develop a HPLC method and mobile phase combination in which both the free fluoride and  $[\text{GaF}_3(\text{L}^3)]$  eluted as single, sharp peaks (with no tailing). In line with the mobile phase reported in the literature for the  $[\text{GaF}_3(\text{BnMe}_2\text{-tacn})]$  system, A = 10 mM ammonium acetate (in  $\text{H}_2\text{O}$ ) and B = MeCN was trialled. The complex eluted at a retention time of  $R_t = 10:12$  min, as a very broad peak in the UV-HPLC trace. However, no  $^{18}\text{F}^-$  uptake was observed under the same conditions ( $3\ \mu\text{mol mL}^{-1}$ ,  $80\ ^\circ\text{C}$ , 10 min).

The previous two results contradict each other — although the use of TFA in the mobile phase led to a very broad baseline in the radio-HPLC trace, it appeared as if two separate products eluted (a minor amount of free  $^{18}\text{F}^-$  and a second, unidentified major peak, which was initially

assumed to be  $[\text{Ga}^{18}\text{FF}_2(\text{L}^3)]$ . However, only one radio-product ( $^{18}\text{F}^-$ ) was observed when ammonium acetate was used. Therefore, to ascertain the nature of the second, unidentified peak in the initial experiments, a new HPLC method was developed in which TFA could be used in the mobile phase, and the tailing of the second radio-peak could be minimised.

As the broad baseline in the first experiments was observed as the major product began to elute (in keeping with the UV-HPLC trace, which matched the reference standard), 10% MeOH was added to Solvent B (MeCN) to rule out any issues with the complex sticking to, or precipitating in the column, as well as 0.1% TFA in Solvent A ( $\text{H}_2\text{O}$ ). The gradient was also adjusted so that the complex eluted much later than free fluoride, to ensure a clear difference between the two potential radio-products. As shown in Figure 5.4a, the UV-HPLC trace of the crude reaction mixture clearly shows one single product, which elutes at a retention time of 10:46 min (in line with the reference standard). Free fluoride is expected to elute at around two minutes – this is not observed in the radio-HPLC trace (Figure 5.4b). However, it does show a radioactive species eluting from the column, beginning at approximately the same time as the product in the UV-HPLC trace. At this point in the gradient, the mobile phase consists of almost 100% Solvent B.

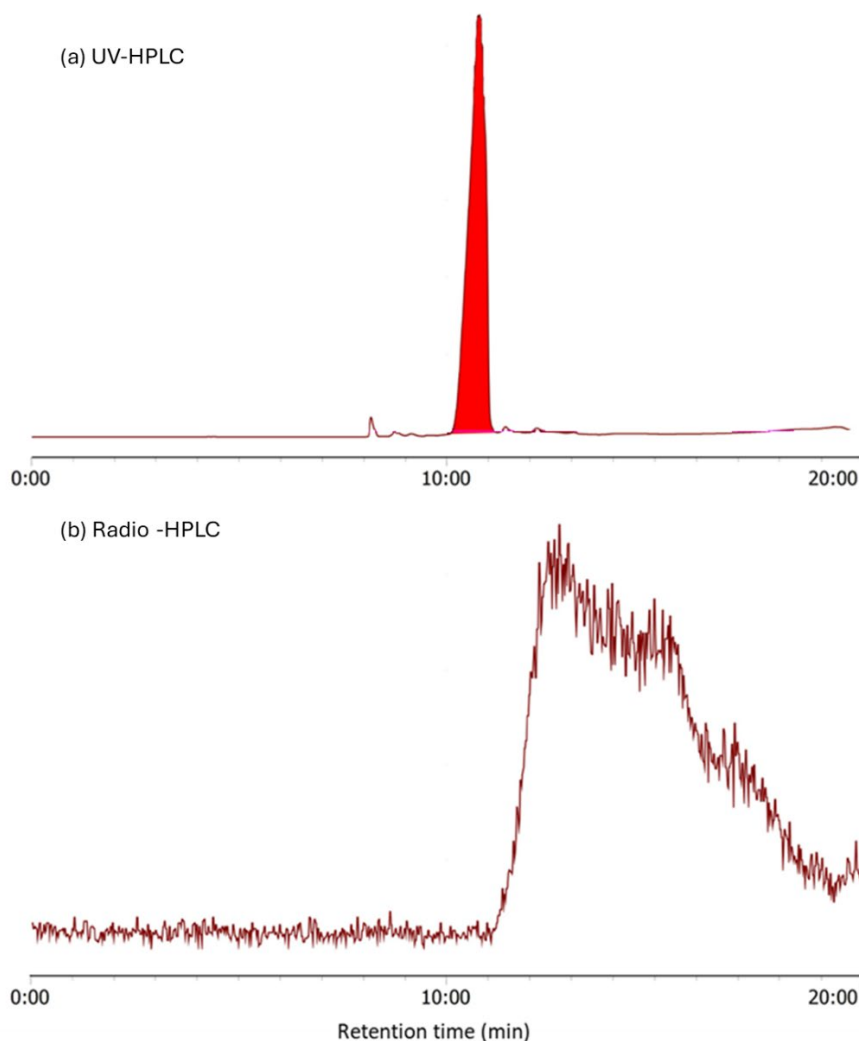


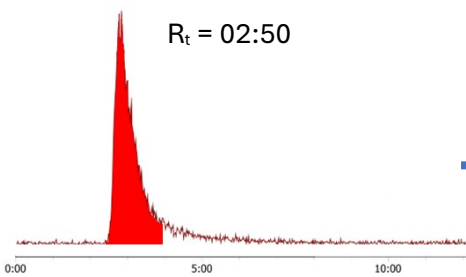

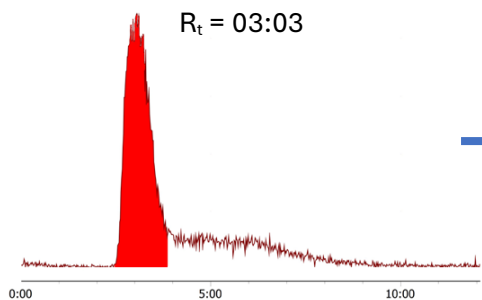

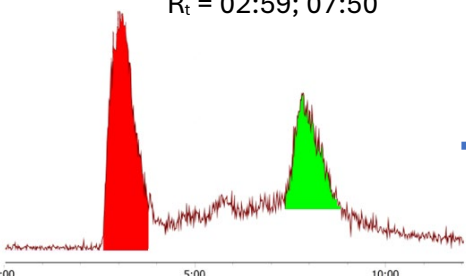
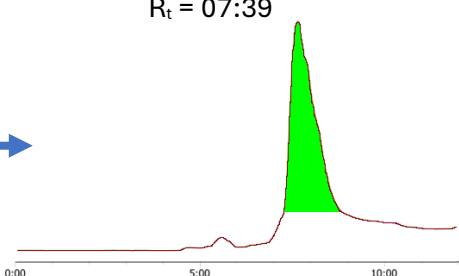
Figure 5.4 – (a) UV-HPLC trace of  $[GaF_3(L^3)]$ ,  $R_t = 10:46$  min; (b) Radio-HPLC trace of  $[GaF_3(L^3)]$ .

A study by Dieter *et al.*<sup>27</sup> found that pH of the mobile phase can strongly influence the retention of  $[^{18}F]$ -fluoride on silica-based reverse-phase HPLC columns. An aqueous solution of 0.1% TFA has a pH of 2.1 (e.g. solvent A of the mobile phase), at which point about 90% of the  $[^{18}F]$ -fluoride is present as  $[^{18}F]HF$ .<sup>28</sup> This can interact strongly with the silica core of the column, which will cause the behaviour observed in this work. When the gradient switches from predominantly aqueous to organic, as above, the pH of the mobile phase will increase. Hence, the fluoride may be seen to elute from the column later than typically expected.

With this in mind, a mobile phase combination was required that contained little-to-no-acid or buffer. Earlier attempts to elute the product with  $H_2O/MeCN$  alone were unsuccessful. However, after the addition of 10% MeOH to the MeCN phase and adjusting the gradient, a reference UV-HPLC of  $[GaF_3(L^3)]$  was obtained. The reaction conditions used for all previous attempts were replicated, with a small aliquot of the crude reaction mixture initially diluted so that it contained

10% organic content. Although a radio-peak relating to free  $[^{18}\text{F}]\text{F}^-$  was present, there was no peak in the UV-HPLC trace. This was also observed when the injected sample contained 20% organic content. To identify whether the complex was retained on the column (and to understand why there was no UV peak), an aliquot of the crude reaction mixture was diluted to contain 50% organic content. This time, a broad peak was observed in the UV-HPLC, alongside a new peak in the radio-chromatogram. Again, it was assumed that the  $[\text{GaF}_3(\text{L}^3)]$  complex underwent some  $[^{18}\text{F}]\text{F}^-$  uptake. Table 5.2 summarises the results.

Table 5.2 – Radio-HPLC and corresponding UV-HPLC traces of the crude  $^{18}\text{F}[\text{GaF}_3(\text{L}^3)]$  reaction mixture, diluted to 10, 20 and 50 percent organic content before injection into the HPLC.

Organic content (%)	Radio-HPLC Trace	UV-HPLC Trace
10	 <p><math>R_t = 02:50</math></p>	 <p>No UV-activity observed</p>
20	 <p><math>R_t = 03:03</math></p>	 <p>No UV-activity observed</p>
50	 <p><math>R_t = 02:59; 07:50</math></p>	 <p><math>R_t = 07:39</math></p>

Under these HPLC conditions, it can be said that the  $[\text{GaF}_3(\text{L}^3)]$  complex appeared to interact strongly with the silica column, and did not elute unless a significant percentage of organic solvent was used. However, the work in Chapter 4 highlighted the increased solubility of this complex (vs.  $[\text{GaF}_3(\text{L}^1)]$ ) under aqueous conditions, by nature of the stability studies undertaken in  $\text{D}_2\text{O}$ . This indicates that neither the solubility or the stability of the complex is the limiting factor in the experiments thus far. At this time, no firm conclusions with respect to the radiochemistry could be made.

Hence, the next and final series of experiments on this complex sought to replace the column entirely. The results above have shown that TFA is required in the mobile phase, to ensure the complex elutes well and consistently. However, they have also shown that the addition of TFA can cause retention of  $^{18}\text{F}$ -fluoride, leading to poor and unusable radio-HPLC baselines. Thus, TFA was added to Solvent B (MeCN/MeOH) rather than the  $\text{H}_2\text{O}$ , with the gradient adjusted to allow any free  $^{18}\text{F}$ -fluoride to elute under purely aqueous conditions before TFA is introduced to the column. The new column was also much shorter than the previous one, minimising the elution time of the  $^{18}\text{F}^-$  ( $R_t = \text{ca. } 1 \text{ min}$ , compared to  $R_t = \text{ca. } 3 \text{ min}$  for the longer column).

The results are shown in Figure 5.5 – (a) shows the UV-HPLC trace of  $[\text{GaF}_3(\text{L}^3)]$  with an  $R_t$  of 5:35 min, and (b) shows the radio-HPLC trace for the crude reaction mixture using the experimental conditions described. Both peaks are much sharper, and importantly, both the fluoride and the complex elute separately. No uptake is observed under these conditions in any of these experiments. The temperature of the reaction was lowered to  $60^\circ\text{C}$  and then to room temperature, but again, no  $^{18}\text{F}^-$  uptake was observed. The complex also showed no  $^{18}\text{F}^-$  uptake with increased reaction time under any temperature (20, 30 and 60 minutes). Given the range of conditions trialled, it is surprising that no radiofluorination was observed. The complex is known to stay intact for at least 4 h in aqueous conditions, so the absence of radiofluorination is not attributed to being a result of degradation (or insolubility, as mentioned above). Instead, it is possible that the ligand architecture hinders the radio-incorporation, possibly by the nature of the steric bulk imposed by isopropyl groups in close proximity to the metal centre.

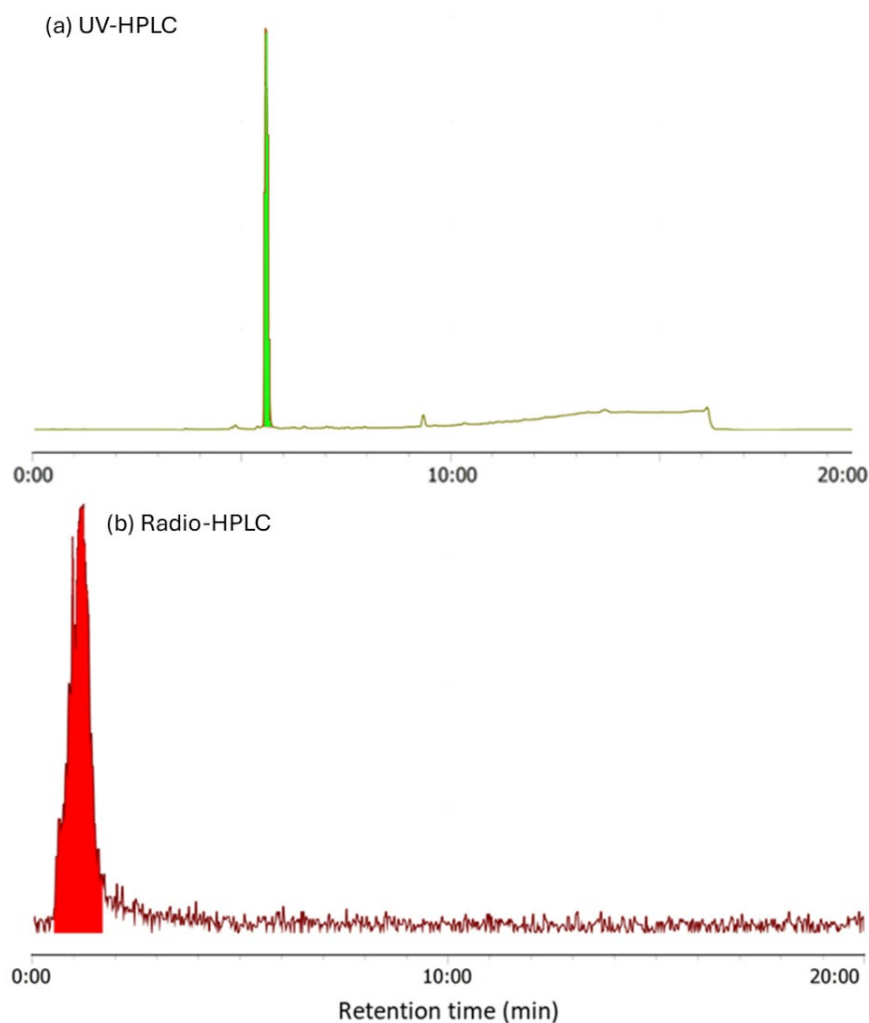


Figure 5.5 – (a) UV-HPLC trace of  $[\text{GaF}_3(\text{L}^3)]$ ,  $R_t = 5:35$  min; (b) Radio-HPLC trace of crude  $^{18}\text{F}$   $[\text{GaF}_3(\text{L}^3)]$  reaction mixture,  $R_t = 1:15$  min ( $[^{18}\text{F}]\text{F}$ ).

Figure 5.6 provides a visual summary of the radiochemical experiments attempted with the  $[\text{GaF}_3(\text{L}^3)]$  complex. Given the results above, attempted radiofluorination of  $[\text{GaF}_3(\text{L}^3)]$  was not pursued further. Instead, attention was turned to  $[\text{GaF}_3(\text{L}^1)]$ , as discussed below.



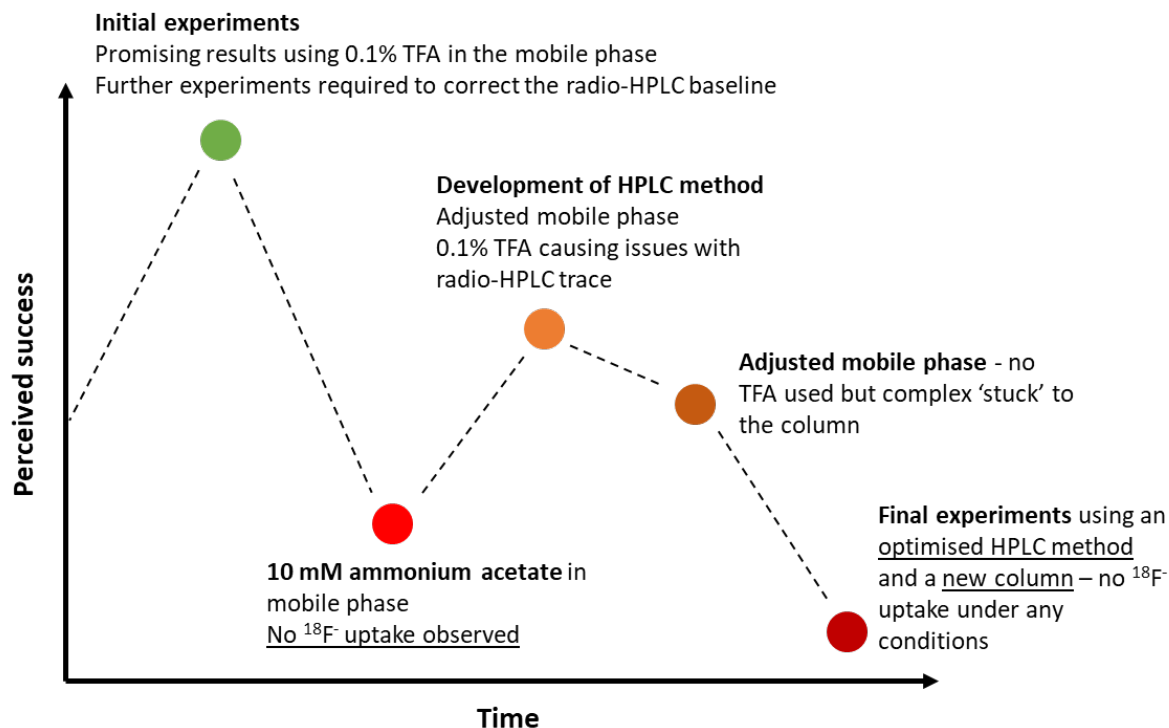
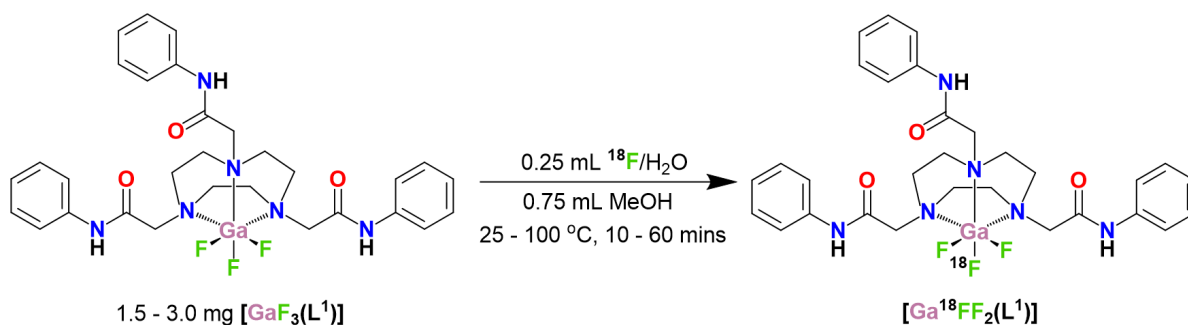


Figure 5.6 – Timeline summary of the development of the HPLC method and conditions for  $[\text{GaF}_3(\text{L}^3)]$ .

## 5.2.2 $^{19}\text{F}/^{18}\text{F}$ exchange reactions using $[\text{GaF}_3(\text{L}^1)]$

### 5.2.2.1 Development of the HPLC Method and Optimisation of Radiofluorination

Previous work in Chapter 4 showed that the  $[\text{GaF}_3(\text{L}^1)]$  complex was poorly soluble in most common solvents, except methanol. For this reason, all radiochemical experiments were carried out in 0.75 mL MeOH and 0.25 mL of target water ( $^{18}\text{F}/\text{H}_2\text{O}$ , 50 – 200 MBq) to give a concentration of 1.5 – 3.0  $\mu\text{mol mL}^{-1}$  (using 1 – 2 mg of complex per 1 mL of solvent). The general reaction for the isotopic exchange is given in Scheme 5.5.



Scheme 5.5 – General isotopic exchange experimental conditions for the target  $[\text{Ga}^{18}\text{FF}_2(\text{L}^1)]$  complex.

The initial HPLC method was again based on previous work in the group and used a mobile phase consisting of A =  $\text{H}_2\text{O}$  and B = MeCN. However, the limited solubility of the complex meant that most of the complex was retained on the column, and the UV-HPLC peak was very weak. The

mobile phase B was therefore changed to MeOH. Although the complex now eluted well and as a sharp peak, a radio-HPLC reference of [ $^{18}\text{F}$ ]-fluoride gave a very broad peak. The gradient was adjusted to sharpen the [ $^{18}\text{F}$ ]-fluoride peak, such that the first two minutes consisted predominantly of water in the mobile phase. Fully aqueous conditions were not used, as this caused the complex to precipitate on the column, causing a blockage. Details of the final mobile phase and the gradient used are given in Section 5.4.1.2. With a working HPLC method, several different conditions could be explored, which are summarised in Table 5.3.

Table 5.3 – Summary of the results from  $^{18}\text{F}/^{19}\text{F}$  isotopic exchange with  $[\text{GaF}_3(\text{L}^1)]$  using a range of conditions. Numbers highlighted in blue correlate with the optimised conditions i.e. the conditions which gave the highest RCY%.

Precursor concentration / $\mu\text{mol mL}^{-1}$	Temperature / $^{\circ}\text{C}$	Time / min	RCY / %
1.5	80	10	7
1.5	80	10	6
1.5	100	10	0
<b>3.0</b>	<b>80</b>	<b>10</b>	<b>20</b>
<b>3.0</b>	<b>80</b>	<b>10</b>	<b>19</b>
<b>3.0</b>	<b>80</b>	<b>10</b>	<b>18</b>
<b>3.0</b>	<b>80</b>	<b>10</b>	<b>15</b>
3.0	80	20	15
3.0	80	30	17
3.0	60	10	9
3.0	60	20	13
3.0	60	30	16
3.0	RT	15	7
3.0	RT	30	10
3.0	RT	45	11
3.0	RT	60	14

Interestingly,  $[\text{GaF}_3(\text{L}^1)]$  initially shows greater  $^{18}\text{F}^-$  uptake at room temperature compared to the  $[\text{FeF}_3(\text{BnMe}_2\text{-tacn})]$  complex (up to 14% vs. 6% at a similar concentration)<sup>1</sup>, but this observation does not continue at elevated temperatures. The highest RCY of ca. 20% was achieved reproducibly using 2 mg of the complex in MeOH, followed by the addition of  $[\text{F}^{18}]\text{F}^-$  in target water (to give a  $3.0 \mu\text{mol. mL}^{-1}$  solution in 75%:25% MeOH:H<sub>2</sub>O) and heating to 80  $^{\circ}\text{C}$  for 10 min (Scheme 5.5). Exceeding 80  $^{\circ}\text{C}$  led to no uptake, which is likely to be due to the temperature sensitivity of the amide bond.

Using a lower precursor concentration ( $1.0\text{ mg}$ ,  $1.5\text{ }\mu\text{mol mL}^{-1}$ ) also led to some radiofluorine incorporation, however, the RCY was lower (typically *ca.* 7%). Figure 5.7 shows the UV-HPLC (a) and radio-HPLC (b) from the optimised radiochemical reaction, which achieved the highest RCY of *ca.* 20%. It is possible that a higher radiochemical yield could be achieved at higher concentrations; however, given this was not pursued since radiolabelling is ideally performed using nano- to micro-molar concentrations of precursor (to replicate the conditions that would be used for radiotracers used in the clinic).

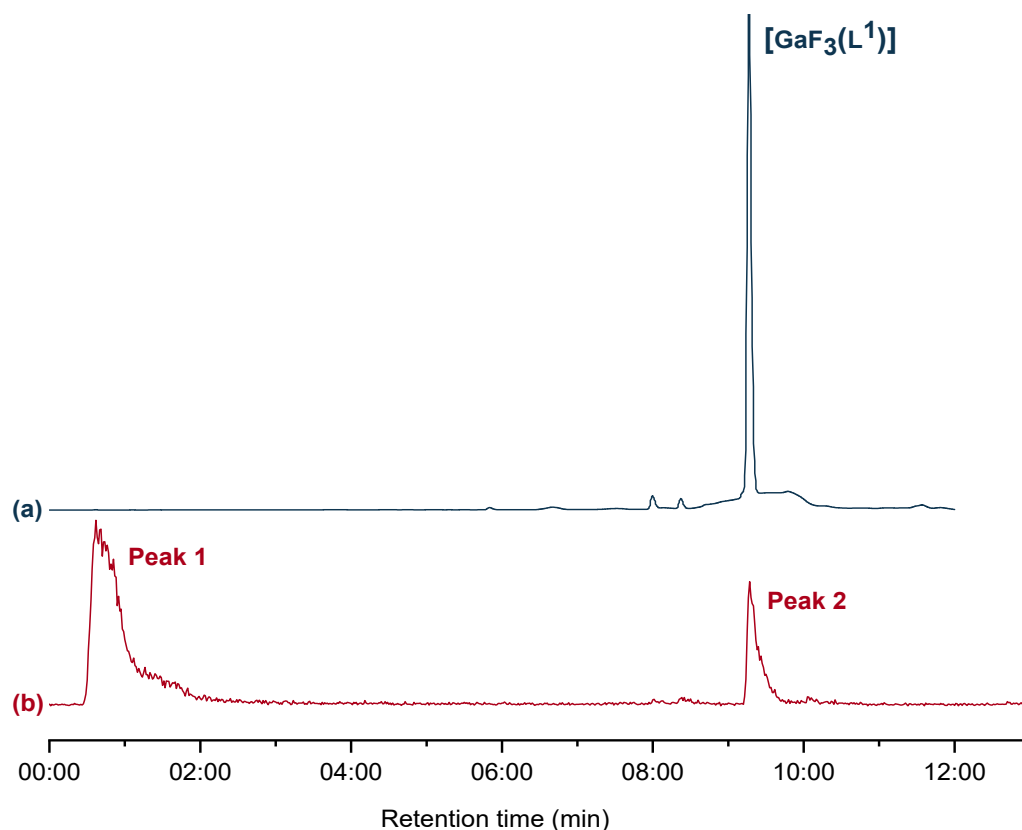


Figure 5.7 – (a) Analytical UV-HPLC trace of the reference standard compound  $[\text{GaF}_3(\text{L}^1)]$ ,  $R_t = 09:16\text{ min}$ ; (b) Analytical radio-HPLC trace of the crude product from radiofluorination of  $[\text{GaF}_3(\text{L}^1)]$ . Peak 1:  $R_t = 00:37\text{ min}$  80% ( $[\text{F}^{18}\text{F}]^-$ ). Peak 2:  $R_t = 09:17\text{ min}$  20% ( $[\text{Ga}^{18}\text{FF}_2(\text{L}^1)]$ ).

The observed radiochemical yields are lower than those reported for other gallium (tri)fluoride complexes with tacn-derivatives, which have been reported to have yields of up to 81% under similar conditions.<sup>20</sup> The exact reason for this behaviour is unknown, but it is likely that the limited solubility of the complex in the partially aqueous reaction solution is a significant factor.

### 5.2.3 Purification Protocol Using Solid-Phase Extraction (SPE)

Purification was attempted using a hydrophobic lipid-balanced (HLB) solid-phase extraction (SPE) cartridge method (see Section 5.4.3 for full details). The radio-product was formulated in

either 90:10 H<sub>2</sub>O/EtOH or 90:10 PBS/EtOH to investigate the radiochemical stability over a period of 2 h. Figure 5.8 shows the stacked radio-HPLC traces for both formulations.

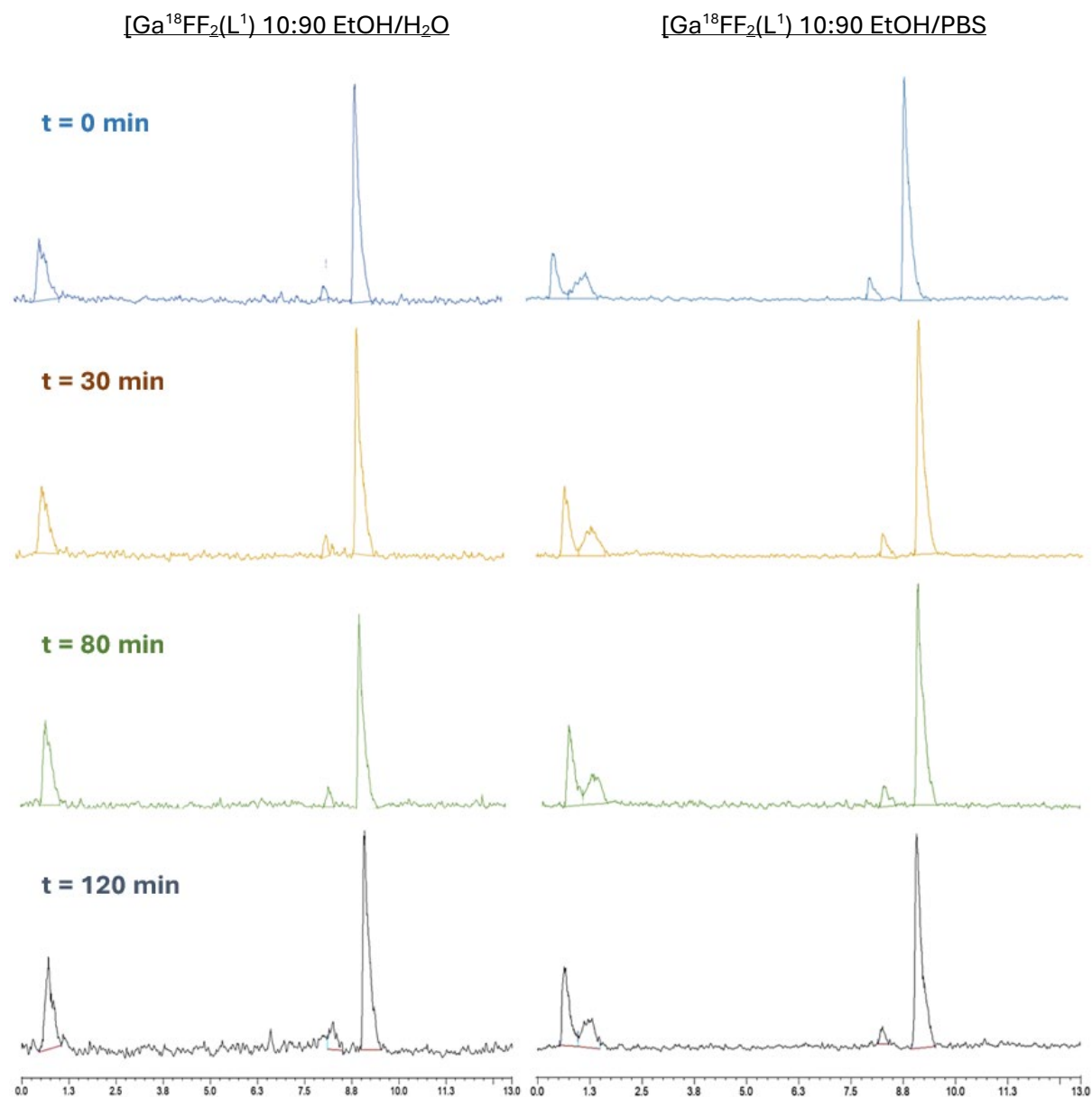


Figure 5.8 – Analytical radio-HPLC traces of the SPE purified  $[Ga^{18}FF_2(L^1)]$  in 10:90 EtOH:H<sub>2</sub>O (left) and 10:90 EtOH:PBS (right) at:  $t = 0, 30, 80$  and  $120$  min.

Over two hours, the radiochemical purity (RCP) decreases by ca. 7% in EtOH/H<sub>2</sub>O, and by ca. 5% in EtOH/PBS. The results are given in Table 5.4. Although the radiochemical yield of  $[Ga^{18}FF_2(L^1)]$  is much lower than those observed for  $[Ga^{18}F(Bn-NODA)]$ , the complex shows good stability in PBS and is not limited to acidic conditions. The purification method used was ineffective at removing all of the free  $[^{18}F]F^-$ , and given the high amount of radioactivity which was still present after purification (ca. 30 – 40%), these results are very promising. High levels of radiation often lead to increasing instability *via* radiolysis (decomposition induced *via*

radiation).<sup>29</sup> Efforts to improve the purification were not pursued further in the interest of time. However, the amide pendant clearly shows some favourable properties in terms of radiolabelling. This is consistent with the literature; many radiotracers (including those in clinical trials) often feature conjugation to biomolecules *via* amide-bond formation.<sup>30,31</sup>

Table 5.4 – Summary of the results from SPE purification of  $[\text{Ga}^{18}\text{FF}_2(\text{L}^1)]$  in  $\text{H}_2\text{O}/\text{EtOH}$  and  $\text{PBS}/\text{EtOH}$  over 2 h.

$[\text{Ga}^{18}\text{FF}_2(\text{L}^1)]$ in 90:10 $\text{H}_2\text{O}:\text{EtOH}$		$[\text{Ga}^{18}\text{FF}_2(\text{L}^1)]$ in 90:10 $\text{PBS}:\text{EtOH}$	
Time / min	RCP / %	Time / min	RCP / %
0	68	0	64
30	67	30	61
80	59	80	57
120	61	120	59

### 5.3 Conclusions

The work in this chapter presents the first examples of (attempted) radiofluorination on  $\text{GaF}_3$  complexes with amide-functionalised triazacyclononane ligands.

The first radiochemical experiment involving  $[\text{GaF}_3(\text{L}^3)]$  appeared promising, with two distinct peaks observed in the radio-HPLC trace. The first, minor peak appeared to correspond with free  $^{18}\text{F}^-$ , and the second, major peak was initially assumed to be  $[\text{Ga}^{18}\text{FF}_2(\text{L}^3)]$ . Adjustments to the HPLC method and mobile phase were required to address the broad nature of the radio-HPLC baseline, and after several iterations, it was later realised to be a result of the interaction of TFA with  $^{18}\text{F}^-$  forming  $^{18}\text{F}]\text{HF}$  (which does not elute well from silica  $\text{C}_{18}$  columns). Using a new column, a final method was developed, resulting in sharp and separate peaks for free  $^{18}\text{F}^-$  and  $[\text{GaF}_3(\text{L}^3)]$ . Several experimental conditions were trialled a minimum of two times each, with no  $^{18}\text{F}^-$  uptake observed under any conditions. These observations are very interesting, and not consistent with previously reported  $\text{GaF}_3$  (and  $\text{GaF}$ ) complexes.<sup>20,13,14</sup> Solubility and stability of the complex are not assumed to be limiting factors, based on previous work in Chapter 4. Instead, it is possible the ligand framework itself hinders any radio-incorporation.

The HPLC method development process used for the  $[\text{GaF}_3(\text{L}^3)]$  complex was useful in assisting the design of an appropriate HPLC method for the  $[\text{GaF}_3(\text{L}^1)]$  complex. As expected, solubility was a major limiting factor, and reactions could only be performed in MeOH. The radiochemical yields obtained for the  $[\text{GaF}_3(\text{L}^1)]$  complex are much lower than those previously obtained for  $[\text{GaF}_3(\text{BnMe}_2\text{-tacn})]$ , but are not dissimilar from some of the initially reported  $^{18}\text{F}^-$ - $[\text{AlF}(\text{NOTA})]$  complexes. This includes the first  $\text{Al}^{18}\text{F}$ -NOTA-peptide conjugate reported by McBride *et al.*<sup>6</sup> with

radiochemical yields between 5–20%, and also the  $[\text{Al}^{18}\text{F}(\text{NOTA-octreotide})]$  conjugate, with automated synthetic techniques achieving an RCY of 26.1% after 10 min with heating to 100 °C (which has also been used in clinical trials).<sup>32,8</sup> For  $[\text{GaF}_3(\text{L}^1)]$ , a max. RCY of 20% was achieved at 80 °C and 10 min, using 3  $\mu\text{mol}$  of the complex in 0.75 mL MeOH and 0.25 mL  $^{18}\text{F}^-/\text{H}_2\text{O}$ . Extending the time or the temperature of the radiochemical reaction did not lead to any improvements. It is possible that increasing the concentration of the  $^{18}\text{F}^-$  prior to radiofluorination experiments may increase the radiochemical yield. This could be done by first trapping the  $^{18}\text{F}^-$  on a QMA cartridge, eluting with a solution containing  $\text{K}^+/\text{Kryptofix 2.2.2}$ , azeotropic drying, and finally taking up the  $[\text{}^{18}\text{F}]\text{KF}/\text{Kryptofix 2.2.2}$  in the reaction solvent.<sup>33</sup> This would also minimise the amount of water in the reaction, which could assist with increasing solubility.

As the radiofluorination of the tris-amide complex was reproducible, and consistent, the optimised conditions were used to ascertain the stability of the radiolabelled  $[\text{Ga}^{18}\text{FF}_2(\text{L}^1)]$  complex. Purification was carried out using an SPE protocol, using a HLB cartridge. This resulted in an initial radiochemical purity of 68% and 64%, which decreased by 7% and 5% over two hours in EtOH/ $\text{H}_2\text{O}$  and EtOH/PBS, respectively. This is a significant improvement to the  $[\text{Ga}^{18}\text{F}(\text{Bn-NODA})]$  system, which is unstable above pH 6.5. Altering the purification method to increase the initial radiochemical purity may increase the stability over time by minimising any adverse effects of radiolysis. This could be done by using a dual-purification method, by first trapping the unreacted  $^{18}\text{F}^-$  from the crude reaction mixture on a QMA cartridge, followed by purification using a HLB cartridge.

In this work, only the radiochemistry of the gallium complexes of  $\text{L}^1$  and  $\text{L}^3$  have been studied. Future work could attempt the radiofluorination of the iron complexes, which would also help to understand the effect of the central metal ion on the radiochemistry of amide-triazacyclononane complexes. Additionally, the (sterically-bulky) isopropyl groups of  $\text{L}^3$  could be exchanged for methyl groups, to closer resemble the  $\text{BnMe}_2\text{-tacn}$  ligand (which has been demonstrated to be successful with  $\text{GaF}_3$  and  $\text{FeF}_3$  complexes). This may ease access of  $^{18}\text{F}^-$  to the metal centre, but could also alter the lipophilicity of the ligand, both which may affect the radiolabelling efficiency.

## 5.4 Experimental

Details of the instrumentation used are given in Appendix A.  $[\text{GaF}_3(\text{L}^1)]$  and  $[\text{GaF}_3(\text{L}^3)]$  used as prepared in Chapter 4. Solvents used were of HPLC-chromatography grade.  $^{18}\text{F}/\text{H}_2\text{O}$  used as supplied from the Positron Emitting Radionuclide Laboratory (PERL) facility at St Thomas' Hospital, London.

### 5.4.1 Analytical HPLC Method

#### 5.4.1.1 [GaF<sub>3</sub>(L<sup>3</sup>)]

The final, optimised HPLC method for [GaF<sub>3</sub>(L<sup>3</sup>)] is given in Table 5.5 below, where the mobile phase A = 100% H<sub>2</sub>O ; B = (90% MeCN + 10% MeOH) +0.1 % TFA. Flow rate: 1 mL min<sup>-1</sup>. Column: Agilent Zorbax 1.8 µm CB-C18 4.6 x 50 mm.

Table 5.5 – Gradient used for analytical HPLC analysis of [GaF<sub>3</sub>(L<sup>3</sup>)].

Time / min	% A	% B
0	100	0
2	100	0
12	90	10
13	50	50
14	100	0
20	100	0

#### 5.4.1.2 [GaF<sub>3</sub>(L<sup>1</sup>)]

The final, optimised HPLC method for [GaF<sub>3</sub>(L<sup>1</sup>)] is given in Table 5.6 below, where the mobile phase A = 90% H<sub>2</sub>O + 10% MeOH; B = 100% MeOH; C = 100% H<sub>2</sub>O. Flow rate: 1 mL min<sup>-1</sup>. Column: Agilent Zorbax 1.8 µm CB-C18 4.6 x 50 mm.

Table 5.6 – Gradient used for analytical HPLC analysis of [GaF<sub>3</sub>(L<sup>1</sup>)].

Time / min	% A	% B	% C
0	0	0	100
1.5	50	0	50
2	100	0	0
10	0	100	0
10.5	0	100	0
11	50	0	50
12	0	0	100
13	0	0	100

## 5.4.2 $^{19}\text{F}/^{18}\text{F}$ Isotopic Exchange Radiolabelling Procedure

### 5.4.2.1 $[\text{Ga}^{18}\text{FF}_2(\text{L}^3)]$

In a typical experiment,  $[\text{GaF}_3(\text{L}^3)]$  (1 mg,  $3.0 \mu\text{mol mL}^{-1}$ ) was added to a small Eppendorf and dissolved in MeCN (0.75 mL). 0.25 mL of an aqueous solution containing  $[^{18}\text{F}]\text{F}^-$  (50 – 200 MBq) was added to this solution. This was heated to  $80^\circ\text{C}$  for 10 minutes in a heating block. An aliquot of 0.1 mL of the crude reaction mixture was then diluted in 0.9 mL of  $\text{H}_2\text{O}$  so that approximately 10% of the solvent composition was organic. A small sample ( $\sim 20 \mu\text{L}$ ) of the diluted crude reaction solution was removed for analysis by analytical HPLC, to deduce the percentage incorporation of  $[^{18}\text{F}]\text{F}^-$  into the metal complex (based upon integration of the radio peaks). A range of HPLC conditions were trialled, but no uptake was observed.

### 5.4.2.2 $[\text{Ga}^{18}\text{FF}_2(\text{L}^1)]$

In a typical experiment,  $[\text{GaF}_3(\text{L}^3)]$  (1 – 2 mg,  $1.5 - 3.0 \mu\text{mol mL}^{-1}$ ) was added to a reaction vessel and dissolved in MeOH (0.75 mL). 0.25 mL of an aqueous solution containing  $[^{18}\text{F}]\text{F}^-$  (50 – 200 MBq) was added to this solution. This was left to stand at room temperature (up to 60 minutes) or heated to  $60^\circ\text{C}$  or  $80^\circ\text{C}$  (up to 30 minutes) using the FastLAB heating block. An aliquot of 0.1 mL of the crude reaction mixture was then diluted in 0.9 mL of  $\text{H}_2\text{O}$  so that approximately 10% of the solvent composition was organic. A small sample ( $\sim 20 \mu\text{L}$ ) of the diluted crude reaction solution was removed for analysis by analytical HPLC, to deduce the percentage incorporation of  $[^{18}\text{F}]\text{F}^-$  into the metal complex (based upon integration of the radio peaks). A maximum RCY of 20% was observed using 2 mg of sample and heating at  $80^\circ\text{C}$  for 10 minutes.

## 5.4.3 SPE Purification Protocol

The crude reaction mixture (1 mL) was diluted with 9 mL of water and loaded onto an HLB (hydrophobic-lipophilic-balance) solid phase extraction (SPE) cartridge. This was washed with water (30 mL) to remove  $[^{18}\text{F}]\text{F}^-$ , and then the product was eluted from the cartridge with ethanol (2 mL). The eluted portion was split into two 1 mL fractions and diluted with (i) water to result in a formulated product in 90:10  $\text{H}_2\text{O}/\text{EtOH}$  or (ii) PBS to result in a formulated product in 90:10 PBS/EtOH. The formulated products were analysed by HPLC at  $t = 0$  and various time intervals up to two hours.



## 5.5 References

1. P. J. Blower, W. Levason, S. K. Luthra, G. McRobbie, F. M. Monzittu, T. O. Mules, G. Reid and M. Nadeem Subhan, *Dalton Trans.*, 2019, **48**, 6767.
2. K. Chansaenpak, B. Vabre and F. P. Gabbaï, *Chem. Soc. Rev.*, 2016, **45**, 954.
3. H. Hong, L. Zhang, F. Xie, R. Zhuang, D. Jiang, H. Liu, J. Li, H. Yang, X. Zhang, L. Nie and Z. Li, *Nat. Commun.*, 2019, **10**, 1.
4. K. R. Scroggie, M. V. Perkins and J. M. Chalker, *Front. Chem.*, 2021, **9**, 687678.
5. M. Namavari, Z. Cheng, R. Zhang, A. De, J. Levi, J. K. Hoerner, S. S. Yaghoubi, F. A. Syud and S. S. Gambhir, *Bioconjug. Chem.*, 2009, **20**, 432.
6. W. J. McBride, R. M. Sharkey, H. Karacay, C. A. D'Souza, E. A. Rossi, P. Laverman, C. H. Chang, O. C. Boerman and D. M. Goldenberg, *J. Nucl. Med.*, 2009, **50**, 991.
7. S. J. Archibald and L. Allott, *EJNMMI Radiopharm. Chem.*, 2021, **6**, 30.
8. T. Long, N. Yang, M. Zhou, D. Chen, Y. Li, J. Li, Y. Tang, Z. Liu, Z. Li and S. Hu, *Clin. Nucl. Med.*, 2019, **44**, 452.
9. W. Wan, N. Guo, D. Pan, C. Yu, Y. Weng, S. Luo, H. Ding, Y. Xu, L. Wang, L. Lang, Q. Xie, M. Yang and X. Chen, *J. Nucl. Med.*, 2013, **54**, 691.
10. C. A. D'Souza, W. J. McBride, R. M. Sharkey, L. J. Todaro and D. M. Goldenberg, *Bioconjug. Chem.*, 2011, **22**, 1793.
11. D. Shetty, S. Y. Choi, J. M. Jeong, J. Y. Lee, L. Hoigebazar, Y. S. Lee, D. S. Lee, J. K. Chung, M. C. Lee and Y. K. Chung, *Chem. Commun.*, 2011, **47**, 9732.
12. W. J. McBride, R. M. Sharkey and D. M. Goldenberg, *EJNMMI Res.*, 2013, **3**, 36.
13. R. Bhalla, W. Levason, S. K. Luthra, G. McRobbie, G. Sanderson and G. Reid, *Chem. Eur. J.*, 2015, **21**, 4688.
14. D. E. Runacres, V. K. Greenacre, J. M. Dyke, J. Grigg, G. Herbert, W. Levason, G. McRobbie and G. Reid, *Inorg. Chem.*, 2023, **62**, 20844.
15. C. J. Broan, E. Cole, K. J. Jankowski, D. Parker, K. Pulukkody, B. A. Boyce, N. R. A. Beeley, K. Millar and A. T. Millican, *Synthesis*, 1992, 63.
16. R. Bhalla, C. Darby, W. Levason, S. K. Luthra, G. McRobbie, G. Reid, G. Sanderson and W. Zhang, *Chem. Sci.*, 2014, **5**, 381.
17. W. Levason, S. K. Luthra, G. McRobbie, F. M. Monzittu and G. Reid, *Dalton Trans.*, 2017, **46**, 14519.
18. R. Bhalla, J. Burt, A. L. Hector, W. Levason, S. K. Luthra, G. McRobbie, F. M. Monzittu and G. Reid, *Polyhedron*, 2016, **106**, 65.
19. R. Bhalla, W. Levason, S. K. Luthra, G. McRobbie, G. Reid, G. Sanderson and W. Zhang, *Chem. Commun.*, 2014, **50**, 12673.

20. F. M. Monzittu, I. Khan, W. Levason, S. K. Luthra, G. McRobbie and G. Reid, *Angew. Chem. Int. Ed.*, 2018, **57**, 6658.
21. J. Holub, M. Meckel, V. Kubiček, F. Rösch and P. Hermann, *Contrast Media Mol. Imaging*, 2015, **10**, 122.
22. T. Weyhermüller, K. Weighardt and P. Chaudhuri, *J. Chem. Soc., Dalton Trans.*, 1998, 3805.
23. F. M. Monzittu, PhD, University of Southampton, 2018.
24. B. Cai and J. Li, *Anal. Chim. Acta*, 1999, **399**, 249.
25. H. G. Barth, *LC GC N. Am.*, 2019, **37**, 824.
26. K. Sikora, M. Jaśkiewicz, D. Neubauer, D. Migoń and W. Kamysz, *Pharmaceuticals*, 2020, **13**, 442.
27. D. Ory, J. Van Den Brande, T. De Groot, K. Serdons, M. Bex, L. Declercq, F. Cleeren, M. Ooms, K. Van Laere, A. Verbruggen and G. Bormans, *J. Pharm. Biomed. Anal.*, 2015, **111**, 209.
28. N. R. Johnston and S. A. Strobel, *Arch. Toxicol.*, 2020, **94**, 1051.
29. K. Vermeulen, M. Vandamme, G. Bormans and F. Cleeren, *Semin. Nucl. Med.*, 2019, **49**, 339.
30. A. Schmidtke, T. Läppchen, C. Weinmann, L. Bier-Schorr, M. Keller, Y. Kiefer, J. P. Holland and M. D. Bartholomä, *Inorg. Chem.*, 2017, **56**, 9097.
31. D. Shetty, J. M. Jeong, C. H. Ju, Y. J. Kim, J.-Y. Lee, Y.-S. Lee, D. S. Lee, J.-K. Chung and M. C. Lee, *Biorg. Med. Chem.*, 2010, **18**, 7338.
32. T. Tshibangu, C. Cawthorne, K. Serdons, E. Pauwels, W. Gsell, G. Bormans, C. M. Deroose and F. Cleeren, *EJNMMI Radiopharm. Chem.*, 2020, **5**, 4.
33. L. Y. F. Haveman, D. J. Vugts and A. D. Windhorst, *EJNMMI Radiopharm. Chem.*, 2023, **8**, 28.

## Chapter 6 Exploring Routes Towards Group 13 Fluoride Complexes with Penta- and Hexa-dentate Triazacyclononane Ligands

### 6.1 Introduction

This chapter will investigate potential alternative routes towards Group 13 metal fluoride complexes with the ligands  $L^1$ ,  $L^3$ ,  $H_3$ -NOTA,  $H_2$ -Bn-NODA and  $H_2$ -Bn-NODP, whilst expanding on their known behaviours and coordination chemistry with different metal ions. Both the effect of Lewis acidity and ionic radii will be studied by comparison of the trivalent metal ions,  $Al^{3+}$ ,  $Ga^{3+}$  and  $In^{3+}$ , as well as to the divalent transition metal complexes described in Chapter 3.

#### 6.1.1 Radiochemical Applications of $M^{3+}$ (M = Al, Ga, In, Fe)

##### 6.1.1.1 Amide Pendant Arm Donors

$^{68}Ga$  is another prominent radioisotope used for PET imaging, and its clinical radiopharmaceuticals typically involve DOTA-like ligands (tetraazamacrocycles).<sup>1</sup> However, triaza-macrocyclic ligands have been shown to be more suitable for the  $Ga^{3+}$  ion than the conventional DOTA-derivatives.<sup>2</sup> In particular, NOTA-monoamides have appeared as a promising class of ligands in recent years owing to their relative ease of synthesis, and bifunctionality through amide formation.<sup>3,4</sup> With this in mind, Holub *et al.*<sup>5</sup> have reported the synthesis of two novel NOTA-bis(phosphonate) ligands – including one with mono-amide functionality, NOTAM<sup>BP</sup> – shown in Figure 6.1. Their properties and behaviour with  $Ga^{3+}$  are described, with the aim of finding suitable candidates for the  $^{68}Ga$  PET imaging of bone metastases. Bone metastases are a common complication of cancer, and therefore, bone tissue is an often-sought target of diagnostic imaging.<sup>6</sup> Many examples involve bis(phosphinate) groups, as these have a high affinity for hydroxyapatite (a mineral found in bone tissue).<sup>7</sup>

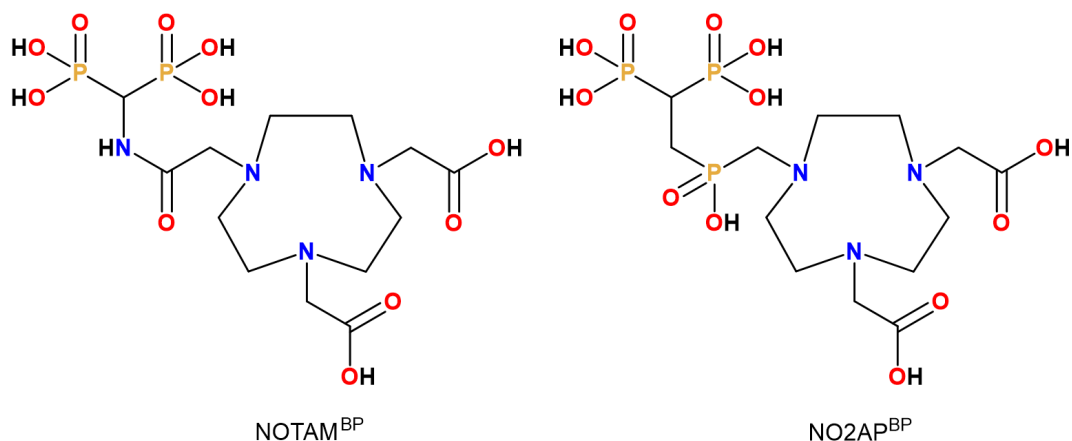


Figure 6.1 – Structures of the two bis(phosphonate) triazacyclononane ligands reported by Holub *et al.*<sup>5</sup>

The two different gallium complexes, [Ga(NOTAM<sup>BP</sup>)] and [Ga(NO2AP<sup>BP</sup>)], showed considerably different properties. For both, the initial mixing of reagents immediately formed an intermediate ‘out-of-cage’ species, with the Ga<sup>3+</sup> ion bound only to the oxygen atoms of the bis(phosphonate) groups and the pendant arms. However, much faster complexation was observed for the methylenephosphinate complex compared to the acetamide complex; it is suggested that the phosphinate group is much better at facilitating the ion transfer from an ‘out-of-cage’ species to an ‘in-cage’ complex. At elevated temperatures (> 60 °C), hydrolysis of the amide pendant arm of NOTAM<sup>BP</sup> was observed, which progressed at a much faster rate with increasing pH (from pH 2 – pH 4). This is attributed to the presence of hydroxide anions. Upon complexation, Ga<sup>3+</sup> is coordinated to the tacn-nitrogen atoms, the carboxylate oxygens of the acid groups, and the amide. In this case, coordination to a small trivalent metal ion with hard Lewis acid character decreases the electron density on the amide carbon atom, making it vulnerable to nucleophilic attack (e.g. by OH<sup>-</sup>). The <sup>71</sup>Ga NMR spectrum of the product indicated some decomposition to form the known [Ga(NOTA)] complex, which was later confirmed by SCXRD analysis.

Shetty *et al.*<sup>8</sup> have also reported two similar mono-amide derivatives of H<sub>3</sub>-NOTA for <sup>68</sup>Ga radiolabelling, with methylacetamide and benzylacetamide amide pendant arms. Interestingly, they discuss the formation of gallium complexes with both ligands that are stable at physiological pH and at higher temperatures (85 °C). Complexation was achieved *via* the reaction of the gallium nitrate hydrate precursor with the ligands in an aqueous solution (buffered to pH 3 or pH 5), whilst heating to 100 °C for 15 min. No hydrolysis was observed, although it is noteworthy to mention that the product mixture was purified by RP-HPLC prior to characterisation. However, for the benzylacetamide complex, different coordination was observed depending on the pH of the reaction (Figure 6.2). No pH-dependent preference was observed for the methylacetamide equivalent (which shows N<sub>4</sub>O<sub>2</sub> coordination in both

instances). In this case, the amide is deprotonated, and shows similar coordination observed for the  $\text{Cr}^{3+}$  complex of TCMT<sup>9</sup>, and the  $\text{Co}^{3+}$  complex of L<sup>1</sup>, both discussed in Chapter 3. It is suggested that the  $\text{N}_3\text{O}_3$  coordination arises at low pH due to protonation of the carbonyl oxygen, which leads to the formation of an imide bond due to isomerism. These observations contrast with other reported amide derivatives of  $\text{H}_3\text{-NOTA}$ , which have shown that the oxygen always coordinates to the gallium under any conditions.<sup>3</sup>

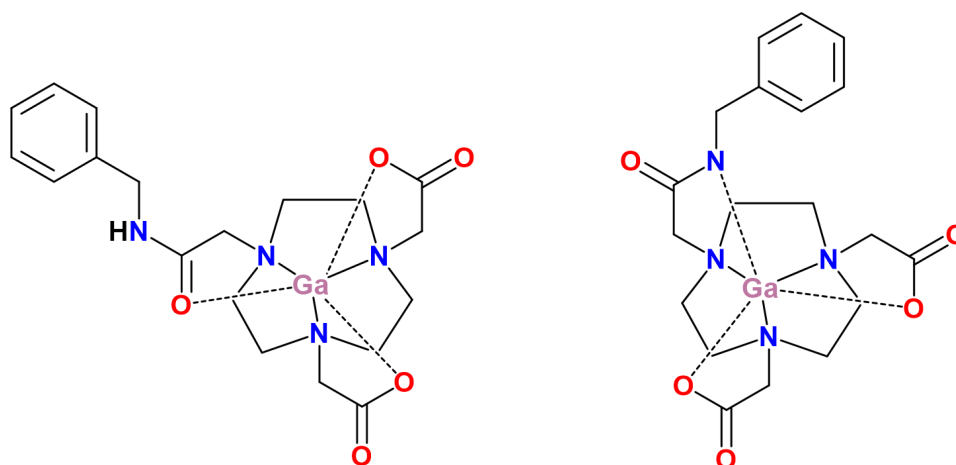


Figure 6.2 – Structures of the two gallium complexes with the benzylacetamide mono-amide derivative of  $\text{H}_3\text{-NOTA}$ . The gallium ion is bound to the oxygen of the amide at pH = 3, and to the nitrogen of the amide at pH = 5.<sup>8</sup>

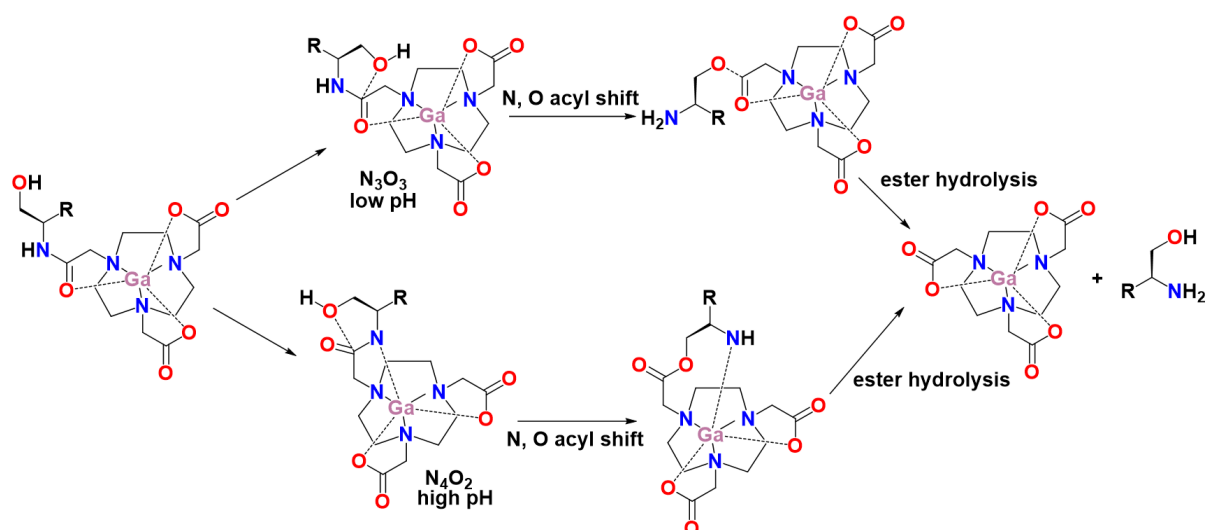
#### 6.1.1.1.1 Metal-Mediated Autolytic Amide Bond Cleavage in Radio-Metallopharmaceuticals

Selective metal ion-mediated peptide bond cleavage is well-documented in a range of natural processes and, in recent years, has been harnessed towards pro-drug applications.<sup>10</sup> Pro-drugs represent an emerging class of pharmaceuticals, particularly important when the physiochemical properties of a target drug limit formulation options, or when the pharmacokinetics are unfavourable.<sup>11</sup> This approach involves the use of a parent compound that can undergo controlled bond cleavage reactions *in vivo* to release the active drug.<sup>12</sup> The requirement for an external stimulus to activate the bond cleavage has traditionally been a limiting factor in the development of pro-drugs.<sup>13</sup>

However, recent work by the Boros group has sought to exploit the Lewis acidic properties of trivalent  $\text{Ga}^{3+}$  to selectively cleave amide bonds to release (radio)-metallopharmaceuticals.<sup>14</sup> The development, optimisation, and *in vivo* studies of  $[\text{Ga}(\text{NO}_2\text{A})]$  complexes conjugated to a biological targeting vector (Bn-PSMA) and a prodrug cap or solid support are reported.

Initial findings utilising a serine- $\text{NO}_2\text{A}$  complex concur with the gallium mono-amide complexes described above, which demonstrate the pH dependency of the coordination mode. At low pH (< 4.5),  $\text{N}_3\text{O}_3$  coordination involving the three carboxamide-oxygens was observed, but above pH

= 5.5, deprotonation of and subsequent binding to the amide-nitrogen was observed. Both coordinative modes – which involve coordinative polarisation of the amide bond from the highly Lewis acidic metal centre – can induce an N, O acyl shift rearrangement, which is followed by ester hydrolysis (Scheme 6.1). However, accelerated rearrangement and ester hydrolysis was observed for the  $N_3O_3$  mode, at a lower pH. The rate of hydrolysis was also observed to proceed at an accelerated rate upon heating to 37 °C and 80 °C.



Scheme 6.1 – N, O-acyl rearrangement of mono-amide (serine)  $[Ga(NO_2A)]$  complexes for both  $N_3O_3$  (low pH) and  $N_4O_2$  coordination modes.

The selective release of high molar activity  $^{67}Ga$ -radiolabelled pharmaceuticals at tracer concentration is then described, with the target drug synthesised on a solid support. This demonstrates an improvement upon current radiochelation methods, which require a significant excess of free ligand (4-5 orders of magnitude) and inhibits the effective binding of *in vivo* targets. The desired radiometal complex is released into solution through metal-mediated autolytic amide bond cleavage, whilst the unreacted precursor remains bound to the solid support. This was applied to the pro-drug release of the  $[Ga(NO_2A)]$ -Bn-conjugate *in vivo* (Figure 6.3). Interestingly, greater steric encumbrance was observed to lead to an increased rate of hydrolysis at 37 °C.

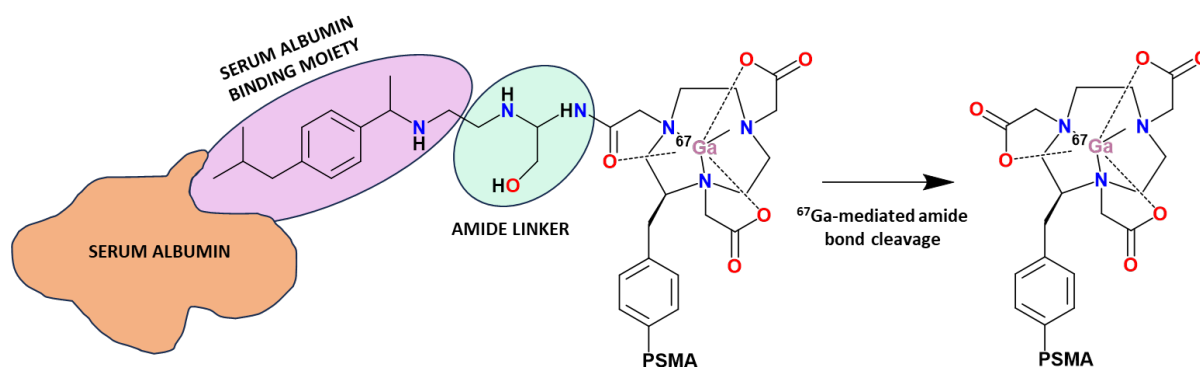


Figure 6.3 –  $[^{67}\text{Ga}(\text{NO}_2\text{A-Bn-PSMA})]$  conjugate bound to a serum albumin binding moiety via a serine (amide) linker. Polarisation of the carbonyl-amide bound to the Lewis acidic  $\text{Ga}^{3+}$  centre leads to the autolytic cleavage of the amide bond.

#### 6.1.1.2 Anionic Carboxylate and Phosphinate Pendant Arm Donors

This work, including the above, has discussed a range of literature examples involving NOTA derivatives and their increasing clinical use within  $^{68}\text{Ga}$  PET imaging. Likewise, due to their favourable ligand binding properties and excellent *in vivo* stability,  $\text{H}_3\text{-NOTA}$  derivatives are also well-known chelators for aluminium and indium, for radiometal ( $^{111}\text{In}$ ) and  $\text{Al-}^{18}\text{F}$  PET imaging applications.<sup>15,16</sup>

$[\text{In}(\text{NOTA})]$  was first discovered by Craig *et al.*<sup>17</sup> in 1989, who aimed to form kinetically inert  $^{111}\text{In}$ -radiolabelled macrocyclic-antibody conjugates for tumour imaging. This early work showed that the  $[\text{In}(\text{NOTA})]$  complex was impervious to demetallation, and showed good *in vivo* stability after 24 h. Later work by the group reported its spectroscopic data, alongside that for  $[\text{Ga}(\text{NOTA})]$ .<sup>18</sup> Whilst a crystal structure of  $[\text{In}(\text{NOTA})]$  was not isolated, both complexes share very similar properties and spectroscopic assignments, and the molecular structure of  $[\text{Ga}(\text{NOTA})]$  showed the (expected) six-coordinate, *pseudo*-octahedral complex, following deprotonation of the pendant acid groups and coordination to the metal centre. It is also assumed the indium complex is hexacoordinate, although an early study comparing  $\text{Fe}^{3+}$ ,  $\text{Ga}^{3+}$  and  $\text{In}^{3+}$  complexes of NOTA reports that the  $[\text{In}(\text{NOTA})]$  complex forms hydroxo species more readily (at lower pH) than the Ga and Fe analogues.<sup>19</sup> It is suggested that  $[\text{In}(\text{NOTA})]$  may form seven-coordinate complexes in solution, with the seventh site occupied by a hydroxo ( $\text{OH}^-$ ) ligand.

Several  $[\text{In}(\text{NOTA})]$  derivatives have been reported since; a notable example includes the radiotracer,  $^{111}\text{In}$ -HEHEHE-Z08698-NOTA (Figure 6.4).<sup>20</sup> This has been shown to be a promising candidate for the imaging of human epidermal growth factor receptor type 3 (HER3) in malignant tumours, which has been associated with resistance to various anticancer therapies.<sup>21</sup> Similar work has also described the labelling of HEHEHE-Z08698-NOTA with  $^{68}\text{Ga}$  for preclinical PET

imaging, due to the improved imaging resolution, sensitivity and accuracy provided with PET imaging (in comparison to SPECT).<sup>22</sup>

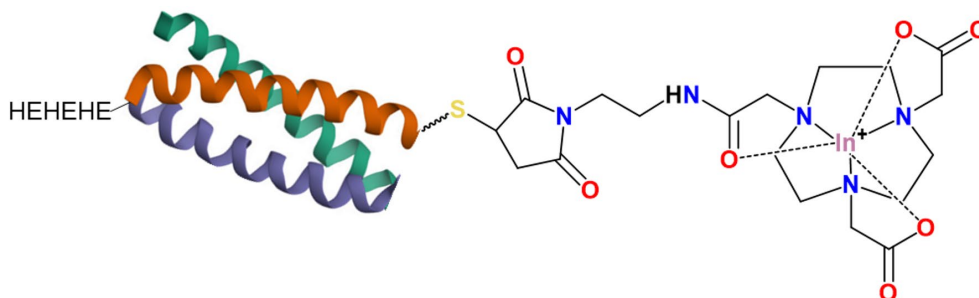


Figure 6.4 – Structure of  $[^{111}\text{In}]\text{-}[\text{In}(\text{NOTA-Z08698-HEHEHE})]^+$ .

Shorter-lived isotopes are also better suited to the pharmacokinetics of HEHEHE-Z08698 ( $^{111}\text{In}$  = 2.8 days;  $^{68}\text{Ga}$  = 68 min), which is an example of an affibody molecule. An affibody consists of a small, three-helical scaffold protein which can undergo rapid blood clearance, and they are characterised by high target specificity (e.g. good tumour uptake). With consideration towards the half-life of  $^{18}\text{F}$  (110 min), Da Pieve *et al.*<sup>23</sup> have reported an  $\text{Al-}^{18}\text{F}$  radiolabelled NOTA-Z08698 conjugate, using radiolabelling strategies based on methods initially reported by McBride and co-workers.<sup>24</sup> Addition of the affibody,  $\text{AlCl}_3$ , and  $^{18}\text{F}^-$  in a one-pot method (pH 4, 100 °C, 15 min) led to the radiofluorinated product with a RCY of 38.8%. Radio-chromatograms obtained for the crude mixture also indicated some decomposition of the radio-conjugate due to the elevated temperatures, but an RCP of 98% was achieved following HPLC purification.  $[^{18}\text{F}]\text{-}[\text{AlF}(\text{NOTA-Z08698})]$  was shown to still have an RCP of 98% after 1 h *in vitro* (mouse serum), and *in vivo* evaluation indicated the tracer had high tumour accumulation. This demonstrates that (tris)carboxylate-functionalised  $\text{H}_3\text{-NOTA}$  ligand is effective in binding all three trivalent  $\text{Al}^{3+}$ ,  $\text{Ga}^{3+}$  and  $\text{In}^{3+}$  metal ions, and is well-known for a wide range of radiopharmaceutical applications.

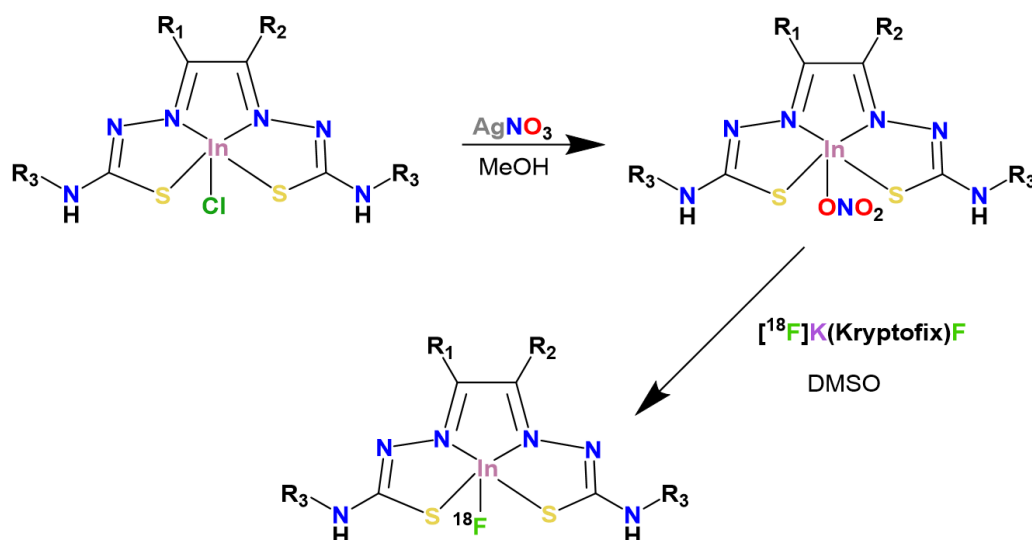
However, as discussed in Chapter 1, more recent examples surrounding the  $\text{Al-}^{18}\text{F}$  chemistry describe the use of  $\text{H}_2\text{-Bn-NODA}$  derivatives, based upon enhanced radiochemical yields due to lack of competition from a third pendant arm donor.<sup>25,26</sup> However, unlike the varied radiochemistry of the trivalent  $[\text{M}(\text{NOTA})]$  systems ( $\text{M} = \text{Al}^{3+}$ ,  $\text{Ga}^{3+}$ ,  $\text{In}^{3+}$ ), the  $[\text{Ga}^{18}\text{F}(\text{Bn-NODA})]$  radiochemistry does not translate as effectively (due to significantly poorer stability above pH 7.5) in comparison to  $[\text{Al}^{18}\text{F}(\text{Bn-NODA})]$  systems. In this case, the binding properties of the macrocycle are better suited to the highly Lewis-acidic  $\text{Al}^{3+}$ , forming weaker bonds to  $\text{Ga}^{3+}$  due to slightly softer Lewis acidity. Considering this, recent work has reported the successful radiofluorination of a trivalent gallium (and iron) complex of  $\text{H}_2\text{-Bn-NODP}$ , which has a larger chelate bite angle, reducing the strain imposed on the pendant arms (as highlighted in the previous chapter).<sup>27</sup> In this case, the gallium complex has markedly increased stability in a range



of formulations (RCP = 99%, EtOH/H<sub>2</sub>O and 95%, EtOH/PBS). However, given that H<sub>2</sub>-Bn-NODP has only recently been reported, its radiochemistry with the other Group 13 metal ions (Al<sup>3+</sup> and In<sup>3+</sup>) has not yet been explored. Like the carboxylate analogue, differences between the coordinative properties of the ligand, and the behaviours of the complexes (especially with respect to (radio)fluorination) are expected to vary due to the differences in ionic radii and Lewis acidity.

#### 6.1.1.2.1 Coordination Chemistry of In<sup>3+</sup>

Despite the numerous macrocyclic complexes of indium known within a vast array of literature, there are very few examples of indium fluoride species for use in <sup>18</sup>F PET imaging. Although this is most likely due to the weaker In–F bond (506 kJ mol<sup>-1</sup>, in comparison to the C–F bond and other main group-fluoride bonds, e.g. B–F, Si–F, Al–F and Ga–F, values between 536 – 766 kJ mol<sup>-1</sup> and summarised in Table 1.2 of Chapter 1), this still represents a very underexplored area of research. More recently, however, indium(III) bis-thiosemicarbazone complexes have been studied for <sup>18</sup>F incorporation (Scheme 6.2).<sup>28</sup> Halide exchange of the indium nitrate complex using [<sup>18</sup>F]K(Kryptofix)F led to successful radio-incorporation, albeit with low radiochemical yields, with values between 1–14% after two minutes with mild heating (40 °C). No other reaction conditions were reported.



Scheme 6.2 – General synthetic route towards <sup>18</sup>F-radiolabelled indium(III) bis-thiosemicarbazone complexes ( $R_n = \text{Me, Et, Ph, H}$ ).<sup>28</sup>

Although this preliminary route presented low radiochemical yields, it indicates there is some precedent to the <sup>18</sup>F-radiolabelling of indium complexes. With this in mind, this chapter will look towards preliminary fluorination (<sup>19</sup>F) experiments with the well-characterised [In(NOTA)] species, as well as the (unknown) [InX(Bn-NODP)] species (X = Cl, NO<sub>3</sub>), to further assess the suitability of indium complexes for radiochemical reactions. In addition, whilst the reactions of

[InF<sub>3</sub>(dmsO)(OH<sub>2</sub>)<sub>2</sub>] with the tris- and mono-amide ligands (L<sup>1</sup>, L<sup>2</sup> and L<sup>3</sup>, Chapter 4) were mostly unsuccessful, leading to a mixture of unidentified products, the reaction of L<sup>1</sup> and L<sup>3</sup> with a direct source of In<sup>3+</sup> may present an alternative route towards these complexes.

### 6.1.2 Aims

In addition to the surrounding literature, the work within Chapter 3 and Chapter 4 of this thesis has revealed a range of possible coordination modes and behaviours of amide-substituted tacn ligands, dependent upon the nature of the central metal ion. As reported, the carboxamide function of the amide pendant group is predominantly found to coordinate to (divalent) transition metal centres (with some notable exceptions, such as the [Co(L<sup>1</sup>)]<sup>3+</sup> complex). For trivalent main group metals (Ga<sup>3+</sup>), coordination is observed *via* the carboxamide C=O or the amide(N) of the pendant arms, largely depending on the reaction pH. In cases where the carboxamide oxygen is bound to Lewis acidic metal centres (Ga<sup>3+</sup>, Fe<sup>2+</sup>/Fe<sup>3+</sup>), hydrolysis of the amide pendant arms is promoted *via* activation of the highly-polarised C=O bond, resulting in the corresponding carboxylate group. This chapter aims to investigate the behaviour of the tris(amide) ligand, L<sup>1</sup>, with Lewis acidic metals (Ga<sup>3+</sup> > Fe<sup>3+</sup> > In<sup>3+</sup>), assess the coordinative properties and stability of their resulting complexes, and ultimately evaluate whether this could provide a plausible, ‘one-pot’ alternative route towards complexes containing M-F bonds.

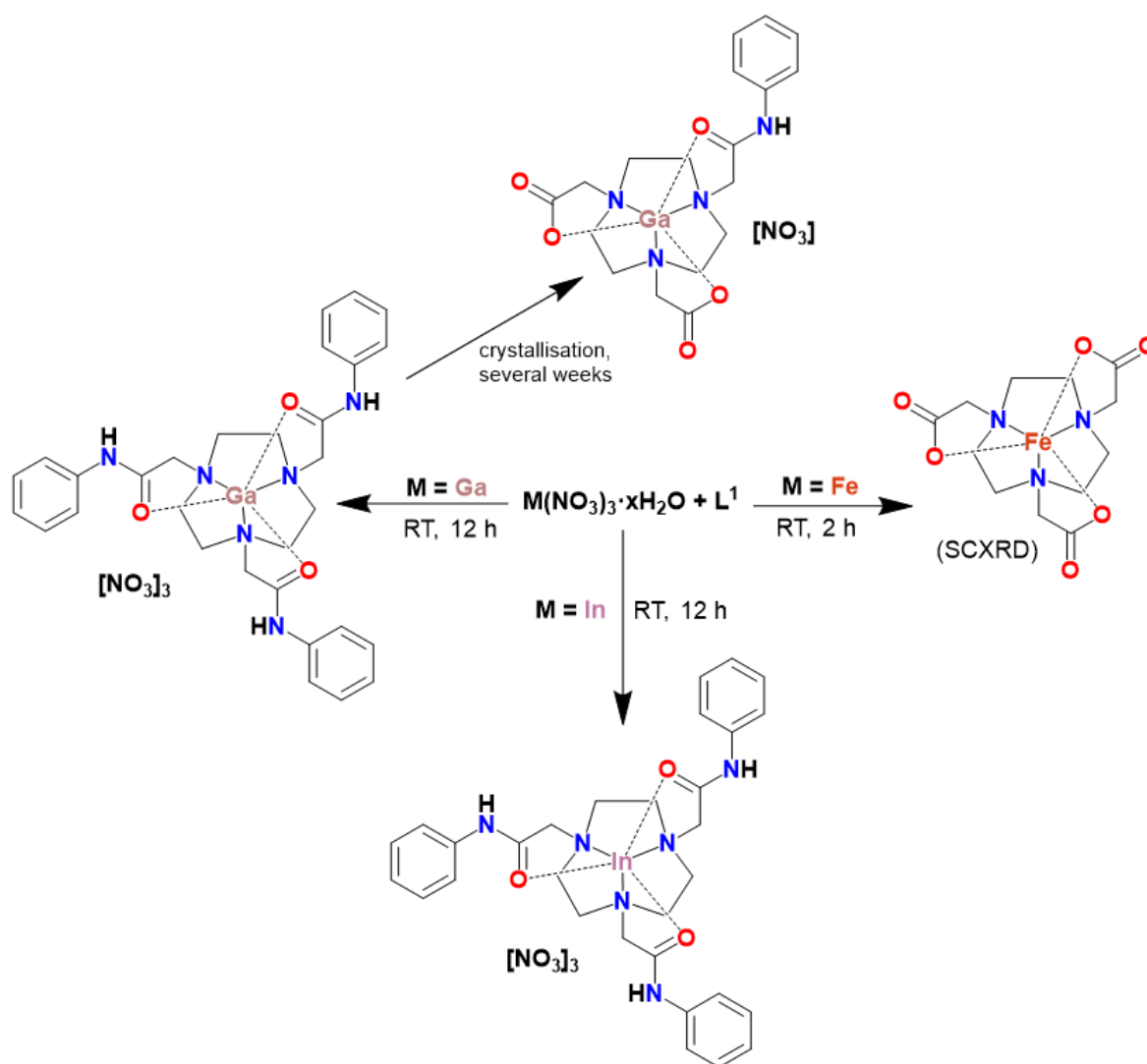
The larger ionic radius of indium(III) is also known to be able to accommodate a higher coordination number, and coordination numbers up to eight are known.<sup>29,30,31</sup> Therefore, it may be possible for the indium complex of L<sup>1</sup> to form a seven-coordinate complex upon the addition of one mol. equiv. of fluoride (N<sub>3</sub>O<sub>3</sub>F coordination sphere). Indeed, shortly after their reporting of the first [In(NOTA)] complex, Craig *et al.*<sup>32</sup> also reported the molecular structure of a seven-coordinate [InCl(NOTA)]<sup>-</sup> complex, although no further chemistry of this product was undertaken. Therefore, to further assess the stability and properties of seven-coordinate indium complexes with regards to fluorination, the conditions for the known [InCl(NOTA)]<sup>-</sup> complex will be replicated, and fluorination of this compound will also be attempted.

In addition, this chapter will also aim to investigate the behaviour of the H<sub>2</sub>-Bn-NODP ligand with aluminium and indium. Although the successful radiofluorination of [GaF(Bn-NODP)] and [FeF(Bn-NODP)] has been reported by the Reid group, this work will help broaden the understanding of the coordinative properties of the ligand, and possibly help to identify any limitations with regard to metal ion size. Based upon the success of the Al-<sup>18</sup>F chemistry with H<sub>2</sub>-Bn-NODA derivatives, it is assumed [AlF(Bn-NODP)] would be a promising candidate for <sup>18</sup>F radiolabelling experiments, provided a suitable synthetic route can be found.

## 6.2 Results and Discussion

### 6.2.1 Amide-Functionalised Triazacyclononane Ligands with Trivalent, Lewis Acidic $\text{Fe}^{3+}$ , $\text{Ga}^{3+}$ and $\text{In}^{3+}$ Cations

In comparison to the divalent transition metal complexes studied in Chapter 3, the coordination of the tris(amide) tacn ligand,  $\text{L}^1$ , to the more Lewis acidic trivalent  $\text{M}^{3+}$  ions was investigated, *via* the reaction of the ligand and the metal nitrate salts of  $\text{Fe}^{3+}$ ,  $\text{Ga}^{3+}$  and  $\text{In}^{3+}$  (Scheme 6.3). All reactions were carried out in methanol solutions at room temperature, between 1 – 12 h.



Scheme 6.3 – Reaction pathways of  $\text{L}^1$  with the Lewis acidic cations  $\text{Fe}^{3+}$ ,  $\text{Ga}^{3+}$  and  $\text{In}^{3+}$  and the various reaction conditions used.  $[\text{Fe}(\text{NOTA})]$  and the  $\text{Ga}^{3+}$  complex were isolated as single-crystals from a product mixture containing multiple (unidentified) species/hydrolysis products.

#### 6.2.1.1 Stability of $\text{L}^1$ with $\text{Fe}^{3+}$

Addition of  $\text{Fe}(\text{NO}_3)_3 \cdot 9\text{H}_2\text{O}$  to a methanol solution of  $\text{L}^1$  resulted in a dark orange solution. Subsequent work-up led to the isolation of a deep red solid. As  $\text{Fe}^{3+}$  is paramagnetic ( $d^5$ ), NMR

spectra were not obtained. However, a few colourless crystals were isolated from the slow evaporation of methanol containing the product. These were shown to be the known [Fe(NOTA)] complex (Figure 6.5), arising from complete amide hydrolysis. Weyhermüller also reported the same [Fe(NOTA)] complex, obtained as a hydrolysis product *via* the reflux of the iron(II) tris(amide) complex, [Fe(TCMT)][ClO<sub>4</sub>]<sub>2</sub>, in water.<sup>9</sup> The metrics for the structure below are directly comparable to the structures for [Fe(NOTA)] previously reported.<sup>33</sup> Solid-state analysis of the bulk red solid (IR spectroscopy and elemental analysis) was indicative of multiple species present in the product mixture, which are likely to be various stages of hydrolysis.

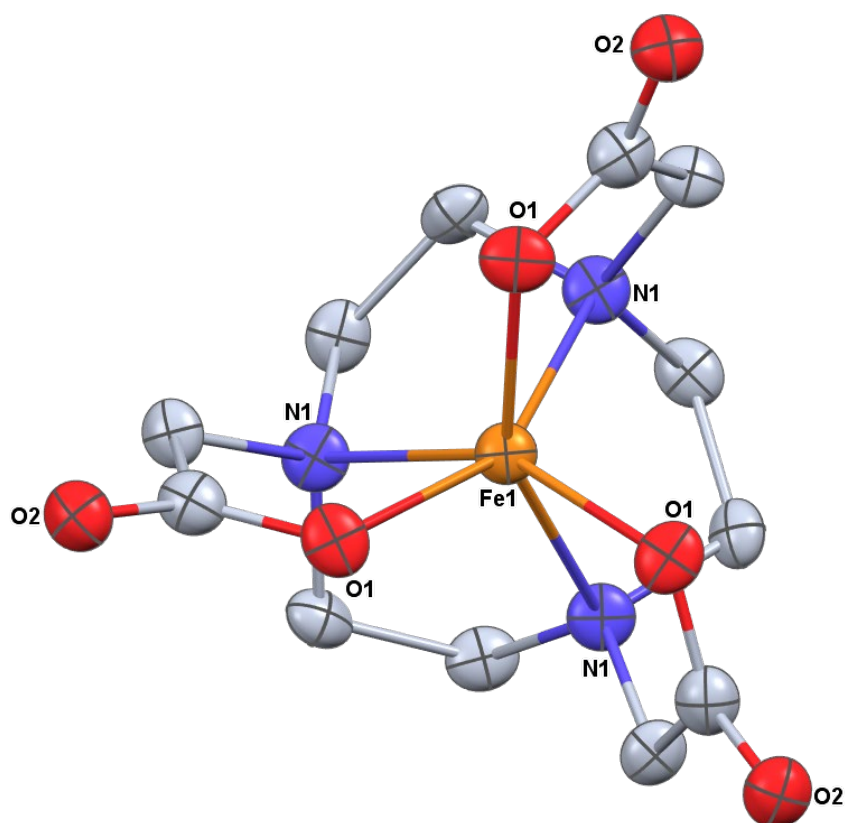


Figure 6.5 – View of the structure of the [Fe(NOTA)] complex with the atom numbering scheme. Ellipsoids are drawn at the 50% probability level and H atoms are omitted for clarity.

#### 6.2.1.2 Stability of L<sup>1</sup> with Ga<sup>3+</sup> vs. In<sup>3+</sup>

As discussed above, several literature examples have shown the tendency of amide-pendant arms to hydrolyse when bound to a Lewis acidic Ga<sup>3+</sup> metal centre. To assess the reactivity and behaviour of L<sup>1</sup> with Ga<sup>3+</sup>, two parallel NMR-scale reactions, each combining L<sup>1</sup> (10 mg, 0.019 mmol) and Ga(NO<sub>3</sub>)<sub>3</sub>·9H<sub>2</sub>O (7.9 mg, 0.019 mmol) in CD<sub>3</sub>OD, were carried out. One reaction was allowed to stir at room temperature, whilst the second was heated to 80 °C. The progress of both reactions was monitored *via* <sup>1</sup>H NMR spectroscopy at various time intervals (Figure 6.6).

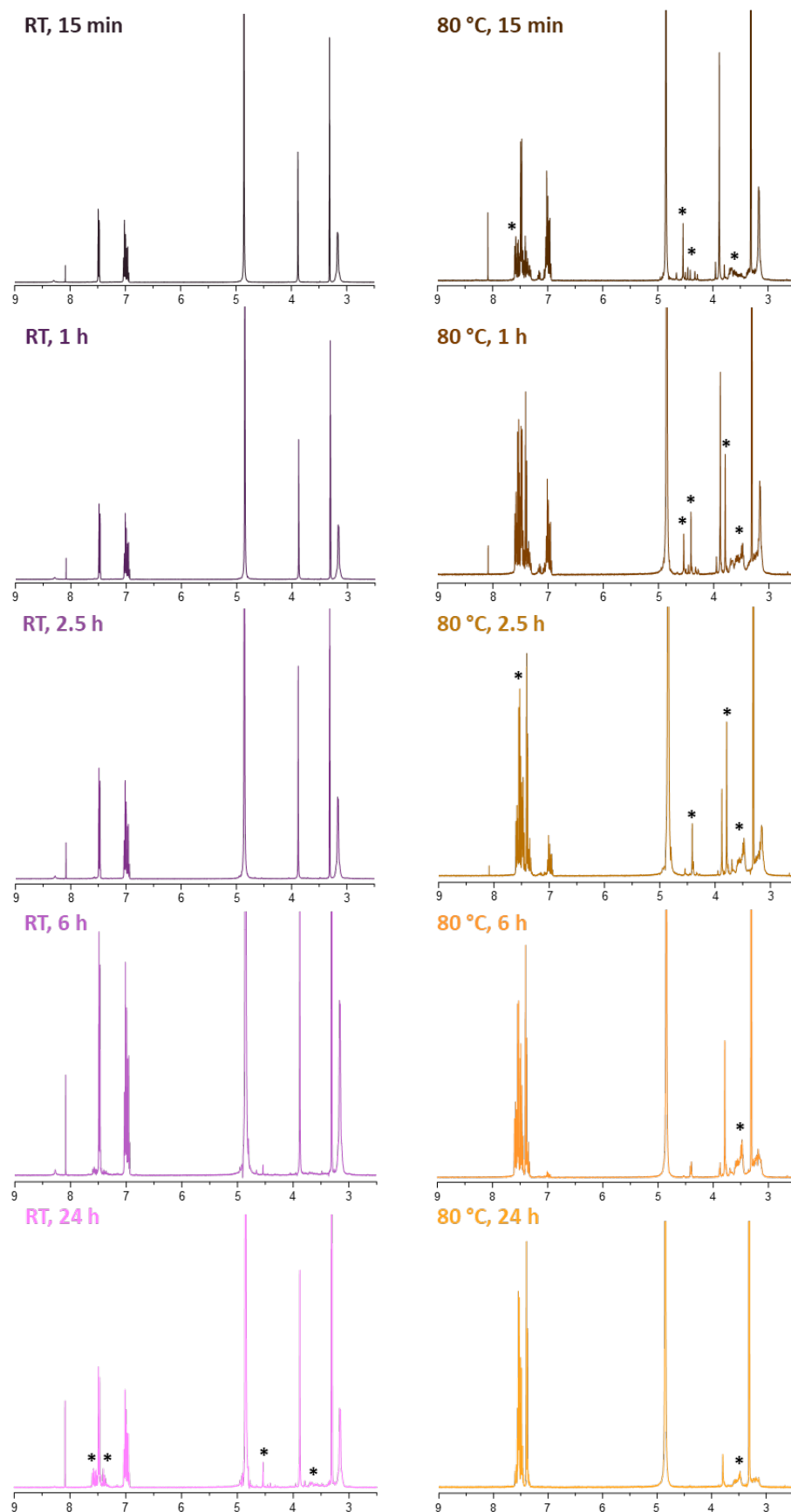


Figure 6.6 –  $^1\text{H}$  NMR spectra following the reaction of  $\text{Ga}(\text{NO}_3)_3 \cdot 9\text{H}_2\text{O}$  and  $\text{L}^1$  (left, room temperature and right, 80 °C) taken at time intervals 15 min, 60 min, 2.5 h, 6 h, and 24 h ( $\text{CD}_3\text{OD}$ ). Peaks relating to hydrolysis products annotated with ‘\*’.

The  $^1\text{H}$  NMR spectrum obtained after 15 min with heating to  $80\text{ }^\circ\text{C}$  suggests these reaction conditions favour rapid formation of hydrolysis products, with the appearance of new (minor) resonances annotated with '\*'. After 4 h, the heated reaction solution was observed to turn from colourless to pink, and a small amount of white solid precipitate had formed (which was poorly soluble in common NMR solvents), suggesting significant decomposition. Precipitation continued until 24 h, at which point the  $^1\text{H}$  NMR spectrum depicts one major, aromatic species. However, this was not consistent with the  $^1\text{H}$  NMR spectrum of the expected hydrolysis product, aniline. The radiochemical experiments undertaken in Chapter 5 involved heating of the  $[\text{GaF}_3(\text{L}^1)]$  complex to  $80\text{ }^\circ\text{C}$ , and no by-products from the reaction were observed in the subsequent UV-HPLC traces. However, to ensure that this behaviour was due to the presence of the Lewis acidic  $\text{Ga}^{3+}$  ion rather than the reaction conditions ( $80\text{ }^\circ\text{C}$ ), a solution of  $\text{L}^1$  was also heated to  $80\text{ }^\circ\text{C}$ . This caused no change in the  $^1\text{H}$  NMR spectrum after 2 h.

In contrast to the reaction heated to  $80\text{ }^\circ\text{C}$ , the  $^1\text{H}$  NMR spectrum of the reaction mixture obtained after 15 min at room temperature shows little change from the uncoordinated ligand. After 2-3 h, the  $^1\text{H}$  NMR spectrum of the colourless solution indicates one major species, consistent with the target  $[\text{Ga}(\text{L}^1)][\text{NO}_3]_3$ , with the tacn- $\text{CH}_2$  protons resonating as a multiplet characteristic of the  $\kappa^3$ -coordinated tacn-ring. Extending the reaction time beyond ca. 5 h leads to slow emergence of additional resonances (although very minor), resembling those formed when the reaction was heated.

Addition of  $\text{Et}_2\text{O}$  to a solution produced from  $\text{Ga}(\text{NO}_3)_3 \cdot 9\text{H}_2\text{O}$  and  $\text{L}^1$  in MeOH after 12 hours stirring at room temperature precipitated a white solid following the addition of diethyl ether. Microanalytical data supported the formation of the complex with a solvated ether molecule, which was also observed in its respective  $^1\text{H}$  NMR spectrum. This also showed the expected product resonances, with the tacn- $\text{CH}_2$  protons appearing as a broad multiplet (3.20 – 3.09 ppm) rather than a singlet in the uncoordinated ligand. IR data also gave the expected C=O stretches, observed at 1661, 1620 and  $1599\text{ cm}^{-1}$ .

From this product, crystals suitable for single crystal X-ray analysis were grown *via* slow evaporation from a methanol solution of the product. This occurred over several weeks, and were found to be a hydrolysis product – as shown in Figure 6.7 – with the loss of two amide pendant arms to form the carboxylate functions. This is in line with the trends observed in the  $^1\text{H}$  NMR studies for the complex detailed above, whereby an increasing amount of hydrolysis products are observed over time. The structure reveals a distorted octahedral coordination environment at  $\text{Ga}^{3+}$  (twist angle,  $\theta = 46.79(7)^\circ$ ) *via* the three tacn N-donor atoms, one pendant O-bonded carboxamide pendant arm and two carboxylate groups.

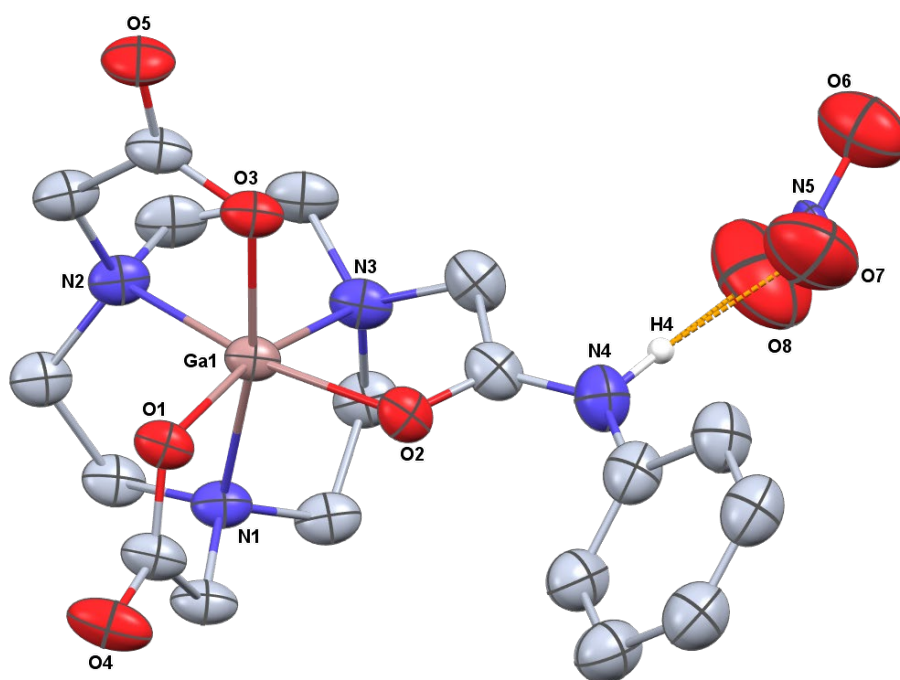


Figure 6.7 – View of the structure of the hydrolysis product from the reaction of  $\text{Ga}(\text{NO}_3)_3 \cdot 9\text{H}_2\text{O} + \text{L}^1$  with the atom numbering scheme and showing the H-bonding between the amide NH group and the nitrate counter-anion. Ellipsoids are drawn at the 50% probability level and H atoms (except those involved in H-bonding) are omitted for clarity.

Hydrolysis at the amide functions of  $\text{L}^1$  on reaction with  $\text{Ga}(\text{NO}_3)_3 \cdot 9\text{H}_2\text{O}$  contrasts with the behaviour discussed in Chapter 4 for the  $[\text{MF}_3(\text{L}^1)]$  complexes. However, as discussed, previous work has shown the tendency of amide pendant arms to undergo hydrolysis in solution when bound to hard, trivalent, Lewis acid cations such as  $\text{Ga}^{3+}$ ,  $\text{Fe}^{3+}$  and  $\text{Fe}^{2+}$ . This is also in line with the observation of the fully hydrolysed  $[\text{Fe}(\text{NOTA})]$  species observed upon reaction of  $\text{L}^1$  with  $\text{Fe}(\text{NO}_3)_3$  under similar (room temperature) conditions. This would suggest that amide-appended tacn ligands are better suited to molecular  $\text{MF}_3$  fragments, in which the three hard Lewis base anions (fluoride ligands) better stabilise the +3 state of the metal.

The reaction of  $\text{In}(\text{NO}_3)_3 \cdot 9\text{H}_2\text{O}$  with  $\text{L}^1$  (12 h, RT) led to the isolation of a white powder solid in good yield (84%). Microanalytical data was in accord with the target  $[\text{In}(\text{L}^1)][\text{NO}_3]_3$  complex, and the IR spectrum depicted three bands, at 1622, 1594, and 1574 relating to the C=O stretch. The  $^1\text{H}$  NMR spectrum was also consistent with coordinated, hexadentate ligand, with broadened resonances observed due to the high quadrupolar moment of indium. The  $\text{CH}_2$  protons of the pendant arm resonate as a singlet, shifted to higher frequency at 4.22 ppm. The tacn- $\text{CH}_2$  protons resonate as two broadened multiplets, at 3.44 – 3.35 and 3.25 – 3.06 ppm. These are very similar to the shifts observed for the divalent  $[\text{Zn}(\text{L}^1)][\text{NO}_3]_2$  complex reported in Chapter 3.  $^1\text{H}$  NMR studies also showed that prolonged heating in MeOH (overnight) leads to some decomposition of the complex, although this did not appear to happen as rapidly as the

analogous gallium complex, which may reflect on the slightly softer Lewis acidic nature of  $\text{In}^{3+}$  vs.  $\text{Ga}^{3+}$ . The formation of the  $[\text{In}(\text{L}^1)][\text{NO}_3]_3$  complex may present an alternative route towards the  $[\text{InF}_3(\text{L}^1)]$  complex – which could not be formed cleanly in Chapter 4 when using the molecular  $[\text{InF}_3(\text{dmsO})(\text{OH}_2)_2]$  precursor.

Hence, a solution of  $[\text{In}(\text{L}^1)][\text{NO}_3]_3$  in MeOH was treated with 3 mol. eqv. KF as a source of  $^{19}\text{F}$  and heated to 80 °C for 2 h. The  $^{19}\text{F}\{^1\text{H}\}$  NMR spectrum (Figure 6.8) revealed a single resonance at -191 ppm, suggesting the formation of a new In–F species. This shift is in line with previously reported  $\text{InF}_3$  triazacyclononane complexes,  $[\text{InF}_3(\text{Me}_3\text{-tacn})]$  and  $[\text{InF}_3(\text{BnMe}_2\text{-tacn})]$ , which appeared as broad resonances at -215 ppm (MeCN), -192.5 ( $\text{D}_2\text{O}$ ) and -220 ppm (MeCN), respectively.<sup>34</sup> However, the  $^1\text{H}$  NMR spectrum of the same sample showed multiple resonances, suggesting the presence of a mixture of species. It is possible these new resonances are due to hydrolysis products, rather than multiple indium fluoride species, or from an incomplete reaction. Further work could be done to optimise the reaction conditions to prevent hydrolysis (e.g. lower temperature) and ensure a complete reaction, and also to ascertain the exact nature of the In–F species responsible for the  $^{19}\text{F}\{^1\text{H}\}$  NMR spectrum below.

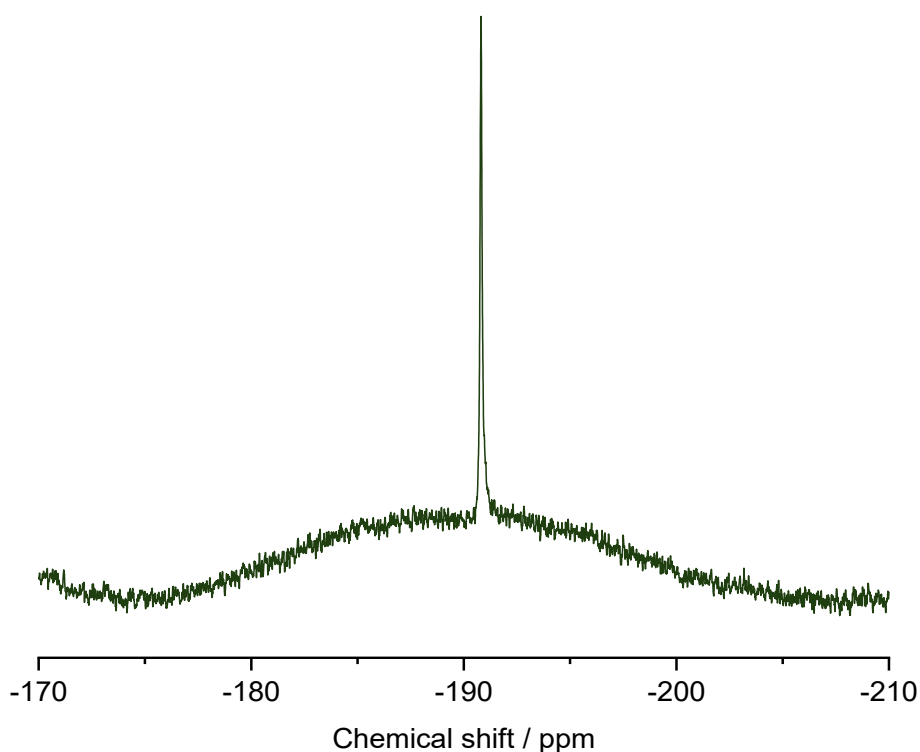


Figure 6.8 –  $^{19}\text{F}\{^1\text{H}\}$  NMR spectrum from the reaction of  $[\text{In}(\text{L}^1)][\text{NO}_3]_3$  with 3 mol. eqv. KF ( $\text{CD}_3\text{OD}$ ).

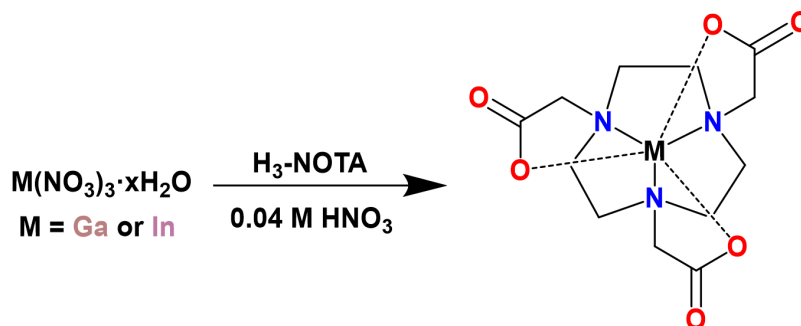
Similarly, the formation of  $[\text{InF}_3(\text{L}^3)]$  was also attempted *via* the addition of  $\text{L}^3$  to the  $\text{In}(\text{NO}_3)_3 \cdot 9\text{H}_2\text{O}$  precursor (NMR-scale). To prevent hydrolysis of the amide pendant arm, heating was avoided. The two starting materials were allowed to stir at room temperature for 30 minutes before 3 mol.



eqv. of KF was added. After 30 minutes, no resonance in the  $^{19}\text{F}\{^1\text{H}\}$  NMR spectrum was observed, so the reaction was left to continue overnight. Unlike the  $\text{L}^1$  complex, the  $^{19}\text{F}\{^1\text{H}\}$  NMR spectrum gave no evidence of a new  $\text{In-F}$  species. However, the  $^1\text{H}$  NMR spectrum was consistent with coordination of the ligand, with broadened resonances and the expected shifts from the uncoordinated ligand. This would suggest that complexation of  $\text{L}^3$  to the  $\text{In}^{3+}$  centre was successful, but fluorination was not. It is possible this behaviour may be associated with the trends in the radiochemical reactions of  $[\text{GaF}_3(\text{L}^1)]$  and  $[\text{GaF}_3(\text{L}^3)]$  discussed in Chapter 5, but given the weaker  $\text{In-F}$  bond (compared to  $\text{Al-F}$ ,  $\text{Ga-F}$ ), there is less thermodynamic driving force for coordination of the fluoride anion, and the results are inconclusive. Although an interesting observation, in the interests of time, this was not pursued further.

### 6.2.2 Synthesis of $\text{Ga}^{3+}$ and $\text{In}^{3+}$ Complexes of NOTA and Attempted Fluorination

The  $\text{Ga}^{3+}$  and  $\text{In}^{3+}$  complexes of  $\text{H}_3\text{-NOTA}$  were prepared based on a previously reported method (Scheme 6.4).<sup>18</sup> Both products were isolated as white powder solids, with the gallium complex in a reasonable yield (72%), and the indium complex in a significantly poorer yield (28%). The products were precipitated from the reaction solution following the addition of acetone – it is likely that some product from the latter reaction remained in solution and, as a result, was not isolated.



Scheme 6.4 – Synthesis of  $[\text{M}(\text{NOTA})]$  complexes ( $M = \text{Ga}$  or  $\text{In}$ ).

The  $^1\text{H}$  and  $^{13}\text{C}\{^1\text{H}\}$  NMR spectra for both complexes were in line with the data reported previously, and consistent with coordinated ligand.<sup>18</sup> The  $\text{tacn-CH}_2$  resonances in both products appear as two multiplets, which relate to the inequivalent axial and equatorial protons, at 3.27 – 3.13, 3.09 – 2.94 ppm for  $[\text{Ga}(\text{NOTA})]$  and 3.49 – 3.38, 3.21 – 3.09 ppm for  $[\text{In}(\text{NOTA})]$ . The  $\text{CH}_2$  protons of the pendant arm resonate at 3.81 ppm and 3.66 ppm, respectively. The  $\text{ESI}^+$  MS obtained for both complexes also depicted  $m/z$  peaks relating to the protonated  $[\text{M}(\text{NOTA})][\text{H}]^+$  species. The IR spectra obtained for both complexes showed two bands relating to the  $\text{C=O}$  stretch of the pendant arm, at 1702 and 1675  $\text{cm}^{-1}$  for  $[\text{Ga}(\text{NOTA})]$ , and at 1663 and 1619  $\text{cm}^{-1}$  for  $[\text{In}(\text{NOTA})]$ . The IR for the indium complex also gave indication of a reasonable amount of

water, with a strong, broad feature at  $3415\text{ cm}^{-1}$  (O-H stretch). Microanalysis of both products are consistent with the IR analysis, giving hydrated complexes:  $[\text{Ga}(\text{NOTA})] + \frac{1}{2} \text{H}_2\text{O}$  and  $[\text{In}(\text{NOTA})] + 3\frac{1}{4} \text{H}_2\text{O}$ .

#### 6.2.2.1 Comparison of Seven-Coordinate $\text{In}^{3+}$ Complexes

Some product precipitated directly from the reaction towards the  $[\text{In}(\text{NOTA})]$  species (over 4 h) was microcrystalline and suitable for electron diffraction analysis. The ED data was collected and reprocessed by Dr Rob Bannister, and the observed structure is shown in Figure 6.9.

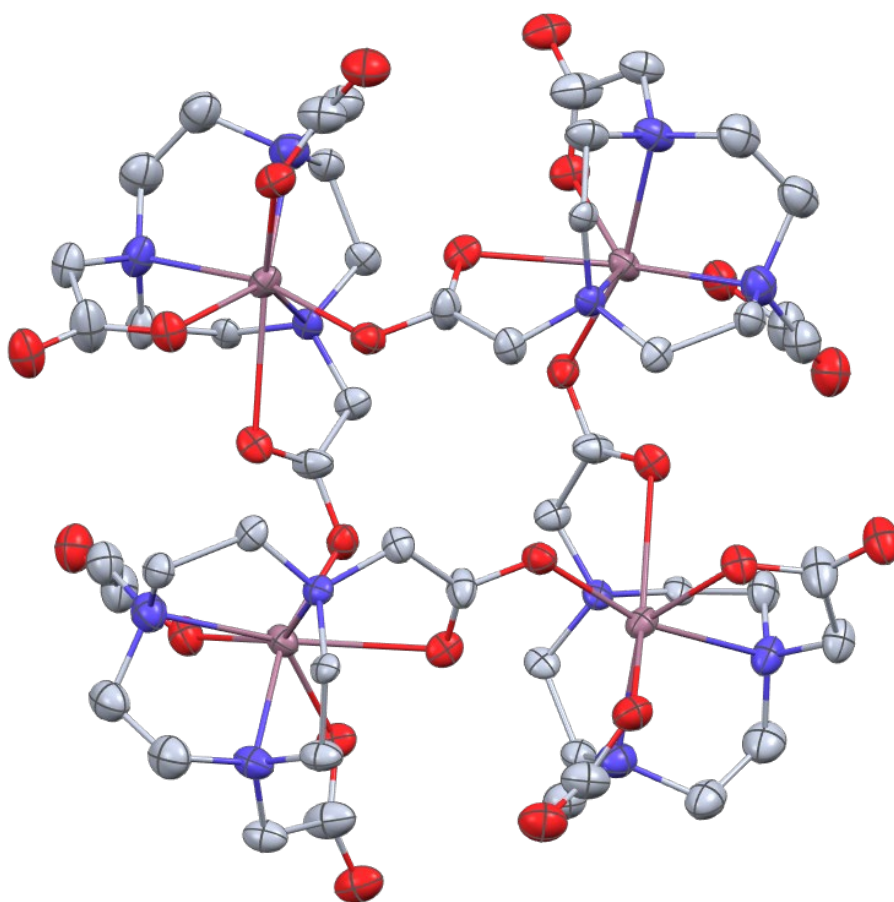


Figure 6.9 – View of the electron diffraction structure of the  $[\text{In}(\text{NOTA})]$  tetramer. Ellipsoids are drawn at the 50% probability level and H atoms are removed for clarity. Atom colours: beige-pink, In; red, O; blue, N; grey, C.

Unexpectedly, this shows the  $[\text{In}(\text{NOTA})]$  complex as a seven-coordinate tetrameric species. Each  $\text{In}^{3+}$  has an  $\text{N}_3\text{O}_4$  coordination sphere, with the (deprotonated) NOTA ligand appearing as a pentadentate chelator *via* the three *facial*  $\text{tacn}(\text{N})$  atoms, and two carboxylate-O atoms of two pendant arms. The third pendant forms a weak In-O bond (reflected in the uncharacteristically long bond length,  $2.623(3)\text{ \AA}$ ), which is also coordinated to a second, adjacent indium. The seventh site is occupied by a weak, asymmetrically bridging carboxylate (i.e. the third pendant arm) of a neighbouring molecule. This latter bond length,  $2.192(18)\text{ \AA}$ , is much more similar to

the In-O bond lengths observed for the non-bridging carboxylate arms, 2.221(18) Å and 2.125(18) Å.

This unusual coordination is shown schematically in Figure 6.10, alongside the relevant atom numbering scheme (for further discussion of the bond lengths below). No other hydrogen-bonding or intermolecular interactions are observed from or between any of the four molecules. This contrasts with the mononuclear and hexacoordinate [In(NOTA)] species, inferred from the literature. Given that the NOTA ligand appears to link two In<sup>3+</sup> ions, it may be a kinetic product that precipitates directly from the reaction solution. Further experiments would be required to determine the exact nature of the bulk material, for example, by recrystallisation of a solution of the product over a longer period of time.

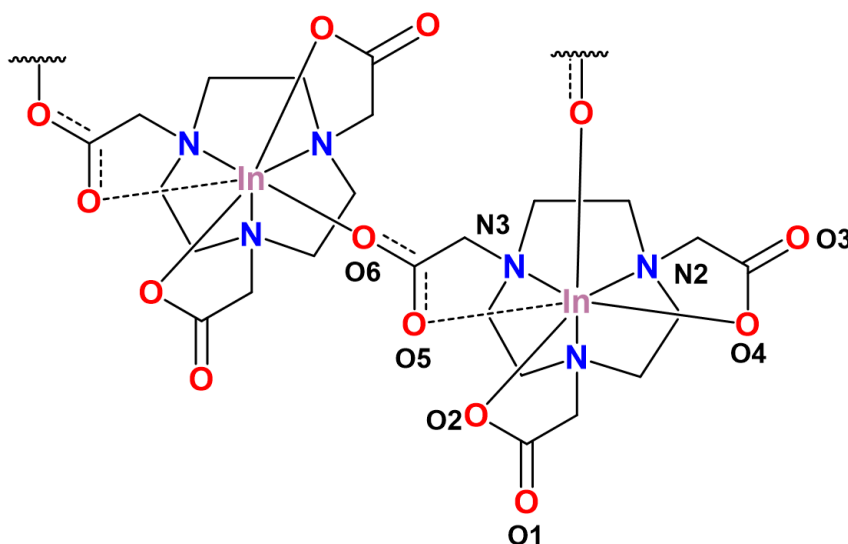


Figure 6.10 – Schematic of the seven-coordinate [In(NOTA)] structure obtained by electron diffraction, which shows an N<sub>3</sub>O<sub>4</sub> coordination sphere. The asymmetric, bridging carboxylate of the third NOTA pendant arm forms only very long-range, and weak interactions with one indium centre (In-O5), whilst coordinated to an adjacent indium (In-O6). Atom numbering scheme is given for N and O atoms.

Although a molecular structure of [In(NOTA)] has not previously been obtained, the molecular structure of a seven-coordinate chloroindium-NOTA complex, [InCl(NOTA)][H], has instead been reported, and was also obtained in this work using the method from the literature.<sup>32</sup> The SCXRD structure for this (anionic) species is shown in Figure 6.11.

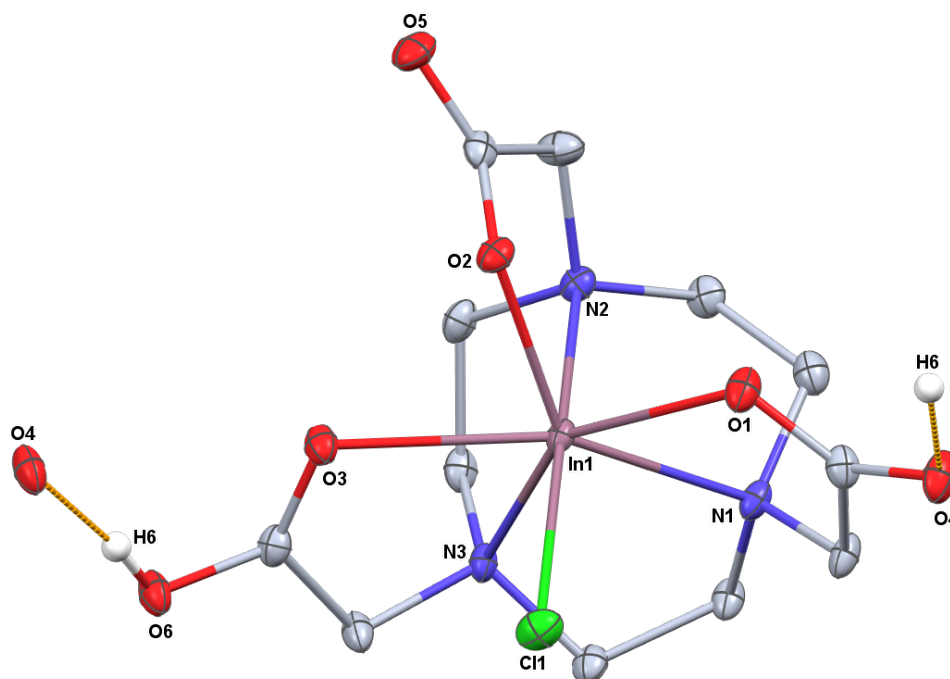


Figure 6.11 – View of the structure of  $[\text{InCl}(\text{NOTA})][\text{H}]$  with the atom numbering scheme and showing the H-bonding between the protonated carboxylate group and a carboxylate of an adjacent molecule. Ellipsoids are drawn at the 50% probability level and H atoms (except those involved in H-bonding) are omitted for clarity.

The metrics for the  $[\text{InCl}(\text{NOTA})][\text{H}]$  structure above are directly comparable with those reported previously, although the R factor is slightly improved (0.0259 vs. 0.039). The complex possesses *pseudo*-pentagonal bipyramidal geometry, and elongation of the In–O3 and In–Cl bonds observed (2.3865(16) Å and 2.4512(6) Å, respectively). The In–Cl bond length is *ca.* 0.1 Å longer than the In–Cl bond lengths observed in the hexacoordinate,  $[\text{InCl}_3(\text{BnMe}_2\text{-tacn})]$  complex.<sup>34</sup> However, In–L bonds are expected to be slightly longer in seven-coordinate species than in (less coordinatively-saturated) hexacoordinate species.

These observations are also not dissimilar from the  $[\text{In}(\text{NOTA})]$  tetramer above, in which each  $\text{In}^{3+}$  ion also adopts a *pseudo*-pentagonal bipyramidal geometry, with significant elongation of the bridging In–O5 bond observed, as discussed above. The C10–O6 bond distance is 1.325(3) Å, some 0.1 Å longer than the C10–O5 bond (1.212(2) Å). The other C–O bond distances for the non-bridging  $\kappa^1$  carboxylate groups only differ by *ca.* 0.04 Å. This reflects on the strain imposed on the asymmetric carboxylate arm upon bridging two indium metal centres. The In–N bond distances and N–In–N bond angles are in good accord with those for previously reported indium triazacyclononane complexes.<sup>34</sup> Selected bond distances for both of the seven-coordinate indium species are summarised in Table 6.1.

Table 6.1 – Selected bond distances (Å) for the seven-coordinate [In(NOTA)] and [InCl(NOTA)][H]·2H<sub>2</sub>O complexes.

Complex	d(In-N)	d(In-O), d(In-Cl)	d(C-O)
	/ Å	/ Å	/ Å
[In(NOTA)]	In-N1 = 2.431(2) In-N2 = 2.355(12) In-N3 = 2.395(2)	In-O2 = 2.221(18) In-O4 = 2.125(18) In-O6 = 2.192(18) In-O5 = 2.623(3)	C8-O1 = 1.292(3) C8-O2 = 1.316(3) C10-O5 = 1.212(2) C10-O6 = 1.325(3) C12-O3 = 1.273(3) C12-O4 = 1.319(3)
[InCl(NOTA)][H]·2H <sub>2</sub> O	In-N1 = 2.3370(18) In-N2 = 2.3119(19) In-N3 = 2.3331(17)	In-O1 = 2.2802(16) In-O2 = 2.1190(15) In-O3 = 2.3865(16) In-Cl = 2.4512(6)	C8-O1 = 1.265(3) C8-O4 = 1.255(3) C10-O3 = 1.223(3) C10-O6 = 1.300(3) C12-O2 = 1.293(3) C12-O5 = 1.219(3)

#### 6.2.2.2 Attempted Fluorination of [Ga(NOTA)], [In(NOTA)] and [InCl(NOTA)][H]

Based on the structures above, preliminary (NMR-scale) experiments were carried out on the complexes, [Ga(NOTA)], [In(NOTA)] and [InCl(NOTA)]<sup>-</sup>, to ascertain whether seven-coordinate fluoride species could be formed *via* the addition of <sup>19</sup>F<sup>-</sup> (one mol. eqv. Me<sub>4</sub>N<sup>19</sup>F or K<sup>19</sup>F) since, if successful, this may provide a basis for future <sup>18</sup>F-radiolabelling experiments. The reactions were followed by <sup>19</sup>F{<sup>1</sup>H} and <sup>1</sup>H NMR spectroscopy.

The observed <sup>19</sup>F{<sup>1</sup>H} NMR spectra for the reactions of [Ga(NOTA)] with Me<sub>4</sub>NF or KF gave no evidence of any new gallium fluoride species, suggesting the three anionic carboxylate pendant arms remained bound; only resonances at around -120 ppm and -150 ppm relating to F<sup>-</sup> and [HF<sub>2</sub>]<sup>-</sup>, respectively, were observed. This is as expected, as seven-coordinate complexes of gallium are not observed due to its smaller ionic radii.

For [In(NOTA)], fluorination was not observed with Me<sub>4</sub>NF, but addition of 1 mol. eqv. KF<sub>(aq)</sub> to a solution of [In(NOTA)] in CD<sub>3</sub>CN led to the emergence of a new, broad resonance in the <sup>19</sup>F{<sup>1</sup>H} NMR, at -172.1 ppm (D<sub>2</sub>O). This was monitored over 24 h, with no change or loss of fluoride observed. However, this was a small-scale reaction, and further work to scale-up the reaction and obtain complete characterisation data is required, to determine the product responsible for the observed <sup>19</sup>F{<sup>1</sup>H} NMR resonance. However, the <sup>19</sup>F{<sup>1</sup>H} NMR spectra of the (six-coordinate) InF<sub>3</sub> complexes with Me<sub>3</sub>-tacn and BnMe<sub>2</sub>-tacn also gave resonances in a similar region (-192.5 to -220 ppm), with considerable shifts observed depending on the NMR solvent used.<sup>34</sup> For example, [InF<sub>3</sub>(Me<sub>3</sub>-tacn)] gave a broad resonance at -192.5 ppm in D<sub>2</sub>O, which shifted to lower-frequency in CD<sub>3</sub>CN (-215 ppm).

As above, the crystalline solid isolated from the reaction of  $\text{InCl}_3$  and NOTA (in 0.04 M HCl) was shown by SCXRD analysis to be the seven-coordinate  $[\text{InCl}(\text{NOTA})][\text{H}]$  complex. A  $\text{Cl}/^{19}\text{F}$  halide exchange reaction was attempted on the remaining crystals (room temperature in  $\text{D}_2\text{O}$ ). The results are given in Figure 6.12 below, which summarises the progression of the reaction, monitored at various time intervals (10 min, 6 h, and 24 h) via  $^{19}\text{F}\{^1\text{H}\}$  NMR spectroscopy.

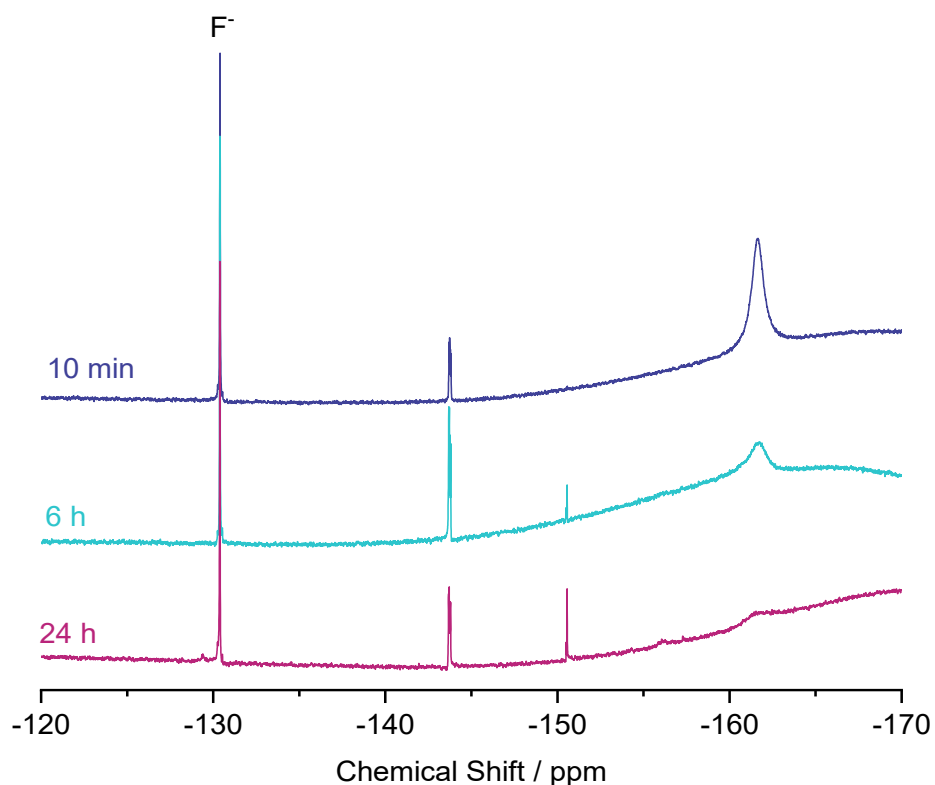
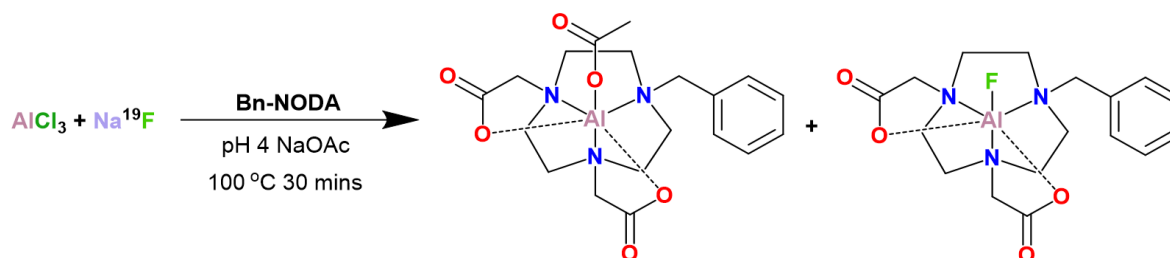


Figure 6.12 –  $^{19}\text{F}\{^1\text{H}\}$  NMR spectra following the reaction of  $[\text{InCl}(\text{NOTA})]^-$  and  $\text{KF}$ , at 10 min, 6 h and 24 h ( $\text{D}_2\text{O}$ ).

The initial  $^{19}\text{F}\{^1\text{H}\}$  NMR spectrum obtained after 10 min is promising, with a new, broad singlet at -161.7 ppm. This is within a reasonable range for an indium fluoride species, and is similar to the experiment described above, with solvent effects likely to cause deviations in shifts. The broad nature may reflect on the large quadrupole moment of the  $^{115}\text{In}$  nuclei ( $0.77 \times 10^{-28} \text{ m}^2$ ). There is also the presence of free fluoride, indicated by the sharp resonance at -130 ppm, and also another (minor) unidentified species around -145 ppm. After 6 h, however, the broad peak at -161.7 ppm appears diminished, and a small resonance around -150 ppm appears, which relates to  $[\text{HF}_2]^-$ . At 24 h, the latter resonance is no longer the major species, and the amount of  $[\text{HF}_2]^-$  has increased. These results would suggest that a new In–F species is formed upon the fluorination of  $[\text{InCl}(\text{NOTA})]^-$ , but it is not stable over extended periods of time (in  $\text{D}_2\text{O}$ ), with loss of fluoride observed (as  $[\text{HF}_2]^-$ ). Further work is required, first to confirm if the product is  $[\text{InF}(\text{NOTA})]^-$  as intended, then to assess its general stability in various solvents and competitive media.

### 6.2.3 Attempted Formation of {MF(L)} Complexes (M = Al, In; L = Bn-NODA, Bn-NODP)

As discussed in Chapter 5 and above (Section 6.1.1.2), the successful radiofluorination of Fe- $^{18}\text{F}$  and Ga- $^{18}\text{F}$  species has been reported with the bis(phosphinate) triazacyclononane ligand, H<sub>2</sub>-Bn-NODP.<sup>27</sup> With this in mind, the attempted formation of aluminium and indium complexes is reported below, following methods based upon prior literature.<sup>24,27,35</sup> Typically, the Al- $^{18}\text{F}$  radiochemistry is performed on a radiopharmaceutical scale (nmol – pmol) and immediately purified using a prep-HPLC protocol. However, the work in this project is interested in the formation of well-defined molecular precursors, such that the radiofluorination step is the only procedure necessary to produce the tracer compound. Hence, formation and characterisation of the precursor complex is ideally performed prior to the radiolabelling experiments. To allow this, the reactions are conducted on a preparative scale to ensure enough product is formed for the various analytical techniques (IR and NMR spectroscopy, ESI<sup>+</sup> MS, etc.). This approach also allows the fluorination step to be optimised using  $^{19}\text{F}^-$  so that the conditions for future radiolabelling are better understood. With this in mind, the chelation of 'Al- $^{19}\text{F}^{2+}$ ', the F-19 analogue of the purported 'Al- $^{18}\text{F}^{2+}$ ', to H<sub>2</sub>-Bn-NODA was attempted, replicating a previously reported method by Shetty and co-workers.<sup>35</sup> The observed reaction is shown in Scheme 6.5, with the product isolated as a white powdered solid.



Scheme 6.5 – Formation of  $[\text{AlX}(\text{Bn-NODA})]$  complexes following  $[\text{Al}^{18}\text{F}]^{2+}$  chelation methods previously reported ( $X = \text{OAc}, \text{F}$ ).

Various characterisation methods (NMR spectroscopy, ESI<sup>+</sup> MS) suggested that the isolated product contained a mixture of species. The  $^1\text{H}$  NMR spectrum was more complicated than expected, with multiple resonances that could not be definitively assigned to a single complex. The  $^{19}\text{F}\{^1\text{H}\}$  NMR spectrum was consistent with the previously reported literature for  $[\text{AlF}(\text{Bn-NODA})]$ , for which the Al–F resonance occurs at -167.1 ppm; the product mixture in the present study showed a single resonance at -167.2 ppm (along with a minor amount of free fluoride at -122.4 ppm).<sup>36</sup> However, the ESI<sup>+</sup> MS showed an  $m/z$  peak relating to  $[\text{Al}(\text{Bn-NODA})(\text{OAc})][\text{H}]^+$  at 420.1 (relative abundance = 100%), with the expected isotope pattern also observed. A further  $m/z$  peak (relative abundance = 14%) at 380.2 corresponds to the  $[\text{AlF}(\text{Bn-NODA})+\text{H}]^+$  complex, suggesting that the target  $[\text{AlF}(\text{Bn-NODA})]$  complex is also present. That the characterisation

data points to a product mixture, rather than the target  $[\text{AlF}(\text{Bn-NODA})]$  complex as a single product, is unsurprising. Much of the literature surrounding these complexes includes HPLC-purification of the reaction solution, and the nature of any other species remains unknown. For example, Shetty and co-workers<sup>35</sup>, whose preparative-scale method provided the basis for this work, only reported the ESI<sup>+</sup> MS and structural analysis of the product post-purification. Cleeren and co-workers<sup>37</sup>, however, reported the synthesis of  $[\text{AlF}(\text{Bn-NODA})]$  alongside its  $^1\text{H}$  and  $^{19}\text{F}\{^1\text{H}\}$  NMR spectra, in which the complex was ‘prepared and identified with HPLC-HRMS’. It is unclear if the isolated product was formed as a single species.

In an effort to further characterise the products from the  $^{19}\text{F}$  reaction, crystallisation was attempted *via* slow evaporation from the NMR solution ( $\text{CD}_3\text{OD}$ ). SCXRD confirmed that the crystals were in fact the  $[\text{Al}(\text{Bn-NODA})(\text{OAc})]$  complex, as observed in the ESI<sup>+</sup> mass spectrum. The structure is shown in Figure 6.13 below. The complex adopts a *pseudo*-octahedral geometry (twist angle,  $\theta = 53.16(5)^\circ$ ), with the (deprotonated) Bn-NODA ligand pentadentate as expected, and the acetate ligand occupying the sixth coordination site.

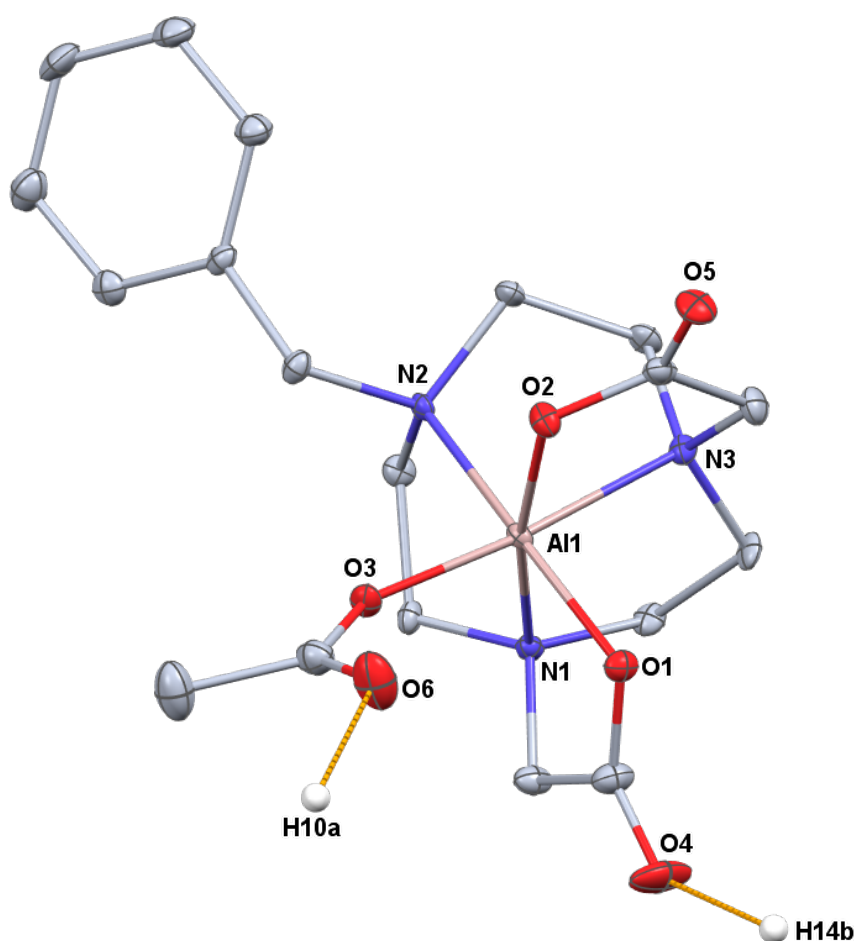


Figure 6.13 – View of the structure of  $[\text{Al}(\text{Bn-NODA})(\text{OAc})]\cdot 2\text{H}_2\text{O}$  showing the atom numbering scheme and H-bonding between carboxylate and lattice  $\text{H}_2\text{O}$  molecules. Ellipsoids are drawn at the 50% probability level and H and solvent atoms (except those involved in H-bonding) are omitted for clarity.



It is known from previous work on the pentadentate  $N_3O_2$ -donor phosphinate analogues, that two different geometric isomers are possible for  $[MX(\text{Bn-NODP})]$  complexes, and therefore, also for  $[MX(\text{Bn-NODA})]$  complexes (Figure 6.14).<sup>27</sup> This includes one isomer in which the pendant arm groups (phosphinate; carboxylate) are inequivalent, with one coordinated O-donor lying *trans* to a *tacn*(N) bonded to a second pendant arm, and the other coordinated O-donor lying *trans* to the *tacn*(N) bonded to the benzyl group. The second isomer is observed if the pendant arm groups are equivalent, with their respective O-donors both lying *trans* to a *tacn*(N) bearing the other pendant arm. In the structure above, the asymmetric isomer is observed, which is also the same for the previously reported  $[\text{AlF}(\text{Bn-NODA})]$ <sup>35</sup>,  $[\text{GaCl}(\text{Bn-NODA})]$ <sup>38</sup> and  $[\text{GaF}(\text{Bn-NODP})]$ <sup>27</sup> complexes.

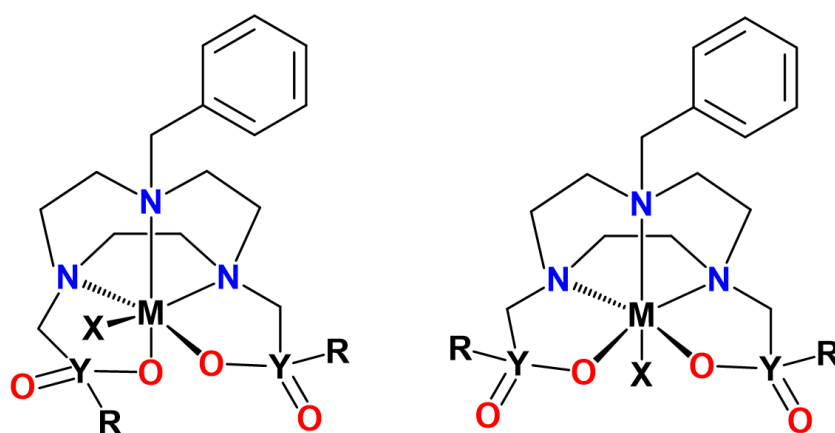
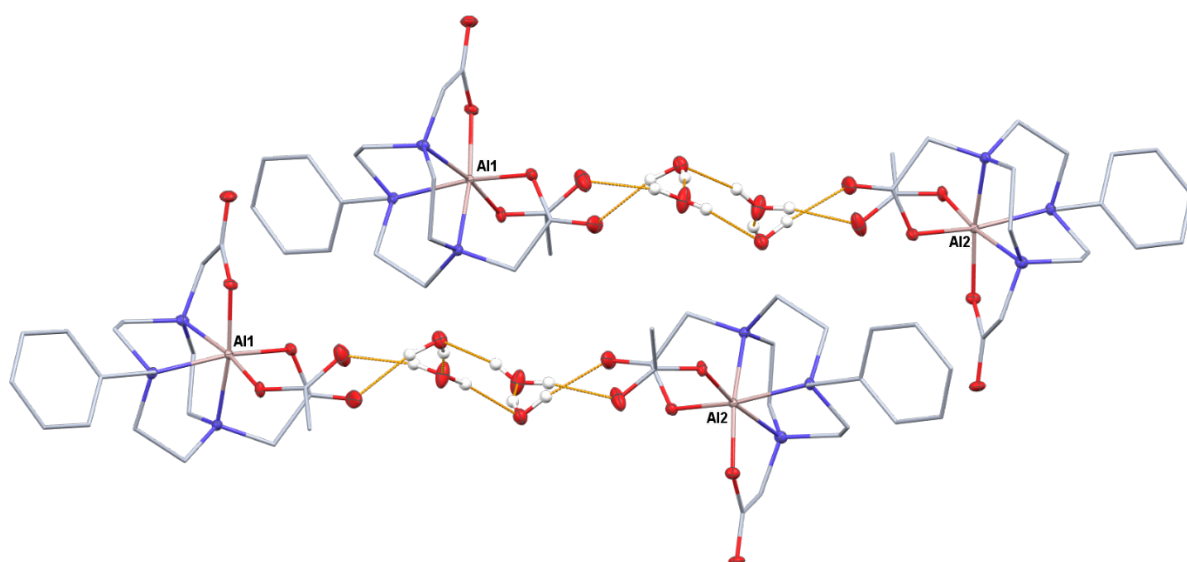


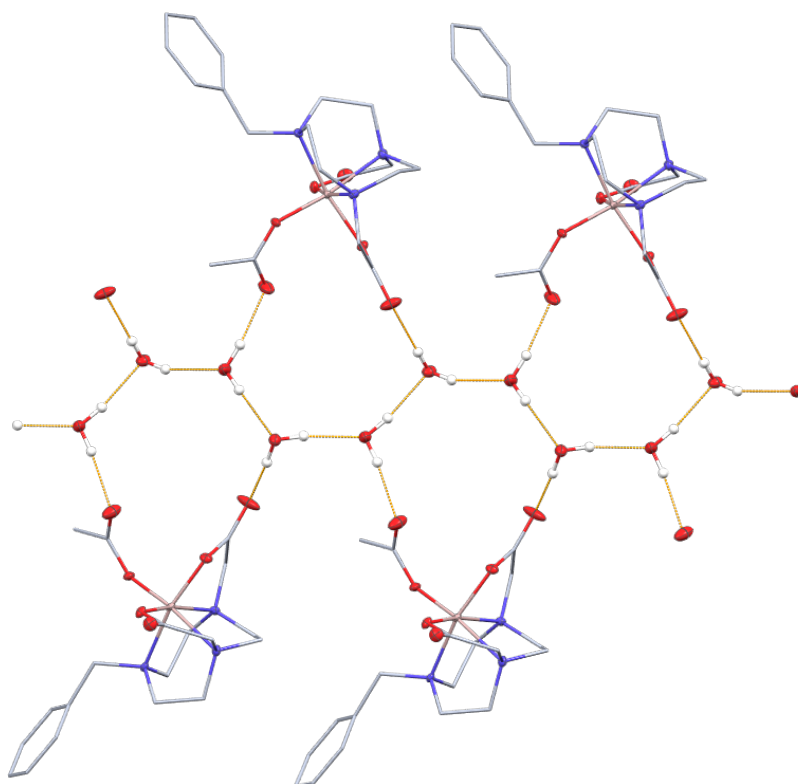
Figure 6.14 – Structures of the two different geometric isomers which are possible for  $[MX(\text{Bn-NODP})]$  and  $[MX(\text{Bn-NODA})]$  complexes, relative to the position of the coordinated P-O donor to the other *tacn*(N)-substituents. When  $Y = \text{C}$ , the R group is not present. When  $Y = \text{P}$ ,  $R = \text{Ph}$ .

The Al-N(*tacn*) bond lengths are in good accord with previously reported aluminium complexes with various triazacyclononane derivatives<sup>34</sup>, including  $[\text{AlF}(\text{Bn-NODA})]$ <sup>35</sup> and  $[\text{AlF}(\text{NODA-MPAA})]$ <sup>25</sup>. The Al1-O1 and Al1-O2 bond lengths (1.8517(17) Å and 1.8327(17) Å, respectively) associated with the coordinated Bn-NODA, are slightly longer than the Al1-O3 bond (1.8047(18) Å), involving the  $\kappa^1$ -acetate ligand. This may be due to the increased strain involved in the two five-membered chelate rings vs. the  $\kappa^1$ -acetate ligand.

The asymmetric unit of the structure shows two  $[\text{Al}(\text{Bn-NODA})(\text{OAc})]$  molecules (Al1 and Al2), linked in the solid-state *via* hydrogen-bonding between one pendant arm carboxylate group and the acetate ligand, to lattice water molecules. The second pendant arm does not appear to engage in any intermolecular interactions. This gives rise to an extended two-dimensional sheet due to a network of hydrogen-bonded water molecules, which is similar to that observed for the  $[\text{AlF}_3(\text{Me}_3\text{-tacn})]$  complex.<sup>34</sup> These extended structures can be viewed in Figure 6.15.



(a)



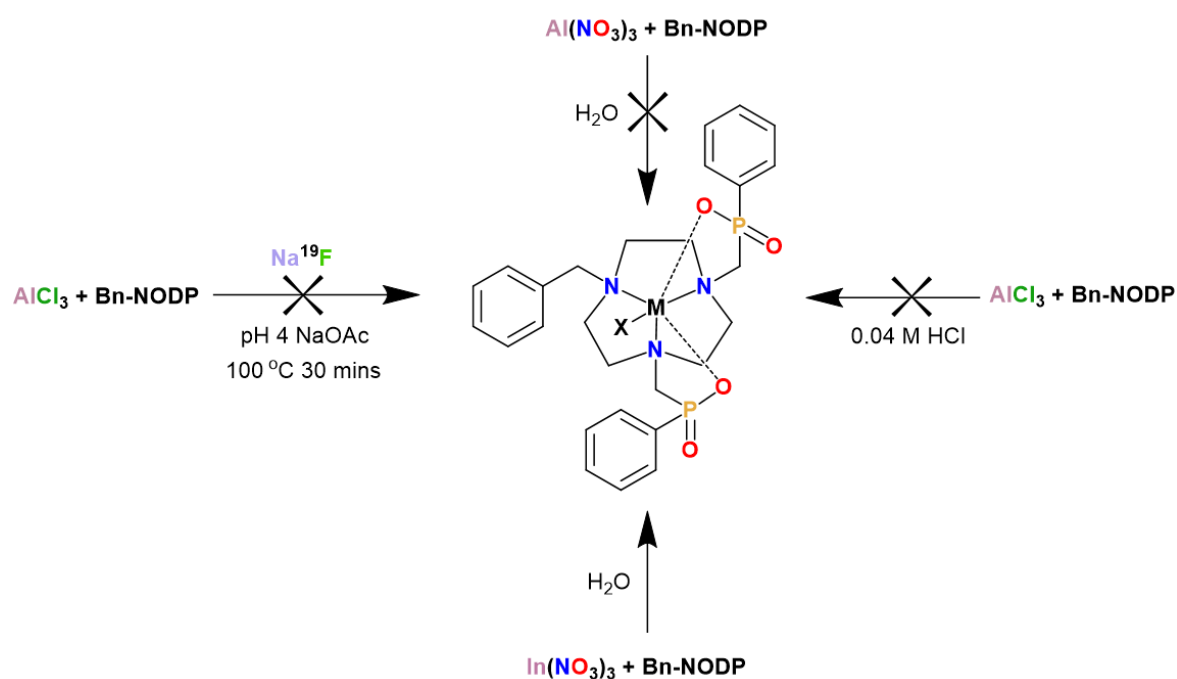
(b)

Figure 6.15 – (a) View of the two  $[Al(Bn-NODA)(OAc)] \cdot 2H_2O$  molecules in the asymmetric unit linked via hydrogen-bonding interactions arising from carboxylate and acetate groups and lattice  $H_2O$ ; (b) View of the extended structure assembled through intermolecular H-bonding between  $[Al(Bn-NODA)(OAc)] \cdot 2H_2O$  and lattice  $H_2O$  molecules. Atom colours: light-pink, Al; red, O; blue, N; white, H.

Although the reaction of  $AlCl_3 \cdot 6H_2O$  with  $H_2$ -Bn-NODA led to a mixture of products, it showed that complexation of the ligand was feasible using a larger molar concentration of precursors. It

is typically accepted that the  $[\text{Al-}^{18}\text{F}]^{2+}$  moiety first forms with aquo ligands which are then displaced by coordination of the macrocycle. However, this work shows the reaction chemistry may not require initial formation of  $[\text{Al-F}]^{2+}$  prior to complexation to the macrocycle, as assumed in the literature. If the  $[\text{Al}(\text{Bn-NODA})(\text{OAc})]$  complex can be isolated in good yield as the pre-formed precursor complex, it may present a new pathway towards  $\text{Al-}^{18}\text{F}$  complexes without the very narrow pH and temperature constraints currently required in the wider Al-F chemistry.

As these results confirmed that the reaction can be scaled up from tracer level, a similar approach was used in the attempted formation of the  $\text{H}_2\text{-Bn-NODP}$  equivalent. Likewise, the previously reported methods towards the  $[\text{GaCl}(\text{Bn-NODP})]$  complex were also attempted with aluminium and indium.<sup>27</sup> The various reaction pathways are given in Scheme 6.6.



Scheme 6.6 – Various pathways towards  $[\text{MX}(\text{Bn-NODP})]$  complexes ( $\text{M} = \text{Al}, \text{In}$ ;  $\text{X} = \text{Cl}, \text{F}, \text{NO}_3$ ).

All attempts to form an aluminium complex of the  $\text{H}_2\text{-Bn-NODP}$  ligand were unsuccessful, and no complexation was observed under any conditions. Conversely,  $^1\text{H}$  and  $^{31}\text{P}\{^1\text{H}\}$  NMR spectra for the product isolated from the reaction of  $\text{H}_2\text{-Bn-NODP}$  with  $\text{In}(\text{NO}_3)_3 \cdot 9\text{H}_2\text{O}$  suggested that complexation of the ligand was successful. The  $^1\text{H}$  NMR spectrum of this product was very similar to the  $^1\text{H}$  NMR spectrum of the gallium complex prepared in the same way, with the coupling of  $^1\text{H}$  and  $^{31}\text{P}$  nuclei leading to complex coupling patterns and assigned accordingly. The  $^{31}\text{P}\{^1\text{H}\}$  NMR spectrum showed two distinct singlets at 24.9 and 24.2 ppm, which integrate in a 1:1 ratio, indicating the product was isolated as the asymmetrical isomer. The obtained  $\text{ESI}^+$  MS gave an  $m/z$  peak at 320.8, corresponding with the  $[\text{In}(\text{Bn-NODP})+\text{H}]^{2+}$  ion.

Preliminary, NMR-scale fluorination using KF (80 °C, 1 h) was then attempted on this complex. A single, broad resonance was observed in the  $^{19}\text{F}\{^1\text{H}\}$  spectrum, at -205.9 ppm. However, the resultant  $^1\text{H}$  and  $^{31}\text{P}\{^1\text{H}\}$  NMR spectra were complicated. The latter NMR spectra depicted multiple phosphorus resonances, possibly due to different isomers or multiple products. A scaled-up reaction may help to decipher the exact nature of the species responsible.

### 6.3 Conclusions

The behaviour of the neutral tris(amide)  $\text{L}^1$  ligand was explored with the trivalent  $\text{Fe}^{3+}$ ,  $\text{Ga}^{3+}$  and  $\text{In}^{3+}$  cations, to investigate the effect of varying Lewis acidity on the stability of the amide-pendant arms. Reaction of the  $\text{Fe}(\text{NO}_3)_3 \cdot 9\text{H}_2\text{O}$  precursor was found to result in a mixture of products, most likely due to various degrees of hydrolysis of the amide arms in  $\text{L}^1$ . Some crystals obtained from this reaction were shown to be the fully hydrolysed  $[\text{Fe}(\text{NOTA})]$  complex. This behaviour is in line with that previously observed for  $\text{Fe}^{2+}$  complexes of  $\text{L}^1$  and TCMT. The reaction of  $\text{L}^1$  with  $\text{Ga}(\text{NO}_3)_3 \cdot 9\text{H}_2\text{O}$  produced the target  $[\text{Ga}(\text{L}^1)][\text{NO}_3]_3$  complex, although  $^1\text{H}$  NMR analysis indicated that slow hydrolysis of the amide pendant arms occurs at room temperature, with the slow emergence of minor resonances after 5-6 hours. The formation of these resonances rapidly increases upon heating to 80 °C, which can be directly attributed to the effect of the Lewis acidic  $\text{Ga}^{3+}$  centre ( $\text{L}^1$  appears to be stable when heated to 80 °C after 2 h in  $\text{CD}_3\text{OD}$  in the absence of  $\text{Ga}^{3+}$ ). Crystals grown following the slow evaporation of a solution containing  $[\text{Ga}(\text{L}^1)][\text{NO}_3]_3$  (over several weeks) were identified as a central  $\text{Ga}^{3+}$  ion bound to an  $\text{L}^1$  ligand in which two of the phenylacetamide arms have been hydrolysed to the corresponding carboxylates. In this instance, the resultant complex is not dissimilar from the mono-amide NOTA derivatives discussed earlier in the chapter.

The  $[\text{In}(\text{L}^1)][\text{NO}_3]_3$  complex formed successfully, and the  $^1\text{H}$  NMR spectrum did not reveal additional resonances over time, suggesting that this complex is more stable than either the gallium or iron analogues. This is consistent with the weaker and softer Lewis acid character of  $\text{In}^{3+}$  vs.  $\text{Ga}^{3+}$  and  $\text{Fe}^{3+}$ . Fluorination of this complex was attempted, resulting in a single  $\text{In-F}$  species as determined by the  $^{19}\text{F}\{^1\text{H}\}$  NMR spectrum. However, the  $^1\text{H}$  NMR spectrum of the product showed multiple resonances, suggesting the reaction conditions (80 °C, 2 h) lead to hydrolysis.

Crystal structure determination by electron diffraction confirmed an unexpected seven-coordinate  $[\text{In}(\text{NOTA})]_4$  tetrameric species, with an  $\text{N}_3\text{O}_4$  coordination sphere at each  $\text{In}$  atom *via* pentadentate coordination to the NOTA ligand, a weak  $\text{In-O}$  interaction between an asymmetric, bridging carboxylate of the third NOTA pendant arm, and coordination to an O-donor atom of this

bridging carboxylate moiety of an adjacent [In(NOTA)] molecule. Bulk analysis of this product would mirror that of a six-coordinate [In(NOTA)] monomeric species, but it is also possible it may be a kinetic product. Further work will be required to establish whether this is the only product present in the isolated solid. Fluorination of this complex, and the seven-coordinate [InCl(NOTA)]<sup>-</sup> species, leads to the appearance of a new resonance in their respective <sup>19</sup>F{<sup>1</sup>H} NMR spectra, which may correspond to [InF(NOTA)]<sup>-</sup> or a derivative thereof. However, this product appears to be unstable in a D<sub>2</sub>O solution over time, with loss of fluoride as [HF<sub>2</sub>]<sup>-</sup> observed.

This chapter also reports the novel, and unexpected, [Al(Bn-NODA)(OAc)] complex, which is formed from the reaction of AlCl<sub>3</sub>·6H<sub>2</sub>O with Bn-NODA in an acetate buffer. This structure sheds some insight into the nature of the ‘Al<sup>18</sup>F<sup>2+</sup>’ reaction with NODA-based ligands, which has been used extensively throughout the literature since it was first reported (in 2009).<sup>24</sup> The literature typically implies that ‘Al<sup>18</sup>F<sup>2+</sup>’ (with aquo ligands) forms initially and it then coordinates to the Bn-NODA derivatives. Further work could look towards the targeted formation and isolation of this complex, and then assess its suitability as a well-defined molecular precursor for <sup>18</sup>F exchange reactions; rather than the ‘one-pot’ formation of the Al-<sup>18</sup>F complexes, which requires tightly controlled pH and temperature. It is possible this acetate species would radiolabel, but with milder temperature and/or less constrained pH conditions, which would be extremely advantageous for broadening the range of potential bioconjugates that may be incorporated. This is a very interesting avenue for future work.

This chapter also sought to investigate routes towards other indium fluoride complexes, as well as novel aluminium complexes, involving the pentadentate H<sub>2</sub>-Bn-NODP ligand. Whilst no reaction conditions favoured the successful formation of an aluminium complex, a route towards an indium complex is reported. It is likely that the Al<sup>3+</sup> ion is insufficiently small to bind favourably to the H<sub>2</sub>-Bn-NODP ligand, whereas the ligand is better suited to the larger In<sup>3+</sup> instead. Preliminary ‘cold’ fluorination experiments of the indium complex suggest an In-F species was formed, but this would need further work for confirmation, and for optimised reaction conditions.

## 6.4 Experimental

For general experimental methods, see Appendix A. The ligands L<sup>1</sup>, L<sup>3</sup> and H<sub>2</sub>-Bn-NODA were used as prepared in Chapter 2. H<sub>2</sub>-Bn-NODP was used as prepared by Dr Rhys King using the method previously established in the Reid group.<sup>27</sup> H<sub>3</sub>-NOTA (ChemATech), AlCl<sub>3</sub>·6H<sub>2</sub>O,

$\text{Fe}(\text{NO}_3)_3 \cdot 9\text{H}_2\text{O}$ ,  $\text{Ga}(\text{NO}_3)_3 \cdot 9\text{H}_2\text{O}$ ,  $\text{InCl}_3$ , KF (Sigma-Aldrich),  $\text{In}(\text{NO}_3)_3 \cdot 9\text{H}_2\text{O}$  (Alfa Aesar) used as supplied. All solvents used were of HPLC-chromatography grade.

#### 6.4.1 Trivalent $\text{M}^{3+}$ Complexes of $\text{L}^1$

##### 6.4.1.1 $[\text{Fe}(\text{L}^1)][\text{NO}_3]_3$

$\text{Fe}(\text{NO}_3)_3 \cdot 9\text{H}_2\text{O}$  (38.5 mg, 0.095 mmol) was added to a solution of  $\text{L}^1$  (50.4 mg, 0.095 mmol) in MeOH (5 mL), causing the solution to turn from colourless to dark orange. This was stirred at room temperature for 1 h. The solvent volume was then decreased *in vacuo* to approximately 1 mL. Excess  $\text{Et}_2\text{O}$  was added, causing precipitation of a deep red solid. This was filtered and dried *in vacuo*. Yield: 48 mg. IR (Nujol,  $\nu / \text{cm}^{-1}$ ): 3400 br (OH), 1752 w (HOH), 1614 m, 1592 m, 1571 m (C=O). Crystals suitable for X-ray diffraction were grown *via* the slow evaporation of a methanol solution containing the product mixture. These were found to be  $[\text{Fe}(\text{NOTA})]$ , indicating extensive hydrolysis of the amide functions.

##### 6.4.1.2 $[\text{Ga}(\text{L}^1)][\text{NO}_3]_3$

Method 1: A solution of  $\text{Ga}(\text{NO}_3)_3 \cdot 9\text{H}_2\text{O}$  (24.4 mg, 0.095 mmol) in MeOH (3 mL) was added to a solution of  $\text{L}^1$  (50.0 mg, 0.095 mmol) in MeOH (3 mL). This was left to stir at room temperature overnight. The solvent volume was then reduced *in vacuo*, and  $\text{Et}_2\text{O}$  was added causing precipitation of an off-white solid. This was isolated *via* filtration and dried *in vacuo*. Yield: 35.0 mg, 0.045 mmol (47%). Analysis required for  $\text{C}_{30}\text{H}_{36}\text{N}_9\text{O}_{12}\text{Ga} \cdot \text{Et}_2\text{O}$ : C, 47.57; H, 5.40; N, 14.68. Found: C, 47.61; H, 5.41; N, 14.41%.  $^1\text{H}$  NMR (295 K,  $\text{CD}_3\text{OD}$ ):  $\delta$  (ppm) = 7.49 – 7.47 (m, [6H], ArH), 7.41 – 7.38 (m, [3H], ArH), 7.03 – 6.94 (m, [6H], ArH), 4.85 ( $\text{H}_2\text{O}$ ), 3.87 (s, [6H],  $\text{CH}_2$ ), 3.20 – 3.09 (m, [12H], tacn- $\text{CH}_2$ ). The NMR indicates the presence of diethyl ether, and a minor amount of one or more other species, likely to be a product (or products of) hydrolysis. IR (Nujol,  $\nu / \text{cm}^{-1}$ ): 3437 br, 3313 br (OH), 3203 w, 3151 w (NH), 1687 m (HOH), 1661 m, 1620 sh, 1599 m (C=O). Crystals suitable for X-ray diffraction were grown *via* the slow evaporation of a methanol solution containing the product mixture (over a period of several weeks). These were found to be trivalent gallium bound to a (hydrolysed)  $\text{L}^1$  with a single amide pendant arm.

##### 6.4.1.3 $[\text{In}(\text{L}^1)][\text{NO}_3]_3$

A solution of  $\text{In}(\text{NO}_3)_3 \cdot 9\text{H}_2\text{O}$  (61.4 mg, 0.160 mmol) in MeOH (5 mL) was added to a solution of  $\text{L}^1$  (84.8 mg, 0.160 mmol) in MeOH (5 mL). This was left to stir at room temperature overnight. The solvent volume was then reduced *in vacuo*, and  $\text{Et}_2\text{O}$  was added causing precipitation of an off-white solid. This was isolated *via* filtration and dried *in vacuo*. Yield: 112 mg, 0.135 mmol (84%). Analysis required for  $\text{C}_{30}\text{H}_{36}\text{N}_9\text{O}_{12}\text{In} \cdot 0.3\text{Et}_2\text{O}$ : C, 44.00; H, 4.62; N, 14.80%. Found: C, 43.69; H,

4.53; N, 14.35.  $^1\text{H}$  NMR (295 K,  $\text{CD}_3\text{OD}$ ):  $\delta$  (ppm) = 7.67 – 7.46 (m, [7H], ArH), 7.36 – 7.25 (m, [6H], ArH), 7.16 – 7.06 (m, [1H], ArH), 4.85 ( $\text{H}_2\text{O}$ ), 4.22 (br s, [6H],  $\text{CH}_2$ ), 3.44 – 3.35 (br m, [6H], tacn- $\text{CH}_2$ ), 3.25 – 3.06 (br m, [6H], tacn- $\text{CH}_2$ ). IR (Nujol,  $\nu$  /  $\text{cm}^{-1}$ ): 3450 br, 3250 br (OH), 3151 w (NH), 1746 w (HOH), 1622 s, 1594 s, 1574 s (C=O).

#### 6.4.1.4 Attempted Fluorination of $[\text{In}(\text{L}^1)][\text{NO}_3]_3$

Aqueous KF (10.5 mg, 0.180 mmol, 3 mol. eqv.) was added to a solution of  $[\text{In}(\text{L}^1)][\text{NO}_3]_3$  (50 mg, 0.060 mmol) in MeOH (5 mL). A slight warming was observed upon addition. The solution was then heated to 80 °C for 2 h. The solvent was removed *in vacuo* and the resultant white solid washed with MeCN. Any undissolved solid was removed *via* filtration. After removal of the solvent *in vacuo*, the product was isolated as a white powder solid. Yield: 22.2 mg.  $^{19}\text{F}\{^1\text{H}\}$  NMR (295 K,  $\text{CD}_3\text{OD}$ ):  $\delta$  (ppm) = -191 ppm (s).  $^1\text{H}$  NMR spectrum was indicative of multiple species, or products of hydrolysis.

### 6.4.2 Complexes of 1,4,7-Triazacyclononane-1,4,7-Triacetic acid ( $\text{H}_3\text{-NOTA}$ )

$[\text{Ga}(\text{NOTA})]$  and  $[\text{In}(\text{NOTA})]$  were synthesised according to a method reported by Broan *et al.*<sup>18</sup>  $[\text{InCl}(\text{NOTA})]^+$  was also prepared according to a method initially reported by Craig *et al.*<sup>32</sup> For all complexes, their spectroscopic data is consistent with that previously reported.

#### 6.4.2.1 $[\text{Ga}(\text{NOTA})]$

A solution of  $\text{Ga}(\text{NO}_3)_3 \cdot 9\text{H}_2\text{O}$  (68.9 mg, 0.165 mmol) in 0.04 M  $\text{HNO}_3$  (approx. 1.5 mL) was added to a solution of  $\text{H}_3\text{-NOTA}$  (50 mg, 0.165 mmol) in 0.04 M  $\text{HNO}_3$  (approx. 1.5 mL). The reaction solution was left to stir at room temperature overnight. Acetone was then added slowly until a slight precipitation was observed. After leaving to stand for four hours, the solid precipitate was filtered and dried *in vacuo*. White solid product. Yield: 44.5 mg, 0.120 mmol (72 %). Analysis required for  $\text{C}_{12}\text{H}_{18}\text{GaN}_3\text{O}_6 \cdot 0.5\text{H}_2\text{O}$ : C, 37.77; H, 4.81; N, 11.37. Found: C, 38.03; H, 5.05; N, 11.09%.  $^1\text{H}$  (295 K,  $\text{D}_2\text{O}$ ):  $\delta$  (ppm) = 3.81 (br s, [6H],  $\text{CH}_2$ ), 3.27 – 3.13 (br m, [6H], tacn- $\text{CH}_2$ ), 3.09 – 2.94 (br m, [6H], tacn- $\text{CH}_2$ ).  $^{13}\text{C}\{^1\text{H}\}$  (295 K,  $\text{D}_2\text{O}$ ):  $\delta$  (ppm) = 174.9 ( $\text{C}=\text{O}$ ), 61.9 ( $\text{CH}_2$ ), 53.2 (tacn- $\text{CH}_2$ ). ESI<sup>+</sup> MS ( $\text{H}_2\text{O}$ ): found:  $m/z$  = 370.2  $[\text{Ga}(\text{NOTA})+\text{H}]^+$  (calculated for  $[\text{Ga}(\text{NOTA})+\text{H}]^+$ :  $m/z$  = 370.1). IR (Nujol,  $\nu$  /  $\text{cm}^{-1}$ ): 1702 sh, 1675 s (C=O).

#### 6.4.2.2 $[\text{In}(\text{NOTA})]$

A solution of  $\text{In}(\text{NO}_3)_3 \cdot 9\text{H}_2\text{O}$  (63.1 mg, 0.165 mmol) in 0.04 M  $\text{HNO}_3$  (approx. 1.5 mL) was added to a solution of  $\text{H}_3\text{-NOTA}$  (50 mg, 0.165 mmol) in 0.04 M  $\text{HNO}_3$  (approx. 1.5 mL). The reaction solution was left to stir at room temperature overnight. Acetone was then added slowly until a slight precipitation was observed. After leaving to stand for four hours, the solid precipitate was

filtered and dried *in vacuo*. White solid product. Yield: 19.7 mg, 0.047 mmol (28%). Analysis required for  $C_{12}H_{18}InN_3O_6 \cdot 3.25H_2O$ : C, 29.92; H, 5.13; N, 8.72. Found: C, 30.01; H, 4.79; N, 9.14%.  $^1H$  (295 K,  $D_2O$ ):  $\delta$  (ppm) = 3.65 (br s, [6H],  $\underline{CH_2}$ ), 3.27 – 3.12 (br m, [6H], tacn- $\underline{CH_2}$ ), 3.10 – 2.93 (br m, [6H], tacn- $\underline{CH_2}$ ).  $^{13}C\{^1H\}$  (295 K,  $D_2O$ ):  $\delta$  (ppm) = 175.4 ( $\underline{C=O}$ ), 61.1 ( $\underline{CH_2}$ ), 51.6 (tacn- $\underline{CH_2}$ ). ESI<sup>+</sup> MS ( $H_2O$ ): found:  $m/z$  = 416.1 [In(NOTA)+H]<sup>+</sup> (calculated for [In(NOTA)+H]<sup>+</sup>:  $m/z$  = 416.0). IR (Nujol,  $\nu$  /  $cm^{-1}$ ): 3415 (br, OH), 1663 sh, 1619 s (C=O).

#### 6.4.2.3 [InCl(NOTA)][H]

A solution of  $InCl_3$  (36.4 mg, 0.165 mmol) was stabilised in 0.04 M HCl (approx. 2 mL) and added to a solution of  $H_3$ -NOTA (50 mg, 0.165 mmol) in 0.04 M HCl (approx. 2.5 mL). This was left to stand at room temperature for over one week, during which time crystals suitable for X-ray diffraction had grown. A white solid had also precipitated. This was collected and dried *in vacuo*. Yield: 37.4 mg, 0.083 mmol (50%).  $^1H$  NMR (295 K,  $D_2O$ ):  $\delta$  (ppm) = 3.66 (br s, [6H],  $\underline{CH_2}$ ), 3.25 – 3.12 (br m, [6H], tacn- $\underline{CH_2}$ ), 3.08 – 2.94 (br m, [6H], tacn- $\underline{CH_2}$ ).  $^{13}C\{^1H\}$  NMR (295 K,  $D_2O$ ):  $\delta$  (ppm) = 175.7 ( $\underline{C=O}$ ), 61.0 ( $\underline{CH_2}$ ), 51.5 (tacn- $\underline{CH_2}$ ). ESI<sup>+</sup> MS ( $H_2O$ ): found:  $m/z$  = 416.3 [In(NOTA)+H]<sup>+</sup> (calculated for [In(NOTA)+H]<sup>+</sup>:  $m/z$  = 416.0). IR (Nujol,  $\nu$  /  $cm^{-1}$ ): 3550 br, 3217 br (OH), 1737 sh (HOH), 1719 m, 1698 sh (C=O), 271 (In-Cl).

#### 6.4.2.4 Attempted Fluorination of [InCl(NOTA)][H]

An NMR-scale reaction was carried out, involving the addition of KF (1.3 mg, 0.022 mmol) to a solution of [InCl(NOTA)][H] (10.0 mg, 0.022 mmol) in  $D_2O$  (2 mL). This was left to stand at room temperature for 10 min.  $^1H$  NMR (295 K,  $D_2O$ ):  $\delta$  (ppm) = 3.64 (br s, [6H],  $\underline{CH_2}$ ), 3.20 – 3.13 (m, [6H], tacn- $\underline{CH_2}$ ), 3.06 – 2.99 (m, [6H], tacn- $\underline{CH_2}$ ).  $^{19}F\{^1H\}$  NMR (295 K,  $D_2O$ ):  $\delta$  (ppm) = -161.6 (br s).

### 6.4.3 Complexes of 1-Benzyl-4,7-Diacetic Acid-1,4,7-Triazacyclononane ( $H_2$ -Bn-NODA)

#### 6.4.3.1 Attempted Formation of [AlF(Bn-NODA)]

$AlCl_3 \cdot 6H_2O$  (18.0 mg, 0.075 mmol), and  $H_2$ -Bn-NODA (25.0 mg, 0.075 mmol) were combined in a sodium acetate buffer solution (pH 4, 5 mL). This was heated to 100 °C for 30 min. Then, NaF (3.1 mg, 0.075 mmol) was added. Heating was continued at 100 °C for a further 30 minutes. The solvent was then removed *in vacuo*, leaving a white solid which was washed with MeCN. The solution was filtered from any undissolved solid, and the solvent removed *in vacuo*. Crystals grown from an NMR solution containing the product mixture were shown to be [Al(Bn-NODA)(OAc)]. The  $^1H$  NMR spectrum ( $D_2O$ ) was indicative of multiple species.  $^{19}F\{^1H\}$  NMR (295 K,  $D_2O$ ):  $\delta$  (ppm) = -167.2 (s). ESI<sup>+</sup> MS ( $H_2O$ ): found:  $m/z$  = 420.1 [Al(Bn-NODA)(OAc)+H]<sup>+</sup>



(calculated for  $[\text{Al}(\text{Bn-NODA})(\text{OAc})+\text{H}]^+$ :  $m/z = 420.2$ ); 380.2  $[\text{AlF}(\text{Bn-NODA})+\text{H}]^+$  (calculated for  $[\text{AlF}(\text{Bn-NODA})+\text{H}]^+$ :  $m/z = 380.1$ ).

#### 6.4.4 Complexes of 1,4-Diphosphinate-7-Benzyl-1,4,7-Triazacyclononane ( $\text{H}_2\text{-Bn-NODP}$ )

##### 6.4.4.1 $[\text{In}(\text{NO}_3)(\text{Bn-NODP})]$

A solution of  $\text{In}(\text{NO}_3)_3 \cdot 9\text{H}_2\text{O}$  (22.6 mg, 0.059 mmol) in  $\text{H}_2\text{O}$  (2.5 mL) was added to a solution of  $\text{H}_2\text{-Bn-NODP}$  (31.1 mg, 0.059 mmol) in  $\text{H}_2\text{O}$  (2.5 mL). This was left to stir at room temperature overnight, during which time a white solid precipitated from the solution. This was filtered from the solution and dried *in vacuo*. Yield: 15.6 mg, 0.022 mmol (37%).  $^1\text{H}$  NMR (295 K,  $\text{CD}_3\text{OD}$ ):  $\delta$  (ppm) = 8.15 – 8.08 (m, [1H], ArH), 8.00 – 7.90 (m, [2H], ArH), 7.89 – 7.67 (m, [2H], ArH), 7.64 – 7.42 (m, [10H], ArH), 4.85 ( $\text{H}_2\text{O}$ ), 4.62 – 4.59 (d,  $^2J_{\text{H-H}} = 14.1$  Hz, [1H],  $\text{NCH}_2\text{Bn}$ ), 4.06 – 4.03 (d,  $^2J_{\text{H-H}} = 14.1$  Hz, [1H],  $\text{NCH}_2\text{Bn}$ ), 3.90 – 3.72 (m, [2H],  $\text{NCH}_2\text{P}$ ), 3.57 – 3.43 (m, [2H],  $\text{NCH}_2\text{P}$ ), 3.42 – 3.33 (m, [4H],  $\text{tacn-CH}_2$ ), 3.26 – 3.06 (m, [6H],  $\text{tacn-CH}_2$ ), 2.99 – 2.87 (br t,  $^2J_{\text{H-H}} = 14.9$  Hz,  $\text{tacn-CH}_2$ ), 2.75 – 2.69 (br dd,  $^2J_{\text{H-H}} = 13.1$  Hz,  $^4J_{\text{H-31P}} = 4.4$  Hz,  $\text{tacn-CH}_2$ ).  $^{31}\text{P}\{^1\text{H}\}$  NMR (295 K,  $\text{CD}_3\text{OD}$ ):  $\delta$  (ppm) = 24.9 (s, [1P]), 24.2 (s, [1P]). ESI<sup>+</sup> MS ( $\text{CH}_3\text{OH}$ ): found:  $m/z = 320.8$   $[\text{In}(\text{Bn-NODP})+\text{H}]^{2+}$  (calculated for  $[\text{In}(\text{Bn-NODP})+\text{H}]^{2+}$ :  $m/z = 320.6$ ). IR (Nujol,  $\nu$  /  $\text{cm}^{-1}$ ): 3417 (br, OH), 1639 (br, HOH), 1128 (m,  $\text{P=O}$ ).

#### 6.4.5 X-ray Crystallographic Data

Complex	<b>[Fe(NOTA)]</b>	<b>[Ga(1-phenylacetamide-4,7-dicarboxylate-1,4,7-tacn)][NO<sub>3</sub>]·1.5H<sub>2</sub>O</b>
Formula	C <sub>12</sub> H <sub>18</sub> FeN <sub>3</sub> O <sub>6</sub>	[C <sub>18</sub> H <sub>24</sub> GaN <sub>4</sub> O <sub>5</sub> ][NO <sub>3</sub> ]·1.5H <sub>2</sub> O
<i>M</i>	356.14	535.166
Crystal system	Trigonal	Monoclinic
Space group (no.)	<i>R</i> 3c (161)	<i>P</i> 1 21/n 1 (14)
<i>a</i> /Å	13.4709(7)	8.7590(5)
<i>b</i> /Å	13.4709(7)	20.1534(14)
<i>c</i> /Å	13.1548(5)	12.8678(6)
$\alpha$ /°	90	90
$\beta$ /°	90	108.467(6)
$\gamma$ /°	120	90
<i>U</i> /Å <sup>3</sup>	2067.3(2)	2154.5(2)
<i>Z</i>	6	4
$\mu$ (Mo-K $\alpha$ ) /mm <sup>-1</sup>	1.130	1.342
<i>F</i> (000)	1110	1110.005
Total no. reflns	15310	20958
<i>R</i> <sub>int</sub>	0.1515	0.0526
Unique reflns	1187	5491
No. of params, restraints	67, 1	505 (552)
GOF	1.120	1.0381
<i>R</i> <sub>1</sub> , <i>wR</i> <sub>2</sub> [ <i>I</i> > 2σ( <i>I</i> )] <sup>b</sup>	0.0792, 0.1981	0.0503, 0.1147
<i>R</i> <sub>1</sub> , <i>wR</i> <sub>2</sub> (all data)	0.0965, 0.2116	0.0797, 0.1250

Complex	<b>[InCl(NOTA)][H]·2H<sub>2</sub>O</b>	<b>[Al(Bn-NODA)(OAc)]·2H<sub>2</sub>O</b>
Formula	C <sub>12</sub> H <sub>19</sub> ClInN <sub>3</sub> O <sub>6</sub> ·2H <sub>2</sub> O	C <sub>19</sub> H <sub>26</sub> AlN <sub>3</sub> O <sub>6</sub> ·2H <sub>2</sub> O
<i>M</i>	487.60	455.447
Crystal system	Monoclinic	Orthorhombic
Space group (no.)	<i>P</i> -2yn (14)	<i>P</i> 2c -2n (33)
<i>a</i> /Å	6.9961(2)	14.5874(3)
<i>b</i> /Å	17.4718(5)	8.5886(2)
<i>c</i> /Å	14.3835(4)	33.2170(9)
$\alpha$ /°	90	90
$\beta$ /°	97.454(3)	90
$\gamma$ /°	90	90
<i>U</i> /Å <sup>3</sup>	1743.30(9)	4161.60(17)
<i>Z</i>	4	8
$\mu$ (Mo-K $\alpha$ ) /mm <sup>-1</sup>	1.555	0.151
<i>F</i> (000)	984	1937.935
Total no. reflns	13374	62274
<i>R</i> <sub>int</sub>	0.0201	0.0490
Unique reflns	4440	12864
No. of params, restraints	209, 0	578, 28
GOF	1.074	1.0457
<i>R</i> <sub>1</sub> , w <i>R</i> <sub>2</sub> [ <i>I</i> > 2σ( <i>I</i> )] <sup>b</sup>	0.0259, 0.0625	0.0589, 0.1471
<i>R</i> <sub>1</sub> , w <i>R</i> <sub>2</sub> (all data)	0.0277, 0.0631	0.0661, 0.1510

<sup>a</sup> common items: T = 100 K; wavelength (Mo-K $\alpha$ ) = 0.71073 Å;  $\theta$ (max) = 27.5°;

<sup>b</sup>  $R_1 = \Sigma ||F_o| - |F_c|| / \Sigma |F_o|$ ;  $wR_2 = [\Sigma w(F_o^2 - F_c^2)^2 / \Sigma wF_o^4]^{1/2}$

#### 6.4.6 Electron Diffraction Crystallographic Data

The crystallographic data of the [In(NOTA)] structure is tabulated below. However, this has been collected from electron diffraction analysis, so the parameters cannot be directly compared with those obtained from SCXRD structural data.

Complex	[In(NOTA)]
Formula	C <sub>12</sub> H <sub>18</sub> InN <sub>3</sub> O <sub>6</sub>
<i>M</i>	415.111
Crystal system	Tetragonal
Space group (no.)	<i>I</i> -4ad (88)
<i>a</i> /Å	15.27(11)
<i>b</i> /Å	15.27(11)
<i>c</i> /Å	28.27(12)
$\alpha$ /°	90
$\beta$ /°	90
$\gamma$ /°	90
<i>U</i> /Å <sup>3</sup>	6590(73)
<i>Z</i>	16
$\mu$ (Mo-K $\alpha$ ) /mm <sup>-1</sup>	n/a
<i>F</i> (000)	1097.091
Total no. reflns	n/a
<i>R</i> <sub>int</sub>	n/a
Unique reflns	1780
No. of params, restraints	210, 251
GOF	1.2129
<i>R</i> <sub>1</sub> , <i>wR</i> <sub>2</sub> [ <i>I</i> > 2σ( <i>I</i> )] <sup>b</sup>	0.1524, 0.3516
<i>R</i> <sub>1</sub> , <i>wR</i> <sub>2</sub> (all data)	0.1867, 0.3784

## 6.5 References

1. D. Shetty, Y.-S. Lee and J. M. Jeong, *Nucl. Med. Mol. Imaging*, 2010, **44**, 233.
2. I. Velikyan, *Theranostics*, 2014, **4**, 47.
3. L. Hoigebazar, J. M. Jeong, S. Y. Choi, J. Y. Choi, D. Shetty, Y.-S. Lee, D. S. Lee, J.-K. Chung, M. C. Lee and Y. K. Chung, *J. Med. Chem.*, 2010, **53**, 6378.
4. A. De Sá, Á. A. Matias, M. I. M. Prata, C. F. G. C. Geraldés, P. M. T. Ferreira and J. P. André, *Bioorg. Med. Chem. Lett.*, 2010, **20**, 7345.
5. J. Holub, M. Meckel, V. Kubiček, F. Rösch and P. Hermann, *Contrast Media Mol. Imaging*, 2015, **10**, 122.
6. G. J. R. Cook, *Cancer Imaging*, 2010, **10**, 153.
7. D. Ulmert, L. Solnes and D. L. Thorek, *Bone Research*, 2015, **3**, 15024.
8. D. Shetty, S. Y. Choi, J. M. Jeong, L. Hoigebazar, Y. S. Lee, D. S. Lee, J. K. Chung, M. C. Lee and Y. K. Chung, *Eur. J. Inorg. Chem.*, 2010, 5432-5438.
9. T. Weyhermüller, K. Weighardt and P. Chaudhuri, *J. Chem. Soc., Dalton Trans.*, 1998, 3805.
10. V. B. Unnikrishnan, V. Sabatino, F. Amorim, M. F. Estrada, C. D. Navo, G. Jimenez-Oses, R. Fior and G. J. L. Bernardes, *J. Am. Chem. Soc.*, 2024, **146**, 23240.
11. J. Rautio, N. A. Meanwell, L. Di and M. J. Hageman, *Nat. Rev. Drug Discov.*, 2018, **17**, 559.
12. C. Wang, M. Xu, Z. Zhang, S. Zeng, S. Shen, Z. Ding, J. Chen, X.-Y. Cui and Z. Liu, *Sci. Bull.*, 2024, **69**, 2745.
13. M. Markovic, S. Ben-Shabat and A. Dahan, *Pharmaceutics*, 2020, **12**, 1031.
14. D. Śmiłowicz, S. Eisenberg, R. Laforest, J. Whetter, A. Hariharan, J. Bordenca, C. J. Johnson and E. Boros, *J. Am. Chem. Soc.*, 2023, **145**, 16261.
15. T. Wadas, J. E. H. Wong, G. R. Weisman and C. J. Anderson, *Chem. Rev.*, 2010, **110**, 2858.
16. V. Bernard-Gauthier, M. L. Lepage, B. Waengler, J. J. Bailey, S. H. Liang, D. M. Perrin, N. Vasdev and R. Schirmacher, *J. Nucl. Med.*, 2018, **59**, 568.
17. A. S. Craig, I. M. Helps, K. J. Jankowski, D. Parker, N. R. A. Beeley, B. A. Boyce, M. A. W. Eaton, A. T. Millican, K. Millar, A. Phipps, S. K. Rhind, A. Harrison and C. Walker, *J. Chem. Soc., Chem. Commun.*, 1989, 794.
18. C. J. Broan, J. P. L. Cox, A. S. Craig, R. Kataký, D. Parker, A. Harrison, A. M. Randall and G. Ferguson, *J. Chem. Soc., Perkin Trans. 2*, 1991, 87.
19. E. T. Clarke and A. E. Martell, *Inorg. Chim. Acta*, 1991, **181**, 273.
20. K. G. Andersson, M. Rosestedt, Z. Varasteh, M. Malm, M. Sandström, V. Tolmachev, J. Löfblom, S. Ståhl and A. Orlova, *Oncol. Rep.*, 2015, **34**, 1042.

21. S. S. Rinne, C. D. Leitaó, B. Mitran, T. Z. Bass, K. G. Andersson, V. Tolmachev, S. Ståhl, J. Löfblom and A. Orlova, *Sci. Rep.*, 2018, **9**, 655.
22. M. Rosestedt, K. G. Andersson, B. Mitran, V. Tolmachev, J. Löfblom, A. Orlova and S. Ståhl, *Sci. Rep.*, 2015, **5**, 15226.
23. C. Da Pieve, L. Allott, C. D. Martins, A. Vardon, D. M. Ciobota, G. Kramer-Marek and G. Smith, *Bioconjug. Chem.*, 2016, **27**, 1839-1849.
24. W. J. McBride, R. M. Sharkey, H. Karacay, C. A. D'Souza, E. A. Rossi, P. Laverman, C. H. Chang, O. C. Boerman and D. M. Goldenberg, *J. Nucl. Med.*, 2009, **50**, 991.
25. C. A. D'Souza, W. J. McBride, R. M. Sharkey, L. J. Todaro and D. M. Goldenberg, *Bioconjug. Chem.*, 2011, **22**, 1793.
26. W. J. McBride, C. A. D'Souza, R. M. Sharkey and D. M. Goldenberg, *Appl. Radiat. Isot.*, 2012, **70**, 200.
27. D. E. Runacres, V. K. Greenacre, J. M. Dyke, J. Grigg, G. Herbert, W. Levason, G. McRobbie and G. Reid, *Inorg. Chem.*, 2023, **62**, 20844.
28. T. K. Venkatachalam, P. V. Bernhardt, G. K. Pierens, D. H. R. Stimson, R. Bhalla and D. C. Reutens, *Aust. J. Chem.*, 2019, **72**, 383.
29. M. T. Andras, A. F. Hepp, S. A. Duraj, E. B. Clark, D. A. Scheiman, P. E. Fanwick and D. G. Hehemann, *Inorg. Chem.*, 1993, **32**, 4150.
30. M. A. Malyarick, A. B. Ilyuhin, S. P. Petrosyants and P. Petrosyants, *Main Group Met. Chem.*, 1994, **17**, 707.
31. C. Avila-Montiel, H. Tlahuext, A. Ariza, C. Godoy-Alcántar, A. R. Tapia-Benavides and D. M. Tlahuextl, *Eur. J. Inorg. Chem.*, 2022, e202200178.
32. A. S. Craig, I. M. Helps, D. Parker, H. Adams, N. A. Bailey, M. G. Williams, J. M. A. Smith and G. Ferguson, *Polyhedron*, 1989, **8**, 2481.
33. K. Wieghardt, U. Bossek, P. Chaudhuri, W. Herrmann, B. C. Menke and J. Weiss, *Inorg. Chem.*, 1982, **21**, 4308.
34. R. Bhalla, C. Darby, W. Levason, S. K. Luthra, G. McRobbie, G. Reid, G. Sanderson and W. Zhang, *Chem. Sci.*, 2014, **5**, 381.
35. D. Shetty, S. Y. Choi, J. M. Jeong, J. Y. Lee, L. Hoigebazar, Y. S. Lee, D. S. Lee, J. K. Chung, M. C. Lee and Y. K. Chung, *Chem. Commun.*, 2011, **47**, 9732.
36. F. Cleeren, J. Lecina, E. M. Billaud, M. Ahamed, A. Verbruggen and G. M. Bormans, *Bioconjug. Chem.*, 2016, **27**, 790.
37. F. Cleeren, J. Lecina, M. Ahamed, G. Raes, N. Devoogdt, V. Caveliers, P. McQuade, D. J. Rubins, W. Li, A. Verbruggen, C. Xavier and G. Bormans, *Theranostics*, 2017, **7**, 2924.
38. R. Bhalla, W. Levason, S. K. Luthra, G. McRobbie, G. Sanderson and G. Reid, *Chem. Eur. J.*, 2015, **21**, 4688.

## Chapter 7 Summary and Outlook

The work in this thesis has demonstrated a considerable advancement in the coordination chemistry of transition metal and Group 13 complexes with new and known N-functionalised triaza-macrocyclic ligands. This includes amide-functionalised ligands,  $L^1$ ,  $L^2$  and  $L^3$ , and the known NOTP-OMe,  $H_3$ -NOTA and  $H_2$ -Bn-NODP ligands. The properties and behaviours of these complexes has been explored, with focus towards Group 13 fluoride complexes for potential applications in  $^{18}\text{F}$ -based PET imaging. This has been achieved through the successful formation and characterisation of the various complexes, following the development of synthetic routes towards the new ligands, in addition to the development of automated purification techniques. The latter may be translated to future tacn-based scaffolds, allowing for improved synthetic yields and increased ease of synthesis.

Chapter 3 and Chapter 4 of this work focused on the properties and behaviours of the ligands,  $L^1$ ,  $L^2$  and  $L^3$  with divalent transition metals, iron trifluoride and the Group 13 fluorides ( $L^1$ ,  $L^2$  and  $L^3$ ). Characterisation of the amide-tacn complexes, but particularly single-crystal X-ray analysis, indicated the coordination mode of the ligands was dependent on the nature of the metal ion, and its immediate coordination sphere. For example,  $L^1$  and  $L^2$  were shown to be hexadentate upon coordination to  $\text{Co}^{3+}$ ,  $\text{Ni}^{2+}$  and  $\text{Cu}^{2+}$ . Interestingly, but in line with the literature, the molecular structures of the cobalt complexes indicated the presence of the oxidised  $\text{Co}^{3+}$ . The  $[\text{Co}(L^1\text{-H})][\text{NO}_3]_2$  complex was deprotonated, not unlike the tris(amide) complex,  $[\text{Cr}(\text{TCMT})]^{3+}$ , reported by Weyhermüller and co-workers.<sup>1</sup> Preliminary work towards divalent  $\text{Ni}^{2+}$ ,  $\text{Cu}^{2+}$  and  $\text{Zn}^{2+}$  complexes of NOTP-OMe also suggested a similar  $\text{N}_3\text{O}_3$  coordination mode, *via* coordination of the P=O bond, but further work will be required understand the true nature of the complexes in the solid-state.

Meanwhile, molecular structures obtained for several  $\text{MF}_3$  species,  $[\text{GaF}_3(L^1)]$ ,  $[\text{InF}_3(L^2)]$ ,  $[\text{GaF}_3(L^3)]$  and  $[\text{FeF}_3(L^3)]$ , showed that the amide-functionalised ligands  $L^1$ ,  $L^2$  and  $L^3$  were tridentate  $\text{N}_3$ -donors *via* the *facial* tacn(N) atoms – the amide arms did not displace the fluoride ligands. This was as expected, given the high strength of the M–F bond with Lewis acidic ( $\text{M}^{3+}$ ) metal centres. For all amide-tacn complexes analysed *via* SCXRD analysis, extensive hydrogen bonding was observed from the amide(NH) groups. For the divalent transition metals, this was between neighbouring and adjacent carboxamide-oxygens, or lattice solvent molecules. For  $[\text{GaF}_3(L^1)]$ , hydrogen-bonding was observed between the amide(NH) group and neighbouring, adjacent fluoride ligands – it was initially thought that these interactions may assist with

directing incoming  $^{18}\text{F}^-$  to the metal centre. For the  $\text{MF}_3$  complexes of  $\text{L}^3$  (Ga and Fe), hydrogen-bonding interactions were observed to lead to the formation of dimers, resulting in an interesting supramolecular array and the formation of solvent-accessible voids.

This work then describes the attempted radiofluorination of the amide-tacn species,  $[\text{GaF}_3(\text{L}^1)]$  and  $[\text{GaF}_3(\text{L}^3)]$ . Previous work has shown the successful radiofluorination of various  $\text{Ga-}^{18}\text{F}$  complexes with various ligands, most notably the  $\text{BnMe}_2\text{-tacn}$  ligand, and more recently, the  $\text{H}_2\text{-Bn-NODP}$  ligand.<sup>2,3</sup> Based on previous methods, and following optimisation of the reaction conditions, the successful radiofluorination of  $[\text{GaF}_3(\text{L}^1)]$  is reported, achieving a radiochemical yield of 20% after 10 min with heating to 80 °C (using a concentration of 3  $\mu\text{mol mL}^{-1}$ ). This is not dissimilar from the yields from the first  $\text{Al-}^{18}\text{F-NOTA}$  conjugates. Radio-incorporation was also observed at room temperature after 30 min (RCY = 10%). Purification used an SPE protocol, using a HLB cartridge, with an initial radiochemical purity of 68% and 64% observed in  $\text{H}_2\text{O/EtOH}$  and  $\text{PBS/EtOH}$ . This decreased by only 7% and 5% after 2 h, in both formulations respectively. Although the purification stage was not pursued further at this time, the radiochemical purity may be improved using an alternative SPE protocol.  $[\text{GaF}_3(\text{L}^3)]$  did not undergo any radiofluorination under any conditions trialled, which is unexpected. Stability studies of the precursor complex displayed high solubility and stability in water (after 4 h), so it is assumed that the ligand architecture may be a limiting factor for this complex. Future work could look towards replacing the sterically-bulky and highly lipophilic isopropyl groups for methyl groups, to better resemble the  $\text{BnMe}_2\text{-tacn}$  ligand. There is some motivation for this, based on the promising stability displayed by the  $[\text{GaF}_3(\text{L}^1)]$  complex.

Alternative routes towards radiolabelled metal (fluoride) complexes are presented by Lewis acidic  $\text{M}^{3+}$  cations, and the stability of  $\text{L}^1$  with  $\text{Fe}^{3+}$ ,  $\text{Ga}^{3+}$  and  $\text{In}^{3+}$  was assessed. Rapid hydrolysis was observed in the attempted formation of the iron complex, with  $[\text{Fe}(\text{NOTA})]$  isolated as one of several (assumed) species.  $\text{Ga}^{3+}$  also promoted the hydrolysis of the pendant arms, which proceeded at a much faster rate upon heating (80 °C vs. room temperature), with increasing hydrolysis products observed with an increase in time (as confirmed by  $^1\text{H}$  NMR spectral analysis, and SCXRD). Similar behaviour was also observed with  $\text{In}^{3+}$ , but at a much slower rate, reflecting on the softer Lewis acid nature in comparison. This behaviour is not uncommon, with some literature examples describing the controlled hydrolysis of the amide-bond for pro-drug applications.<sup>4</sup> Attempted fluorination *via* the addition of 3 mol. eqv.  $\text{KF}$  of the latter complex gave a single  $\text{In-F}$  species, although further work would be required to ascertain its exact nature. However, it does present a possible alternative pathway to  $\text{InF}_3$  complexes, where the  $[\text{InF}_3(\text{dmsO})(\text{OH}_2)_2]$  complex instead leads to multiple species.



Many examples of radiometal and Al-<sup>18</sup>F-based pharmaceuticals contain Lewis acidic M<sup>3+</sup> cations bound to H<sub>3</sub>-NOTA (and its derivatives), including <sup>111</sup>In for SPECT imaging. Prior to this work, the molecular structure of [In(NOTA)] has not been reported. However, electron diffraction structural analysis confirmed the unusual and unexpected seven-coordinate tetrameric [In(NOTA)]<sub>4</sub>. This behaviour has not previously been reported, although the hexacoordinate complex is well-known; this represents a very interesting addition to the possible coordination and properties of the H<sub>3</sub>-NOTA ligand, and may indicate a kinetic product. Further work could look at probing the exact nature of the complex.

H<sub>2</sub>-Bn-NODA is also well-known in both Al-<sup>18</sup>F and Ga-<sup>18</sup>F radiolabelling applications, and this work sought to establish a preparative-scale method towards Al-<sup>18</sup>F complexes. Unexpectedly, the [Al(Bn-NODA)(OAc)] complex was subsequently isolated alongside the target [AlF(Bn-NODA)] complex, and its molecular structure was determined. This complex presents an alternative avenue for further exploration of the Al-<sup>18</sup>F chemistry, which typically requires tightly controlled temperature and pH (typically, 100 – 120 °C, pH 4). It is possible that the isolation of this intermediate species prior to the addition of <sup>18</sup>F<sup>-</sup> may lend itself to milder radiolabelling conditions. If this route proves viable, it could greatly enhance the scope of Al-<sup>18</sup>F-based PET imaging pharmaceuticals, with the possibility of bioconjugation to more temperature and pH-sensitive peptides. In terms of the wider impact, this may assist with broadening the scope of inorganic radiotracers for a greater variety of biological targets.

## 7.1 References

1. T. Weyhermüller, K. Weighardt and P. Chaudhuri, *J. Chem. Soc., Dalton Trans.*, 1998, 3805.
2. F. M. Monzittu, I. Khan, W. Levason, S. K. Luthra, G. McRobbie and G. Reid, *Angew. Chem. Int. Ed.*, 2018, **57**, 6658.
3. D. E. Runacres, V. K. Greenacre, J. M. Dyke, J. Grigg, G. Herbert, W. Levason, G. McRobbie and G. Reid, *Inorg. Chem.*, 2023, **62**, 20844.
4. D. Śmiłowicz, S. Eisenberg, R. Laforest, J. Whetter, A. Hariharan, J. Bordenca, C. J. Johnson and E. Boros, *J. Am. Chem. Soc.*, 2023, **145**, 16261.

## Appendix A General Experimental Details

Ligand and complex synthesis was carried out under atmospheric conditions unless otherwise stated, then standard Schlenk line and glovebox techniques were employed, under a dry N<sub>2</sub> atmosphere. Anhydrous solvents when required were dried by distillation from Na/benzophenone (THF, Et<sub>2</sub>O) or Mg/I (MeOH) and subsequently stored over 3 Å (MeOH) or 4 Å (THF, Et<sub>2</sub>O) molecular sieves. Aqueous reactions were performed using milliQ H<sub>2</sub>O.

Infrared spectra were recorded over a range of 200-4000 cm<sup>-1</sup> using a Perkin Elmer Spectrum 100 spectrometer and samples were prepared as Nujol mulls between CsI plates.

NMR spectra were recorded using a Bruker AV400 or DPX400, with <sup>1</sup>H and <sup>13</sup>C{<sup>1</sup>H} being referenced to the solvent resonance. <sup>19</sup>F{<sup>1</sup>H} spectra were referenced to CFCl<sub>3</sub>, <sup>31</sup>P{<sup>1</sup>H} to 85% H<sub>3</sub>PO<sub>4</sub>, <sup>27</sup>Al to aqueous [Al(OH<sub>2</sub>)<sub>6</sub>]<sup>3+</sup> and <sup>71</sup>Ga to [Ga(OH<sub>2</sub>)<sub>6</sub>]<sup>3+</sup> at pH 1. All spectra were recorded at 298 K. Due to Teflon in the probe, the <sup>19</sup>F{<sup>1</sup>H} and <sup>27</sup>Al NMR spectra have a broad, rolling baseline. Multinuclear NMR experiments were collected by Dr Rhys King (<sup>27</sup>Al) or Dr Danielle Runacres (<sup>71</sup>Ga).

UV/visible spectra were recorded in solution (MeOH) using a Perkin Elmer 750S spectrometer.

Low resolution mass spectra were obtained in MeOH by positive ion electrospray MS using a Waters (Manchester, UK) Acquity TQD tandem quadrupole mass spectrometer. Samples were introduced to the mass spectrometer *via* an Acquity H-Class quaternary solvent manager (with TUV detector at 254 nm, sample and column manager). High resolution positive ion electrospray mass spectra were recorded using a MaXis (Bruker Daltonics, Bremen, Germany) time of flight (TOF) mass spectrometer. Samples were infused into the ion source using a syringe driver at a constant flow rate of 3 μL min<sup>-1</sup>. Direct injection and high-resolution MS were run by Dr Julie Herniman.

Microanalyses were outsourced to Medac Ltd. While majority of measurements are within +/- 0.4% of the theoretical value, in a few cases the values are slightly outside this range, reflecting the inherent variability of microanalytical measurements across different facilities.<sup>1</sup>

Single crystal X-ray diffraction data was collected using a Rigaku AFC12 goniometer equipped with an enhanced sensitivity (HG) Saturn724+ detector mounted at the window of an FR-E+ SuperBright molybdenum (λ = 0.71073 Å) rotating anode generator with HF Varimax optics (100 μm focus) with the crystal held at 100 K, or a Rigaku UG2 goniometer equipped with a Rigaku

hybrid pixel array detector (Hypix 6000 HE detector) mounted at the window of an FR-E+ SuperBright molybdenum ( $\lambda = 0.71073 \text{ \AA}$ ) rotating anode generator with Arc)Sec VHF Varimax confocal mirrors (70  $\mu\text{m}$  focus), with the crystal held at 100 K. Structure solution and refinement were performed using SHELX(T/S/L)97, SHELX2013, SHELX-2014/7 via Olex<sup>2,3,4</sup> or using NosphereA2.<sup>5,6</sup> For structures with significant disorder, and for final reprocessing of crystal data prior to publication, help was obtained from Dr Rob Bannister and Dr Victoria Greenacre.

For the 3DED experiment (run and reprocessed by Dr Rob Bannister), the sample was dispersed dry onto a copper-supported lacey carbon TEM grid, after grinding the sample with a pestle and mortar. This was cooled in liquid nitrogen and loaded at  $\sim 175 \text{ K}$  via a Gatan Elsa cryo holder into a Rigaku XtaLAB Synergy-ED electron diffractometer, operated at 200 kV and equipped with a Rigaku HyPix-ED hybrid pixel array area detector. Data for the most suitable crystallites appearing as rods were collected at 175 K using selected area continuous rotation electron diffraction with a selected area aperture of 2  $\mu\text{m}$  apparent diameter. Data were collected and processed using CrysAlisPRO (version 1.171.43.143a (Rigaku Oxford Diffraction, 2023)). The structure was solved using ShelXT<sup>2</sup> and refined in the kinematic approximation using Olex2.refine as implemented in Olex2, version 1.5 alpha using published scattering factors.<sup>7</sup> A global rigid bond restraint was employed to improve the physical sense of the anisotropic displacement parameters for all non-hydrogen atoms. Experimental and refinement information are contained within the CIF along with structure factors and an embedded .RES file.

Radiofluorination experiments were performed using [<sup>18</sup>F]F<sup>-</sup> which was obtained via the irradiation of [<sup>18</sup>O]H<sub>2</sub>O target water (97 atom %, Rotem Industries Ltd., Israel) with a CTI RDS 112 cyclotron (11 MeV, 30  $\mu\text{A}$  beam current) used at St. Thomas' Hospital. Dr Graeme McRobbie or Dr George Herbert (GE Healthcare) supervised all work where the GE equipment was used, and Dr Graeme McRobbie advised on much of the radiochemistry. Crude products formed in the radiofluorination experiments of both [GaF<sub>3</sub>(L<sup>3</sup>)] and [GaF<sub>3</sub>(L<sup>1</sup>)] were analysed on an Agilent 1260 Infinity II HPLC system with an Agilent 1260 DAD UV detector (G7111B) and a LabLogic Systems Ltd sodium iodide 1" PMT. LabLogic Laura radiochromatography data collection and analysis software was used to integrate the peak areas. Crude products from radiofluorination experiments of [GaF<sub>3</sub>(L<sup>1</sup>)], as well as any purified samples (including stability tests) were analysed on an Agilent 1290 HPLC system with an Agilent 1260 DAD UV detector (G4212B) and a Bioscan FC3200 sodium iodide PMT with a rate meter. Dionex Chromeleon 6.8 Chromatography data recording software was used to integrate the peak areas. SPE purification used a HLB cartridge purchased from Waters (P/N 186000132).

## A.1 References

1. R. E. H. Kuveke, L. Barwise, Y. Van Ingen, K. Vashisth, N. Roberts, S. S. Chitnis, J. L. Dutton, C. D. Martin and R. L. Melen, *ACS Cent. Sci.*, 2022, **8**, 855.
2. G. M. Sheldrick, *Acta Crystallogr. Sect. C: Cryst. Struct. Commun.*, 2015, **71**, 3.
3. G. M. Sheldrick, *Acta Crystallogr. Sect. A: Found. Crystallogr.*, 2008, **64**, 112.
4. O. V. Dolomanov, L. J. Bourhis, R. J. Gildea, J. A. L. Howard and H. Puschmann, *J. Appl. Crystallogr.*, 2009, **42**, 339.
5. F. Kleemiss, O. V. Dolomanov, M. Bodensteiner, N. Peyerimhoff, L. Midgley, L. J. Bourhis, A. Genoni, L. A. Malaspina, D. Jayatilaka, J. L. Spencer, F. White, B. Grundkötter-Stock, S. Steinhauer, D. Lentz, H. Puschmann and S. Grabowsky, *Chem. Sci.*, 2021, **12**, 1675.
6. L. Midgley, L. J. Bourhis, O. V. Dolomanov, S. Grabowsky, F. Kleemiss, H. Puschmann and N. Peyerimhoff, *Acta Crystallogr. A Found. Adv.*, 2021, **77**, 519.
7. A. Saha, S. S. Nia and J. A. Rodríguez, *Chem. Rev.*, 2022, **122**, 13883.

## Appendix B Crystallographic Information Files

Cif files are located in the supplementary information.

The following complexes can also be found by their corresponding CCDC numbers, below:

$L^1 \cdot HCl$  ..... 2355936

$[Co(L^1-H)][NO_3]_2$  ..... 2405335

$[Ni(L^1)][NO_3]_2 \cdot 1.5MeOH$  ..... 2405334

$[Ni(L^2)][NO_3]_2 \cdot 0.443H_2O$  ..... 2405336

$[Cu(L^1)][NO_3]_2 \cdot 1.25Et_2O \cdot MeOH$  ..... 2405333

$[Cu(L^2)][NO_3]_2$  ..... 2405332

$[GaF_3(L^1)] \cdot 1.5MeOH \cdot 0.5H_2O$  ..... 2355938

$[InF_3(L^2)]$  ..... 2355939

$[FeF_3(L^3)] \cdot 2.4H_2O$  ..... 2355940

$[GaF_3(L^3)] \cdot 0.067H_2O$  ..... 2355941

$[Ga(1\text{-phenylacetamide-4,7-dicarboxylate-1,4,7-tacn})][NO_3] \cdot 1.5H_2O$  ..... 2405331